Extended Dark Sector of the Universe, dynamics and detection possibilities

Dipankar Pradhan

A thesis
submitted for the degree of

Doctor of Philosophy

Supervisor

Dr. Subhaditya Bhattacharya

Department of Physics
Indian Institute of Technology Guwahati
Guwahati - 781039, Assam, India

Extended Dark Sector of the Universe, dynamics and detection possibilities

A thesis submitted by

Dipankar Pradhan

to

Indian Institute of Technology Guwahati
in partial fulfillment of the requirements
for the award of the degree of
Doctor of Philosophy in Physics

Supervisor

Dr. Subhaditya Bhattacharya

Department of Physics
Indian Institute of Technology Guwahati
Guwahati - 781039, Assam, India

To
my
Mother & Elder Sister

"The important thing is not to stop questioning.
Curiosity has its own reason for existing."

-Albert Einstein

Declaration

Dipankar Pradhan
Roll No. 196121009
Department of Physics
Indian Institute of Technology Guwahati
Guwahati, India
E-mail: d.pradhan@iitg.ac.in

I hereby declare that works presented in the thesis entitled "**Extended Dark Sector of the Universe, dynamics and detection possibilities**" has been carried out by me under the supervision of Dr. Subhaditya Bhattacharya at the Department of Physics, Indian Institute of Technology Guwahati, India. The thesis has not been submitted anywhere else for any degree. Works presented in the thesis are all my own unless referenced to the contrary in the thesis.

Date: 28/02/2025 **Dipankar Pradhan**

Certificate

Dr. Subhaditya Bhattacharya
Professor
Department of Physics
Indian Institute of Technology Guwahati
Guwahati, India
E-mail: subhab@iitg.ac.in

It is certified that the work contained in the thesis entitled "**Extended Dark Sector of the Universe, dynamics and detection possibilities**" by Mr. Dipankar Pradhan (Roll No - 196121009), a Ph.D. student in the Department of Physics, Indian Institute of Technology, Guwahati is carried out under my supervision and has not been submitted elsewhere for the award of any other degree.

Date: 28/02/2025 **Subhaditya Bhattacharya**

Acknowledgements

First and foremost, I would like to convey my sincere gratitude to my supervisor, Prof. Subhaditya Bhattacharya, for his constant support, guidance, and advice throughout my Ph.D. journey. I am truly privileged to have him as my supervisor, as he has not only assisted me academically but also consistently kept me motivated, especially during challenging times. His suggestions for becoming a proficient speaker have always helped me refine my presentation skills. I genuinely appreciate his understanding and patience in accommodating my limitations. With him, it has truly been a profoundly enriching learning experience for me.

I would also like to express my gratitude to my DC committee members: Dr. Debasish Borah (Chairperson), Dr. M. C. Kumar, and Dr. Sayan Chakrabarti. Their continuous feedback and guidance during my annual progress reviews have been crucial to my growth and development. I am also thankful to Prof. Arunansu Sil for his continuous feedback and guidance during my research development.

The most cherished part of my Ph.D. journey belongs to my dearest friends: Banashree Baishya, Lipika Kolay, Gargi Sen, Samik Mitra, Seshadri Majumder, Chinmoy Dey, and Shantanu Sahoo. I am also profoundly grateful to my excellent juniors, Avik Sarkar, Nilay Modal, and Vipin Anand, as well as my esteemed seniors, Dr. Purushottam Ghosh, Dr. Basabendu Barman, Dr. Jayita Lahiri, and Dr. Sahabub Jahedi, for their unwavering support and guidance. I also want to express my gratitude to my seniors (Dr. Pulak Banerjee, Dr. Surojit Dalui, Dr. Arghyajit Datta, Sourav Pal, Monu Singh, Golam Masud Karim) and juniors (Amit, Ankan, Indrajit, Rajesh Mondal, Himanshu, Sanu, Dipendu, Dipendu, Nayan, Disha, Niraj, Hemanta, Nihar, Arkodip, Subhajit, Rajesh), friends (Soumalya, Koushik, Debabrata, Swarup, Soumen), and others who have been close to me.

I wholeheartedly extend my deepest gratitude to my beloved parents, brothers, and sisters, whose boundless love, steadfast support, and unwavering understanding have been the guiding lights of my life. Their sacrifices, encouragement, and belief in me have been the pillars upon which I have built my dreams. Without their presence, patience, and profound care, this journey would not have been possible.

Acronyms

SM	:	Standard Model of particle physics
BSM	:	Beyond the Standard Model
DM	:	Dark Matter
CDM	:	Cold Dark Matter
NP	:	New Physics
NR	:	Non-relativistic
EW	:	Electroweak
SSB	:	Spontaneous Symmetry Breaking
EWSB	:	Electroweak Symmetry Breaking
v	:	vacuum expectation value (of Higgs)
dof	:	degrees of freedom
RHN	:	Right Handed Neutrino
LHC	:	Large Hadron Collider
ILC	:	International Linear Collider
BEQ	:	Boltzmannan Equation
cBEQ	:	coupled Boltzmannan Equation
FLRW	:	Friedmann Lemaître Robertson Walker (equations)
CMB	:	Cosmic Microwave Background
CMBR	:	Cosmic Microwave Background Radiation
WMAP	:	Wilkinson Microwave Anisotropy Probe
C.L.	:	Confidence Level
BBN	:	Big Bang Nucleosynthesis
BR	:	Branching Ratio
CPT	:	CP times Time reversal
CR	:	Cosmic Rays

DIS : Deep Inelastic Scattering
EFT : Effective Field Theory
dof : degree of freedom
FLRW : Friedmann-Lemaître-Robertson-Walker (equations)
FS : Free Streaming
GC : Galactic Center of the Milky Way
GT : Galilean Transformation
GCH : Galactic Center Halo (a 'small' region around the GC)
GH : Galactic Halo
GR : General Relativity
GRB : Gamma Ray Burst
GUT : Grand Unified Theory
GW : Gravitational Wave
HDM : Hot Dark Matter
HEP : High Energy Physics
HST : Hubble Space Telescope
DD : Direct Detection (of Dark Matter)
ID : Indirect Detection (of Dark Matter)
IDM : Inert Doublet Model/Inert Higgs
IGM : InterGalactic Medium
ΛCDM : The standard cosmological model featuring a CC and CDM
LEP : the most recent $e\bar{e}$ collider at CERN
LHC : Large (or Last) Hadron Collider
LSP : Lightest (Stable) SuperSymmetric Particle
LSS : Large Scale Structure
MACHO : Massive Astrophysical Compact Halo Object
MB : Maxwell-Boltzmann distribution
MD : Matter Domination
MDM : Minimal Dark Matter
MOND : MOdified Newtonian Dynamics
MReq : Matter-Radiation equality
MW : Milky Way
NFW : Navarro, Frenk and White DM density distribution
PDF : Parton Distribution Function
PDF : Probability Distribution Function

pNGB	:	pseudo-Nambu-Goldstone boson
QFT	:	(Relativistic) Quantum Field Theory
QCD	:	Quantum Chromo Dynamics
QED	:	Quantum Electro Dynamics
RD	:	Radiation Domination
SHM	:	Standard Halo Model
SIDM	:	Self-Interacting Dark Matter
FIMP	:	Feebly Interacting Massive Particles
WIMP	:	Weakly Interacting Massive Particle
SIMP	:	Strongly Interacting Massive Particle
pFIMP	:	pseudo-Feeble Interacting Massive Particle
WDM	:	Warm Dark Matter

Basic notations and conventions

$a_0 = 1/\alpha m_e \approx 1/3.7\ keV$, Bohr radius.

$c \approx 3 \times 10^8\ \mathrm{m/sec}$, speed of light in a vacuum.

$\alpha = e^2/4\pi \approx 1/137.036$, fine-structure constant.

$\alpha_{\mathrm{s}} = g_{\mathrm{s}}^2/4\pi$, strong $\mathrm{SU(3)_c}$ coupling constant.

$\alpha_{\mathrm{w}} = g_{\mathrm{w}}^2/4\pi$, weak $\mathrm{SU(2)_L}$ coupling constant.

$\alpha_Y = g_{\mathrm{Y}}^2/4\pi$, hypercharge coupling constant.

η_B: baryon-to-photon number density ratio, $\eta_B = n_{\mathrm{B}}/n_\gamma$.

g_{s}: strong gauge coupling.

g_{w}: weak $\mathrm{SU(2)_L}$ gauge coupling.

g_{Y}: hypercharge gauge coupling.

h: Higgs boson

h: the scaling factor for Hubble expansion rate defined through $H_0 = \mathrm{h} \times 100\mathrm{km/sec \cdot Mpc}$.

H_0: present-day Hubble expansion rate.

H: Standard Model Higgs doublet.

$\mathcal{H}$: Hubble expansion rate.

$\Lambda_{\mathrm{QCD}} \approx 300\ MeV$, non-perturbative QCD scale.

$m_h \approx 125.20\,GeV$, Higgs boson mass.

$m_N \approx 0.939\ GeV$, nucleon mass. We mostly work in the isospin limit $m_N = m_p = m_n$.

$m_n = 939.565\ MeV$, neutron mass.

$m_p = 938.272\ MeV$, proton mass.

$m_{\mathrm{Pl}} \approx 1.2 \times 10^{19} GeV$, Planck mass.

$M_{\mathrm{Pl}} = m_{\mathrm{Pl}}/\sqrt{8\pi}$ reduced Planck mass.

$m_t \approx 172.76 GeV$, top quark mass.

n_{B}: number density of baryons.

n_γ: number density of photons.

Ω_{b}: cosmological abundance of normal baryonic matter.

Ω_{DM}: cosmological abundance of dark matter.

$s_{\mathrm{w}} \equiv \sin\theta_{\mathrm{w}} \simeq \sqrt{0.22305}$, θ_{w} is the weak mixing angle (Weinberg Angle).

$\tau_{\mathrm{univ}} \approx 13.7\ \mathrm{Gyr}$, the age of the Universe.

$T_0 \approx 2.726\,\mathrm{K}$, present CMB temperature.

$\theta_{\mathrm{w}} \simeq \sqrt{0.23129}$, weak mixing angle.

$m_{\rm W} = 80.3692\ {\rm G}eV$, $W^{\pm}$ boson mass.

$m_{\rm Z} = 91.1880\ {\rm G}eV$, Z^0 boson mass.

$\mathtt{v} \approx 246\ {\rm G}eV$, the Higgs vacuum expectation value.

$\mathtt{Y}$: hypercharge, normalized such that the electric charge is $Q_e = {\rm I}_3 + \mathtt{Y}/2$.

$G_F \approx 1.1664 \times 10^{-5}\ {\rm G}eV^{-2}$, Fermi coupling constant.

$G_N = 6.709 \times 10^{-39}\ {\rm G}eV^{-2}$, Gravitational constant.

σ^i: three Pauli spin matrices.

$\rho_{\rm DM}$: physical energy density of DM.

$\phi,\ \phi_i$: real scalar fields with $i = 1, 2, ...$

$\Phi,\ \Phi_i$: Complex scalar fields with $i = 1, 2, ...$

Φ_i: Complex scalar fields with $i = 1, 2.$

$\psi_i,\ \chi_i$: Dirac fermion fields with $i = 1, 2, ...$

N_i: Majorana fermion fields with $i = 1, 2, ...$

Abstract

Despite the remarkable success of explaining the fundamental constituents of the visible universe via weak, electromagnetic and strong interactions, the Standard Model (SM) of particle physics fails to explain many observations, for example, the presence of a non luminous dark matter (DM), matter-antimatter asymmetry, tiny but non-zero neutrino masses amongst several other issues. In this thesis we primarily aim to address different possibilities of DM appearing in extensions of the SM, which has both theoretical and phenomenological implications. Amongst many possibilities of DM genesis, we focus mainly on Weakly Interacting Massive Particles (WIMPs), Feebly Interacting Massive Particles (FIMPs), and Strongly Interacting Massive Particles (SIMPs). Our interest mainly lies when we have more than one different kinds of DM present in the universe, and consequent phenomenology in direct, indirect and collider searches. We compare the consequence of DM freeze-out and freeze-in before and after Electroweak Symmetry breaking (EWSB), to show that it leaves an important imprint in DM mass, in an analysis involving a vector boson WIMP and a scalar FIMP. When the interaction between WIMP and FIMP exceeds a certain limit, the FIMP equilibrates to the thermal bath and freezes out, giving rise to a new kind of particle called pseudo-FIMP (pFIMP). The dynamics and detection possibilities of pFIMP through loop induced direct and indirect searches are studied. Leveraging its phenomenological advantages, we are also able to explain the non-observation of lepton flavor-violating (LFV) decays. The possibility of pFIMP appearing in presence of SIMP is also discussed. We also propose a UV-complete model that could show a distinct signal in the direct detection recoil rate spectrum, indicating the presence of two DM components, after addressing all the relevant cosmological and collider constraints. We also investigate the possibility of having two stable DM components under a single discrete symmetry, by taking kinematic constraints into account, which shows some remarkable possibilities. Apart, we demonstrate that two DM components can also play an important role in determining the small active neutrino masses and generating the CP violating decays in addressing baryon asymmetry of the universe.

List of publications/preprints included in this thesis

[I]. Title: Electroweak symmetry breaking and WIMP-FIMP dark matter.

Authors: Subhaditya Bhattacharya (IIT Guwahati), Sreemanti Chakraborti (Annecy, LAPTH), **Dipankar Pradhan** (IIT Guwahati).

DOI: 10.1007/JHEP07(2022)091.

[II]. Title: Dynamics of the pseudo-FIMP in presence of a thermal Dark Matter.

Authors: Subhaditya Bhattacharya (IIT Guwahati), Jayita Lahiri (Hamburg University), **Dipankar Pradhan** (IIT Guwahati)

DOI: 10.1103/PhysRevD.108.L111702.

[III]. Title: Detection possibility of a Pseudo-FIMP in the presence of a thermal WIMP.

Authors: Subhaditya Bhattacharya (IIT Guwahati), Jayita Lahiri (Hamburg University), **Dipankar Pradhan** (IIT Guwahati).

DOI: 10.1103/PhysRevD.109.095031.

[IV]. Title: Multiparticle scalar dark matter with $\mathbb{Z}_N$ Symmetry.

Authors: Subhaditya Bhattacharya (IIT Guwahati), Lipika Kolay (IIT Guwahati), **Dipankar Pradhan** (IIT Guwahati).

e-Print: 2410.16275.

[V]. Title: The Influence of Lepton Portal on the WIMP-pFIMP framework.

Authors: Jayita Lahiri (Hamburg University), **Dipankar Pradhan** (IIT Guwahati), Abhik Sarkar (IIT Guwahati).

e-Print: 2410.19734.

[VI]. Title: Pseudo-FIMP dark matter in presence of a SIMP.

Authors: Subhaditya Bhattacharya (IIT Guwahati), Jahaan Thakkar (TIFR) and **Dipankar Pradhan** (IIT Guwahati).

e-Print: 2411.15108.

[VII]. Title: Direct Search signal of two-component Dark Matter.

Authors: Subhaditya Bhattacharya (IIT Guwahati), and **Dipankar Pradhan** (IIT Guwahati).

e-Print: 2501.17862.

[VIII]. Title: Two-component Dark Matter and low scale Thermal Leptogenesis.

Authors: Subhaditya Bhattacharya (IIT Guwahati), Devabrat Mahanat (Pragjyotish College, Guwahati University), Nilay Mondal (IIT Guwahati), and **Dipankar Pradhan**(IIT Guwahati).

e-Print: 2412.21202.

[IX]. Title: Lepton Collider as a window to Reheating*.

Authors: Basabendu Barman (SRM University), Subhaditya Bhattacharya (IIT Guwahati), Sahabub Jahedi (IIT Guwahati), **Dipankar Pradhan** (IIT Guwahati), and Abhik Sarkar (IIT Guwahati).

e-Print: 2406.11963.

[X]. Title: Lepton Collider as a window to Reheating: II*.

Authors: Basabendu Barman (SRM University), Subhaditya Bhattacharya (IIT Guwahati), Sahabub Jahedi (IIT Guwahati), **Dipankar Pradhan** (IIT Guwahati), and Abhik Sarkar (IIT Guwahati).

e-Print: 2410.18198.

[XI]. Title: Up-type FCNC in presence of Dark Matter*.

Authors: Subhaditya Bhattacharya (IIT Guwahati), Lipika Kolay (IIT Guwahati), **Dipankar Pradhan** (IIT Guwahati), and Abhik Sarkar (IIT Guwahati).

e-Print: 2504.20045.

[XII]. Title: Multi-messenger FIMP*.

Authors: Debasish Borah (IIT Guwahati), Nayan Das (IIT Guwahati), Sahabub Jahedi (IIT Guwahati), **Dipankar Pradhan** (IIT Guwahati).

e-Print: 2506.13860.

[XIII]. Title: WIMP-FIMP Phenomenology Before and After EWSB*.

Authors: Subhaditya Bhattacharya (IIT Guwahati), Sreemanti Chakraborti (Annecy, LAPTH), **Dipankar Pradhan** (IIT Guwahati).

DOI: Springer Proc.Phys. 304 (2024) 48-51.

[XIV]. Title: A real scalar singlet pseudo-FIMP in presence of a real scalar WIMP*.

Authors: Subhaditya Bhattacharya (IIT Guwahati), Jayita Lahiri (Hamburg University), **Dipankar Pradhan** (IIT Guwahati).

DOI: Springer Proc.Phys. 361 (2025) 73-80.

Note: Publications marked with asterisk (∗) are not included in this thesis.

Permissions and Attributions

- The content of the Chapter 3 is based on following work
  (a) **arXiv:2501.17862**, in collaboration with Subhaditya Bhattacharya.
- The content of the Chapter 4 is based on following works
  (a) **JHEP 07 (2022) 091**, in collaboration with Subhaditya Bhattacharya and Sreemanti Chakraborti.
- The content of the Chapter 5 is based on following work
  (a) **Phys.Rev.D 108 (2023) 11, L111702**, in collaboration with Subhaditya Bhattacharya, and Jayita Lahiri.
  (b) **arXiv:2411.15108**, in collaboration with Subhaditya Bhattacharya and Jahaan Thakkar.
- The content of the Chapter 6 is based on following work
  (a) **Phys.Rev.D 109 (2024) 9, 095031**, in collaboration with Subhaditya Bhattacharya and Jayita Lahiri.
  (a) **arXiv:2410.19734**, in collaboration with Jayita Lahiri and Abhik Sarkar.
- The content of the Chapter 7 is based on following work
  (a) **arXiv:2410.16275**, in collaboration with Subhaditya Bhattacharya and Lipika Kolay.
- The content of the Chapter 8 is based on following work
  (a) **arXiv:2412.21202**, in collaboration with Subhaditya Bhattacharya, Devabrat Mahanta and Niloy Mondal.

Contents

Chapter 1

Introduction

Contents

THEORETICAL frameworks for studying physical phenomena range from small-scale ($\sim 10^{-15}$ m, corresponding to the size of elementary particles) governed by the Standard Model (SM) of particle physics, to large-scale ($\sim 10^{27}$ m, the observable cosmic scale) governed by the General Theory of Relativity and Cosmology. They have shaped our understanding of the universe and its evolution to a great extent. SM of particle physics has been remarkably successful in predicting the interactions between the visible sector fundamental particles. After the discovery of the Higgs Boson in 2012, it can be deemed complete. However, observations from various astrophysical and cosmological studies [1–6] suggest that the universe is composed of about 4.9% baryonic matter, 26.8% non-luminous matter which is called as Dark Matter (DM), and 68.3% dark energy (DE) (see Fig . 1.1). This striking assertion mainly stems from the observation of anisotropies in the Cosmic Microwave Background Radiation (CMB) experiments via Wilkinson Microwave Anisotropy Probe (WMAP) and Planck collaborations [7], based on the Friedmann-Lemaître-Robertson-Walker (FLRW) [8, 9] metric within the Lambda Cold Dark Matter (ΛCDM) model. Both DM and DE are unaccounted for in the SM. Another puzzle of the universe is the dominance of matter over antimatter. The matter-antimatter asymmetry remains an open question and also calls for physics beyond the Standard Model (BSM). In addition, there are several questions for which we do not have an answer within the SM of particle physics. In this chapter, we review the key aspects of the SM of particle physics and the issues to go beyond, some of which are pertinent for problems dealt with in the thesis.

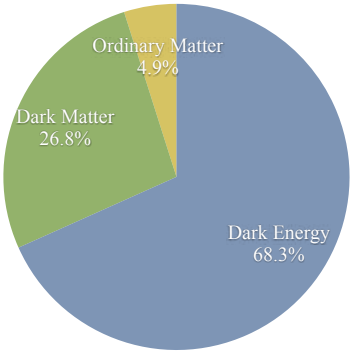

Figure 1.1: Energy content of the universe.

1.1 Standard Model of particle physics

The observed universe, made up of visible particles, is decipherable to a great extent via the model proposed by Weinberg and Salam around 1967-68 [10–12], and well known as the Standard Model (SM) of particle physics. What constitutes the SM, are the elementary particles having electromagnetic, weak, and strong interactions. The present form of SM is realised via years of research and dedication.

The quest for fundamental particles started long back, and the most promising one was the discovery of the electron by J. J Thomson in the Cathode Ray Tube Experiment around 1897 [13, 14]. The discovery of the muon happened much later in 1936, by Carl Anderson and Seth Neddermeyer in cosmic rays. Discovery of electron neutrino in 1956, by Clyde Cowan and Frederick Reines in nuclear reactor experiments, followed by muon neutrino discovery in 1962, by Leon M. Lederman, Melvin Schwartz, and Jack Steinberger in accelerator experiments opened the window of weak interaction physics. Discovery of up, down and strange quarks, proposed by Murray Gell-Mann and George Zweig to explain hadron structure in 1964, was confirmed via deep inelastic scattering experiments at SLAC at 1968. Charm quark discovery was in 1974, by Burton Richter and Samuel Ting in the J/Ψ particle. Tau lepton was discovered in 1975 by Martin Perl and collaborators at SLAC, bottom quark in 1977 by Leon M. Lederman's team at Fermilab in bottomonium states, Gluon in 1979 via indirect observation in three-jet events at the PETRA collider. W and Z boson discovery in 1983 by Carlo Rubbia, Simon van der Meer, and the UA1/UA2 Collaborations at CERN was an important milestone in achieving SM. Top quark being heavy, remained hidden for a long time, and was discovered in 1995, by the CDF and D$\emptyset$ Collaborations at Fermilab. The recent discovery of the Higgs boson [15] at LHC in 2012 [16, 17] completes the SM. The full SM particle content is shown in Table 1.1.

The mathematical framework which governs the interactions in the SM is based on quantum field theory (QFT). The theoretical development towards achieving the SM also started long back. The discovery of Maxwell's equations (1860), which unified electricity and magnetism can be marked as the beginning of this exciting journey. Around 1900-1905, quantum physics started developing with pioneering efforts of Planck, Einstein, Bohr etc., which slowly shaped in quantum mechanics by 1920s, majorly developed by Schrödinger, Heisenberg, and Dirac. The construction of Dirac equation and the proposal of antiparticles in 1928 unified quantum physics and special relativity. One of the most remarkable discoveries is the formulation of

Quantum Electrodynamics in 1940s, by Feynman, Schwinger, and Tomonaga. Theory of weak interactions proposed by Fermi in 1933 was taking a concrete shape with developments of non-abelian gauge theory around 1954, proposed by Yang and Mills. A unified electroweak theory could be achieved in 1960s, with the pioneering proposal of Glashow, Weinberg, and Salam, which is at the heart of SM. The Quark model as proposed by Gell-Mann, Zweig in 1964 to classify the hadrons, got a robust footing around 1970s with the developments of Quantum Chromodynamics (QCD) as a gauge theory based on the $\mathrm{SU}(3)$ symmetry, with Gluons mediating the interaction. As a whole, the vision of SM as a gauge theory of $\mathrm{SU}(3)_{\mathrm{c}}\otimes\mathrm{SU}(2)_{\mathrm{L}}\otimes\mathrm{U}(1)_{\mathrm{Y}}$, where the gauge bosons mediate electromagnetic, weak and strong interactions between the constituent leptons and quarks could be built. However, one point kept bothering us, was the masses of the particles, which couldn't be written within the unbroken gauge symmetry. This gives rise to another phenomenal proposal of SM gauge symmetry to be spontaneously broken $\mathrm{SU}(2)_{\mathrm{L}}\otimes\mathrm{U}(1)_{\mathrm{Y}}\rightarrow\mathrm{U}(1)_{\mathrm{EM}}$ at the electroweak scale around $246\ GeV$ via Higgs field acquiring non-zero vacuum expectation value (VEV), proposed by several authors including Peter Higgs, and Francois Englert. This is called Electroweak Symmetry breaking (EWSB) and was experimentally verified via Higgs discovery at the LHC.

The SM Lagrangian involving particles mentioned in Table 1.1, is [26–30],

$$\begin{aligned}\mathcal{L}_{\mathrm{SM}} =& -\frac{1}{4}\mathbf{W}_{\mu\nu}.\mathbf{W}^{\mu\nu} - \frac{1}{4}B_{\mu\nu}B^{\mu\nu} + \overline{\ell_{\mathrm{L}}^{\alpha}}i\not{\mathcal{D}}\ell_{\mathrm{L}}^{\alpha} + \overline{Q_{\mathrm{L}}^{\alpha}}i\not{\mathcal{D}}Q_{\mathrm{L}}^{\alpha} + \overline{\ell_{\mathrm{R}}^{\alpha}}i\not{\partial}'\ell_{\mathrm{R}}^{\alpha} + \overline{u_{\mathrm{R}}^{\alpha}}i\not{\partial}'u_{\mathrm{R}}^{\alpha} \\ &+ \overline{d_{\mathrm{R}}^{\alpha}}i\not{\partial}'d_{\mathrm{R}}^{\alpha} - (\mathrm{y}^{\ell}_{\alpha\beta}\overline{\ell_{\mathrm{L}}^{\alpha}}H\ell_{\mathrm{R}}^{\beta} + \mathrm{y}^{d}_{\alpha\beta}\overline{Q_{\mathrm{L}}^{\alpha}}Hd_{\mathrm{R}}^{\beta} + \mathrm{y}^{u}_{\alpha\beta}\overline{Q_{\mathrm{L}}^{\alpha}}H^{c}u_{\mathrm{R}}^{\beta} + h.c.) \\ &+ |\mathcal{D}_{\mu}H|^2 - \mu_H^2H^{\dagger}H - \lambda_H(H^{\dagger}H)^2 + \mathcal{L}_{\mathrm{QCD}}\,,\end{aligned} \tag{1.1}$$

where $\partial'_{\mu} = \partial_{\mu} - ig_{\mathrm{Y}}\frac{1}{2}\mathrm{Y}B_{\mu}$, $\mathcal{D}_{\mu} = \partial_{\mu} - ig_{\mathrm{w}}\frac{1}{2}\boldsymbol{\sigma}.\mathbf{W}_{\mu} - ig_{\mathrm{Y}}\frac{1}{2}\mathrm{Y}B_{\mu}$ and $H^{c} = i\sigma_2H^{\star}$. The gauge field strength tensors are defined as $B_{\mu\nu} = \partial_{\mu}B_{\nu} - \partial_{\nu}B_{\mu}$, $W^{a}_{\mu\nu} = \partial_{\mu}W^{a}_{\nu} - \partial_{\nu}W^{a}_{\mu} + g_{\mathrm{w}}\epsilon_{abc}W^{b}_{\mu}W^{c}_{\nu}$ where B_{μ} is the hypercharge gauge boson, W^{a}_{μ} are the $\mathrm{SU}(2)_{\mathrm{L}}$ gauge bosons and anti-symmetric Levi-Civita tensor ϵ^{abc} are the structure constants for $\mathrm{SU}(2)_{\mathrm{L}}$ gauge group, with $a,\ b,\ c = \{1,\ 2,\ 3\}$. Left-handed leptons ($\ell_{\mathrm{L}}^{\alpha}$), left-handed quarks ($Q_{\mathrm{L}}^{\alpha}$), right-handed leptons ($\ell_{\mathrm{R}}^{\alpha}$), and right-handed quarks are represented as,

$$\ell_{\mathrm{L}}^{\alpha} = \left\{\begin{pmatrix}\nu_{e\mathrm{L}}\\ e_{\mathrm{L}}\end{pmatrix}, \begin{pmatrix}\nu_{\mu\mathrm{L}}\\ \mu_{\mathrm{L}}\end{pmatrix}, \begin{pmatrix}\nu_{\tau\mathrm{L}}\\ \tau_{\mathrm{L}}\end{pmatrix}\right\}, \quad Q_{\mathrm{L}}^{\alpha} = \left\{\begin{pmatrix}u_{\mathrm{L}}\\ d_{\mathrm{L}}\end{pmatrix}, \begin{pmatrix}c_{\mathrm{L}}\\ s_{\mathrm{L}}\end{pmatrix}, \begin{pmatrix}t_{\mathrm{L}}\\ b_{\mathrm{L}}\end{pmatrix}\right\}; \tag{1.2}$$

$$\ell_{\mathrm{R}}^{\alpha} = \{e_{\mathrm{R}},\ \mu_{\mathrm{R}},\ \tau_{\mathrm{R}}\}, \quad u_{\mathrm{R}}^{\alpha} = \{u_{\mathrm{R}},\ c_{\mathrm{R}},\ t_{\mathrm{R}}\}, \quad d_{\mathrm{R}}^{\alpha} = \{d_{\mathrm{R}},\ s_{\mathrm{R}},\ b_{\mathrm{R}}\}\,; \tag{1.3}$$

where $\alpha = 1, 2, 3$ represents the generation index. Left(right) handed fermions are defined by the chirality operator, $\psi_{\mathrm{L,R}} = \frac{1}{2}(1 \mp \gamma_5)\psi$, where ψ is a Dirac spinor. In SM right-handed neutrinos are absent. The $\mathrm{U}(1)_{\mathrm{Y}}$ hypercharges correspond to $\ell_{\mathrm{L}}^{\alpha},\ Q_{\mathrm{L}}^{\alpha},\ \ell_{\mathrm{R}}^{\alpha},\ u_{\mathrm{R}}^{\alpha},\ d_{\mathrm{R}}^{\alpha},\ H$ are $-1,\ 1/3,\ -2,\ 4/3,\ -2/3,\ 1$, respectively, while the weak isospins of the weak isodoublets are formulated using $\mathrm{I}_3 = Q_e - \mathrm{Y}/2$. Here, $\boldsymbol{\sigma}$s are the pauli spin matrices and $\boldsymbol{\sigma}/2$ are the generators of $\mathrm{SU}(2)_{\mathrm{L}}$ gauge group.

[1] Using the isotropy of the CMB to place stringent constraints on a possible electrical charge asymmetry of the universe: $Q_e^{\gamma} < 10^{-35}$ [19], $Q_e^{\nu} < 4\times10^{-35}$ [20] and for heavy (light) DM, $Q_e^{\mathrm{DM}} < 4\times10^{-24}$ (10^{-30}) [20].

[2] The various observational studies are suggested that the photon is not entirely massless and derive a stringent upper limit [21–25]: $< 1.5\times10^{-24}m_e$.

Fundamental Particles		Electric Charge (Q_e)	Spin	Mass (GeV)
Quarks	Up (u)	$+\frac{2}{3}$	$\frac{1}{2}$	$(2.16 \pm 0.07) \times 10^{-3}$
	Down (d)	$-\frac{1}{3}$	$\frac{1}{2}$	$(4.70 \pm 0.07) \times 10^{-3}$
	Cherm (c)	$+\frac{2}{3}$	$\frac{1}{2}$	1.2730 ± 0.0046
	Strange (s)	$-\frac{1}{3}$	$\frac{1}{2}$	$(93.5 \pm 0.8) \times 10^{-3}$
	Top (t)	$+\frac{2}{3}$	$\frac{1}{2}$	172.57 ± 0.29
	Bottom (b)	$-\frac{1}{3}$	$\frac{1}{2}$	4.183 ± 0.007
Leptons	Electron (e)	-1	$\frac{1}{2}$	0.511×10^{-3}
	Electron neutrino (ν_e)	0[1]	$\frac{1}{2}$	≈ 0
	Muon (μ)	-1	$\frac{1}{2}$	105.658×10^{-3}
	Muon neutrino (ν_μ)	0[1]	$\frac{1}{2}$	≈ 0
	Tau (τ)	-1	$\frac{1}{2}$	$(1776.93 \pm 0.09) \times 10^{-3}$
	Tau neutrino (ν_τ)	0[1]	$\frac{1}{2}$	≈ 0
Gauge bosons	Photon (γ)	0[1]	1	0[2]
	W boson ($W^\pm$)	± 1	1	80.3692 ± 0.0133
	Z boson (Z^0)	0	1	91.188 ± 0.002
	Gluon (g)	0	1	0
Scalar	Higgs (h)	0	0	125.20 ± 0.11

Table 1.1: The SM Particles, their electric charges (Q_e) and Masses [18].

The *Yukawa* couplings are, in general, complex and non-diagonal. However, after the rotation to the physical state with a defined mass, it is achieved by defining mass eigenstate as a linear combination of flavor eigenstate. After the spontaneous EWSB, for $\mu_H^2 < 0$, Higgs acquire non-zero vacuum expectation value/vev (v) $H = (H^+,\ H^0)^T \to \frac{1}{\sqrt{2}}(0,\ h + \mathrm{v})^T$, and the gauge bosons ($W^\pm,\ Z$) become massive, $m_W = \frac{\mathrm{v}}{2} g_\mathrm{w}$ and $m_Z = \frac{\mathrm{v}}{2}\sqrt{g_\mathrm{w}^2 + g_\mathrm{Y}^2}$, following the Goldstone theorem [31, 32]. The leptons and quarks also get mass through Yukawa interactions proportional to v. The unbroken gauge group is $\mathrm{U}(1)_\mathrm{EM}$, and the photon remains massless. Absent a right handed neutrino, neutrinos remain massless in SM [33–36]. Neutrino flavor oscillation however, indicates the presence of a tiny neutrino mass; we will come back to this issue later. After EWSB, the QCD gauge symmetry $\mathrm{SU}(3)_\mathrm{c}$ remains unbroken, under which quarks are triplet. The QCD Lagrangian reads,

$$\mathcal{L}_\mathrm{QCD} = \sum_q \overline{\Psi}_{q,a} \left(i\not{\partial}\delta_{ab} + g_s \frac{1}{2}\gamma^\mu G_\mu^c \lambda_{ab}^c - m_q \delta_{a,b} \right) \Psi_{q,b} - \frac{1}{4}\mathbf{G}_{\mu\nu}.\mathbf{G}^{\mu\nu}\,, \tag{1.4}$$

where $\Psi_{q,a}$ represents the quark fields with flavor q and color index a, which runs

from 1 to 3; as quarks come with three colors. G^c_μ corresponds to the gluon fields with color index c running from 1 to 8 as Gluons transforms under adjoint representation of $\mathrm{SU(3)_c}$. $\frac{\lambda^c_{ab}}{2}$s are the $\mathrm{SU(3)_c}$ gauge group generators and this eight 3×3 matrices (λ^c) are known as Gell-Mann matrices. $g_s = \sqrt{4\pi\alpha_s}$ is the QCD coupling constant while α_s is the strong coupling constant, which measures the interaction strength between quarks and gluons. The field strength tensor of the gluon fields: $G^c_{\mu\nu} = \partial_\mu G^c_\nu - \partial_\nu G^c_\mu - g_s f^{abc} G^a_\mu G^b_\nu$ and $[\lambda^a, \lambda^b] = 2\, i\, f^{abc}\lambda^c$ where f_{abc} is the structure constants of the $\mathrm{SU(3)_c}$ group. The gluon-gluon interaction arises from the last non-linear term. Neither quarks, anti-quarks, nor gluon are observed as free particles in nature. More importantly, the color confinement mechanism ensures that any observable particle is color-neutral or colorless.

Following the Eq . (1.1), we can identify all possible interaction terms among the fundamental particles. The discovery of a $125\ GeV$ scalar in 2012 at the LHC [16, 17] confirmed that the SM is an extremely well-verified theory at the EW scale, with only a few exceptions. For example, we are yet to confirm whether the $125\ GeV$ scalar originate from SM Higgs doublet unless all its associated couplings are measured. This also gives rise to the question what kind of phase transition the universe went through at the EWSB scale, or whether the Higgs vacuum is stable/metastable up to the scale of gravity, all relevant for NP search prospects.

1.2 Issues with the Standard Model

Despite the significant achievements of the SM in explaining elementary particles and their interactions, many unsolved issues remain. The challenges include explaining the existence of a non-luminous DM, tiny yet non-zero masses of neutrinos, the hierarchy problem [37–39], gauge coupling unification [40–43], the stability of the Higgs vacuum [44–47], the strong CP problem in QCD [48–51], matter-antimatter asymmetry prevailing in the universe, flavor anomalies etc. We discuss some of these issues below.

1.2.1 Evidences of a non-luminous dark matter

The existence of a non-luminous DM, which accounts for about 85% of matter present in the universe [7], can't be accommodated within the SM and has been a key motivation for studying physics beyond the SM. The hint for DM mainly comes from astrophysical and cosmological observations [1]. In 1930, J. H. Oort first realized that the motion of stars in the Milky Way required more mass than was previously imagined [2]. Later, in 1933, F. Zwicky also found a similar indication of missing mass but at a large scale when he calculated the velocity dispersion of galaxies in coma clusters using the Doppler shift effect [4]. Around the 1970's V. Rubin's group performed a long study of the rotation curves of 60 isolated galaxies, observed rotation curves are constant up to very large radius instead of falling as $v \sim 1/\sqrt{r}$ in the absence of non-luminous matter due to Keplerian behavior [5]. Another supporting observation related to this comes from the $21-\mathrm{cm}$ rotation curve of the nearby galaxy $\mathrm{M33}$ out to a galactocentric distance of $16\ \mathrm{kpc}$ [52, 53].

Gravitational lensing provides another way of probing the presence of non-luminous matter, as it can map the total gravitating mass of a galaxy cluster by exploiting

the fact that gravitational fields affect the propagation of light. In the strong lensing regime, where we have a very dense region between the source and observer, light emitted from the source follows several geodesics to reach the observer and results in multiple images of the same physical source in the observer's view. In the weak lensing regime, the presence of some non-luminous massive object between the source and observer results in distortions of the apparent shape of the luminous object by changing its gravitational potential. This methodology was adopted in the observation of "Bullet Cluster" (1E0657-56) [6]. In a collision of galaxy clusters, the hot gas of both systems has dissipated energy due to electromagnetic interactions, which is held up at the point of collision, but DM halos pass straight through without sufficient collision, and their presence could be inferred from this weak gravitational lensing. On the cosmological scale, Cosmic Microwave Background (CMB) Radiation gives us strong evidence of the existence of DM. The analysis of CMB anisotropies provides us with an accurate estimate of cosmological models and strong constraints on cosmological parameters. Wilkinson Microwave Anisotropy Probe (WMAP) [54] and Planck [7] data suggest that the universe is made up of around 4.9% baryonic matter (like baryons, leptons), 26.8% non-baryonic matter known as DM and rest 68.3% dark energy assuming FRW model or Standard Model of Cosmology. In literature, the content is commonly expressed in terms of relic density,

$$\Omega_{\rm DM} h^2 = 0.1200 \pm 0.0012\,, \tag{1.5}$$

where h refers to reduced Hubble constant. Observations from Big Bang Nucleosynthesis (BBN) and the Cosmic Microwave Background (CMB) provide robust evidence for the existence of a non-baryonic component of the universe, DM. The observational evidences in support of DM are summarised in Fig . 1.2. We elaborate upon the evidence below.

Observations from Galaxy Clusters

A galaxy cluster is a massive structure that consists of hundreds to thousands of galaxies bound together by gravity.

- **Coma Cluster:** In 1933, F. Zwicky analyzed the motion of galaxies in the Coma cluster (1000 galaxies within 1 Mpc) using the Virial theorem:

  $$\langle V \rangle + 2\langle K \rangle = 0, \quad \text{where } \langle V \rangle = -\frac{N^2}{2} G_N \frac{\langle m^2 \rangle}{R}, \quad \langle K \rangle = N \frac{\langle m v^2 \rangle}{2}.$$

  The cluster mass M is related to the velocity dispersion by:

  $$M \sim \frac{2R\langle v^2 \rangle}{G_N}.$$

  The derived mass-to-luminosity ratio, $\frac{M}{L} \sim 300 h \frac{M_\odot}{L_\odot}$, exceeds the solar value by 300 times, indicating that most of the mass is non-luminous, or *dark*.

- **X-ray Observations:** The gravitational potential of galaxy clusters is also determined via X-ray emission from hot gas. The electron number density $n_e(r)$ and temperature $T_e(r)$ are measured, yielding the baryon number density $n_b(r) =$

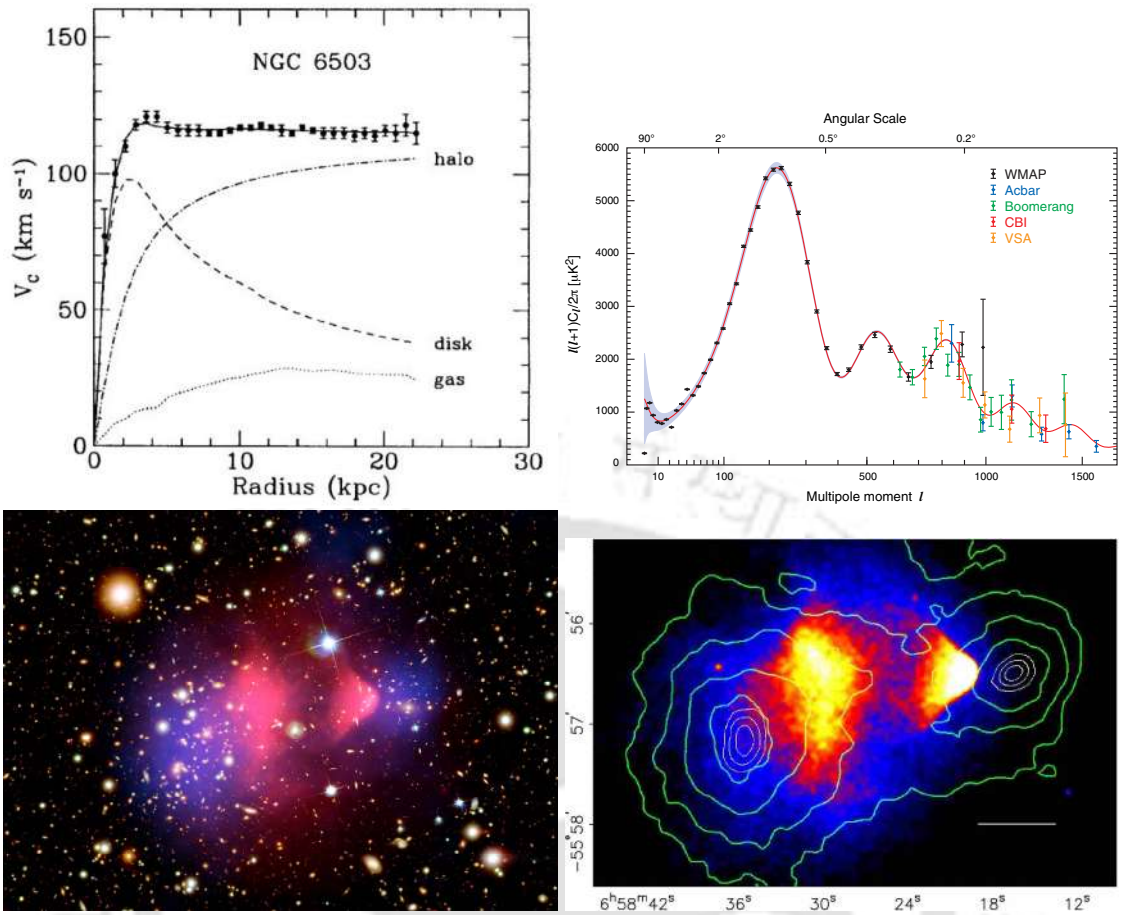

Figure 1.2: *Top-Left*: Galactic rotation curve for NGC 6503, illustrating the contributions from the stellar disk (dashed), gaseous components (dotted), and the DM halo (dashed-dot) required to achieve consistency with observational data [55]. *Top-Right*: Powered spectrum [56], the first peak says that the universe is flat, the second peak provides the baryonic matter content of the universe, and the third peak indicates the presence of DM in the universe. *Bottom-Left*: The collision of galaxy clusters $1E0657-56$, known as the Bullet Cluster, demonstrates a distinct separation between baryonic matter (represented in pink) and DM (depicted in blue). The spatial distribution of DM is inferred through the effects of gravitational lensing, image courtesy: Chandra X-ray Observatory. *Bottom-Right*: The green contours denote the reconstructed lensing signal, proportional to the projected mass in the system [57].

$\mu n_e(r)$ (where μ is a composition factor) and pressure $P(r) = n_e(r)T_e(r)$. Using hydrostatic equilibrium:

$$\frac{dP}{dR} = -n_b(r)m_b\frac{G_N M(R)}{R^2}, \quad M(R) = 4\pi\int_0^R \rho(r)r^2 dr.$$

X-ray spectra constrain $M(R)$, consistently revealing mass exceeding the visible baryonic contribution.

- **Gravitational Lensing:** The distortion of distant galaxy images due to gravitational lensing enables the reconstruction of cluster mass distribution. Results indicate the presence of non-visible, differently distributed matter.

- **Bullet Cluster:** The "bullet cluster" provides direct evidence for DM. In this merging cluster, the collisional baryonic gas lags due to energy dissipation, whereas collisionless DM components pass through, aligning with gravitational potential contours but not with visible gas.

Observations from Galaxies

The rotation curve of a galaxy, $v(R) = \sqrt{\frac{G_N M(R)}{R}}$, reflects mass distribution. Luminous matter predicts $v(R) \propto R^{-1/2}$ at large radii. Observations, however, show $v(R) \simeq$ constant (see Fig. 1.2), implying $M_{\rm DM} \propto R$, consistent with a DM density distribution $\rho_{\rm DM}(r) \propto 1/r^2$.

Large-Scale Structures

Without DM, density perturbations would begin growing only post-recombination, precluding structure formation today. Structure growth depends on DM types; **Hot DM** helps forming large structures and then fragment (top-down). **Cold DM** helps small structures merge into larger ones hierarchically (bottom-up). Cosmological observations and simulations strongly favor the cold DM scenario.

What can be dark matter

According to recent Planck data [7], the total matter density of the universe is $\Omega_m h^2 \sim 0.31$, where $\Omega = \frac{\rho}{\rho_c}$ is the cosmological density, the critical energy density is given by $\rho_c = \dfrac{3H^2}{8\pi G_N} \sim 1.054 \times 10^{-5} h^2\ GeV/\text{cm}^3$, with G_N denoting gravitational constants, and $h = H_0/(100\ \text{km/s/Mpc})$ is the reduced Hubble parameter with $H_0 = (73.0 \pm 1.0)\ \text{km}^{-1}\ \text{s}^{-1}\ \text{Mpc}^{-1}$ [58] denoting the present day Hubble parameter value. Luminous matter, including stars and dust clouds, accounts for $\Omega_{lum} h^2 \sim 0.005$, while baryonic matter contributes $\Omega_b h^2 \sim 0.04$. This inequality suggests that DM can be baryonic or non-baryonic. However, the baryonic nature of DM is strongly constrained by big-bang nucleosynthesis (BBN). Apart from astrophysical objects like Massive Compact Halo Objects (MACHOs) [59] that can address the macroscopic behavior of DM and constitute part of baryonic DM [60], an overwhelming belief that DM consists of fundamental particles and non-baryonic [61] is widely studied. All of the evidence gathered so far suggests that the DM candidates should [62]:

- **Dark matter should be Electromagnetic charge neutral**, with minimal interaction with photons, consistent with CMB observation. There are possibilities that it may have a tiny effective charge and interact via "dark photons" [63] although it is strongly constrained [64, 65].
- **DM is stable with a lifetime larger than the age of the universe**. Otherwise, it would decay into observable particles and won't provide the observed relic density.
- **DM should be massive particles**, as the evidence of DM comes from the gravitational effects only, and contributes significantly to the energy density of the universe. The mass can vary widely as shown in Fig. 1.3. An upper bound on Primordial Black Hole (PBH) DM is $\lesssim 1.12 \times 10^{50}\ GeV$ obtained from the gravitational micro lensing by Kepler satellite [66]. Another limit on PBH has come from a comprehensive analysis of high resolution high-redshift $\text{Lyman}-\alpha$ forest data, $\lesssim 1.12 \times 10^{59}\ GeV$ [67]. The lower limit on DM mass is around $(1-10) \times 10^{-22}\ eV$ using the $\text{Lyman}-\alpha$ forest data [68, 69], while that for the

Fuzzy DM is around 10^{-22} eV [70]. This bound turns larger, around 10^{-19} eV [71], if the DM is produced after inflation via a process with finite correction length.

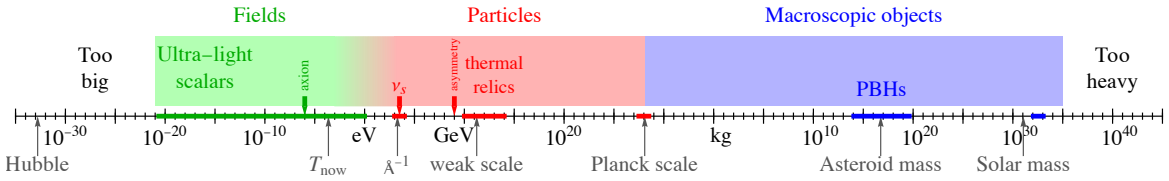

Figure 1.3: Possible mass range for DM with some notable candidates. Adapted from [72].

- **Dark matter should be non-baryonic** except for MACHOs [59], as the observed gravitational effects in the galaxies and galaxy clusters cannot be explained only by the baryonic DM [73].
- The interaction strength of DM with visible sector depends on the proposed particle type, as we elaborate later.

As briefly mentioned above, non-baryonic DM can be classified into:

- **Cold Dark Matter (CDM):** CDMs are non-relativistic in nature and are keystones of the ΛCDM model, explains accelerated expansion of the universe, large-scale structure formation and DM halos. The most popular CDM candidates are Weekly Interacting Massive Particles (WIMPs), Feebly Interacting Massive Particles (FIMP) and Strongly Interacting Massive Particles (SIMP), amongst several other possibilities. Thermal DM has a large mass range around $10\,MeV - 100\,TeV$ [74, 75], while it can extend to $10^{14} GeV$ for Superheavy thermal DM [76] and can also go down to few keV [77]. For non thermal DM, the lower mass bound is around $15\ keV$ [78, 79].
- **Hot Dark Matter (HDM):** HDM is relativistic and has large free streaming lengths due to tiny mass. For example, SM active neutrinos and sterile neutrinos [80] can be HDM. However, the structure formation of the universe goes against the existence of only HDM candidates. The constraints from cosmological data, including CMB, baryon acoustic oscillations (BAO), large-scale structure formation, on the HDM masses imply $\sum m_\nu < 0.12$ eV [81], while for sterile neutrinos the mass $\lesssim 1\ keV$ [82].
- **Warm Dark Matter (WDM):** This type of DM candidates have properties falling between cold and hot regimes, and masses are usually in the KeV range. Sterile neutrinos and gravitons are the most popular WDM candidates encountered in literature. Again, WDM candidates satisfying all the above credentials are a challenging task for DM model building.
- **Fuzzy Dark Matter (FDM):** This is ultralight DM [70] that leads to wavelike properties rather than discrete point-like particles and follows the quantum mechanical behavior. Its mass is around 10^{-22} eV and potentially affects the structure formation and density profile of galaxies. Axion is a possible FDM candidate.

We will come back to the DM model and detection possibilities in detail in the next chapter.

1.2.2 Neutrino mass

Around 1930, Wolfgang Pauli first postulated the existence of neutrinos, although Pauli called it "neutron", to explain the non-conservation of spin and energy in the beta−decay [83]. The characteristics of this particle were defined by (i) electromagnetically charge neutrality, (ii) nearly masslessness, and (iii) having 'weak interaction' with the visible sector. Later, around 1934, Enrico Fermi renamed the particle as neutrino and postulated the theory of beta decay via effective weak interactions. In 1956, Clyde Cowan and Frederick Reines experimentally detected the neutrino by observing antineutrino interactions from a nuclear reactor [84, 85]. In SM, neutrinos are assumed to be massless. However, in 1960, the Homestake experiment [86] observed a discrepancy in the solar neutrino flux, and this led to a hypothesis that neutrinos could be massive and undergo oscillations in flavor [87] during propagation. This phenomenon was confirmed in 1998 with the Super-Kamiokande experiment [88, 89] and later supported by SNO [90] and KamLAND [91], which provided evidence for solar and atmospheric neutrino oscillations. Around 1957, the neutrino oscillation was first proposed by Bruno Pontecorvo [92, 93] and later, around 1962, Maki, Nakagawa, and Sakata [94] pointed out the mismatch between the propagation and interaction eigenstates, which was further developed by Pontecorvo [95].

The basic idea behind neutrino oscillation is that neutrinos are massive, so the flavor and mass eigenstates don't coincide. Both are related to each other via a unitary mixing matrix, similar to the quark mixing matrix Cabibbo-Kobayashi-Masakawa (CKM). We thus introduce a 3×3 unitarity matrix $\mathrm{U_{PMNS}}$, known as the Pontecorvo Maki Nakagawa Sakata (PMNS) matrix [18, 94, 95] for three generations of neutrinos, propagating with mass eigenstates ν_i $(i = 1, 2, 3)$ with mass m_i, which are in linear combination of the three flavor eigenstates ν_α $(\alpha = e, \mu, \tau)$ via $|\nu_\alpha\rangle = \mathrm{U_{PMNS}}|\nu_i\rangle$. The PMNS matrix inherits the scope of having neutrinos as Majorana particles (self conjugate) via two Majorana [96] phases (ρ, σ) [97, 98] without affecting the neutrino oscillation data, but having consequences in lepton number violating processes [99] as [100],

$$\mathrm{U_{PMNS}} = \begin{bmatrix} c_{12}c_{13} & s_{12}c_{13} & s_{13}e^{-i\delta_{CP}} \\ -s_{12}c_{23} - c_{12}s_{23}s_{13}e^{i\delta_{CP}} & c_{12}c_{23} - s_{12}s_{23}s_{13}e^{i\delta_{CP}} & s_{23}c_{13} \\ s_{12}s_{23} - c_{12}c_{23}s_{13}e^{i\delta_{CP}} & -c_{12}s_{23} - s_{12}c_{23}s_{13}e^{i\delta_{CP}} & c_{23}c_{13} \end{bmatrix} \times \mathrm{Diag}[e^{i\rho},\ e^{i\sigma},\ 1] \quad (1.6)$$

where $c_{ij} \equiv \cos\theta_{ij}$ and $s_{ij} \equiv \sin\theta_{ij}$ (for $ij = 12, 13, 23$), δ is the Dirac CP-violating phase together with two Majorana CP-violating phases $(\rho,\ \sigma)$.

In vacuum[3], the mass eigenstates ν_i are eigenstates of free Hamiltonian, $H_0|\nu_i\rangle = E_i|\nu_i\rangle$ and evolve with time as $e^{-i\ E_i t}$. So, the flavor eigenstates at time t are superposition of flavor eigenstates at time $t = 0$, and therefore the probability of an initial neutrino flavor α oscillating into a flavor β at time t is given by,

$$P_{\alpha\beta}(t) = |\langle\nu_\beta|\nu_\alpha(t)\rangle|^2 = U_{\alpha i}U^*_{\beta i}U_{\beta j}U^*_{\alpha j}e^{-i(E_i - E_j)t}\,. \quad (1.7)$$

For relativistic neutrinos, $E_i \approx E + \dfrac{m_i^2}{2E}$, and assuming every neutrino have same

[3]While we discuss neutrino propagation in vacuum, neutrinos travel through dense media, such as solar neutrinos, for which matter effects need to be incorporated [100].

momentum $E = |\mathbf{p}_i|$ while travelling a distance L in time t yields Eq. (1.7),

$$P_{\alpha\beta}(t) = U_{\alpha i}U^*_{\beta i}U_{\beta j}U^*_{\alpha j}e^{-i\frac{\Delta m^2_{ij}}{2E}L}, \tag{1.8}$$

where $\Delta m^2_{ij} = m^2_i - m^2_j$; with $\Delta m^2_{21} = \Delta m^2_{\text{sol}}$ and $\Delta m^2_{31} = \Delta m^2_{\text{atm}}$. So, the oscillation probability depends on the three mixing angles, the Dirac CP phase, and the mass square splittings, which are experimentally observed quantities. As we can only probe $|\Delta m^2_{31}|$, two mass hierarchies can occur, Normal Ordering (NO) and Inverted Ordering (IO), depending on which is the lightest neutrino mass eigenstate ν_1 or ν_3, see Fig. 1.4. A recent global fit result [101] corresponding to these oscillation

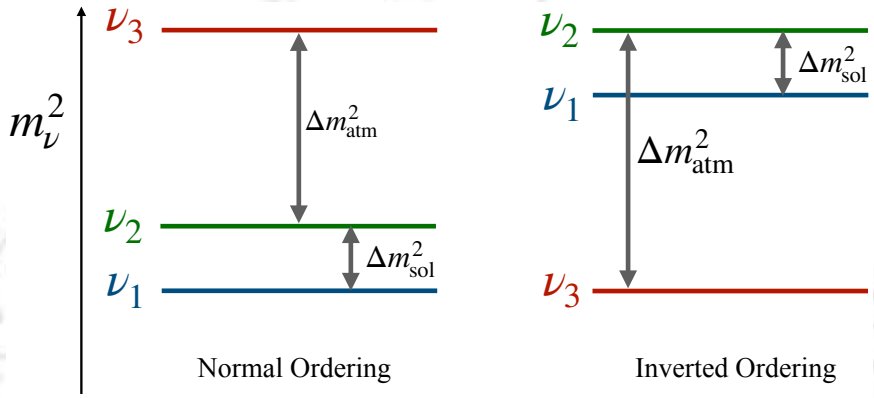

Figure 1.4: A schematic depiction of the ordering of the two neutrino mass eigenstates, Normal Ordering (NO) and Inverted Ordering (IO), supported by neutrino oscillation data.

parameters is shown in Table 1.2.

The cosmological observation also puts limits on the sum of the neutrino masses as neutrinos contribute to the energy density of the universe and the growth of large-scale structures. The limits from CMB: $\sum m_\nu < 0.12\ (0.15)$ eV for NO (IO) [7], KATRIN puts bounds on the effective electron neutrino mass: $m_{\nu_e} < 0.45$ eV at 90% CL [102]. Apart, neutrinoless double beta decay experiment like KamLAND-Zen puts an upper limit to the square of the effective Majorana neutrino mass $\langle m_{\beta\beta}\rangle \equiv |\sum_i U^2_{PMNS_{ei}} m_{\nu_i}|^2 < 28-122$ meV at 90% CL [103]. We may note here, whether neutrinos are Dirac or Majorana type, still remains an open question. Neutrino oscillation yield identical probabilities for both the cases, making them indistinguishable. Detecting a lepton number violating process, like neutrinoless double beta decay, could provide a hint towards that.

Accommodating neutrino masses require an extension beyond the SM. Introducing a right-handed neutrino, we can write the following mass terms:

$$m_D\overline{\nu}_R\nu_L + \frac{1}{2}m_L\overline{\nu}^c_L\nu_L + \frac{1}{2}m_R\overline{\nu}^c_R\nu_R + \text{h.c.}\,. \tag{1.9}$$

In the above, m_D represents a Dirac mass term, while m_L and m_R represent Majorana mass term.

The dimension five SM effective operator, called Weinberg operator [104, 105], which is SM gauge invariant but violates Lepton number, can generate Majorana mass for the left handed neutrinos, after Spontaneous symmetry breaking,

$$\mathcal{O}_W = \frac{\lambda_{\alpha\beta}}{\Lambda}(\overline{L}_\alpha\tilde{H})(\tilde{H}^T L^c_\beta) + h.c.\,, \tag{1.10}$$

parameters	best fit $\pm 1\sigma$	2σ range	3σ range
$\Delta m^2_{21}[10^{-5}\text{eV}^2]$	$7.50^{+0.22}_{-0.20}$	7.12–7.93	6.94–8.14
$\lvert\Delta m^2_{31}\rvert[10^{-3}\text{eV}^2]$ (NO)	$2.55^{+0.02}_{-0.03}$	2.49–2.60	2.47–2.63
$\lvert\Delta m^2_{31}\rvert[10^{-3}\text{eV}^2]$ (IO)	$2.45^{+0.02}_{-0.03}$	2.39–2.50	2.37–2.53
$\sin^2\theta_{12}/10^{-1}$	3.18 ± 0.16	2.86–3.52	2.71–3.69
$\theta_{12}/^\circ$	34.3 ± 1.0	32.3–36.4	31.4–37.4
$\sin^2\theta_{23}/10^{-1}$ (NO)	5.74 ± 0.14	5.41–5.99	4.34–6.10
$\theta_{23}/^\circ$ (NO)	49.26 ± 0.79	47.37–50.71	41.20–51.33
$\sin^2\theta_{23}/10^{-1}$ (IO)	$5.78^{+0.10}_{-0.17}$	5.41–5.98	4.33–6.08
$\theta_{23}/^\circ$ (IO)	$49.46^{+0.60}_{-0.97}$	47.35–50.67	41.16–51.25
$\sin^2\theta_{13}/10^{-2}$ (NO)	$2.200^{+0.069}_{-0.062}$	2.069–2.337	2.000–2.405
$\theta_{13}/^\circ$ (NO)	$8.53^{+0.13}_{-0.12}$	8.27–8.79	8.13–8.92
$\sin^2\theta_{13}/10^{-2}$ (IO)	$2.225^{+0.064}_{-0.070}$	2.086–2.356	2.018–2.424
$\theta_{13}/^\circ$ (IO)	$8.58^{+0.12}_{-0.14}$	8.30–8.83	8.17–8.96
δ/π (NO)	$1.08^{+0.13}_{-0.12}$	0.84–1.42	0.71–1.99
$\delta/^\circ$ (NO)	194^{+24}_{-22}	152–255	128–359
δ/π (IO)	$1.58^{+0.15}_{-0.16}$	1.26–1.85	1.11–1.96
$\delta/^\circ$ (IO)	284^{+26}_{-28}	226–332	200–353

Table 1.2: A summary of the neutrino oscillation parameters; taken from [101].

with $\tilde{H} = i\sigma_2 H^*$, and Λ denoting the New Physics (NP) that has been integrated out. Thus, the mass term approximately can be written as $m_L \sim \lambda_{\alpha\beta}(\text{v}^2/\Lambda)$ where v is the vev of the SM Higgs. For sub-eV neutrino masses and $\lambda_{\alpha\beta} \sim \mathcal{O}(1)$, the NP scale $\Lambda \sim \mathcal{O}(10^{14})$ GeV turns huge. The smallness of coupling $(\lambda_{\alpha\beta}/\Lambda)$ could generally be explained using even higher dimensional operators along with the Weinberg operator following, $\mathcal{O}_d = \mathcal{O}_W(H^\dagger H)^{(d-5)/2}$, where one can append powers of $H^\dagger H$, given that it is a SM singlet. So, this operator can be generated by introducing a NP particle, at the tree or n-loop level $(n \geq 1)$, when the generated neutrino mass for this d-dimensional operator induced at the n-loop level is approximately given by $m_\nu \sim \lambda_{\alpha\beta}(16\pi^2)^{-n}(v/\Lambda)^{d-5}$. In Fig. 1.5, the typical scale of λ is shown by using $\mathcal{O}_d$, explaining the observed neutrino masses for a given dimension d and the order of loop n, following [106]. This suggests the enhanced possibility of collider detection

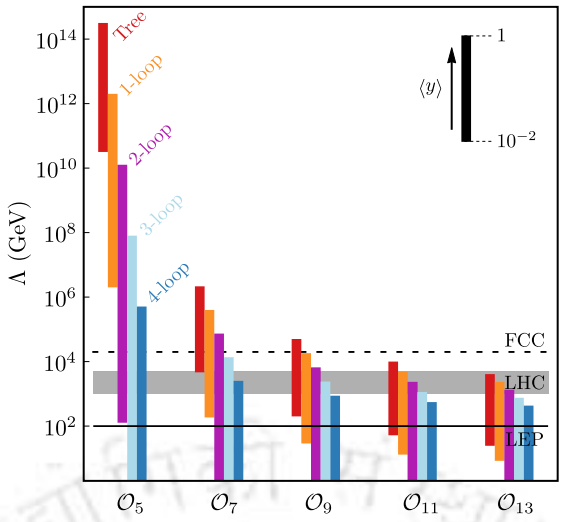

Figure 1.5: A rough estimate of the mass scale Λ at which a neutrino mass model with dimension d and $n-$loops accurately explains the observed neutrino masses. Adapted from [106].

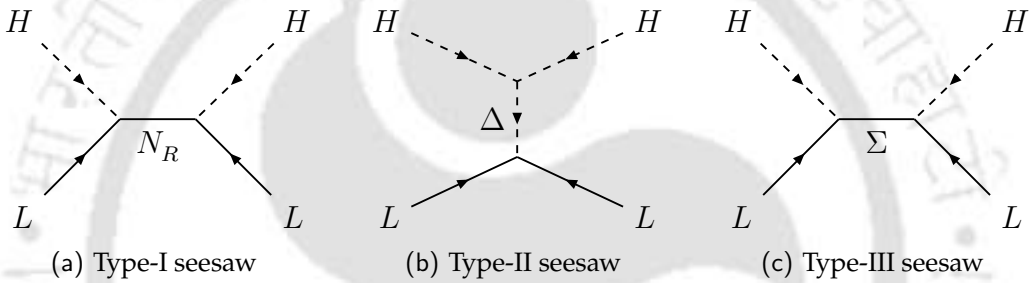

(a) Type-I seesaw (b) Type-II seesaw (c) Type-III seesaw

Figure 1.6: Seesaw mechanisms for neutrino mass generation via Weinberg operator at the tree level.

of NP, for generating neutrino masses via higher-dimensional operators and with larger loops.

The Weinberg operator can be generated at the tree level through three well-known seesaw mechanisms, Type-I, Type-II, and Type-III [107–113]. Apart, there are numerous non-minimal models that can lead to the realization of this dimension-five Wienberg operator. The main goal of these mechanisms is to introduce additional heavy degrees of freedom into the SM, thereby enabling $\mathrm{B}-\mathrm{L}$ violation. We will briefly discuss these mechanisms, see Fig . 1.6.

Type-I seesaw

In this mechanism, three right handed neutrinos (RHN) are appended to the SM. The relevant Lagrangians corresponding to these RHNs are given by [114–117],

$$-\mathcal{L}_{N_R} = \bar{\ell} Y_\nu \tilde{H} N_R + \frac{1}{2}\overline{N_R^c} M_R N_R + \text{h.c.}\,, \tag{1.11}$$

where M_R is the symmetric Majorana mass matrix. See the left plot of Fig . 1.6, where the RHN mediates $LHLH$ interaction. It is easy to understand that the NP scale in the Weinberg operator corresponds to the RHN mass, $\Lambda = M_R$, after we integrate it out. The phenomenological possibilities are limited here, given the heavy RHN mass here.

Type-II seesaw

In this mechanism, a scalar triplet with hypercharge 2, $\Delta = (\Delta^{++}, \Delta^{+}, \Delta^{0})$, couples to the lepton doublet and the Higgs doublet following [117–122],

$$-\mathcal{L}_{\Delta} \supset \frac{1}{2}\overline{\ell_{\rm L}} Y_{\Delta} \Delta i\sigma_2 \ell_{\rm L}^{c} - \lambda_{\Delta} M_{\Delta} H^{T} i\sigma_2 \Delta H + \text{h.c.}\,, \tag{1.12}$$

where the $SU(2)_{\rm L}$ doublet representation of this triplet is,

$$\Delta = \frac{1}{\sqrt{2}} \begin{pmatrix} \Delta^{+} & \sqrt{2}\Delta^{++} \\ \sqrt{2}\Delta^{0} & -\Delta^{+} \end{pmatrix}. \tag{1.13}$$

The Weinberg operator is generated via a t-channel mediation of Δ as shown in the middle panel of Fig. 1.6, after it is integrated out.

Type-III seesaw

In this mechanism, triplet fermions (Σ) are added to the SM. The relevant interaction terms of the Lagrangian, are given by [123–125],

$$-\mathcal{L}_{\Delta} \supset \overline{\ell_{\rm L}} Y_{\Sigma} \Sigma^{c} \tilde{H} + \frac{1}{2}\text{Tr}(\overline{\Sigma} M_{\Sigma} \Sigma^{c}) + h.c.\,, \tag{1.14}$$

where the fermion triplet is defined as,

$$\Sigma = \frac{1}{\sqrt{2}} \begin{pmatrix} \Sigma^{0} & \sqrt{2}\Sigma^{+} \\ \sqrt{2}\Sigma^{-} & -\Sigma^{0} \end{pmatrix}. \tag{1.15}$$

The Weinberg operator is generated via a s-channel mediation of Σ as shown in the right panel of Fig. 1.6, after it is integrated out. In summary, the Weinberg operator results via, [100],

$$\mathcal{O}_{W} \equiv \begin{cases} \frac{1}{2}\left(Y_{\nu} M_{R}^{-1} Y_{\nu}^{T}\right)_{\alpha\beta} \overline{\ell}_{{\rm L}\alpha} \tilde{H} \tilde{H}^{T} \ell_{{\rm L}\beta}^{c} + \text{h.c.} & (\text{Type}-\text{I})\,, \\ -\frac{\lambda_{\Delta}}{M_{\Delta}} \left(Y_{\Delta}\right)_{\alpha\beta} \overline{\ell}_{{\rm L}\alpha} \tilde{H} \tilde{H}^{T} L_{{\rm L}\beta}^{c} + \text{h.c.} & (\text{Type}-\text{II})\,, \\ \frac{1}{2}\left(Y_{\Sigma} M_{\Sigma}^{-1} Y_{\Sigma}^{T}\right)_{\alpha\beta} \overline{L}_{\alpha} \tilde{H} \tilde{H}^{T} L_{\beta}^{c} + \text{h.c.} & (\text{Type}-\text{III})\,. \end{cases} \tag{1.16}$$

After spontaneous EWSB, $\tilde{H}$ achieves VEV ($\mathtt{v} \sim 246\ GeV$), $\langle \tilde{H} \rangle = \mathtt{v}/\sqrt{2}$, and the effective Majorana neutrino mass for the three light neutrinos (ν_L) are generated, following Eq. (1.16), as $\frac{1}{2}\overline{\nu_L} M_{\nu} \nu_L^{c} + \text{h.c.}$, where the symmetric mass matrix (M_{ν}) is written as,

$$M_{\nu} = \begin{cases} -\frac{1}{2} Y_{\nu} \frac{v^2}{M_{R_2}} Y_{\nu}^{T} & (\text{Type}-\text{I})\,, \\ \lambda_{\Delta} Y_{\Delta} \frac{v^2}{M_{\Delta}} & (\text{Type}-\text{II})\,, \\ -\frac{1}{2} Y_{\Sigma} \frac{v^2}{M_{\Sigma}} Y_{\Sigma}^{T} & (\text{Type}-\text{III})\,. \end{cases} \tag{1.17}$$

From the above equation Eq. (1.17), it is clear that the smallness of M_{ν} can be ascribed to the large values of $M_R,\ M_{\Delta},\ M_{\Sigma}$ in the seesaw mechanism, limiting its phenomenological possibilities. Efforts to bring down the RHN mass scale results in variants of the model like linear and inverse seesaw mechanisms [126–129].

Radiative models

Neutrino masses can also be generated radiatively at one-loop level. Some of the most studied models in this direction are the Zee model [130], and scotogenic model [124]. There are examples of generating neutrino mass at higher loops, for example, Zee-Babu model at two loop [131], KNT (Krauss-Narsi-Trodden) model [132], Cocktail model [133] at three loop etc. Here, we discuss the scotogenic model [134] briefly, as it involves DM in the loop. The scotogenic model contains three RHNs

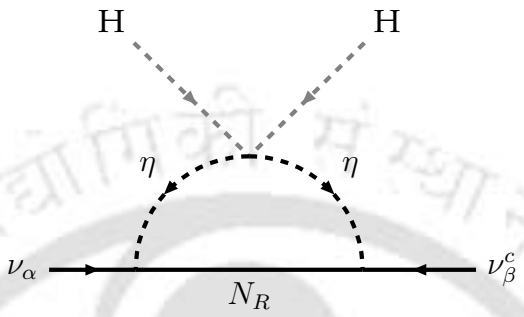

Figure 1.7: Radiative neutrino mass generation at one loop in the scotogenic model [134].

N_{R_i}, singlets under the SM gauge group, and a scalar doublet (η^+, η^0), both odd under $\mathcal{Z}_2$ so that the lightest one becomes a stable DM. The symmetry also forbids the tree-level neutrino mass generation via Type-I seesaw. The Yukawa interaction for this model is given by [134],

$$\mathcal{L}^{\rm Yuk}_{\rm scoto} = f_{ij}(\phi^- \nu_i + \overline{\phi_0}\ell_i)\ell^c_j + h_{ij}(\nu_i\eta^0 - \ell_j\eta^+)N_{R_j} + h.c.\,, \tag{1.18}$$

and the Majorana mass and the quadratic scalar terms are,

$$\frac{1}{2}M_{R_i}N_{R_i}N_{R_i} + h.c.\,, \tag{1.19}$$

$$\frac{1}{2}\lambda_5(H^\dagger\eta)^2 + h.c.\,, \tag{1.20}$$

with i and j are the generation indices. Using the interaction terms in Eq. (1.18) and Eq. (1.20), the one-loop radiatively generated neutrino mass matrix M_ν (see Fig. 1.7) is given by [134],

$$(M_\nu)_{ij} = \sum_k \frac{h_{ik}h_{jk}M_k}{16\pi^2}\left[\frac{m_R^2}{m_R^2 - M_{R_k}^2}\ln\frac{m_R^2}{M_{R_k}^2} - \frac{m_I^2}{m_I^2 - M_{R_k}^2}\ln\frac{m_I^2}{M_{R_k}^2}\right], \tag{1.21}$$

where m_R and m_I are the masses of the real and imaginary part of η^0. Upon further simplification, the neutrino mass turns out to be,

$$(M_\nu)_{ij} = \frac{\lambda_5 v^2}{16\pi^2}\sum_k \frac{h_{ik}h_{jk}}{M_k}\,, \tag{1.22}$$

which is basically the seesaw scale reduced by roughly the factor $\lambda_5/16\pi^2$. Thus, the RHN mass is down to 1 TeV from 10^9 TeV for the choice of benchmark: $m_\nu \sim 1$ eV, $\lambda_5 \sim$ h$^2 \sim 10^{-4}$, allowing a possibility of detection in future collider experiments in the scotogenic model.

Among the open questions in neutrino physics, the nature of neutrinos, whether Dirac or Majorana, is the most significant. See some references on the Dirac neutrino mass models [135–140] . In this thesis, our discussion focuses majorly on the radiative Majorana neutrino mass generation, which will be presented in Chapter 8 in the context of a two-component DM framework.

1.2.3 Matter-Antimatter asymmetry

Our observations suggests that matter dominates over antimatter in the observable universe. On Earth, matter surrounds us, while antimatter is mainly produced in accelerators. Both our Solar System and galaxy exhibit a distinct matter-antimatter asymmetry. One might propose that matter and antimatter exists in separate cosmic regions. However, such regions would produce detectable high-energy photons from annihilations ($B + \bar{B} \to \gamma\,\gamma$) at their borders. But, the absence of this signature indicates a global matter-antimatter asymmetry in the universe. Furthermore, two distinct cosmological observations, rooted in very different physics, give us similar probes. The matter-antimatter asymmetry is usually expressed as,

$$\eta_B = \left.\frac{n_B - n_{\bar{B}}}{n_\gamma}\right|_0 , \tag{1.23}$$

where n_B, $n_{\bar{B}}$ and n_γ are the number density of baryons, antibaryons, and photons, respectively, and the subscript 0 indicate that the value is measured at the present cosmic time. It is sometimes expressed in terms of the baryon density $(\Omega_{\rm b}{\rm h}^2)$ as $\eta_B = 274 \times 10^{-10}\Omega_{\rm b}{\rm h}^2$ [18]. However, there might be lepton excess over antileptons as well [141–144], but its contribution to the energy density of the universe is very small compared to the contribution of baryons.

The baryon density can be inferred in two ways: *First*, from the abundances of light elements (^{4}He, D, ^{3} He, and ^{7} Li), which directly probe the primordial abundances formed during Big Bang nucleosynthesis (BBN) at redshifts $z \sim 10^{10}$. Among these, deuterium abundance is most sensitive to the baryon-to-photon ratio η_B, while the other elements have a weaker dependence. A combined measurement of their abundances provides [145], see left plot of Fig . 1.8:

$$\Omega_{\rm b}^{\rm BBN}{\rm h}^2 = 0.0224 \pm 0.0007\,. \tag{1.24}$$

On the other hand, the photon density is proportional to T^3, and the universe's temperature is inferred from the CMB radiation, which exhibits an almost perfect blackbody spectrum. The anisotropies reflect acoustic oscillations of the photon-baryon fluid at decoupling, dependent on the baryon-to-photon ratio at redshift $z \sim 10^3$. Higher baryon density boosts odd peaks in the angular power spectrum relative to even ones, as shown in the right figure of Fig . 1.8. CMB anisotropy measurements from the 7−year WMAP data provides [7]:

$$\Omega_{\rm b}^{\rm CMB}{\rm h}^2 = 0.02242 \pm 0.00014\,. \tag{1.25}$$

The agreement of these two measurements at vastly different redshifts is a key success of standard big-bang cosmology. While one might consider this asymmetry an initial condition of the universe, there are two significant arguments against it. *First*, such a condition would be highly fine-tuned, implying that for every 100 million

quark-antiquark pairs, there would be one extra quark. *Second*, the widely accepted theory of inflationary expansion in the early universe would erase any asymmetry present after the Big Bang. Thus, it must be assumed that the universe was initially matter-antimatter symmetric, and a mechanism that generates $\eta_B \neq 0$ after inflation, but before the freeze-out of baryon-antibaryon annihilations dynamically, known as baryogenesis, is needed.

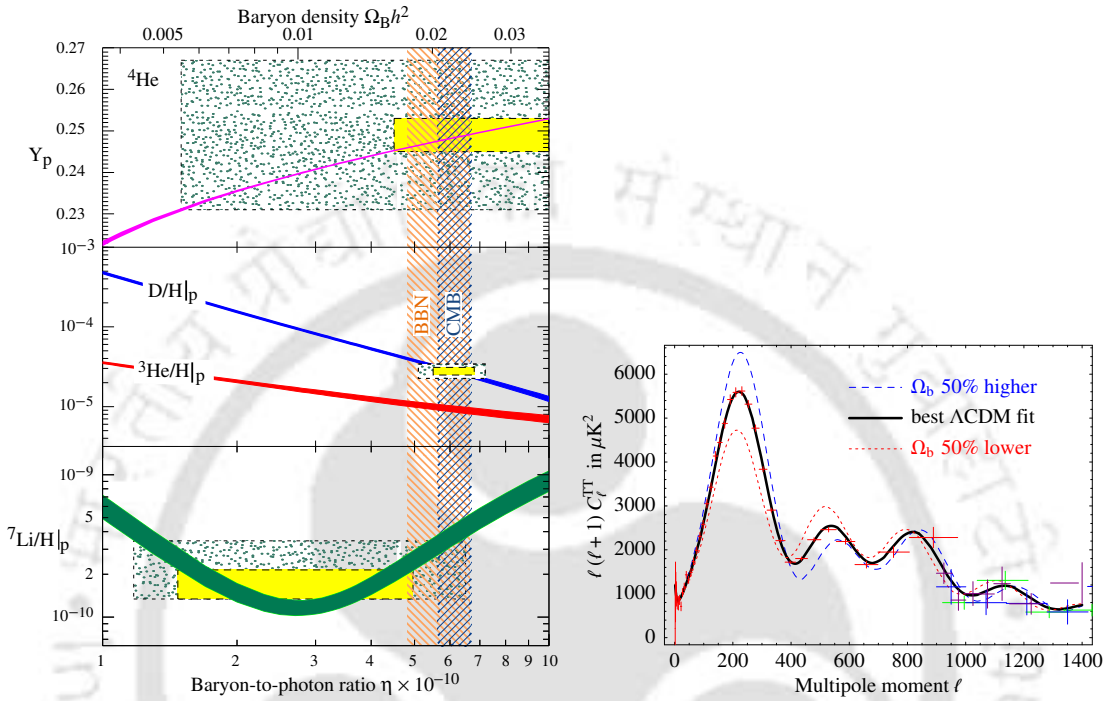

Figure 1.8: *Left figure:* The standard model of big-bang nucleosynthesis predicts the abundances of ^{4}He, D, ^{3} He, and ^{7} Li. Boxes represent observed light element abundances, with smaller boxes showing 2σ statistical errors and larger boxes indicating combined $\pm 2\sigma$ statistical and systematic errors. The narrow vertical band represents the CMB measurement of cosmic baryon density. *Right figure:* illustrates how the anisotropy magnitude at an angular scale of $1/l$ varies with n_B/n_γ. The left (right) figures are taken from [146] ([147]).

Sakharov's conditions

The necessary conditions for the generation of asymmetry dynamically in the universe starting from the symmetric initial state are known as the Sakharov conditions[148],

- *Baryon number* (**B**) *non-conservation:* The baryon number violating process is responsible for baryon asymmetry.

- **C** (*Charge conjugation*) *and* **CP** (*charge*×*parity*) *symmetry violation:* The **B** violating processes that create baryons occur at the same rate as their **C** and **CP** conjugated processes, which produce an equal amount of antibaryons. Therefore, **C** and **CP** symmetry violation is necessary.

- *Departure from the thermal equilibrium:* In chemical equilibrium, entropy is maximized when the chemical potentials of non-conserved quantum numbers, like **B**, vanish. Due to **CPT** invariance, the equal masses of quarks and antiquarks lead to identical phase space densities in thermal equilibrium and,

consequently, equal number densities. Therefore, the deviation from thermal equilibrium is necessary to generate the required baryon asymmetry.

Although all three of these conditions are met in the SM, they are still insufficient to produce the correct baryon asymmetry of the universe [149] for the following reasons:

- *Baryon Number Violation is too weak at low temperatures:* In SM, the **B** violation can occur through sphaleron processes at high temperatures. However, as the universe cools after the electroweak phase transition (EWPT), these processes become inefficient. Consequently, any baryon asymmetry generated earlier could be washed out unless constrained by very specific conditions.

- *Insufficient* **CP** *Violation:* In SM, weak interactions violate **C** maximally, and the **CP** violation in the SM arises mainly from the CKM matrix (in the quark sector) and, to a lesser extent, from the PMNS matrix (in the lepton sector). However, the **CP** violation provided by these matrices is far too small to explain the observed baryon asymmetry of the universe. Therefore, any reasonable baryogenesis theory needs additional sources for **CP** violation.

- *Electroweak Phase Transition is not strongly first-order:* The deviation from equilibrium occurs in particle interactions through the bubble walls between the broken and the unbroken phases. In order to obtain an irreversible asymmetry, the potential barrier between the two phases has to be large enough; that is, the phase transition has to be strongly first order. In the SM, for the observed Higgs mass ($\sim 125\ GeV$), the EWPT is a smooth crossover rather than a strongly first-order transition. Without a strongly first-order transition, the necessary departure from thermal equilibrium is inefficient unless we add additional mechanisms.

Successful baryogenesis requires two main key ingredients: *first*, new sources of **CP** violation, and *second*, a mechanism that causes a departure from thermal equilibrium. Furthermore, any mechanism that generates a **B** or **L** asymmetry at higher temperatures must also violate $\mathbf{B}-\mathbf{L}$, as failure to do so would result in the asymmetry being washed out by sphaleron interactions. Several approaches to satisfy these conditions have been explored, including grand unified theory (GUT) baryogenesis [150–152], electroweak baryogenesis [153, 154], the Affleck-Dine mechanism [155, 156], leptogenesis [157–162] and other [163].

The leptogenesis mechanism has garnered attention over the years within the class of models related to baryogenesis. Sphalerons violate $\mathbf{B}+\mathbf{L}$ through the effective interaction [113, 164, 165] $\Pi_\alpha q_{\mathrm{L}}^\alpha q_{\mathrm{L}}^\alpha q_{\mathrm{L}}^\alpha \ell_{\mathrm{L}}^\alpha$, but preserve $\mathbf{B}-\mathbf{L}$. In the proposal of leptogenesis, the lepton asymmetry is generated from the out-of-equilibrium decays of heavy particles, which coupled with the SM leptons, and is at least partly converted into the baryon asymmetry. The baryon (**B**) and lepton (**L**) asymmetries are determined by the $\mathbf{B}-\mathbf{L}$ asymmetry through sphaleron-induced chemical equilibrium. In the SM, this relationship is given by [166, 167]:

$$\mathbf{B} = \frac{8N_G + 4N_H}{22N_G + 13N_H}\mathbf{B} - \mathbf{L}, \tag{1.26}$$

where N_G denotes the number of generations (3 in the SM), and N_H represents the number of Higgs doublets (1 in the SM). However, in the presence of supersymmetric particles, this formula is slightly modified [168]. The key features of this mechanism is to connect the observed baryon asymmetry of the universe to the still unexplained fact that neutrinos have mass. Several such frameworks [169–179] have been studied to simultaneously explain neutrino masses, DM, and leptogenesis; one possibility is to invoke Scotogenic model, by introducing heavy RHNs and additional scalar doublet [180–187]. We study some such example in Chapter 8.

1.2.4 Lepton flavor enigma

The Landé g-factor of a charged elementary particle with half-integer intrinsic spin is equal to 2 at the tree level, as predicted by Dirac in 1928 for electron [188]. Any departure from this occurs due to higher order quantum correction and is generally known as the "anomalous magnetic moment", mathematically parametrised by,

$$a_\ell = \frac{g_\ell - 2}{2}\,, \tag{1.27}$$

where $g_\ell = 2$ for charged leptons ($\ell = e,\ \mu,\ \tau$).

An overall 3.2σ deviation between the theory (*incorporating correction due to QED (upto 5-loop)* [189–191], *SM EW contribution upto 2-loops* [192–199] *and leading three-loops* [200, 201], *incorporating QCD corrections via hadronic light-by-light scattering* [202–206], *hadronic vacuum polarisations* [207–214], *higher order hadronic correction at NNLO* [215, 216]) and experimental [217, 218] prediction of a_μ is [18],

$$\Delta a_\mu \equiv a_\mu^{\rm exp} - a_\mu^{\rm SM} = (1.13 \pm 0.35) \times 10^{-9}\,. \tag{1.28}$$

On the other hand, the recent measurement of (a_e), show a disagreement [219–221] with the SM prediction [191, 222]. The SM prediction depends on the measurement of the fine-structure constant, which is derived from the recoil velocity or frequency of atoms absorbing a photon. In the recent measurements of a_e, there exists a 5.5σ discrepancy between the measurements obtained using Rubidium-87 [219] and Cesium-133 [220]:

$$\Delta a_e \equiv a_e^{\rm exp} - a_e^{\rm SM} = \begin{cases} (-8.8 \pm 3.6) \times 10^{-13}\ (-2.4\sigma) & ({\rm Cs})\,, \\ (+4.8 \pm 3.0) \times 10^{-13}\ (+1.6\sigma) & ({\rm Rb})\,. \end{cases} \tag{1.29}$$

On the other hand, the anomalous magnetic moment of the tau lepton, $a_\tau = g_\tau/2 - 1$, serves as a sensitive probe for potential NP [223, 224]. However, obtaining a precise measurement of a_τ is significantly more challenging compared to the magnetic moments of electrons and muons.

On the other hand, no experimental evidence of charged lepton flavor-violating (cLFV) decay has been observed so far, thereby establishing an upper limit on the observables. We highlight the current (and projected) experimental upper limits

(90% confidence level) on the branching ratios of some cLFV decays:

$$\texttt{Br}(\mu \to \mathrm{e}\gamma) < 3.1 \times 10^{-13}\ (6 \times 10^{-14}) \quad [225]\ ([226])\,, \tag{1.30}$$
$$\texttt{Br}(\mu \to 3\mathrm{e}) < 1.0 \times 10^{-12}\ (1 \times 10^{-16}) \quad [227]\ ([228])\,, \tag{1.31}$$
$$\texttt{Br}(\tau \to \mathrm{e}\gamma) < 3.3 \times 10^{-8} \quad [18]\,, \tag{1.32}$$
$$\texttt{Br}(\tau \to \mu\gamma) < 4.2 \times 10^{-8} \quad [18]\,, \tag{1.33}$$
$$\texttt{Br}(\tau \to 3\mathrm{e}) < 2.7 \times 10^{-8} \quad [18]\,, \tag{1.34}$$
$$\texttt{Br}(\tau \to 3\mu) < 2.1 \times 10^{-8} \quad [18]\,. \tag{1.35}$$

We will discuss one model example in this thesis, where lepton flavor turns crucial.

With this brief introduction to SM of particle physics and some of its shortcomings, we would like to move on to describe the DM physics in detail, which the thesis is primarily based upon.

Chapter 2

Dark Matter Phenomenology

Contents

The existence of DM is well motivated from different astrophysical and cosmological observations, as elaborated in the last chapter, but laboratory discoveries are still awaited. The observations accumulated in support of DM has mainly come from gravitational interaction. One of the known numbers associated with DM is the relic density of DM in the universe, $\Omega_{\rm DM}^{\rm planck}h^2 \sim 0.12$. But, how the DM is produced is a question and gives rise to several possibilities of particle DM. We will illustrate them via some simple examples in extension to the Standard Model. Equally important question is how to detect DMs in upcoming experiments. This chapter will be devoted in exploring such possibilities as that will be pivotal to the thesis.

2.1 Dark Matter in extension of the Standard Model

Cold DM (CDM) is one of the most optimistic DM candidates that satisfy all the observed characteristics, and in this report, we focus mostly on them. Unfortunately we do not have a particle that can account for a CDM within SM, necessitating an extension of the SM. Apart from the characteristics pointed out in the previous chapter, CDM can produce the correct relic density broadly through two different mechanisms: (i) thermal freeze-out and (ii) non-thermal freeze-in[1] . Interestingly, not

[1]Beyond the two broad set ups that we discuss here, several kinds of DMs have been proposed, such as, Asymmetric DM [229–233], DM production from phase transition [234–236], Formation of

only the DM genesis, but their detectability is also very much dependent on such classifications. The observations made so far also do not clarify the detailed quantum properties like DM spin, and the possibility whether there are more than one DM component that constitute the dark sector, providing plethora of possibilities for DM model building. In this thesis, we will discuss possibilities of multiparticle DM sector. This feature is interesting as it gives rise to different phenomenological possibilities as we elaborate upon. The cartoon in Fig . 2.1 shows possible CDM candidates in a single and multi-component frameworks, some of which we address in the thesis.

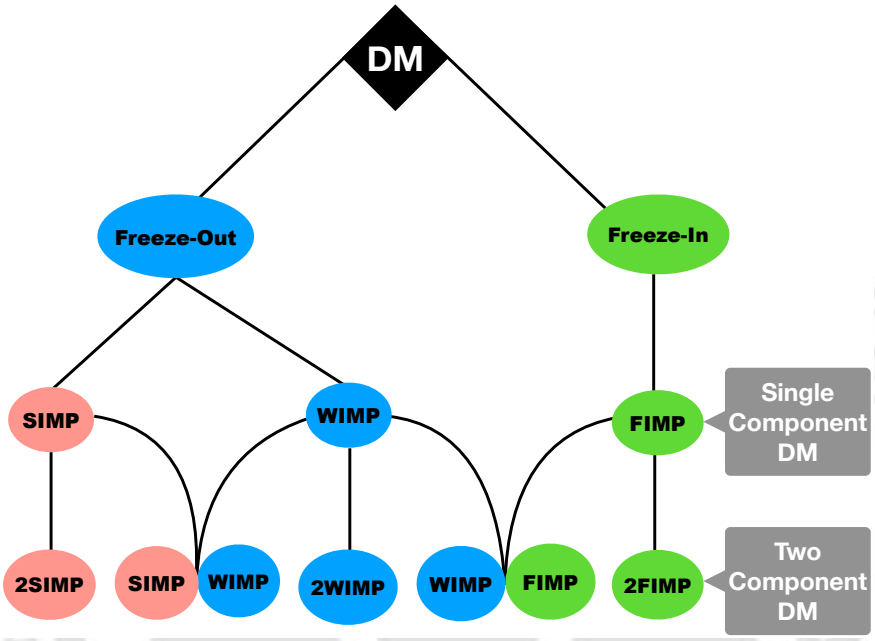

Figure 2.1: Possible CDM candidates and combinations that can produce multipartite dark sector.

2.1.1 Thermal freeze-out

In this case, DM particles are assumed to be in thermal and chemical equilibrium with the SM particles in the early universe. As the temperature falls and the universe expands, at a particular epoch when the interaction rates (Γ) become smaller than the expansion rate $(\mathcal{H})$ (Hubble constant), the DM particles freeze out from the thermal bath and become relic. WIMP and SIMP type DMs fall within this regime, as discussed below.

`WIMP: An example`

Freeze-out of DM dominantly occurs through $\mathrm{DM\ DM} \to \mathrm{SM\ SM}$ annihilation process. To attain correct relic density, the annihilation cross-section needs to be in the order of weak interaction cross-section, and this is the reason for calling such DM candidate Weakly Interacting Massive Particle (WIMP). The DM masses in such cases are usually $\sim 100\ GeV$, accessible to the present and future detectors and have been studied widely.

DM as primordial black hole [237–241], Gravitational DM [242–247] etc.

Let us discuss the WIMP possibility in a simple model, where the DM is assumed to be a real scalar (ϕ_i), which remains a singlet under SM gauge symmetries, and transforms under $\mathcal{Z}_2$ symmetry ($\phi_i \to -\phi_i$) to render its stability. The SM extended Lagrangian is given by,

$$\mathcal{L}_{\phi_i} = \frac{1}{2}\partial_\mu\phi_i\partial^\mu\phi_i - \frac{1}{2}\mu_{\phi_i}^2\phi_i^2 - \frac{1}{2}\lambda_{iH}\phi_i^2 H^\dagger H - \frac{1}{4!}\lambda_i\phi_i^4 \,. \tag{2.1}$$

The mass of the DM, after EWSB, turns out to be $m_{\phi_i}^2 = (\mu_{\phi_i}^2 + \frac{1}{2}\lambda_{iH}v^2)$. One of the main parameters of this model which governs DM-SM interaction is the Higgs portal term λ_{iH}, the strength of which dictates whether the DM is in thermal bath, and when it can freeze out. The number density is governed by the BEQ,

$$\dot{n}_{\phi_i} + 3\mathcal{H}n_{\phi_i} = -\langle\sigma v\rangle_{\phi_i\,\phi_i\to \mathrm{X}\,\mathrm{X}}\left[n_{\phi_i}^2 - n_{\phi_i,0}^2\right] \,, \tag{2.2}$$

where dot over n_{ϕ_i}denotes the time derivative, and $\mathrm{X} \in \{\text{leptons, quarks, } \mathrm{W}^\pm\text{, Z, and Higgs}\}$. Instead of using number density, we often define yield, $Y_{\phi_i} = n_{\phi_i}/s$, which is a dimensionless quantity and remains unaffected by the expansion rate in radiation dominated (RD) era, where $s = \dfrac{2\pi^2}{45}g_*^s T^3$ denotes entropy density. It is easy to show that $\dot{n}_{\phi_i} + 3\mathcal{H}n_{\phi_i} = s\dot{Y}_{\phi_i}$. The time ($t$) is related to the bath temperature during the RD epoch by $t = 1/(2\mathcal{H})$ where $\mathcal{H} = 1.67\sqrt{g_*^\rho}T^2/M_{\rm pl}$. The entropy and matter degrees of freedom are g_*^s and g_*^ρ respectively [248], and $M_{\rm pl} = 1.22 \times 10^{19}\ GeV$. The equilibrium number density ($n_{\phi_i}^{\rm eq}$) is defined as, $n_{\phi_i}^{\rm eq} = n_{\phi_i,0} = \dfrac{g_i}{2\pi^2}m_{\phi_i}^2 T K_2\left(m_{\phi_i}/T\right)$. We provide a detailed discussion on constructing BEQ for DM in Appendix A.

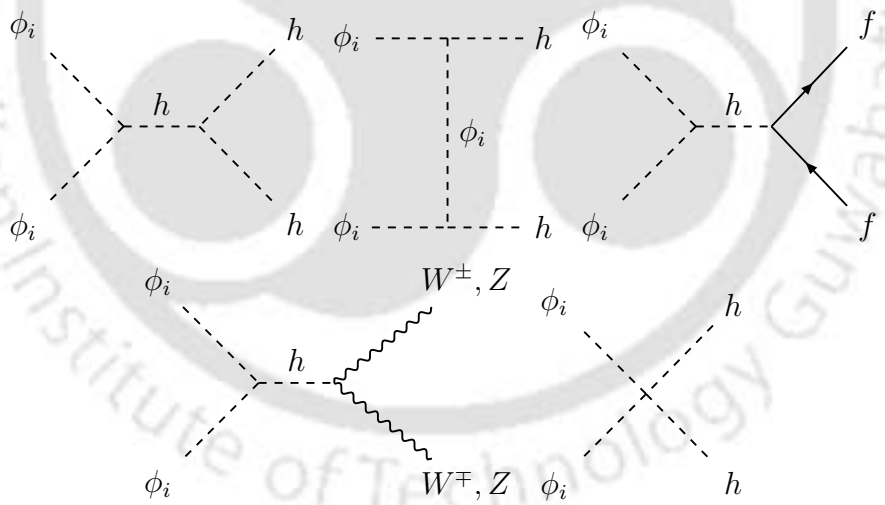

Figure 2.2: Feynman diagrams relevant to the production of singlet scalar WIMP as in Eq. (2.1), where f denotes the SM leptons and quarks.

The relic density is defined in terms of the yield Y_{ϕ_i} after freeze out, as,

$$\Omega_{\phi_i}h^2 = 2.744 \times 10^8 m_{\phi_i}Y_{\phi_i}\left[x_0\right] \,, \tag{2.3}$$

where $x_0 = m_{\phi_i}/T_0$, with $T_0 = (2.34855 \pm 0.00049) \times 10^{-13}\ GeV\ (1\sigma)$ [249] is the present-day CMB temperature. In Fig. 2.3, we present the solution of Eq. (2.2), indicated by the thick lines. Increase in the parameter λ_{iH} leads to enhancement in the rate of $\phi_i\,\phi_i \to \mathrm{X}\,\mathrm{X}$ interactions, which progressively delays the freeze out and reduces the relic density. For a comprehensive analysis and the constraints derived from direct, indirect, and collider searches for this model, see [250–252].

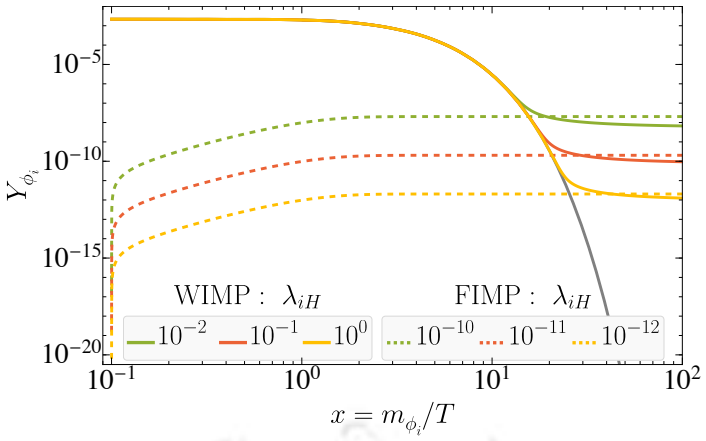

Figure 2.3: Plot represents the relic yields for the conventional freeze-out (solid colored) and freeze-in (dashed colored) as a function of m_{ϕ_i}/T, while the grey thick line indicates DM yield in equilibrium. Different colored lines correspond to different choices of Higgs portal coupling (λ_{iH}) as mentioned in the figure inset, for a fixed DM mass $m_{\phi_i} = 40\ GeV$.

SIMP: An example

Freeze-out of DM may also occur via number changing processes like $3_{\rm DM} \to 2_{\rm DM}$ (or $4_{\rm DM} \to 2_{\rm DM}$) annihilations within the dark sector, while the $2_{\rm DM} \to 2_{\rm SM}$ annihilation is suppressed. The order of DM mass has to account for the suppression in the phase space and usually comes around MeV to provide the correct relic density. The coupling for such a number-changing process within the dark sector also requires to be quite large. Hence, such a class of DM is called Strongly Interacting Massive Particle (SIMP) [253, 254]. The simplest model example could be that of a real scalar DM as described in Eq. (2.1). As the freeze-out occurs here mainly through

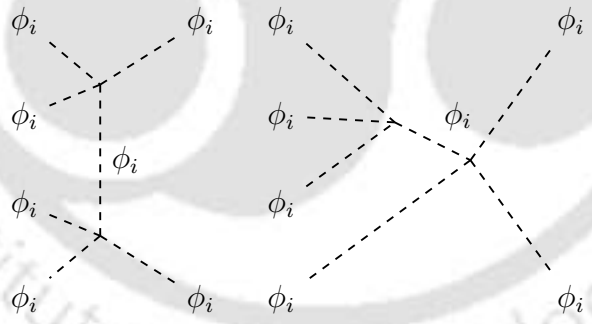

Figure 2.4: Feynman diagrams relevant to the possible self-annihilation of a real scalar DM as in Eq. (2.1) for SIMP like solution.

$N_{\rm DM} \to N'_{\rm DM}$ ($N_{\rm DM} \geq N'_{\rm DM}$) interactions, the dominant process will be $4_{\rm DM} \to 2_{\rm DM}$ annihilation channels, as illustrated in Fig. 2.4, since the $3_{\rm DM} \to 2_{\rm DM}$ interactions are forbidden by $\mathcal{Z}_2$ symmetry. The Higgs portal suppressed BEQ, assuming that the dark sector and SM bath share the same temperature when kinetic equilibrium is maintained via $\phi_i + {\rm SM} \to \phi_{\rm i} + {\rm SM}$ scattering, is [254]

$$\dot{n}_{\phi_i} + 3\mathcal{H} n_{\phi_i} = -\frac{1}{2}\langle \sigma v^3 \rangle_{4\to 2} \left[n^4_{\phi_i} - n^2_{\phi_i} n^2_{\phi_i,0} \right] , \tag{2.4}$$

where a factor of $1/2$ arises to account for $4 \to 2$ processes. Correct relic abundance is achieved for $m_{\phi_i} \lesssim 1$ MeV, although the parameter space is strongly constrained

by self-interaction bounds derived from cluster observations. However, this restriction on m_{ϕ_i} is alleviated when kinetic equilibrium is not maintained, leading to significant deviations between the dark sector temperature and the SM thermal bath temperature. For a detailed phenomenological discussion regarding such implications, refer to [255]. Substantial research efforts have been devoted in exploring the SIMP mechanism in various contexts, like too big to fail and core vs cusp problem, see for example, [256–264].

2.1.2 Non-thermal freeze-in

In this mechanism, DMs never reach equilibrium with the thermal bath particles due to its feeble interaction, and are produced from thermal bath particles out of equilibrium and freeze-in when the bath temperature falls below DM mass. The main proposition of such DM came in 2009 [265] , where they proposed Feebly Interaction Massive particle (FIMP) to be the DM.

`FIMP: An example`

The BEQ governing FIMP production is same as that of the WIMP, excepting for the fact that we omit the DM annihilation to SM, owing it to be out of thermal bath, and additionally we include the decay of thermal bath particles to DM[2]. Depending on the temperature at which DM is predominantly produced, two types of freeze-in (FI) mechanisms are proposed: (i) IR (infrared) freeze-in [265] and (ii) UV (ultraviolet) freeze-in [266]. In the case of infrared freeze-in, DM particles are produced at low energies (IR scale) through interactions involving lighter mediators or thermal particles present in the IR regime. Here, the relic density is particularly sensitive to the infrared regime, where thermal effects and low-energy interactions dominate. In contrast, in the UV FI scenario, DM production occurs at high energies (UV scale) through processes such as decay or scattering involving very energetic bath particles or mediated by very heavy particles with masses close to the UV/cutoff scale [267–272]. UV FI is often obtained from DM-SM higher dimensional effective interaction. Here, we focus mainly on the IR type freeze in. We can resort to the same scalar singlet DM model as described by Eq . (2.1), to be a FIMP like DM. Following Eq . (2.2), we can rewrite the BEQ for the production of FIMP type ϕ_i, as,

$$\dot{n}_{\phi_i} + 3\mathcal{H}n_{\phi_i} = 2\langle\Gamma\rangle_{\mathrm{X}\to\phi_i\ \phi_i}\left(n_{X,0} - n_{\phi_i}\frac{n_{X,0}}{n_{\phi_i,0}}\right) + 2\langle\sigma v\rangle_{\mathrm{X\ X}\to\phi_i\ \phi_i}\left(n^2_{X,0} - n^2_{\phi_i}\frac{n^2_{X,0}}{n^2_{\phi_i,0}}\right)\ , \quad (2.5)$$

where the factor 2 arises because of the production of two identical DMs in the final state. The main points behind the above equation are, (i) the tiny initial DM number density and, (ii) production rate is much smaller than the expansion rate ($\Gamma << \mathcal{H}$). Therefore, $\frac{n_{\phi_i}}{n_{\phi_i,0}} \ll 1$ is maintained, and we can always neglect the terms $\propto \frac{n_{\phi_i}}{n_{\phi_i,0}}$. The Feynman graphs for the scalar FIMP is shown in Fig . 2.5, and the solution of Eq . (2.5) is shown in Fig . 2.3 where the FIMP yield is dictated by the dashed lines where yield increases with the gradual enhancement of λ_{iH} and freezes in when $T \sim m_{\phi_i}$. Interestingly, if we gradually enhance the Higgs portal coupling λ_{iH} beyond a

[2]If the parent particles aren't in the thermal equilibrium, then one has to solve coupled BEQ, related to DM and parent particle simultaneously. It will be further added by a temperature equation if the parent particle is not in kinetic equilibrium with the thermal bath particles.

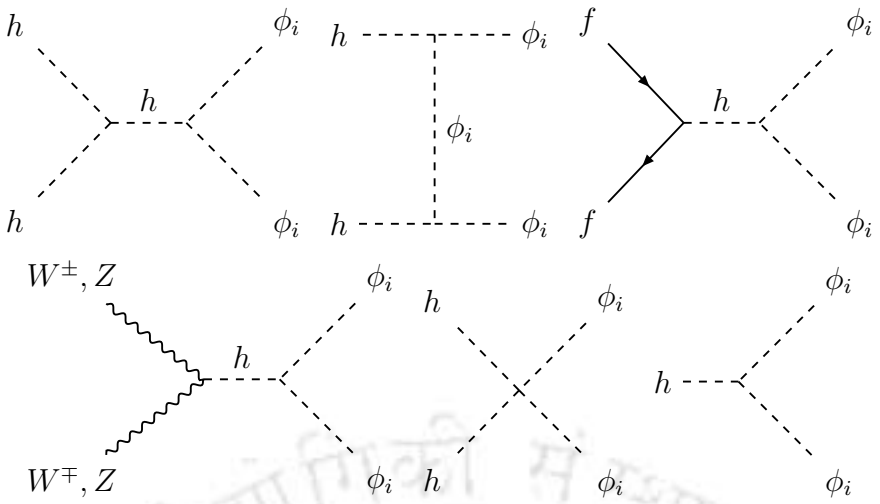

Figure 2.5: Feynman diagrams relevant for production of a real scalar DM following Eq. (2.1) as FIMP, where f denotes the SM leptons and quarks.

certain limit, then the DM reaches thermal equilibrium, when the production rate becomes larger than the Hubble rate [273]. It then provides either a WIMP or SIMP like solution as discussed before. Numerous scholarly articles are available in the literature [274–276] that can serve as references for exploring the potential of FIMP scenarios beyond the simplest case described here, providing deeper insights to its applicability and relevance.

2.1.3 Multicomponent dark matter

Multicomponent DM assumes the presence of more than one DM particle to constitute the dark sector. Why one should think of such possibilities ? Firstly, assuming that one particular kind of DM constitute 26% energy budget of the universe seems to be simplified as an assumption, where the 4% visible sector carries so many different kinds of particles and interactions. But how do we bother having more than one DM component in the universe? The answer to this that the DM-DM interaction crucially governs the DM freeze-out or freeze in, while it also affects the detectability. Another motivation for a multi-component DM model stems from the small-scale structure formation related issues [277, 278], such as the "Core – Cusp problem" [279–281], "Missing Satellites problem" [282–285], "Too Big to Fail problem" [286–288], or "Diversity problem" [289, 290], which arise because of the assumption of pure CDM consideration. One of the possibilities is to incorporate WDM along with CDM, which can help resolving these issues. While WDM smooths out small-scale structures, CDM continues to dominate on larger scales, ensuring that the formation of large-scale structures, such as the galaxy clusters, remains largely unaffected. Together, CDM and WDM preserve large-scale structures while improving the fit to the observed power spectrum of large-scale structures, which would be overproduced in presence of WDM alone. However, the feedback mechanism from baryonic matter (baryon feedback) [291–295], modified gravity theory [296, 297][3] etc., are adopted within pure CDM.

[3]Although these models have been constrained especially in light of cosmic microwave background observations [298], they may offer intriguing phenomenological fit at smaller scales [299].

In multicomponent frameworks, the constituent particles may be WIMP, FIMP, SIMP, etc. In this report, we consider two-component DM for simplicity, which encapsulates the DM-DM interaction. Some generic features of multipartite DM frameworks include:

- Relic under abundance of each individual DM component so that the total relic density satisfies the observed limit:

$$\Omega_{\rm DM}h^2 = \sum_i \Omega_i h^2 \,. \tag{2.6}$$

  This includes the possibility of dominance by one component, as well as equal sharing between them.

- The other important aspect is the effect in direct and indirect search, where each individual DM component possesses a modified effective scattering cross section limited by its fraction in the relic density:

$$\sigma^{\rm eff}_{\rm DD} = \frac{\Omega_i}{\Omega_{\rm DM}}\sigma^i_{\rm DD} \,, \tag{2.7}$$

$$\sigma^{\rm eff}_{\rm ID} = \frac{\Omega_i^2}{\Omega_{\rm DM}^2}\sigma^i_{\rm ID} \,. \tag{2.8}$$

- The most important aspect of two-component DM depends on the strength of DM-DM interaction. If the conversion rate is comparable to their individual production or annihilation rates, the DM-DM conversion affects their relic densities, as well as their detection prospects, as shown in WIMP-WIMP [300], WIMP-FIMP [301], SIMP-SIMP [302, 303], and FIMP-FIMP [304] setups.

A quick note here that conversion can even be instrumental in identifying a new class of DM, such as pseudo-FIMP (pFIMP) [305, 306], as we elaborate later.

A simple example

The simplest two component DM can arise with two real scalar DM components (ϕ_1 and ϕ_2) which are stable under $\mathcal{Z}_2 \otimes \mathcal{Z}_2'$ symmetry [300], extensively studied in literature. The Lagrangian is:

$$\mathcal{L} = \mathcal{L}_{\rm SM} + \mathcal{L}_{\phi_1} + \mathcal{L}_{\phi_2} - \frac{1}{4}\lambda_{\phi_1\phi_2}\phi_1^2\phi_2^2 \,, \tag{2.9}$$

where $\mathcal{L}_{\phi_{1,2}}$ is identical to that of Eq . (2.1), with $i = 1, 2$. The presence of mutual DM-DM interaction via $\lambda_{\phi_1\phi_2}$ makes the situation different from the single component case and results in a distinguishable feature. The Feynman graphs that produce the DM-DM conversion in this model is shown in Fig . 2.6. This two-component framework is dictated by five free parameters, $\{m_{\phi_1}, m_{\phi_2}, \lambda_{\phi_i}, \lambda_{\phi_1\phi_2}\}$. The choices of λ_i produce different kinds of DM combinations as illustrated in Table 2.1. To get the cosmological evolution of the DM components, one needs to solve the coupled BEQ (cBEQ),

$$\begin{aligned}
\dot{n}_{\phi_1} + 3\mathcal{H}n_{\phi_1} &= -\left[\langle\sigma v\rangle_{\phi_1\phi_1\to \rm X\,X}\left(n_{\phi_1}^2 - n_{\phi_1,0}^2\right) + \langle\sigma v\rangle_{\phi_1\phi_1\to\phi_2\phi_2}\left(n_{\phi_1}^2 - \frac{n_{\phi_1,0}^2}{n_{\phi_2,0}^2}n_{\phi_2}^2\right)\right] \,, \\
\dot{n}_{\phi_2} + 3\mathcal{H}n_{\phi_2} &= -\left[\langle\sigma v\rangle_{\phi_2\phi_2\to \rm X\,X}\left(n_{\phi_2}^2 - n_{\phi_2,0}^2\right) + \langle\sigma v\rangle_{\phi_2\phi_2\to\phi_1\phi_1}\left(n_{\phi_2}^2 - \frac{n_{\phi_2,0}^2}{n_{\phi_1,0}^2}n_{\phi_1}^2\right)\right] \,,
\end{aligned} \tag{2.10}$$

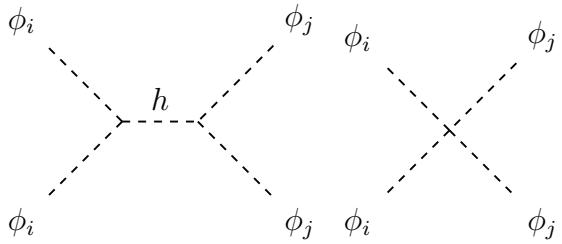

Figure 2.6: Feynman diagrams correspond to DM-DM conversion, where $\{i, j = 1, 2\}$.

where the presence of the conversion term makes the equations coupled. Solving the cBEQ numerically we compute the relic density of the DM species, see for details, Fig . 2.7 where in the left plot we show the WIMP-WIMP solution, and in the right plot we show the WIMP-FIMP solution.

Scenario	λ_{1H}	λ_{2H}	$\lambda_{\phi_1\phi_2}$	ϕ_1 detection possibility	ϕ_2 detection possibility
FIMP-FIMP	Feeble	Feeble	Feeble	No	No
WIMP-FIMP	Weak	Feeble	Feeble	Yes	No
FIMP-WIMP	Feeble	Weak	Feeble	No	Yes
WIMP-WIMP	Weak	Weak	Feeble	Yes	Yes
WIMP-WIMP	Weak	Weak	Weak	Yes	Yes
WIMP-pFIMP	Weak	Feeble	Weak	Yes	Yes
pFIMP-WIMP	Feeble	Weak	Weak	Yes	Yes

Table 2.1: Generic two-component real scalar DM scenario while some of them are studied and some of them not yet studied. "No" means it's very hard to detect in future experiments, and "Yes" means that there might be future detection possibilities.

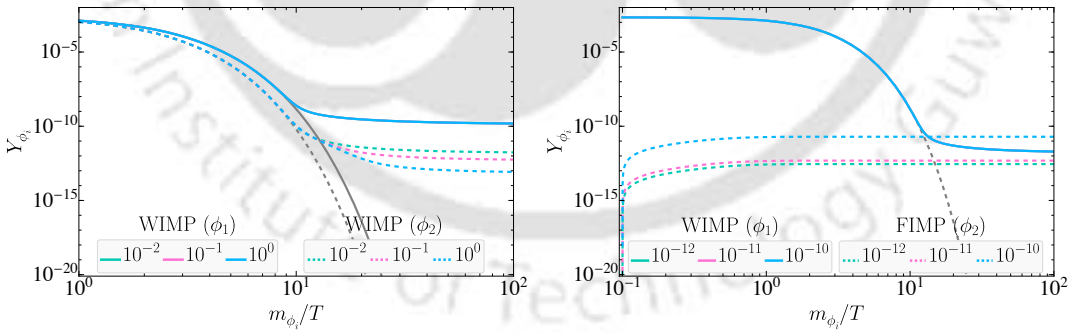

Figure 2.7: Figures representing the evolution of DM yields in two component model as in Eq . (2.9) with m_{ϕ_i}/T. *Left:* Freeze out for WIMP-WIMP ϕ_1 (solid colored), ϕ_2 (dashed colored) as a function of m_{ϕ_i}/T, while the grey lines indicate DM yields in equilibrium. Different colors correspond to different DM-DM interaction couplings ($\lambda_{\phi_1\phi_2}$) as mentioned in the figure inset, while $\lambda_{1H} = 10^{-2}$, $\lambda_{2H} = 10^{-1}$ and $m_{\phi_1} = 110$ GeV, $m_{\phi_2} = 130$ GeV are kept fixed. *Right:* Same as left, but for WIMP-FIMP scenario with $\lambda_{1H} = 10^{-1}$, $\lambda_{2H} = 10^{-11}$ making ϕ_2 FIMP (dashed) and ϕ_1 WIMP (thick). Different colors correspond to different $\lambda_{\phi_1\phi_2}$ as mentioned in the figure inset.

The detection possibilities of these two scalar DM arises through Higgs portal interactions. In presence of another DM, the DM-nucleon cross-section has to be further modified,

$$\sigma^{\rm eff}_{\phi_i {\rm N}} = \frac{\Omega_{\phi_i} h^2}{\Omega_{\rm DM} h^2} \sigma_{\phi_i {\rm N}} \,, \tag{2.11}$$

where, $\sigma_{\phi_i \mathrm{N}}$ is the ϕ_i-nucleon scattering cross section. In a similar way, the DM annihilation cross section into SM particles relevant in indirect searches can also be further modified as,

$$\langle \sigma v \rangle^{\mathrm{eff}}_{\phi_i \phi_j \to \mathrm{SM\ SM}} = \frac{\Omega_{\phi_i} h^2}{\Omega_{\mathrm{DM}} h^2} \frac{\Omega_{\phi_j} h^2}{\Omega_{\mathrm{DM}} h^2} \langle \sigma v \rangle_{\phi_i \phi_j \to \mathrm{SM\ SM}} \,. \tag{2.12}$$

We will come back to the specific features of the two component DM in a more focused discussion in the following chapters, but one may consult the following literature for some examples of WIMP-WIMP [300, 307–312], WIMP-FIMP [301, 313], and FIMP-FIMP[304, 314, 315] setups.

2.2 Dark Matter detection

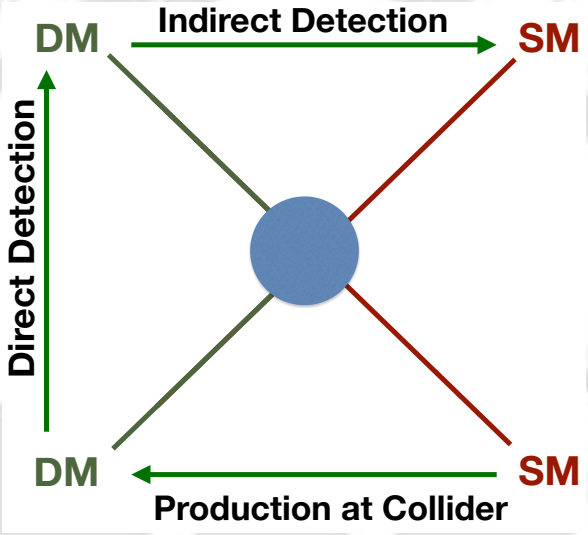

Figure 2.8: WIMP DM interaction with the SM particles via $2 \to 2$ process leads to different DM search strategies; DM annihilation produces indirect detection (ID) in the center of the galaxies, scattering of DM with SM provides direct detection (DD) of DM, and production of DM in collider experiments provide collider search strategies.

The possibility of DM detection lies in its non-gravitational interactions with visible sector. First of all, if the DM possesses feeble interaction with SM, the detection becomes difficult. This makes primarily the WIMPs prone to detections. Different ways of DM detection are shown in a cartoon in Fig . 2.8. The signals of DM annihilation in the Galactic center can be registered on Earth via indirect detection (ID). DM can be produced in colliders and might account for momentum or energy imbalance signatures (collider search). The possibility of DM scattering off a nucleus or electron can provide a direct detection (DD). We will discuss all such possibilities one by one.

2.2.1 Direct Detection

Direct detection experiments aim to measure the energy deposited when galactic DM particles scatter off detector materials [316–325]. Since Earth resides within the DM halo, DM particles continuously traverse terrestrial detectors and may occasionally interact with the detector material. However, detecting such events presents

significant challenges due to the extremely low scattering rates and the small energy deposits, typically ranging from $\mathcal{O}(\mathrm{k}eV)$ to $\mathcal{O}(\mathrm{e}V)$. To minimize background noise, these experiments are conducted deep underground, utilizing detectors constructed from ultra-pure materials. Direct detection experiments are categorized into two types: (i) DM scattering off atomic nuclei and (ii) DM scattering off electrons. The energy transferred (E_R) from DM to the target particle is approximately equal to the kinetic energy of the DM-nucleus (or DM-electron) system, given by $\sim \mu_r v_r^2/2$, where $\mu_r = m_{\rm DM} M/(m_{\rm DM}+M)$ represents the reduced mass of the system with $M = m_N$ (m_e), mass for nuclei (electrons), and $v_r \sim 10^{-3}c$ is the DM relative velocity in the galactic halo. The transferred momentum in non-relativistic elastic scattering is $\sim \sqrt{E_R m_{\rm DM}}$. Alternatively, inelastic scattering processes can occur, where DM is absorbed rather than scattered [326–329]. Our thesis focuses on elastic scattering, where electrons and nuclei are bound within the detector material. Beyond standard electron-nucleus scattering, several non-standard DM signals have been proposed, like (i) **Composite DM** [330, 331], where DM comprises composite objects rather than point-like particles and produces novel signals; (ii) **Self-Destructing DM** [332, 333], involving dark sector particles that decay inside the detector to produce SM particles; (iii) **Multi-Scattering** [334, 335], where ultra-heavy DM ($m_{\rm DM} \gtrsim 10\,\mathrm{T}eV$) undergoes multiple scatterings within the detector; (iv) **Boosted DM** [336–340], where DM particles, boosted via interactions with cosmic rays or energetic particles, allow exploration of lighter DM masses ($m_{\rm DM} \sim 100\,\mathrm{k}eV$); (v) **Secluded DM** [341–343], involving DM decoupled from SM particles but coupled to a lighter mediator, which subsequently decays into SM particles prior to Big Bang Nucleosynthesis (BBN) and interacts with detector material via mediator exchange; and (vi) **Exothermic DM** [344–346], where heavy dark sector particles transform into DM during DD scattering, resulting in exothermic reactions depositing significant energy in the detector. As non-observation of a DM signal via direct detection limit is progressively approaching the 'neutrino floor', a significant challenge arises in differentiating DM-nucleon scattering cross-sections from neutrino-induced backgrounds, see for example [347, 348].

Scattering with atomic nuclei

Let's assume that DM interacts weakly enough with SM particles so that it can reach the underground detectors. The DM-nucleus scattering ($\mathrm{DM},\ \mathrm{A} \to \mathrm{DM},\ \mathrm{A}$) event rate (number of events per time interval per target mass, m_T) is [324],

$$\frac{dR_{\rm ev}(E_R,t)}{dE_R} = \frac{dN_e}{dt}\frac{1}{m_T} = \sum_i \frac{N_{T,i}}{m_T}\int_{v>v_{\rm min}}^{\infty} \frac{d\sigma_{A,i}(E_R,v)}{dE_R} v \frac{\rho_\oplus}{m_{\rm DM}} f_\oplus(\boldsymbol{v}+\boldsymbol{v}_E(t))d^3\boldsymbol{v}\,, \quad (2.13)$$

where N_T denotes the number of target nuclei in the target mass m_T, and E_R represents the nuclear recoil energy. For multiple nuclei ($i > 1$), the integration over the DM velocity in the Earth's frame is performed, with the local DM density $\rho_\oplus$ assumed to match the solar neighborhood value, $\rho_\oplus = \rho_\odot \approx 0.4\ \mathrm{GeV/cm^3}$. $v = |\boldsymbol{v}|$ is the speed of DM in the experiment rest frame, and the velocity distribution $f_\oplus(\boldsymbol{v}+\boldsymbol{v}_\oplus(t))$ is measured in the Earth's frame. The differential cross-section is proportional to the inverse square speed of DM, and the velocity distribution can be

expressed as:

$$\eta(v_{\rm min}, t) = \int_{v>v_{\rm min}} \frac{f_{\oplus}(\boldsymbol{v} + \boldsymbol{v}_{\oplus}(t))}{v} d^3v \,. \tag{2.14}$$

The minimum velocity required, $v_{\rm min} = \sqrt{m_A E_R/(2\mu_r^2)}$, ensures the transfer of the kinetic energy E_R to the nucleus with, $E_R = E_{\rm th}$. The minimum threshold energy, $E_{\rm th}$, is determined by the properties of the detector materials. The maximum velocity is defined by the DM escape velocity from the Galaxy ($v_{\rm esc} \approx 550$ km/s), transformed into the Earth's reference frame using Galilean Transformation. The underlying particle physics is encapsulated in the DM-nucleus scattering cross-section, $\frac{d\sigma_A}{dE_R}$. Rather than directly calculating DM-nucleus scattering, we evaluate DM-nucleon scattering (assuming the nucleons within the nucleus are non-relativistic) and then extrapolate to the nucleus level. Depending on the nuclear spin, the non-relativistic interaction can be classified as (i) spin-dependent (SD) scattering involving the nuclear spin or (ii) spin-independent (SI) scattering, which is independent of nuclear spin. If an SI interaction is present, it predominantly contributes to DM-nucleus scattering due to coherent enhancement effects.

The time average of DM-nucleus scattering cross-section is the sum of the SI and SD contributions [72],

$$\frac{d\sigma^A_{\rm SI}}{dE_R} = \frac{m_A}{2v^2\mu_N^2} A^2 \sigma^N_{\rm SI} F^2_{\rm SI}(E_R) \,, \tag{2.15}$$

$$\frac{d\sigma^A_{\rm SD}}{dE_R} = \frac{m_A}{2v^2\mu_N^2} A^2 \sigma^N_{\rm SD} S(q) \,, \tag{2.16}$$

where $\sigma^N_{\rm SI}$ ($\sigma^N_{\rm SD}$) is the SI (SD) DM-nucleon scattering cross-section, $F_{\rm SI}(E_R)$ is the SI nuclear form factor [349, 350] and $S(q)$ is the SD nuclear response function [350–353]. The DM-nucleon scattering cross-section is given by,

$$\sigma^N_{\rm SI} = \left(\frac{Z f^p_N + (A-Z) f^n_N}{A f^{p(n)}_N} \right)^2 \sigma^{p(n)}_{\rm SI} \,, \tag{2.17}$$

$$\sigma^N_{\rm SD} = \sigma^p_{\rm SD} + \sigma^n_{\rm SD} \,, \tag{2.18}$$

where $\sigma^{p(n)}_{\rm SI(SD)}$ is the SI (SD) DM scattering cross-section with a single proton (neutron), and $f^{p(n)}_N$ is the coupling of DM with non-relativistic proton (neutron). A is the atomic mass number of the nucleus with charge Z, $\mu_N = m_N m_{\rm DM}/(m_N + m_{\rm DM})$ is the reduced mass of the DM-nucleon system, the momentum exchange rate is $q = \sqrt{2 m_A E_R}$ and the mass of the nucleus is defined as $m_A \approx A m_N$. As the transfer energy is $\sim \mathcal{O}(10 - 100)$ keV, much smaller than binding energy per nucleon and gives transfer momentum $q \sim \mathcal{O}(10 - 100)$ MeV, while $1/q$ is the same order as of the nuclear radius $A^{1/3}$ fm, nuclei are not point-like objects to a DM, and require nuclear form factor. In the limit of small momenta transfers, $q \to 0$, the integrated cross section for DM scattering on the nucleus is,

$$\sigma^A_{\rm SI}|_{q\to 0} = A^2 \sigma^N_{\rm SI} \frac{\mu^2_{\rm DM\ A}}{\mu^2_{\rm DM\ N}} \,, \tag{2.19}$$

$$\sigma^A_{\rm SD}|_{q\to 0} = \sigma^N_{\rm SD} S(q \to 0) \frac{\mu^2_{\rm DM\ A}}{\mu^2_{\rm DM\ N}} \,. \tag{2.20}$$

From the above equations, we can say that compared to the SI scattering cross-section, the SD cross-section lacks the A^2 coherent enhancement factor, resulting in a weaker experimental constraint. So, in the left plot of Fig . 2.9, we only have illustrated the most stringent constraints on the SI scattering cross-section to date, derived from underground detectors employing various target materials. During the calculation of Eq . (2.18), we integrated out the heavier mediator if the mediator mass significantly exceeds the typical momentum transfer in DD[4], and the rest of the calculation follows the effective theory approach. The stringent lower bounds, from different experiments, on the SI DM-nucleon scattering cross section are shown in Table 2.2.

However, the event rate in Eq . (2.13) should be modified in the presence of one or more additional DM components [354, 355]. This modification induces a kink in the recoil rate spectrum, which could serve as a signature of multicomponent DM if a viable signal is detected in future DM-nuclear scattering experiments. We elaborate on it later.

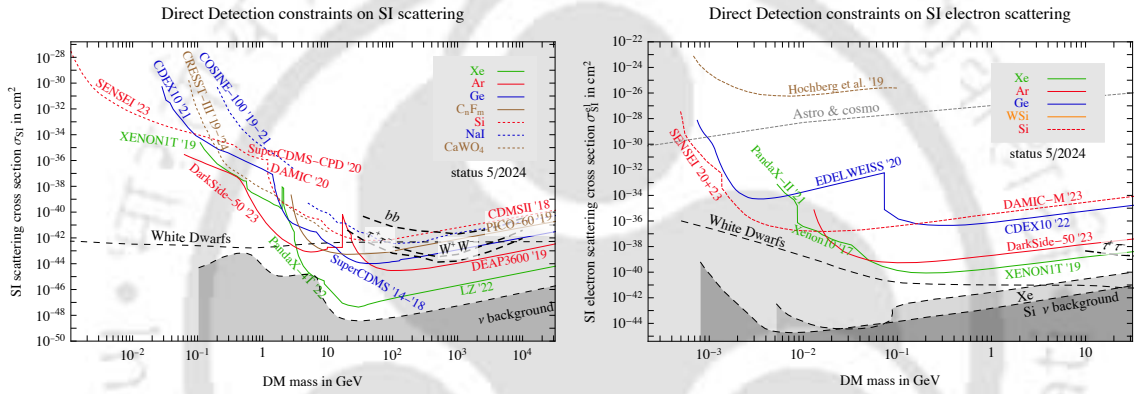

Figure 2.9: The upper limits on the SI DM-nucleon (left) and electron (right) scattering cross-section as a function of DM mass. Adapted from [72].

Experiment	Target	Fiducial Mass (kg)	Cross Section (cm^2)	Ref.
SI high mass ($> 5\ GeV$)				
LUX-ZEPLIN	Xe	4200	2.1×10^{-48}	[356]
PandaX-4T	Xe	2670	3.8×10^{-47}	[357]
XENONnT	Xe	4180	2.6×10^{-47}	[358]
SuperCDMS	Ge	12	1.0×10^{-44}	[359]
DarkSide-50	Ar	20	1.9×10^{-43}	[360]
DEAP-3600	Ar	2000	3.9×10^{-45}	[361]
SI low mass ($< 5\ GeV$)				
LUX (Migdal)	Xe	118	6.9×10^{-38}	[362]
XENON1T (Migdal)	Xe	1042	3×10^{-40}	[363]
XENON1T (ionisation only)	Xe	1042	3.6×10^{-41}	[364]

[4]For a light mediator ($q \gg m_{\text{mediator}}$), the point interaction assumption is replaced by long-range interactions, causing the amplitude to depend on q^2. This dependence is directly incorporated into the expression for the differential cross section for DM scattering on nuclei, Eq . (2.18).

Experiment	Target	Fiducial Mass (kg)	Cross Section (cm^2)	Ref.
DarkSide-50 (ionisation only)	Ar	20	1.4×10^{-42}	[360]
SuperCDMS (CDMSlite)	Ge	0.6	2×10^{-40}	[365]
SuperCDMS (CDMSlite, Migdal)	Ge	0.6	6×10^{-38}	[366]
CRESST	$CaWO_4$-O	0.024	1×10^{-39}	[367]
CRESST	Si	0.0035	4.5×10^{-32}	[368]
DAMIC	Si	0.3	1×10^{-40}	[369]
NEWS-G	Ne	0.3	1×10^{-38}	[370]

Table 2.2: The limits from DD experiments on SI (for high $> 5\ GeV$ and low $< 5\ GeV$ masses) DM-nucleon scattering cross section. These data are taken from [18].

Scattering with electrons

The phenomenology of DM-electron scattering is mainly governed by the fact that electrons are bound in atomic, molecular, and solid-state systems. The lighter DM implies smaller kinetic energy and thus deposits smaller momentum exchange in the scattering events. The current constraints on DM-electron scattering are presented in the right plot of Fig. 2.9. Let us discuss the methodology of determining limits from experiments. The event rate per unit target mass for DM scattering with bound electrons in a target material of volume V and mass m_T is expressed as [371, 372]:

$$R_{\rm ev} = \frac{1}{\rho_T} \int dn_{\rm DM} \frac{V d^3\mathbf{p}_2}{(2\pi)^3} \sum_f |\langle f, \mathbf{p}_2 | H_{\rm int} | i, \mathbf{p}_1 \rangle|^2 (2\pi) \delta(E_f - E_i + E_2 - E_1)\,, \quad (2.21)$$

where $\rho_T = m_T/V$ represents the mass density of the target material, $p_{1(2)}$ denotes the four-momentum of the incoming (outgoing) DM, and $H_{\rm int}$ is the non-relativistic Hamiltonian describing the interaction between DM and electrons. The states $|i\rangle$ and $|f\rangle$ are the initial and final states of the detector, with corresponding energies E_i and E_f. Additionally, $n_{\rm DM}$ denotes the number density of DM particles, with their velocity given by $\boldsymbol{v} = \mathbf{p}_1/m_{\rm DM}$. However, the interaction can be written in terms of the products of DM and electron currents as [373],

$$\begin{aligned} \langle f, \mathbf{p}_2 | H_{\rm int} | i, \mathbf{p}_1 \rangle &\equiv \int \frac{d^3\mathbf{q}}{(2\pi)^3} \langle \mathbf{p}_2 | \mathcal{O}_{\rm DM} | \mathbf{p}_1 \rangle \langle f | \mathcal{O}_{\rm el} | i \rangle \\ &= \frac{1}{V} \sqrt{\frac{\pi \bar{\sigma}(q)}{\mu^2_{\rm DM-e}}} \langle f | \mathcal{O}_{\rm el} | i \rangle\,, \end{aligned} \quad (2.22)$$

where $q = |\mathbf{q}|$, $\mu_{\rm DM-e} = m_{\rm DM} m_e/(m_{\rm DM} + m_e)$. The $\mathcal{O}_{\rm el}$ and $\mathcal{O}_{\rm DM}$ operators only act on the target system and DM states, respectively. In the above equations, we have used the plane wave state for DM (e.g., $e^{i\mathbf{q}_1 \cdot \mathbf{r}}/\sqrt{V}$) and $\mathbf{q} = \mathbf{q}_1 - \mathbf{q}_2$. Using the Eq. (2.22),

Eq . (2.21) becomes,

$$R_{\rm ev} = \frac{1}{\rho_T}\frac{\rho_\oplus}{m_{\rm DM}}\int d^3\boldsymbol{v} f_{\rm DM}(\boldsymbol{v})\int \frac{d^3\mathbf{q}}{(2\pi)^3}d\omega\delta(\omega+E_2-E_1)\frac{\pi\overline{\sigma}(q)}{\mu^2_{\rm DM-e}} \times \underbrace{\frac{2\pi}{V}\sum_f |\langle f|\mathcal{O}_{\rm el}(\mathbf{q})|i\rangle|^2\delta(E_f-E_i-\omega)}_{S(\mathbf{q},\omega)} . \tag{2.23}$$

In the above expression, the term $S(\mathbf{q},\omega)$ is called the dynamic structure factor, and it depends on the dynamics of the target material; the momentum transfer $\mathbf{q}$ with energy deposited ω by DM in the target material,

$$\omega = E_2 - E_1 = \mathbf{q}.\boldsymbol{v} - \frac{\mathbf{q}^2}{2m_{\rm DM}} . \tag{2.24}$$

Therefore, the minimum required velocity

$$v_{\rm min}(q,\omega) = E_2 - E_1 = \frac{\omega}{q} - \frac{q}{2m_{\rm DM}} . \tag{2.25}$$

For the isotropic approximation for the target materials (only dependent on q, not on $\mathbf{q}$), we obtain [371],

$$R^{\rm iso}_{\rm ev} = \frac{1}{\rho_T}\frac{\rho_\oplus}{m_{\rm DM}}\int \frac{qdq}{(2\pi)^2}d\omega\,\eta(v_{\rm min}(q,\omega))\frac{\pi\overline{\sigma}(q)}{\mu^2_{\rm DM-e}}\delta(\omega+E_2-E_1)S(\mathbf{q},\omega) , \tag{2.26}$$

where $\eta(v_{\rm min}) = \int_{v_{\rm min}}^{\infty} d^3\boldsymbol{v}\frac{f_{\rm DM}(\boldsymbol{v})}{v}$. The term $\overline{\sigma}(q)$ is reduced to scattering of DM on 'free electrons' in the limit of the heavy mediator with momentum transfer $q \to 0$. However, in the literature, the fiducial cross-section is commonly used with $\sigma_T = \overline{\sigma}(q_0)$ where $q_0 = 1/a_0 \simeq 3.7\ keV$ and $\overline{\sigma}(q) = \sigma_T F^2_{\rm DM}(q)$, where $F_{\rm DM}(q)$ is called the *DM form factor*. If we assume DM interacts directly with electrons, then the cross-section $\overline{\sigma}_e$ is written as [372],

$$\overline{\sigma}_e \equiv \frac{\mu^2_{\rm DM-e}}{16\pi m^2_{\rm DM} m_e^2}\overline{|\mathcal{M}_{\rm DM-e}(q)|^2}|_{q^2=\alpha^2 m_e^2} . \tag{2.27}$$

For a bound electron with a binding energy E_B, DM particle of mass $m_{\rm DM} \geq 250\,{\rm keV}\times\frac{E_B}{1\,{\rm eV}}$ can, in principle, be probed. The resulting signal depends on the material, which may consist of one or more electrons (in semiconductors, noble liquids, or graphene), one or more photons (in scintillators), phonons (in superconductors and superfluids), or quasiparticles (in superconductors). In general, the differential event rate for ionization is written as [372],

$$\frac{dR_{\rm ion}}{dE_e} = \frac{1}{E_e}\frac{1}{\rho_T}\frac{\rho_\oplus}{m_{\rm DM}}\frac{1}{8\mu^2_{\rm DM-e}}\int dq\, q\,\overline{\sigma}|f_{\rm ion}(k_e,q)|^2\eta(v_{\rm min}) , \tag{2.28}$$

where the minimum DM velocity for obtaining an ionizing state with an outgoing electron with energy E_e is given by $v_{\rm min} = (E_e + E_B)/2 + q/2m_{\rm DM}$ and $f_{\rm ion}$ is the ionization form factor given in [372].

The Migdal effect

The DM scattering on atoms can induce a process in which DM initially interacts with the atomic nucleus, causing the nucleus to recoil. This recoil generates a perturbation that transfers momentum to the surrounding electron cloud, resulting in an electron ejection. This phenomenon is known as the Migdal effect [374–378]. It is a $2 \to 3$ process, where an incoming DM particle and an atom scatter, producing a final state comprising of an outgoing DM particle, an ionized atom, and a free electron. This mechanism is distinct from elastic DM/nucleus (or DM/atom) scattering, as discussed previously. Elastic and inelastic DM/atom scatterings yield different experimental signatures: while elastic scatterings produce only nuclear recoils, inelastic processes result in both nuclear recoils and the ejection of free electrons within the detector. The latter signature is more analogous to those arising from DM-electron scatterings. Because the detection thresholds for electron excitations are generally lower, the Migdal effect provides an way to enhance the sensitivity of conventional DM detectors to DM/nucleus scattering, particularly for lower DM mass ranges. In this thesis, our focus is mainly on DM-nuclear scattering.

2.2.2 Indirect Detection

The DM, despite being a microscopic constituent, can exert significant and measurable macroscopic effects on astrophysical systems. The indirect searches of DM, which entails searching for SM particles produced through DM interactions, represent another method for DM detection, as illustrated in Fig . 2.8. This detection method focuses on identifying an excess in cosmic ray fluxes observed on or near Earth, which may result from the annihilation or decay of DM particles within the galactic halo or beyond [379]. These byproducts include detectable species such as gamma rays, neutrinos, and antimatter particles[5]. The production rate of these particles depends on three key factors: (i) the annihilation (or decay) rate of DM particles, (ii) the density of particle pairs (or individual particles, in the case of decay) in the region of interest, and (iii) the number of final-state particles produced per annihilation (or decay) event. The production rate of a final-state particle f per unit volume, arising from DM annihilation and decay, can be expressed as [18]:

$$\Gamma_f^A = c\frac{\rho_{\rm DM}^2}{m_{\rm DM}^2}\langle\sigma v\rangle N_f^A\,; \qquad \Gamma_f^D = c\frac{\rho_{\rm DM}}{m_{\rm DM}}\frac{1}{\tau_{DM}}N_f^D\,; \tag{2.29}$$

where $\langle\sigma v\rangle$ is the thermally averaged cross-section times relative velocity (we will define it more precisely later), $\rho_{\rm DM}$ is the physical density of the DM, N_f^A is the number density of the final state particles f produced by an individual annihilation event, $c = 1/2$ $(1/4)$ when particle and antiparticle are the same (different) and $\tau_{\rm DM}$ is the lifetime of DM.

In general, the particles produced by DM annihilations or decays, which we aim to detect, consist of all the stable Standard Model species: photons [381–383], neutrinos [384–386], positrons [387–389], anti-helium [390–392], antiprotons [393–395], anti-deuterons [396–398] amongst others.

[5]Typically, DM annihilation could produce both particle and antiparticle with equal amount, while, in the astrophysical background, the anti-matter production is less likely compared to matter particles [380].

Photons: High-energy photons ($\gamma-$rays) freely propagate in the galaxy, carrying information about DM in their energy spectrum and angular distribution. Being electrically neutral, DM produces photons only via subdominant mechanisms, such as charged-particle loops or ancillary radiation, resulting in a suppressed, model-dependent photon flux. These photons, generated directly through DM-related processes without environmental interactions, are called prompt $\gamma-$rays. On the other hand, low-energy photons (e.g., X-rays, radio waves) from DM can arise indirectly via interactions like inverse Compton scattering, synchrotron emission, or bremsstrahlung, depending on astrophysical factors such as magnetic fields and gas density. These are termed secondary radiation. Low-energy photons can however originate directly from the decay of light DM particles with masses in the keV to MeV range.

Positrons: They diffuse through galactic magnetic fields, randomizing their directions and obscuring direct traces to the DM distribution. Information of DM is thus contained in the energy spectrum, which is altered as positrons lose energy through synchrotron emission, Coulomb scattering, ionization, bremsstrahlung, and inverse Compton scattering. Below a few GeV, solar activity distorts the spectrum, and below $\sim 1\ GeV$, positrons are deflected and cannot penetrate the solar system. High-energy positrons from nearby galactic regions are less affected by diffusion and losses, offering clearer indication to DM contributions.

Neutrinos: Being electrically charge neutral, neutrinos travel freely through the Galaxy and can also pass through the dense matter of the Earth and the Sun, up to multi$-TeV$ energies. Due to their small interaction cross-sections, detecting neutrinos is more challenging than detecting gamma rays or positrons. Additionally, their energy is often only partially reconstructed, as they are measured indirectly through charged particles (e.g., up-going muons) produced when a neutrino interacts with the material of a neutrino telescope or the surrounding rock, water, or ice. However, neutrino interaction cross-section increases with energy, partially compensating the reduced flux at larger DM masses. Potential sources of neutrinos from DM are similar to those of photons, with the Sun's center being a significant source and to a lesser extent, the Earth.

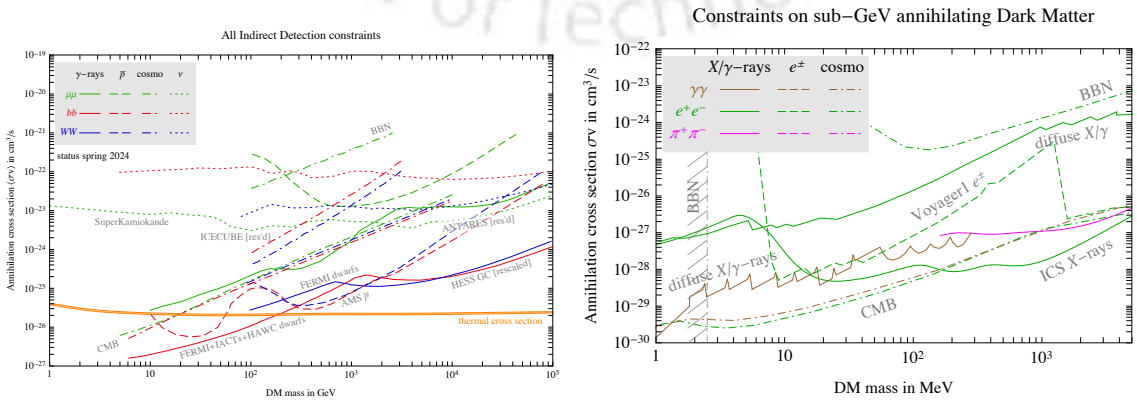

Figure 2.10: The current most stringent bounds on weak-scale DM annihilations for $GeV \lesssim$ (left) and $GeV \gtrsim$ (right) DM mass. Adapted from [72].

Numerous searches for DM annihilation or decay signals via ID yielded no conclusive excess. As a result, these measurements only establish upper bounds on the DM annihilation cross-section or decay rate. These limits are derived by ensuring that the flux from DM, potentially combined with known or assumed astrophysical backgrounds, does not exceed the observed flux. The results are typically presented in the $m_{\rm DM} - \langle\sigma v\rangle$ and $(m_{\rm DM} - \tau_{\rm DM})$ planes, where for annihilation (decay), regions above (below) the limiting lines are excluded. Extensive searches have focused on weak-scale DM with masses ranging from GeV to $100\ TeV$ over the past decades. The left plot in Fig . 2.10 presents a selection of the most relevant bounds from various observations ($gamma$: FERMI-LAT [399–405], VERITAS [406, 407], MAGIC [408–410], HESS [411–413] etc,. $neutrino$: ANTARES [384, 414, 415], IceCube [416–418], BAIKAL [419, 420] and so on), obtained by DM annihilations to SM particles listed in [72]. For the DM with masses ranging from MeV to GeV, the ID constraints are shown in the right plot of Fig . 2.10. The kinematically allowed annihilation or decay channels include $\gamma\gamma$, neutrinos, e^+e^-, and $\mu^+\mu^-$, which are dominant for the indirect searches of low-mass DM; for an exclusive list, see [421]. For super-heavy DM with $m_{\rm DM} > 100\ TeV$, a special mechanism for DM annihilation is needed to avoid unitarity constraints; and the indirect constraints are mainly applicable to the DM decay time. Several collaborations, including HAWC [422], MAGIC [423], and LHAASO [424], have placed limits on decay time based on data from high-energy cosmic ray observations, such as IceCube, Telescope Array, and the Pierre Auger Observatory among others. Recently, the HAWC collaboration also derived constraints on the annihilation of super-heavy DM [425]. This thesis focuses mainly on the annihilation of DM within the mass range of MeV to GeV.

2.2.3 Collider Searches

An important method for detecting DM involves its production in particle colliders, as schematically depicted in Fig . 2.8, where it can be investigated rigorously in a manner comparable to the searches for SM particles. Investigations in this area yield viable signal predictions, despite the lack of any positive detection yet, across a wide range of DM masses, interaction couplings, and spin states, which constitute the most critical parameters for DM signal identification alongside experimental sensitivity. The indication of DM production at collider is obtained via missing energy $\not{E}$[6], or missing transverse momentum $\not{E}_T$[7], as DM interacts minimally with ordinary matter and traverses the detector undetected, thereby creating energy and momentum imbalance. This signature is further constrained by background processes. Beyond this scope, DM may coexist with additional states, such as new heavy mediators (referred to as long-lived particles, LLP), which may decay into SM particles, resulting in detectable signatures in particle detectors. These signatures are mostly model-dependent, and extensive literature has been devoted to their investigation. To date, no statistically significant DM signal have been confirmed.

[6]The missing energy is defined as the difference between the center-of-mass-energy and the sum of the energies of all detected particles, as $E_{\rm miss} = \sqrt{s} - \sum_i E_{{\rm detected},i}$. Naturally, this requires precise knowledge of the center-of-mass energy of the collider, which is possible at ILC, but not at LHC.

[7]$\not{E}_T$, is defined as the magnitude of the vector sum of the transverse momenta (p_T) of all detected particles, as: $\not{E}_T = \sqrt{\left(\sum_i p_{x,i}\right)^2 + \left(\sum_i p_{y,i}\right)^2} \equiv |\vec{p}_T^{\rm miss}|$, where, $\vec{p}_T^{\rm miss}$, is given by: $\vec{p}_T^{\rm miss} = -\sum_i \vec{p}_{T,i}^{\rm vis}$, where, $\vec{p}_{T,i}^{\rm vis}$ represents the transverse momentum of the i-th visible particle.

Amongst several types of colliders [426] designed to explore the different aspects of HEP, the ongoing (I) Large Hadron Colliders, and proposed (II) Lepton Collider can be useful for DM searches.

Hadron Colliders accelerate hadrons (mainly proton or anti protons) to very high energy and collide them. Examples include: (i) the Tevatron [427], a proton-antiproton collider, which ran in Fermilab, and was decommissioned in 2011 ; (ii) the Large Hadron Collider (LHC) [428–430], currently the most powerful proton-proton collider in operation at CERN, has played a pivotal role in the discovery of the Higgs boson and the investigation of BSM phenomena ; (iii) the Superconducting Super Collider (SSC) [431], was proposed in 1990s, but never started ; (iv) the Future Circular Collider (FCC) [432–434], a proposed project at CERN, aims to achieve unprecedented energy levels to facilitate the exploration of DM, supersymmetry, and other BSM physics ; (v) the Super Proton-Proton Collider (SPPC) [435] is another proposed collider designed to extend the frontiers of high-energy particle physics .

Lepton Colliders accelerate leptons for high energy collisions. The salient feature of this collider is the absence of QCD backgrounds, as leptons do not participate in strong interactions, unlike hadrons. The operational and proposed lepton colliders are detailed as follows: (i) the Large Electron-Positron Collider (LEP) [436] was decommissioned after providing essential data for the exploration of the EW sector and Z-boson physics. (ii) the International Linear Collider (ILC) [437, 438] is a proposed high-precision electron-positron collider, designed to investigate HEP phenomena, including the Higgs boson, DM, and other beyond Standard Model (BSM) phenomena. (iii) the Circular Electron-Positron Collider (CEPC) [439] is another proposed collider aimed at exploring both the SM and BSM phenomena. (iv) the Compact Linear Collider (CLIC) [440] is a proposed linear collider at CERN, designed to probe SM and BSM physics at energy scales exceeding those of the ILC.

In addition, several other kinds of colliders are either operational, proposed, or decommissioned: (i) the Relativistic Heavy Ion Collider (RHIC) [441], which is currently operational; (ii) the Nuclotron-based Ion Collider Facility (NICA) [442], which is proposed; (iii) the Hadron-Electron Ring Accelerator (HERA) [443], which has been decommissioned; and (iv) The Plasma Wakefield Accelerators (PWFA) [444], etc. In this thesis, we will address BSM physics associated with the ongoing LHC and the proposed ILC.

A conventional particle detector is capable of detecting only the lightest particles, which are either stable or possess sufficiently long lifetimes on the timescales associated with particle colliders. It generates measurable signatures, such as electrons, photons, muons, quarks, gluons, and neutrinos. However, heavier particles can be identified through the analysis of their decay products. Discriminating between the missing energy associated with light particles (e.g., neutrinos) and heavy particles (e.g., DMs) presents a non-trivial challenge [445–447]. Following production, DM particles typically escape the detector without interacting with the detector materials. Consequently, the signal from these particles can only be detected if SM particles are produced in conjunction with the DMs. In presence of heavy dark sector particles, signals like multi lepton, or multi jet along with missing energy or missing transverse momentum emerges.

In the absence of extended dark sector, signals such as mono-X plus E_T^{miss} provides the only option, (where X can be a radiated photon, jet, Higgs boson, W, or Z^0 boson) [448–451]. The lack of any NP signal at the LHC thus far suggests that the NP scale is either too high to be produced at the LHC or light but too weakly coupled to the SM particles, making it insufficiently detectable. In low energies, these heavy NP particles can be integrated out and made a non-renormalizable effective operator, and DMs are produced via these higher dimensional operators [452, 453]. The DM searches via the EFT operator attempt to avoid dealing with a plethora of DM model possibilities, but here, it does not capture the on-shell production of a mediator. For that, *'simplified model'* approach is adopted, to describe the physics of mediators between DM and SM [454–459].

Apart, one also looks for (i) *Excess in Resonant Peaks*, (ii) *Long-Lived Particle tracks or displaced vertices*, (iii) *Anomalous Jet Structures*, (iv) *Rare Decay Channels* including (a) Higgs invisible decay [8], (b) Z boson invisible decay [9], (c) Rare Flavor-Changing Neutral Currents (FCNCs) events with MET, (d) Lepton Flavor Violating Decays with Missing Energy, (e) B-meson decays to invisible states to search for DM. In this thesis, we discuss some mono-X and di-lepton plus missing energy signals for a simplified model in Chapter 6.

2.3 Objective of the Thesis

After the introduction to physics beyond the SM, and DM physics, we are ready to define the objective of the thesis. We wish to explore extended dark sector of the universe, having more than one particle, that may be a second DM component, or a heavy dark sector particle decaying to DM. In this context, we wish to assume them of different kinds, like WIMP, FIMP, or SIMP. The existing literature mostly focuses onto WIMP-WIMP combination, but here we go beyond that. Our approach has been to address both cosmological and phenomenological features that such models bring forth and we wish to find out the generic features of such frameworks in a model independent and minimalistic way.

One of the major questions asked is, if we can find a novel signature of multiparticle DM sector. There was a proposal that a kink in the recoil energy spectrum for the DM direct search can provide such a hint for WIMP-WIMP scenarios. However, no UV complete model could be thought of. We study a model where such signals can be seen after addressing cosmological and other constraints. Actually, our analysis hints towards a class of models where such features can be observed. This is elaborated in Chapter 3.

When we take up WIMP-FIMP set up, the DM-DM conversion process being feeble, hardly affects either WIMP or FIMP physics. However, depending whether the freeze-in of the FIMP and freeze-out of the WIMP happening before or after Electroweak Symmetry breaking (EWSB), provides some interesting phenomenological distinctions. We study such a prospect in Chapter 4 for a scalar-vector boson WIMP-FIMP set up.

[8] The observed (expected) upper limit on the branching fraction of the 125 GeV Higgs boson to invisible particles at the ATLAS and CMS detector is 0.107 (0.077) [460] and 0.15 (0.08) [461], respectively, at 95% C.L.

[9] The ATLAS and CMS observation put a strong constraint on the Z-invisible decay width: $\sim$ 506 MeV [462] and $\sim$ 523 MeV [463], respectively.

Importantly, when the interaction between WIMP and FIMP is enhanced, then the FIMP equilibrates to thermal bath and freezes out. We study in details the freeze out dynamics of such FIMPs turning to a new kind of thermal bath particles, which we call pseudo FIMP (pFIMP). We find out whether such pFIMP solutions can be obtained in presence of SIMP. All of these is elaborated in Chapter 5.

The search prospects of pFIMP are not obvious, with loop induced interactions. We study all such pFIMP possibilities that connect via WIMP loop for scalar, fermion and vector boson DM. We elaborate upon a specific model, where we can make some prediction for direct detection at future sensitivities. We also study some interesting connection with LFV set ups, and collider signals in Chapter 6.

In general, two DM components arise when we impose two discrete symmetries to stabilize them. However, under a single discrete symmetry, it is also possible to achieve stability for both DM components, imposing specific kinematic conditions. This is analyzed for both the WIMP-WIMP and WIMP-pFIMP scenarios within the context of two complex scalar fields as DM, as we illustrate in Chapter 7.

We also study the effect of multicomponent DM frameworks in explaining the small neutrino masses and matter-antimatter asymmetry of the universe. This is discussed in Chapter 8. Finally, we summarize the thesis and discuss future research directions in Chapter 9.

Chapter 3

Direct Search signal of two-component Dark Matter

Contents

How do we know if the dark sector consists of more than one dark matter (DM) component is an important question, for which the answer is not very definite. In this chapter we study such a possibility in context of direct DM search. It was pointed out earlier in a model independent analysis that a kink in the nuclear recoil energy spectrum may indicate to the presence of two DM components. However, realizing one such model was difficult due to experimental constraints. Here we propose and study a model containing a vector boson DM and a scalar DM, aided by a light scalar mediator, where a kink in the nuclear recoil spectrum arises after addressing individual relic densities, direct search limits, collider constraints and theoretical limits. We find out the allowed parameter space of the model and those regions likely to show such distinctive signal. The discussion in this chapter is based on Ref . [464].

3.1 Introduction

In a model-independent analysis of two-component DM setup [354, 355],[1] it was shown that a kink may appear in the recoil energy spectrum of DD, when one DM is of low mass $\sim 10\ GeV$, and the other is heavy, $\gtrsim 40\ GeV$. The only physical observable in the event rate analysis is the curvature of the event rate spectrum, which would serve as evidence for the presence of more than one DM particle in the dark sector. The position and properties of this curvature depend not only on the DM masses but also on local DM densities and the DM scattering rates with detector nuclei. The study motivated us to look into a UV complete set up where such observations can be realised. This is challenging as having a low mass WIMP faces severe constraint from experimental data, particularly invisible decay constraints of Higgs or the DM-SM portal. Further, the relative relic densities and DM masses are closely related in a realistic model, so that finding a parameter space where such novel feature can be seen in future sensitivities of DD becomes an interesting exercise.

In this work, SM is extended by a gauge singlet vector boson DM (VBDM), which acquires mass through the spontaneous breaking of a $\mathrm{U}(1)_X$ symmetry via a complex scalar. Apart we postulate the presence of a real scalar DM (RSDM). The stability of both is ensured by an appropriate $\mathcal{Z}_2 \otimes \mathcal{Z}_2'$ symmetry. Through the mixing with CP-even part of the SM Higgs doublet, a new real scalar particle emerges along with the SM Higgs [468, 469], playing a crucial role in the analysis. Our goal is to study the allowed parameter space satisfying relic density, DD, ID, and the collider constraints, that result in a visible kink in the total event rate spectrum indicating the presence of more than one DM components.

This chapter is organized as follows: in Section 3.2, we discussed the possibility of getting two stable vector and scalar DM components transforming under a single $\mathcal{Z}_2 \otimes \mathcal{Z}_2'$ symmetry and in Section 3.3 we have discussed the coupled Boltzmann equation and its solution- relic density of DMs. The direct detection signal for this vector-scalar DM model is discussed in Section 3.4. We finally summarise in Section 8.6. Appendices B.1 and B.2 provide some necessary details omitted in the main text.

3.2 The Model

This chapter aims to come up with a UV-complete model that produces a visible kink in the time-averaged event rate spectrum while satisfying all the current theoretical and observational constraints. Its worth mentioning that all the simple minded two component DM models, consisting of singlet or doublet scalar or fermion, leaves in a mass regime where such distinguishability is difficult to address.

To alleviate this, we extend the SM gauge symmetry by a global $\mathrm{U}(1)_X$ symmetry under which the complex scalar S is charged. The associated dark gauge boson X_μ is stabilized by a $\mathcal{Z}_2$ symmetry, making it a viable vector boson DM candidate. We further include a real scalar ϕ singlet, stable under a $\mathcal{Z}_2'$ symmetry, representing a second DM candidate. The charges of these particles under the $\mathcal{Z}_2 \otimes \mathcal{Z}_2'$ symmetry

[1] In context of colliders, references [465, 466] have shown that a two-component DM scenario can lead to the appearance of two peaks in the missing energy ($\not{E}$) distribution; reference [467] attempted to explore how the indirect signal (specifically the photon flux) is altered in the presence of two DMs.

are listed in Table 3.1. The SM extended dark sector Lagrangian is written as [301],

Dark Fields	$\mathcal{Z}_2 \otimes \mathcal{Z}_2'$	
Real scalar ϕ	ϕ	$-\phi$
Complex scalar S	S^*	S
$\mathrm{U}(1)_X$ Gauge Boson X_μ	$-X_\mu$	X_μ

Table 3.1: Model particles and their charges under $\mathcal{Z}_2 \otimes \mathcal{Z}_2'$ symmetry.

$$\mathcal{L} = \mathcal{L}_{\rm SM} + |\partial_\mu \phi|^2 + |D_\mu S|^2 + \frac{1}{4} X_{\mu\nu} X^{\mu\nu} - V(\phi, S, H)\,, \tag{3.1}$$

where,

$$D_\mu = \partial_\mu + i g_X X_\mu; \quad X_{\mu\nu} = \partial_\mu X_\nu - \partial_\nu X_\mu;$$

and,

$$\begin{aligned} V(\phi, S, H) =& -\mu_H^2 (H^\dagger H) + \lambda_H (H^\dagger H)^2 + \frac{1}{2}\mu_\phi^2 \phi^2 + \frac{1}{4!}\lambda_\phi \phi^4 - \mu_S^2 (S^* S) + \lambda_S (S^* S)^2 \\ &+ \frac{1}{2}\lambda_{\phi H} \phi^2 (H^\dagger H) + \frac{1}{2}\lambda_{\phi S} \phi^2 (S^* S) + \lambda_{HS} (H^\dagger H)(S^* S)\,. \end{aligned} \tag{3.2}$$

The potential $V(\phi, S, H)$ in Eq. (3.2), for $\lambda_H, \lambda_S, \lambda_\phi, \mu_\phi^2 > 0$ and $\mu_H^2 < 0, \mu_S^2 < 0$, so that it provides the following vacuum:

$$H = \begin{pmatrix} \phi^+ \\ \frac{\mathrm{v}+h+i\phi_0}{\sqrt{2}} \end{pmatrix} \to \langle H \rangle = \begin{pmatrix} 0 \\ \frac{\mathrm{v}}{\sqrt{2}} \end{pmatrix}; \tag{3.3}$$

$$S = \frac{v_s + s + i\mathcal{A}}{\sqrt{2}} \to \langle S \rangle = \frac{v_s}{\sqrt{2}};\ \langle \phi \rangle = 0\,. \tag{3.4}$$

In the above, $\phi^{\pm,0}$, $\mathcal{A}$ denote Nambu-Goldstone Bosons [32, 470–472], which disappear in the unitary gauge after EWSB. The breaking of $\mathrm{U}(1)_X$ makes the associated gauge boson massive:

$$m_X = v_s g_X\,, \tag{3.5}$$

where g_X denotes $\mathrm{U}(1)_X$ gauge coupling constant and v_s denotes the $\mathrm{U}(1)_X$ symmetry breaking scale. Let us have a quick look into the relevant constraints.

• Tree level unitarity

The tree-level unitarity of the theory comes from all possible $2 \to 2$ scattering amplitude and can be ensured by [473, 474],

$$\lambda_H < 4\pi,\ \lambda_S < 4\pi,\ \lambda_{HS} < 8\pi\,. \tag{3.6}$$

• Perturbativity

To maintain the perturbativity of the theory, the couplings of the theory obey [475],

$$\lambda_H < 4\pi, \quad \lambda_S < 4\pi, \quad g_X < \sqrt{4\pi}, \quad \lambda_{HS} < 4\pi\,. \tag{3.7}$$

• Limits on the thermal Dark Matter mass

There is a unitarity bound that sets an upper limit on the mass of symmetric and asymmetric thermal DM, is $\sim$ 110 TeV [75, 476–478]. The combined Big Bang Nucleosynthesis (BBN) and Cosmic Microwave Background (CMB) provides the lower limits to the WIMP masses is $\sim 0.5 - 5$ MeV [74, 479–486].

• Relic density

The Planck data [7] constrains the present DM relic density,

$$\Omega_{\rm DM}{\rm h}^2 = 0.1200 \pm 0.0012\,. \tag{3.8}$$

where h is the reduced Hubble parameter $\rm H_0/(100\ km/s/Mpc)$ with $\rm H_0 = 67.4 \pm 0.5\ km/s/Mpc$ being the current Hubble constant.

• Ranges of mixing angle sin ϑ

As the scalar mass matrix is real, symmetric and non-diagonal, it can be diagonalised by an orthogonal matrix, resulting in mass eigenstates (h_1, h_2).

$$\begin{pmatrix} h_1 \\ h_2 \end{pmatrix} = \begin{pmatrix} \cos\vartheta & -\sin\vartheta \\ \sin\vartheta & \cos\vartheta \end{pmatrix} \begin{pmatrix} h \\ s \end{pmatrix}\,. \tag{3.9}$$

Here we assume h_1 to be SM like, and h_2 is lighter. The relations between the parameters in the Lagrangian, to the physical ones and mixing are,

$$\mu_H^2 = (\lambda_H v^2 + \frac{1}{2}\lambda_{HS} v_s^2)\,, \tag{3.10}$$

$$\mu_S^2 = (\lambda_S v_s^2 + \frac{1}{2}\lambda_{HS} \mathrm{v}^2)\,, \tag{3.11}$$

$$\lambda_{HS} = \frac{\sin 2\vartheta}{2 v_s \mathrm{v}} \left(m_{h_2}^2 - m_{h_1}^2\right)\,, \tag{3.12}$$

$$\lambda_H = \frac{1}{2\mathrm{v}^2} \left(m_{h_1}^2 \cos^2\vartheta + m_{h_2}^2 \sin^2\vartheta\right)\,, \tag{3.13}$$

$$\lambda_S = \frac{1}{2 v_s^2} \left(m_{h_2}^2 \cos^2\vartheta + m_{h_1}^2 \sin^2\vartheta\right)\,. \tag{3.14}$$

The Higgs precision measurement set an upper limit on the $h - s$ mixing angle ϑ at 95% CL for 125.1 GeV Higgs [487–494],

$$|\sin\vartheta| \lesssim 0.29\,. \tag{3.15}$$

In our analysis, we have chosen a small but not overly tiny mixing angle ($10^{-4} \lesssim |\sin\vartheta| \lesssim 10^{-2}$), ensuring h_2 stays in thermal equilibrium during DM freeze-out, has a lifetime shorter than the BBN era ($\tau_{h_2} < 1\,\text{sec}$), and does not disrupt BBN or induce invisible Higgs decays.

• Higgs invisible decay

If DM's connected via Higgs portal, have smaller mass than half of the SM Higgs, then Higgs can invisibly decay to DM pair. The most sensitive limits on $\mathcal{B}_{h_1\to\text{inv}}$ are obtained in VBF searches exploring data collected at $\sqrt{s} = 13\ TeV$, excluding $\mathcal{B}_{h_1\to\text{inv}} < 0.18\ (0.10)$ observed (expected) at 95% C.L using 138 fb^{-1} of CMS data, [495], and $\mathcal{B}_{h_1\to\text{inv}} < 0.15\ (0.10)$ using 139 fb^{-1} of ATLAS data [496]. Together, searches for invisible decays of the Higgs boson using 139 fb^{-1} of $p\,p$ collision data at $\sqrt{s} = 13\ TeV$ recorded in Run 2 data of LHC set an upper limit on the invisible Higgs boson branching ratio of $\mathcal{B}_{h_1\to\text{inv}} < 0.113\ (0.080^{+0.031}_{-0.022})$ observed (expected) at the 95% CL. Here we assume that the dark Higgs h_2 decays instantaneously inside the detector, with DMs long-lived. In our context, therefore, the invisible decay width of the SM Higgs is,

$$\Gamma^{\text{inv}}_{\text{h}_1} = \frac{\mathcal{B}_{\text{h}_1\to\text{inv}}}{1-\mathcal{B}_{\text{h}_1\to\text{inv}}}\Gamma^{\text{SM}}_{\text{h}_1}\,, \tag{3.16}$$

where, $\Gamma^{\text{inv}}_{\text{h}_1} = \Gamma_{\text{h}_1\to\text{XX}} + \Gamma_{\text{h}_1\to\text{h}_2\text{h}_2}$ and $\Gamma^{\text{SM}}_{h_1} = 4.100\times10^{-3}\ GeV\ (\pm1.4\%)$ [497] for $m_{h_1} = 125.09\ GeV$.

• Can h_2 be a 95 GeV scalar?

The latest CMS analysis confirms an excess of di-photon events around 95 GeV. By combining data from the first three years of Run 2, collected at $\sqrt{s} = 13\ TeV$ with integrated luminosities of 36.3 fb^{-1}, 41.5 fb^{-1}, and 54.4 fb^{-1}, CMS reports a local (global) significance of 2.9 $(1.3)\sigma$ at a mass of 95.4 GeV [498]. In contrast, ATLAS reported di-photon search results below 125 GeV using 80 fb^{-1} of Run 2 data [499] to show only a mild excess, with the largest deviation at 95.4 GeV, yielding a local significance of 1.7σ [500]. A combined analysis gives a signal strength of $\mu^{\text{ATLAS+CMS}}_{\gamma\gamma} = 0.24^{+0.09}_{-0.08}$ [501], corresponding to a 3.1σ excess. Some studies explored the possibility with $\text{U}(1)_X$ gauge boson DM model, containing a real scalar h_2 along with the SM Higgs h_1 [502], investigating the processes $q\bar{q} \to t\bar{t}X_\mu X^\mu$ and $q\bar{q} \to VX_\mu X^\mu$ with $V \to \ell\bar{\ell}$, with $m_{h_2} = 95.4\ GeV$ and $V = Z_\mu, h_1$. No exclusions apply to our region of interest, provided that $g_X < 10^{-2}$ and $|\sin\vartheta| < 10^{-2}$. The reference [503] provides theoretical predictions for signal strengths in $\gamma\gamma$, $\tau\bar{\tau}$, and $b\bar{b}$ channels in the $\text{U}(1)_X$SSM model, which aligns well with the excesses observed by CMS. Interestingly, LEP data strongly disfavor the production of 95 GeV scalar particle, as well as any other new physics interpretation in the 95-100 GeV mass range [504]. We do not intend to perform a full analysis of h_2 to diphoton decay, which can cause this excess near $95\ GeV$.

• Bounds on light mediator h_2 mass from thermalization condition

The decay or annihilations of the light scalar h_2 into SM fermions is restricted by BBN data, because the precision measurement of the baryon density through BBN and CMB are well measured [505–507] and restricts h_2 lifetime $\tau_{\rm h_2} \lesssim 1$ sec [508, 509]. The h_2 decay life time in our case turns,

$$\tau_{\rm h_2} = [\Gamma_{\rm h_2\to SM\ SM} + \Gamma_{\rm h_2\to X\ X} + \Gamma_{\rm h_2\to\phi\ \phi}]^{-1} \ . \tag{3.17}$$

Equivalently, the total decay width of $\rm h_2$ ($\Gamma_{\rm h_2}$) should be greater than $6.58\times10^{-25}\ GeV$, which puts a stringent limit on the model parameters. For other relevant constraints for the light scalar h_2 in presence of VBDM see [510]. Also, you may visit ref . [511, 512] for relevant bounds on light scalar DM from LEP, LHC, light meson decay, and fixed target experiments. For h_2 to remain in chemical equilibrium with thermal bath, the interaction rate of $\rm h_2$ must be larger than the Hubble expansion rate,

$$\sum_{\mathcal{F}} \left[\langle\Gamma\rangle_{\rm h_2\to\mathcal{F}\ \mathcal{F}} + {\rm n}^{\rm eq}_{\rm h_2}\langle\sigma v\rangle_{\rm h_2\ h_2\to\mathcal{F}\ \mathcal{F}}\right]_{\rm T^{DM}_{FO}} \gtrsim {\rm H(T^{DM}_{FO})}\,, \tag{3.18}$$

where $\mathcal{F} \in \{\text{SM particles},\ \phi,\ \rm X\}$, and $\rm T^{DM}_{FO} \sim m_{DM}/25$. In Fig . B.2, see the variation of interaction rate of h_2 with the bath temperature. However, the kinematic equilibrium of h_2 is maintained by the inelastic scattering with light SM fermions ($\rm h_2\ \mathcal{F} \to h_2\ \mathcal{F}$), sharing the same SM bath temperature ($\rm T$), so that we use $\rm n_{h_2}(T) \simeq n_{h_2,0}(T)$ throughout the analysis; one can also study the departure from the aforementioned condition via solving the three coupled Boltzmann equations (cBEQ) simultaneously.

• Limits on thermal dark matter annihilation

CMB anisotropies constrain energy injection from DM annihilation, providing limits on WIMP annihilation cross-sections that complement indirect DM searches. Planck 2018 data constrains DM mass and annihilation cross-section; the strongest bounds are obtained assuming s-wave annihilation into bottom quark pairs, $\langle\sigma v\rangle_{\rm DM\ DM\to b\bar{b}} \sim 8\times10^{-27}{\rm cm^3/s}$ for $m_{\rm DM} = 6\ GeV$ [7]. On the other hand, the 95% confidence level upper limits on the thermally-averaged cross-section for DM particles annihilating into $b\bar{b}$, derived from a combined analysis of 158 hours of Segue 1 observation with MAGIC, and 6-year observations of 15 dwarf satellite galaxies by the Fermi-LAT, is $\sim 10^{-26}\,{\rm cm^3/s}$ for $\rm m_{DM} = 6\ GeV$ [401].

3.3 Coupled Boltzmann Equation and Relic density

In this study, we have considered both the dark sector particles as WIMP-like DM, so that both components can be probed in future DD experiments. In particular, we are interested in the possibility of getting a kink in the recoil energy spectrum. But before that, we will address the possibility of the DM components to acquire correct relic density. WIMPs are initially in thermal equilibrium with the bath particles and

undergo freeze-out when their interaction rate falls below the Hubble expansion rate. The Feynman diagrams, which provide the annihilation of DMs and DM-DM conversion processes, are shown in Fig . B.1. The freeze out of DM components are evaluated by solving the coupled Boltzmann Equations (cBEQs), which in our case, reads:

$$\begin{aligned}
\frac{dY_\phi}{dx} &= -\frac{\mathrm{s}}{x\,H(x)}\left[\left(Y_\phi^2 - Y_{\phi,0}^2\right)\langle\sigma v\rangle_{\phi\;\phi\to \mathrm{SM\;SM}} + \left(Y_\phi^2 - Y_X^2\frac{Y_{\phi,0}^2}{Y_{X,0}^2}\right)\langle\sigma v\rangle_{\phi\;\phi\to X\;X}\right], \\
\frac{dY_X}{dx} &= -\frac{\mathrm{s}}{x\,H(x)}\left[\left(Y_X^2 - Y_{X,0}^2\right)\langle\sigma v\rangle_{\mathrm{X\;X}\to \mathrm{SM\;SM}} + \left(Y_X^2 - Y_\phi^2\frac{Y_{X,0}^2}{Y_{\phi,0}^2}\right)\langle\sigma v\rangle_{XX\to\phi\;\phi}\right] \\
&\quad + \frac{2}{x\,H(x)}\sum_{i=1}^{2}\left[Y_{h_i,0} - Y_{h_i,0}\frac{Y_X^2}{Y_{X,0}^2}\right]\langle\Gamma\rangle_{h_i\to X\;X}\,.
\end{aligned} \tag{3.19}$$

In the above, notations have very standard meaning, some of them worth noting are, $x = \mu_{\phi X}/T$, where $\mu_{\phi X} = m_\phi m_X/(m_\phi + m_X)$ denotes reduced mass for the two DM components, T denotes temperature of the thermal bath, $Y_{i,0} = n_{i,0}/\mathrm{s}$ denotes equilibrium yield, with $\mathrm{s} = \frac{2\pi^2}{45}g_*^s T^3$ denoting entropy density, $n_{i,0} = \frac{T}{2\pi^2}g_i m_i^2 K_2\left(\frac{m_i}{T}\right)$ indicate to equilibrium number density, annihilation final states include $\mathrm{SM} \in \{\mathrm{h_1},\ \mathrm{h_2},\ \mathrm{W^\pm},\ \mathrm{Z},$ leptons and quarks$\}$, and

$$\langle\sigma v\rangle_{\mathrm{a\;b}\to\mathrm{c\;d}}\, n_{a,0}n_{b,0} = \langle\sigma v\rangle_{\mathrm{c\;d}\to\mathrm{a\;b}}\, n_{c,0}n_{d,0}\,, \tag{3.20}$$

indicate the thermal average of annihilation cross-section. The total DM relic density is the sum of the individual relic densities, derived from the solution of the cBEQ in Eq . (3.19), to provide,

$$\Omega_{\mathrm{DM}}\mathrm{h}^2 = 2.744\times 10^8\left[m_\phi Y_\phi + m_X Y_X\right]_{x\to\infty}\,. \tag{3.21}$$

The free parameters in this model that crucially dictates DM phenomenology are,

$$\{m_\phi,\ m_X,\ m_{h_2},\ g_X,\ \lambda_{\phi H},\ \lambda_{\phi S},\ \sin\vartheta\}\,. \tag{3.22}$$

The parameter space which is scanned here is : $\{10^{-3} < \lambda_{\phi S} < 1,\ 10^{-4} < \lambda_{\phi H} < 10^{-1},\ 10^{-3} < g_X < 10^{-1},\ 10^{-4} < |\sin\vartheta| < 10^{-2},\ 1 < m_X < 550,\ 1 < m_{h_2} < 10^3,\ 1 < m_\phi < 10^3\}$ where masses are in GeV unit. We have calculated the DM relic densities and the spin-independent (SI) DM-nucleon inelastic scattering cross-section using MicrOMEGAs 6.0 [513], and the findings are presented and discussed below.

In the left plot of Fig . 3.1, we illustrate the relic density allowed points in the $m_{\mathrm{DM}} - \sigma^{\mathrm{eff}}_{\mathrm{DM-N}}$ plane. The orange points represent real scalar DM (ϕ), while the light blue points correspond to VBDM (X). The effective SI DM-nucleon scattering cross-section is defined as $\sigma^{\mathrm{eff}}_{i\mathrm{N}} = (\Omega_i/\Omega_{\mathrm{tot}})\sigma^{\mathrm{SI}}_{i\mathrm{N}}$, where the individual direct search cross-section is scaled by the ratio of its relative abundance with respect to the total one. The grey (LZ-2022 [514]) and pink (XENONnT [515]) shaded regions indicate the DD exclusion limits, while the projected limits are shown by the dashed blue (PandaX-xT [516]) and green (DARWIN-200 t y [517, 518]) lines. The points scanned here already obey indirect detection and collider search limits. Additionally, two peaks in the indirect detection signal $\langle\sigma v\rangle_{\mathrm{DM\;DM}\to\mathrm{b\;\bar{b}}}$ occur near the h_1 and h_2 resonances, leading to the exclusion of some points in these regions. The major

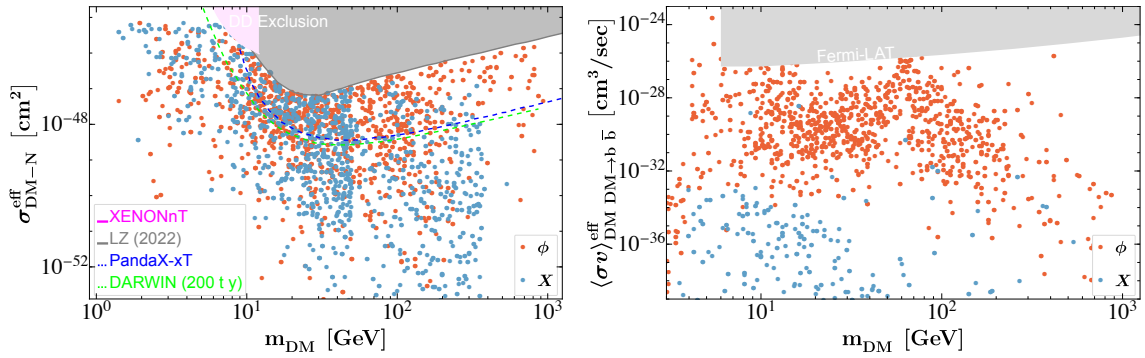

Figure 3.1: *Left:* Allowed parameter space of the model in the $m_{\rm DM} - \sigma^{\rm eff}_{\rm DM-N}$ plane (ϕ in blue, X in red points) that satisfies $\mathcal{B}_{h_1\to \rm inv} \leq 0.113$ and $\tau_{h_2} < 1$ sec, relic abundance and indirect search (DM DM $\to$ b $\bar{\rm b}$) constraints from Fermi-LAT and CMB. The bounds and future sensitivities from experiments like XENONnT, LZ, PandaX-xT, DARWIN are shown. *Right:* points allowed by relic density, and recent direct detection constraint from LZ-2022 in $m_{\rm DM} - \langle\sigma v\rangle^{\rm eff}_{\rm DM\ DM\to b\ \bar{b}}$ plane are shown with Fermi-LAT bound.

stumble block in coming up with a realistic model that produces a curvature in the direct search signal is that one of the DM components must have small mass, therefore susceptible to the invisible branching ratio of either the Higgs or Z boson or whatever the DM-SM portal is. In our case, we need to adhere to the Higgs invisible decay bound, and we can address that by choosing a very small mixing angle $|\sin\vartheta| \lesssim 10^{-2}$. This was one of the reasons of having the second light scalar present in the scenario. From the figure, it is clear that there is plenty of breathing space for the model to survive the non-observation of direct search limit after addressing the observed relic density, with both the DM components providing detectable points in the vicinity of the exclusion limit and beyond. Notably, we are considering spin independent direct search cross-section and the corresponding limits as obtained by the DM interactions in this model.

In the right plot in Fig. 3.1, we have shown the relic density allowed points in $m_{\rm DM} - \langle\sigma v\rangle^{\rm eff}_{\rm DM\ DM\to b\ \bar{b}}$ plane, where the color coding remains the same as the left plot. All the points shown here are also allowed by direct and collider search constraints. This particular annihilation channel to the bottom quark pair is relevant as some points are excluded near the Higgs resonance region from the Fermi-LAT [519–521] limit. There are points below the Higgs mass, which also get restricted because of the resonance enhancement due to the presence of the light mediator h_2.

3.4 Two component dark matter signal in direct detection

After finding out the allowed parameter space of the model from the existing bounds, we now turn to the direct search observability of two DM components. Its worth repeating that we wish to focus on the direct search signal where a kink or a curvature in the recoil energy spectrum is observed [354, 355]. Absent any background, this indicates the presence of more than one DM components. In the context of the model presented above, it is therefore the exploration of the region of parameter space where the presence of two DM components can be realised.

Let us now turn to the formalism a little. The total observed differential event rate is the sum of the individual event rates from each DM component interacting

with the target nuclei. The DM relic densities as obtained from the solution of cBEQ are given by,

$$\Omega_X h^2 = \frac{\rho_X}{\rho_{\rm crit}}\,, \quad \Omega_\phi h^2 = \frac{\rho_\phi}{\rho_{\rm crit}}\,, \quad \text{with} \quad \rho_{\rm loc} = \rho_X + \rho_\phi\,, \tag{3.23}$$

where the critical density is given by $\rho_{\rm crit} = \dfrac{3H_0^2}{8\pi G}$, with $\rm H_0$ and G representing the Hubble and gravitational constants respectively. Following the above relations, we can evaluate the DM densities in terms of relic densities,

$$\rho_\phi = \rho_{\rm loc}\frac{\Omega_\phi h^2}{\Omega_\phi h^2 + \Omega_X h^2}\,, \quad \text{and} \quad \rho_X = \rho_{\rm loc}\frac{\Omega_X h^2}{\Omega_\phi h^2 + \Omega_X h^2}\,, \tag{3.24}$$

and

$$\rho_\phi \sigma_\phi^N = \rho_{\rm loc}\frac{\Omega_\phi h^2}{\Omega_\phi h^2 + \Omega_X h^2}\sigma_\phi^N \equiv \rho_{\rm loc}\sigma_{\phi-N}^{\rm eff}\,, \quad \text{and} \quad \rho_X \sigma_X^N = \rho_{\rm loc}\sigma_{X-N}^{\rm eff}\,. \tag{3.25}$$

The time-averaged event rate for recoil, typically measured in events/(kg keV day), for a detector with a target nucleus[2] of mass m_A and characterized by the standard notation (A, Z), is given by the sum of the individual contributions,

$$R_A(E_R) = R_A^{(1)}(E_R) + R_A^{(2)}(E_R) = F_A^2(E_R)\sum_{\alpha=X,\phi}(A_\alpha^{\rm eff})^2\frac{\rho_\alpha\sigma_\alpha^p}{2m_\alpha\mu_{\alpha p}^2}\eta_\alpha(v_m^\alpha, m_A, t)\,, \tag{3.26}$$

where the nuclear form factor of the detector element with the mass number A is denoted by $F_A(E_R)$, where E_R denotes recoil energy. For the spin-independent (SI) form factor, we use the Helm parameterization [525, 526]. The velocity integral $(\eta_\alpha(v_m^\alpha, m_A, t))$ is defined as,

$$\eta_\alpha(v_m^\alpha, m_A, t) = \int_{v_{m,A}^{(\alpha)}} d^3v\frac{f_{\rm det}^{(\alpha)}(\boldsymbol{v}, t)}{v}, \tag{3.27}$$

where $v_{m,A}^{(\alpha)} = \sqrt{\dfrac{m_A E_R}{2\mu_{\alpha A}^2}}$ is the minimum velocity required for a DM particle α to produce a nuclear recoil with energy E_R (the detector's threshold) in a nucleus of mass m_A. The velocity distribution of DM particles in the detector frame, $f_{\rm det}^{(\alpha)}(\boldsymbol{v}, t)$, satisfies $f_{\rm det}^{(\alpha)}(\boldsymbol{v}, t) \geq 0$ and $\int f_{\rm det}^{(\alpha)}(\boldsymbol{v}, t)d^3v = 1$. The velocity distributions in the detector and galaxy rest frames are related further by a Galilean transformation: $f_{\rm det}(\boldsymbol{v}, t) = f_{\rm gal}(\boldsymbol{v} + \boldsymbol{v}_e(t))$, where $\boldsymbol{v}_e(t)$ is the Earth's velocity in the galaxy's rest frame. Here, we have used the Standard Halo Model, assuming a local DM density of $\rho_{\rm loc} \simeq 0.4\ GeV/cm^3$ and a Maxwellian velocity distribution [527–529],

$$f_{\rm gal}(v) = \frac{1}{(2\pi v_\alpha^2)^{3/2}}\exp\left(-\frac{3}{2}\frac{v^2}{v_\alpha^2}\right)\,, \tag{3.28}$$

[2]In this chapter, we have considered the $^{132}\rm Xe_{54}$ as our detector nuclei. However, we can do a similar analysis for other nuclei such as germanium (EDELWEISS [522]) and sodium (COSINE-100 [523]) for the spin-independent case, while fluorine (PICO [524]) for the spin-dependent case, etc.

with a cutoff at the escape velocity, $v_{\rm esc} = 550\ {\rm km\ s^{-1}}$ [530, 531]. The velocity dispersion v_α depend on the DM masses within the model following,

$$v_\alpha = v_0\,(\overline{m}/m_\alpha)^{1/2}\ , \tag{3.29}$$

where the canonical value for the velocity dispersion is $v_0 \sim 270\ {\rm km\ s^{-1}}$ [532, 533], and

$$\overline{m} = \sum_{k=1,2} n_k m_k / \sum_{l=1,2} n_l = \rho_{\rm loc}/(n_1+n_2) = \left(\sum_{k=1,2}\Omega_k h^2\right)\left(\sum_{l=1,2}\frac{\Omega_l h^2}{m_l}\right)^{-1}\ . \tag{3.30}$$

The scattering cross-section of DM particle α with the protons at zero momentum transfer is denoted by σ^p_α, while $\mu_{\alpha p}$ represents the reduced mass of the DM particle α and the proton. The nuclear form factor of the nucleus j is denoted by $F_j(E_R)$. The effective mass number of nucleus j, interacting with the DM particle α, is $A^{\rm eff}_\alpha = Z + (A-Z) f^n_\alpha/f^p_\alpha$ with $f^{n,p}_\alpha$ representing the SI coupling strengths of the DM particle α to neutrons and protons respectively. For the SI form factors, we use the Helm parametrization in our numerical analysis [525, 526].

Benchmarks	m_ϕ [GeV]	m_X [GeV]	$\Omega_\phi h^2$	$\Omega_X h^2$	$\sigma^{\rm eff}_{\phi-N}$ [cm^2]	$\sigma^{\rm eff}_{X-N}$ [cm^2]
A	109.65	8.77	0.0352	0.0851	2.00×10^{-47}	1.98×10^{-47}
B	77.17	12.16	0.0264	0.0934	5.38×10^{-49}	2.06×10^{-48}
C	66.07	12.42	0.0005	0.11902	4.99×10^{-48}	1.91×10^{-47}
D	51.29	8.42	2.8×10^{-5}	0.1202	3.95×10^{-49}	4.55×10^{-48}
E	40.74	8.46	2.4×10^{-5}	0.1208	1.18×10^{-48}	2.09×10^{-47}
F	199.53	13.18	0.0379	0.0822	3.23×10^{-48}	4.41×10^{-48}
G	83.18	4.27	0.0294	0.0915	1.10×10^{-47}	1.10×10^{-47}

Table 3.2: The benchmark points noted above are capable of displaying a noticeable kink in the recoil rate spectrum while also meeting the constraints from relic density, DD, ID, and collider searches of DM.

In Table 3.2, we present several benchmark points that account for the current DM relic density, stringent direct detection limits from LZ (2022), indirect detection constraints on DM annihilation into bottom quarks, and collider limits on the Higgs invisible decay. We also have accounted for the limits on the mixing angle $\sin\vartheta$ and the BBN limit on the h_2 lifetime. Each benchmark, labeled A to G, shows a noticeable kink in the recoil energy spectrum following the methodology described above. The variation of the total time-averaged event rate as a function of recoil energy (E_R) is shown in Fig. 3.2. All the benchmark points described in Table 3.2 are shown here by different colored lines. The kink typically appears around $E_R \lesssim 10$ keV. Its position depends not only on the DM mass but also on the relic density and the SI DM-nucleon scattering cross-section. In the left panel, E_R ranges up to 40 keV, while in the right panel, it is limited to 10 keV for a closer inspection of the kink. We also show on the right panel, how the different slopes in R_ϕ and R_X adds to the kink. It is obvious that there are regions of parameter space, where the slope for both DM components are same in the recoil spectrum, where the distinguishability is submerged. So it is legitimate to ask, what is the parameter that crucially governs the

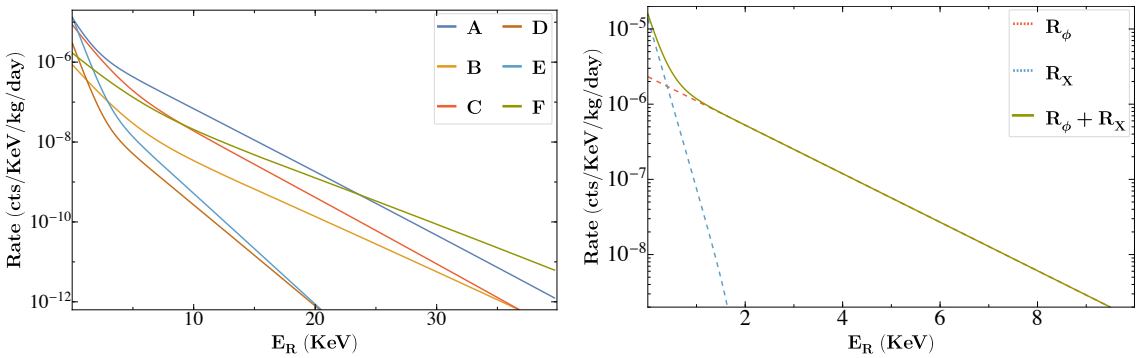

Figure 3.2: Recoil rate spectrum for the benchmark points as in Table 3.2. We show the variation of total event rate $(R_\phi + R_X)$ with the recoil energy (E_R). The right plot shows benchmark G, while the left plot demonstrates benchmark points A to F from Table 3.2. The dashed blue and orange lines on the right panel correspond to the individual rates from vector boson and real scalar DM respectively.

kink. The answer to that is DM mass. So, the larger the mass is, the smaller the slope is. Whenever, there is a substantial gap in the slope between the DM components, having similar direct search cross-section, such distinctive curvature will appear to indicate the presence of two DM components.

The angles between the linear fit of the vector and scalar DM event rate curves, measured from the positive E_R axis, are represented as θ_X and θ_ϕ, respectively. The resultant angle between these two curves is defined as $\theta = \theta_X - \theta_\phi$. If $m_X > m_\phi$, then $\theta_\phi < \theta_X$, resulting in a positive angle. Conversely, if $m_X < m_\phi$, then $\theta_\phi > \theta_X$, yielding a negative angle. However, other parameters, such as DM relic density and DD cross-section, can influence the slope, though their effects are mild and flexible, with a considerable impact on event rates.

Finally, in Fig. 3.3, we show the points in the $m_\phi - m_X$ plane that satisfy the DM relic density and respect the DD, ID, and collider constraints. Importantly, the rainbow color bar represents the angle (θ, in degrees) between the two linear fit lines for the event rates of the two DM particles, X and ϕ in the recoil energy spectrum. We see the presence of bluish or yellow-reddish points, where the angle is large to make the kink visible, spanning at large m_ϕ with small m_X. This also validates the claim made in model independent way in the references [354, 355] that the kink appears only when one mass is around $10\ GeV$, and the other is $\gtrsim 40\ GeV$. On the contrary, for the opposite mass hierarchy, i.e. $m_X > m_\phi$, energy densities are widely different with $\rho_\phi \ll \rho_X$, and the event rates for ϕ is way smaller as $R_\phi \ll R_X$ across the entire range of E_R. Consequently, this hierarchy is less promising for discriminating between the two DM components, although a finite slope difference exists between the two linear-fitted event rate curves. However, the situation alters if we can have $\rho_\phi > \rho_X$ for $m_\phi < m_X$ by incorporating new degrees of freedom into our model. Thus, our work provides an example of a UV-complete vector-scalar model, where the distinguishability in direct search could be demonstrated. This is possible due to the presence of light scalar (h_2), which helps keep the VBDM under relic, even below the Higgs resonance. We also note that as a result, the benchmark points where VBDM is light, provides the majority of the relic density contribution. However, the possibility of having equal share of relic density is difficult, at least in this model, to provide a distinctive direct search signal for the presence of both.

A statistical method using frequentist statistics for assessing the sensitivity of future experiments to distinguish between a single- and two-component DM scenario

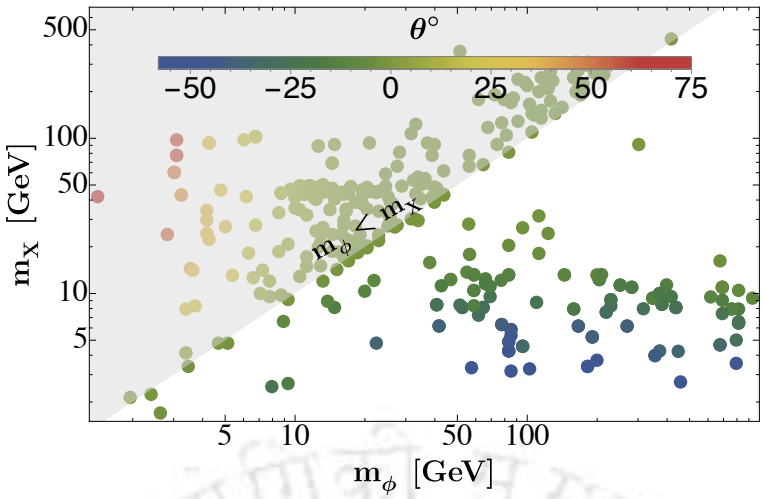

Figure 3.3: Rainbow color bar shows the variation of angle between the two event rate lines w.r.t E_R, while the θ is in degree. The grey-shaded region is insensitive for experiments to discriminate the slope due to the difference in even rates, although accommodates large θ; for details, see the main text.

was discussed in detail by [355]. It involves hypothesis testing and parameter estimation, where DM masses, the DM-nucleon scattering cross-section, and the energy density of each component and the same velocity dispersion assuming SHM are assumed free. In contrast, these parameters excepting for the DM mass are evaluated in our model following their interactions, adhering to all observation constraints.

3.5 Summary

There are many possibilities embedded in multi-component DM, both in construction and phenomenology. The limits on the self-interaction of DM from the galaxy cluster observations like Bullet, Abell clusters does not clarify the ambiguity of its component type, as the self-interaction could be among the same or different kinds of particles that constitute the 26.8% dark sector of the observed universe. An extended dark sector provides different phenomenological advantages specifically due to the DM-DM conversion, however an observational signal can only testify such hypothesis. Therefore, observation of two component DM signals in direct detection (DD), indirect detection (ID), and collider experiments are important to study. In this chapter, we have focused on multi-component DM signals in direct detection experiments.

In model independent analysis [354, 355], it was argued that a kink in the nuclear recoil rate can provide such a useful hint of having two different DMs coexisting and producing direct search signal. However, we don't know of an analysis where a UV complete model was studied to discuss such possibilities. Now, this is important as several constraints both from theoretical consistency as well as from observations like collider searches, indirect searches limit such models heavily with a potential possibility that the region of the parameter space where such distinguishability is observed, is actually discarded. This was the main point of concern and rationale behind our study. Many of the simple kind of two-component DM models studied so far fails to provide such distinguishability, where the model is valid, like having two scalar/fermion singlets; one singlet, one doublet etc.

In the proposed model, we extend the SM by introducing a SM gauge-singlet real

scalar (ϕ) stable under $\mathcal{Z}_2'$ and a complex scalar S respecting $\mathrm{U}(1)_X$ gauge symmetry. The associated gauge boson X, stable under $\mathcal{Z}_2$, serves as the second DM candidate. The singlet-doublet mixing generates a new scalar (h_2) together with the SM Higgs (h_1). The mixing angle (ϑ) serves as a crucial variable, that can make one DM light, after addressing Higgs invisible decay and (in)direct detection of DMs, by choosing $|\sin\vartheta| \lesssim 10^{-2}$. The individual relic densities are calculated by solving the cBEQ. We assume the light scalar h_2 to be in thermal bath, the rationale of which is explained in Appendix B.2. Another strong constraint comes from the BBN, as the presence of a light scalar can alter the BBN prediction of the ΛCDM model. Therefore, the lifetime of this light scalar should be smaller than 1 sec. Further, for direct and indirect detection, we calculate the 'effective' DM-nucleon scattering and annihilation cross-sections, as they most often contribute to total relic density unequally.

Further, we calculate the time-averaged event rate, assuming that both DMs scatter off the detector nuclei and making it recoil. We plot the time-averaged event rate with the recoil energy for several benchmark points, respecting all relevant constraints to show that a kink in the recoil rate can be observed. The event rate depends not only on DM masses, DM number densities, DM-nucleon scattering cross-section, but also on the detector materials, and their sensitivity decides the minimum recoil energy required to produce detectable signals. Our analysis is based mainly on $^{132}\mathrm{Xe}_{54}$ material used in LZ, XENON, PandaX, and the threshold recoil energy for nuclear recoil events is 1 KeV as used for XENONnT experiments. The curvature of the resultant event rate spectrum, which is the summation of event rates corresponding to the two DMs, provides the proof of the existence of more than one DM. Here, we measure the curvature by measuring the angle between two asymptotic lines corresponding to the event rates of two DMs. The position of the resultant kink depends upon several parameters, like DM mass, relative abundances, DM-nucleon scattering cross-section etc. The observability of the kink, or what is the minimum angle (θ_{min}) below which we are unable to differentiate between single-component and two-component DM frameworks is another question. This is discussed partly via statistical analysis in [355]. According to our model, the maximum achieved angle is $\sim 75°$, where $m_\phi \lesssim 5$ GeV and $m_X \gtrsim 40$ GeV, and $\sim -60°$, where $m_X \lesssim 5$ GeV and $m_\phi \gtrsim 40$ GeV. However, for $m_X > m_\phi$, the energy densities are highly different, $\rho_\phi \ll \rho_{\mathrm{X}}$, and the event rates for ϕ is way smaller than X, as $\mathrm{R}_\phi \ll \mathrm{R}_{\mathrm{X}}$ across the entire range of E_{R}, thus making the observability of the kink in the recoil rate nearly impossible.

Therefore, the requirement that the recoil rates can't differ too much for the DM components by having DM-nucleon cross-section at the same ballpark, but the slope in recoil rate requires to be different by having different DM masses, favors a specific mass hierarchy $m_X < m_\phi$ for our model to show the kink. The difference in DM mass results in different relic density contributions. Such a conclusion was not possible to draw from a model independent analysis. Further, the possibility of having a kink in the direct search signal together with that of a double bump signal in the collider is an interesting question, or of their complementarity, if exists, which we plan to study later.

Chapter 4

WIMP-FIMP in the non-interacting limit, an example

Contents

The Electroweak Symmetry Breaking (EWSB) is known to produce a massive universe that we live in. However, it may also provide an important boundary for freeze-in or freeze-out of dark matter (DM) connected to Standard Model via Higgs portal as processes contributing to DM relic differ across the boundary. We explore such possibilities in a two-component DM framework, where a massive $\mathrm{U}(1)_X$ gauge boson DM freezes-in and a scalar singlet DM freezes-out, that inherits the effect of EWSB for both the cases in a correlated way. Amongst different possibilities, we study two sample cases; first when one DM component freezes in and the other freezes out from thermal bath both necessarily *before* EWSB and the second, when both freeze-in and freeze-out occur *after* EWSB. We find some prominent distinctive features in the available parameter space of the model for these two cases after addressing relic density and the recent most direct search constraints from XENON1T, some of which can be borrowed in a model-independent way. The discussion in this chapter is based on Ref . [301].

4.1 Introduction

Electroweak Symmetry Breaking (EWSB) is one of the most important phenomena that fundamental particle physics has taught us. The discovery of the Higgs-like boson with mass $125\ GeV$ in 2012 at the LHC [16, 17], has established EWSB as a law of nature and Standard Model (SM) of particle physics as the most appropriate theory to describe electromagnetic, weak and strong interactions amongst fundamental particles. Weak gauge boson (W and Z) masses provide the scale of EWSB to be $\sim 246\ GeV$, (equivalent to a temperature of $\sim 160\ GeV$) when the phase transition occurs. Albeit the plethora of knowledge accumulated for EWSB, there are several unanswered questions like whether the Higgs boson responsible for EWSB is SM like, how to stabilize the *metastable* vacua [45, 534] that we live in, or how to solve the gauge hierarchy problem [535], together with other experimental observations like tiny but non-zero neutrino mass [119, 536, 537], dark matter, baryon asymmetry of the universe [538, 539], that leave ample scope to study physics beyond the SM (BSM).

Our aim of this analysis is to study the effect of EWSB as a boundary for DM freeze-in and freeze-out. EWSB can provide an important boundary, mainly because of two reasons: first SM particles become massive and second, additional channels open up for DM production or annihilation after EWSB, particularly for DM that connects to SM via Higgs portal, both of which alter the yield. Specifically, we are interested in exploring the difference between the resulting relic density and direct search allowed parameter spaces of the model, if the DM freezes in (or freezes out) before EWSB (bEWSB) to that when it freezes-in (or freezes out) after EWSB (aEWSB). Although the phenomena is well understood, the authors are not aware of any systematic comparative analysis that distinguishes these two possibilities in details. It is worthy to point out that freeze-in production of a light (KeV-MeV) scalar has been studied [540] in five steps with emphasis on finite temperature effects and quantum statistics around EWSB scale to show that the production magnifies around that scale, although the results do not apply to our case, as heavy DMs are considered. To study the effect in both freeze-in and freeze-out context, we choose a two component DM setup with one WIMP and one FIMP like DM.

We choose an abelian vector boson DM (VBDM) in an $\mathrm{U}(1)_X$ gauge extension of SM [267, 510, 541–543] to constitute a FIMP like DM. A scalar singlet on the other hand, is considered as WIMP (such DM is perhaps the most popular, amongst many studies, see [250, 251, 544–547]). VBDM has also been studied extensively as single component DM, both in the context of WIMP [548–560] and FIMP [267, 510, 541–543]. The stability of both DM components is ensured by added $\mathcal{Z}_2 \times \mathcal{Z}_2'$ symmetry under which they transform non-trivially. While the model serves as an example of a two component WIMP-FIMP set up where the effect of EWSB is studied, VBDM freeze-in provides an additional scale via $\mathrm{U}(1)_X$ breaking, which helps achieving a rich phenomenology both before and after EWSB as we illustrated. Apart from that, the interplay of the scalar fields to address the correct Higgs mass and bounds can also be adopted in other WIMP-FIMP frameworks having extended scalar sector and Higgs portal interaction.

The chapter is organised as follows: first we discuss the model in Section 8.2, features of the model with VBDM as FIMP and scalar singlet as WIMP is discussed next in Section 4.3; FIMP freeze-in and WIMP freeze-out before EWSB is discussed

in Section 4.4, while the case when freeze-in and freeze-out both occur after EWSB is elaborated in Section 4.5, we finally conclude in Section 4.6. Appendices C.1 to C.4 provide some necessary details omitted in the main text.

4.2 The Model

The model consists of two DM components: (i) an abelian vector boson X (VBDM) arising from an $\mathrm{U}(1)_X$ gauge extension of SM and (ii) a real scalar singlet (ϕ) having Higgs portal interaction with the SM. The scalar doublet H is responsible for spontaneous EWSB. Both DM candidates are rendered electromagnetic charge neutral by having zero SM hypercharge. $\mathrm{U}(1)_X$ symmetry spontaneously breaks (to no remnant symmetry) via non-zero vacuum expectation value (vev) of a complex scalar singlet (S) transforming under $\mathrm{U}(1)_X$,[1] to yield X massive. A stabilising symmetry (we choose the simplest possibility $\mathcal{Z}_2$) is further imposed under which $X \to -X$ to make it a stable VBDM. The real scalar singlet (ϕ) also needs to be stabilised for becoming the second DM component of the universe and the simplest possibility is yet again to consider an additional symmetry $\mathcal{Z}_2' : \phi \to -\phi$, different from $\mathcal{Z}_2$[2]. However, X does not have a direct renormalizable coupling to ϕ; X couples to complex scalar S, which has portal interactions to both ϕ and SM Higgs (H). Therefore, ϕ is *apparently stable* even if it transforms under the same $\mathcal{Z}_2$ symmetry as of X, absent a direct interaction with each other. However, an effective dimension five operator involving $\mathrm{U}(1)_X$ gauge field strength tensor $X^{\mu\nu}$, SM hypercharge field strength tensor $B_{\mu\nu}$ and ϕ can be written as:

$$\mathcal{L}_{\text{dim 5}} \supset \frac{1}{\Lambda} X^{\mu\nu} B_{\mu\nu} \phi \,; \tag{4.1}$$

invariant under $\mathrm{SM} \times \mathrm{U}(1)_X \times \mathcal{Z}_2$ symmetry. This will in turn allow the heavier between ϕ and X to decay into the other and provides a single component DM model. The phenomenology of such higher dimensional operator to study DM production of X in context of both freeze-in (see [267, 561]) and freeze out limit [352, 562–569] has been studied. Therefore having two different symmetries for two DM components is necessary, which prohibits an operator like in Eq. (4.1) and renders both DM components stable. The charges of the fields under $\mathcal{Z}_2 \times \mathcal{Z}_2' \times \mathrm{U}(1)_X$ are mentioned in Table 4.1. Note that none of the SM fields possess any charge under the dark symmetry and none of the additional fields has SM charges. The Lagrangian for the model having field content and charges, as in Table 4.1 is:

$$\mathcal{L} = \mathcal{L}_{\text{SM}} + \frac{1}{2}|\partial_\mu \phi|^2 + |D_\mu S|^2 + \frac{1}{4} X^{\mu\nu} X_{\mu\nu} - V(H, \phi, S) \,; \tag{4.2}$$

where,

$$D_\mu = \partial_\mu + i g_X X_\mu; \;\; X^{\mu\nu} = \partial^\mu X^\nu - \partial^\nu X^\mu \,; \text{ and}$$

[1] The $\mathrm{U}(1)_X$ charge of S remains indetermined in absence of any term containing a single S field to cater to $\mathcal{Z}_2$ invariance.

[2] Two different symmetries $\mathcal{Z}_2 \times \mathcal{Z}_2'$ are required to stabilise two DM, as the lightest particle under a symmetry is stable, while the heavier ones transforming under the same symmetry, decay to the lightest.

Particles	$\mathcal{Z}_2$	$\mathcal{Z}_2'$
$\mathrm{U}(1)_X$ Gauge Boson X	$-X$	$+X$
Complex scalar S	S^*	S
Real scalar ϕ	ϕ	$-\phi$
Complex scalar doublet H	H	H

Table 4.1: Fields beyond the SM together with SM Higgs doublet (H) and their charges under the symmetry $\mathcal{Z}_2 \times \mathcal{Z}_2'$.

$$\begin{aligned} V(H,\phi,S) = \; & \mu_H^2(H^\dagger H) + \lambda_H(H^\dagger H)^2 + \tfrac{1}{2}\mu_\phi^2\phi^2 + \tfrac{1}{4!}\lambda_\phi\phi^4 + \mu_S^2(S^*S) + \lambda_S(S^*S)^2 \\ & + \tfrac{1}{2}\lambda_{\phi H}\phi^2(H^\dagger H) + \lambda_{HS}(H^\dagger H)(S^*S) + \tfrac{1}{2}\lambda_{\phi S}\phi^2(S^*S)\,. \end{aligned} \tag{4.3}$$

It is apparent that the model that is studied here, is the same as that studied previously in Chapter 3. In the scalar potential $V(H,\phi,S)$ above (in Eq. (4.3)), we choose $\lambda_H, \lambda_S, \mu_\phi^2 > 0$ and $\mu_H^2, \mu_S^2 < 0$ so that it provides a minimum with the following vacuum:

$$\begin{aligned} H =& \begin{pmatrix} \phi^+ \\ \frac{\mathrm{v}+h+i\phi_0}{\sqrt{2}} \end{pmatrix} \to \langle H\rangle = \begin{pmatrix} 0 \\ \frac{\mathrm{v}}{\sqrt{2}} \end{pmatrix}; \\ S =& \frac{1}{\sqrt{2}}(v_s + s + iA) \to \langle S\rangle = \frac{1}{\sqrt{2}}v_s;\ \langle\phi\rangle = 0\,. \end{aligned} \tag{4.4}$$

Therefore, two scalar fields acquire non-zero vev: $\langle S\rangle = v_s/\sqrt{2}$, which breaks $\mathrm{SM} \times \mathrm{U}(1)_\mathrm{X} \to \mathrm{SM}$ and $\langle H\rangle = \mathrm{v}/\sqrt{2}$, which causes spontaneous EWSB: $\mathrm{SU}(2)_\mathrm{L} \times \mathrm{U}(1)_\mathrm{Y} \to \mathrm{U}(1)_\mathrm{EM}$. In the above, $\phi^{\pm,0}, A$ denote Nambu-Goldstone Bosons, which disappear in the unitary gauge after EWSB. We draw the reader's attention here to a notation used further in the draft, where S refers to the complex scalar singlet field, while s refers to the physical scalar particle after $\mathrm{U}(1)_X$ breaking. Note also that v_s renders the $\mathrm{U}(1)_X$ gauge boson massive via:

$$m_X = g_X v_s\,, \tag{4.5}$$

where g_X denotes $\mathrm{U}(1)_X$ gauge coupling constant. The value of v_s denotes the scale of $\mathrm{U}(1)_X$ symmetry breaking and is crucially governed by the condition whether X is FIMP or WIMP. EWSB scale (v) is known from SM gauge boson masses to be $\mathrm{v} = 246\,GeV$. Physical particles that arise in the model, depends on the scale (before or after EWSB) and will be elaborated in the respective regimes.

We further note that X being odd under $\mathcal{Z}_2$, requires:

$$\mathcal{Z}_2 : X \to -X, \quad \implies \mathcal{Z}_2 : S \to S^*. \tag{4.6}$$

The last relation follows from straightforward calculation. First of all,

$$\begin{aligned} |D^\mu S|^2 \quad &= [(\partial^\mu + ig_X X^\mu)S]^*\,[(\partial^\mu + ig_X X^\mu)S]\,, \\ &= (\partial^\mu - ig_X X^\mu)S^*(\partial^\mu + ig_X X^\mu)S\,. \end{aligned} \tag{4.7}$$

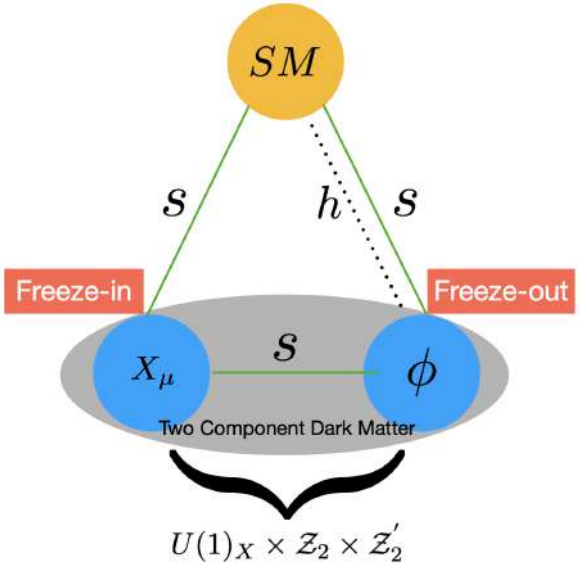

Possible two component DM cases

Vector DM	Scalar DM
Freezes out (WIMP)	Freezes out (WIMP)
Freezes in (FIMP)	Freezes in (FIMP)
Freezes out (WIMP)	Freezes in (FIMP)
Freezes in (FIMP)	Freezes out (WIMP)

Figure 4.1: Left: A cartoon depicting the DM components in the model and their interactions to visible sector and amongst them (see text for notation); Right: Possible scenarios in the two component DM set-up, the one in color is considered in this analysis.

The transformation of the kinetic piece $|D^\mu S|^2$ under $\mathcal{Z}_2$ goes as,

$$\begin{aligned} \mathcal{Z}_2 : |D^\mu S|^2 \quad &= (\partial^\mu - i g_X X^\mu) S^* (\partial^\mu + i g_X X^\mu) S \\ &\to (\partial^\mu + i g_X X^\mu) S^* (\partial^\mu - i g_X X^\mu) S \,. \end{aligned} \tag{4.8}$$

Comparing Eq . (4.8) with Eq . (4.7), we get $\mathcal{Z}_2 : S \to S^*$.

To summarise, the model inherits two DM components, a VBDM X and a scalar singlet ϕ in $\mathrm{U}(1)_X \times \mathcal{Z}_2 \times \mathcal{Z}_2'$ extension of SM. Both of them interact with each other and with SM via scalar particle s[3], while ϕ also interacts via SM Higgs (H) portal. The dark sector particles and their interactions are sketched in a cartoon in the left panel of Fig . 4.1. Four different phenomenological situations emerge depending on which DM freezes in (FIMP) and which freezes out (WIMP), as shown in the right panel of Fig . 4.1. We explore the possibility when X is a FIMP and ϕ is an WIMP like DM.

4.3 Possibilities with X freezing-in and ϕ freezing-out

The first noteworthy feature of the model is the presence of two widely different symmetry-breaking scales: (i) $\mathrm{SM} \times \mathrm{U}(1)_\mathrm{X} \to \mathrm{SM}$, and (ii) EWSB: $\mathrm{SU}(2)_\mathrm{L} \times \mathrm{U}(1)_\mathrm{Y} \to \mathrm{U}(1)_\mathrm{EM}$, which are pictorially depicted in Fig . 4.2. While EWSB scale is known, $\mathrm{U}(1)_X$ breaking scale crucially depends on whether X freezes in or freezes out. It is explained in a moment. X as FIMP and ϕ as WIMP inherit yet another set of phenomenological possibilities that the model offers and are noted in the bottom panel of Fig . 4.2.

• **Freeze-in of X and $\mathrm{U}(1)_X$ breaking scale**: The VBDM X to be a cold DM dictates the scale for $\mathrm{U}(1)_X$ breaking. The $\mathrm{U}(1)_X$ gauge coupling (g_X) which provides

[3] $s - H$ mixing after EWSB also connects VBDM to SM via SM Higgs.

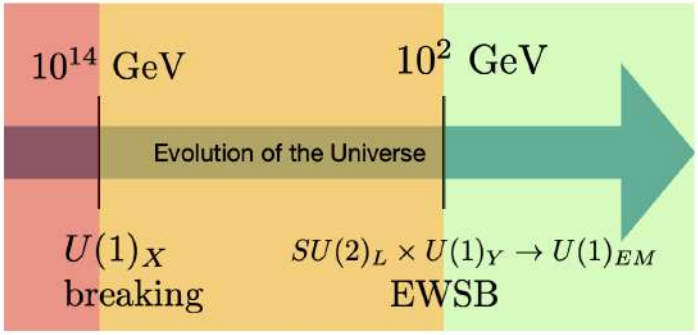

Possible situations	X freezes-in	ϕ freezes-out
(i)	Before EWSB	Before EWSB
(ii)	Before EWSB	After EWSB
(iii)	After EWSB	Before EWSB
(iv)	After EWSB	After EWSB

Figure 4.2: The relevant symmetry breaking scales of the model : $\mathrm{U}(1)_X$ breaking and EWSB (top panel) and different phenomenological situations for X to freeze-in and ϕ to freeze-out (bottom panel).

DM-SM interaction, is required to be feeble (roughly $g_X \sim 10^{-11}$) to keep it out of equilibrium. The DM yield that generates the correct relic is proportional to the production cross-section (or decay width). For $m_X \sim TeV$, so that it behaves as a cold dark matter (CDM), the $\mathrm{U}(1)_X$ breaking scale turns out to be $v_s \sim 10^{14}\ GeV$ (following Eq. (4.5)). On the other hand, EWSB occurs at $T_{\rm EW} \sim 160\ GeV$ [570, 571], corresponding to $v_{\rm EW} \sim \mathrm{v} = 246\ GeV$. Therefore, the hierarchy $v_s \gg \mathrm{v}$ implies $T_{U(1)} \gg T_{\rm EW}$ (see Fig. 4.2), which further aids to the distinction between freeze-in before EWSB (bEWSB) and after EWSB (aEWSB).

1. Freeze-in bEWSB ($T_{\rm EW} < m_X < T_{U(1)}$): When the DM freezes in completely bEWSB, the DM production saturates before $T_{\rm EW}$; then characteristic freeze-in scale is depicted by $T_{\rm FI}$ or $x_{\rm FI} = \frac{m_X}{T_{\rm FI}}$ requires

$$T_{\rm FI} > T_{\rm EW}; \quad \Longrightarrow \quad x_{\rm FI} < x_{\rm EW}\,. \tag{4.9}$$

   Note also, that the characteristic freeze-in temperature is correlated to the DM mass, $T_{\rm FI} \sim m_X$. Obviously, $x_{\rm EW} = \frac{m_X}{T_{\rm EW}}$. In this regime, only the singlet scalar S acquires a vev (v_s) to give mass to X. Other scalars (Higgs and ϕ) are also massive due to bare mass term, while all the SM fields are massless. In such a situation, X has no connection to SM, and the production occurs via the interaction with the physical scalar s, which is assumed to be in the thermal bath due to sizeable portal coupling with SM Higgs (H). The details of the production processes will be discussed in Section 4.4 when we elaborate such a scenario[4].

2. Freeze-in aEWSB ($m_X \lesssim T_{\rm EW}$): When DM production from thermal bath continues even aEWSB, we have,

$$T_{\rm FI} \sim m_X < T_{\rm EW}; \quad \Longrightarrow \quad x_{\rm FI} > x_{\rm EW}\,. \tag{4.10}$$

[4]We shall also note that freeze-in bEWSB does not include the possibility of $T_{\rm FI} > T_{U(1)}$, as X is massless in that regime.

After EWSB, the Higgs doublet (H) acquires a vev (v); H and s mix to yield physical scalars h_1 and h_2, where h_1 is assumed to be SM Higgs (dominantly doublet), the one observed at LHC with $m_{h_1} \sim 125\,GeV$, while h_2 is dominantly a singlet, heavier or lighter than the SM Higgs following the existing bounds. Naturally, DM can be additionally produced from the SM particles in thermal bath aEWSB, providing a different allowed parameter space. The detailed discussion is taken up in Section 4.5.

A cartoon of freeze-in bEWSB (in blue) and aEWSB (in red) is shown in the left panel of Fig . 4.3 in $Y-x$ plane, where $Y = \frac{n}{s}$ refers to DM yield with s denoting to entropy density and $x = \frac{m}{T}$, with m denoting DM mass and T denoting temperature of the bath (details in Section 4.4.4). From left to right along x-axis, x becomes larger with T dropping. In Fig . 4.3 (left panel) we consider two DM species denoted by ① and ② with $m_2 > m_1$. Following $T_{\rm FI} \sim m_X$, we have $x_{\rm FI} \sim 1$ for both cases. Then following, $x_{\rm FI} < x_{\rm EW}$ for freeze-in bEWSB, we need $m > T_{\rm EW}$, while for freeze-in aEWSB, $x_{\rm FI} > x_{\rm EW}$ requires $m < T_{\rm EW}$. Therefore, we can have $m_2 > T_{\rm EW} > m_1$ where ② freezes in bEWSB and ① freezes in aEWSB. The red vertical dotted line shows $x_{\rm FI} \sim 1$, while pink and blue dotted vertical lines indicate $(x_1)_{\rm EW}$ and $(x_2)_{\rm EW}$ with $(x_2)_{\rm EW} > (x_1)_{\rm EW}$. The relative abundance shown here depends on DM-SM interaction and has no implication unless discussed in context of the model.

• **Freeze-out of ϕ and EWSB**: The real scalar singlet ϕ is assumed to be in thermal bath via non-suppressed portal couplings. It freezes out through the dominant $2 \to 2$ annihilation to SM and also to other DM candidate (if kinematically allowed). The freeze-out do not crucially dictate any scale in the model unlike freeze-in. Here also, two possibilities emerge:

1. Freeze-out bEWSB : For ϕ to freeze out bEWSB, one requires the characteristic freeze-out temperature ($T_{\rm FO}$) to follow,

$$T_{\rm FO} > T_{\rm EW} \implies x_{\rm FO} < x_{\rm EW}\,; \tag{4.11}$$

where $x_{\rm FO} = \frac{m_\phi}{T_{\rm FO}}$. The processes that are responsible for freeze out of ϕ bEWSB are only through the coupling with the physical scalar s and will be elaborated in Section 4.4.

2. Freeze-out aEWSB : Freeze out of ϕ aEWSB implies:

$$T_{\rm FO} < T_{\rm EW} \implies x_{\rm FO} > x_{\rm EW}\,. \tag{4.12}$$

In this regime, the interaction between ϕ and SM arises through $h-s$ mixing and occurs via both the physical scalars h_1 and h_2. Therefore, new channels contribute to DM number depletion, we discuss them in detail in Section 4.5.

Unlike freeze-in, freeze-out of DM does not directly constrain the DM mass. However, for freeze-out to render correct relic density, $x_{\rm FO}$ remains in the ballpark $x_{\rm FO} \sim 20-25$. Inevitably, freeze-out bEWSB or aEWSB can be realized for different DM masses (m), which changes $x_{\rm EW} = \frac{m}{T_{\rm EW}}$ to lie above or below $x_{\rm FO}$, as depicted in the right panel of Fig . 4.3. We again consider two DM species denoted by ① and ② with $m_2 > m_1$ (shown by green and pink lines); so that $(x_2)_{\rm EW} > (x_1)_{\rm EW}$ (vertical

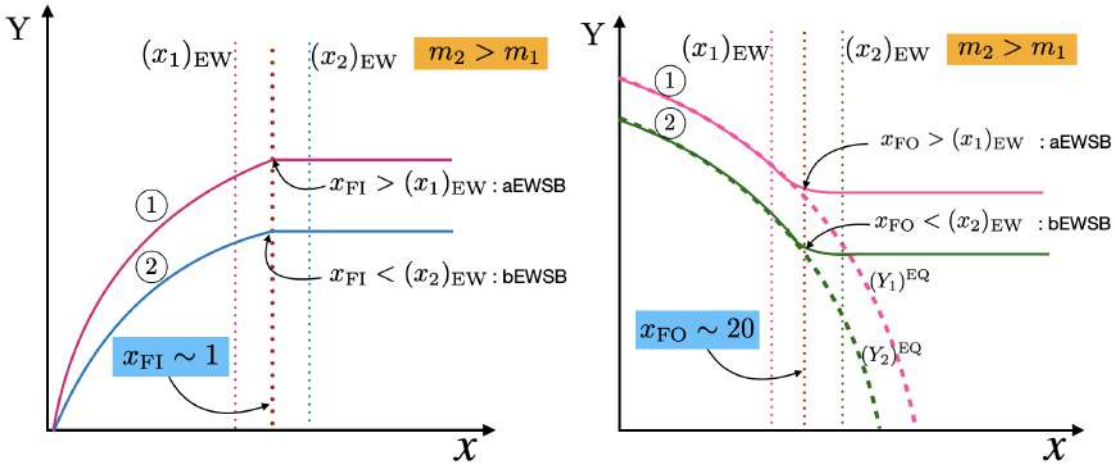

Figure 4.3: Left: A cartoon freeze-in in the $Y - x$ plane for two sample DMs with $m_2 > m_1$ which shows freeze-in aEWSB (in red) and bEWSB (in blue). Right: Cartoon freeze-out which shows freeze-out aEWSB (in pink) and bEWSB (in green) from the respective equilibrium distributions (in dashed curves) shown in the right panel.

dotted lines) depicts freeze-out bEWSB ($x_{\rm FO} < (x_2)_{\rm EW}$) and aEWSB ($x_{\rm FO} > (x_1)_{\rm EW}$) respectively from their equilibrium distributions. The distributions and the relative yields in this figure have not been sketched for a particular model or interaction, so the relative strengths have no implications, this is just for illustration purposes.

Out of different freeze-in epochs of X and freeze-out of ϕ, as noted in the bottom panel of Fig . 4.2, we explore two sample cases here with (i) both freeze-in and freeze-out occurring bEWSB and (ii) both occurring aEWSB, which capture the most interesting distinctions of allowed parameter space of the model.

4.4 Dark Matter phenomenology bEWSB

Here, we address in detail the freeze-in of X and freeze-out of ϕ, both occurring bEWSB (option (i) of the bottom panel in Fig . 4.2.). To be specific, the temperatures around which freeze-in ($T_{\rm FI}$) and freeze-out ($T_{\rm FO}$) occur, lie between $\mathrm{U}(1)_X$ breaking and EWSB, i.e.

$$T_{U(1)} > T_{\rm FI} > T_{\rm EW};\;\; T_{U(1)} > T_{\rm FO} > T_{\rm EW}\,. \tag{4.13}$$

In the following subsections, we discuss the physical particles and interactions in this regime for DM freeze-in and freeze-out via coupled BEQ, relic density and direct search allowed parameter space of the model.

4.4.1 Physical states and parameters

As the regime is dictated by interactions after spontaneous $\mathrm{U}(1)_X$ breaking and bEWSB, in unitary gauge we have,

$$S = \frac{1}{\sqrt{2}}(v_s + s) \to \langle S\rangle = \frac{1}{\sqrt{2}}v_s,\;\; \langle H\rangle = 0,\;\; \langle\phi\rangle = 0\,. \tag{4.14}$$

The scalar potential in this limit reads:

$$V_{\text{scalar}} = \mu_H^2(H^\dagger H) + \lambda_H(H^\dagger H)^2 + \frac{1}{2}\mu_\phi^2\phi^2 + \frac{1}{4!}\lambda_\phi\phi^4 + \frac{1}{2}\mu_S^2(v_s+s)^2 + \frac{1}{2}\lambda_{\phi H}(H^\dagger H)\phi^2 + \frac{1}{4}\lambda_S(v_s+s)^4 + \frac{\lambda_{HS}}{2}(H^\dagger H)(v_s+s)^2 + \frac{\lambda_{\phi S}}{4}\phi^2(v_s+s)^2 . \tag{4.15}$$

The physical scalars can be identified from the extremization of the potential, which provides the following relations between the neutral physical scalars and parameters of the model:

$$\begin{aligned}
\frac{\partial V_{\text{scalar}}}{\partial s} &= 0 \to \mu_S^2 = -\lambda_S v_s^2 , \\
\frac{\partial^2 V_{\text{scalar}}}{\partial H^\dagger \partial H} &= m_H^2 \to \mu_H^2 = m_H^2 - \frac{\lambda_{HS}}{2}v_s^2 , \\
\frac{\partial^2 V_{\text{scalar}}}{\partial \phi^2} &= m_\phi^2 \to \mu_\phi^2 = m_\phi^2 - \frac{\lambda_{\phi S}}{2}v_s^2 , \\
\frac{\partial^2 V_{\text{scalar}}}{\partial s^2} &= m_s^2 \to \mu_S^2 = m_s^2 - 3\lambda_S v_s^2 ;
\end{aligned} \tag{4.16}$$

where m_H is the mass of the SM like Higgs bEWSB and m_ϕ is the mass of real scalar DM (ϕ) bEWSB. We must note here that H bEWSB represents *four* massive scalar degrees of freedom (d.o.f) [270, 540, 572, 573] being part of the complex isodoublet, while ϕ has only one d.o.f being a real scalar singlet. Using Eq. (4.15) and Eq. (4.16), it is easy to show that the mass of the $\mathrm{U}(1)_X$ complex scalar turns out to be $m_s^2 = 2\lambda_S v_s^2$. Although m_H and m_s can be treated as free parameters, they must reproduce correct Higgs mass and mixing, see discussions in the next Section 4.4.2 and Appendix C.2.

This allows us further to identify the parameters of the model that are relevant for the analysis. All the physical masses and the couplings controlling the relic density of DM are chosen as the external parameters. Quartic self couplings like λ_H and λ_ϕ are fixed at values within the limit of DM self-scattering (~ 0.1) and play a minimal role in DM-SM interaction. All the other parameters are considered as internal parameters, which are defined by the relations described in Eqs. (4.5) and (4.16). Table 4.2 summarises the parameters of the model bEWSB. The parameters of the model are subject to further constraints as explained in the next subsection.

External parameters	Internal parameters
$m_H, m_s, m_\phi, m_X, g_X, \lambda_H, \lambda_\phi, \lambda_{HS}, \lambda_{\phi S}, \lambda_{\phi H}$	$\mu_H, \mu_\phi, \mu_S, v_s, \lambda_S$

Table 4.2: External and internal parameters of the model bEWSB.

4.4.2 Constraints and bounds

In this section, we discuss the possible theoretical and experimental constraints on the parameters of the model relevant to our analysis.

- **Stability:**
  In order to get the potential bounded from below, the quadratic couplings of the potential $V_{\rm scalar}$ must satisfy the following co-positivity conditions as [574–576],

$$\begin{gathered}\lambda_H \geq 0, \lambda_\phi \geq 0, \lambda_S \geq 0, \\ \lambda_{\phi H} + 2\sqrt{\lambda_H \lambda_\phi} \geq 0, \lambda_{HS} + 2\sqrt{\lambda_H \lambda_S} \geq 0, \lambda_{\phi S} + 2\sqrt{\lambda_\phi \lambda_S} \geq 0\,.\end{gathered} \tag{4.17}$$

  In this analysis, we choose all the couplings positive, which satisfy the above conditions trivially.

- **Perturbativity:**
  In order to maintain the perturbativity of the theory, the quartic couplings of the scalar potential $V_{\rm scalar}$ and the gauge couplings obey [473, 475],

$$\begin{aligned}&\lambda_H < 4\pi, && \lambda_S < 4\pi, && \lambda_\phi < 4\pi, && g_X < \sqrt{4\pi}, \\ &\lambda_{HS} < 4\pi, && \lambda_{\phi S} < 4\pi, && \lambda_{\phi H} < 4\pi\,.\end{aligned} \tag{4.18}$$

- **Tree level unitarity:**
  Tree level unitarity of the theory, coming from all possible $2 \to 2$ scattering amplitude, can be ensured [473–475] via following constraints

$$|\lambda_\phi| < 8\pi,\ |\lambda_S| < 4\pi,\ |\lambda_H| < 4\pi,\ |\lambda_{\phi S}| < 8\pi,\ |\lambda_{HS}| < 8\pi,\ |\lambda_{\phi H}| < 8\pi\,. \tag{4.19}$$

- **Constraints on DM mass bEWSB:**
  For freeze-in of X to complete bEWSB, it is required that the freeze-in scale ($T_{\rm FI} \sim m_X$) has to be larger than $T_{\rm EW} \sim 160\ GeV$; then, $m_X \gtrsim 160\ GeV$. Similarly, freeze-out of ϕ bEWSB forces the freeze-out temperature $T_{\rm FO}$ to be larger than $T_{\rm EW}$, i.e, $T_{\rm FO} \gtrsim 160\ GeV$. This condition automatically implies that $x_{\rm FO} = m_\phi/T_{\rm FO}$, which is typically ~ 25 for WIMP freeze-out, requires the following conditions on WIMP and FIMP masses:

$$\text{WIMP}: \ m_\phi \gtrsim 4\ TeV; \ \ \text{FIMP}: \ m_X \gtrsim 160\ GeV. \tag{4.20}$$

- **Relic density**: One of the most important constraints on the parameters of the model comes from the observed relic abundance of DM. The latest observations from anisotropies in CMBR in experiments like WMAP [577], and PLANCK [7] indicate

$$\Omega_{\rm DM}h^2 = \Omega_X h^2 + \Omega_\phi h^2 = 0.1200 \pm 0.0012\,, \tag{4.21}$$

  where $\Omega = \frac{\rho}{\rho_c}$ refers to cosmological density, with ρ_c indicating critical density, h is the present Hubble parameter scaled in units of 100 km/s/Mpc. In the two-component WIMP-FIMP setup that we explore here, the individual relic densities of X and ϕ shall add to the total observed relic, where each of the individual components will be under-abundant, *ie*, $\Omega_{X,\phi}h^2 \lesssim 0.12$. We elaborate on the relic density of the WIMP and FIMP components of the model in the next section.

- **Direct detection (DD) constraints**: WIMP (ϕ) has a direct search prospect, while the FIMP (X) does not [5]. In this regime, although freeze out of ϕ occurs bEWSB, after EWSB ϕ couples to SM, yielding a possibility of direct search of ϕ. Non-observation of DM from ongoing experiments like XENON1T [578] sets a stringent upper limit on WIMP-nucleon spin-independent elastic scattering cross-section at 90% C.L,

$$\sigma_{\rm SI} \sim \begin{cases} 4.1 \times 10^{-47}\ {\rm cm}^2 & \text{at } 30\ {\rm GeV/c}^2\ \ ({\rm XENON1T}) \\ 1.4 \times 10^{-48}\ {\rm cm}^2 & \text{at } 50\ {\rm GeV/c}^2\ \ ({\rm XENONnT}) \end{cases} \tag{4.22}$$

  Here, we also mention the projected XENONnT [579] sensitivity. The relevant couplings g_X and $\lambda_{\phi S}$,[6] are constrained to be $\sim 10^{-12}$ both from the freeze-in requirements and direct search bounds. In addition, $\lambda_{\phi H} \sim 10^{-3}$ keeps the DD cross-section safely below the experimental direct search bounds. We provide a detailed account for the direct search of the model in the Appendix C.4.

- **Higgs mass and mixing**: It is important to note that independent of DM freeze-out or freeze-in to occur bEWSB or aEWSB, there is a mixing of Higgs (h) with s after EWSB to render two physical states: h_1, assumed to be SM like Higgs with $m_{h_1} = 125.1\ GeV$ and a heavy or light h_2, dominantly a singlet. $h - s$ mixing angle (θ) is restricted by LHC data [489] within:

$$|\sin\theta| \lesssim 0.3\,. \tag{4.23}$$

  The requirement of correct Higgs mass, as well as mixing, puts a limit on parameters m_H, m_s, λ_{HS}, etc. For details of the mass eigenstates, mixing, and relations with model parameters, refer to the discussions in Appendix C.2. We note here one important exception: if $m_s \gtrsim 2m_X$ then dominant FIMP production occurs from s decay, and additionally, if the FIMP production from late decay of s saturates bEWSB, then there is no s which remains in the bath to mix with h and consequently no h_2 state to appear aEWSB. Then Higgs mass bEWSB and aEWSB are related by $m_H^2 = \frac{m_{h_1}^2}{2}$. Note further, collider bound on scalar singlet WIMP DM mass m_ϕ is mild [580, 581], while no significant bound on FIMP mass can be obtained.

- **Invisible Decay of Higgs :** SM Higgs (h_1) can decay into pairs of DM (X and ϕ) as well as to pairs of h_2 in our model if kinematically allowed. Since these decays contribute to the invisible decay of Higgs, corresponding $h_1\phi\phi,\ h_1XX,\ h_1h_2h_2$ couplings get severely constrained by the experimental data. They can be traced from expressions of Higgs decay width to ϕ, X, h_2 as provided in Appendix C.3. As per the latest experimental data given by ATLAS (for 139 fb^{-1} luminosity at $\sqrt{s} = 13\ TeV$), the strictest upper limit on $\mathcal{B}_{h_1\to\text{inv}}$ can be set to $\sim$

[5] The interaction of X with SM occurs via physical scalars $h_{1,2}$. Due to tiny λ_{HS} coupling ($\sim 10^{-12}$) and heavy mass of the mediators $\sim \mathcal{O}(100)$GeV as considered here, FIMP X does not have any direct search prospect. But, the smallness of the dominantly singlet scalar mass $m_{h_2} \sim$ MeV may bring X under the DD scanner [510].

[6] Also, as $v_s \sim 10^{14}\ GeV$, the requirement of keeping X out-of-equilibrium demands that the coupling $\lambda_{\phi S}$ should be as small as $\sim 10^{-12}$.

0.13 at 95% CL [582–584]. A comparison of the invisible Higgs decay bound from the latest ATLAS and CMS data are given by:

$$\begin{aligned} \mathcal{B}_{h_1\to\text{inv}} &< \begin{cases} 0.13 & \text{(ATLAS)} \\ 0.19 & \text{(CMS)} \end{cases} \\ \Gamma_{h_1\to\text{inv}} &< \begin{cases} 0.61\ \text{MeV} & \text{(ATLAS)} \\ 0.95\ \text{MeV} & \text{(CMS)} \end{cases} \end{aligned} \tag{4.24}$$

For simplicity, we do not scan the region of parameter space where Higgs invisible decay to DM is possible, with $m_X > m_{h_1}/2$, and $m_\phi > m_{h_1}/2$. However, $h_2 \to XX$ is considered for the analysis, where there is no bound.

4.4.3 Processes contributing to DM Relic

The processes that contribute to the freeze-in of vector boson X bEWSB are shown in Fig . 4.4. The initial abundance of X in the early universe is assumed negligible, while it builds up via production from the particles in thermal bath, namely s, ϕ and H. Decay of s contributes the most, subject to the kinematic constraint $m_s \geq 2m_X$. Scattering processes $ss \to XX$ also contribute, but it is suppressed compared to the decay. In addition, $HH^\dagger \to XX$ and $\phi\phi \to XX$ also contribute, mediated by s-channel s. The process $\phi\phi \to XX$ is WIMP-FIMP conversion, and it occurs as ϕ is assumed present in the thermal bath. We will discuss the effect of such conversion contributions in detail. It is worth noting that unsuppressed $ss \to H^\dagger H$, $\phi\phi \to H^\dagger H$, $\phi\phi \to ss$ keep ϕ, s, and H, all in equilibrium in early universe. The processes which contribute to the freeze out of ϕ bEWSB are shown in Fig . 4.5. They are all known and include $\phi\phi \to HH^\dagger$ via the quartic coupling as well as that mediated by s; additionally, $\phi\phi \to ss$ occurs via quartic portal coupling, and s-channel mediation by s and t-channel mediation by ϕ. Finally, WIMP-FIMP conversion $\phi\phi \to XX$ via s-channel mediation of s is also possible as shown in the bottom panel of Fig . 4.5, otherwise absent in single component case. Let us recall again that all the processes initiated by H and those produce H assume four massive scalar d.o.f.

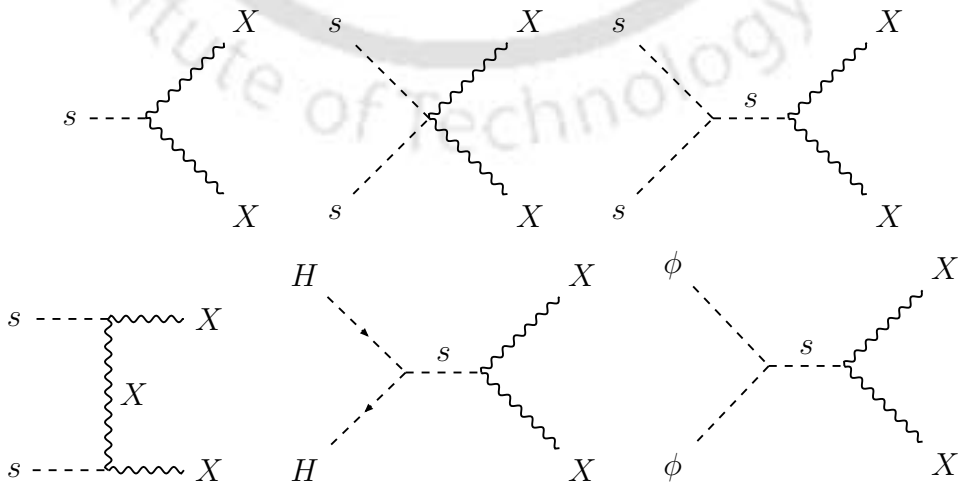

Figure 4.4: Feynman diagrams showing non-thermal production channels of X bEWSB.

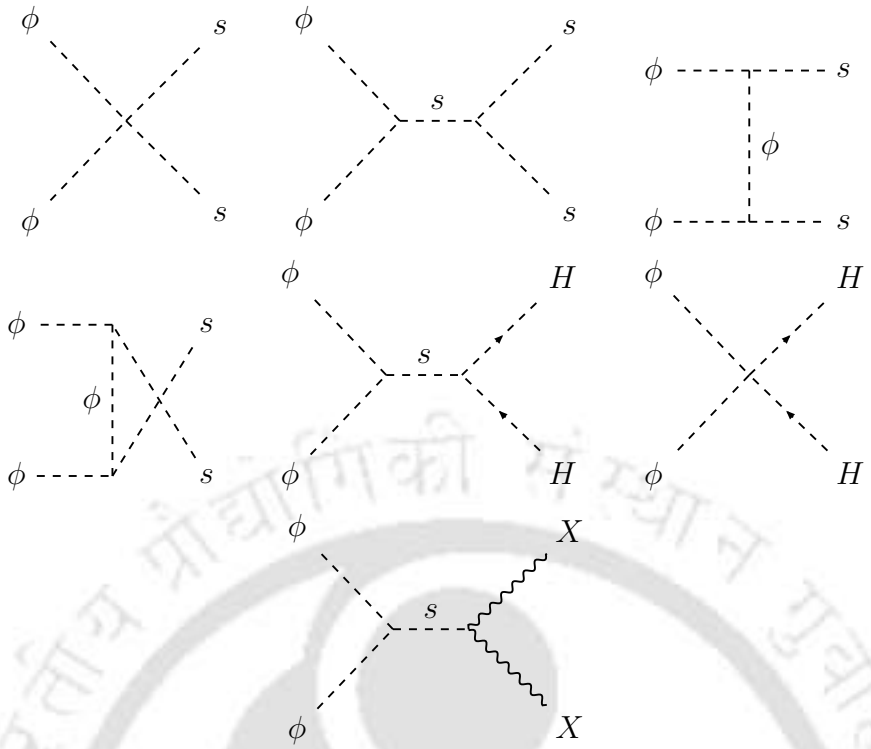

Figure 4.5: Feynman diagrams contributing to ϕ freeze-out via $2 \to 2$ depletion processes bEWSB.

4.4.4 Coupled Boltzmann Equations and conversion

The DM number density for the WIMP-FIMP scenario can be evaluated by the coupled Boltzmann equations (cBEQs):

$$\frac{dY_X}{dx} = -\frac{2\,\mathrm{M_{Pl}}}{1.66}\frac{x}{m_X^2}\frac{\sqrt{g_*(x)}}{g_s^*(x)}\langle\Gamma_{s\to XX}\rangle\,(Y_X - Y_s^{eq}) - \frac{4\pi^2\mathrm{M_{Pl}}\sqrt{g_*(x)}}{45\times 1.66}\frac{m_X}{x^2}\left[\sum_{i=s,H}\langle\sigma v\rangle_{ii\to XX}\left(Y_X^2 - (Y_i^{eq})^2\right) - \langle\sigma v\rangle_{\phi\phi\to XX}\left(Y_\phi^2 - \frac{(Y_\phi^{eq})^2}{(Y_X^{eq})^2}Y_X^2\right)\right], \tag{4.25}$$

$$\frac{dY_\phi}{dx} = -\frac{2\pi^2\,\mathrm{M_{Pl}}\sqrt{g_*(x)}}{45\times 1.66}\frac{m_\phi}{x^2}\left[\sum_{i=s,H}\langle\sigma v\rangle_{\phi\phi\to ii}\left(Y_\phi^2 - (Y_\phi^{eq})^2\right) + \langle\sigma v\rangle_{\phi\phi\to XX}\left(Y_\phi^2 - \frac{(Y_\phi^{eq})^2}{(Y_X^{eq})^2}Y_X^2\right)\right]. \tag{4.26}$$

In the above, $x = m/T$, $Y_{X,\phi} = \frac{n_{X,\phi}}{\boldsymbol{s}}$, where $n_{X,\phi}$ refers to the number of X and ϕ respectively, and $\boldsymbol{s}$ represents entropy density given by $\boldsymbol{s} = \frac{2\pi^2}{45}g_*^s(T)T^3$. The equilibrium number density with respect to comoving volume for non-relativistic species (X, ϕ) is given by Boltzmann distribution (assuming chemical potential to be zero)

$$Y^{eq} = \frac{n^{eq}}{\boldsymbol{s}} = 0.145\frac{g}{g_*^s}x^{3/2}e^{-x}.$$

Further note $\sqrt{g_*(T)} \simeq \frac{g_*^s(T)}{\sqrt{g_*^\rho(T)}}$, where g_*^s and g_*^ρ denote d.o.f corresponding to entropy and energy density of the universe. Further, $\mathrm{M_{Pl}} = 1.22\times 10^{19}$ GeV denotes

reduced Planck mass. Thermal average of decay width $\langle\Gamma_{A\to BB}\rangle$ and annihilation cross-section times the velocity $\langle\sigma v\rangle_{AA\to BB}$ are given by,

$$\langle\Gamma_{A\to BB}\rangle = \Gamma_{A\to BB}\frac{K_1\left(m_B/T\right)}{K_2\left(m_B/T\right)}\,, \tag{4.27}$$

$$\langle\sigma v\rangle_{AA\to BB} = \frac{1}{8m_A^4TK_2^2(m_A/T)}\int_{4m_B^2}^{\infty} d\mathtt{s}\;\sigma_{AA\to BB}(\mathtt{s})(\mathtt{s}-4m_A^2)\sqrt{\mathtt{s}}\,K_1\left(\sqrt{\mathtt{s}}/T\right)\,, \tag{4.28}$$

$K_{1,2}$ are modified Bessel functions of first and second kind respectively and v refers to Möllar velocity defined by $v=\frac{\sqrt{(p_1.p_2)^2-m_1^2m_2^2}}{E_1E_2}$. In $\langle\Gamma_{A\to BB}\rangle$, the particle (A) is decaying at rest and the thermal average do not involve an integration over the centre-of-mass energy $\sqrt{\mathtt{s}}$, while for annihilation cross-section $\langle\sigma v\rangle_{AA\to BB}$, a lower limit $\mathtt{s}=4m_B^2$ is required for the reaction to occur, and it diminishes at high $\sqrt{\mathtt{s}}$, owing to the presence of $K_1\left(\sqrt{\mathtt{s}}/T\right)$ for a particular T.

One important point to note before we proceed further. The WIMP-FIMP conversion $\phi\phi\to XX$, which makes the BEQs (Eq. (4.25) and 4.26) coupled, requires to be of the order of freeze-in production cross-section, as otherwise it will thermalize the FIMP, suppressing the non-thermal production (this exercise will be discussed in detail elsewhere). This, in turn, makes the conversion process negligible compared to other annihilation cross-sections of ϕ (first term in Eq. (4.26)). However, this conversion can still be significant for non-thermal production of X. This feature is generic to any two-component WIMP-FIMP model, where the freeze-out of WIMP can be marked unaffected by the conversion to FIMP, while the FIMP production can be substantial due to WIMP. This feature importantly reduces the cBEQs as in Eq. (4.25) and Eq. (4.26) to two individual uncoupled BEQs, where the conversion can be dropped from Eq. (4.26) to yield:

$$\begin{aligned}\frac{dY_X}{dx} =& \frac{2\,\mathrm{M_{Pl}}}{1.66\sqrt{g_*^\rho(x)}}\frac{x}{m_X^2}\langle\Gamma_{s\to XX}\rangle Y_s^{eq}\\ &+\frac{4\pi^2\,\mathrm{M_{Pl}}}{45\times1.66}\frac{g_*^s(x)}{\sqrt{g_*^\rho(x)}}\frac{m_X}{x^2}\left(\sum_{i=s,H}\langle\sigma v\rangle_{ii\to XX}(Y_i^{eq})^2+\langle\sigma v\rangle_{\phi\phi\to XX}Y_\phi^2\right)\,,\end{aligned} \tag{4.29}$$

$$\frac{dY_\phi}{dx} = -\frac{2\pi^2\,\mathrm{M_{Pl}}}{45\times1.66}\frac{g_*^s(x)}{\sqrt{g_*^\rho(x)}}\frac{m_\phi}{x^2}\sum_{i=s,H}\langle\sigma v\rangle_{\phi\phi\to ii}\left(Y_\phi^2-(Y_\phi^{eq})^2\right)\,. \tag{4.30}$$

Eqs. (4.29) and (4.30) allow us to treat the freeze-in of X and freeze-out of ϕ separately as we do next. It also allows to treat $x=m_X/T$ in Eq. (4.29) and $x=m_\phi/T$ in Eq. (4.30) as two separate variables [7]. We further note that in view of small Y_X and feeble interaction, we have dropped the terms $\propto Y_X$ and Y_X^2 ($X\,X\to s$ and $X\,X\to i\,i$) in Eq. (4.25) to obtain Eq. (4.29).

4.4.5 Freeze-in of X

Now let us discuss the freeze-in of X, bEWSB in details. The main point is that the initial abundance of X in the early universe is negligible, builds up from the decay or

[7] Otherwise in cBEQ, one needs to define a common $x=\mu/T$, where $\mu=\frac{m_Xm_\phi}{m_X+m_\phi}$ (see [585]).

scattering of the particles in the thermal bath, and saturates when the photon temperature falls below DM mass. One essentially then needs to solve BEQ . (4.29) from $x \simeq 0$ to $x = m_X/T_{\rm EW}$, using non-thermal production of X, indicated in Fig . 4.4, and include:

(i) s decays to X pair while in thermal equilibrium and after s freezes out,

(ii) s and H scattering to X pairs,

(iii) ϕ pair annihilation to X pairs.

However, there is a slight twist to the story. The decay contribution of s to X pairs, as written in Eq . (4.29), is only applicable when the decaying particle is in equilibrium with the thermal bath. The decay process, however, continues even after s freezes out from the thermal bath, i.e. beyond $x \geq x_D$, where x_D denotes the freeze-out point of s. The decay contribution after freeze-out of s from the thermal bath is often termed as 'late decay' (LD) of s. The dynamics of such effect can be captured by yet another coupled BEQ written together with the evolution of yield Y_s (see Appendix C.1), where the freeze out of s is governed by its annihilation channels to SM[8], as shown in the Feynman graph in Fig . 4.6. The coupled BEQ for this case can be simplified to a single BEQ with an additional term to in-equilibrium decay (for derivation, see [268, 586]):

$$\begin{aligned}\frac{dY_X}{dx} =& \frac{45}{3.32\pi^4}\frac{g_s\, M_{\rm Pl}\, m_s^2\, \Gamma_{s\to XX}}{m_X^4}\left(\frac{x^3 K_1\left[\frac{m_s}{m_X}x\right]}{g_*^s(x)\sqrt{g_*^\rho(x)}}\Theta\left(x_D - x\right)\right.\\ &\left. + e^{-\frac{0.602\, M_{\rm Pl}\,\Gamma_{s\to XX}}{m_X^2\sqrt{g_*^\rho(x)}}(x^2-x_D^2)}\frac{x^2 x_D}{\eta(x,x_D)}K_1\left[\alpha(x,x_D)\frac{m_s}{m_X}\frac{x^2}{x_D}\right]e^{\frac{m_s}{m_X}\left(\alpha(x,x_D)\frac{x^2}{x_D}-x_D\right)}\Theta(x-x_D)\right)\\ &+ \frac{4\pi^2\,{\rm M_{Pl}}}{45\times 1.66}\frac{g_*^s(x)}{\sqrt{g_*^\rho(x)}}\frac{m_X}{x^2}\left(\sum_{i=s,H}\langle\sigma v\rangle_{ii\to XX}(Y_i^{eq})^2 + \langle\sigma v\rangle_{\phi\phi\to XX}Y_\phi^2\right). \end{aligned} \tag{4.31}$$

In the above, the term proportional to $\Theta(x_D - x)$ in the first parenthesis indicates FIMP production from 'in-equilibrium' decay of s, and the second term in the first parenthesis captures the late decay contribution with $\Theta(x - x_D)$ denoting the Heaviside theta function. Also note that g_s (internal d.o.f for s) is 1. The freeze-out point of s is denoted by x_D, which can be found out by the following expression:

$$x_D = \ln[\Lambda] - \frac{1}{2}\ln[\ln[\Lambda]],\ \Lambda = 0.038\,\frac{g_s m_s {\rm M_{Pl}}}{\sqrt{g_*^\rho}}\sum_{\rm SM=H,\phi,X}\sigma^0_{ss\to {\rm SM\ SM}}, \tag{4.32}$$

where $\sigma^0_{ss\to {\rm SM\ SM}}$ denotes annihilation cross-section of s to SM particles at threshold ($\mathtt{s} = 4\,m_{\rm s}^2$) and corresponding expressions are provided in the Appendix C.1. Also

[8]The presence of the $s \to H^\dagger H$ decay ensures that s always remains in thermal equilibrium for $\lambda_{HS} \sim 10^{-14}$, preventing the LD of s during the FI of X. However, for $\lambda_{HS} \sim 10^{-20}$, the late decay of s during the freeze-in of X occurs. Our results mainly consider such possibilities, as the FO of s is controlled by a comparatively larger coupling $\lambda_{\phi S}$ in the $ss \to \phi\phi$ process. However, in the absence of s-decay (scattering-dominant regime), we have chosen $\lambda_{HS} \sim 10^{-10}$ so that s always remains in thermal equilibrium during the FO of ϕ and the FI of X, where $ss \to H^\dagger H$ processes will also take part in FIMP relic.

note in Eq. (4.31), the factor $\eta(x, x_D)$ and $\alpha(x, x_D)$ are given by:

$$\eta(x, x_D) = \alpha(x, x_D) g_*^s(x) \sqrt{g_*^\rho(x)}, \quad \alpha(x, x_D) = \left[\frac{g_*^s(x_D)}{g_*^s(x)}\right]^{1/3} \left[\frac{g_*^\rho(x_D)}{g_*^\rho(x)}\right]^{1/4}. \tag{4.33}$$

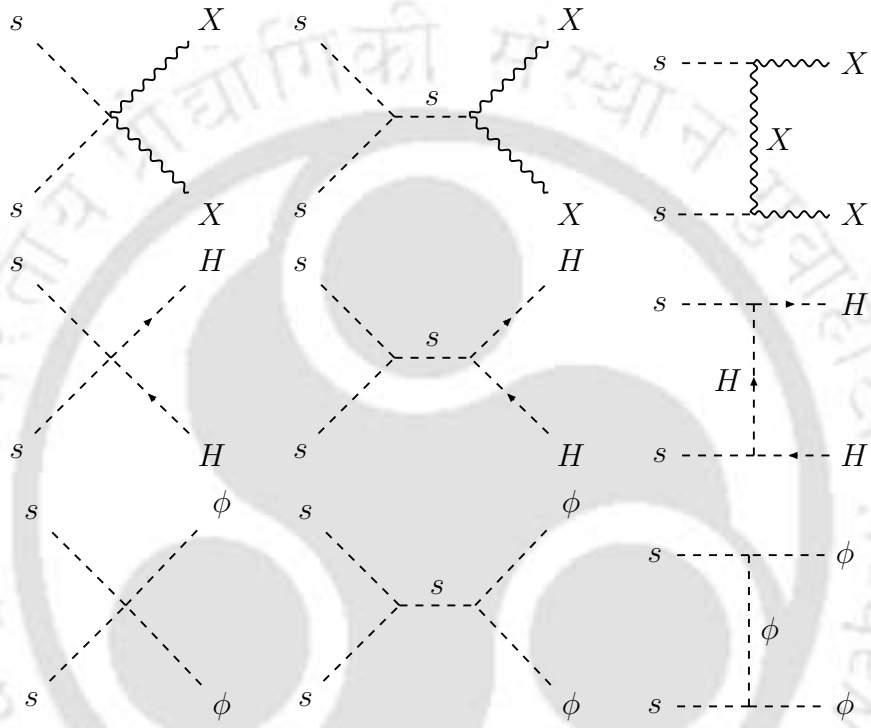

Figure 4.6: Feynman diagrams showing all possible annihilation channels of s, which causes s to freeze out from thermal bath bEWSB.

Late decay contribution provides a significant contribution to DM yield. However, when we consider freeze-in to occur bEWSB, late decay contribution should also accumulate fully bEWSB. This evidently requires freeze-out of s to occur bEWSB with $T_D > T_{\rm EW}$, with $x_D = \frac{m_s}{T_D}$ (see Eq. (4.32) for details) varying typically in the range of $\sim 20 - 25$. We can achieve this limit by having heavy m_s for which $x_D \leq m_s/T_{\rm EW}$, resulting a limit on m_s as:

$$T_{\rm EW} \lesssim \frac{m_s}{25} \implies m_s \gtrsim 4\ {\rm TeV}\,, \tag{4.34}$$

which is not surprisingly the same limit on WIMP mass to freeze-out bEWSB as in Eq. (4.20).

The yield of X in the pre-EWSB regime is given by,

$$
\begin{aligned}
Y_X^{\rm bEWSB} = & \frac{45}{3.32\pi^4}\frac{\mathrm{M_{Pl}}\, m_s^2\, \Gamma_{s\to XX}}{m_X^4}\int_0^{m_X/T_{\rm EW}}\Bigg[\frac{x^3 K_1\left[\frac{m_s}{m_X}x\right]}{\sqrt{g_*^\rho(x)}g_*^s(x)}\Theta\left(x_D-x\right) \\
& + e^{-\frac{0.602\,\mathrm{M_{Pl}}\,\Gamma_{s\to XX}}{m_X^2\sqrt{g_*^\rho(x)}}(x^2-x_D^2)}\frac{x^2 x_D}{\eta(x,x_D)}K_1\left[\alpha(x,x_D)\frac{m_s}{m_X}\frac{x^2}{x_D}\right]e^{\frac{m_s}{m_X}\left(\alpha(x,x_D)\frac{x^2}{x_D}-x_D\right)}\Theta(x-x_D)\Bigg]dx \\
& + \frac{45\,\mathrm{M_{Pl}}}{4\pi^6\times 1.66}\int_0^{m_X/T_{\rm EW}}\sum_{i=s,H}\langle\sigma v\rangle_{ii\to XX}\frac{m_i^4}{m_X^3}\frac{x^2K_2^2\left[\frac{m_i}{m_X}x\right]}{g_*^s(x)\sqrt{g_*^\rho(x)}}dx \\
& + \frac{4\pi^2\mathrm{M_{Pl}m_X}}{45\times 1.66}\int_0^{m_X/T_{\rm EW}}\langle\sigma v\rangle_{\phi\phi\to XX}\frac{g_*^s(x)}{\sqrt{g_\rho^*(x)}}\frac{Y_\phi^2}{x^2}dx\,. \qquad (4.35)
\end{aligned}
$$

We note that although the limit of x integration above is taken up to EWSB scale ($x:0\to m_X/T_{\rm EW}$), the result does not alter if we extend the limit to smaller temperature or larger $x\to\infty$, as the parameters are chosen in a way that freeze-in occurs bEWSB. Freeze-in bEWSB is ensured by checking $Y_{x>x_{EW}}=Y_{x_{EW}}$. Finally, the relic density for X can be written in terms of Y_X, and we want to probe under abundant region as X constitutes a part of two-component framework, then,

$$
\Omega_X\mathrm{h}^2\simeq 2.744\times 10^8\,\mathrm{m_X Y_X^{bEWSB}};\;\;\Omega_X\mathrm{h}^2\leq 0.1212\,. \qquad (4.36)
$$

where the FIMP dark matter relic density is written in terms of the reduced Hubble parameter, h in units of 100 km/s/Mpc.

Phenomenology

As argued before, FIMP production from decay is always dominant over the scattering processes in our model due to the presence of either feeble couplings at both vertices, a heavy mediator or heavy initial state particles for the latter. Therefore, in this study, we can divide the FIMP parameter space into two purely separate mass regimes, where decay and scattering contributions to FIMP production are mutually exclusive. However, in cases where scattering can create a heavy mediator on-shell with unsuppressed production and decays subsequently to DM, there may arise a potential double counting when both decay and scattering processes are considered together [587], which needs to be accounted. For us, there is no such issue with the following segregation of kinematic regimes, which yield different phenomenology:

- **Case-I** ($m_s\geq 2m_X$): X is produced mainly from s decay, annihilation processes are smaller and neglected.
- **Case-II** ($m_s<2m_X$): Decay channel ($s\to XX$) is forbidden, scattering processes contribute to X production.

Case-I ($m_s\geq 2m_X$) **:**
In this kinematical region, given that even late decay of s occurs bEWSB, it leaves no trace of s aEWSB. So, there is no $s-H$ mixing, and the dark sector remains detached from the SM. As mentioned previously, for this case, we need to choose $m_H^2=m_{h_1}^2/2$

to get the correct Higgs mass aEWSB. Together, we also demand that ϕ freezes out bEWSB, then DM components do not have any *direct* coupling to SM, except the quartic interaction $\phi\phi \to HH$ proportional to $\lambda_{\phi H}$. But as discussed, constraints from Direct search on $\lambda_{\phi H}$ make this coupling weak, this particular kinematical region with freeze-in and freeze-out both occurring bEWSB, is difficult to probe by any experiment in the near future and is thus constrained very feebly by direct detection or collider search constraints.

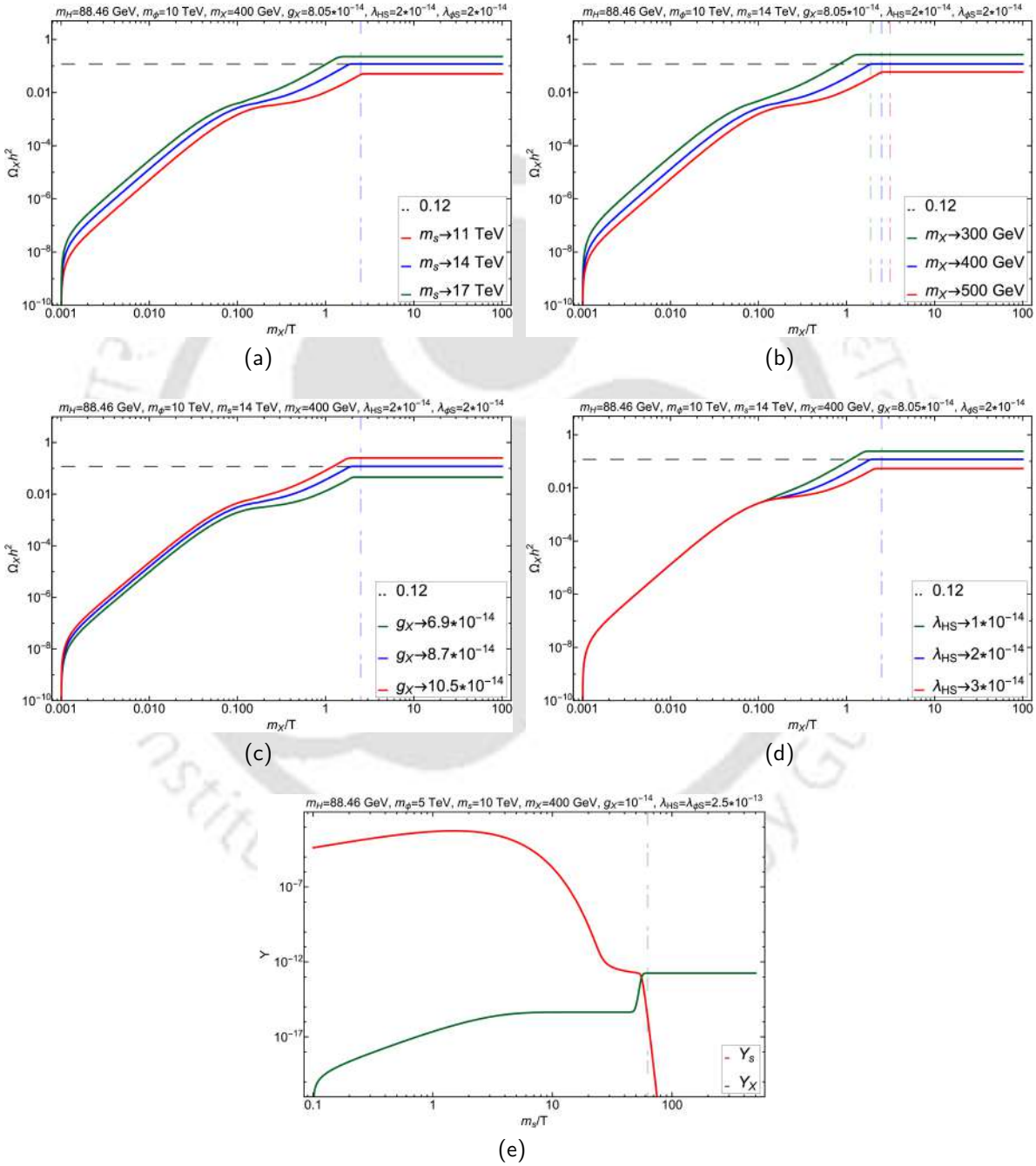

Figure 4.7: Freeze-in for X bEWSB in relic density ($\Omega_X h^2$) versus $x = \frac{m_X}{T}$ plane obtained by solving BEQ (Eq. (4.31)) for the kinematic region $2m_X \leq m_s$. Figs. 4.7a to 4.7d shows variation with respect to parameters $m_s, m_X, g_X, \lambda_{HS}$, having three different values where one provides correct relic, one under abundance and one over abundance. Parameters chosen for the plot are mentioned in figure inset and heading. Horizontal black dashed line shows correct relic density. The vertical dot-dashed lines indicate EWSB. Fig. 4.7e shows late decay contribution of s to freeze-in of X bEWSB, obtained by solving cBEQ (Eq. (C.1)) using Mathematica.

The plots in Fig . 4.7 show change in $\Omega_X h^2$ in terms of $x = m_X/T$ where freeze-in necessarily occurs bEWSB. All the plots are generated by solving BEQ (Eq . (4.31)) using Mathematica. In Fig . 4.7a, three different colored lines in red, blue, green correspond to three different values of m_s (mentioned in figure inset with other parameters kept fixed are mentioned in the figure heading), so that X freezes-in bEWSB. The vertical blue dotted line shows EWSB ($x_{\rm EW} = m_X/T_{\rm EW}$). As X is produced from s decay (and late decay of s), where the decay width of s is proportional to m_s, it is clear that with larger m_s, the X abundance increases. We also see that the entire freeze-in of X, takes place in two steps. Firstly, when s is in equilibrium i.e., for $T > T_D$ (T_D denotes freeze-out point of s), then X yield increases from zero and reaches the first plateau when $T < m_X$. Afterwards, when T drops to $T \lesssim T_D$, then s freezes out and the late decay of s into X is activated, X yield rises again, eventually producing the second plateau. The horizontal black dotted line represents the central value of the present DM relic abundance. We see that the blue line with $m_s = 14\ {\rm T}eV$ matches to correct relic, given other parameters fixed as mentioned in the figure heading. Also note here that we choose $x = 0.001$ to start the freeze-in production, although ideally the maximum temperature of the bath ($T_{\rm RH}$) should be very high $T_{\rm RH} \sim T_{U(1)}$. This is simply because, in both decay and scattering dominated freeze-in of X in this model, the yield is independent of $T_{\rm RH}$, a typical feature of IR freeze-in.

In Figs . 4.7b to 4.7d, we show how the freeze-in of X depends on the parameters m_X, g_X and λ_{HS} when s decay is the main source of X production. In each plot three cases are shown, one for correct relic, one for under abundance and one for over abundance. The values of the parameters kept fixed to achieve them can be read from figure insets and headings. As the resultant yield is proportional to the decay width of s, the dependence of these parameters on the decay width solely determine the relic density accumulated. For example, m_X is inversely proportional to s decay width. Therefore, with larger m_X, the relic density decreases in Fig . 4.7b. On the other hand, s decay width is proportional to g_X, therefore X relic density increases with larger g_X as is clear from Fig . 4.7c. In Fig . 4.7d, we have shown the dependence on λ_{HS}. The decoupling of s from thermal bath depends on λ_{HS}. With larger λ_{HS}, s annihilation cross-section increases, delaying the decoupling of s which in turn reduces the late decay contribution to X yield, as evident from Fig . 4.7d.

The very fact that the late decay contribution of s is essentially that of freeze-out abundance of s converting into X yield, is clear when we solve the coupled BEQ for s freeze-out and X freeze-in together as elaborated in Appendix C.1 (see Eq . (C.1)) and demonstrated in Fig . 4.7e. Here, the green line represents the variation of X yield (Y_X) with m_s/T and the red line represents Y_s. Y_s shows the freeze-out of s from the equilibrium distribution and then late decay to X (descending part of s yield after freeze out). The freeze-out yield of Y_s matches to Y_X yield completely. The vertical green dashed line confirms that the entire phenomenon occurs bEWSB for the chosen parameters of the model.

We find out next the relic under abundant parameter space of the model (Eq . (4.36)) via numerical scan for the kinematic region $2m_X \leq m_s$ in Fig . 4.8. Fig . 4.8a shows the parameter space in g_X vs. m_X plane. The color shades in light yellow, light red and light blue indicate different ranges of relic density (see Fig. inset). The scattered points with shades as in the color bar signify the percentage of 'late decay' contribution to the relic density of X ($\Omega_{\rm LD}h^2$) with respect to the total X relic density

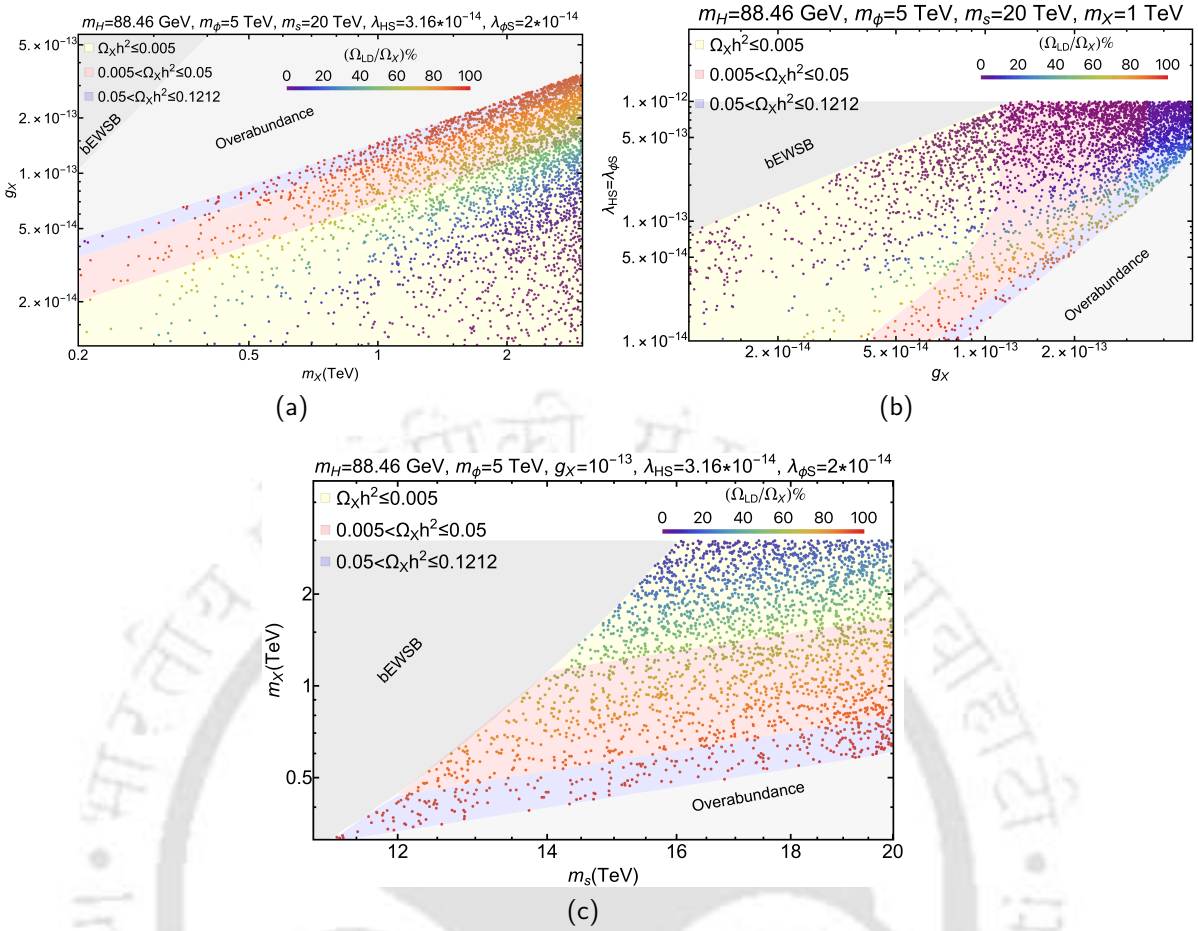

Figure 4.8: Numerical scan of the under-abundant region of X relic (Eq. (4.36)) for freeze in bEWSB, when $(2m_X \leq m_s)$. Fig. 4.8a shows scan in $m_X - g_X$ plane, 4.8b in $g_X - \lambda_{HS} = \lambda_{\phi S}$ plane and 4.8c in $m_s - m_X$ plane. Different color shades indicate different ranges of relic density for fixed values of other parameters within our said bound as mentioned in figure inset and caption. The rainbow color bar represents the contribution of the late decay of s in X freeze-in by the ratio $(\Omega_{\rm LD}/\Omega_X)$. This kinematic region is free from collider and direct search constraints, see text for details.

$(\Omega_X h^2)$. The variation of relic density with g_X and m_X is consistent with the behaviour already noted in Fig. 4.7b and 4.7c, as we show that relic density increases with increasing g_X and decreasing m_X. This is also true for the scattered points, as the functional dependence of the parameters are the same for both in-equilibrium decay and the late decay of s. In other two correlation plots, i.e., Fig. 4.8b (scan in $g_X - \lambda_{HS}$ plane) and Fig. 4.8c (scan in $m_s - m_X$ plane), we find that the change in relic density is consistent with Fig. 4.7a and Fig. 4.7d. In all these three correlation plots, we mark the overabundant region with light grey shaded region and the deep grey area signifies the parameter region where freeze-in bEWSB condition is not maintained. We further note that as only decay of s dominates the production of X, Higgs mixing does not appear aEWSB and so collider bound is mostly absent. DD cross-section (the discussion is postponed to Appendix C.4 as it is a standard exercise) is only affected by $\lambda_{\phi H}$ parameter, which is not very sensitive to the decay dominated production, especially when m_ϕ is in TeV range. This makes the parameter space free from the experimental constraints. We must also note that for all plots bEWSB in the kinematic region $2m_X \leq m_s$, the choice of $m_H = m_{h_1}/\sqrt{2} = 88.46\ GeV$ is consistent with a SM Higgs with $m_{h_1} = 125.1\ GeV$.

Case-II: $(m_s \lesssim 2m_X)$ **:**
Now, we consider a kinematic region where s decay is kinematically forbidden to produce X, with $m_s < 2m_X$. Absence of decay (and late decay) indicates that scattering, as shown in Fig. 4.4, plays a crucial role in the production of X. If X is produced through scattering or WIMP-FIMP conversion bEWSB, then s remains in the thermal bath to mix with h after EWSB, eventually connecting DM to SM. In this case, DD remains a viable option for detection of WIMP (see Appendix C.4). Also the mixing angle $(\sin\theta)$ of s and the CP-even neutral component of Higgs doublet is restricted by the upper bound on mixing obtained from collider search as $\sin\theta \leq \mathcal{O}(0.3)$ [489]. On top of that, following the correlation between λ_{HS} and $\sin\theta$ as in Eq. (C.15), λ_{HS} will get further constrained by the mixing bounds, and constrain the parameter space bEWSB. On the contrary, when FIMP production completes bEWSB via s decay (and late decay), λ_{HS} remains mostly unconstrained due to absence of s aEWSB.

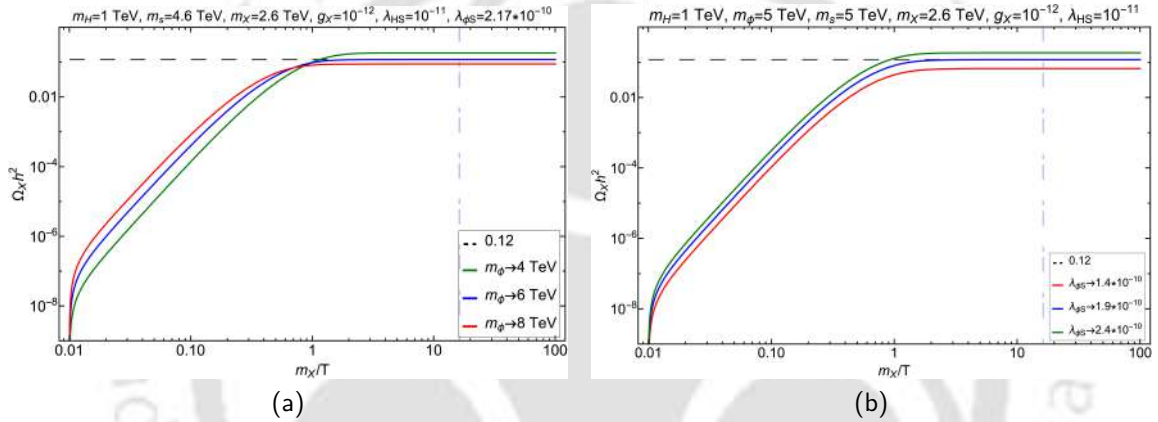

Figure 4.9: Freeze-in production for X bEWSB in relic density $(\Omega_X h^2)$ versus $x = \frac{m_X}{T}$ plane for the kinematic region $m_s < 2m_X$, when scattering processes contribute to DM production. Variation with respect to m_ϕ (left) and $\lambda_{\phi S}$ (right) for three representative values that provide under, correct and over relic abundance are shown by red, blue, green lines. Horizontal black dashed line shows observed relic density. The vertical dot-dashed lines denote the boundary of EWSB. The parameters kept fixed are written in the figure insets as well as in the figure heading.

We first depict the freeze-in patterns in Fig. 4.9, in terms of $\Omega_X h^2$ as a function of $x = m_X/T$. This is similar to Fig. 4.7, where the vertical dot-dashed lines denote EWSB and in each case we ensure that X freezes in bEWSB $(x_{\rm FI} < x_{\rm EW})$, but for kinematic region $m_s < 2m_X$. In Fig. 4.9a and Fig. 4.9b the variation of $\Omega_X h^2$ is shown with respect to m_ϕ and $\lambda_{\phi S}$ respectively. In each case three choices of parameters provide under, correct and over abundance to indicate their role in DM production. For example, with the increase of m_ϕ, the X production cross-section decreases, which in turn, decreases FIMP abundance as evident from Fig. 4.9a. Similarly, larger $\lambda_{\phi S}$ enhances DM production cross-section and FIMP relic, as seen in Fig. 4.9b. The parameters kept fixed for the plots are mentioned in Figure captions and respect the constraints elaborated in Section 4.4.2.

In both the freeze-in patterns observed in Fig. 4.7 and Fig. 4.9, we see that the abundance builds slowly upto $x \sim 1$ which is usually classified as Infra Red (IR) freeze in, where the mass effect turns important. This is contrasted to the Ultra Violet (UV) freeze-in pattern advocated usually for DM EFT theories as in [352, 561, 588, 589], where the abundance builds up at very high temperature or low x and saturates. One may also notice the *slight* difference in freeze-in pattern due to

decay and annihilation dominated productions; for the decay, the yield builds up even slower with late decay contribution adding up as in Fig . 4.7, compared to the production via scattering as in Fig . 4.9.

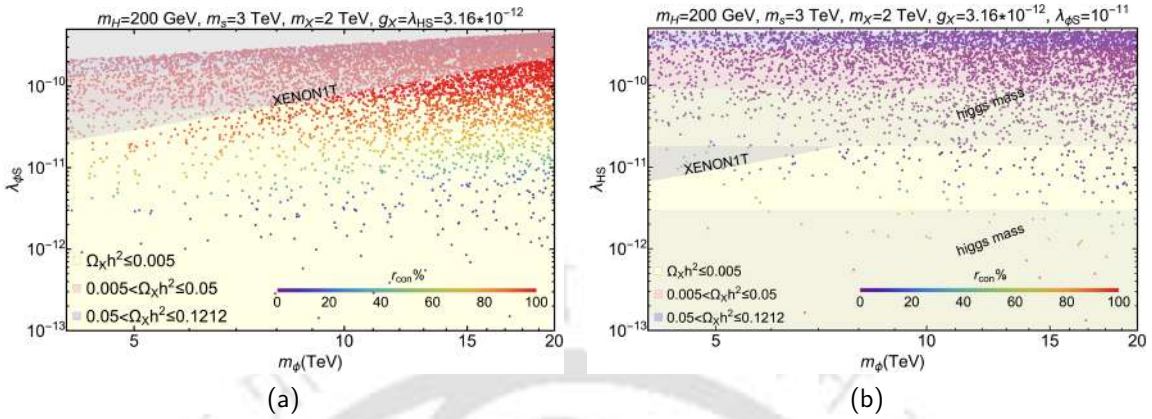

Figure 4.10: Numerical scan of the under-abundant region of X relic for freeze-in bEWSB, when $m_s < 2m_X$. Fig . 4.10a and 4.10b show correlation in $m_\phi - \lambda_{\phi S}$ and $m_\phi - \lambda_{HS}$ planes respectively. Three different color shades indicate different ranges of relic density (see figure inset) for fixed values of other parameters written in figure heading. The rainbow color bar represents how much the WIMP-FIMP conversion ($\phi\phi \to XX$) is contributing in production of X by the ratio $r_{\rm con}$ (see Eq . (4.37)). Grey shaded areas signify the regions excluded by direct detection and Higgs mass constraints.

We turn next to the parameter space scan for the FIMP under abundance in the kinematic region $m_s < 2m_X$ as shown in Fig . 4.10, correlating different parameters relevant for scattering/conversion processes. While the light yellow, light red and the light blue shaded regions signify different ranges of relic density (see figure inset), the scattered points with different colors as in the color bar signify the percentage of WIMP-FIMP conversion channels with respect to the total FIMP production via the following ratio:

$$r_{\rm con} = \frac{\langle \sigma v \rangle_{\phi\phi \to XX}}{\langle \sigma v \rangle_{\rm Tot}} \,. \tag{4.37}$$

As mentioned before, the presence of s after EWSB, when FIMP production is prohibited from the decay of s, ensures direct search and collider search possibilities of the model, which in turn puts appropriate bounds on the parameter space in absence of a signal. These constraints are superimposed on the parameter space by grey shaded exclusion regions. Fig . 4.10a shows scan in $m_\phi - \lambda_{\phi S}$ plane and we see that XENON1T bound heavily constrains $\lambda_{\phi S} \lesssim 2 \times 10^{-11}$. WIMP-FIMP conversion is then restricted significantly as $\lambda_{\phi S}$ affects conversion contribution directly and FIMP becomes heavily under abundant $\Omega_X h^2 \lesssim 0.005$. In Fig . 4.10b we show scan in $m_\phi - \lambda_{HS}$ plane. As expected Higgs mass bound plays a crucial role together with DD constraints to limit $3 \times 10^{-12} \lesssim \lambda_{HS} \lesssim 2 \times 10^{-11}$, again to make the FIMP heavily under abundant ($\Omega_X h^2 \lesssim 0.005$), particularly with the choice of $\lambda_{\phi S} = 10^{-11}$ as done for the scan. The conversion contribution is large when m_ϕ is small, as expected.

We further intend to highlight that in all these scans, the parameters directly affecting Higgs mass and mixing after EWSB, ie, m_s, m_X and g_X (see Eq . (C.8)) are all very fined-tuned. Owing to this requirement, there is not enough range to show the variations of these parameters in a scan. Therefore, we choose to vary the parameters in the dark sector that does not affect Higgs mass; λ_{HS} being the only exception, shows a very narrow viable region, as pointed out in Fig . 4.10b.

4.4.6 Freeze-out of ϕ

The scalar singlet dark matter ϕ is assumed to be in thermal bath as WIMP, tracking the equilibrium (non-relativistic and Maxwell-Boltzmann) distribution in early universe. When the bath temperature (T) goes below the decoupling temperature of ϕ, i.e. $T \lesssim T_D^{\phi}$, the interaction rate of DM with the bath particles eventually becomes less than the Hubble expansion rate H. This causes the DM to decouple from the thermal bath and freeze out to give the saturation abundance. In this section, we assume the freeze-out to occur bEWSB and find the region of parameter space where it happens and produces under abundance. As mentioned previously, there are several constraints to ensure freeze-out bEWSB such as $m_\phi \geq$4 TeV. Further constraints on model parameters come from DD and collider searches as discussed before. We indicate the bounds in resulting parameter space. The annihilation channels of WIMP ϕ, through which it depletes the number density can be divided into two main categories:

- **Annihilation to visible sector**:

  The channels bEWSB, include ϕ pair-annihilation into s and H pairs. The relevant Feynman diagrams are in Fig . 4.5. The couplings relevant to the above scatterings are $\lambda_{\phi S}$, λ_{HS}, $\lambda_{\phi H}$ and λ_S $(= \frac{m_s^2}{2v_s^2})$. As already mentioned, $v_s = m_X/g_X$ must always be very large ($\sim 10^{14}$ GeV) throughout the analysis in order to have a successful FIMP (X) production as a CDM. Hence, unless we choose $\lambda_{\phi S} \sim 1/v_s$, couplings like $\phi\phi s$ $(\propto v_s\lambda_{\phi S})$, will make the annihilation cross-sections very large, resulting in negligible ϕ abundance. Hence, in order to get a reasonable annihilation of ϕ,

  $$\lambda_{\phi S} \lesssim 10^{-12} \text{ for } g_X \sim 10^{-12}.$$

  Such a choice is consistent with both the freeze-in of X and direct detection constraints on $\lambda_{\phi S}$. Although such small $\lambda_{\phi S}$ makes the four-point scattering cross section, such as the top left channel in Fig . 4.5, practically negligible, ϕ mainly annihilates via the s and t-channel diagrams in Fig . 4.5, where presence of v_s in one of the vertices like $\phi\phi s$ make the contribution sizeable. We further note that $\lambda_{\phi H}$ should also be greater than 10^{-3} to get a reasonable annihilation via $\phi\phi \to HH$. Although ϕ freezes out bEWSB, we recall that s and h mixes due to EWSB. As a result, λ_{HS} is traded off as a parameter dependent on mixing. So, the collider searches of Higgs at the LHC, restricts λ_{HS}. We indicate the effect of such constraints on the allowed parameter space.

- **Conversion to FIMP DM** :

  ϕ annihilates into X pair via s mediation (bottom panel of Fig . 4.5). But since freeze-in requires g_X to be very small ($\lesssim 10^{-12}$), one vertex of conversion diagram (XXs) proportional to $g_X^2 v_s$ is also minuscule; this evidently implies that unless the other vertex $\lambda_{\phi S}$ is chosen sufficiently large (~ 1), the conversion contribution is negligible. However, $\lambda_{\phi S}$ requires to be small from DD, makes the conversion very small. Secondly, large conversion cross section to FIMP production automatically implies that X production will be too fast for the non-thermal freeze-in and it will drive X towards equilibrium, seizing the

FIMP nature of X. Hence, WIMP↔FIMP conversion is negligible in the context of WIMP, but plays an important role in the FIMP production as already demonstrated in previous subsection.

Upon neglecting the WIMP-FIMP conversion, the cBEQ reduces to two individual uncoupled BEQs; the one for ϕ is given by Eq. (4.30), which can be easily solved numerically (we use Mathematica 12.3.1.0 [590]). The parameters are chosen in such a way that the freeze-out occurs bEWSB. The relic density for ϕ can then be written in terms of freeze-out yield [62] and we again focus on the under abundant region of the parameter space, given ϕ is one of the two DM components that we assume to constitute the dark sector:

$$\Omega_\phi \mathrm{h}^2 \simeq 2.744 \times 10^8 \, m_\phi Y_\phi^{\mathrm{bEWSB}}; \;\; \Omega_\phi \mathrm{h}^2 \leq 0.1212 \, .$$

where WIMP dark matter relic density is written in terms of the reduced Hubble parameter, h in units of 100 km/s/Mpc.

Phenomenology

We first study ϕ freeze-out bEWSB as a solution of the BEQ. (4.30) in Fig. 4.11, where we plot $\Omega_\phi h^2$ with $x = m_\phi/T$ for parameters $\lambda_{HS}, \lambda_{\phi S}, m_\phi, g_X$. We choose three representative values of these parameters so that we produce correct relic, under abundance and over abundance. The horizontal black dotted line denotes the current central value of DM abundance. Vertical dot-dashed lines indicate EWSB ($x_{\mathrm{EW}} = m_\phi/160$ GeV) and each freeze out occurs bEWSB with $x_{\mathrm{FO}} < x_{\mathrm{EW}}$. The parameters kept fixed for these plots, as mentioned in the figure insets and headings, comply with all the constraints mentioned earlier.

As already mentioned, to ensure the WIMP freeze-out to take place bEWSB, the allowed mass of ϕ is constrained to $m_\phi \gtrsim 4 \; TeV$. To comply with this bound, in Fig. 4.11a, the freeze out of ϕ is shown for $m_\phi = 7 \, TeV, 8.5 \, TeV$ and $10 \, TeV$, depicted by red, blue and green colored lines respectively. As annihilation cross-section is inversely proportional to WIMP mass, and freeze-out yield is also inversely proportional annihilation cross-section, we see that as m_ϕ increases, the WIMP relic density also enhances and the case with $m_\phi = 8.5 \; TeV$ matches with correct relic. In Figs. 4.11b to 4.11d, we show the effects in WIMP relic due to variation of $\lambda_{HS}, \lambda_{\phi S}, g_X$ respectively. As the annihilation cross-section of WIMP (ϕ) increases with larger couplings, we see that the relic density reduces expectedly with larger $\lambda_{HS}, \lambda_{\phi S}$ in Figs. 4.11b and 4.11c. The scenario changes in Fig. 4.11d, where variation with respect to g_X is shown. In annihilation cross-section, g_X enters inversely through $v_s \; (= m_X/g_X)$, as a result, annihilation to H, s reduces with the increase of g_X, resulting in an enhancement of relic with g_X as shown in Fig. 4.11d.

DD of ϕ occurs through Higgs mediation (see Appendix C.4). Even if WIMP freezes-out bEWSB, direct search of ϕ is possible at present epoch, so the constraints apply. However, the constraints depend on kinematical regions: (i) $m_s \geq 2m_X$ and (ii) $m_s < 2m_X$ in a similar vein as discussed before.

<u>Case-I:</u> ($m_s \geq 2m_X$) :
When $m_s \geq 2m_X$, and we ensure X freeze-in to saturate bEWSB, the decay of s totally depletes its number density, so that any $s - h$ mixing aEWSB is non-existent,

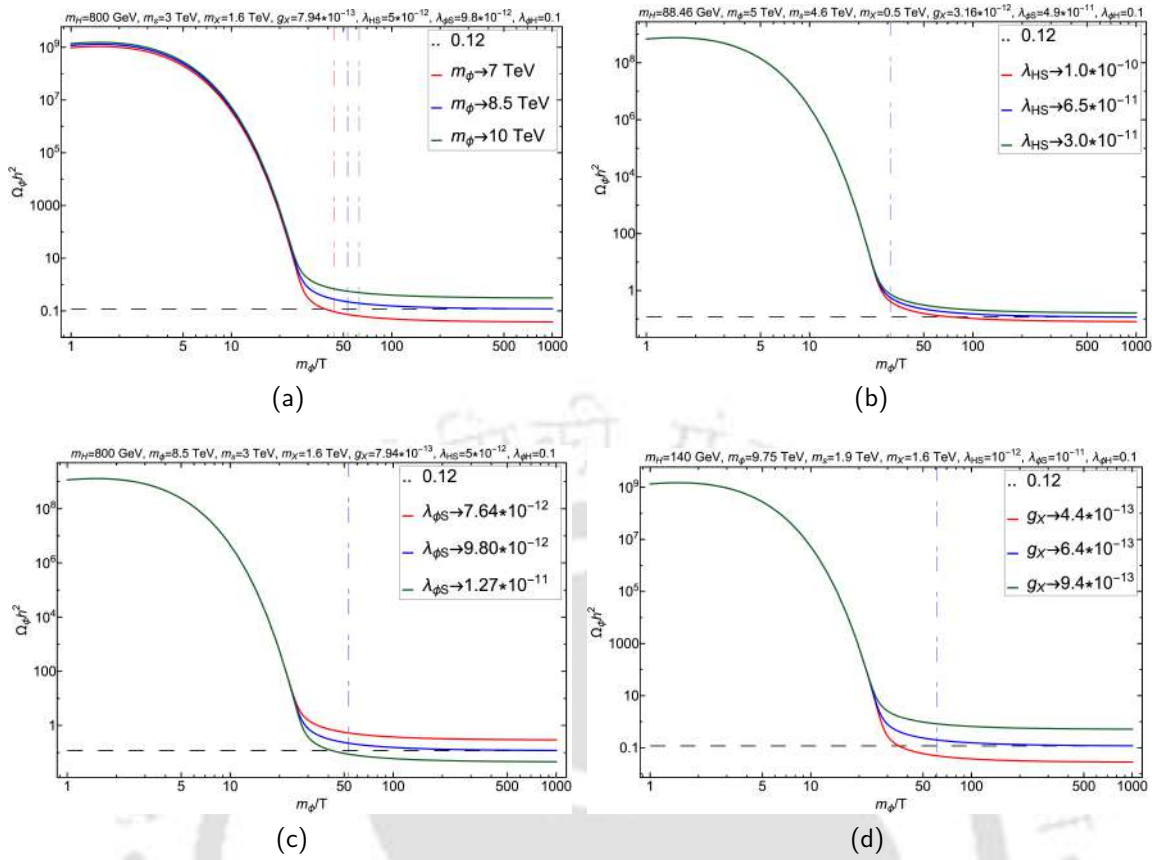

Figure 4.11: WIMP relic density ($\Omega_\phi h^2$) in terms of $x = m_\phi/T$ for three different values of parameters $\lambda_{HS}, \lambda_{\phi S}, m_\phi, g_X$ (from left to right and top to bottom) to provide correct relic, under and over abundance. The parameters kept fixed are mentioned in the insets as well as in the figure headings. The horizontal black dotted line denotes correct relic abundance and the vertical dot-dashed lines depict EWSB, $x_{\rm EW} = m_\phi/160$.

resulting only SM Higgs mediating direct search for ϕ. So the situation is similar to the DD of single component scalar singlet ϕ.

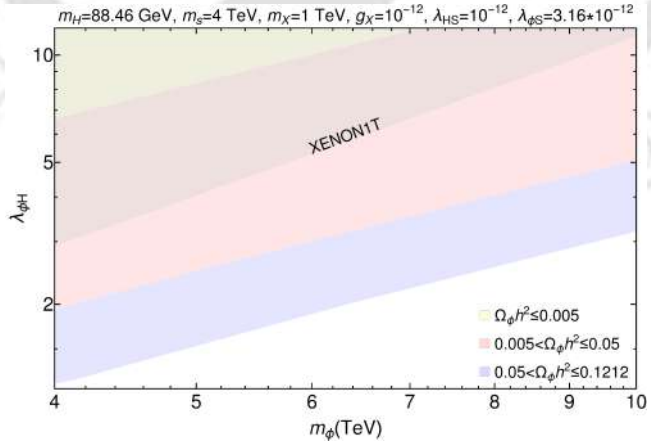

Figure 4.12: Under abundant region for ϕ ($\Omega_\phi \mathrm{h}^2 \leq 0.1212$) with respect to variation of $\lambda_{\phi H}$ vs. m_ϕ for kinematic region $m_s \geq 2m_X$ when freeze-out occurs bEWSB. Spin independent XENON1T direct search excluded region is showed by the grey shaded area at the top for large $\lambda_{\phi H}$. Light yellow, light red and light blue shades indicate different ranges of $\Omega_\phi \mathrm{h}^2$ as mentioned in figure inset. Parameters kept fixed for the plot are mentioned in the figure heading and comply with all other constraints.

Fig. 4.12 shows the under abundant parameter space in $m_\phi - \lambda_{\phi H}$ plane where ϕ freezes out bEWSB, in the kinematic region $m_s \geq 2m_X$. Three color shades in-

dicate different ranges of $\Omega_\phi h^2$ (mentioned figure inset). The grey shaded region is excluded by the present spin-independent XENON1T limit, which restricts only very high values of $\lambda_{\phi H} \gtrsim 3$, given other parameters are kept constant at values mentioned in the figure heading. As $m_s > 4\ TeV$ (see Eq. (4.34)) for late decay to complete bEWSB, WIMP annihilation mostly occur through the four point interaction $\phi\phi \to HH^\dagger$. The correlation between $m_\phi - \lambda_{\phi H}$ is consistent with two features already discussed: (a) WIMP annihilation cross-section via four point interaction increases with $\lambda_{\phi H}$ which in turn reduces the abundance and (b) WIMP annihilation cross-section decreases with m_ϕ, which causes $\Omega_\phi h^2$ to increase with the WIMP mass.

Case-II: $(m_s < 2m_X)$ **:**
When $m_s \leq 2m_X$, $s - h$ mixing occurs aEWSB and direct search occurs via mediation of both physical states h_1, h_2. Therefore, mixing plays an important role in the direct detection of WIMP. In this case, the parameter space and the constraints are expectedly different from the previous case where mixing was absent. Correlations of relevant parameters for under abundance of ϕ ($\Omega_\phi h^2 \leq 0.1212$) in this kinetic regime is shown in Fig. 4.13 together with direct search and Higgs mixing constraint.

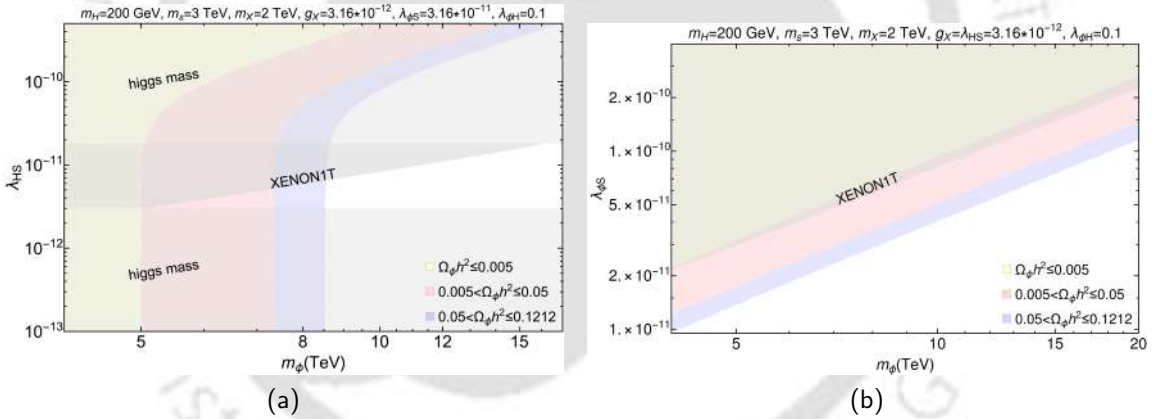

Figure 4.13: Under abundance for ϕ ($\Omega_\phi h^2 \leq 0.1212$) in the kinematic region $m_s < 2m_X$. Fig. 4.13a shows the correlation between $m_\phi - \lambda_{HS}$ and Fig. 4.13b shows the correlation between $m_\phi - \lambda_{\phi S}$. Different color shades in light yellow, light red and light blue indicates under abundance within ranges as mentioned in figure inset. Grey shaded regions are excluded by latest XENON1T bound, Higgs mass and collider bound on scalar mixing (see text for details).

Fig. 4.13a shows the under abundant parameter space in m_ϕ vs. λ_{HS} plane where grey shaded regions are excluded by XENON1T direct search bound and Higgs mass/scalar mixing constraints. The functional dependence of m_ϕ as in Fig. 4.11a and of λ_{HS} as in Fig. 4.11b are retained here. We conclude that $\lambda_{HS} \sim 5\times10^{-12}$ is safe for m_ϕ varying within 7 to 8.5 TeV, given the other model parameters are kept fixed as mentioned in the figure caption. Fig. 4.13b shows the correlation between $m_\phi - \lambda_{\phi S}$. Recall that Y_ϕ increases with larger $\lambda_{\phi S}$ (see Fig. 4.11c) as well as with larger WIMP mass (m_ϕ), which is also evident in Fig. 4.13b. Once $\lambda_{HS} \sim 3.16 \times 10^{-12}$ is fixed in Fig. 4.13b, it fixes the mixing angle within experimental limit, there is no other constraint on this parameter space excepting for the direct search bounds, depicted in grey shade.

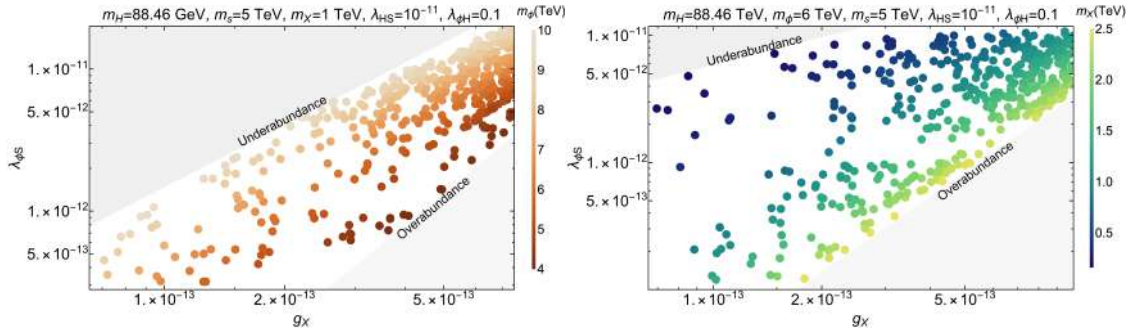

Figure 4.14: Scan in $g_X - \lambda_{\phi S}$ plane when both WIMP and FIMP components add to observed relic density, $\Omega_X h^2 + \Omega_\phi h^2 = 0.1200 \pm 0.0012$, simultaneously addressing other constraints when both freeze in and freeze out occur bEWSB in kinematic region $m_s \geq 2m_X$. In Fig. 4.14a, we keep FIMP mass fixed at $m_X = 1\ TeV$ and vary WIMP mass m_ϕ as shown in the SiennaTones color bar. In Fig. 4.14b, we keep $m_\phi = 6\ TeV$ fixed and vary m_X as shown by the BlueGreenYellow color bar. Other parameters kept fixed are mentioned in the figure heading. Under abundance and over abundance constraints from freeze-in/freeze-out bEWSB are shown by grey shaded regions.

4.4.7 Putting WIMP and FIMP together

Scenario	Benchmark points	m_H, m_ϕ, m_s, m_X (TeV)	$g_X, \lambda_{HS}, \lambda_{\phi S}, \lambda_{\phi H}$	$\Omega_\phi h^2$	$\Omega_X h^2$	$\frac{\Omega_\phi}{\Omega_T}\%$	$\frac{\Omega_X}{\Omega_T}\%$	$\sigma^{\rm SI}_{\phi_{\rm eff}}$ (cm^2)
$m_s \geq 2m_X$	BP1	0.088, 8.0, 7.0, 1.0	$10^{-13}, 10^{-11}, 5.69\times10^{-13}, 0.1$	0.1176	0.0014	98.82	1.18	1.44×10^{-48}
	BP2	0.088, 7.0, 6.0, 1.5	$10^{-12}, 10^{-11}, 1.07\times10^{-11}, 0.1$	0.0626	0.0571	52.30	47.70	9.99×10^{-49}
	BP3	0.088, 6.0, 5.0, 2.0	$2.33\times10^{-12}, 10^{-11}, 2.6\times10^{-11}, 0.1$	0.0087	0.1112	7.26	92.74	1.89×10^{-49}
$m_s < 2m_X$	BP4	0.2, 8.3, 3.0, 2.0	$10^{-11}, 10^{-11}, 10^{-10}, 0.3$	0.1062	0.0138	88.50	11.50	2.05×10^{-45}
	BP5	0.2, 14.5, 3.0, 2.0,	$10^{-11}, 10^{-11}, 2.74\times10^{-10}, 0.3$	0.0592	0.0605	49.46	50.54	3.09×10^{-45}
	BP6	0.2, 11.0, 3.0, 2.0	$10^{-11}, 10^{-11}, 3.32\times10^{-10}, 0.2$	0.0056	0.1154	4.63	95.37	7.55×10^{-46}

Table 4.3: Some sample benchmark points for the WIMP-FIMP model, when both freeze-in of X and freeze-out of ϕ occur bEWSB respecting the total relic density, direct search, Higgs mass/mixing, and other constraints. The benchmark points depict the possibilities when one component dominates over the other as well as the case when they have almost equal share for the total DM relic density.

So far we discussed the under abundant parameter space for both WIMP (ϕ) and FIMP (X) individually when they freeze-out and freeze-in bEWSB. However, the fact that the total DM relic density has to be achieved (Eq. (4.21)) from both these components, will correlate these two cases. Two such example scans are shown in Fig. 4.14, where we show the relic density allowed parameter space in $\lambda_{\phi S} - g_X$ plane for the kinematic region $m_s \geq 2m_X$, abiding by other relevant constraints. In Fig. 4.14a, we keep FIMP mass fixed at $m_X = 1\ TeV$ and vary WIMP mass m_ϕ as shown in the SiennaTones color bar. In Fig. 4.14b, we keep $m_\phi = 6\ TeV$ fixed and vary m_X as shown by the BlueGreenYellow color bar. The other parameters kept fixed are mentioned in the figure headings.

In Fig. 4.14a, we see that for a fixed g_X, when we make $\lambda_{\phi S}$ larger, the FIMP (X) relic almost remains the same, but WIMP (ϕ) relic decreases due to larger annihilation cross-section; so m_ϕ requires to be larger to keep the WIMP relic in the similar ballpark and total relic density constant. This is why we see darker points with smaller m_ϕ populating smaller $\lambda_{\phi S}$ regions, while for larger $\lambda_{\phi S}$, the WIMP mass(m_ϕ) requires to be larger with brighter points populating such regions. In the same figure, we see that when we enhance g_X, FIMP relic gets larger, and ac-

cordingly WIMP relic needs to be smaller by having larger $\lambda_{\phi S}$ as well as small m_ϕ. Of course, if we keep $\lambda_{\phi S}$ unchanged with larger g_X, the total relic density goes beyond the experimental observation and provides over abundance, shown by grey shaded region. In a similar way, when $\lambda_{\phi S}$ is larger than a specific value for a given g_X, then WIMP relic is so tiny that it leads to under abundant total relic, also marked by the grey shaded region. A complementary behaviour is observed in Fig . 4.14b. Here, for a fixed g_X, with larger $\lambda_{\phi S}$, WIMP relic decreases, but with m_ϕ kept constant, there is only one way to keep the observed relic density constant, by enhancing FIMP contribution i.e. by decreasing m_X. This is why we see darker points with small m_X favouring larger $\lambda_{\phi S}$ regions and brighter points with larger m_X populating smaller $\lambda_{\phi S}$ regions. Grey shaded over abundance for small $\lambda_{\phi S}$ and under abundance for large $\lambda_{\phi S}$ regions can be described in a similar way as in Fig . 4.14a. A similar correlation can be made when FIMP production occurs dominantly via scattering processes with $m_s \leq 2m_X$, but the allowed parameter space becomes tinier due to the involvement of $\lambda_{\phi S}$ into both freeze-in and freeze-out processes. We next furnish some characteristic benchmark points in Table 4.3, where the abundance of FIMP (X) and WIMP (ϕ) adds to the total observed relic density together with addressing direct search and Higgs mixing constraints ensuring that freeze-in of X and freeze-out of ϕ both occur bEWSB. The benchmark points BP1 and BP4 depict the possibilities when ϕ dominates over X, BP3, BP6 show the other possible hierarchy when X dominates over ϕ, while BP2 and BP5 demonstrate the case when they have almost equal share for the relic density. Before concluding this section, we would like to comment that if both freeze-in/freeze-out has to occur bEWSB the masses m_ϕ, m_s need to be very heavy, and possibility of any collider production is difficult. The FIMP is anyway very feebly coupled to SM. The WIMP can still have a direct search possibility, larger when the FIMP can be produced via scattering, smaller when it is produced via $s \to XX$ decay, providing an interesting correlation between the WIMP and FIMP DM components.

4.5 Dark Matter phenomenology aEWSB

In this section, we address a situation where the freeze-in of X and freeze-out of ϕ both occur after EWSB. This is equivalent to saying that both the DM components attain saturation at a temperature smaller than $T_{\rm EW}$, i.e.:

$$T_{U(1)} > T_{\rm EW} > T_{\rm FI}; \;\; T_{U(1)} > T_{\rm EW} > T_{\rm FO}\,. \tag{4.38}$$

The methodology of finding the allowed parameter space for such a situation is similar to the previous case; to solve BEQ for both WIMP and FIMP cases individually including all the processes that contribute aEWSB, and choosing model parameters in such a way that we satisfy Eq . (4.38). This is the case usually considered for most of the DM analysis, excepting for checking the validity of Eq . (4.38), which we additionally ensure. However, as the approach remains the same as elaborated in the last section, we highlight on the main features that this possibility offers, without going too much of the details.

4.5.1 Physical states and interactions

The physical particles and interactions aEWSB is obtained when both S and H acquire non-zero VEVs v_s and v respectively. In unitary gauge we write,

$$S = \frac{v_s + s}{\sqrt{2}} \to \langle S \rangle = \frac{1}{\sqrt{2}} v_s, \; H = \begin{pmatrix} 0 \\ \frac{h+v}{\sqrt{2}} \end{pmatrix} \to \langle H \rangle = \frac{1}{\sqrt{2}} v, \; \langle \phi \rangle = 0 \,. \tag{4.39}$$

Evidently, this induces mixing between the two scalars $(s - h)$, the strength of which is dictated by the mixing angle θ. Upon diagonalization, two physical scalars h_1 and h_2 emerge, where h_1 is assumed to be the SM Higgs with $m_{h_1} \sim 125.1\ GeV$, whereas h_2 may be assumed heavy with mass $m_{h_1} \ll m_{h_2}$. The physical and the unphysical fields are related through an orthogonal matrix,

$$\begin{pmatrix} h_1 \\ h_2 \end{pmatrix} = \begin{pmatrix} \cos\theta & -\sin\theta \\ \sin\theta & \cos\theta \end{pmatrix} \begin{pmatrix} h \\ s \end{pmatrix} \,. \tag{4.40}$$

For details, see Appendix C.2, where the minimization of the scalar potential and emergent conditions are specified. We may note one point here that λ_{HS}, which was an external parameter bEWSB, can now be considered as an internal parameter and it is dictated by the mixing angle as given below:

$$\lambda_{HS} = \frac{\sin 2\theta}{2 v_s v} \left(m_{h_2}^2 - m_{h_1}^2 \right) . \tag{4.41}$$

In Table 4.4, we list all the relevant parameters of the model considered for the analysis, classified into external (parameters that we choose to vary as input) and internal (or derived) parameters. We further note, that excepting for the constraints on dark sector particle masses imposed to make the freeze-in/freeze-out occur bEWSB, we adhere to all the other constraints as in Section 4.4.2.

External parameters	Internal parameters
$m_{h_1}, m_\phi, m_{h_2}, m_X, g_X, \lambda_\phi, \lambda_{\phi S}, \lambda_{\phi H}, \sin\theta$	$\mu_H, \mu_\phi, \mu_S, v_s, \lambda_H, \lambda_S, \lambda_{HS}$

Table 4.4: The parameters used in the aEWSB analysis.

We further note here that WIMP mass for ϕ aEWSB is changed due to the additional contribution proportional to DM-Higgs portal interaction $\lambda_{\phi H}$. See Eq . (C.13) in Appendix C.2, where $\mathfrak{m}_\phi$ refers to WIMP mass aEWSB, although we have used the same notation m_ϕ in the text to avoid clutter. This essentially does not affect the phenomenology to a great extent.

4.5.2 BEQ in aEWSB scenario

The BEQ does not change aEWSB, the change is only in the processes of DM production and annihilation, and in the limit of x which goes beyond $x_{\rm EW}$. First point

to note that even aEWSB, the WIMP-FIMP conversion is still small to keep X out-of-equilibrium, so that it is only relevant for FIMP production, and the cBEQs reduce to two independent BEQs as before,

$$\begin{aligned}
\frac{dY_X}{dx} =& \left\{ \frac{45}{3.32\pi^4} \frac{g_s \, \mathrm{M_{Pl}} \, m_s^2 \Gamma_{s\to XX}}{m_X^4} \frac{x^3 K_1\left[\frac{m_s}{m_X}x\right]}{g_*^s(x)\sqrt{g_*^\rho(x)}} \right. \\
&\left. + \frac{4\pi^2 \mathrm{M_{Pl}}}{45\times 1.66} \frac{g_*^s(x)}{\sqrt{g_*^\rho(x)}} \frac{m_X}{x^2} \left(\sum_{i=s,H} \langle\sigma v\rangle_{ii\to XX} (Y_i^{eq})^2 + \langle\sigma v\rangle_{\phi\phi\to XX} Y_\phi^2 \right) \right\} \Theta[x_{\rm EW} - x] \\
&+ \left\{ \frac{45}{3.32\pi^4} \sum_{A=h_1,h_2} \frac{g_A \, \mathrm{M_{Pl}} \, m_A^2 \Gamma_{A\to XX}}{m_X^4} \left(\frac{x^3 K_1\left[\frac{m_A}{m_X}x\right]}{g_*^s(x)\sqrt{g_*^\rho(x)}} \Theta[x_D^A - x] \right. \right. \\
&\left. \left. + e^{-\frac{0.602\,\mathrm{M_{Pl}}\,\Gamma_{A\to XX}}{m_X^2\sqrt{g_*^\rho(x)}}(x^2 - x_D^{A^2})} \frac{x^2 x_D^A}{\eta(x,x_D^A)} K_1\left[\alpha(x,x_D^A)\frac{m_A}{m_X}\frac{x^2}{x_D^A}\right] e^{\frac{m_A}{m_X}\left(\alpha(x,x_D^A)\frac{x^2}{x_D^A} - x_D^A\right)} \Theta[x - x_D^A] \right) \right. \\
&\left. + \frac{4\pi^2 \, \mathrm{M_{Pl}}}{45\times 1.66} \frac{g_*^s(x)}{\sqrt{g_*^\rho(x)}} \frac{m_X}{x^2} \left(\sum_{i=h_2,\mathrm{SM}} \langle\sigma v\rangle_{ii\to XX} (Y_i^{eq})^2 + \langle\sigma v\rangle_{\phi\phi\to XX} Y_\phi^2 \right) \right\} \Theta[x - x_{\rm EW}],
\end{aligned} \tag{4.42}$$

$$\begin{aligned}
\frac{dY_\phi}{dx} =& -\frac{2\pi^2 \, \mathrm{M_{Pl}}}{45\times 1.66} \frac{g_*^s(x)}{\sqrt{g_*^\rho(x)}} \frac{m_\phi}{x^2} \left[\left\{ \sum_{i=H,s} \langle\sigma v\rangle_{\phi\phi\to ii} \Theta[x_{\rm EW} - x] \right. \right. \\
&\left. \left. + \sum_{j=h_2,\mathrm{SM}} \langle\sigma v\rangle_{\phi\phi\to jj} \Theta[x - x_{\rm EW}] \right\} (Y_\phi^2 - Y_\phi^{eq^2}) \right].
\end{aligned} \tag{4.43}$$

It is worthy mentioning that $x = \frac{m_X}{T}$, $\frac{m_\phi}{T}$ in BEQ of FIMP and WIMP respectively and $\mathrm{SM} = \mathrm{h_1}, \mathrm{W^\pm}, \mathrm{Z}, \ell, \mathrm{q}$ includes all possible massive particles. Note that the $\Theta[x - x_{\rm EW}]$ functions present in both eqs. (4.42) and (4.43) denote processes that take part in DM production/annihilation before and after EWSB. While the Θ function separates the FIMP production into two distinct regions, before and after EWSB, this does not include the third possibility of DM production during EWSB at $x \sim x_{\rm EW}$. Such contribution may arise in certain models as explored in [540, 591, 592], where it is shown that a significant amount of FIMP production via oscillations from Higgs is possible during phase transition when $m_h(T) \sim m_{\rm DM}$, if the DM remains out of equilibrium, has a Higgs portal coupling and having mass less than the Higgs mass. However, in our case, such contributions do not arise. This is because the scalar (s) having a Higgs portal, is not a DM, rather a particle present in the thermal bath producing X via in-equilibrium or late decays or scattering. If s remains in thermal bath during EWSB, the oscillations cannot help to enhance the number density of s and therefore of X; on the other hand, if it needs to be out-of-equilibrium during EWSB, the mass turns out to be pretty heavy ~ 4 TeV, as pointed out in Eq. (4.34), way beyond the Higgs mass $(\gg m_h)$ for the oscillations to produce additional s.

Let us discuss a few salient features of freeze-in/freeze out aEWSB here. For example, in scattering dominated FIMP production regime, with $m_s < 2m_X$, all scattering processes $(ss \to XX; \phi\phi \to XX \text{ and } HH \to XX)$ play important role in FIMP (X) production bEWSB $(x < x_{\rm EW})$; but aEWSB $(x > x_{\rm EW})$ new scattering channels open up, as shown in Fig. 4.15. Again, one needs to remember, that the Goldstone

degrees of freedom for H is now converted to massive gauge bosons $W^{\pm}, Z$, but contributions from massive fermions add to the production. Now, consider $m_s \geq 2m_X$ but $m_s \lesssim 4\ TeV$, then FIMP is dominantly produced from s decay bEWSB, but the decoupling of s occurs aEWSB and $s-h$ mixing occurs to produce h_1, h_2. Then dominating FIMP production aEWSB comes from the decay (and late decay) of $h_{1,2}$ as shown in Fig . 4.15. Both the processes bEWSB and aEWSB contribute to the freeze-in yield aEWSB as indicated in Eq . (4.42). For WIMP (ϕ) however, when it freezes out aEWSB, annihilation channels bEWSB do not matter much as they only maintain the WIMP in thermal bath, the freeze-out (or decoupling) of WIMP as well as the consequent relic density ($\Omega_\phi h^2$) are mainly governed by the processes aEWSB. The corresponding Feynman graphs for ϕ freeze-out aEWSB is shown in Fig . 4.16. WIMP-FIMP conversion aEWSB is shown in Fig . 4.17.

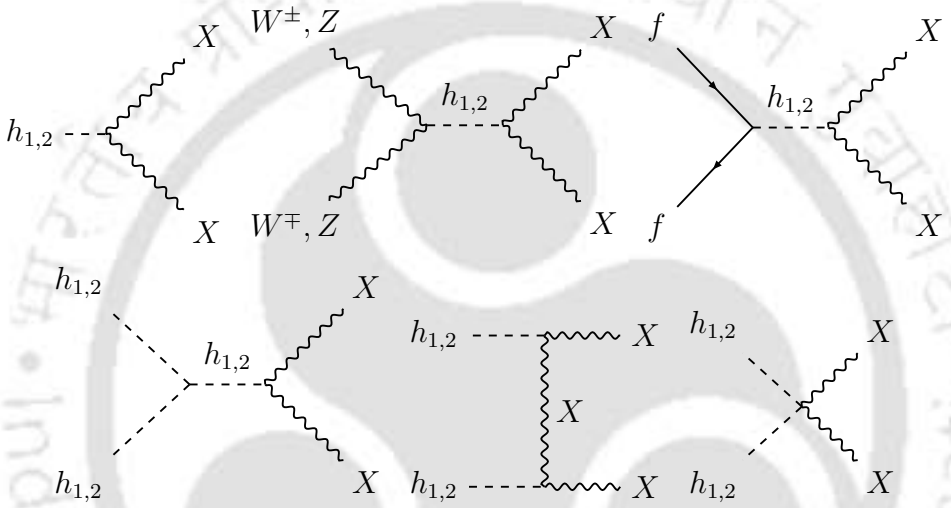

Figure 4.15: Feynman diagrams showing non-thermal production channels of X aEWSB

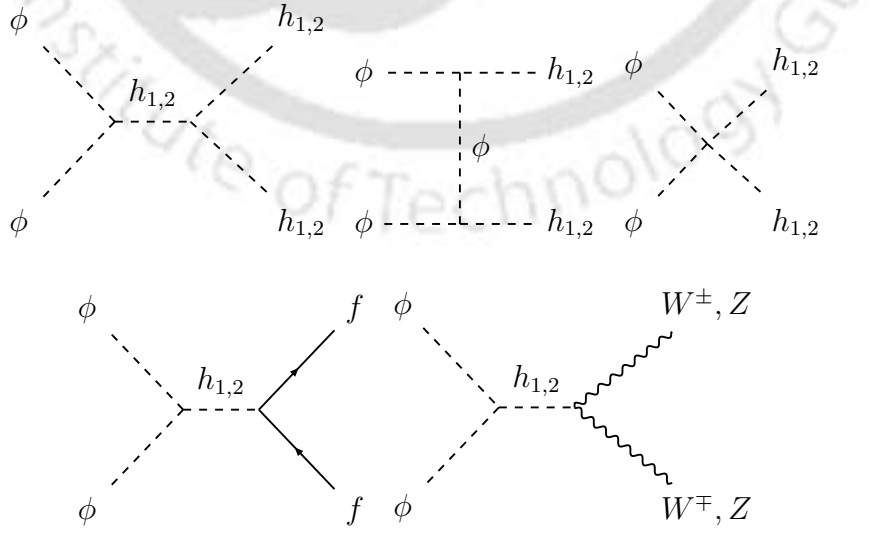

Figure 4.16: Feynman diagrams showing annihilation channels of ϕ aEWSB

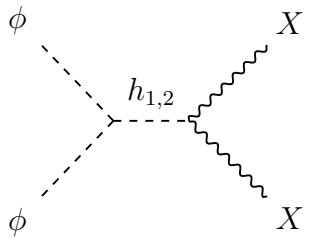

Figure 4.17: WIMP-FIMP conversion channel aEWSB.

4.5.3 Freeze-in of X

As evident from Eq . (4.42), X freeze-in has an important contribution accumulated from processes bEWSB, while aEWSB ($x > x_{\rm EWSB}$), X production occurs mainly via h_2 decay (h_1 decay to XX is assumed kinematically forbidden by considering $m_{h_1} < 2m_X$), and scattering processes as shown in Fig . 4.15, in absence of decay. Freeze-in aEWSB is ensured by checking $Y_{x_{\rm EW}} < Y_{x>x_{\rm EW}}$. Since the essential phenomenology of aEWSB freeze-in is not entirely different from bEWSB, we show a few representative plots to demonstrate the viable parameter space in this region. We show the first freeze-in production of X in Fig . 4.18 in terms of $\Omega_X h^2$ as a function of m_X/T. In Fig . 4.18a, we show the case where $h_2 \to XX$ is the dominant DM production channel, as the decay is kinematically allowed. Here we show the freeze-in pattern for three different g_X values (mentioned in the figure inset) by red, blue and green colored lines, respectively. FIMP relic density increases with g_X, which is already discussed, and correct relic density is obtained for $g_X = 2 \times 10^{-12}$. The horizontal dashed line depicts the central value of the observed DM relic. The vertical dot-dashed line refers to EWSB and we ensure the freeze-in to happen aEWSB. We again see that in decay dominated production, late decay adds significantly to the FIMP yield Y_X. In Fig . 4.18b, we show the same $\Omega_X h^2$ vs. m_X/T variation, but for scattering dominated production, absent the kinematically forbidden $h_2 \to XX$ decay mode for different $\lambda_{\phi S}$ represented by the red, blue and green lines. Expectedly, FIMP relic is enhanced with larger $\lambda_{\phi S}$, similar to the bEWSB case. Again, freeze-in abundance to settle aEWSB is explicitly seen when compared to vertical dot-dashed lines depicting EWSB ($x_{\rm EW}$).

As the dependence of freeze-in relic density on the parameters remain almost the same aEWSB, it is needless to repeat all the features here once again. Nevertheless, in order to demonstrate the viable parameter space complying with aEWSB freeze-in, we show three plots in Fig . 4.19. The top left plot, i.e., Fig . 4.19a shows a correlation in m_X vs. g_X plane and corresponds to the decay dominant FIMP production. We find that excepting for very small g_X regions constrained by direct search of ϕ (with the direct search cross-section being proportional to $v_s \sim 1/g_X$), the rest of the parameter space shows under relic abundance indicated by color codes as mentioned in the figure inset. This is an important contrast to the bEWSB case, where the parameter space for the decay dominant FIMP production is completely unconstrained (see Fig . 4.8). Also, one can conclude from this plot that after EWSB, large part of parameter space can be saved from DD limits if the FIMP production is decay dominated. The right panel plot, i.e., Fig . 4.19b shows a correlation in $m_\phi - \lambda_{\phi S}$ plane, which corresponds to scattering dominant FIMP production absent $h_2 \to XX$ decay.

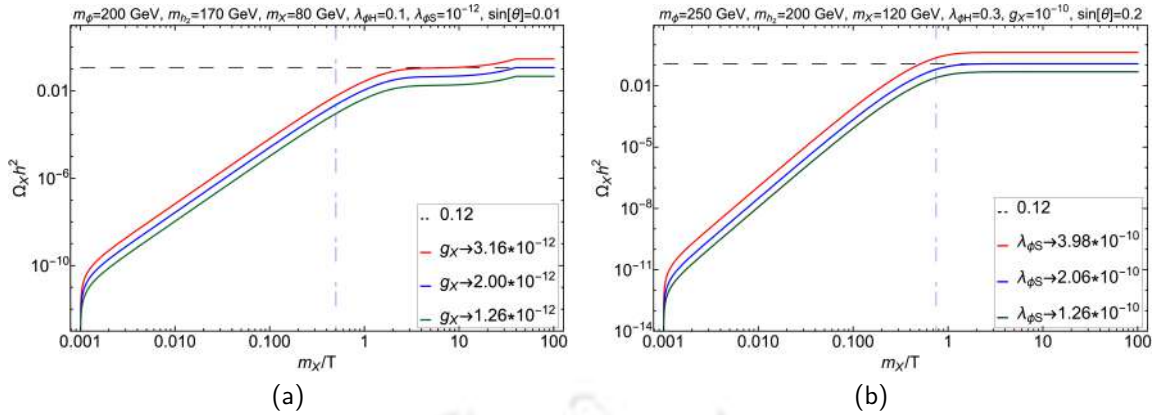

Figure 4.18: Variation of X relic density as a function of $x = m_X/T$ to demonstrate freeze-in aEWSB; In left panel (Fig . 4.19a) we show decay dominant case where freeze-in production aEWSB occurs via $h_2 \to XX$ for three discrete g_X values. In the right panel Fig . 4.19b, decay is kinematically forbidden and scattering processes dominate freeze-in production. Vertical dot-dashed line indicates EWSB and black dashed line shows the central value of observed relic density. Parameters kept fixed for the plot are mentioned in the figure heading.

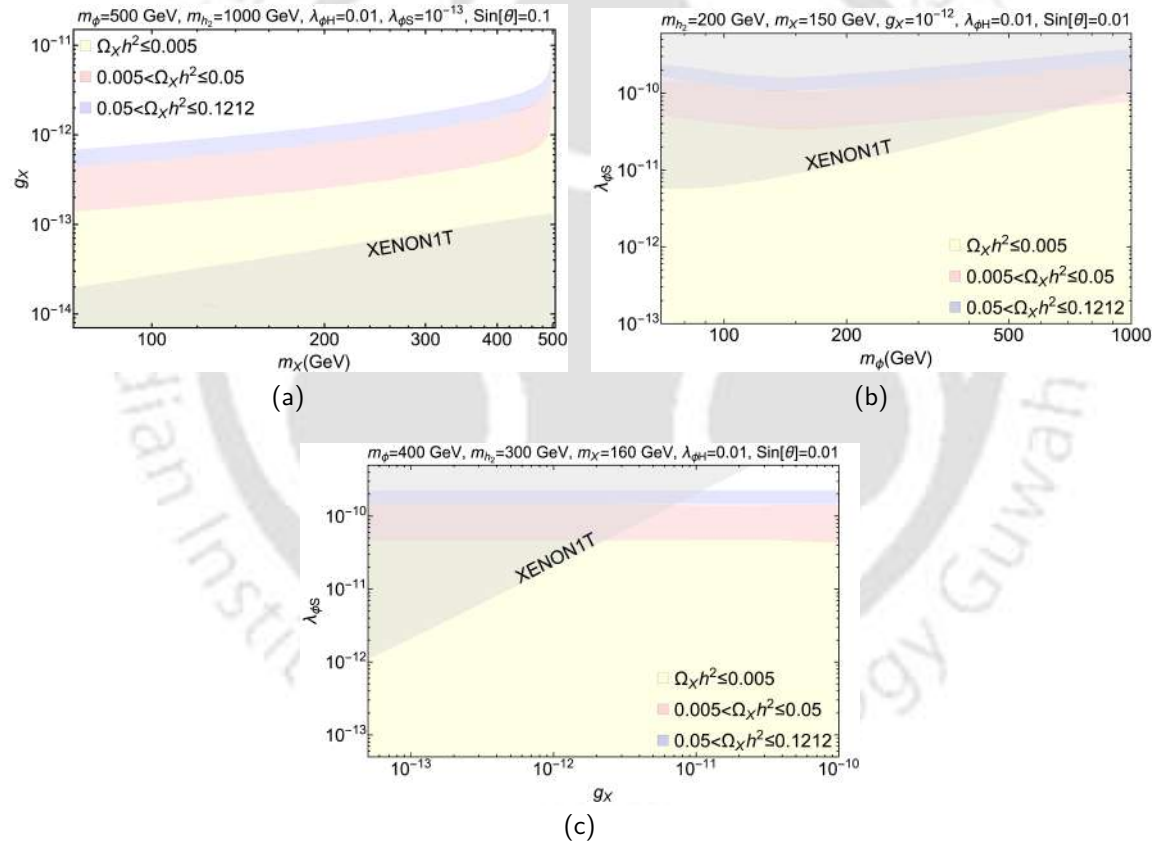

Figure 4.19: Under abundant ($\Omega_X h^2 \leq \Omega_T h^2$) parameter space for DM freeze-in aEWSB. Fig . 4.19a shows a correlation in g_X vs. m_X plane with direct search constraint restricting the smaller g_X values shown by the grey shaded region. In Fig.4.19b, the under abundant region in $\lambda_{\phi S}$ vs. m_ϕ plane is shown, with grey shaded region ruled out by the XENON1T direct search bound. The relic density of FIMP DM is indicated by color code in the figure inset. In Fig.4.19c, we show the viable parameter space in $\lambda_{\phi S}$ vs. g_X plane for the scattering dominated production of FIMP. Direct search limits weaken for smaller $\lambda_{\phi S}$ and larger g_X. Parameters kept fixed are mentioned in figure headings.

Here we see that a large region of the parameter space is ruled out by DD data particularly for larger $\lambda_{\phi S}$. Since the DD cross-section has very strong dependence on both $\lambda_{\phi S}$ and g_X, in Fig . 4.19c at the bottom panel, we show a correlation in the $\lambda_{\phi S}$ vs. g_X plane. Here, FIMP relic density, although increases with $\lambda_{\phi S}$, remains almost con-

stant with the variation of g_X, as the scattering dominant production cross-section has no explicit dependence on g_X. On the other hand, the direct detection cross-section, having explicit dependence on $\lambda_{\phi S}$ and $v_s \sim 1/g_X$, shows weaker bounds for small $\lambda_{\phi S}$ and large g_X. Parameters kept fixed for the scans, are mentioned in the respective figure headings and ensure all the other constraints.

4.5.4 Freeze-out of ϕ

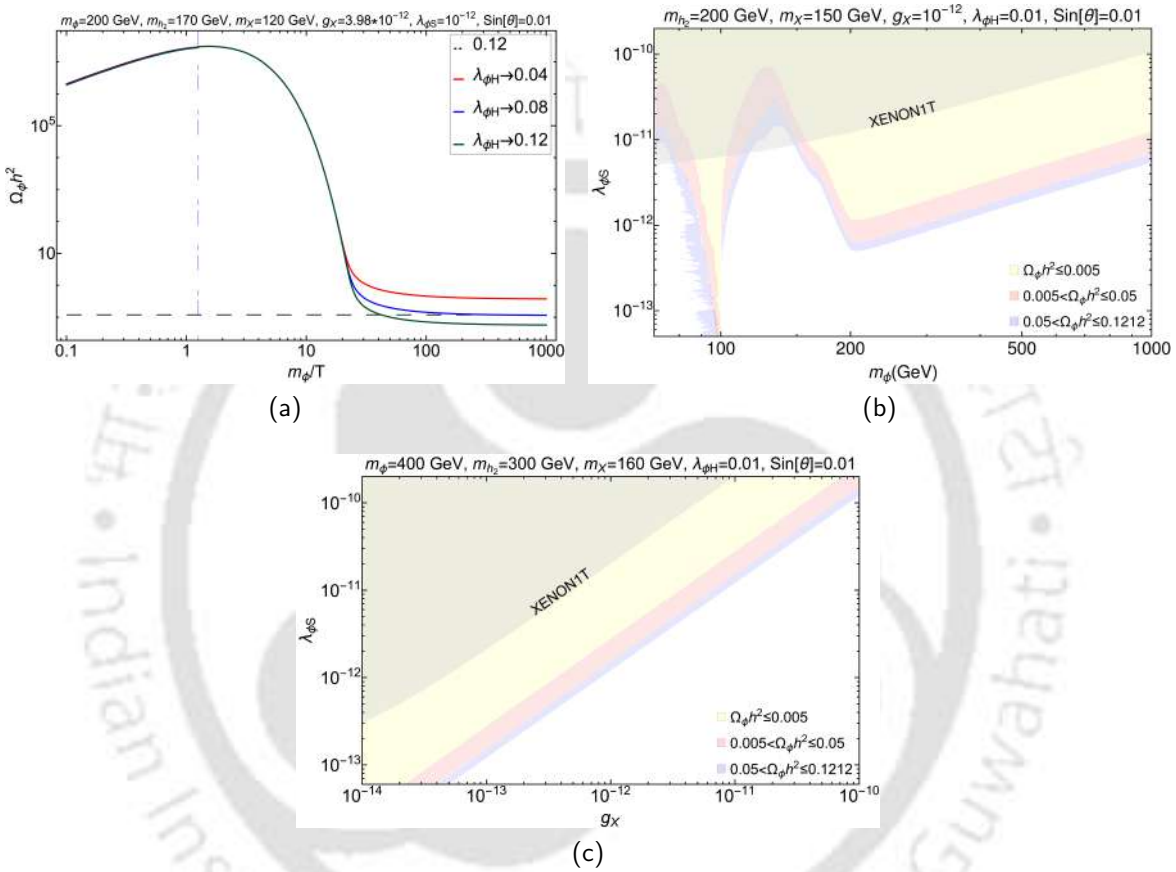

Figure 4.20: Figure 4.20a shows freeze-out pattern for WIMP (ϕ) relic density as a function of m_ϕ/T for some fixed values of $\lambda_{\phi H}$, which also ensures freeze-out aEWSB. The vertical dot-dashed line corresponding to EWSB ($x_{\rm EW}$). Fig. 4.20b denotes a correlation plot for the under-abundant ϕ in $m_\phi - \lambda_{\phi S}$ plane. The constraints from spin independent DD cross-section obtained from XENON1T data are shown in grey shades. The parameters kept fixed for are mentioned in figure heading. The color shades in light blue, light red and light yellow show the ranges of under abundance as mentioned in figure inset. In Fig. 4.20c, we show the under abundant ϕ in $\lambda_{\phi S}$ vs. g_X plane.

ϕ freezes out aEWSB through the annihilation channels as shown in Fig. 4.16. New annihilation channels open up through for *e.g :* $h\phi\phi$ vertex aEWSB. The trilinear couplings of ϕ with Higgs become relevant in the DM phenomenology, in contrast to only quartic DM-Higgs interaction bEWSB for ϕ freeze-out. We demonstrate aEWSB freeze-out with three representative plots in Fig. 4.20. Fig. 4.20a shows the evolution of WIMP abundance ($\Omega_\phi h^2$) with m_ϕ/T for three discrete values (mentioned in the figure inset) represented by red, blue and green colored lines respectively. If we increase $\lambda_{\phi H}$, this enhances the annihilation cross-section and in turn decrease the relic abundance, which we show in the figure. The blue one with $\lambda_{\phi H} = 0.08$ satisfies the correct relic. The vertical dot-dashed line ensures that the ϕ freeze out occurs aEWSB and the horizontal dashed line represents the central value of the observed

DM relic. Also note in Fig . 4.20a, a small bump appearing in the equilibrium distribution due to the change of WIMP mass at EWSB boundary as given by Eq . (C.13) in Appendix C.2.

In Fig . 4.20b, we show the (under-) relic and direct search allowed parameter space in $m_\phi - \lambda_{\phi S}$ plane. The three shades light yellow, light red and light blue represent different ranges for under-abundance, as mentioned in the legend. The grey shaded region is excluded by present spin independent direct search (XENON1T) bound. With smaller $\lambda_{\phi S}$, relic density expectedly increases. Also, we see the maximum annihilation around the m_{h_2} resonance at 100 GeV, as we fixed m_{h_2} at 200 GeV for this scan. Owing to the fact that m_{h_2} is unknown and loosely constrained, a large amount of relic density allowed parameter space can be brought under the direct search bound if one focuses on the m_{h_2} resonance. We also see that a large parameter space opens up whenever the annihilation channel to h_2 pair opens up with $m_\phi > m_{h_2}$. To demonstrate the effect of the two relevant couplings g_X and $\lambda_{\phi S}$ on WIMP relic density and DD, we show a correlation plot in the bottom panel Fig . 4.20c. DD limits show the same trend as Fig . 4.19c, whereas the WIMP annihilation cross-section, also being proportional to $\lambda_{\phi S}\, v_s$, shows under abundance for large $\lambda_{\phi S}$ and small g_X. Importantly we see that for WIMP, under abundant regions face more exclusion from direct search limit while it is the other way round for FIMP, which obviously stems from the reverse dependence on the cross-section to the DM yield for these two cases.

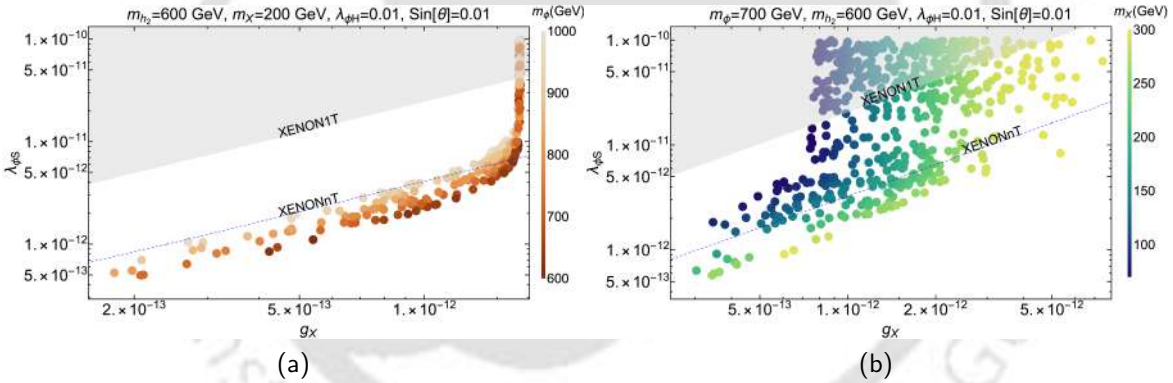

Figure 4.21: Scan in $g_X - \lambda_{\phi S}$ plane when both WIMP and FIMP components add to observed relic density, $\Omega_X h^2 + \Omega_\phi h^2 = 0.1200 \pm 0.0012$, simultaneously addressing other constraints when both freeze in and freeze out occur aEWSB in the kinematic region $m_{h_2} \geq 2m_X$. In Fig . 4.21a, we keep FIMP mass fixed at $m_X = 200\ GeV$ and vary WIMP mass m_ϕ as shown in the SiennaTones color bar. In Fig . 4.21b, we keep WIMP mass $m_\phi = 700\ GeV$ fixed and vary FIMP mass (m_X) as shown by the BlueGreenYellow color bar. Other parameters kept fixed are mentioned in the figure heading. Direct search constraint from XENON1T is shown by grey shaded regions, while the future sensitivity of XENONnT is shown by the blue dotted line.

4.5.5 Putting WIMP and FIMP together

We again discuss a couple of example plots where the WIMP (ϕ) and FIMP (X) add to the total observed DM relic density. In Fig . 4.21, we show the scan in $g_X - \lambda_{\phi S}$ plane where both freeze-in of X and freeze-out of ϕ occur aEWSB. In Fig . 4.21a, we keep FIMP mass (m_X) fixed, while vary WIMP mass (m_ϕ) as shown by the SiennaTones color bar. In Fig . 4.21b, we instead keep WIMP mass (m_ϕ) fixed, while vary FIMP mass (m_X) as shown by the BlueGreenYellow color bar. In both cases, we adhere to a parameter space where FIMP production is decay dominated. Observations are pretty similar to what we got bEWSB.

In Fig . 4.21a, we again see that with larger g_X, FIMP relic enhances, which in turn requires $\lambda_{\phi S}$ to enhance as well, so that Ω_ϕ decreases (the inclined region). Now, g_X can maximally enhance to $\sim 2 \times 10^{-12}$, when FIMP relic completely dominates over WIMP, with a sharp rise in $\lambda_{\phi S}$ to bring WIMP relic to very small value. We also see that keeping the g_X fixed (so that FIMP relic remains almost unchanged), if we enhance $\lambda_{\phi S}$, WIMP relic decreases unless we adjust m_ϕ to larger values to keep the total relic within experimental observed value. In Fig . 4.21b, larger $\lambda_{\phi S}$ diminishes Ω_ϕ, which is adjusted by larger FIMP contribution, by having smaller m_X for a fixed g_X. Further, when g_X is enhanced, FIMP contribution becomes larger, then WIMP contribution is adjusted to smaller values by larger $\lambda_{\phi S}$. Importantly, present direct search bound from XENON1T (on spin independent cross-section) plays an important role here, shown by grey shaded region, which discards part of large $\lambda_{\phi S}$ region. Future projected direct search sensitivity of XENONnT experiment is also shown by the blue dashed line, which will probe a large part of the allowed parameter space.

As can be easily seen, that the phenomenology aEWSB is richer and as the masses (m_ϕ, m_s, m_X) turn out to be much smaller. Such regions are prone to both direct search and collider experiments for the WIMP, which interestingly correlates to the FIMP under abundance as some of the parameters are common. We leave the exercise, where collider signal and direct search sensitivity of WIMP-FIMP model will be discussed, for a separate work. We finally tabulate some characteristic benchmark points for this scenario in Table 4.5, where the total relic obtained from X and ϕ adds to the observed one abiding by all the other constraints. Here also, AP1 and AP4 point out to the cases when X dominates over ϕ, AP3, AP6 show when ϕ dominates over X and AP2, AP5 depict the case when both DM contribute equally.

Scenario	Benchmark points	m_ϕ, m_{h_2}, m_X (GeV)	$g_X, \lambda_{\phi S}, \lambda_{\phi H}, \sin\theta$	$\Omega_\phi h^2$	$\Omega_X h^2$	$\frac{\Omega_\phi}{\Omega_T}$ (%)	$\frac{\Omega_X}{\Omega_T}$ (%)	$\sigma^{\rm SI}_{\phi_{\rm eff}}$ (cm^2)
$m_{h_2} \geq 2m_X$	AP1	200, 150, 70	$1.82\times10^{-12}, 3.30\times10^{-12}, 10^{-2}, 10^{-2}$	0.0117	0.1088	9.71	90.29	1.60×10^{-48}
	AP2	400, 300, 130	$1.51\times10^{-12}, 2.80\times10^{-12}, 10^{-2}, 10^{-2}$	0.0545	0.0663	45.08	54.92	9.52×10^{-50}
	AP3	350, 300, 100	$3.00\times10^{-13}, 4.85\times10^{-13}, 10^{-2}, 10^{-2}$	0.1141	0.0053	95.54	04.46	1.52×10^{-48}
$m_{h_2} < 2m_X$	AP4	700, 400, 250	$5.22\times10^{-11}, 1.58\times10^{-10}, 10^{-2}, 10^{-2}$	0.0186	0.1002	15.68	84.32	9.41×10^{-49}
	AP5	1000, 300, 200	$3.33\times10^{-11}, 1.63\times10^{-10}, 10^{-2}, 10^{-2}$	0.0599	0.0604	49.77	50.23	2.29×10^{-48}
	AP6	600, 250, 150	$9.97\times10^{-12}, 2.50\times10^{-11}, 10^{-2}, 10^{-2}$	0.1187	0.0018	98.54	01.46	5.45×10^{-50}

Table 4.5: Some sample benchmark points for the WIMP-FIMP DM model, when both freeze-in and freeze-out occur aEWSB respecting the total relic density, direct search, Higgs mass/mixing and other constraints. The benchmark points depict the possibilities when one component dominates over the other as well as the cases when they have almost equal share for the relic density.

4.6 Summary

In this analysis, we show that EWSB plays an important boundary condition for DM freeze-out and freeze-in. To be specific, we ask, if it is possible to identify the region of parameter space where saturation of DM yield occurred bEWSB or aEWSB. We see that there are mainly two effects to this end; the main point is the mass of the DM or the decaying particle, which plays an important role to saturate the freeze-in or freeze-out abundance before or after EWSB, and second is the change in the

depletion or production channels for DM across EWSB, particularly for those DM particles that couple to visible sector via Higgs portal. Here we have demonstrated the changes in relic density allowed parameter space of a two component WIMP-FIMP model when both freeze-in and freeze-out occurs before EWSB to that when both occur aEWSB. Some broad characteristics emerge from the study. For example, when FIMP freezes in bEWSB, we see that the requirement that even 'late decay' of the bath particle to occur bEWSB puts constraints on the mass on the decaying particle to be larger than some threshold. This is equivalent to freeze-out of a particle to occur bEWSB, where the WIMP mass requires to be sufficiently heavy (~ 4 TeV); the exact limit depends on the nature and interactions of the DM considered. On the other hand for freeze-in or freeze-out to occur aEWSB, the mass of the bath particle for FIMP, or the mass of DM for WIMP can be in the range of $\sim \mathcal{O}(100)\ GeV$. We have demonstrated the above features by solving appropriate Boltzmann equations, taking care of all constrains on the model parameters . This in turn provides with a nice distinguishability of the parameter space of the model; the case bEWSB is difficult to probe at collider having heavier masses (be it WIMP mass or the particle in thermal bath that decays to FIMP), direct search (for WIMP) serves as the only viable option, while the case aEWSB is more accessible to both collider and direct search prospects with masses of the order of TeV.

Regarding the model we choose for illustration, we have a vector DM (X) transforming under additional $\mathrm{U}(1)_X$ symmetry, which remains out-of-equilibrium and freezes in, while a scalar singlet DM ϕ remains in thermal bath and freezes-out to acquire correct relic. The effect of EWSB is pronounced in such a case with a larger $\mathrm{U}(1)_X$ breaking scale necessitated by the freeze-in of X. On the contrary, if we imagine a situation, where ϕ is WIMP and X is FIMP, then unnatural fine tuning will only be applicable to the portal couplings $\lambda_{\phi H}, \lambda_{\phi S}$, bringing down the $\mathrm{U}(1)_X$ breaking scale close to EWSB, leaving a very small region of parameter space for a massive X freeze-out bEWSB. Further, in such a two component set up, WIMP and FIMP parameters get correlated to produce the observed relic. For example, given a $\mathrm{U}(1)_X$ coupling g_X, it is possible to adjudge a portal $\lambda_{\phi S}$ and vice versa. Direct search constraints on the WIMP ϕ also limits the FIMP abundance due to the presence of some common coupling parameters like $\lambda_{\phi S}$.

While both the models as single component DM have been studied in literature, we find out that the presence of both DM components together provides additional features for their respective abundances. For example, ϕ has channels to deplete its number density due to the scalar s required to break $\mathrm{U}(1)_X$ symmetry, which allows a larger allowed parameter space for ϕ in the resonance region $m_\phi \sim m_s/2 \sim m_{h_2}/2$. Further, regions where annihilation to this scalar $m_\phi > m_s$ (or the physical one h_2 after mixing) opens up, it is easier to satisfy relic under abundance after adhering to direct search bounds. For FIMP (X), conversion from WIMP (ϕ) plays a major role, which is only possible in a two component set up like this. On the contrary, in order to keep X out-of-equilibrium, the WIMP-FIMP conversion is never sizeable enough to alter the effective annihilation cross-section and relic density of ϕ. This feature is generic beyond the specific model taken up here. We also note that, the coupled BEQ required to address a two component WIMP-FIMP case, reduces to two uncoupled BEQs in the limit of tiny annihilation from WIMP to FIMP. However, one may think of a situation where the FIMP has very tiny coupling with SM, but a sizeable one with the WIMP, which may bring it to thermal bath and then freezes it

out. The consequences of such a situation are interesting and will be addressed in the next chapter.

Chapter 5

WIMP-FIMP with substantial interaction: Pseudo-FIMP

Contents

In a two-component dark matter (DM) set-up, when DM_1 is in equilibrium with the thermal bath, the other DM_2 can be equilibrated just by sizeable interaction with DM_1, even without any connection with the visible-sector particles. We show that such DM candidates (DM_2) have unique 'freeze-out' characteristics impacting the relic density, direct and collider search implications, and propose to classify them as 'pseudo-FIMP' (pFIMP). The dynamics of pFIMP is studied in a model-independent manner by solving generic coupled Boltzmann Equations (cBEQ) for both WIMP and SIMP partners, followed by concrete model illustrations. The discussion in this chapter is based on Refs . [305] and [593].

5.1 pFIMP phenomenology in the presence of WIMP

Let us first consider DM_1 to be WIMP.

5.1.1 Introduction

When the interaction between a WIMP and a FIMP remains 'feeble', the FIMP continues to be out of equilibrium [301, 594, 595], but enhanced interaction (of weak strength) can make the FIMP equilibrate to thermal bath and undergo *freeze-out* with

some unique features, which are essentially model-independent, but relies on the properties of its thermal DM partner. We propose to classify such a particle into a category called 'pseudo-FIMP' (pFIMP), as it is a thermal DM in spite of having feeble connection with the SM. Also, pFIMP can be realized in presence of *any* thermal DM like Strongly Interacting Massive Particle (SIMP), independent of the depletion mechanism. Some model-dependent studies which mimic a pFIMP-like situation, have been studied [308, 596–598], but without elaborating the generic features that such particles possess. This letter illustrates the pFIMP characteristics in a model-independent way followed by a concrete model illustration and detection possibilities. Actually the idea of pFIMP has been conceptualised and demonstrated here for the first time, that occurs in a particular limit of the DM-DM and DM-SM interactions in a multicomponent set up. This leads to several model possibilities to be explored in the pFIMP limit as detailed in [306].

5.1.2 Model Independent analysis

The evolution of DM number density in WIMP-FIMP framework is governed by a set of coupled Boltzmann equations (cBEQ) as shown in Eq. (D.1), in terms of yield ($Y = \frac{n}{s}$) as a function of $x = \mu_{12}/T$, where $\mu_{12} = m_1 m_2/(m_1 + m_2)$ denotes the reduced mass of the two DMs, and T denotes the temperature of the thermal bath.

$$\begin{aligned}
\frac{dY_1}{dx} &= -\frac{s}{x\,\mathcal{H}(x)}\left[\langle\sigma v\rangle_{11\to \mathrm{SM}}\left(Y_1^2 - Y_1^{\mathrm{eq}^2}\right) + \langle\sigma v\rangle_{11\to 22}\left(Y_1^2 - \frac{Y_1^{\mathrm{eq}^2}}{Y_2^{\mathrm{eq}^2}}Y_2^2\right)\right], \\
\frac{dY_2}{dx} &= \frac{2\,s}{x\,\mathcal{H}(x)}\left[\frac{1}{s}\langle\Gamma_{\mathrm{SM}\to 22}\rangle(Y_{\mathrm{SM}}^{\mathrm{eq}} - \frac{Y_2^2}{Y_2^{\mathrm{eq}^2}}Y_{\mathrm{SM}}^{\mathrm{eq}}) + \langle\sigma v\rangle_{\mathrm{SM}\to 22}\left(Y_{\mathrm{SM}}^{\mathrm{eq}^2} - \frac{Y_2^2}{Y_2^{\mathrm{eq}^2}}Y_{\mathrm{SM}}^{\mathrm{eq}^2}\right)\right. \\
&\quad \left. + \langle\sigma v\rangle_{11\to 22}\left(Y_1^2 - \frac{Y_1^{\mathrm{eq}^2}}{Y_2^{\mathrm{eq}^2}}Y_2^2\right)\right].
\end{aligned} \tag{5.1}$$

In the above equation, $s = \frac{2\pi^2}{45} g_*^s \left(\frac{\mu_{12}}{x}\right)^3$, $\mathcal{H}(x) = 1.67\sqrt{g_*^\rho}\,\mu_{12}^2 x^{-2} \mathrm{M}_{\mathrm{pl}}^{-1}$. Subscripts $1,\ 2$ in Eq. (D.1) and in the rest of the draft denote WIMP and FIMP (pFIMP) components respectively. Interactions that crucially determine the DM densities are WIMP depletion to SM governed by $\langle\sigma v\rangle_{11\to \mathrm{SM}}$, FIMP production from the SM bath via annihilation $\langle\sigma v\rangle_{\mathrm{SM}\to 22}$ and/or decay $\langle\Gamma_{\mathrm{SM}\to 22}\rangle$, and WIMP-FIMP conversion $\langle\sigma v\rangle_{11\to 22}$ ($\langle..\rangle$ denotes thermal average and v is Möllar velocity). The cBEQ for a two component WIMP case is also the same as Eq. (D.1). The difference lies in the (i) strength of the DM-SM interactions; $\langle\sigma v\rangle_{\mathtt{WIMP}} \sim 10^{-8}\ GeV^{-2}$, whereas $\langle\sigma v\rangle_{\mathtt{FIMP}} \sim 10^{-20}\ GeV^{-2}$ and (ii) initial conditions, $Y_{\mathtt{WIMP}}|_{x\sim 0} = Y^{\mathrm{eq}} \sim x^{3/2}e^{-x}$, $Y_{\mathtt{FIMP}}|_{x\sim 0} = 0$. In the following, the conversion $\langle\sigma v\rangle_{11\to 22}$ is varied from 'feeble' to 'weak' strength to show the transition from FIMP to pFIMP state. Other notations in Eq. (D.1) are all standard and available in any DM text [300].

For solving Eq. (D.1) to obtain DM yields in a model-independent way, we choose some benchmark values of the DM masses and $\langle\sigma v\rangle$. As the temperature dependence in $\langle\sigma v\rangle$ requires $\sigma(s)$ (s is c.o.m energy) i.e. diagrams that contribute to annihilation, in absence of which we assume here $\langle\sigma v\rangle \approx \sigma^{\mathrm{T}}$; a temperature-independent threshold value representing (σv) at the *freeze-out* (*freeze-in*) temperature for WIMP/pFIMP (FIMP). Full $\langle\sigma v\rangle$ is used for a model-specific analysis and the dynamical features remain the same.

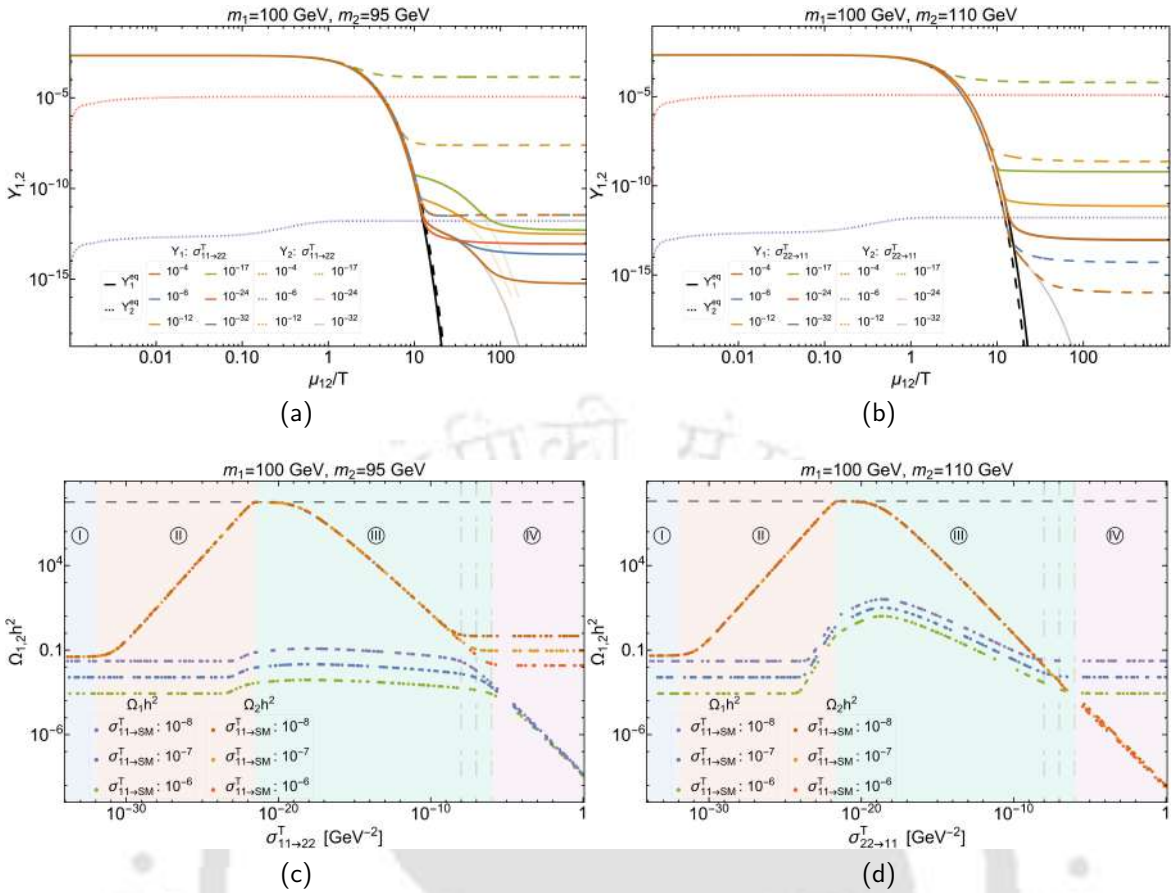

Figure 5.1: (a) $Y_{1,2}(x)$ for mass hierarchy 1, where solid (dotted) [dashed] curves denote WIMP (FIMP) [pFIMP] with equilibrium distributions marked in black; (b) Same as (a) for hierarchy 2; (c) $\Omega_{1,2}h^2$ as a function of $\sigma^T_{11\to22}$ for hierarchy 1; red/yellow/orange dotted lines represent FIMP(pFIMP), while green/blue/pink ones represent WIMP; (d) same as (c) for hierarchy 2. For all the plots $\Gamma^T_{SM\to22} = 10^{-23}\text{GeV}^{-1}$, $\sigma^T_{SM\to22} = 10^{-32}\text{GeV}^{-2}$. For upper panel plots, we choose $\sigma^T_{11\to SM} = 10^{-7}\text{GeV}^{-2}$. See figure inset/caption for other parameters kept fixed.

Plots in Fig . 5.1 summarise the main outcome of the model independent analysis. In Figs . 5.1a, 5.1b, $Y_{1,2}$ are plotted as a function of x, for different conversion rates. In Figs . 5.1c, 5.1d, $\Omega_{1,2}h^2$ are plotted as a function of $\sigma^T_{11\to22}$ (left), $\sigma^T_{22\to11}$ (right). Note, that $\langle\sigma v\rangle_{11\to22} = \langle\sigma v\rangle_{22\to11}(Y_2^{eq}/Y_1^{eq})^2$. All the cross-sections are in the units of GeV^{-2} and in the following text we may omit writing it explicitly. Both the mass hierarchies (1) $m_1 > m_2$ (on left) and (2) $m_1 < m_2$ (on right) are shown. In hierarchy (1), conversion from WIMP to pFIMP is kinematically allowed, while the reverse process is Boltzmann suppressed ($\sim e^{-2\delta m\, x}$, $\delta m = m_1 - m_2$). For hierarchy (2), its the other way round. The whole analysis can be divided into four different regions of varying conversion cross-section, Ⓘ : $\sigma^T_{11\to22} < \sigma^T_{SM\to22}$, Ⓘⓘ : $\sigma^T_{SM\to22} \lesssim \sigma^T_{11\to22} \ll \sigma^T_{11\to SM}$, Ⓘⓘⓘ : $\sigma^T_{SM\to22} \ll \sigma^T_{11\to22} < \sigma^T_{11\to SM}$, Ⓘⓥ : $\sigma^T_{11\to SM} \lesssim \sigma^T_{11\to22}$, as shown by the colour bars in Figs . 5.1c, 5.1d.

In region Ⓘ, when the conversion rate is very small ($\sigma^T_{11\to22} \sim 10^{-32}$) it has no role in FIMP or WIMP relic density. The FIMP remains out-of-equilibrium and freeze-in occurs via $\sigma^T_{SM\to22}, \Gamma^T_{SM\to22}$, see the blue dotted lines in Figs . 5.1a, 5.1b and horizontal red/yellow/orange dotted lines in Figs . 5.1c, 5.1d.

In region Ⓘⓘ, when $\sigma^T_{11\to22} \gtrsim \sigma^T_{SM\to22}$, the FIMP is still out of equilibrium but the freeze-in is guided by the conversion process, see the red dotted lines in Figs . 5.1a, 5.1b ($\sigma^T_{11\to22} \sim 10^{-24}$) and the growing red/yellow/orange dotted lines with larger

$\sigma^{\rm T}_{11\to 22}$ in Figs . 5.1c, 5.1d. The WIMP still remains unaffected, evident from the red/violet solid lines in Figs . 5.1a, 5.1b, and horizontal blue/green/violet dotted lines in Figs . 5.1c, 5.1d.

In region (III), as the conversion rate $\sigma^{\rm T}_{11\to 22}$ is increased further, the FIMP starts following the thermal distribution, see green ($\sigma^{\rm T}_{11\to 22} = 10^{-17}$) and orange ($\sigma^{\rm T}_{11\to 22} = 10^{-12}$) dashed lines in Figs . 5.1a, 5.1b. This is when the FIMP turns into pFIMP and undergoes "freeze-out". Larger conversion cross-section keeps pFIMP longer in the thermal bath resulting smaller relic density; see the steady decline in red/yellow/orange dotted lines with larger $\sigma^{\rm T}_{11\to 22}(\approx 10^{-17})$ in Figs . 5.1c, 5.1d. Notably, the freeze-out point of pFIMP is governed purely by its conversion rate from (to) the WIMP. However, the WIMP freeze-out is additionally dictated by $\sigma^{\rm T}_{11\to \rm SM}$. Therefore pFIMP always decouples before or together with the WIMP (compare dashed and solid lines in Figs . 5.1a, 5.1b) and provides an important difference between WIMP-WIMP and pFIMP-WIMP case. For heavier WIMP (hierarchy 1), the WIMP freeze-out shows a bump (see Fig . 5.1a), as it attains a modified equilibrium distribution following Eq . (5.2), after pFIMP decouples [597],

$$\mathrm{n}_1^{\mathrm{eq}'} = \mathrm{n}_1^{\mathrm{eq}} \left(\frac{\sigma^{\rm T}_{11\to \rm SM} + \sigma^{\rm T}_{11\to 22} \left(\mathrm{n}_2/\mathrm{n}_2^{\mathrm{eq}}\right)^2}{\sigma^{\rm T}_{11\to \rm SM} + \sigma^{\rm T}_{11\to 22}} \right)^{1/2} . \tag{5.2}$$

When pFIMP is heavier (hierarchy 2), the conversion from WIMP to pFIMP is kinematically suppressed, and no modified freeze-out pattern for WIMP is observed (see Fig . 5.1b). This provides another distinction of pFIMP-WIMP scenario from the WIMP-WIMP one. After FIMP equilibrates to thermal bath, larger production of WIMP from pFIMP enhances WIMP relic density, see the jump from red thick line ($\sigma^{\rm T}_{11\to 22} = 10^{-24}$) to green thick line ($\sigma^{\rm T}_{11\to 22} = 10^{-17}$) in Figs . 5.1a, 5.1b. This feature is also observed in the violet/blue/green dashed lines in Figs . 5.1c, 5.1d. For hierarchy (1), the departure of the WIMP from the original equilibrium distribution to modified equilibrium (Eq . (5.2)) depends on $\sigma^{\rm T}_{11\to 22}$ (compare green and orange thick lines in Fig . 5.1a), however the freeze-out from modified equilibrium is primarily governed by $\sigma^{\rm T}_{11\to \rm SM}$, yielding same $\Omega_1 \mathrm{h}^2$ for different $\sigma^{\rm T}_{11\to 22}$. On the contrary, for hierarchy (2), when pFIMP is heavier, the WIMP production from pFIMP is substantial due to kinematic accessibility, as a result the WIMP freeze out is delayed, and the WIMP yield goes down with enhanced conversion rate (see Fig . 5.1d), providing a crucial hierarchical distinction.

In region (IV), with $\sigma^{\rm T}_{11\to 22} > \sigma^{\rm T}_{11\to \rm SM}$, we see even more interesting consequences. For hierarchy (1), the WIMP relic density falls drastically with larger $\sigma^{\rm T}_{11\to 22}$ due to larger depletion (violet/green/blue dotted lines in Fig . 5.1c), while the pFIMP yield remains the same, and is dependent only on $\sigma^{\rm T}_{11\to \rm SM}$ (horizontal brown/yellow/red dotted lines in Fig . 5.1c, or overlapping dashed lines in Fig . 5.1a for $\sigma^{\rm T}_{11\to 22} = 10^{-6}, 10^{-4}$). This is because pFIMP yield in hierarchy (1) is governed by two quantities, WIMP number density and conversion rate. Now, the WIMP number density falls with larger $\sigma^{\rm T}_{11\to 22}$, while that is compensated by the enhanced production via $\sigma^{\rm T}_{11\to 22}$ which keeps the pFIMP yield almost constant in this region. For hierarchy (2), the situation is however different. With increasing conversion, pFIMP yield decreases significantly, while the WIMP yield remains almost constant (see Fig . 5.1d). This is attributed again to the combined effect of decreasing pFIMP number density along with larger WIMP production from pFIMP with larger conversion rate. Since pFIMP

has no SM interaction, it goes out of the original equilibrium distribution as WIMP freezes out. However, due to considerable conversion to WIMP, it achieves a modified equilibrium distribution as seen from the orange and blue dashed lines in Fig . 5.1b.

$DM_1 - DM_2$	$\langle\sigma v_{SM-DM_1}\rangle$	$\langle\sigma v_{SM-DM_2}\rangle$	$\langle\sigma v_{DM_1-DM_2}\rangle$	Observed Relic	Direct-Detection	Indirect-Detection
WIMP-WIMP	Weak	Weak	Weak/Feeble	Yes [300]	Yes-Yes [300, 599]	Yes-Yes[600]
WIMP-pFIMP	Weak	Feeble	Weak	Yes [308, 597]	Yes-Yes[597]	Yes-Yes
FIMP-FIMP	Feeble	Feeble	Weak/Feeble	Yes [304, 601, 602]	No-No [602]	No-No

Table 5.1: Generic two-component DM scenarios, order of the interaction with SM as well as between DMs, possibilities of satisfying relic abundance and being probed in direct (indirect) search experiments.

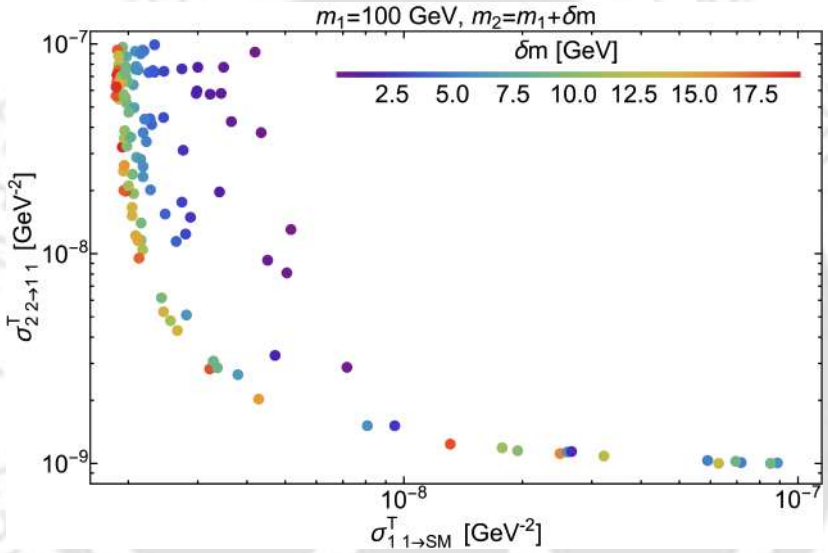

Figure 5.2: Relic density allowed points in the $\sigma^{T}_{11\to SM} - \sigma^{T}_{22\to 11}$ plane for $m_2 > m_1$ in WIMP-pFIMP limit. $\delta m = |m_1 - m_2|$ is varied as shown in the colour-bar. We choose $\Gamma^{T}_{SM\to 22} = 10^{-20}\ GeV^{-1}$, $\sigma^{T}_{SM\to 22} = 10^{-30}\ GeV^{-2}$, $m_1 = 100\ GeV$ and decaying particle mass $m_s = 300$ GeV.

We now perform a model-independent scan of the WIMP-pFIMP parameter space, where we assume that annihilation cross-sections and masses have adequate freedom to be varied independently. In Fig . 5.2, we scan points that satisfy relic density ($\Omega_1 h^2 + \Omega_2 h^2 = 0.12 \pm .0012$) in $\sigma^{T}_{11\to SM} - \sigma^{T}_{22\to 11}$ plane for hierarchy (2). WIMP mass is kept fixed at $100\ GeV$ and the mass splitting between WIMP and pFIMP $\delta m = |m_1 - m_2|$ is varied as shown in the colour bar. When the conversion rate is small, $\sigma^{T}_{11\to SM}$ requires to be large in order to achieve WIMP density within the limit. Understandably δm does not play a major role here, and a large range of δm is allowed (right side of Fig . 5.2). With larger conversion rate, smaller $\sigma^{T}_{11\to SM}$ is required (left of Fig . 5.2). If we decrease $\sigma^{T}_{11\to SM}$ keeping $\sigma^{T}_{22\to 11}$ fixed, the WIMP tends to become overabundant, unless the conversion contribution from pFIMP to WIMP is decreased by increasing δm via Boltzmann suppression. However, for hierarchy (1), the situation is different and the whole $\sigma^{T}_{11\to SM} - \sigma^{T}_{11\to 22}$ parameter space within $\delta m = |m_1 - m_2| \lesssim 10\ GeV$ becomes allowed.

In summary, the allowed points accommodate mostly small mass difference ($\delta m \lesssim 10\ GeV$) and the mass hierarchy between WIMP and pFIMP play a crucial role in the

$m_{\phi_1}[GeV]$	$m_{\phi_2}[GeV]$	λ_{1H}	λ_{12}	loop factor	$\Omega_{\phi_1}h^2$	$\Omega_{\phi_2}h^2$	$\sigma^{SI}_{\phi_{1\,eff}}[cm^2]$	$\sigma^{SI}_{\phi_{2\,eff}}[cm^2]$	Gluon fusion (fb)	
									WIMP	pFIMP
63.33	60.50	0.10	4	2.53×10^{-3}	0.0002	0.1203	3.3×10^{-47}	5.0×10^{-48}	8.4	13.9
104.1	100.0	0.22	6	8.40×10^{-3}	0.0002	0.1210	7.89×10^{-47}	2.15×10^{-47}	0.69	1.18×10^{-3}
405.0	402.9	0.30	8	1.52×10^{-2}	0.0101	0.1091	4.06×10^{-46}	7.49×10^{-48}	9×10^{-4}	2.34×10^{-6}

Table 5.2: Some benchmarks for the two-component scalar singlet model (Eq. (5.3)) in WIMP-pFIMP limit, where the loop factor is approximated as $\sim (\lambda_{1H}\lambda_{12})/(16\pi^2)$. The last two columns depict the WIMP and pFIMP production cross-section at LHC via Gluon fusion yielding mono-jet+$\not{E}_T$ in the final state at $\sqrt{s} = 14$ TeV.

consequent DM phenomenology, absent in usual WIMP-WIMP set up. Here we have ensured that the conversion cross-section remains well below the bullet cluster observational data [57] that suggests the upper limit on the self-interaction cross-section of DM(s) per unit mass to be, $\sigma/m < 0.7\ cm^2 g^{-1} \sim 3.2 \times 10^3\ GeV^{-3}$.

In Table 5.1, we depict a few examples of two component DM scenarios, with their strength of DM-DM conversion, possibility of producing correct relic abundance, along with direct (indirect) detection prospects at present/future experiments. Generically, the pFIMP detection is heavily dependent on the detection prospects of the WIMP, as the pFIMP direct search or collider search signal proceeds via WIMP loop as shown in Fig. 5.3. The strength of the pFIMP interaction is less than the WIMP, but can be of similar order when the loop factor is compensated by the large pFIMP-WIMP interaction.

5.1.3 A simple model example

We would now like to validate our claims of pFIMP characteristics for a specific model. Here we use temperature dependent $\langle\sigma v\rangle$ in terms of the model parameters. We choose the simplest model consisting of two real scalar singlets, where ϕ_1 behaves as WIMP and ϕ_2 as FIMP/(pFIMP), both of which are rendered stable under $\mathcal{Z}_2 \otimes \mathcal{Z}_2'$ symmetry. The Lagrangian density is given by,

$$\begin{aligned}\mathcal{L} = \mathcal{L}_{SM} + \frac{1}{2}\partial_\mu\phi_1\partial^\mu\phi_1 + \frac{1}{2}\partial_\mu\phi_2\partial^\mu\phi_2 - \frac{1}{2}\mu_{\phi_1}^2\phi_1^2 - \frac{1}{2}\mu_{\phi_2}^2\phi_2^2 - \frac{1}{4!}\lambda_{\phi_1}\phi_1^4 \\ - \frac{1}{4!}\lambda_{\phi_2}\phi_2^4 - \frac{1}{2}\lambda_{1H}\phi_1^2 H^\dagger H - \frac{1}{2}\lambda_{2H}\phi_2^2 H^\dagger H - \frac{1}{4}\lambda_{12}\phi_1^2\phi_2^2\,.\end{aligned} \tag{5.3}$$

This model in WIMP-WIMP limit has been explored in many texts including [300]. Here we focus on the pFIMP regime, partly explored in [308]. For that, we choose ϕ_2 to have negligible coupling with the SM, $\lambda_{2H} \approx 10^{-12}$. However, in presence of the WIMP-like ϕ_1, the conversion governed by λ_{12} plays a key role and with large $\lambda_{12} \sim 1$ it reproduces all the characteristics of pFIMP. Relic density as a function of λ_{12} is plotted in the supplementary material, which shows similar features to that of Figs. 5.1c, 5.1d and validates the pFIMP characteristics. The WIMP-pFIMP limit of this model has also been verified with the code micrOMEGAs4.1 [603].

Direct search of pFIMP is possible via WIMP loop, absent a tree-level connection to SM. The Feynman graph is shown in Fig. 5.3, while the detailed calculations are provided in the supplementary material. Large WIMP-pFIMP interaction (λ_{12}) helps in the detection of pFIMP, the loop suppression factor $\sim 1/(16\pi^2)$ allows it to

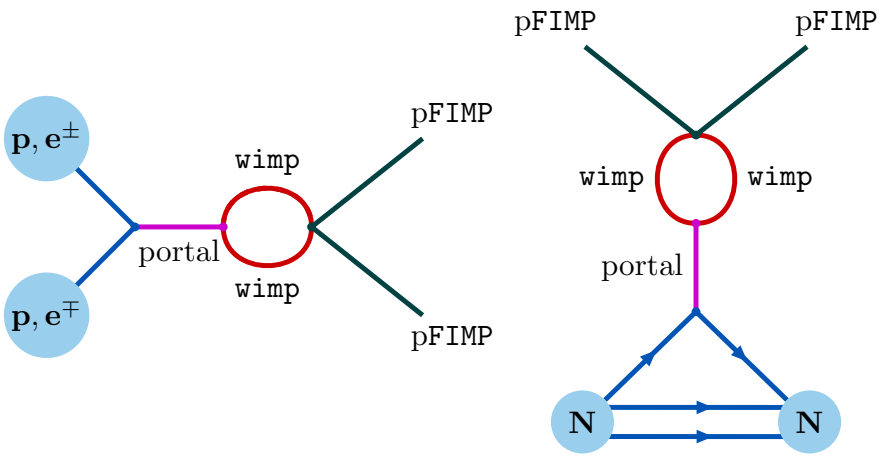

Figure 5.3: A schematic Feynman diagram for collider (left) and direct-detection (right) of pFIMP via one-loop WIMP interaction.

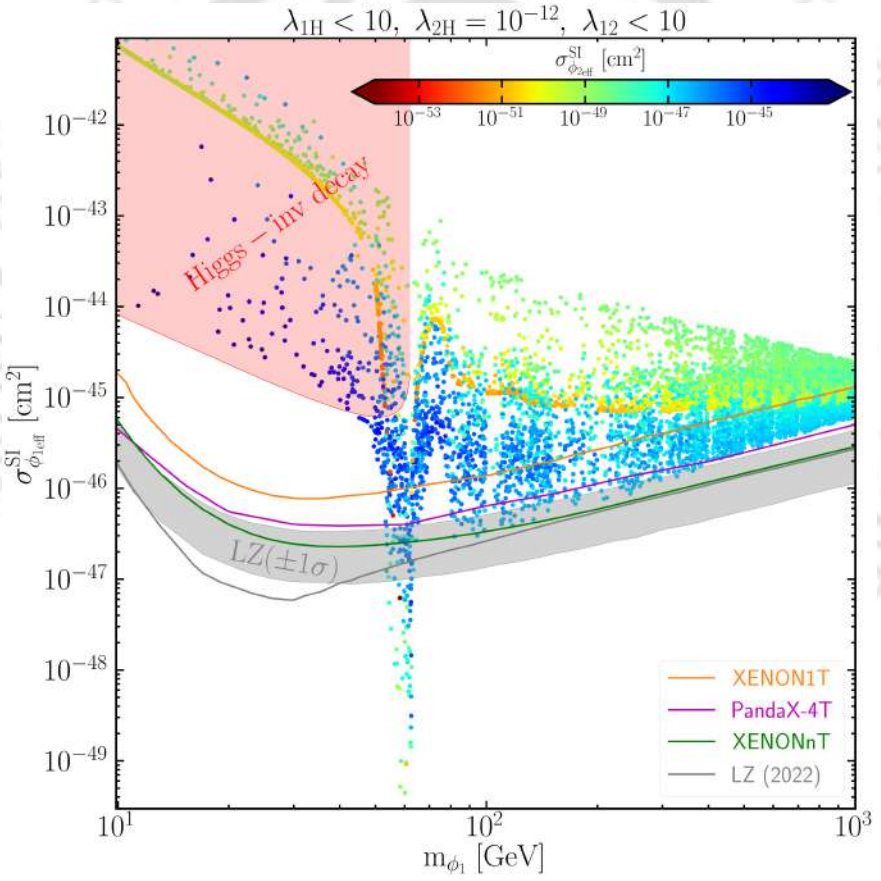

Figure 5.4: Relic density allowed points of the model described by Eq. (5.3) in $\sigma^{SI}_{\phi_{1eff}} - m_{\phi_1}$ plane. The parameters varied are $\{m_{\phi_2}, \lambda_{1H}, \lambda_{12}\}$. $\sigma^{SI}_{\phi_{2eff}}$ is shown in colour bar. See heading and figure inset for other parameters and experimental limits.

evade existing bound and make it accessible to future sensitivities. In Fig. 5.4, spin-independent (SI) direct detection cross-section for the WIMP (ϕ_1) and pFIMP (ϕ_2) is shown as a function of WIMP mass for relic density allowed points of the model. The sensitivity of existing direct search data have all been compared [357, 358, 514, 578]. A clear dip is seen in the resonance region $m_{\phi_1} \sim m_h/2$, where due to resonance enhancement λ_{1H} is relaxed and points satisfy direct search constraints. One should

however remember the limitations of Lee-Weinberg mechanism in the vicinity of resonance as pointed out by [604, 605].

When $m_{\phi_1} > m_{\phi_2}$, small δm enhances the $\phi_1\phi_1 \to \phi_2\phi_2$ conversion, consequently decreasing Ω_{ϕ_1} and effective direct detection cross-section $\sigma^{\rm SI}_{i_{\rm eff}} = \frac{\Omega_i}{\Omega_{\rm tot}}\sigma^{\rm SI}_i$, where $i = \{\phi_1,\ \phi_2\}$. However, most of the parameter space of this WIMP-pFIMP limit of the two component scalar DM model is on the verge of exclusion by the LZ (2022) data, leaving the Higgs resonance, $m_{\phi_1} \sim m_h$ regions and some points close to the $\pm 1\sigma$ exclusion limit up to 500 GeV survive to be explored. Unlike WIMP-WIMP case, where two DMs may have widely different masses, pFIMP limit necessitates the mass splitting to be small and therefore serves as a guiding principle for searching both DM components. Similarly pFIMPs can also be produced in collider via one-loop WIMP graphs yielding mono-X plus missing energy signals as estimated in the Table 5.2 for some benchmark points where the model satisfies relic density and direct search bounds. In this case, detection of pFIMP seems only possible in the resonance region, owing to a resonant enhancement in the production. Interesting to note that, even in this region, the effective coupling between Higgs and pFIMP is rather small due to loop suppression, thereby making it safe from the Higgs invisible decay constraints. One can have plethora of other possibilities, like a fermion WIMP instead of a scalar WIMP, which enhances the detection possibility of a scalar pFIMP, see for example, [306]. We again note here that the model chosen for illustration is not the best for detection, rather it is the simplest one.

Furthermore, pFIMP having a similar mass to that of the WIMP provides a challenge in distinguishing the DM components in direct and collider searches, as the distinguishability (a kink in the recoil spectrum for direct search [354, 355] or two bumps in missing energy at colliders [465, 466]) often depends on the mass splitting of the DM components. However mono-X signal can be useful, as the position of the peak here primarily depends on the operator structure, angular momentum conservation etc. We are exploring such possibilities, however the two component scalar case will be difficult to disentangle.

5.1.4 Summary

We have shown that the FIMP can reach equilibrium in presence of a thermal DM component and sizeable conversion cross-section. We call it pFIMP. The freeze-out of pFIMP precedes that of its thermal partner and requires a small mass splitting with it. The numerical solution of Eq. (D.1) presented here and approximate analytical solution provided in the supplementary material validates all the pFIMP properties in a model independent way. The pFIMP realization in presence of SIMP is also provided in the supplementary material. The freeze-out properties of pFIMP is verified for the simplest two-component DM model with two scalar singlets. The detection prospect of pFIMP via WIMP loop in future direct, indirect and collider search experiments opens up new possibilities. Such investigations in context of direct DM search for two-component WIMP–pFIMP model has been pursued in [306].

5.2 pFIMP phenomenology in the presence of SIMP

Let us now consider DM_1 to be SIMP. The freeze-out characteristics of pFIMP then depend very much on those of its SIMP partner. We establish this in a model-independent analysis via solving coupled Boltzmann Equations, so that it is applicable to any kind of pFIMP-SIMP combination, immaterial to their particle properties. Second, we establish the same via a concrete model example involving two scalar fields, one real, and the other complex, stabilized by $\mathcal{Z}_2 \otimes \mathcal{Z}_3$ symmetry. This is arguably the simplest scenario yielding pFIMP-SIMP model. The search strategies for DM known so far, like direct detection (DD), indirect detection (ID), or collider searches are difficult to reveal such DM combinations unless the SIMP is accessible to the detector via light mediator.

This chapter is organized as follows: Section 5.2.1 provides a brief discussion on a single component SIMP, Section 5.2.2 explores the dynamics and phenomenology of pFIMP in a model-independent manner, and Section 5.2.3 presents a model example. Finally, we summarize in Section 5.2.4. Appendices D.5 to D.8 provide additional details that were omitted in the main text.

5.2.1 A brief discussion on the simplest SIMP model

For WIMP, the DM freeze out depends on the thermal average of annihilation cross-section ($2_{\rm DM} \to 2_{\rm SM}$). For SIMP, DM freeze out (FO) occur mainly via self-interaction like $3_{\rm DM} \to 2_{\rm DM}$ [253] (or $4_{\rm DM} \to 2_{\rm DM}$ [255]) annihilations within the dark sector, while $2_{\rm DM} \to 2_{\rm SM}$ annihilation is suppressed. The equilibration of SIMP to thermal bath is maintained by scattering with SM particles (DM+SM $\to$ DM+SM), the rate of which is given by $\Gamma = n_{eq}\langle\sigma v\rangle$, which can be larger than the Hubble expansion rate (H) due to the large relativistic SM number density (n_{eq}), in spite of the small annihilation cross-section to SM. The hierarchy of interactions that keeps SIMP in thermal bath without heating up the dark sector is therefore,

$$\Gamma_{\rm DM+SM\to DM+SM} \gtrsim \Gamma_{3_{\rm DM}\to 2_{\rm DM}} \gtrsim \Gamma_{2_{\rm DM}\to 2_{\rm SM}} \,. \tag{5.4}$$

However for the five body ($3_{\rm DM} \to 2_{\rm DM}$) or six body depletion process ($4_{\rm DM} \to 2_{\rm DM}$) that governs SIMP freeze out, the DM mass needs to be adjusted to account for the larger phase space volume and is of the order of MeV to address correct relic density. The coupling for such a number-changing process within the dark sector must also be significantly large to take into account of the phase space suppression. Hence, such a class of DM is called Strongly Interacting Massive Particle (SIMP) [253, 255, 257, 262, 606]. We may stress here again that strong interaction here doesn't refer to strong interaction between dark and SM particles, but it is within the dark sector particles.

Concerning SIMP, the simplest possibility emerges when we take a complex scalar singlet (Φ), which transforms under $\mathcal{Z}_3$ symmetry. Corresponding Lagrangian is [253],

$$\mathcal{L} = \mathcal{L}_{\rm SM} + |\partial_\mu \Phi|^2 - m_\Phi^2 |\Phi|^2 - \lambda_\Phi |\Phi|^4 - \lambda_{\Phi H}\left(H^\dagger H - v^2/2\right)|\Phi|^2 - \frac{\mu_3}{2}\left(\Phi^3 + \Phi^{\star 3}\right) \tag{5.5}$$

where $\mu_3, \lambda_\Phi, \lambda_{\Phi H} > 0$. Note here that the above Lagrangian is valid for any charge of Φ or Φ^* as ω, ω^2, where $\omega^3 = 1$.

• Unitarity and Perturbativity

Using the unitarity of the S-matrix, *i.e*. the optical theorem, the maximum value of the inelastic cross-section for an identical particle is [75, 478, 607, 608],

$$\left\langle \sigma_{k\to 2} v_{rel}^{k-1} \right\rangle_{\max} = \sum_{l} (2l+1) \frac{2^{\frac{3k-2}{2}} (\pi x)^{\frac{3k-5}{2}}}{g_{\rm DM}^{k-2} m_{\rm DM}^{3k-4}} \,, \tag{5.6}$$

and for non-identical particles in non-relativistic approximation with s-wave contribution [609],

$$\left\langle \sigma_{k\to 2} v_{\rm rel}^{k-1} \right\rangle \;\leq\; 2^{(3k-1)/2} (T/\pi)^{(5-3k)/2} S_k \frac{g_4 g_5}{g_1..g_k} \left(\frac{m_1 + ... + m_k}{m_1 ... m_k} \right)^{3/2} \,, \tag{5.7}$$

where S_k is the symmetry factor associated with identical particles in the initial state, and g_k counts the degrees of freedom of i^{th} particle. In our case maximum value of $3\text{DM} \to 2\text{DM}$ annihilation are,

$$\left\langle \sigma_{\Phi\Phi\Phi\to\Phi\Phi^*} v_{\rm rel}^2 \right\rangle \;\leq\; \frac{48\sqrt{3}\pi^2}{m_\Phi^3 T^2} 3! \text{ and } \left\langle \sigma_{\Phi\Phi\Phi^*\to\Phi^*\Phi^*} v_{\rm rel}^2 \right\rangle \;\leq\; \frac{48\sqrt{3}\pi^2}{m_\Phi^3 T^2} 2! \,. \tag{5.8}$$

However, these constraints are very mild for MeV scale DMs. The unitarity bound in the infinite scattering energy limit is given by [474, 610–613],

$$|\lambda_{\Phi H}| \leq 8\pi \,, \; |\lambda_\Phi| \leq 4\pi \,. \tag{5.9}$$

The perturbative bound for this model is given by [253, 302],

$$|\lambda_{\Phi H}| \leq 4\pi \,, \; |\lambda_\Phi| \leq \pi \,. \tag{5.10}$$

• Vacuum Stability

The necessary condition to stabilise the potential (Eq. (5.5)) is,

$$\lambda_H > 0 \,, \; \lambda_\Phi > 0 \,, \; \lambda_{\Phi H} + 2\sqrt{\lambda_\Phi \lambda_H} > 0 \,. \tag{5.11}$$

The maximal allowed value of the cubic parameter μ_3 is approximately equal to $\mu_3|_{\max} \approx 2\sqrt{2}\sqrt{\lambda_\Phi/\delta}\, m_\Phi$ where dimensionless parameter δ parameterises the energy difference of vacua [614]. For $\delta = 2$, the $\mathcal{Z}_3$ breaking minimum is approximately degenerate with the SM minimum and gives the absolute stability bound [611, 613].

• Kinetic equilibrium

The dominating FO process for SIMP is $3_{\rm DM} \to 2_{\rm DM}$, which converts some fraction of DM (SIMP) mass into dark matter kinetic energy and gets distributed among themself and the scattering with SM bath particles transfer energy to the thermal bath, otherwise this will heat up the dark sector core and violates the astrophysical constraints derived from the structure formation [615]. The kinetic equilibrium should be maintained between DM and SM bath minimally up to the freeze out of Φ so that $\mathrm{T_{SM}} = \mathrm{T_{DM}}$. The required condition to achieve this is $\langle \Gamma_{\Phi\ \rm SM\to\Phi\ SM} \rangle_{T=T_\Phi^{\rm FO}} \gtrsim \mathcal{H}(T_\Phi^{\rm FO})$ and is one the most important conditions for SIMP. DM can scatter with relativistic SM fermions, which is in thermal equilibrium during FO. As the relativistic fermions (f) are abundant in the radiation-dominated era, the scattering process $\Phi f \to \Phi f$

is fast enough to keep dark and the visible sector in kinetic equilibrium during FO, respecting $\mathrm{T_{DM}} = \mathrm{T_{SM}}$ [262, 263, 278]. We have estimated a bound on the portal coupling ($\lambda_{\Phi H}$) for a sample of DM mass (m_Φ) in Appendix D.8 to maintain kinetic equilibrium. Another way to achieve the kinetic equilibrium between two sectors is to extend the dark sector by introducing a relativistic new particle during FO [616]. However, if the dark sector temperature is much less than the SM bath temperature, these two sectors can never reach kinetic equilibrium [255, 617].

• Dark matter self scattering

As SIMP type DM has sizeable self-interaction, which helps to solve the small-scale problems [278, 618] but is constraint by several observation constraints like,

⋆ Bullet cluster [619–621]: $\frac{\sigma_{\rm self}}{m_{\rm DM}} \lesssim 1\ \mathrm{cm^2 gm^{-1}}$.

⋆ Abell cluster [622]: $1\ \mathrm{cm^2 gm^{-1}} \lesssim \frac{\sigma_{\rm self}}{m_{\rm DM}} \lesssim 3\ \mathrm{cm^2 gm^{-1}}$.

A similar kind of bound is also available from cosmological simulation on self-interacting DM in galaxy cluster [623, 624].

• Dark Matter Mass limits

BBN has a put significant constraint from different cosmological observations [480, 481, 625]. So, it is an obvious choice for DM to freeze out before BBN; *i.e*. $\mathrm{T_{FO}} > \mathrm{T_{BBN}} \sim 0.1\,\mathrm{MeV}$ gives an essential constraint on the masses of thermal DM. For DM masses above $10\,MeV$, BBN constitutes an important probe for the annihilation cross section of DM [482, 626].

• Boltzmann Equation

To get the present number density of SIMP DM, we have to solve the BEQ,

$$\frac{dY_\Phi}{dx} = -\frac{s}{x\,\mathcal{H}(x)}\left[\langle\sigma v\rangle_{\Phi\Phi^*\to \mathrm{SM\ SM}}(Y_\Phi^2 - Y_\Phi^{eq^2}) + s\langle\sigma v^2\rangle_{3\Phi\to 2\Phi}(Y_\Phi^3 - Y_\Phi^2 Y_\Phi^{eq})\right], \quad (5.12)$$

where $x = m_\Phi/T$, $\mathcal{H}(x) = 1.67\sqrt{g_*^\rho}m_\Phi^2/\left(x^2 \mathrm{M_{pl}}\right)$, $\mathrm{s} = \frac{2\pi^2}{45} g_*^{\mathrm{s}} \left(m_\Phi/x\right)^3$ and $g_*^{\mathrm{s}(\rho)}$ is the entropy (matter) degrees of freedom. The total DM yield is twice Y_Φ as its conjugate particle (Φ^*) also has the same yield. Also note the presence of second term inside the parenthesis, absent in the WIMP, which dominates the SIMP like freeze out. A semi-analytical solution of Eq. (5.12) has been shown in Appendix D.5 and a comparison with the numerical solution to match closely.

The parameter space scan of the numerical solution of Eq. (5.12) for a complex scalar SIMP (Φ) described by the Lagrangian in Eq. (5.5) is shown in Fig. 5.5. In Figs. 5.5a and 5.5b, we show the relic under abundant parameter space in $\mathrm{m_\Phi} - \Omega_\Phi \mathrm{h}^2$ planes and the color bar represents variation in cubic parameter μ_3 (left) and quadratic coupling λ_Φ (right) within appropriate limits. The SIMP relic density is inversely proportional to the DM mass and proportional to μ_3 and λ_Φ parameters, which is also reflected in Figs. 5.5a and 5.5b respectively. With the enhancement of SIMP mass, DM self-annihilation cross section decreases, and the relic density is enhanced. To adjust the relic density, we have to increase the couplings within the theoretical limits. We are getting DM mass up to $\mathrm{m_\Phi} \lesssim 200\,\mathrm{MeV}$ in a single-component complex scalar SIMP scenario to acquire correct relic density. The self-scattering cross-section over DM mass, Eq. (D.45) strongly constrains the relic density allowed

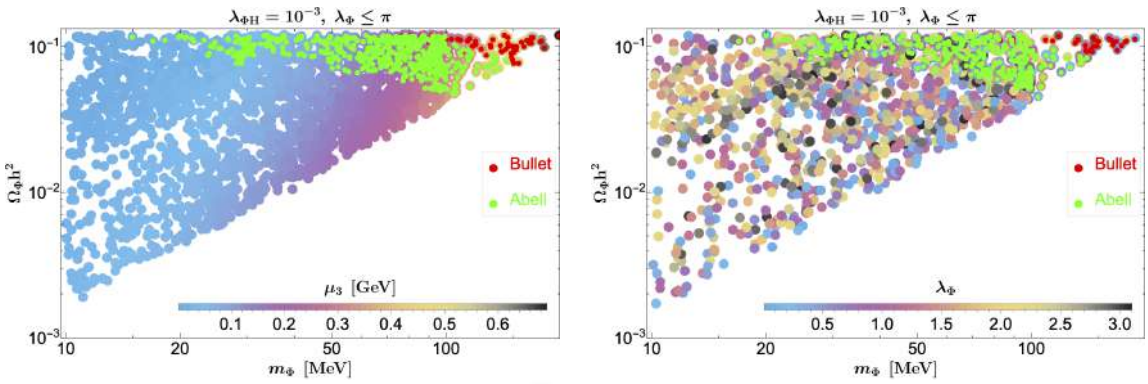

Figure 5.5: Figs. 5.5a and 5.5b represent the relic and unitarity allowed parameter space in $m_\Phi - \Omega_\Phi h^2$ plane for a complex scalar SIMP (Φ) described by the Lagrangian in Eq. (5.5). The variation of the relevant couplings (μ_3, λ_Φ) is shown in the color bar, while the ones fixed is mentioned in the figure heading. Red and green points satisfy the self interaction limits from Bullet and Abell cluster bounds, respectively.

parameter space. After considering all of the available theoretical and cosmological constraints, few points respect the presently available DM self-interaction bound from Bullet and Abell cluster, marked by red and green points respectively as shown in Fig. 5.5. This preliminary analysis helps us addressing the phenomenological distinction with the two component scenario considered later in this chapter. Before concluding this section, let us furnish some of the two component DM frameworks in combination with SIMP in Table 5.3 and remind that we focus on the pFIMP-SIMP combination, which was briefly mentioned in [305].

Scenario	w − s	$\Gamma_{\text{SM SM}\to\text{w w}}$	$\Gamma_{\text{SM SM}\to\text{s s}}$	$\Gamma_{\text{s s}\to\text{w w}}$	Self Annihilation
I	FIMP-SIMP	Feeble	Weak	Feeble	Weak-Strong
II	pFIMP-SIMP [this work]	Feeble	Weak	Weak	Weak-Strong
III	WIMP-SIMP	Weak	Weak	Weak/Feeble	Weak-Strong
IV	SIMP-SIMP [302, 303]	Weak	Weak	Weak/Feeble	Strong-Strong

Table 5.3: Generic two-component DM scenarios in the presence of a SIMP where w and s stand for two different or the same kind of dark sector particles, and $\Gamma_{i\ j\to k\ l}$ indicate the annihilation or production rate of the respective particle.

5.2.2 pFIMP in presence of a SIMP: model independent analysis

Let us briefly recapitulate the essence of pFIMP [305, 306] first. pFIMP is a kind of thermal DM, which has feeble interaction with the visible sector, but remains in equilibrium via interaction with the thermal DM partner. pFIMP therefore, can only be realised in a multicomponent DM scenario, when its partner is in thermal equilibrium. pFIMP freeze out therefore heavily depends on the partner's character, and the partner's detectability decides pFIMP's detection possibility [306].

The existence of pFIMP was demonstrated in presence of WIMP in [305, 306]. Here we show that SIMP being another kind of thermal DM, can accommodate a pFIMP DM in a multicomponent set up (the second possibility in Table 5.3), with

substantial interactions between them. The analysis has been done in two steps: firstly, a model-independent analysis on the pFIMP-SIMP scenario, in Section 5.2.2, showing that the pFIMP dynamics is possible in the presence of a SIMP. Secondly, we do the same exercise for the simplest two-component real (pFIMP) and complex scalar SIMP DM model, in Section 5.2.3. In terms of yield $Y = n/\mathbf{s}$ the two component cBEQ becomes,

$$\frac{dY_{\rm s}}{dx} = -\frac{\mathbf{s}}{x\,\mathcal{H}(x)}\Bigg[\left(Y_{\rm s}^2 - Y_{\rm s}^{\rm eq^2}\right)\langle\sigma v\rangle_{\rm s\ s\to SM\ SM} + \mathbf{s}\left(Y_{\rm s}^3 - Y_{\rm s}^2 Y_{\rm s}^{\rm eq}\right)\langle\sigma v^2\rangle_{3s\to 2s} + \left(Y_{\rm s}^2 - Y_{\rm s}^{\rm eq^2}\frac{Y_{\rm w}^2}{Y_{\rm w}^{\rm eq^2}}\right)\langle\sigma v\rangle_{\rm s\ s\to w\ w}\Bigg]. \tag{5.13}$$

$$\frac{dY_{\rm w}}{dx} = \frac{2\,\mathbf{s}}{x\,\mathcal{H}(x)}\Bigg[\frac{1}{\mathbf{s}}\left(Y_{\rm SM}^{\rm eq} - Y_{\rm SM}^{\rm eq}\frac{Y_{\rm w}^2}{Y_{\rm w}^{\rm eq^2}}\right)\langle\Gamma\rangle_{\rm SM\to w\ w} + \left(Y_{\rm SM}^{\rm eq^2} - Y_{\rm SM}^{\rm eq^2}\frac{Y_{\rm w}^2}{Y_{\rm w}^{\rm eq^2}}\right)\langle\sigma v\rangle_{\rm SM\ SM\to w\ w} + \left(Y_{\rm s}^2 - Y_{\rm s}^{\rm eq^2}\frac{Y_{\rm w}^2}{Y_{\rm w}^{\rm eq^2}}\right)\langle\sigma v\rangle_{\rm s\ s\to w\ w}\Bigg], \tag{5.14}$$

In the above, $Y_{\rm w}$ refers to pFIMP yield, and $Y_{\rm s}$ defines SIMP yield. $\mathcal{H}(x) = 1.67\sqrt{g_*^\rho}\mu_{\rm sw}^2/\left(x^2 {\rm M_{pl}}\right)$, $\mathbf{s} = \frac{2\pi^2}{45} g_*^{\mathbf{s}}\left(\mu_{\rm sw}/x\right)^3$, $Y_i^{\rm eq} = \frac{45}{4\pi^4}\frac{g_i}{g_*^{\mathbf{s}}}\left(\frac{m_i}{\mu_{\rm sw}}x\right)^2 K_2\left(\frac{m_i}{\mu_{\rm sw}}x\right)$.

The solution of cBEQ, Eqs. (5.14) and (5.13), is shown in Figs. 5.6a, 5.6c for ${\rm m_w} > {\rm m_s}$ and in Figs. 5.6b, 5.6d for ${\rm m_w} < {\rm m_s}$. In the top panel of Fig. 5.6, we have varied the conversion cross-section, shown by different color thick (SIMP) and dotted/dashed (pFIMP) lines, while others m_s, ${\rm m_w}$, $\langle\sigma v\rangle_{\rm s\ s\to SM\ SM}$, $\langle\sigma v\rangle_{\rm w\ w\to SM\ SM}$ and $\langle\sigma v^2\rangle_{\rm 3\ s\to 2\ s}$ values are kept fixed as mentioned in the figure inset. In this model-independent analysis, we have used the numerical values for thermal average cross-sections instead of a temperature-dependent functional form. The DM self-interaction constraints from different cosmological observations are yet to be considered, we do the same for model-dependent discussion.

The simplest way to explain Fig. 5.6 by dividing the whole scenario into four regions, Ⓘ $\gamma_{\rm sw} < \gamma_{\rm ww}$; Ⓘ$\!$Ⓘ $\gamma_{\rm ww} \lesssim \gamma_{\rm sw} \ll \gamma_{3s\to 2s}$; Ⓘ$\!$Ⓘ$\!$Ⓘ $\gamma_{\rm ww} \ll \gamma_{\rm sw} < \gamma_{3s\to 2s}$; Ⓘ$\!$Ⓥ $\gamma_{3s\to 2s} \lesssim \gamma_{\rm sw}$. We define, $\gamma_{\rm ww} = \langle\sigma v\rangle_{\rm sm\ sm\to w\ w} n_{\rm sm}^2 \equiv \langle\Gamma\rangle_{\rm sm\to w\ w} n_{\rm sm}$, $\gamma_{\rm sw} = \langle\sigma v\rangle_{\rm s\ s\to w\ w} n_{\rm s}^2$ and $\gamma_{3s\to 2s} = \langle\sigma v^2\rangle_{3s\to 2s} n_{\rm s}^3 = \langle\sigma v^2\rangle_{2s\to 3s} n_{\rm s}^2$.

Region Ⓘ shown by the light blue shaded region in Figs. 5.6c and 5.6d, FIMP number density $n_{\rm w}$ is independent of the $\sigma^T_{s\ s\to {\rm w\ w}}$ due to the negligible DM-DM conversion cross-section compared to DM production rate from SM particles. This is also visible in Figs. 5.6a (${\rm m_s} > {\rm m_w}$) and 5.6b (${\rm m_s} < {\rm m_w}$) from blue dot-dashed lines. This scenario corresponds to a pure FIMP for $Y_{\rm w}$ and pure SIMP for $Y_{\rm s}$.

Region Ⓘ$\!$Ⓘ refers to light red regions in Figs. 5.6c, 5.6d and is also represented by red dot-dashed lines in Figs. 5.6a, 5.6b. In this regime, $\gamma_{\rm ww} \lesssim \gamma_{\rm sw} \ll \gamma_{3s\to 2s}$, SIMP number density remains unaffected due to small conversion rate compared to $\sigma^{\rm T}_{\rm 3s\to 2s}$ but FIMP number density $({\rm n_w})$ is enhanced with larger conversion from SIMP, as reflected in all the four figs. This limit still represents a combination of SIMP and FIMP DMs, where FIMP production is affected by conversion from SIMP, but is mostly overabundant.

Suppose we further enhance the DM-DM conversion rate. In that case, FIMP $({\rm w})$ reaches thermal equilibrium and follows equilibrium before freeze out. At the

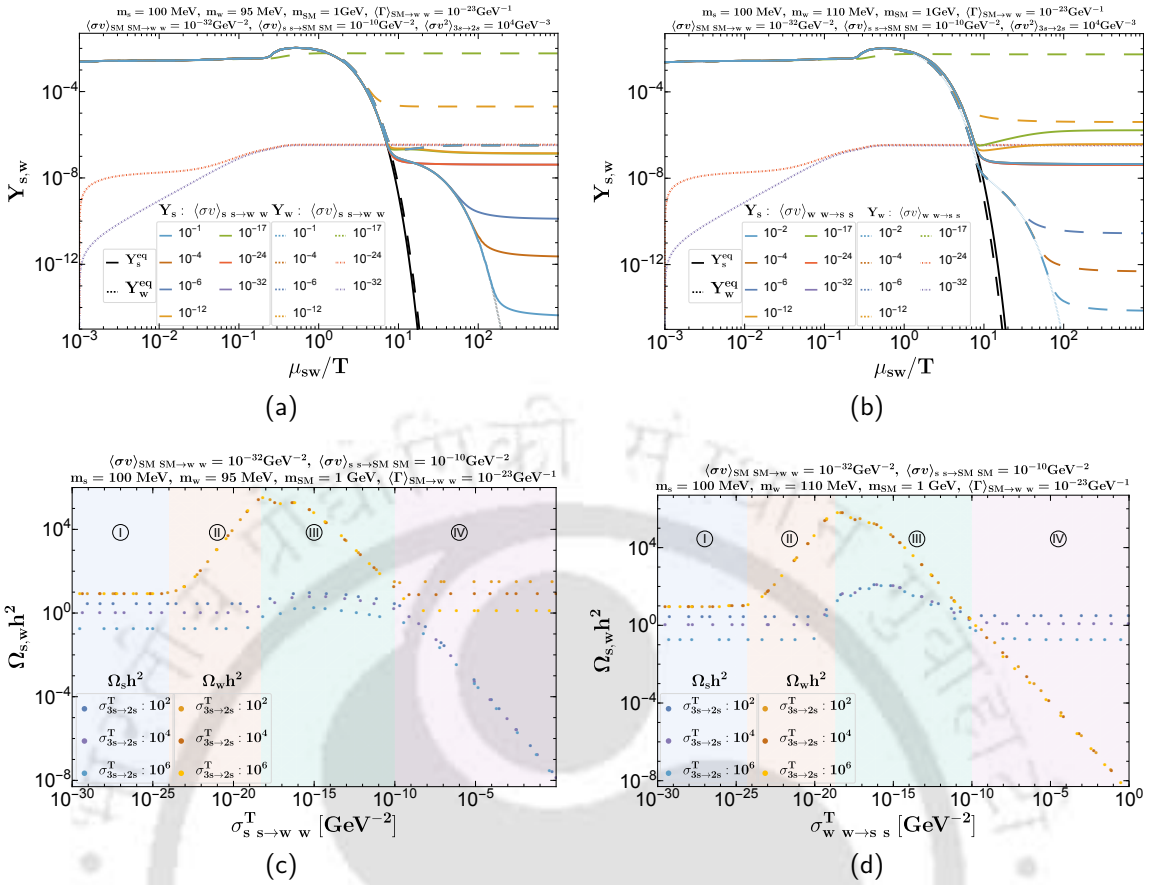

Figure 5.6: Solution to cBEQs, Eqs. (5.13) and (5.14) for pFIMP-SIMP scenario; Figs. 5.6a, 5.6c represent $m_s > m_w$ case, while Figs. 5.6b, 5.6d represent $m_s < m_w$ case. Figs. 5.6a, 5.6b represent the variation of DM yield with dimensionless parameter μ_{sw}/T for different values of conversion cross-section illustrated by different colored lines, solid for SIMP, dashed for pFIMP. Figs. 5.6c, 5.6d represent DM relics as a function of DM-DM conversion cross-sections. Different colored dotted lines correspond to different SIMP annihilation cross-sections as mentioned in the plot legends.

same time, SIMP number density is slightly enhanced due to opening up a new annihilation or production channel, see region Ⓘ in Figs. 5.6c, 5.6d and green, yellow dashed lines in Figs. 5.6a, 5.6b. After equilibration, we call the FIMP (w) as pFIMP as it has a feeble visible connection but is weakly connected with partner SIMP type DM and makes it a two-component SIMP-pFIMP scenario. With further enhancement of conversion rate (γ_{sw}), both SIMP and pFIMP number density decreases, but before freeze out, they follow a modified equilibrium distribution depending on the choice of mass hierarchy, as shown by the dotted yellow and green lines in Fig. 5.6a. In this regime, for $(m_s < m_w)$ (in Fig. 5.6b) SIMP number density is suddenly enhanced after decoupling from the thermal bath due to the production from pFIMP, which is also seen in Fig. 5.6c. The expression of modified equilibrium number densities that the particles acquire in Figs. 5.6a and 5.6b for two hierarchies are given by Eqs. (5.15) and (5.16) respectively,

$$n_w^{eq'} = n_w^{eq}\frac{n_s}{n_s^{eq}} \quad \text{for } m_w > m_s\,, \tag{5.15}$$

$$n_s^{\mathrm{eq}'} = n_s^{\mathrm{eq}} \left[\frac{\langle\sigma v\rangle_{s\ s\to \mathrm{SM\ SM}} + \left(\frac{n_s^2}{n_s^{\mathrm{eq}}}\right)\langle\sigma v^2\rangle_{3s\to 2s} + \left(\frac{n_{\mathrm{w}}}{n_{\mathrm{w}}^{\mathrm{eq}}}\right)^2 \langle\sigma v\rangle_{s\ s\to \mathrm{w\ w}}}{\langle\sigma v\rangle_{s\ s\to \mathrm{SM\ SM}} + n_s\langle\sigma v^2\rangle_{3s\to 2s} + \langle\sigma v\rangle_{s\ s\to \mathrm{w\ w}}} \right]^{1/2} \quad \text{for } \mathrm{m}_s > \mathrm{m}_{\mathrm{w}}\,. \tag{5.16}$$

Even larger enhancement of DM conversion compared to the self-annihilation of SIMP, $\gamma_{3s\to 2s} \lesssim \gamma_{\mathrm{sw}}$, gives a completely different scenario, as shown in Ⓘⓥ of Figs. 5.6c, 5.6d and by deep blue, brown, light blue lines in Figs. 5.6a, 5.6b. The conversion rate depends on the conversion cross-section as well as the number density during or before the heavier component freeze out. When the conversion is larger than SIMP self-annihilation, the heavier component continues to deplete into the lighter ones even after decoupling from the thermal bath. Since the lighter component has frozen out before, the heavier component goes into the modified equilibrium; see the light blue dashed line in Figs. 5.6a, 5.6b. With the enhancement of the conversion cross-section, the number density for lighter one doesn't change much due to the gradual decrease of heavy particle number density with the enhancement of conversion cross-section, and both simultaneously fix the light particle number density in region Ⓘⓥ of Figs. 5.6c and 5.6d. However, here the SIMP is not purely a SIMP as its freeze out is mostly governed by conversion.

5.2.3 A model example of pFIMP-SIMP

Let us now discuss a model example of pFIMP-SIMP set-up. Here we introduce a real scalar ϕ and a complex scalar singlet field Φ as DM components, which are stable under $\mathcal{Z}_2 \otimes \mathcal{Z}_3$ symmetry and charge assignments are shown in Table 5.4. The

Dark Fields	$\mathcal{Z}_2$	$\mathcal{Z}_3$
Φ	Φ	$\omega\Phi$ or $\omega^2\Phi$
ϕ	-ϕ	ϕ

Table 5.4: Dark sector fields (Φ and ϕ) and their quantum numbers where $\omega = e^{i2\pi/3}$.

dark sector Lagrangian obeying the symmetry can be written as,

$$\begin{aligned}\mathcal{L} =& \mathcal{L}_{\mathrm{SM}} + \mu_H^2 H^\dagger H - \lambda_H (H^\dagger H)^2 + \frac{1}{2}|\partial_\mu \phi|^2 - \frac{1}{2}\mu_\phi^2\phi^2 - \frac{1}{4!}\lambda_\phi \phi^4 + |\partial_\mu \Phi|^2 - \mu_\Phi^2 |\Phi|^2 \\ & - \lambda_\Phi |\Phi^* \Phi|^2 - \frac{1}{2}\mu_3(\Phi^3 + \Phi^{*^3}) - \frac{1}{2}\lambda_{\phi H}\phi^2 H^\dagger H - \lambda_{\Phi H}|\Phi|^2 H^\dagger H - \frac{1}{2}\lambda_{\Phi\phi}|\Phi|^2\phi^2\,.\end{aligned} \tag{5.17}$$

After spontaneous symmetry breaking, $H = \begin{pmatrix} 0 \\ \frac{v+h}{\sqrt{2}} \end{pmatrix}^T$. From the interactions as in Eq. (6.31), Φ having $3 \to 2$ depletion, can be a SIMP, while ϕ can be pFIMP. Understandably, this is the simplest model example of pFIMP-SIMP set up. We are interested in a small mass ($\sim$ MeV) scale of pFIMP, as the SIMP is validated in that mass range only, as discussed before. We choose small values of Higgs portal coupling $\lambda_{\phi H}$. This helps the pFIMP to remain out of thermal bath, at the same time, helps evading Higgs to invisible branching ratio. We will also choose the other Higgs

portal coupling $\lambda_{\Phi H}$ to be small as well to adhere to the SIMP limit of Φ. This also takes care of the invisible Higgs branching ratio to Φ pair.

Solution of coupled Boltzmann Equation and relic density

Assuming CP conservation existing inside the dark sector, the coupled Boltzmann Equation for two DMs, where $Y_s = Y_\Phi + Y_{\Phi^*}$ with $Y_\Phi = Y_{\Phi^*}$ is given by,

$$\frac{dY_\phi}{dx} = \frac{2\,\mathbf{s}}{x\,\mathcal{H}(x)}\left[\frac{1}{\mathbf{s}}\left(Y_{\rm h}^{\rm eq} - Y_{\rm h}^{\rm eq}\frac{Y_\phi^2}{Y_\phi^{\rm eq^2}}\right)\langle\Gamma\rangle_{{\rm h}\to\phi\ \phi} + \left(Y_{\rm SM}^{\rm eq^2} - Y_{\rm SM}^{\rm eq^2}\frac{Y_\phi^2}{Y_\phi^{\rm eq^2}}\right)\langle\sigma v\rangle_{{\rm SM\ SM}\to\phi\ \phi}\right.$$
$$\left. + \frac{1}{4}\left(Y_{\rm s}^2 - Y_{\rm s}^{\rm eq^2}\frac{Y_\phi^2}{Y_\phi^{\rm eq^2}}\right)\langle\sigma v\rangle_{\Phi\ \Phi^*\to\phi\ \phi}\right], \tag{5.18}$$

$$\frac{dY_s}{dx} = -\frac{\mathbf{s}}{x\,\mathcal{H}(x)}\left[\frac{1}{2}(Y_s^2 - Y_s^{\rm eq^2})\langle\sigma v\rangle_{\Phi\ \Phi^*\to{\rm SM\ SM}} + \frac{\mathbf{s}}{4}(Y_s^3 - Y_s^2 Y_s^{\rm eq})\langle\sigma v^2\rangle_{3\Phi\to2\Phi}\right.$$
$$\left. + \frac{1}{2}\left(Y_s^2 - Y_s^{\rm eq^2}\frac{Y_\phi^2}{Y_\phi^{\rm eq^2}}\right)\langle\sigma v\rangle_{\Phi\ \Phi^*\to\phi\ \phi}\right]. \tag{5.19}$$

In the above, ${\rm SM} = \{{\rm h},\ {\rm W}^\pm,\ {\rm Z},\ {\rm leptons},\ {\rm quarks}\}$, $\mathbf{s}$ represents entropy density, $Y_i^{\rm eq} = n_i^{\rm eq}/{\rm s}$ is the equilibrium yield of i^{th} particle has mentioned in the previous section, and,

$$\langle\sigma v^2\rangle_{3\Phi\to2\Phi} = 2\left(\langle\sigma v^2\rangle_{\Phi\Phi\Phi\to\Phi\Phi^*} + \langle\sigma v^2\rangle_{\Phi\Phi^*\Phi^*\to\Phi\Phi}\right).$$

The total relic density is written in terms of DM yields obtained from the solution of cBEQ D.1, after freeze out,

$$\Omega_{\rm DM}{\rm h}^2 = 2.74385\times10^8\left[m_\Phi Y_s + m_\phi Y_\phi\right]_{x\to\infty}. \tag{5.20}$$

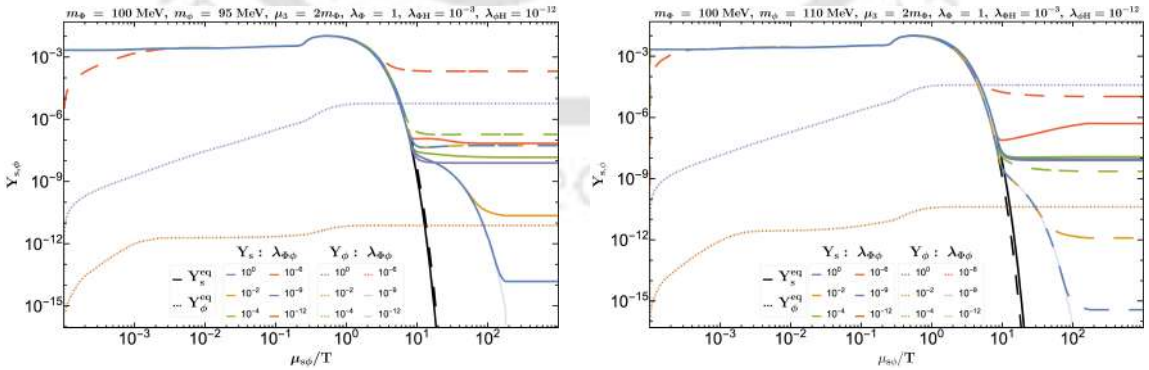

(a) (b)

Figure 5.7: Solution to the cBEQ D.1, where Figs. 5.7a and 5.7b represents $m_\Phi > m_\phi$ and $m_\Phi < m_\phi$ scenarios respectively. The thick, dashed and dotted color lines represent the SIMP, FIMP and pFIMP cases respectively. Different colors show $\lambda_{\Phi\phi}$ variation as mentioned in the figure inset. The thick black and dashed lines represent the SIMP and pFIMP equilibrium yields. Other parameter kept fixed are mentioned in the figure heading.

The solution of cBEQ D.1 provides the yield of SIMP (Y_Φ) and pFIMP (Y_ϕ) as shown in Fig. 5.7 with the variation of $\mu_{s\phi}/T$ for different mass hierarchies; Fig. 5.7a

shows the case for $m_\Phi > m_\phi$ and Fig . 5.7b represents the case for $m_\Phi < m_\phi$. The explanation of this figure is similar to that of Fig . 5.6 (top row). The only change here is that we vary the free-parameter $\lambda_{\Phi\phi}$ in solving cBEQ instead of choosing a numerical value for the conversion cross-section $\sigma^{\rm T}_{\rm ss\to ww}$ as done before. For small values of $\lambda_{\Phi\phi}$ $(10^{-12},\ 10^{-9})$, ϕ shows pure FIMP like behaviour before freezing-in, as shown by the violet and orange dot-dashed lines in figs for both the mass hierarchies. Enhancement of $\lambda_{\Phi\phi}$ $(\sim 10^{-6})$ makes ϕ reach thermal bath and follow the equilibrium distribution before freezing out; ϕ becomes pFIMP here and is represented by dashed red lines in both the figs. At this moment, the number density of SIMP Φ is enhanced due to new production channel opening up via conversion. With further enhancement of $\lambda_{\Phi\phi}$ $(\gtrsim 10^{-6}-10^{-4})$, we observe a decrease in both SIMP and pFIMP number densities, shown by green thick and dashed lines in Fig . 5.7 for both the mass hierarchies. This serve as the ideal pFIMP-SIMP parameter space, where we achieve under abundance for both the DM components. If $\lambda_{\Phi\phi}$ is enhanced further to $\sim \{10^{-2}, 10^{0}\}$ then the annihilation of the heavier DM component to the lighter one is possible even after the freeze out of the lighter component, then the heavier component follows modified equilibrium distribution following Eqs . (5.16), and (5.15) before freezing out. The yellow $(\lambda_{\Phi\phi} \sim 10^{-2})$ and light blue $(\lambda_{\Phi\phi} \sim 10^{0})$ thick (SIMP) and dashed (pFIMP) lines represent DM yields following such modified distributions.

Constraints on the model parameter space

We will provide a short account of the results obtained from the parameter space scan here. In the two-component SIMP-pFIMP scenario, total relic density $(\Omega^{\rm obs}_{\rm DM})$ is gathered from both SIMP and pFIMP, obtained from the solution of cBEQ in Eq . (D.1). In our model, as described by Eq . (6.31), free parameters relevant for the cosmological evolution are $m_\Phi,\ m_\phi,\ \lambda_\Phi,\ \mu_3$ and $\lambda_{\Phi\phi}$. Other parameters like $\lambda_{\Phi H} \sim 10^{-3}$ and $\lambda_{\phi H} \sim 10^{-12}$ are kept fixed to maintain the criteria of keeping Φ as SIMP and ϕ as pFIMP. Also, $\lambda_{\Phi H}$ and $\lambda_{\phi H}$ do not play a direct role in the relic density of the DM components. In Fig . 5.8, we have shown a few variations in the parameters space scan.

DM self-interaction plays a crucial role here. In the SIMP-pFIMP scenario, DM self-interaction cross-section over DM mass $(\sigma_{\rm self}/m_{\rm DM})$ depends not only on their self-scattering cross-sections but also on their individual relic densities, which are restricted by Bullet cluster and Abell cluster observations, see Eq . (D.46). The parameters $\lambda_{\Phi H}$ and λ_ϕ plays a significant role in DM self-interaction processes. If the pFIMP relic is dominant over SIMP, then $\sigma_{\rm self}$ mostly depends on the $\sigma_{\phi\phi\to\phi\phi}$, *i.e* . λ_ϕ, but, in the case of dominant SIMP, the self-scattering cross-section depends primarily on *i.e.* λ_Φ and $\lambda_{\Phi H}$ couplings.

In Figs . 5.8a and 5.8b, we have plotted the relic density allowed parameter space in $m_\Phi - \lambda_\Phi$ plane for both the mass hierarchies. SIMP is heavier in the left plot, while pFIMP is heavier on the right. The main parameter that is varied here is the coupling relevant for conversion cross-section, i.e. $\lambda_{\Phi\phi}$, as shown in the colour bar. Other parameters kept fixed are mentioned in figure heading, they are responsible for keeping the SIMP and pFIMP limit intact and respect unitarity, vacuum stability limits. All the scattered points respect relic density constraint. Those in red respect self interaction limit from Bullet cluster, while those in green respect the limit from

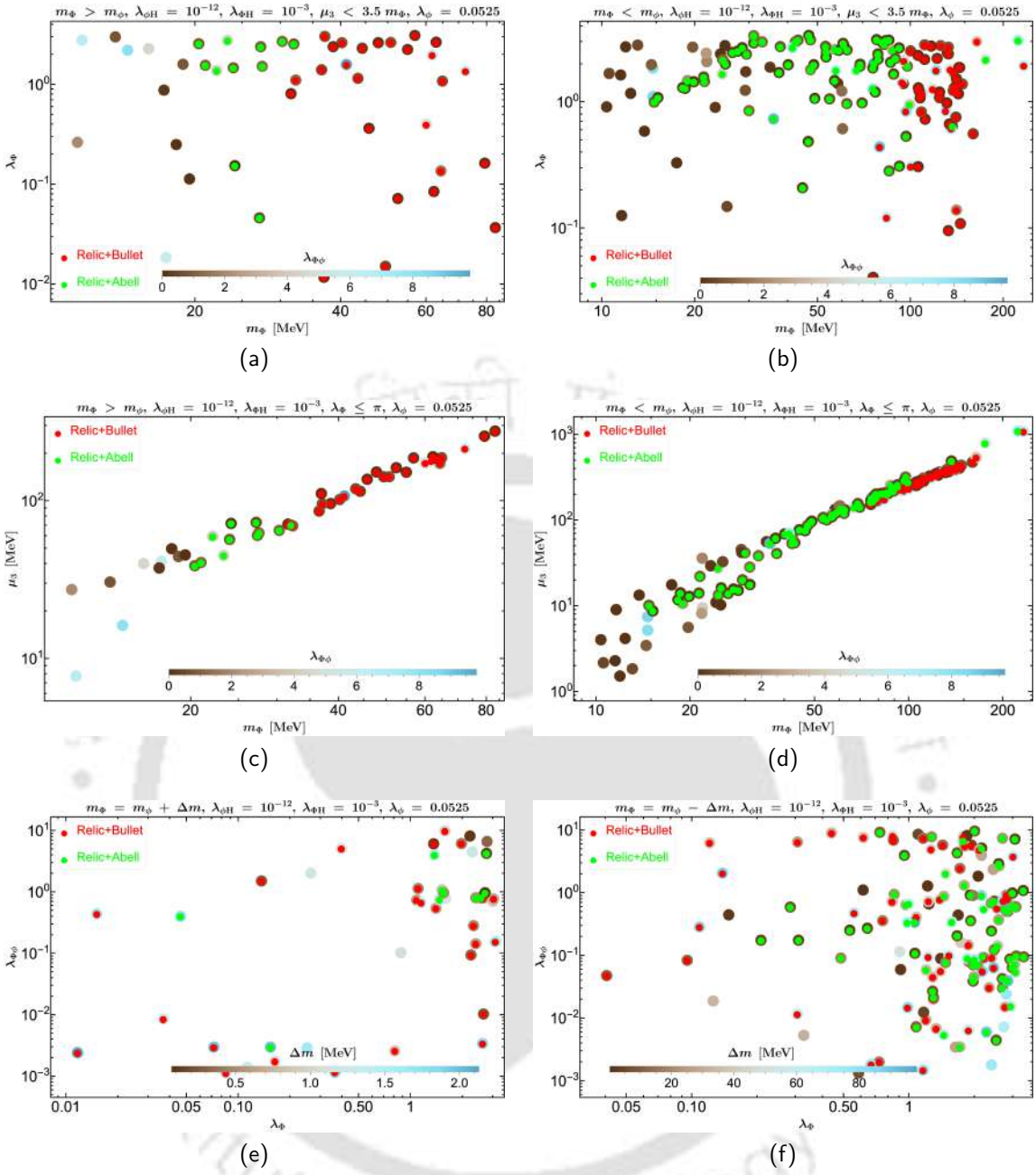

Figure 5.8: Figs . 5.8a, 5.8b and 5.8c, 5.8d are represent the DM relic allowed parameter space in $m_\Phi - \lambda_\Phi$ and $m_\Phi - \mu_3$ plane, respectively. The variation of portal coupling $\lambda_{\Phi\phi}$ is shown by the BrownCyanTones color bar. The red and green points represent the points within the Bullet and Abell cluster self-interaction limit. Figs . 5.8e, 5.8f represents the relic allowed points in $\lambda_\Phi - \lambda_{\Phi\phi}$ plane and BrownCyanTones color bar shows the DM mass separation.

Abell cluster. When SIMP is heavier (Fig . 5.8a), pFIMP freezes out before and SIMP relic is smaller and has a subdominant contribution to the total relic density due to modified freeze out. In such circumstances, self interaction limit is less constrained for SIMP and allows $\lambda_\Phi \sim \times 10^{-2}$. For a lighter SIMP, the constraint is stricter $\lambda_\Phi \sim \times 10^{-1}$. $\lambda_\phi \sim 5.25 \times 10^{-2}$ helps the pFIMP to obey self-interaction bound.

In Figs . 5.8c and 5.8d, we have plotted the relic allowed parameter space in $m_\Phi - \mu_3$ planes. Red points respect self interaction limit from Bullet cluster, while those in green respect the limit from Abell cluster. Almost all the points in the full mass range obeys this limit. We further see a correlation between m_Φ and μ_3, roughly

following $\mu_3 \geq 2m_\Phi$. As before, $\lambda_{\Phi\phi}$ is varied as shown in the colour bar. For larger $\lambda_{\Phi\phi}$, when pFIMP is heavier (right hand plot), it shows modified freeze out, and its relic becomes sub-dominant in total DM relic. Under this circumstance, only SIMP self-interaction contributes dominantly to DM self-interaction bound (Note, we kept $\lambda_{\Phi H}$ is constant). $\lambda_{\Phi H} \sim 10^{-3}$ is preferred for the allowed parameter space to obey both Bullet and Abell cluster bound while λ_ϕ is free. Lower mass limit $m_\Phi \lesssim 15\,MeV$ is disfavoured from the self interaction limit.

In Figs . 5.8e and 5.8f, we have shown the relic density allowed points with DM mass variation in the color bar in $\lambda_\Phi - \lambda_{\Phi\phi}$ plane. As such there is no specific correlation between these parameters to be observed to yield correct relic abundance and self interaction limits. We see that the maximum available DM mass separation is up to $5\ MeV$ for $m_\Phi > m_\phi$, but more relaxed (up to $50\ MeV$) for the opposite mass hierarchy. This is an important result of this pFIMP-SIMP scenario, to agree with the model-independent analysis of pFIMP in the presence of any thermal DM [305, 306].

Before concluding this section, let us briefly summarise the outcome of this analysis. The two-component DM scenario in the presence of SIMP has not been studied much excepting [302, 303]. Here, we have studied pFIMP dynamics in the presence of SIMP that helps a feebly coupled DM to equilibrate to thermal bath and freeze out via substantial interaction with SIMP. The major outcomes of this SIMP-pFIMP analysis are that relic density allowed parameter space of this model surpasses the single component SIMP allowed range, in particular, the SIMP mass is allowed up to $\sim 50\,MeV$ when $m_\phi > m_\Phi$. Second, DM self-interaction provides the most dominant constraint, in particular, λ_ϕ and $\lambda_{\Phi H}$ couplings, which are free parameters in context of DM relic density gets constrained by DM self-interaction bound.

Detection possibility

The required condition to keep the SIMP in kinematic equilibrium is $\Gamma_{\Phi\Phi^*\to f\bar{f}} \lesssim \Gamma_{3\Phi\to 2\Phi} \lesssim \Gamma_{\Phi f\to\Phi f}$, which has motivated us to choose $\lambda_{\Phi H}$ as free parameter (in single component) as long as it doesn't become too high such that the $\mathrm{DM\ DM} \to \mathrm{SM\ SM}$ annihilation dominates over the self-annihilation. As this parameter is suppressed, it doesn't have a significant role in SIMP freeze out and relic density, but this might be constrained by presently available SIMP-electron scattering bound like XENON1T [364], CRESST-III [367], DAMIC-M [627], DarkSide-50 [628], ALETHEIA [629] and DarkSide-20k [630], LDMX [631] (proposed) etc.

Unfortunately, in the case of our two-component real and complex scalar pFIMP-SIMP model, it is difficult to detect both the components via direct or indirect detection due to small values of $\lambda_{\Phi H}$ with detector's low sensitivity as far as the current and immediate future projection goes. The DM-electron cross-section mostly depend upon the mediator mass m_h and Higgs-DM portal coupling $\lambda_{\Phi H}$ for SIMP. Apart from small $\lambda_{\Phi H}$, the presence of a heavy ($\sim$ GeV) mediator decreases the DM-electron scattering cross-section. As we already know [305, 306], the pFIMP detection is possible only via thermal DM loop-mediated interaction with the visible sector, so the difficulty in SIMP detection transmits to the difficulty in pFIMP searches as well, although low mass pFIMP takes part in electron scattering. The pFIMP-electron scattering cross-section depends upon the parameters $\lambda_{\Phi\phi}$, $\lambda_{\Phi H}$ and the mediator mass ($\mathrm{m_h} \sim 125\ \mathrm{GeV}$). In the case of MeV DM (SIMP or pFIMP), the

DM-electron scattering cross-section significantly suffers from the presence of heavy mediator.

Therefore detection possibility of such a framework emerges under the possibility of a low mediator mass ($\sim MeV$). For that the model needs to be augmented further. Besides the particle content of two scalar fields contributing to pFIMP-WIMP model, we consider a vector-like lepton (VLL) ψ with weak hypercharge $\mathtt{Y} = -1$ [632, 633], charged under $\mathcal{Z}_3$ having transformation like $\psi \to \omega\psi$. For simplicity, one may assume that this VLL fermion only couples to the first right-handed lepton generation to avoid the strong bounds from the lepton flavour-violating process. The newly extended Lagrangian can be written as,

$$\mathcal{L}_\psi = \overline{\psi}\left[i\gamma^\mu\left(\partial_\mu + ig'\mathtt{Y}B_\mu\right) - m_\psi\right]\psi - \left(\mathrm{y}\overline{\psi}e_R\Phi + \mathrm{h.c.}\right), \tag{5.21}$$

where $g' = (2/v)\sqrt{m_Z^2 - m_W^2}$ is the $\mathrm{U}(1)_\mathtt{Y}$ gauge coupling. ψ is a vector-like lepton (VLL) with weak hypercharge $\mathtt{Y} = -1$ [632, 633] and charged under $\mathcal{Z}_3$ where transformation is like $\psi \to \omega\psi$. The perturbative limit on real Yukawa coupling is $\mathrm{y} < \sqrt{4\pi}$ and $m_\psi > m_\Phi + m_e$ to ensure the Φ stability. The most important mass bound on this charged particle mass comes from LEP [634–638] to be $\gtrsim 103.5$ GeV. In that way, this also becomes a heavy mediator. The detection possibility and phenomenology of such a framework are discussed in [639], with a focus on dark matter masses in the GeV range.

5.2.4 Summary

To address pFIMP dynamics in the presence of SIMP, we first adopt a model-independent analysis by solving coupled BEQs, one of which addresses SIMP freeze out, the other pFIMP freeze out. For this part, the responsible thermal average cross-sections are taken as numerical numbers. The solution of cBEQ, as shown in Fig . 5.6, confirms the pFIMP dynamics in the presence of SIMP, when conversion cross-section is varied from feeble to weak strength. We show that a pure FIMP having freeze in can be brought to thermal bath and freeze out when the conversion to accompanying SIMP is sizeable. In pFIMP limit, the depletion within the dark sector $3\mathrm{SIMP} \to 2\mathrm{SIMP}$ might be comparable to the conversion process $2\mathrm{SIMP} \to 2\mathrm{pFIMP}$ without affecting the SIMP condition.

In this analysis, we assumed that SM and dark bath are in kinetic equilibrium via elastic scattering of DM with bath particles. This elastic scattering rate measures the momentum exchange rate to/from SM bath from/to the dark sector. If this rate is larger than the Hubble expansion rate, the dark sector and thermal bath are always in kinetic equilibrium, and both sectors follow the same temperature (bath temperature). This has been validated in the appendix for a typical benchmark. Otherwise, the dark sector temperature would be different from the SM bath. It will be an interesting exercise to take up such an analysis in the context of the SIMP-pFIMP setup.

We next discuss the simplest pFIMP-SIMP model with extension of SM with two scalar singlets (one real, one complex) stabilised by $\mathcal{Z}_2 \otimes \mathcal{Z}_3$ symmetry. We chose the model parameter in such a way that the real scalar behaves as pFIMP (ϕ), while the complex scalar (Φ) acts like SIMP. Out of the DM masses, self couplings, portal couplings, and conversion couplings, the conversion coupling $\lambda_{\Phi\phi}$ helps the pFIMP reach thermal equilibrium. The parameter space is crucially constrained by the self

interaction bounds. Interestingly, couplings like λ_ϕ, and $\lambda_{\Phi H}$, which play insignificant role in DM freeze out, gets constrained by DM self-interaction. As usual, DM mass splittings get constrained to yield pFIMP solution, but different depending on mass hierarchy. For example, $\Delta m \lesssim 2\ MeV$ for heavier SIMP, and $\Delta m \lesssim 100\ MeV$ when pFIMP is heavier. Also, relic density allowed parameter space of this model surpasses the single component SIMP allowed range, in particular, the SIMP mass is allowed up to $\sim 50\ MeV$ when $m_\phi > m_\Phi$.

Detectability of pFIMP-SIMP model is difficult as the portal coupling of both pFIMP and SIMP with SM Higgs is suppressed to address their freeze outs. Secondly, their interaction with SM is mediated by SM Higgs, which is way heavier than the DM mass ($\sim MeV$), making the cross-section further subdued. We thus propose a minimal extension of the dark sector by the inclusion of a charged vector-like lepton. This is primarily assumed to interact with electrons only, to avoid conflicts with lepton flavor violation constraints. This provides a different mediator to interact with direct or indirect searches. The presence of such new Yukawa interaction terms opens up direct (via electron scattering) and indirect (annihilation into electron and photon pair) search prospects of the pFIMP-SIMP scenario.

Finally, in this chapter, we establish pFIMP-like solutions to occur both in the presence of WIMP and SIMP. The detectability of pFIMP depends on its partner, and we elaborate on it in the next chapter.

Chapter 6

Pseudo-FIMP detection in direct, indirect, and collider search experiments

Contents

The dynamics of a pseudo-FIMP (pFIMP) has been established in the presence of WIMP and SIMP-type thermal DM previously. pFIMP talks to the visible sector via thermal DM loop. Therefore, the detectability of pFIMP depends on the detectability of the partner DM. It is understood that SIMP having limited detection possibility, the pFIMP that arises alongwith also has limited detectability. In this chapter, we discuss ways to detect a pFIMP in the presence of WIMP in a couple of UV complete models, including direct, indirect, and collider searches.

6.1 Real scalar pFIMP and Fermionic WIMP

In this section, we first provide all one-loop graphs stemming from pFIMP-WIMP interactions involving scalar, fermion and vector boson particles, assuming both of them are stabilised via $\mathcal{Z}_2 \otimes \mathcal{Z}_2'$ symmetries. We elaborate upon a model where a fermionic WIMP has a significant Yukawa interaction with a scalar pFIMP with negligible Higgs portal coupling. We study in detail the loop-induced direct and indirect search prospects of the pFIMP in the relic density allowed region of the

model, along with collider expectations at the LHC. The discussion in this section is based on Ref . [306].

6.1.1 Introduction

Here, we study a two-component DM model with one scalar and one fermion. The scalar sector consists of a singlet and is assumed to be the pFIMP component. The fermion sector consists of a vector like doublet and a singlet, where the lightest state after mixing via electroweak symmetry breaking (EWSB) serves as the WIMP component having gauge interaction with the visible sector[1]. The possibility of bringing the fermion pFIMP under the direct search scanner via WIMP loop has been studied here in detail with some discussions on the indirect search prospects.

Our organisation of topics are as follows. In Section 6.1.2, we present a general discussion on the WIMP-pFIMP scenario and possible interactions between the WIMP and pFIMP that can give rise to the pFIMP detection prospect. In Section 6.1.3, we discuss a model example in WIMP-pFIMP limit. The DM phenomenology including relic density, direct (indirect) and collider detection prospects are discussed in Section 6.1.4. In Section 6.1.5, we summarize and conclude. Several appendices provide the details of the relevant calculations.

6.1.2 WIMP-pFIMP ensemble

A DM having feeble interaction with the SM can still thermalise via sizeable interaction with a WIMP and is called a pFIMP as demonstrated in [305]. We first provide a short account of this set-up and the resulting behavior of pFIMP.

Generic pFIMP characteristics

Most of the pFIMP characteristics can be described in a model-independent way where the freeze-out pattern of both the WIMP and pFIMP are governed via a generic coupled Boltzmann Equations (cBEQ),

$$\begin{aligned}
\frac{d\mathrm{y}_1}{dx} =& -\frac{2\pi^2 \mathrm{M_{pl}}}{45\times 1.66}\frac{g^s_\star}{\sqrt{g^\rho_\star}}\frac{\mu_{12}}{x^2}\left[\langle\sigma v\rangle_{11\to \mathrm{SM}}\left(\mathrm{y}_1^2 - Y_1^{\mathrm{eq}^2}\right) + \langle\sigma v\rangle_{11\to 22}\left(\mathrm{y}_1^2 - \frac{Y_1^{\mathrm{eq}^2}}{Y_2^{\mathrm{eq}^2}}\mathrm{y}_2^2\right)\right],\\
\frac{d\mathrm{y}_2}{dx} =& \frac{2\mathrm{M_{pl}}}{1.66\times\sqrt{g^\rho_\star}}\frac{x}{\mu_{12}^2}\langle\Gamma_{\mathrm{SM}\to 22}\rangle\left(Y^{\mathrm{eq}}_{\mathrm{SM}} - \frac{\mathrm{y}_2^2}{Y_2^{\mathrm{eq}^2}}Y^{\mathrm{eq}}_{\mathrm{SM}}\right) + \frac{4\pi^2\mathrm{M_{pl}}}{45\times 1.66}\frac{g^s_\star}{\sqrt{g^\rho_\star}}\frac{\mu_{12}}{x^2}\\
&\left[\langle\sigma v\rangle_{\mathrm{SM}\to 22}\left(Y^{\mathrm{eq}^2}_{\mathrm{SM}} - \frac{\mathrm{y}_2^2}{Y_2^{\mathrm{eq}^2}}Y^{\mathrm{eq}^2}_{\mathrm{SM}}\right) + \langle\sigma v\rangle_{11\to 22}\left(\mathrm{y}_1^2 - \frac{Y_1^{\mathrm{eq}^2}}{Y_2^{\mathrm{eq}^2}}\mathrm{y}_2^2\right)\right].
\end{aligned} \tag{6.1}$$

In the above and also in the rest of the draft, $\mathrm{M_{pl}} = 1.22091\times 10^{19}$ GeV represents Planck mass, $g^s_\star \simeq g^\rho_\star \approx 106.7$ denotes effective massless degrees of freedom and subscripts $1(2)$ denote WIMP(pFIMP). The interaction channels which govern the freeze-out/freeze-in of the DM components are:

[1]The minimal version of such a framework appears in [597], where the fermion DM acts as pFIMP, while the scalar acts as WIMP. However, the model is ruled out by the present direct search bound.

- $\langle\sigma v\rangle_{11\to\text{SM}}$: annihilation/depletion of the WIMP to the SM states.
- $\langle\sigma v\rangle_{11\to22}$: conversion of the WIMP to the FIMP (pFIMP) or vice versa.
- $\langle\sigma v\rangle_{\text{SM}\to22}$: production of the FIMP (pFIMP) from the thermal (SM) bath.
- $\langle\Gamma_{\text{SM}\to22}\rangle$: decay of the bath particles to the FIMP (pFIMP).

We note here that the cBEQ as shown in Eq . (D.1) describes WIMP-WIMP or WIMP-FIMP or FIMP-FIMP case for different strengths of the DM-SM interactions; $\langle\sigma v\rangle_{\text{WIMP}} \sim 10^{-10}\ \text{GeV}^{-2}$, whereas $\langle\sigma v\rangle_{\text{FIMP}} \sim 10^{-20}\ \text{GeV}^{-2}$. The other distinction lies in the initial conditions, for WIMP: $\text{y}_1|_{x\sim0} = Y_1^{\text{eq}} \sim x^{3/2}e^{-x}$, while for FIMP: $\text{y}_2|_{x\sim0} = 0$. The pFIMP solution for DM_2 from the above cBEQ is obtained when,

$$\langle\sigma v\rangle_{\text{SM}\to22} \ll \langle\sigma v\rangle_{11\to22} \sim \langle\sigma v\rangle_{11\to\text{SM}} \sim 10^{-10}\ \text{GeV}^{-2}\,.$$

We further note the discrepancy of a factor of 2 in the Eq . (D.1), stemming from the symmetry factor in identical particle production for 2 as in the BEQ for y_2, while that is absent in annihilation of 1 as for y_1.

We would like to mention that the production of pFIMP can occur from the decay of some heavy thermal bath particle. But for the pFIMP condition above to be met, the decay has to be suppressed as well (i.e. $\langle\Gamma_{\text{SM}\to22}\rangle \sim n_{\text{SM}}^{\text{eq}}\langle\sigma v\rangle_{\text{SM}\to22}$).

We further note that the cBEQ is written in terms of yields $\text{y}_{1,2} = \frac{n_{1,2}}{s}$, where s refers to the entropy density (per co-moving volume) as,

$$s = \frac{2\pi^2}{45}g_\star^s(T)T^3\,; \quad g_\star^s(T) = \sum_k \mathcal{C}_k g_k \left(\frac{T_k}{T}\right)^3 \theta(T-m_k). \tag{6.2}$$

Here k runs over all particles, T_k is the temperature of particle k, g_k its number of internal degrees of freedom and $\mathcal{C}_k = 1\,(7/8)$ when k is a boson(fermion). We also define the Hubble parameter as

$$\mathcal{H}(T) = 1.66\sqrt{g_\star^\rho}\frac{T^2}{\text{M}_{\text{pl}}}; \tag{6.3}$$

$$g_\star^\rho(T) = \sum_{i=bosons} g_i\left(\frac{T_i}{T}\right)^4 + \frac{7}{8}\sum_{i=fermions} g_i\left(\frac{T_i}{T}\right)^4. \tag{6.4}$$

We will assume the relativistic degrees of freedom (DOF) $g_\star^{\rho,s} \approx 106.7$ to be approximately constant as the temperature during which the FIMP freezes in or the WIMP freezes out is rather high. Further, since the two DM with different masses $m_{1,2}$ are involved, we define a common variable $x = \mu_{12}/T$ where $\mu_{12} = m_1m_2/(m_1+m_2)$ is the reduced mass of the system. This is possible as both the pFIMP and WIMP share the same temperature. With the redefined x we can write the equilibrium yield [640] as,

$$Y_i^{\text{eq}}(x) = \frac{45}{4\pi^4}\frac{g_i}{g_\star^s}\left(\frac{m_i}{\mu_{12}}x\right)^2 K_2\left(\frac{m_i}{\mu_{12}}x\right). \tag{6.5}$$

The expressions of thermal average of annihilation cross-section is given by,

$$\langle \sigma v_{12} \rangle = \frac{1}{8 m_1^2 m_2^2 T} \frac{1}{K_2\left(\frac{m_1}{T}\right) K_2\left(\frac{m_2}{T}\right)} \int_{(m_1+m_2)^2}^{\infty} \sigma(s)(s-(m_1+m_2)^2)\sqrt{s} K_1\left(\frac{\sqrt{s}}{T}\right) ds \quad (6.6)$$

where $v_{12} = (1/(E_1 E_2))\sqrt{(p_1.p_2)^2 - m_1^2 m_2^2}$ denotes Möllar velocity, s denotes center-of-mass (CM) energy and $m_{1,2}$, $E_{1,2}$, $p_{1,2}$ denotes annihilating DM masses, energy and momentum, respectively. K_i's denote the modified Bessel functions of second kind, of order i. We further note that the conversion from one DM species to the other are related by,

$$\langle \sigma v \rangle_{11\to 22} = \langle \sigma v \rangle_{22\to 11} \left(\frac{Y_2^{eq}}{Y_1^{eq}}\right)^2 . \quad (6.7)$$

This indicate that when WIMP is heavier than pFIMP, i.e. $m_1 > m_2$ (hierarchy 1), WIMP to pFIMP conversion is kinematically allowed, while the reverse process is Boltzmann suppressed by a factor $\sim e^{-2x\delta m}$, δm denoting the mass difference between the DM's. It is other way round for $m_2 > m_1$ (hierarchy 2). This feature helps to distinguish the mass hierarchies in the pFIMP-WIMP model. The key features of pFIMP freeze out are discussed in details in [305], a summary of which is as follows:

- pFIMP freezes out together or before WIMP, so the relic density of pFIMP is always larger than the WIMP partner[2]. When the conversion cross-section is of similar order to that of WIMP annihilation to SM, both pFIMP and WIMP share similar relic densities.
- When the conversion rate is higher than the WIMP annihilation, the freeze out and resultant relic density of pFIMP remains constant in hierarchy 1, while the WIMP relic density becomes much smaller. In hierarchy 2, this is exactly the other way round. With larger conversion, the WIMP relic remains constant and pFIMP relic drops sharply.
- The mass splitting between WIMP and pFIMP needs to be small ($\delta m \sim 10$ GeV, for $m_{\rm DM} \sim 100$ GeV) for achieving relic density and direct search allowed parameter space, unless we have resonance, co annihilation, semi annihilation or some other special features of the conversion process.

pFIMP-SM interactions via WIMP loop

pFIMPs having feeble tree level interactions with the SM can interact via WIMP loop. Such one loop interaction vertices are shown in Fig . D.5. Here pFIMPs (on the right) are shown by black lines, WIMPs (in the loop) are denoted by red lines, SM particles (on the left of the interaction vertex) are shown by grey lines. As pFIMPs and WIMPs are stabilized by separate symmetries, the bath particles which complete the loop, as denoted by the teal color lines, transform suitably under both the symmetries. The dashed, solid and wavy lines indicate scalar, fermion and vector bosons for WIMP (pFIMP) and the vertices conserve spin, which in turn fixes the SM portal (Z, h).

[2]Recall that for thermal DM $\Omega h^2 \sim 1/\langle \sigma v \rangle$.

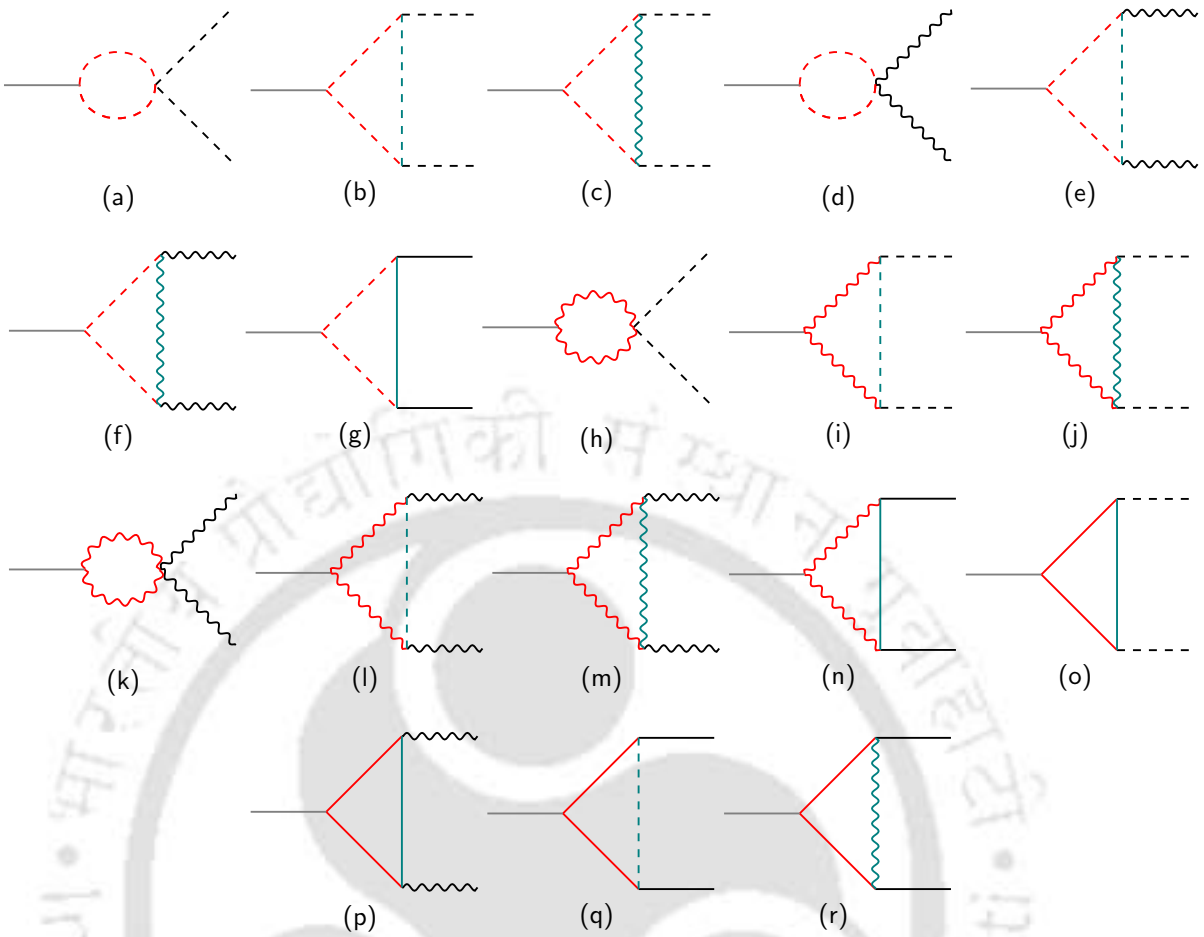

Figure 6.1: Feynman diagrams showing pFIMP (on the right denoted by black lines) interaction with the SM (Z, h) particles (on the left denoted by grey color lines) via WIMP (in red) and heavy thermal bath particles (in teal colour) in loop. All possible interaction vertices having scalar (dashed), fermion (solid) and vector boson (wavy lines) WIMP and pFIMPs transforming under $\mathcal{Z}_2 \otimes \mathcal{Z}_2'$ symmetries as in Table 6.1 have been considered.

In Table 6.1, we have shown all possible renormalizable interactions between WIMPs and pFIMPs in a two component DM scenario stabilised by $\mathcal{Z}_2 \otimes \mathcal{Z}_2'$ symmetry for all combinations of scalar, fermion and vector boson particles. These vertices generate the diagrams shown in Fig. D.5. WIMPs are odd under $\mathcal{Z}_2$ and even under $\mathcal{Z}_2'$, while pFIMPs are odd under $\mathcal{Z}_2'$, and even under $\mathcal{Z}_2$. Particles denoted by prime $(\chi', \psi', \phi', X_\mu')$ are odd under both $\mathcal{Z}_2 \otimes \mathcal{Z}_2'$, which connect WIMP and pFIMP states as shown by the teal color lines in Fig. D.5. This list excludes dark sector particles having non-trivial SM charges, more complicated spin configurations and higher order operators having mass dimension larger than four. A short account of these models and their interactions are as follows:

- Figs. 6.1a to 6.1c correspond to the scenarios where both the WIMPs and pFIMPs are scalars. In Fig. 6.1b (6.1c), DMs are further connected by an extra heavy scalar (vector) bath particle shown in teal colour. Corresponding WIMP-pFIMP interactions that generate these graphs are mentioned in Table 6.1. For Fig. 6.1c, other interaction terms apart from $(\partial^\mu \phi)\Phi X_\mu'$ like $(\partial^\mu X_\mu')\phi\Phi$ or $(\partial^\mu \Phi)\phi X_\mu'$ are also possible.

- Figs. 6.1d to 6.1f depict scalar WIMP and vector boson pFIMP. Fig. 6.1e (6.1f)

Scenarios	WIMP-pFIMP Model			Relic	Detection Possibility
	WIMP	pFIMP	Interaction terms		
(a)	Scalar(ϕ)	Scalar(Φ)	$\phi^2\Phi^2$	✓[305, 308]	✗
(b)	Scalar(ϕ)	Scalar(Φ)	$\mu\phi\Phi\phi'$	✗	✗
(c)	Scalar(ϕ)	Scalar(Φ)	$(\partial^\mu\phi)\Phi X'_\mu$	✗	✗
(d)	Scalar(ϕ)	Vector(V)	$\phi^2 V^\mu V_\mu$	✗	✗
(e)	Scalar(ϕ)	Vector(V)	$(\partial_\mu\phi)V^\mu\phi'$	✗	✗
(f)	Scalar(ϕ)	Vector(V)	$\mu\phi X^\mu X'_\mu$	✗	✗
(g)	Scalar(ϕ)	Fermion(χ)	$\overline{\chi}\chi'\phi$	✓[597]	✓[597]
(h)	Vector(X)	Scalar(Φ)	$X^\mu X_\mu\Phi^2$	✗	✗
(i)	Vector(X)	Scalar(Φ)	$X^\mu(\partial_\mu\phi')\Phi$	✗	✗
(j)	Vector(X)	Scalar(Φ)	$\mu X^\mu X'_\mu\Phi$	✗	✗
(k)	Vector(X)	Vector(V)	$X^\mu X_\mu V^\nu V_\nu$	✗	✗
(l)	Vector(X)	Vector(V)	$\mu X^\mu V_\mu\phi'$	✗	✗
(m)	Vector(X)	Vector (V)	$X^\mu V^\nu(\partial_\mu X'_\nu)$	✗	✗
(n)	Vector(X)	Fermion(χ)	$X_\mu\overline{\chi}\gamma^\mu\chi'$	✗	✗
(o)	Fermion(ψ)	Scalar(Φ)	$\overline{\psi}\psi'\Phi$	This work	This work
(p)	Fermion(ψ)	Vector(V)	$\overline{\psi}\gamma^\mu\psi' V_\mu$	✗	✗
(q)	Fermion(ψ)	Fermion(χ)	$\overline{\psi}\chi\phi'$	✗	✗
(r)	Fermion(ψ)	Fermion(χ)	$\overline{\psi}\gamma^\mu\chi X'_\mu$	✓[596]	✗

Table 6.1: Possible WIMP-pFIMP renormalisable interactions for real scalar, fermion and vector boson particles (see the corresponding Feynman diagrams in Fig. D.5) assuming $\mathcal{Z}_2 \otimes \mathcal{Z}'_2$ symmetries to stabilise both. Particles denoted by prime ($\chi', \psi', \phi', X'_\mu$) are odd under both the $\mathcal{Z}_2$ symmetries, indicated by the teal color lines in Fig. D.5, connect WIMP and pFIMPs. μ represents a dimensionful coupling having one mass dimension.

require a heavy scalar (vector-boson) bath particle connecting them. See the Table 6.1 for corresponding interaction terms. For Fig. 6.1e, other terms like $\phi(\partial_\mu V^\mu)\phi'$, $\phi V^\mu(\partial_\mu\phi')$ are also possible apart from $(\partial_\mu\phi)V^\mu\phi'$ as in Table 6.1.

- Fig. 6.1g represents interaction between a scalar WIMP and fermion pFIMP scenario. In this scenario an extra fermion bath particle is necessary for interaction. This model has been addressed before [597]. For all the scalar WIMP cases discussed so far, the interaction with SM can be governed by the Higgs portal coupling $\phi^2 H^\dagger H$.

- Figs. 6.1h to 6.1j correspond to vector boson WIMP and scalar pFIMP scenario. Fig. 6.1i (6.1j) require extra scalar (vector boson) bath particle for the interaction, see table. For Fig. 6.1i, interaction term like $X^\mu(\partial_\mu\Phi)\phi'$ is also allowed. The WIMP-SM interaction for vector boson WIMP can be driven by $X^\mu X_\mu H^\dagger H$. Note further that we are ignoring the detailed possibility of an abelian/non-abelian gauge origin of the vector boson here.

- Figs. 6.1k to 6.1m correspond to a situation where both WIMP and pFIMPs are vector bosons. The DMs are connected by a scalar (Fig. 6.1l) or a vector bo-

son (Fig . 6.1m) bath particle as shown in the interaction vertices in Table 6.1. Fig . 6.1m can be generated by other interaction terms depending on the field derivative term, as argued before. WIMP-SM portal can also be via Higgs portal as mentioned above. Fig . 6.1n shows the possibility of vector boson WIMP and fermion pFIMP, interacting with each other via another fermion bath particle as shown in teal color.

- Finally, the Figs . 6.1o, 6.1p and (6.1q, 6.1r) correspond to fermion-scalar, fermion-vector and (fermion-fermion) WIMP-pFIMP set-ups. Fig . 6.1q (6.1r) require scalar (vector-boson) bath particles for interaction. Connection of fermion WIMP to SM can occur via effective operator term of the form $\bar{\psi}\psi H^\dagger H$ or via an Yukawa interaction involving a heavy fermion doublet like $\bar{\Psi}\psi H$+h.c. We are going to elaborate upon Fig . 6.1o in a UV complete model next.

The right and cross signs in the relic and detection possibilities in Table 6.1 indicate whether such models have been studied before or not. We can see that amongst various possibilities mentioned, WIMP-pFIMP phenomenology has been explored in a few cases, that too without elaborating upon the characteristics of the pFIMP, its decoupling and/or detectability. Scalar particle as both pFIMP and WIMP has been explored in [305, 308]. In [308], it was pointed out that when pFIMP couples to the SM via a scalar WIMP loop, the direct search detectability becomes difficult, however, in [305], it was shown that the direct search possibility emerges when renormalisation scale is chosen at the freeze-out temperature. We will elaborate more on this later. In [597], fermion pFIMP was studied in a scalar-fermion set up as in Fig . 6.1c, however, the resulting parameter space of this model is almost ruled out by the recent most direct search results. In [596], pFIMP phenomenon was discussed partially, but the detectability of pFIMP via WIMP loop has been neglected.

6.1.3 An example of pFIMP-WIMP model

Our focus will be now on a WIMP-pFIMP two component DM set up where the direct detection possibility of pFIMP is achieved in next generation experiments. We will also make connections to the indirect detection prospects. The model consists of (i) a real scalar-singlet ϕ, which acts like pFIMP and (ii) the lightest admixture of a vector-like fermion doublet $\psi = (\psi^0 \;\; \psi^-)^T$ [599, 641] and a vector-like singlet fermion ψ_1, which acts as WIMP DM. We additionally introduce another vector-like singlet fermion ψ_2, which acts as a messenger between the two DM sectors. Stability of both the DM components is ensured by a $\mathcal{Z}_2 \otimes \mathcal{Z}_2'$ symmetry. The charges of all the relevant fields are given in Table 6.2.

Dark Fields	$SU(3)_c \times SU(2)_L \times U(1)_Y \times \mathcal{Z}_2 \times \mathcal{Z}'_2$				
$\psi = \begin{pmatrix} \psi^0 \\ \psi^- \end{pmatrix}$	1	2	-1	$-$	$+$
ψ_1	1	1	0	$-$	$+$
ψ_2	1	1	0	$+$	$-$
ϕ	1	1	0	$-$	$-$

Table 6.2: Dark sector fields and their corresponding quantum numbers.

Abiding by the symmetry charges, the corresponding Lagrangian is given by,

$$\mathcal{L} = \mathcal{L}_{\rm SM} + \mathcal{L}_{\rm Scalar} + \mathcal{L}_{\rm VF}\,, \tag{6.8}$$

where,

$$\mathcal{L}_{\rm Scalar} = \frac{1}{2}|\partial_\mu\phi|^2 - \frac{1}{2}\mathfrak{m}_\phi^2\phi^2 - \frac{1}{4!}\lambda_\phi\phi^4 - \frac{1}{2}\lambda_{\phi H}\phi^2 H^\dagger H\,, \tag{6.9}$$

and,

$$\begin{aligned}\mathcal{L}_{\rm VF} =& \overline{\psi}\left[i\gamma^\mu\left(\partial_\mu + ig\frac{\sigma^a}{2}W_\mu^a + ig'\frac{Y}{2}B_\mu\right) - m_\psi\right]\psi \\ &+ \sum_{\alpha=1,2}\overline{\psi}_\alpha\left(i\gamma^\mu\partial_\mu - m_{\psi_\alpha}\right)\psi_\alpha - \left(Y_1\overline{\psi}\widetilde{H}\psi_1 + Y_2\overline{\psi}_2\psi_1\phi + \text{h.c.}\right).\end{aligned} \tag{6.10}$$

After Electroweak Symmetry Breaking (EWSB), the SM Higgs H acquires vacuum expectation value (VEV) $v = 246$ GeV, so that In unitarity gauge we can write, $H = \left(0\ \frac{1}{\sqrt{2}}(v+h)\right)^T$. Then the physical mass term of ϕ can be written as $m_\phi^2 = \mathfrak{m}_\phi^2 + \frac{1}{2}\lambda_{\phi H}v^2$. ϕ is a stable DM candidate and serves as the pFIMP component when $\lambda_{\phi H} \to 0$ and conversion to the fermion DM is substantial via large Y_2. From Eq . (6.10), it is straight-forward to calculate the mass terms for the vector-like fermions. The mass eigenstates (χ_1, χ_2) can be obtained via diagonalization of the fermion mass matrix through a unitary transformation from the flavor basis (ψ_1, ψ^0).

$$-\mathcal{L}_{\rm mass} = m_{\chi_1}\overline{\chi}_1\chi_1 + m_{\chi_2}\overline{\chi}_2\chi_2 + m_\psi\psi^+\psi^-\,; \tag{6.11}$$

where,

$$\chi_1 = \cos\theta\psi_1 + \sin\theta\psi^0\,, \tag{6.12}$$

$$\chi_2 = -\sin\theta\psi_1 + \cos\theta\psi^0\,, \tag{6.13}$$

$$m_{\chi_1} = \sin^2\theta m_\psi + \cos^2\theta m_{\psi_1} + \frac{Y_1 v}{\sqrt{2}}\sin 2\theta\,, \tag{6.14}$$

$$m_{\chi_2} = \cos^2\theta m_\psi + \sin^2\theta m_{\psi_1} - \frac{Y_1 v}{\sqrt{2}}\sin 2\theta\,. \tag{6.15}$$

The mixing angle θ can be written as,

$$\tan 2\theta = \frac{\sqrt{2}Y_1 v}{m_{\psi_1} - m_\psi}\,. \tag{6.16}$$

Using Eq . (6.16), we can easily write,

$$Y_1 = \frac{\sin 2\theta}{\sqrt{2}v}(m_{\chi_1} - m_{\chi_2})\,, \tag{6.17}$$

$$m_\psi = m_{\chi_1}\sin^2\theta + m_{\chi_2}\cos^2\theta\,, \tag{6.18}$$

$$m_{\psi_1} = m_{\chi_1}\cos^2\theta + m_{\chi_2}\sin^2\theta\,. \tag{6.19}$$

m_ψ denotes the mass of the charged components of the doublet $\psi^\pm$. The independent parameters of our model are :

$$\{m_{\chi_1},\ m_{\chi_2},\ m_{\psi_2},\ m_\phi,\ \sin\theta,\ Y_2,\ \lambda_{\phi H}\}.$$

χ_1 being the lightest neutral fermion, serves as the WIMP DM component. Note here that χ_1 having gauge interaction with SM via doublet component ψ^0 can't be a pFIMP. In general, any DM having gauge coupling with the SM can never be a pFIMP. The mass difference between χ_1 and the second lightest neutral fermion χ_2, denoted as $\Delta m = m_{\chi_2} - m_{\chi_1}$ serves as an important parameter that controls co-annihilation process and the resulting WIMP relic density. We would like to comment here that the model is perfectly valid as a two component DM scenario without the presence of ψ_2, but can't provide an interaction between ϕ and χ_1. Then it can serve as best as an WIMP-WIMP (in the limit of sizeable $\lambda_{\phi H}$) or WIMP-FIMP (with $\lambda_{\phi H} \to 0$) model. The presence of ψ_2 provides the much needed Yukawa interaction Y_2 between the DM components and allows the model to be explored in pFIMP(ϕ)-WIMP(χ) combination. We can now also correlate with Fig . 6.1o: χ_1 is the fermion WIMP in red colour, ϕ is the pFIMP in dashed black line and ψ_2 is the bath particle connecting them as shown in teal colour. Mass difference between χ_1 and ϕ is denoted in the following text by $\delta m = m_\phi - m_{\chi_1}$, and is also highly constrained by pFIMP freeze-out to yield under abundance.

Following the DM-DM interaction term $Y_2 \overline{\psi}_1 \psi_2 \phi$, we will be interested in the region where $m_{\psi_2} > m_{\chi_1} + m_\phi$, so that ψ_2 can decay to χ_1 and ϕ. The relevant Feynman diagrams for pFIMP production, (co)-annihilation of WIMPs, WIMP-pFIMP conversions and semi-conversion are shown in Figs . 6.2 to 6.4 respectively. In particular, note the presence of a semi-conversion channel $\chi_1 \psi_2 \to h\phi$ in Fig . 6.4, which also helps evading the stringent pFIMP mass constraint on δm. We choose a tiny $\lambda_{\phi H} \sim 10^{-12}$ so that ϕ does not possess a direct SM interaction and behaves as pFIMP, it also helps us evade the upper bound on Higgs invisible branching ratio BR$(h \to invisible) < 19\%$ at 2σ [642] as well as the direct detection constraints to explore the mass range below the Higgs resonance $m_\phi < (m_h/2)$ as well. Its however worthy to mention that the mediator ψ_2 generates ϕ-Higgs portal as a counter term of the loop mediated interaction (see Appendix E.3 for details) and allows for the direct search of pFIMP. For details on Higgs and Z invisible decay width and resulting constraints, see Appendix E.1. Notably, a bound from the LEP experiments on the charged fermion masses [634–638] $\gtrsim 103.5$ GeV also discard the low DM mass region of the relic density allowed parameter space, following Eqs . (6.17)-(6.19).

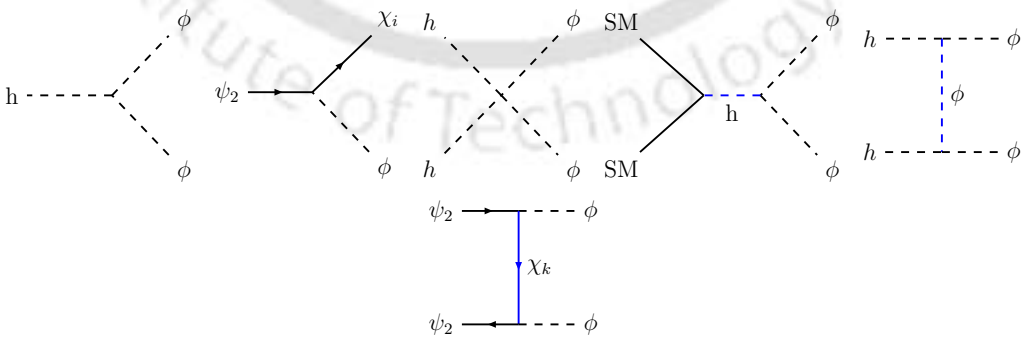

Figure 6.2: Feynman diagrams for pFIMP ϕ production from thermal bath $\{i, k = 1, 2\}$.

Before moving further, we would like to make a couple of comments. The very idea that pFIMP-WIMP conversion governs the pFIMP freeze out distinguishes a scalar pFIMP in a two component scalar DM model from that described here. Also the detectability of pFIMP relies on the loop and the particles involved therein,

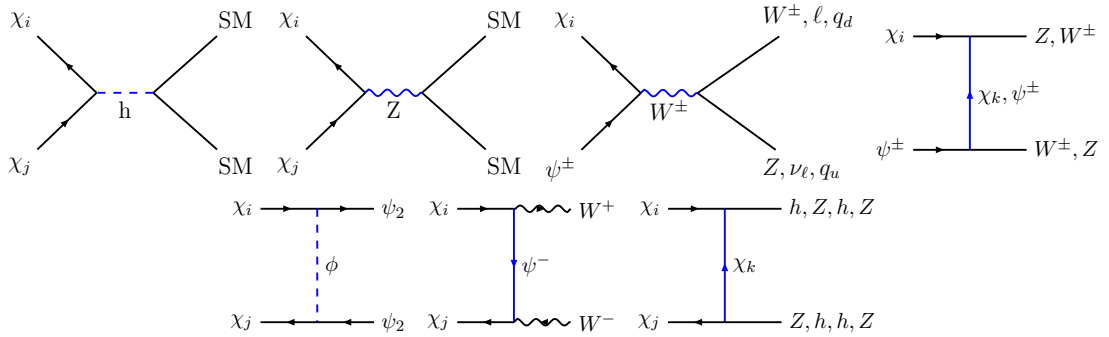

Figure 6.3: Feynman diagrams for the possible annihilation and co-annihilation channels of WIMP χ_1 $\{i, j, k = 1, 2\}$.

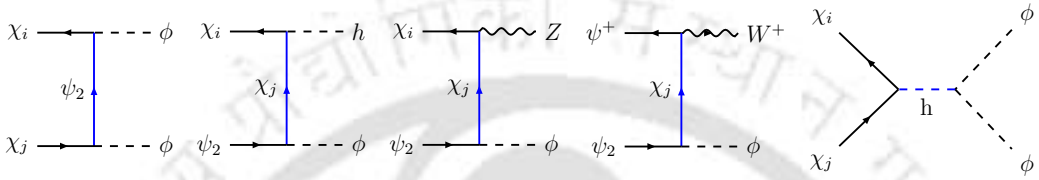

Figure 6.4: Feynman diagrams contributing to WIMP-pFIMP conversion $\{i, j = 1, 2\}$.

which provides a distinct possibility for the model at hand, as we elaborate here. To sum it up, it is not only the pFIMP particle itself, but its WIMP partner, and its interaction with the WIMP holds the key for phenomenological outcome of the two component DM set up.

6.1.4 Dark matter phenomenology

Having discussed the model, we will focus on the DM phenomenology highlighting the pFIMP freeze-out behavior followed up by the scan of the allowed parameter space.

Coupled Boltzmann Equations and relic density

After considering all the relevant processes, the cBEQ's involving the fermion WIMP (χ_1) and scalar pFIMP (ϕ) turn out to be [603, 643–646],

$$\begin{aligned}\frac{dY_\chi}{dx} = &-\frac{2\pi^2 \mathrm{M_{pl}}}{45\times 1.66}\frac{g_\star^s}{\sqrt{g_\star^\rho}}\frac{\mu_{\chi_1\phi}}{x^2}\Bigg[\langle\sigma v\rangle^{\rm eff}_{\rm SM}\left(Y_\chi^2 - Y_\chi^{\rm eq^2}\right) + \langle\sigma v\rangle^{\rm eff}_{\phi}\left(Y_\chi^2 - Y_\chi^{\rm eq^2}\frac{Y_\phi^2}{Y_\phi^{\rm eq^2}}\right)\\ &+ \langle\sigma v\rangle^{\rm eff}_{\psi_2}\left(Y_\chi^2 - Y_\chi^{\rm eq^2}\frac{Y_{\psi_2}^2}{Y_{\psi_2}^{\rm eq^2}}\right) + \left(\langle\sigma v\rangle^{\rm eff}_{\chi_1\overline{\psi}_2\to h\phi} + \langle\sigma v\rangle^{\rm eff}_{\psi^-\overline{\psi}_2\to W^-\phi}\right)\left(Y_{\psi_2}Y_\chi - Y_{\psi_2}^{\rm eq}Y_\chi^{\rm eq}\frac{Y_\phi}{Y_\phi^{\rm eq}}\right)\\ &+ \langle\sigma v\rangle^{\rm eff}_{\chi_1\overline{\psi}_2\to Z\phi}\left(Y_{\psi_2}Y_\chi - Y_{\psi_2}^{\rm eq}Y_\chi^{\rm eq}\frac{Y_\phi}{Y_\phi^{\rm eq}}\right)\Bigg] + \frac{\mathrm{M_{pl}}}{1.66\sqrt{g_\star^\rho}}\frac{x}{\mu_{\chi_1\phi}^2}\langle\Gamma\rangle^{\rm eff}_{\psi_2\to\chi_1\phi}\left(Y_{\psi_2} - Y_{\psi_2}^{\rm eq}\frac{Y_\phi}{Y_\phi^{\rm eq}}\frac{Y_\chi}{Y_\chi^{\rm eq}}\right),\end{aligned} \tag{6.20}$$

$$\begin{aligned}\frac{dY_\phi}{dx} =& \frac{\mathrm{M_{pl}}}{1.66\times\sqrt{g_\star^\rho}}\frac{x}{\mu_{\chi_1\phi}^2}\left[2\langle\Gamma\rangle_{h\to\phi\phi}\left(Y_h^{\rm eq}-Y_h^{\rm eq}\frac{Y_\phi^2}{Y_\phi^{\rm eq^2}}\right)+\langle\Gamma\rangle^{\rm eff}_{\psi_2\to\chi_1\phi}\left(Y_{\psi_2}-Y_{\psi_2}^{\rm eq}\frac{Y_\phi}{Y_\phi^{\rm eq}}\frac{Y_\chi}{Y_\chi^{\rm eq}}\right)\right]\\ &+\frac{2\pi^2\mathrm{M_{pl}}}{45\times1.66}\frac{g_\star^s}{\sqrt{g_\star^\rho}}\frac{\mu_{\chi_1\phi}}{x^2}\left[2\langle\sigma v\rangle_{\rm SM\ SM\to\phi\phi}\left(Y_{\rm SM}^{\rm eq^2}-Y_{\rm SM}^{\rm eq^2}\frac{Y_\phi^2}{Y_\phi^{\rm eq^2}}\right)\right.\\ &+2\langle\sigma v\rangle_{\psi_2\bar\psi_2\to\phi\phi}\left(Y_{\psi_2}^2-Y_{\psi_2}^{\rm eq^2}\frac{Y_\phi^2}{Y_\phi^{\rm eq^2}}\right)+\left(\langle\sigma v\rangle^{\rm eff}_{\chi_1\bar\psi_2\to h\phi}+\langle\sigma v\rangle^{\rm eff}_{\psi^-\bar\psi_2\to W^-\phi}\right)\left(Y_{\psi_2}Y_\chi-Y_{\psi_2}^{\rm eq}Y_\chi^{\rm eq}\frac{Y_\phi}{Y_\phi^{\rm eq}}\right)\\ &\left.+\langle\sigma v\rangle^{\rm eff}_{\chi_1\bar\psi_2\to Z\phi}\left(Y_{\psi_2}Y_\chi-Y_{\psi_2}^{\rm eq}Y_\chi^{\rm eq}\frac{Y_\phi}{Y_\phi^{\rm eq}}\right)+2\langle\sigma v\rangle^{\rm eff}_{\phi}\left(Y_\chi^2-Y_\chi^{\rm eq^2}\frac{Y_\phi^2}{Y_\phi^{\rm eq^2}}\right)\right].\end{aligned}\tag{6.21}$$

In Eqs. (6.20) and (6.21), Y_ϕ is the pFIMP yield and Y_χ is the total WIMP yield (assimilating contributions from the heavy dark sector particles),

$$Y_\chi=\sum_i Y_{\chi_i},\quad \chi_i=\{\chi_1,\overline{\chi}_1,\chi_2,\overline{\chi}_2,\psi^\pm\}\,.\tag{6.22}$$

It is worth reminding that all the unstable heavy states such as $\psi^\pm$, χ_2 take part in co-annihilation processes when in equilibrium. Legitimately $\chi_i,\psi^\pm$ are in equilibrium by rapid annihilations into bath particles. This is also true for ψ_2, via processes as mentioned in Eq. (6.24) for sizeable $Y_2\gtrsim10^{-2}$ when $\langle\Gamma_{\psi_2}\rangle/\mathcal{H}(T)>1$ as shown in Fig. 6.5(a), so that their number densities can be chosen to be the equilibrium number density ($Y^{\rm eq}$) during the DM saturation epoch [3]. We have also shown the variation of $\langle\Gamma_\phi\rangle/\mathcal{H}(T)$ as function of T in Fig. 6.5(b) for different values of Y_2, where $\langle\Gamma_\phi\rangle$ is given by Eq. (6.23). The chemical equilibrium is achieved for $Y_2\gtrsim10^{-4}$.

$$\langle\Gamma_\phi\rangle=2\sum_{i=1,2}\left(\langle\sigma v\rangle_{\phi\chi_i\to h\psi_2}+\langle\sigma v\rangle_{\phi\chi_i\to Z\psi_2}\right)n_{\chi_i}^{\rm eq}+2\langle\sigma v\rangle_{\phi\psi^-\to W^-\psi_2}n_{\psi^-}^{\rm eq}+\langle\sigma v\rangle_{\phi\phi\to\rm SM\ SM}n_\phi^{\rm eq}\,.\tag{6.23}$$

$$\begin{aligned}\langle\Gamma_{\psi_2}\rangle=&\left(\langle\sigma v\rangle_{\psi_2\overline{\chi}_1\to h\phi}+\langle\sigma v\rangle_{\psi_2\overline{\chi}_1\to Z\phi}\right)n_{\chi_1}^{\rm eq}+\left(\langle\sigma v\rangle_{\psi_2\overline{\chi}_2\to h\phi}+\langle\sigma v\rangle_{\psi_2\overline{\chi}_2\to Z\phi}\right)n_{\chi_2}^{\rm eq}+\langle\sigma v\rangle_{\psi_2\psi^+\to W^+\phi}n_{\psi^+}^{\rm eq}\\ &+\left[\langle\sigma v\rangle_{\psi\bar\psi_2\to hh}+\langle\sigma v\rangle_{\psi\bar\psi_2\to hZ}+\langle\sigma v\rangle_{\psi\bar\psi_2\to ZZ}+\langle\sigma v\rangle_{\psi\bar\psi_2\to W^+W^-}+\langle\sigma v\rangle_{\psi\bar\psi_2\to\ell\bar\ell}+\langle\sigma v\rangle_{\psi\bar\psi_2\to q\bar q}\right]n_{\psi_2}^{\rm eq}\,.\end{aligned}\tag{6.24}$$

After the freeze-out, they eventually decay to the lightest stable DM χ_1, contributing to its relic density. This issue is addressed via 'effective' annihilation cross-section to SM $\langle\sigma v\rangle^{\rm eff}$, and effective decay width $\langle\Gamma\rangle^{\rm eff}$ (see [647] and Appendix E.2 for details), where all possible SM final states such as h, $W^\pm$, Z, ℓ, q are considered. Also note that in Figs. 6.20 and 6.21, $\mathrm{M_{pl}}=1.22091\times10^{19}$ GeV represents Planck mass, and $g_\star^s\simeq g_\star^\rho\approx106.7$ denotes effective massless degrees of freedom. The common variable $x=\frac{\mu_{\chi_1\phi}}{T}$ written in terms of the reduced mass $\mu_{\chi_1\phi}=(\frac{1}{m_{\chi_1}}+\frac{1}{m_\phi})^{-1}$

[3] Two points to note here, one, the equilibration is easier when ψ_2 is part of a doublet via gauge interactions. Second, it is not necessary to have ψ_2 in equilibrium for the WIMP (χ)-pFIMP (ϕ) exchange process to be substantial (as required here), although several other terms of the BEQs (6.20) and (6.21) will change to yield a different allowed parameter space.

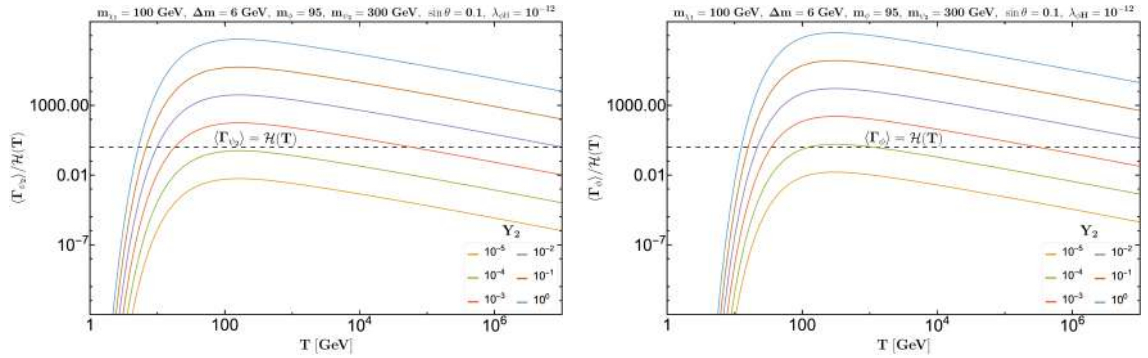

Figure 6.5: Variation of $\langle\Gamma_{\psi_2}\rangle/\mathcal{H}(\mathrm{T})$ as a function of T (GeV) in Fig. 6.5a and $(\langle\Gamma_{\phi}\rangle/\mathcal{H}(\mathrm{T}))$ in Fig. 6.5b for different values of Yukawa couplings Y_2 as shown by different color lines.

caters to the two component DM system in equilibrium. The dark sector particles follow the non-relativistic equilibrium distribution given by,

$$Y_{\phi}^{\rm eq} = \frac{45}{4\pi^4}\frac{g_{\phi}}{g_{\star}^{s}}\left(x\frac{m_{\phi}}{\mu_{\chi_1\phi}}\right)^2 K_2\left(x\frac{m_{\phi}}{\mu_{\chi_1\phi}}\right) , \tag{6.25}$$

$$Y_{\chi}^{\rm eq} = \frac{45}{4\pi^4}\sum_i\frac{g_i}{g_{\star}^{s}}\left(x\frac{m_i}{\mu_{\chi_1\phi}}\right)^2 K_2\left(x\frac{m_i}{\mu_{\chi_1\phi}}\right) . \tag{6.26}$$

In writing the Eqs. (6.20) and (6.21), we also have used [643],

$$\frac{n_i}{n} \approx \frac{n_i^{\rm eq}}{n^{\rm eq}} , \; n^{\rm eq} = \sum_i n_i^{\rm eq} = \frac{T}{2\pi^2}\sum_i g_i m_i^2 K_2\left(\frac{m_i}{T}\right) . \tag{6.27}$$

In the above, T represents the common temperature that DM particles possess, and K_2 represents modified Bessel function of second order. Note further that the scalar DM ϕ is assumed out-of-equilibrium initially due to tiny $\lambda_{\phi H}$, but reaches thermal equilibrium and becomes pFIMP by large conversion from/to WIMP via $\chi_1\chi_1 \to \phi\phi$. A symmetry factor of 2 applies for ϕ (see Eq. (6.21)). Subsequent solution of the cBEQ provides relic density of the DM species by,

$$\Omega_{\rm DM}{\rm h}^2 = 2.744\times10^8\left(m_{\chi_1}Y_{\chi}\left[\frac{m_{\chi_1}}{\mu_{\chi_1\phi}}x_{\infty}\right] + m_{\phi}Y_{\phi}\left[\frac{m_{\phi}}{\mu_{\chi_1\phi}}x_{\infty}\right]\right) , \tag{6.28}$$

where x_{∞} corresponds to the present time/temperature.

The solutions of cBEQ's are presented in terms of DM yield as a function of x in Figs. 6.6 (a) and (b) for two different mass hierarchies. Light brown and violet dotted lines represent pure FIMP situation with $Y_2 = \{10^{-12}, 10^{-8}\}$ respectively, where the DM freezes in. For $Y_2 = 10^{-8}$, with larger conversion from WIMP to FIMP, the FIMP yield increases. However, with Y_2 increasing further ($Y_2 \gtrsim 10^{-3}$), the FIMP thermalises to the equilibrium number density via conversion process and enters into the pFIMP regime (red, green, yellow and deep blue dashed lines) to freeze-out subsequently. The red dashed curve(s) in particular, show how the pFIMP enters into the thermal bath. The pFIMP thermal equilibration is already checked in Fig. 6.5b. The change in the WIMP or pFIMP number density/freeze-out point depends on the mass hierarchy as well as on the conversion cross-section. Here in

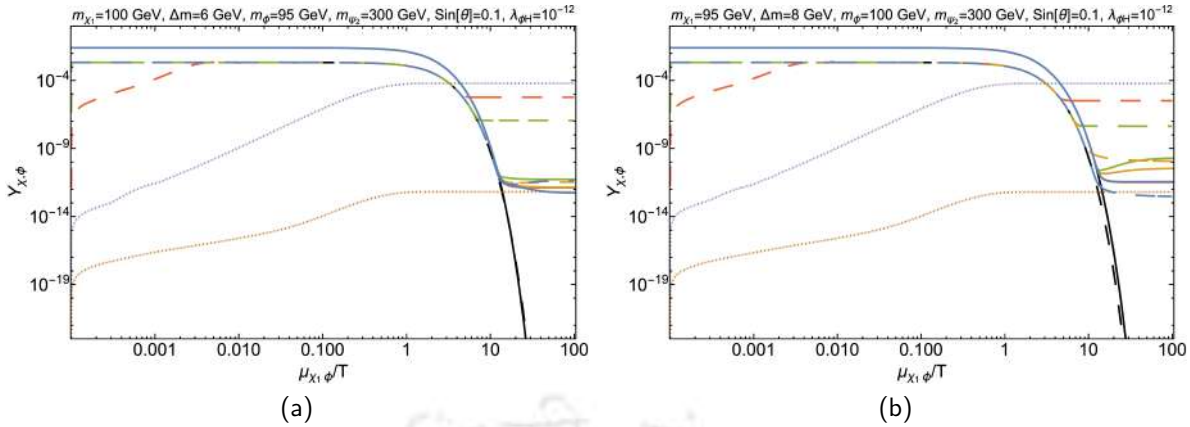

Figure 6.6: Fig . 6.6(a) shows the variation of yield (Y) of WIMP (thick lines), pure FIMP (dotted lines) and pFIMP (dashed lines) as a function of x where light brown, violet, red, green, yellow and deep blue lines correspond to different values of $Y_2 : \{10^{-12}, 10^{-8}, 10^{-4}, 10^{-2}, 1, 2\}$ respectively for $m_{\chi_1} > m_\phi$. Fig . 6.6(b) shows the same for $m_{\chi_1} < m_\phi$ with different values of Yukawa coupling $Y_2 : \{10^{-12}, 10^{-8}, 10^{-4}, 10^{-2}, 10^{-1}, 0.5\}$ represented by light brown, violet, red, green, yellow and deep blue lines respectively. The black thick and dashed lines show the equilibrium distribution of WIMP and pFIMP, respectively. Other parameters kept fixed are mentioned in the figure caption.

both the plots, while the pFIMP relic density decreases with larger Y_2 (via larger conversion cross-section), notice that the WIMP relic density doesn't change much. This is because the WIMP annihilation plus co-annihilation still remains larger than that of the conversion cross-section for the chosen parameters. For detailed pFIMP dynamics see [305].

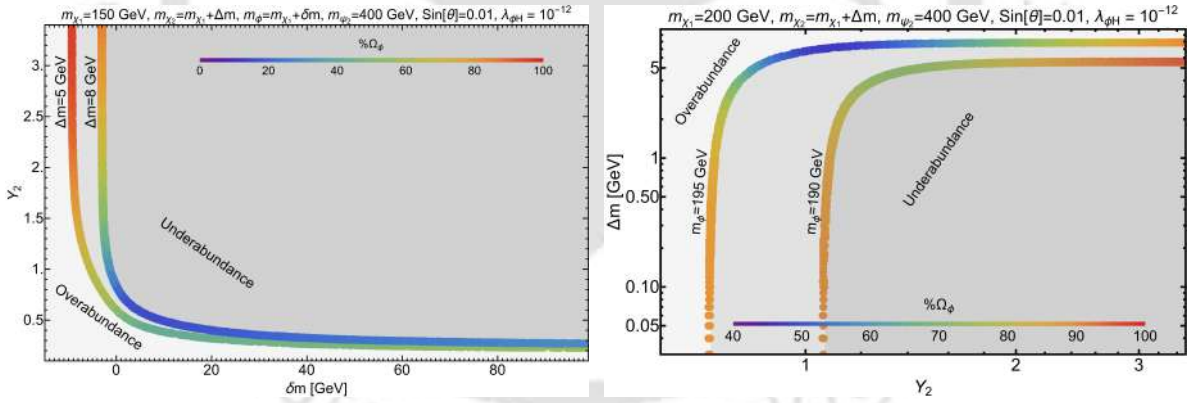

Figure 6.7: Parameter space allowed by the observed relic ($0.1188 \leq \Omega_{\rm DM}h^2 \leq 0.1212$) in (a) $\delta m - Y_2$ plane (b) $Y_2 - \Delta m$ plane. In both the figures percentage contribution of pFIMP (Ω_ϕ) is shown in the color bar. Parameters kept fixed are mentioned in the figure heading.

In Fig . 6.7 (a), we show the relic density allowed parameter space of the model in $\delta m - Y_2$ plane, where the total relic density adds to the observed one ($\Omega h^2 = 0.1200 \pm 0.0012$) [7] for fixed $\{m_\chi, \Delta m, m_{\psi_2}, \sin\theta\}$ as indicated in the figure caption. Two sets of Δm are chosen. Smaller Δm enhances coannihilation of the WIMP and thus reduces the contribution to the total relic. It is clear from the percentage contribution of the pFIMP (ϕ) to the total DM relic as shown in the colour axis. Overabundant and underabundant regions fall below and above the correct choice of Y_2 quite expectedly owing to the inverse dependence of relic density to the conversion cross sections, as indicated. Recall that, $\delta m = m_\phi - m_{\chi_1}$ represents the mass differ-

ence between the pFIMP and WIMP. The parameter space can be divided into two regions: (i) $\delta m > 0$, i.e. pFIMP is heavier than WIMP; (ii) $\delta m < 0$, when WIMP is heavier than pFIMP. The results are different for these cases. When $\delta m > 0$, there is a mild dependence on δm, as the conversion process doesn't depend heavily on it and contribution to the WIMP relic density is small, thus pFIMP contribution remains in 20% ballpark with almost no change in Y_2. However, when $\delta m < 0$, the WIMP has an additional depletion channel, and its relic density decreases with larger conversion to pFIMP with larger splitting, in turn the pFIMP relic enhances significantly, which requires to be adjusted by having larger Y_2 to keep the total relic within the observed one. In Fig . 6.7(b), we show the relic density allowed parameter space in $Y_2 - \Delta m$ plane. As mentioned earlier, here, Δm is the mass difference between the second lightest fermionic dark sector particle χ_2 and the WIMP DM χ_1. With larger Y_2, and therefore larger $\chi_1 \to \phi$ conversion, the co-annihilation effect is required to reduce with larger Δm and the relative contribution of ϕ to the total relic density increases. We further see that a maximum of $\Delta m \lesssim 10$ GeV is possible for pFIMP ϕ to saturate the most of DM abundance. The parameters kept fixed are mentioned in the figure caption and the two choices of m_ϕ used for the scan are mentioned in the plot.

Direct detection prospect

Now we delve into the direct search prospect of the two component DM's, which is our key focus in this study. First we will briefly discuss the direct detection of the WIMP and then explore the pFIMP case in detail.

Direct detection of WIMP

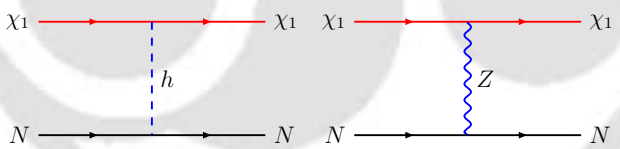

Figure 6.8: The Feynman diagrams for the direct detection of WIMP (χ_1).

In this model, the spin-independent direct detection cross section for WIMP χ_1 ($\sigma^{\rm SI}_{\chi_1 N}$) gets major contribution from Z and Higgs-mediated t-channel diagrams (Fig . 6.22) and therefore the singlet-doublet mixing parameter $\sin\theta$ plays an important role, apart from the DM mass m_{χ_1}. The direct search prospect of this WIMP is similar to that in [599, 648]. The Z mediated contribution is required to be small to abide by the non-observation of a spin-independent direct search of the DM. This is possible when the singlet doublet mixing ($\sin\theta$) is small, since the effective coupling involved in the Z mediated vertex is $\lambda_{Z\overline{\chi}_1\chi_1} = \frac{m_Z}{v}\sin^2\theta$, whereas the effective Higgs coupling is $\lambda_{h\overline{\chi}_1\chi_1} = -\frac{Y_1}{\sqrt{2}}\sin 2\theta$.

In Fig . 6.9 (a) and (b) we show the effective spin-independent direct detection cross-section ($\sigma^{\rm eff}_{\chi_1}$) of the WIMP-like fermion DM χ_1 as a function of its mass (m_{χ_1}) for two different mass hierarchies. We also show the limits from existing direct search data along with future sensitivities. The effective direct search cross-section for the individual DM components are defined [649] as follows,

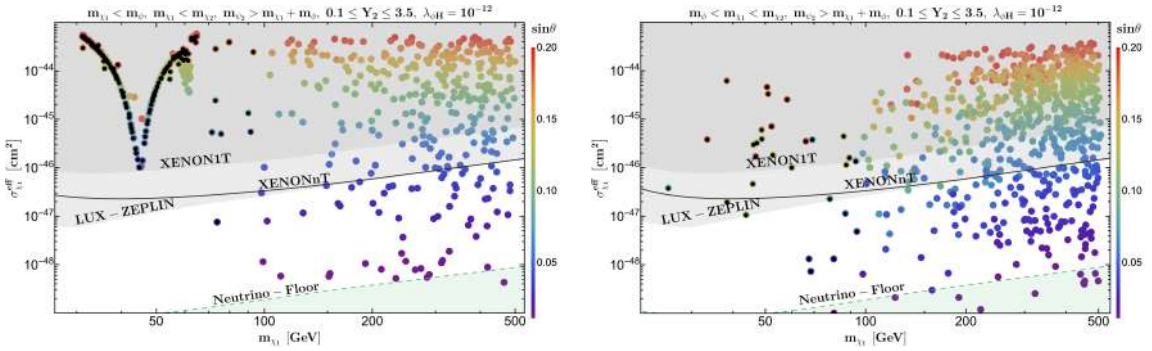

Figure 6.9: Effective spin-independent direct detection cross-section ($\sigma^{\rm eff}_{\chi_1}$) for WIMP χ_1 for (a) $m_{\chi_1} < m_\phi$ and (b) $m_{\chi_1} > m_\phi$. All the points satisfy the present DM relic density bound $0.1188 \leq \Omega_{\chi_1}h^2 + \Omega_\phi h^2 \leq 0.1212$ via the combined contribution of both DM's. $\sin\theta$ is shown as color axis in both the figures. Other parameters kept fixed are shown in figure heading. The limits from XENON1T, LUX-ZEPLIN data and future sensitivities from XENONnT and Neutrino floor are shown. Black dotted points are excluded by the LEP bound on the charged fermion masses.

$$\sigma^{\rm eff}_{\chi_1} = \frac{\Omega_{\chi_1}}{\Omega_{\chi_1}+\Omega_\phi}\sigma^{\rm SI}_{\chi_1 \rm N}\,; \quad \sigma^{\rm eff}_{\phi} = \frac{\Omega_{\phi}}{\Omega_{\chi_1}+\Omega_\phi}\sigma^{\rm SI}_{\phi \rm N}\,. \tag{6.29}$$

In both the Figs. 6.9 (a) and (b) $\sin\theta$ is shown in the colour bar. It is clear that with increasing $\sin\theta$, i.e. with more doublet contribution, the direct detection cross-section for χ_1 increases. One finds in Fig. 6.9 (a), when $m_{\chi_1} \lesssim 100$ GeV, only in the vicinity of Z-resonance, we get points allowed by the relic density, but disfavoured from direct search data. The points allowed by the direct search data requires $m_\chi \gtrsim 100$ GeV with $\sin\theta \lesssim 0.1$. In the reverse hierarchy (Fig. 6.9(b)), the Z-resonance region is not particularly distinct. The reason behind this is the following. When $m_{\chi_1} > m_\phi$, the conversion channel from χ_1 to ϕ is open which helps χ_1 to deplete its number density considerably and become under-abundant, whereas when $m_{\chi_1} < m_\phi$, this conversion is kinematically disfavoured and therefore the under-abundance for χ_1 is achieved primarily near Z-resonance. Here too, small mass difference between χ_1 and χ_2 can facilitate co-annihilation and there exists a possibility of under-abundance with appropriate choice of Δm. The black dots over the rainbow points are disfavoured from the LEP limit on charged fermion masses. The same appears in other parameter space scans. The detailed calculation of the direct detection cross-section of WIMP can be found in Appendix E.4.

Direct detection of pFIMP

The FIMP having negligible coupling with SM states is difficult to probe in direct search experiments. pFIMP on the other hand, despite having negligible couplings to SM, has a prospect of being detected at direct search experiments via substantial coupling with the WIMP. As discussed in Section 8.2, the pFIMP coupling to SM occurs via the WIMP-loop, which can have a non-negligible contribution to the elastic scattering between pFIMP and detector nucleon.

In Fig. 6.10, we show the diagrams which contribute to the direct search cross-section of pFIMP (ϕ) in our model. The diagram (Fig. 6.10 (left)) involving the Higgs portal coupling of pFIMP, contributes negligibly to the total amplitude with $\lambda_{\phi H} \sim 10^{-12}$. Fig. 6.10 (middle) shows the WIMP-loop induced contribution with

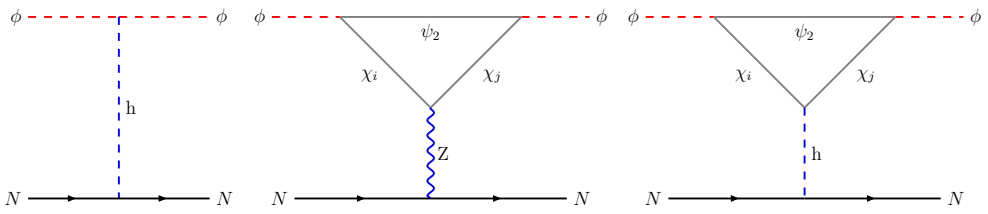

Figure 6.10: The (left) tree-level and (middle) and (right) one-loop Feynman diagram for the direct detection of pFIMP ϕ .

a t-channel Z mediator, whereas Fig . 6.10 (right) shows the same with t-channel Higgs mediation.

The coupling that plays crucial role in determining the loop amplitude is the WIMP-pFIMP coupling (Yukawa coupling Y_2), which was also a key parameter in governing the pFIMP dynamics. On the other hand, one has to also remember that the loop contributions are also a direct consequence of the singlet-doublet mixing in our model. In the absence of mixing, the loop contribution to pFIMP-nucleon interaction vanishes. Therefore, not only the Yukawa coupling Y_2, but also the Yukawa coupling Y_1 is crucial in this context. In addition, the mixing term is directly proportional to the mass difference between the WIMP and the second lightest dark sector particle $(m_{\chi_2} - m_{\chi_1})$, as we have seen in Eq . (6.17). The smaller the mass difference, the weaker is the detectability of the pFIMP at direct detection experiments. Similar to the WIMP case, here too the Higgs mediated diagram contributes much more compared to the Z-mediated case, thanks to the small $\sin\theta$ limit that we need to abide by. For an order-of-magnitude estimate of the Higgs and Z mediated contributions, one can see Figs . E.2 and E.4 in Appendix E.3. We would like to emphasize here that, we get an advantage by choosing a fermionic WIMP candidate over a scalar. It was shown in [308], that the pFIMP in a two-component scalar DM model, will have negligible contribution to the direct detection as the scalar loop-amplitude vanishes at the low transfer momentum limit (unless the WIMP is a warm DM in the KeV mass-range). Although that issue can be alleviated if we choose renormalisation scale at the DM mass scale, however the scale dependence remains. This is not the case with fermion WIMP loop, see the detailed calculations in Appendix E.3. Herein lies a very important motivation behind choosing the model. The detailed calculation of direct detection cross-section of pFIMP is done in Appendix E.4, which we use for the parameter space scan discussed next.

In Fig . 6.11, we present the effective spin-independent direct detection cross-section $(\sigma_\phi^{\rm eff})$ of the pFIMP ϕ as a function of its mass (m_ϕ) for two different mass hierarchies. The definition of $\sigma_\phi^{\rm eff}$ follows from Eq . (6.29). As the major contribution to $\sigma_\phi^{\rm eff}$ comes from the fermion-loop induced diagrams (Fig . 6.10), the parameters Δm, Y_2 and $\sin\theta$ play a crucial role. In order to achieve a considerable direct detection cross-section, a large mass splitting Δm is desirable, as already pointed out. On the other hand, large Δm means absence of co-annihilation and therefore, over-abundance of χ_1. This situation is evident in Fig . 6.11(a), where the parameter space allowed by observed relic density implies direct detection cross-section for the pFIMP not only lies below the existing direct search limits, but a large part remains within the neutrino floor sensitivity. This tension is relaxed when $m_{\chi_1} > m_\phi$, since in this case the conversion channel from χ_1 to ϕ becomes kinematically favoured and under-abundance of χ_1 is possible even with moderate/large Δm. This in turn ensures a moderate direct search cross-section $(10^{-49} - 10^{-47})$ for the pFIMP with

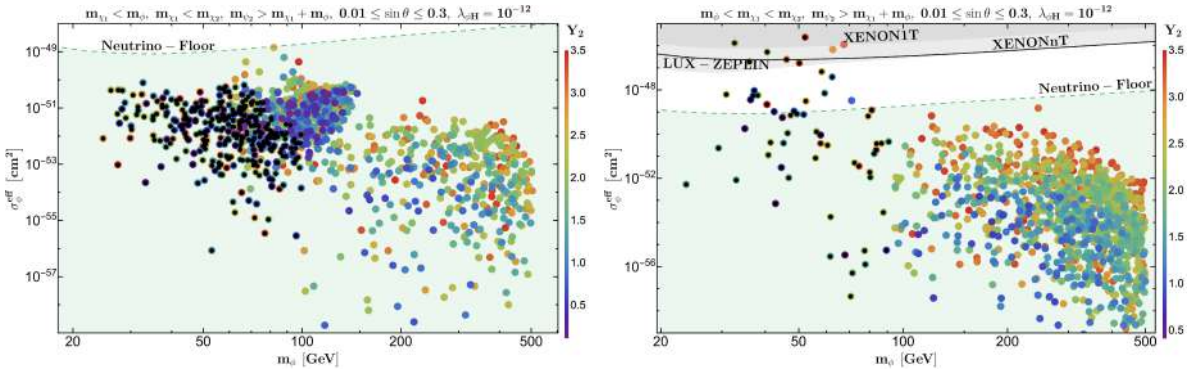

Figure 6.11: Effective spin-independent direct detection cross-section ($\sigma_\phi^{\rm eff}$) for pFIMP ϕ for (a) $m_{\chi_1} < m_\phi$ and (b) $m_{\chi_1} > m_\phi$. All the points satisfy the present DM relic density bound $0.1188 \leq \Omega_{\chi_1}h^2 + \Omega_\phi h^2 \leq 0.1212$ via the combined contribution of both DM's. Y_2 is shown as the color axis in both figures. Other parameters kept fixed are shown in figure heading. The limits from XENON1T, LUX-ZEPLIN data and future sensitivities from XENONnT and Neutrino floor are shown. Black dotted points are excluded by the LEP bound on the charged fermion masses.

mass $\lesssim 100$ GeV, which can be probed in the next generation direct detection experiments like Xenon-nT (projected limit 10^{-49} cm^2), as shown in Fig. 6.11 (b). Hereby, we draw a crucial inference that $m_{\chi_1} > m_\phi$ is more favourable for the direct detection of pFIMP, as compared to the inverse hierarchy in this specific model.

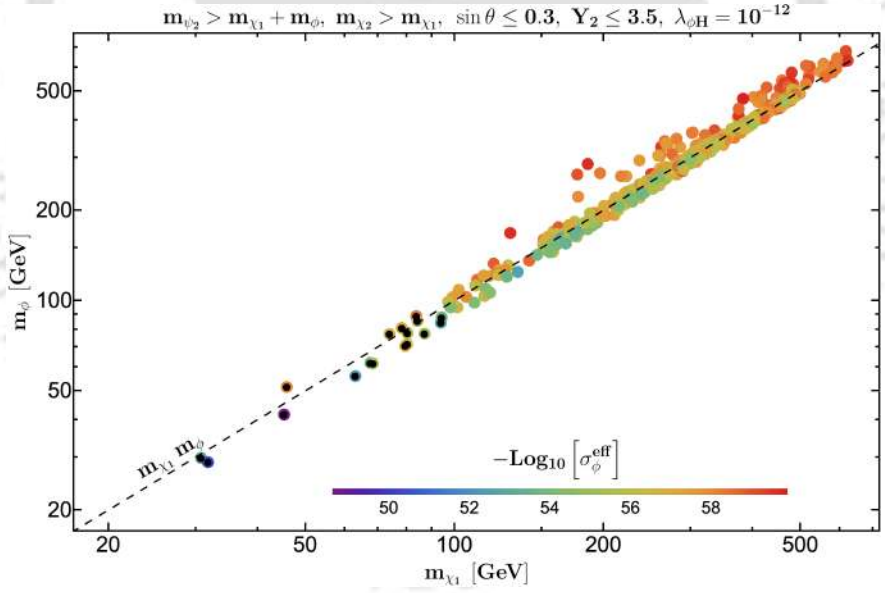

Figure 6.12: Allowed parameter space in $m_{\chi_1} - m_\phi$ plane, which respect the present observed relic density as well as have sensitivities for future direct detection experiments beyond LUX-ZEPLIN bound. The color axis represents the effective spin-independent pFIMP-nucleon scattering cross-section, $\sigma_\phi^{\rm eff}$ in cm^2 in Log scale. Black dotted points are excluded by the LEP bound on the charged fermion masses.

Having discussed the individual aspects of WIMP and pFIMP direct detection, we would also like to make a connection between the two. In Fig. 6.12, we have shown the allowed parameter space which respect the present relic density and direct detection (LUX-ZEPLIN) bound in $m_{\chi_1} - m_\phi$ plane. The color axis represents the effective spin-independent pFIMP-nucleon scattering cross-section, $\sigma_\phi^{\rm eff}({\rm cm}^2)$ in Log scale. One can firstly observe that the allowed region lies in the vicinity of $m_{\chi_1} = m_\phi$ line in accordance with the pFIMP dynamics [305]. When $m_{\chi_1} > m_\phi$,

χ_1 to ϕ conversion is significant, reducing the WIMP contribution and enhancing ϕ contribution to the total relic, and therefore the effective $\sigma_\phi^{\rm eff}$ too increases. Now see the red points above the $m_{\chi_1} = m_\phi$ line, i.e the opposite hierarchy ($m_{\chi_1} < m_\phi$). One can notice the presence of larger $\delta m \sim 100$ GeV points for this hierarchy, which was absent in the other hierarchy in accordance with Fig . 6.7. In addition, if χ_1 is in the Z resonance, under-abundance of χ_1 becomes further enhanced and it becomes easier to achieve large Δm and consequently large direct detection cross-section for the pFIMP (blue points in the vicinity of Z resonance in Fig . 6.12). For the inverse hierarchy on the other hand, the under-abundance of WIMP is solely dependent on its co-annihilation and therefore, large Δm values are disfavoured, resulting in small direct detection cross-section for the pFIMP. We have checked that even with χ_1 in the vicinity Z resonance, the dependence on co-annihilation is not relaxed and therefore, direct detection cross-section for the pFIMP remains below the neutrino floor for almost the entire parameter space.

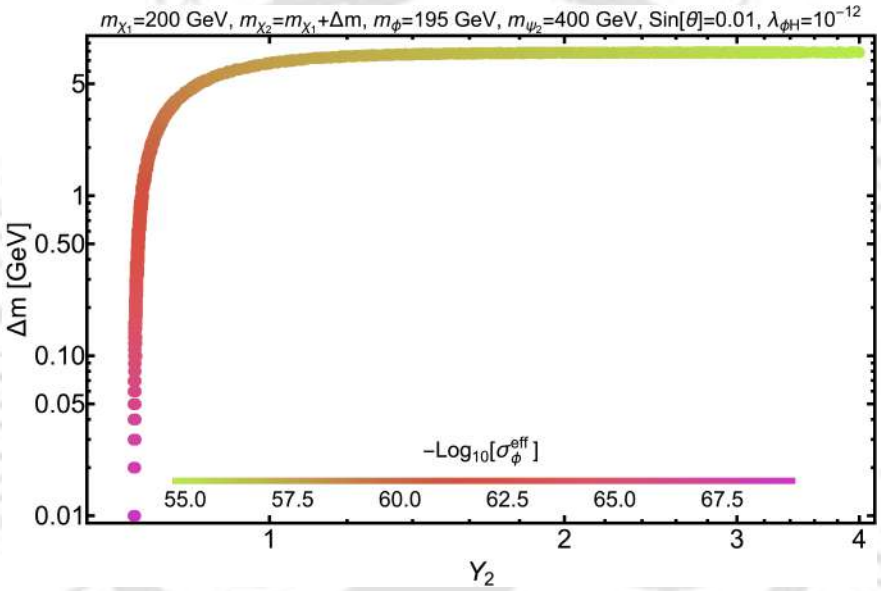

Figure 6.13: Parameter space allowed by observed relic density and direct search constraints in $Y_2 - \Delta m$ plane, where the spin-independent effective DM-nucleon elastic scattering cross-section of scalar DM ($\sigma_\phi^{\rm eff}$ in cm^2) is shown as the color axis in Log scale.

In Fig . 6.13, we show the relic density and direct search allowed points in $Y_2 - \Delta m$ plane, with the color axis denoting the direct detection cross-section of the pFIMP ϕ in Log scale. The shape of the curve is exactly similar to that of Fig . 6.7 (b), dictated by the relic density constraint, which limits $\Delta m \lesssim 10$ GeV to assimilate the effect of annihilation/co-annihilation of the WIMP. Larger Δm imply enhanced contribution from the fermion loop (see Fig . 6.10) resulting larger direct detection cross-section for the pFIMP, evident from the transition in color in Fig . 6.13. Increasing Y_2 is also crucial in obtaining enhanced direct search cross-section $\sigma_\phi^{\rm eff}$, also apparent from the colour of the curve.

Indirect detection possibility

Similar to the direct detection prospects of pFIMP, one can obtain indirect signal evidence of pFIMP, analysing the photon flux [650] in the existing and future indirect detection experiments such as Fermi-LAT [651], SK [652], H.E.S.S [653], IceCube

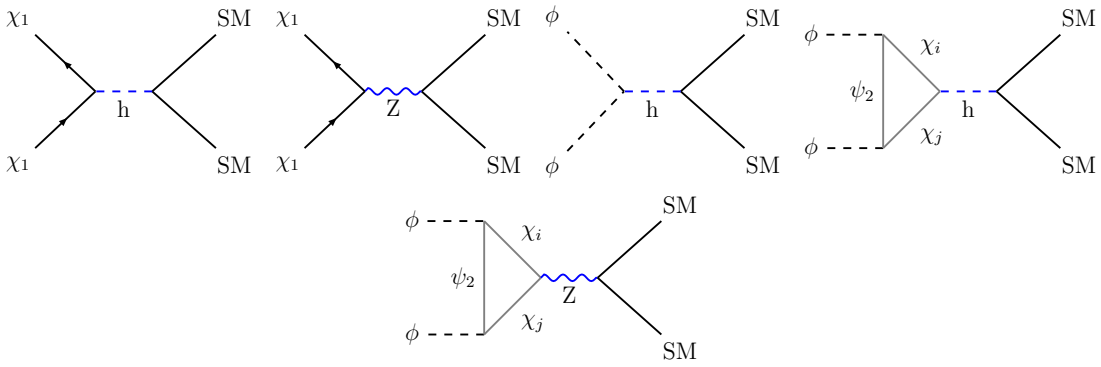

Figure 6.14: The Tree-level (left) and one-loop (right) Feynman diagrams for the Indirect detection of WIMP (χ_1) and pFIMP (ϕ).

[654–656] etc. We have considered the recent data for DM annihilation channels to $b\bar{b}$, $\tau^+\tau^-$ and W^+W^- from various experiments and study their effect on our model parameter space. The strongest bounds come from the $b\bar{b}$ annihilation channel. The effective annihilation cross-section of a DM pair to $b\bar{b}$ final state in a two-component DM set up is given by [657, 658],

$$\langle\sigma v\rangle^{\rm ID}_{\rm DM\ DM\to b\bar{b}} = \frac{\Omega^2_{\rm DM}}{(\Omega_{\chi_1}+\Omega_\phi)^2}\langle\sigma v\rangle_{\rm DM\ DM\to b\bar{b}}\,. \tag{6.30}$$

In the above, DM notation indicates WIMP (χ_1) or pFIMP (ϕ).

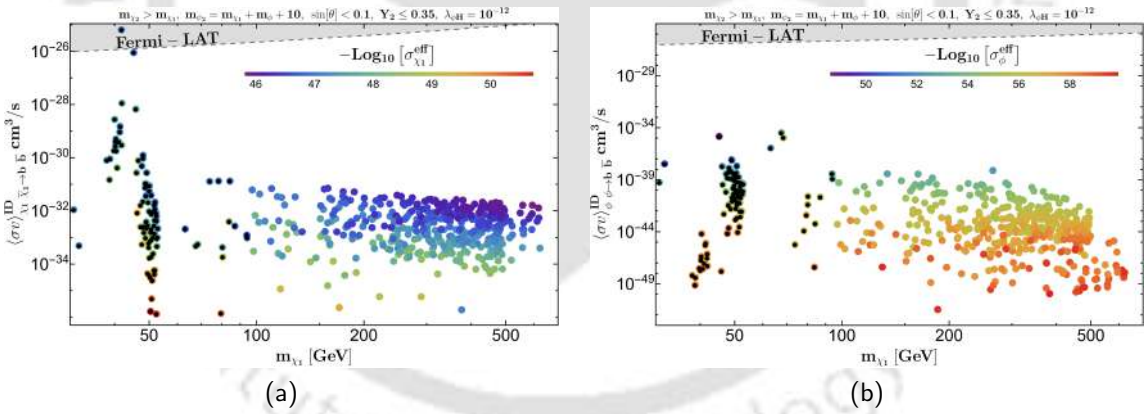

Figure 6.15: DM annihilation cross-section to $b\bar{b}$, $\langle\sigma v\rangle^{\rm ID}_{\chi_1\bar{\chi}_1\to b\bar{b}}$ and $\langle\sigma v\rangle^{\rm ID}_{\phi\phi\to b\bar{b}}$ as a function of DM mass. The color axis denotes effective direct detection cross-section for pFIMP ($\sigma^{\rm eff}_\phi$). All points in $\sigma^{\rm ID}$-m_{χ_1} plane satisfy observed relic and LUX-ZEPLIN bound for both WIMP and pFIMP. Grey shaded region is excluded by DM annihilation to $b\bar{b}$ search at Fermi-LAT [519, 651] and H.E.S.S [653] data. Black dotted points are excluded by the LEP bound.

In Fig . 6.14, we show the processes that contribute to the aforementioned annihilation channels for both WIMP and pFIMP. Note that the tree-level Higgs mediated channel for pFIMP annihilation turns negligible with $\lambda_{\phi H} \to 0$, while the WIMP-loop induced diagrams dominantly contribute to pFIMP annihilation, similar to the direct search case.

In Fig . 6.15, we plot $\langle\sigma v\rangle^{\rm ID}_{\rm DM\ DM\to b\bar{b}}$ as a function of DM mass for WIMP (Fig . 6.15(a)) and pFIMP (Fig . 6.15(b)). The color axis denotes the effective direct detection cross-section for pFIMP ($\sigma^{\rm eff}_\phi$). All the points in both plots satisfy the observed relic and LUX-ZEPLIN bound. It is evident from the figures that the entire parameter space is

allowed by indirect bound from Fermi-LAT (black dashed line) and can be probed in future experiments. Interestingly, the region that is most sensitive to the future indirect detection experiments lies in the vicinity of Z-resonance. The same points also produce maximum direct search cross-section for the pFIMP (dark blue points in Fig. 6.15(b)) and thereby yield best discovery potential.

Collider constraints and prospects at LHC

The WIMP sector of the model having additional particles transforming under the SM gauge group, naturally have collider detectability as well as constraints from the existing data [599, 659, 660]. The hardest limit appears on the model from the LEP exclusion [634] of not observing a singly charged fermion beyond the SM, resulting $m_{\psi^\pm} \gtrsim 103.5$ GeV. The ALTAS [661, 662] and CMS [663] experiments at LHC have looked for DM signal in opposite sign di-leptons (OSD) + jets + $\not{E}_T$ (MET) final state and non-observation of any excess puts a limit on our model, that produces such a signal. In our model, corresponding signal process is predominantly generated by the Drell-Yan production of the charged fermion pair, subsequently decaying via off-shell $W^\pm$ as shown in Fig. 6.16a. In Fig. 6.17, we show the LHC constraints in the plane of charged lepton mass and DM mass. This limit stems from the search for supersymmetric chargino, where the lightest neutralino serves as cold DM (both in gaugino-dominated regions), giving rise to OSD plus MET signal. One can see from here that large mass difference between the DM candidate and charged fermions are disallowed by the experimental data, i.e. the on-shell production of $W^\pm$ from the charged fermion decay is crucial for the parameter point to be sensitive to the experimental data. However, as we have discussed in detail, in the small $\sin\theta$ limit, the requirement of adequate co-annihilation makes the DM and charged fermion masses almost degenerate, see the maroon points that comes from our model checked against the experimental constraints in Fig. 6.17. Therefore, the parameter space of our model, relevant from the DM constraints are allowed by the ATLAS and CMS bounds. It is interesting to note further that, only in the Z resonance region, the requirement for degenerate DM masses with its charged/neutral partners get relaxed, where a large mass gap becomes allowed from relic density constraints. Therefore, some of these points where DM mass lies in the resonance region, can possess $\psi^\pm > 103.5$ GeV and survive all the experimental constraints (See Figs. 6.11 and 6.15). Apart from the OSD final state, the WIMP can be produced via several other channels like $\chi_2\chi_2$, $\chi_2\psi^\pm$ and their subsequent decays to produce $(1\ell, 2\ell, 3\ell, 4\ell)$ signals [599, 659, 660] in association with MET.

On the other hand, pFIMP can only be produced via WIMP loop, yielding a mono-X ($X = j, \gamma, Z, W, h$) signal predominantly via initial state radiation, see Fig. 6.16c. WIMP of this specific model (or any other model) will always be able to produce the same mono-X signal (see Fig. 6.16b) and the WIMP cross-section is larger than the pFIMP one, as the latter is always loop-suppressed. Therefore, $\not{E}_T$ peak produced by the pFIMP will possibly be submerged into that of the WIMP, as the mass difference between them is not large. Note here that the distinguishability of the peaks in $\not{E}_T$ distribution heavily depends on the mass separation [465]. The pFIMP signal can possibly be distinguished from the WIMP partner, if the MET peak is separated due to different effective Lorentz structures for the production [466]. We will elaborate on this possibility concerning pFIMP production in a sep-

arate publication. We present the signal cross-sections in Table 6.3 at some typical benchmark points for illustration. This indicates that the possibility of pFIMP detection of this model at LHC is rather bleak.

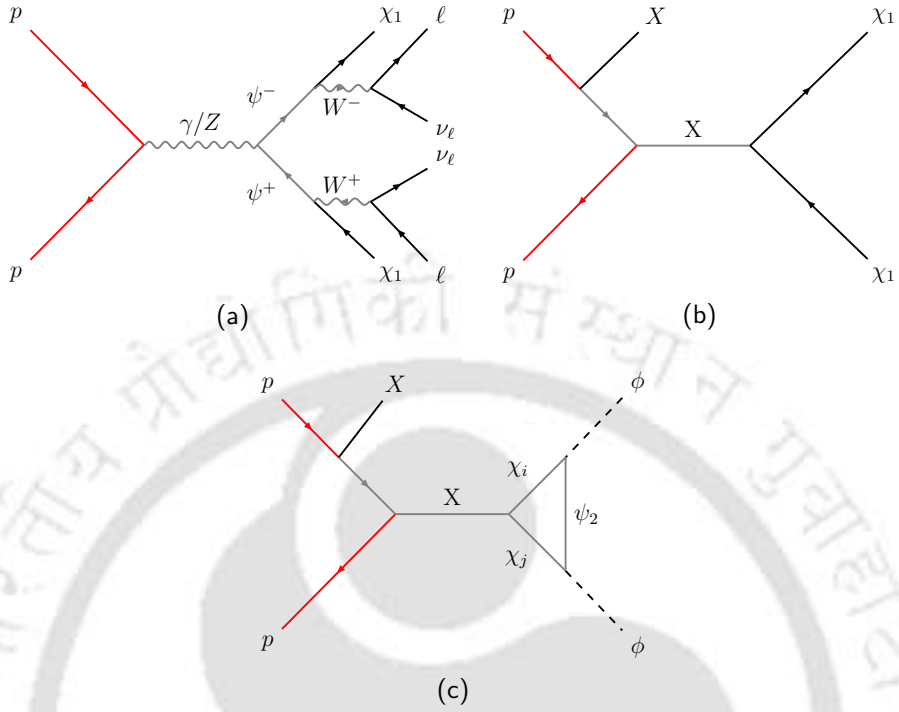

Figure 6.16: Feynman diagrams showing $p\,p \to \psi^+\psi^-$ production and subsequent decays to OSD ($\ell^+\ell^- + \not{E}_T$) events (Fig. 6.16a), mono-X + $\not{E}_T$ signal for WIMP (Fig. 6.16b) and pFIMP (Fig. 6.16c); where $X \in \{jet,\ \gamma,\ h,\ Z\}$ and $i = 1,\ 2$.

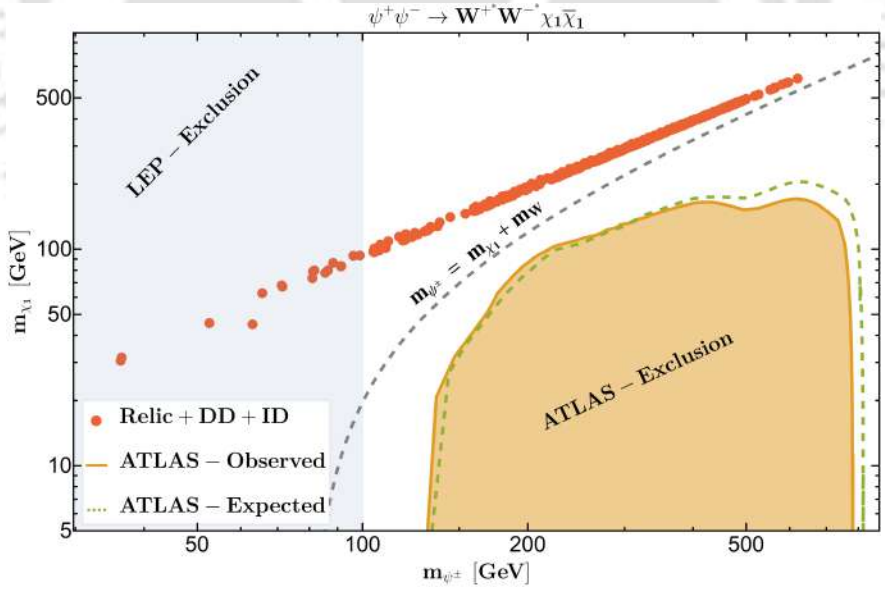

Figure 6.17: WIMP masses $\gtrsim$ 103 GeV are allowed by ATLAS [661, 662] and LEP [634] observed chargino signal.

6.1.5 Summary

We focused on a two-component DM scenario involving a thermal WIMP and a FIMP having negligible interaction with SM. When the interaction between the WIMP

m_{χ_1}	m_{χ_2}	m_ϕ	m_{ψ_2}	$\sin\theta$	Y_2	$\Omega_{\chi_1}h^2$	$\Omega_\phi h^2$	$\sigma^{\rm eff}_{\chi_1}$ [cm^2]	$\sigma^{\rm eff}_{\phi}$ [cm^2]	p-p collision (fb)		
										WIMP		pFIMP
										OSD + $\not{E}_T$	mono-jet+$\not{E}_T$	mono-jet+$\not{E}_T$
98.0	104.7	94.8	202.8	0.02	2.44	0.0092	0.1115	6.30×10^{-49}	1.40×10^{-55}	93.3	2.21×10^{-4}	1.49×10^{-9}
250.3	253.9	242.9	1121.2	0.04	1.61	0.0423	0.0783	2.27×10^{-47}	1.96×10^{-58}	3.67	1.38×10^{-4}	9.16×10^{-12}
456.1	461.4	454.7	920.8	0.02	2.43	0.0954	0.0258	2.11×10^{-48}	1.09×10^{-58}	0.312	8.42×10^{-7}	1.26×10^{-11}

Table 6.3: Relic density, Direct search and Collider signal cross-sections at some benchmark points for the two-component fermion-scalar model. All the masses are in the units of GeV. The last two columns depict the WIMP and pFIMP production cross-section at LHC via Gluon fusion yielding mono-jet+$\not{E}_T$ in the final state at $\sqrt{s} = 14$ TeV. The OSD + MET final state cross-section is estimated only via $\psi^+\psi^-$ production and cascade decay.

and FIMP becomes of weak interaction strength, the FIMP thermalises and freezes-out similar to the WIMP. Such DM candidates can be called pseudo-FIMP (pFIMP) and we explored various aspects of this mechanism in our earlier work [305] in a model independent manner. In this work, we focus on a specific two component DM model to analyze the parameter space in the WIMP-pFIMP limit.

A crucial aspect of this work is to explore the possibility of detection of pFIMP in direct and indirect search experiments. It is well-known that a FIMP having tiny coupling to SM states, evades both present and future (projected) direct detection bounds. However, the pFIMP, aided by its significant interaction with the WIMP, can have considerable DM-nucleon cross-section at the direct search experiments. Although, the pFIMP has no direct connection to the SM, it can produce WIMP-loop induced amplitudes, which can bring the pFIMP under future experimental sensitivities. Having identified all such one-loop possibilities with scalar, fermion and vector boson particles as WIMP and pFIMP, we choose a specific model which is likely to provide a considerable direct and indirect search sensitivity for the pFIMP. It is important to note that pFIMP detectability depends heavily on its WIMP partner, not only due to its presence in the loop induced graphs for the pFIMP interacting with the SM, but also due to the fact that the under-abundant region allowed for pFIMP depends crucially on the WIMP annihilation/co-annihilation channels. We focus on these two aspects of pFIMP dynamics in this model dependent study.

The model we chose to illustrate consists of a fermion WIMP which is an admixture of a singlet and a doublet. The pFIMP is a scalar singlet having negligible Higgs portal interaction and a substantial WIMP-pFIMP conversion via Yukawa interaction. Both possibilities like fermionic WIMP and scalar WIMP at individual level have been studied before, but the pFIMP phenomenology and the detectability that we analyse here is new in the literature. We have scanned the parameter space of our model and identified the region which is most sensitive to both direct and indirect search experiments. We found that one specific mass hierarchy with heavier WIMP is favoured for direct detection. On the other hand, a large mass splitting between the WIMP and the second lightest dark sector particle is required for better pFIMP direct search. This is achieved when the WIMP mass lies in the vicinity of the Z-resonance region. Although low WIMP mass region is strongly constrained from the LEP data as well as as from LHC bound, allowed parameter space points are left in the Z-resonance region, albeit fine-tuned. Importantly, the WIMP being a fermion in this model, also helps to generate a significant loop-induced amplitude. We must note that our model is just one example that is conducive for pFIMP de-

tectability, while there exists a plethora of possibilities as outlined in the beginning of this work.

Collider searches for the WIMP component of this model have been discussed in the literature. The WIMP sector of this model can produce multilepton signal plus MET, thanks to the presence of a doublet. The limits from the current data leaves a large allowed parameter space of the model for signal discovery at the future sensitivities of LHC. The pFIMP on the other hand, can only be produced via WIMP loop and yield mono-X ($X = j, \gamma, Z, W, h$) signal via initial state radiation. WIMPs can also produce the same signal, but with larger cross-section. So pFIMP signal is likely to be submerged into the WIMP signal, having little or no consequence in the final state event numbers or distributions in this scenario.

The other crucial feature that WIMP-pFIMP set up provides, after addressing the correct relic density, is to have a small mass difference between the two DM components, around $\lesssim 10$ GeV, which however gets relaxed to some extent in one particular hierarchy of this model. But broadly we expect two DM signals (either in direct or in collider searches) in the same mass range. While this is very predictive in one hand, but disentangling them may be challenging. We plan to address these issues in a future analysis.

6.2 Real scalar pFIMP and Complex scalar WIMP

Introducing a lepton portal interaction, which connects DM directly to the SM lepton sector, improves the detection prospect of the WIMP, as well as the partner pFIMP. However, such possibilities are constrained strongly by the non-observation of lepton flavor-violating decays. Interestingly, this also makes it possible to probe such models in future low-energy experiments. In this section, we have tried to establish such connections and find parameter space which respects the limits from DM relic, direct, indirect, and lepton flavor violation (LFV). We also recast the constraints from di-lepton/di-tau plus missing energy signal at the LHC on our model and provide projections for HL-LHC and future lepton colliders. Although the LFV and collider limits mainly concern WIMPs, the parameter space for pFIMPs is also constrained due to its strong connection to WIMPs through DM relic density and detection prospects. The discussion in this chapter is based on Ref . [639].

6.2.1 Introduction

In this section, we explore a WIMP-pFIMP framework where the WIMP interacts with the SM sector through the lepton portal in addition to the usual scalar-portal interaction. In lepton portal DM models [633, 664–667], DM couples directly to a charged lepton and mediator. This kind of model has a rich phenomenology at the collider experiments, which will give rise to a unique signature. Not only that, these interactions also lead to lepton-flavor violating decays, which are absent in the SM. Thus, parameter space of such models can be constrained by low energy experiments, on the other hand, it is also possible to look for signals of this model in future low energy experiments as well. Consequently, we are interested in exploring the complementarity between LHC constraints and the limits set by lepton flavor violation. At the same time, we also look into the signal at the direct and indirect

detection experiments coming from such a scenario.

The plan of our work is as follows. In Section 6.2.2, we discuss our model. The constraints on our model from lepton flavor violation are taken into consideration in Section 6.2.3. In Section 6.2.4, the dark matter phenomenology involving WIMP-pFIMP and all the constraints from the direct and indirect searches are discussed. Finally, in Section 6.2.4, we recast LHC constraints on our model and then calculate projections at HL-LHC as well as future lepton colliders. We summarize our results in Section 6.2.5.

6.2.2 The Model

Our main motivation in this work, is to connect the lepton-flavor sector with the dark sector which can be enabled by lepton portal mechanism. In addition, we also want to explore the pFIMP regime, in a lepton portal DM model. Keeping these in mind we write the minimal Lagrangian in Eq . (6.31).

$$\begin{aligned}\mathcal{L} =& \mathcal{L}_{\rm SM} + \mu_H^2 H^\dagger H - \lambda_H (H^\dagger H)^2 + \frac{1}{2}|\partial_\mu \phi|^2 - \frac{1}{2}\mu_\phi^2 \phi^2 - \frac{1}{4!}\lambda_\phi \phi^4 + |\partial_\mu \Phi|^2 \\ &- \mu_\Phi^2 |\Phi|^2 - \lambda_\Phi |\Phi^* \Phi|^2 - \frac{1}{2}\mu_3 \left[\Phi^3 + (\Phi^*)^3\right] - \frac{1}{2}\lambda_{\phi \rm H} \phi^2 H^\dagger H - \lambda_{\Phi \rm H} |\Phi|^2 H^\dagger H \\ &- \frac{1}{2}\lambda_{\Phi\phi} |\Phi|^2 \phi^2 + \overline{\psi}\left[i\gamma^\mu \left(\partial_\mu + ig' \mathrm{Y} B_\mu\right) - m_\psi\right]\psi - \sum_\ell \mathrm{y}_\ell \overline{\psi} \ell_R \Phi + \text{h.c.}\,.\end{aligned} \tag{6.31}$$

In this context, one of the simplest approaches is to define the interaction terms that connect the SM fermions to the DM through charged dark sector particles. In a simplified scenario, this charged partner is coupled to the right-handed SM fermions (f_R) through a renormalizable interaction term, like, $\overline{\Psi} f_R \Phi$ where Ψ and Φ represent a vector-like Dirac fermion and a scalar, respectively. The Ψ could serve as a viable DM candidate if Φ carries SM-like charges, similar to SM fermions. Alternatively, Φ could be a DM candidate [664, 668], provided that Ψ is a charged Dirac fermion having SM hypercharge [666]. Crucially, the charged particle will ultimately decay into DM and SM fermions in both scenarios.

These kinds of interaction terms can influence a connection between SM flavor anomalies, flavor violating decays and DM phenomenology. Here, we only focused on the LFV decays, while other aspects will be addressed elsewhere. Introducing a new co-annihilating partner, such as a charged particle, may lead to an under-abundant parameter space, which could be resolved by introducing an additional DM component to account for the remaining relic density. Different types of multi-particle DM scenarios are possible, depending on the interactions between DM and SM particles, as well as DM-DM interactions. The most promising scenarios: WIMP-WIMP [300, 597], WIMP-FIMP [301, 313], and WIMP-pFIMP [305–307], among others. In this work, we focus exclusively on the WIMP-pFIMP scenario, which provides richer phenomenology than the WIMP-WIMP case, particularly in the presence of lepton portal interactions. The pFIMP does not directly couple to leptons and only interacts via the WIMP loop, which is comparatively suppressed relative to the WIMP. Nevertheless, a correlation can still be established between the parameter space permitted by LFV decay and the parameter space responsible for pFIMP regime.

Our model consists of two DM fields: a real scalar ϕ which transforms under $\mathcal{Z}_2$ and a complex scalar Φ is transformed under $\mathcal{Z}_3$. The dark sector is further extended by introducing a charged vector-like lepton ψ, also transformed under $\mathcal{Z}_3$, that interacts exclusively only with right-handed charged leptons (ℓ_R). The charges of dark fields under $\mathcal{Z}_2 \otimes \mathcal{Z}_3$ symmetry are shown in Table 6.4, and the SM extended

Dark Fields	$\mathcal{Z}_2$	$\mathcal{Z}_3$
ϕ	-1	$+1$
Φ	$+1$	ω/ω^2
ψ	$+1$	ω/ω^2

Table 6.4: Dark sector fields and their corresponding quantum numbers while the charge fermion has $\mathrm{U}(1)_{\mathrm{Y}}$ hypercharge, $\mathrm{Y} = -1$.

Lagrangian is written as,
where $g' = (2/v)\sqrt{m_Z^2 - m_W^2}$ is the $\mathrm{U}(1)_{\mathrm{Y}}$ gauge coupling. ψ[4] is a vector-like lepton (VLL) [632, 633, 664, 665] with weak hypercharge $\mathrm{Y} = -1$ and charged under $\mathcal{Z}_3$. For theoretical constraints on the model parameters, see the following [611].

6.2.3 Constraints on model parameters

The perturbative limit on the lepton portal coupling is $\mathrm{y}_\ell < \sqrt{4\pi}$ and $m_\psi > m_\Phi + m_e$ to ensure the stability of DM candidate Φ. Furthermore, the charged fermion is strongly constrained by the LEP [634–638], $m_\psi \gtrsim 103.5$ GeV. The other theoretical constraints (unitarity, perturbativity, vacuum stability) on the model parameters are available in the following references [302, 669]. Higgs invisible decay constraints are measured by ATLAS $\mathcal{B}(h \to \mathrm{inv}) < 0.107$ [460] and CMS $\mathcal{B}(h \to \mathrm{inv}) < 0.15$ [461] at 95% CL, applicable when $m_{\mathrm{DM}} \leq m_h/2$. The observed total decay width of the Higgs boson (based on indirect measurement) is $\Gamma_h = 3.2^{+2.4}_{-1.7}$ MeV [670], while the SM expectation is 4.1 MeV [497]. The loop-mediated decay of Z boson to WIMP is constrained by recent Z invisible decay width bound has come from various experiments like [36, 463, 671],

$$\Gamma_{\mathrm{Z}\to\mathrm{invisible}} < \begin{cases} 523 \pm 16 \text{ MeV} & (\mathrm{CMS})\,, \\ 503 \pm 16 \text{ MeV} & (\mathrm{LEP})\,, \\ 498 \pm 17 \text{ MeV} & (\mathrm{L3})\,. \end{cases} \tag{6.32}$$

Lepton flavor constraints

A stringent bound on the couplings of the DM particle and the heavy VLL appears from the measurements of the anomalous magnetic moments of leptons [222, 672–678].These processes are lepton flavor conserving in nature. Although the anoma-

[4]The source of origin of low energy lepton portal renormalizable interaction term, $\overline{\psi}\ell_R\Phi$, could be a dimension-5 effective operator $(C_\ell/\Lambda)\,\overline{\psi}H\ell_R\Phi$, where $\psi = (\psi^0\ \psi^-)^{\mathrm{T}}$ is a vector like Lepton doublet, and also transform similarly under $\mathcal{Z}_3$ like Φ. After EWSB, obtain a term like $\left(C_\ell v/\sqrt{2}\Lambda\right)\overline{\psi}\Phi\ell_R \equiv \mathrm{y}_\ell\overline{\psi}\Phi\ell_R$.

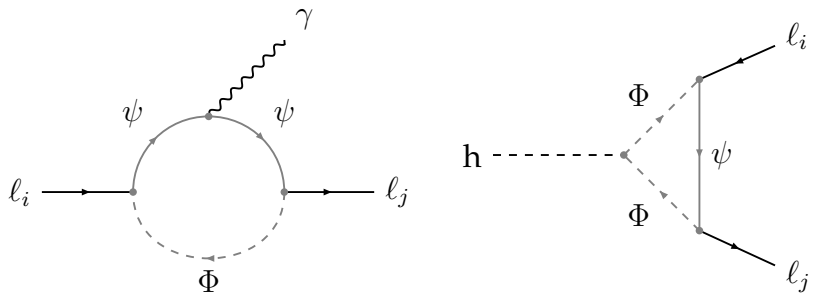

Figure 6.18: *Left*: Diagram contributing to $\ell_i \to \ell_j \gamma$. *Right*: Higgs boson decay to lepton pair, $h \to \ell_i \ell_j$.

lous magnetic dipole moment of electron ($\Delta a_e = g_e/2 - 1$) [27, 29, 679] is known precisely [221], SM prediction [191, 222] relies on the measurement of fine structure constant using the recoil velocity/frequency of atoms that absorb a photon. Currently, there is a 5.5σ discrepancy between the measurements using Rubidium-87 [219] and Cesium-133 [220].

$$\Delta a_e \equiv a_e^{\rm exp} - a_e^{\rm SM} = \begin{cases} (-8.8 \pm 3.6) \times 10^{-13}\ (-2.4\sigma) & ({\rm Cs}) \\ (+4.8 \pm 3.0) \times 10^{-13}\ (+1.6\sigma) & ({\rm Rb}) \end{cases} . \tag{6.33}$$

The anomalous magnetic moment of muon $a_\mu = g_\mu/2 - 1$ has been measured by BNL E821 and FNAL experiments yields a 4.2σ discrepancy [680] from the SM prediction,

$$\Delta a_\mu \equiv a_\mu^{\rm exp} - a_\mu^{\rm SM} = (2.49 \pm 0.48) \times 10^{-9} \quad [217, 681]. \tag{6.34}$$

Fig. 6.19 illustrates the allowed parameter space in the $m_\Phi - {\rm y}_\ell$ plane for the fla-

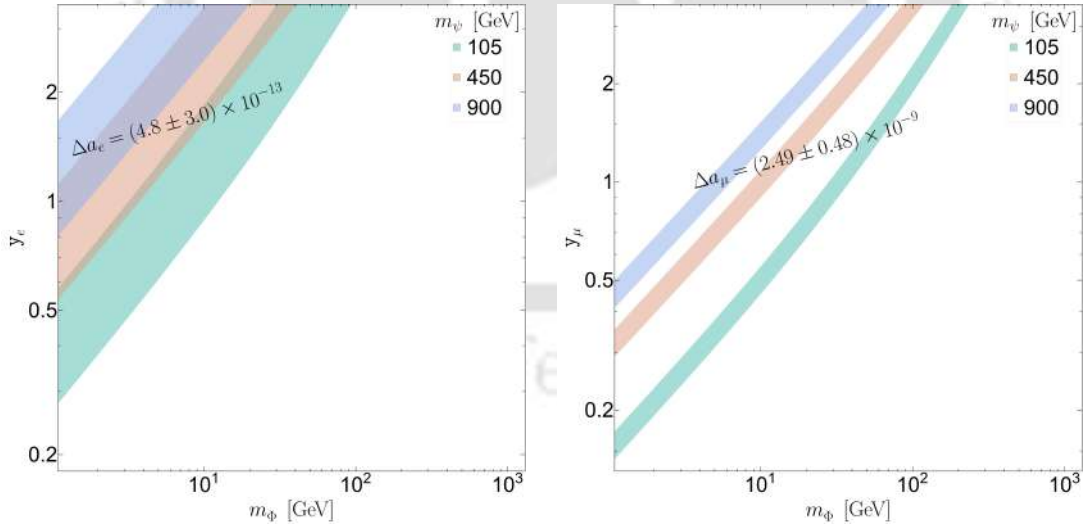

Figure 6.19: Figs. 6.19a and 6.19b represent the bounds on ${\rm y}_\ell - m_\Phi$ parameter space from Δa_e and Δa_μ measurements, respectively.

vor conserving quantities, namely lepton anomalous magnetic moment (Δa_ℓ). We mention that, these anomalies and their significant deviation from the SM expectations cannot be addressed in our analysis, where ${\rm y}_\ell \lesssim 0.1$ due to constraints from lepton-flavor violating decays, which will be discussed in detail. This limitation can

be addressed by further extensions of our model in the future. On the other hand, the anomalous magnetic moment of the tau lepton, $a_\tau = (g_\tau - 2)/2$, can act as a sensitive indicator of potential new physics [223, 224]. However, achieving a precise measurement of a_τ is considerably more challenging than for the magnetic moments of electrons and muons. In addition to the lepton flavor conserving processes, there are potential contributions to lepton flavor violating (LFV) decays, $\ell_i \to \ell_j \gamma$ with $i \neq j$ in our model. The most stringent limits on LFV decays come from $\mathcal{B}_{\mu\to e\gamma}$[5] followed by $\mathcal{B}_{\tau\to e\gamma}$ and $\mathcal{B}_{\tau\to\mu\gamma}$.

$$\begin{aligned}
\mathcal{B}_{\mu\to e\gamma} &< 3.1\times10^{-13}\ (90\%\ \text{C.L.})\ \ [225],\\
\mathcal{B}_{\tau\to e\gamma} &< 3.3\times10^{-8}\ (90\%\ \text{C.L.})\ \ [682],\\
\mathcal{B}_{\tau\to\mu\gamma} &< 4.2\times10^{-8}\ (90\%\ \text{C.L.})\ \ [683].
\end{aligned} \tag{6.35}$$

Fig . 6.18 show the Feynman diagrams contributing to lepton flavor conserving ($i = j$) and violating ($i \neq j$) processes. Fig . 6.19 illustrates the parameter space that can accommodate the anomalies Δa_e and Δa_μ, represented by different color shades according to mass of the mediator ψ. Fig . 6.20 illustrates the allowed parameter space constrained by the lepton flavor violating processes, represented by different color shades according to the WIMP mass. Figs . 6.20a to 6.20c, illustrate the allowed parameter space for the LFV processes $\mu \to e\gamma$, $\tau \to \mu\gamma$, and $\tau \to e\gamma$, respectively, within the experimental bounds (see Eq . (6.35)) in the $y_e - y_\mu$, $y_\mu - y_\tau$, and $y_e - y_\tau$ planes. The varying color shades represent different WIMP masses in each case.

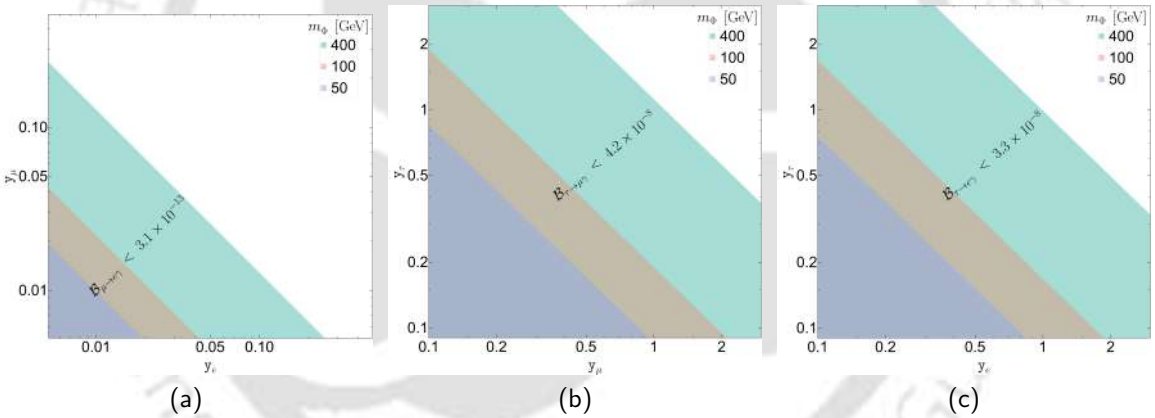

Figure 6.20: Figs . 6.20a to 6.20c represents the $\mu \to e\gamma$, $\tau \to \mu\gamma$ and $\tau \to e\gamma$, respectively. In the analysis, we have set the charged fermion mass as $m_\psi = 450$ GeV.

[5]MEG II claims to achieve a future sensitivity for the $\mu \to e\gamma$ branching ratio of 6×10^{-14} [226].

Higgs decay to lepton pairs

At the LHC, for a Higgs boson mass of 125 GeV, the observed upper limits on the branching fraction of its decay to lepton pairs, at 95% C.L. are given below:

$$\begin{aligned}
&\mathcal{B}_{h\to ee} < 3.0\times10^{-4} \quad [684]\,,\\
&\mathcal{B}_{h\to \mu\mu} < 2.6^{+1.3}_{-1.3}\times10^{-4} \quad [685]\,,\\
&\mathcal{B}_{h\to \tau\tau} < 6.0^{+0.8}_{-0.7}\times10^{-2} \quad [685]\,,\\
&\mathcal{B}_{h\to e\mu} < 4.4\times10^{-5} \quad [686]\,,\\
&\mathcal{B}_{h\to \mu\tau} < 1.5\times10^{-3} \quad [687]\,,\\
&\mathcal{B}_{h\to e\tau} < 2.0\times10^{-3} \quad [688]\,,
\end{aligned} \tag{6.36}$$

where $\mathcal{B}_{h\to\ell_i\ell_j} = \Gamma_{h\to\ell_i\ell_j}/\Gamma_h^{\rm total}$ and $\Gamma_h^{\rm total} = 4.1$ MeV [689, 690]. However, even the most stringent bound on $h \to e\mu$ is far less restrictive compared to the $\mu \to e\gamma$ constraint, hence they do not constrain our parameter spaces any further.

6.2.4 Dark Matter phenomenology

In the extended SM Lagrangian, as presented in Eq. (6.31), we have introduced three new particles ψ, Φ, and ϕ. The real scalar particle ϕ is absolutely stable, in the absence of its decay term owing to $\mathcal{Z}_2$ symmetry. Among the complex scalar and vector-like charged fermion, the lightest one will serve as a stable DM candidate, and the responsible symmetry is $\mathcal{Z}_3$ in this case. The corresponding charges for these particles under these symmetries transformations are provided in Table 6.4. Another key point to highlight is that a charged DM [65, 691–698] is heavily constrained by observations, and hence we do not consider the charged DM possibility in our context. Therefore, we always choose $m_\psi > m_\Phi + m_e$ to ensure that Φ remains a stable DM candidate. Finally, these two DM components (ϕ and Φ) would contribute to the total DM relic density. We emphasize that, the -Higgs-portal coupling of ϕ, $\lambda_{\phi \rm H}$ is taken 10^{-12}, in order to ensure pFIMP dynamics as discussed in [305, 306]. In the rest of the chapter, we exclusively consider this regime.

cBEQ and relic density

Let us assume CP conservation exists inside the dark sector. The coupled Boltzmann equations (cBEQ) for the two DMs, where $Y_{\rm w} = Y_\Phi + Y_{\Phi^*} + Y_{\psi^+} + Y_{\psi^-}$ and $Y_{\rm w}^{\rm eq} = Y_\Phi^{\rm eq} + Y_{\Phi^*}^{\rm eq} + Y_{\psi^+}^{\rm eq} + Y_{\psi^-}^{\rm eq}$, is

$$\begin{aligned}
\frac{dY_\phi}{dx} =& \frac{2\,\mathbf{s}}{x\,\mathcal{H}(x)}\left[\frac{1}{\mathbf{s}}\left(Y_h^{\rm eq} - Y_h^{\rm eq}\frac{Y_\phi^2}{Y_\phi^{\rm eq^2}}\right)\langle\Gamma\rangle_{h\to\phi\,\phi} + \left(Y_{\rm SM}^{\rm eq^2} - Y_{\rm SM}^{\rm eq^2}\frac{Y_\phi^2}{Y_\phi^{\rm eq^2}}\right)\langle\sigma v\rangle_{\rm SM\,SM\to\phi\,\phi}\right.\\
&\left. + \left(Y_{\rm w}^2 - Y_{\rm w}^{\rm eq^2}\frac{Y_\phi^2}{Y_\phi^{\rm eq^2}}\right)\langle\sigma v\rangle_{\rm conv}^{\rm eff}\right]\,,
\end{aligned} \tag{6.37}$$

$$\frac{dY_{\rm w}}{dx} = -\frac{\mathbf{s}}{x\,\mathcal{H}(x)}\left[\left(Y_{\rm w}^2 - Y_{\rm w}^{\rm eq^2}\right)\langle\sigma v\rangle_{\rm ann}^{\rm eff} + \frac{1}{2}\left(Y_{\rm w}^2 - Y_{\rm w}Y_{\rm w}^{\rm eq}\right)\langle\sigma v\rangle_{\rm semi}^{\rm eff} + \left(Y_{\rm w}^2 - Y_{\rm w}^{\rm eq^2}\frac{Y_\phi^2}{Y_\phi^{\rm eq^2}}\right)\langle\sigma v\rangle_{\rm conv}^{\rm eff}\right]\,,$$

where $Y_i = n_i/\mathbf{s}$, n_i is the number density of i^{th} particle, $\mathbf{s}$ is the entropy density, and other terms carry the usual meaning.

$$\langle\sigma v\rangle^{\text{eff}}_{\text{ann}} = \langle\sigma v\rangle_{\Phi\ \Phi^*\to \text{SM}\ \text{SM}} \frac{n^{\text{eq}^2}_{\Phi}}{n^{\text{eq}^2}_{\text{w}}} + \langle\sigma v\rangle_{\psi^-\ \psi^+\to \text{SM}\ \text{SM}} \frac{n^{\text{eq}^2}_{\psi}}{n^{\text{eq}^2}_{\text{w}}} + 2\langle\sigma v\rangle_{\psi^-\Phi^*\to \text{SM}\ \text{SM}} \frac{n^{\text{eq}}_{\psi} n^{\text{eq}}_{\Phi}}{n^{\text{eq}^2}_{\text{w}}}\,, \tag{6.38}$$

$$\langle\sigma v\rangle^{\text{eff}}_{\text{semi}} = 2\langle\sigma v\rangle_{\psi^-\ \Phi\to\Phi^*\ \text{SM}} \frac{n^{\text{eq}}_{\psi} n^{\text{eq}}_{\Phi}}{n^{\text{eq}^2}_{\text{w}}} + 2\left(\langle\sigma v\rangle_{\Phi\ \Phi\to\psi^+\ \text{SM}} + \langle\sigma v\rangle_{\Phi\ \Phi\to\Phi^*\ \text{SM}}\right) \frac{n^{\text{eq}^2}_{\Phi}}{n^{\text{eq}^2}_{\text{w}}}\,, \tag{6.39}$$

$$\langle\sigma v\rangle^{\text{eff}}_{\text{conv}} = \langle\sigma v\rangle_{\Phi\ \Phi^*\to\phi\ \phi} \frac{n^{\text{eq}^2}_{\Phi}}{n^{\text{eq}^2}_{\text{w}}}\,, \tag{6.40}$$

where $\text{SM} = \{h,\ \text{W}^{\pm},\ \text{Z},\ \text{leptons},\ \text{quarks}\}$. The total relic density is given by, in terms of DM yields as the solution of cBEQ,

$$\Omega_{\text{DM}}\text{h}^2 = 2.744\times 10^8 \left[m_{\Phi} Y_{\text{w}} + m_{\phi} Y_{\phi}\right]_{x\to\infty}\,. \tag{6.41}$$

We numerically solved the cBEQ using `micrOMEGAs` [513] after importing the model generated with `FeynRules` [699, 700]. The results of the cBEQ solution and the relic allowed parameter space are illustrated in Figs . 6.22, 6.23 and 6.25.

Direct detection

DM-nucleus scattering is one of the crucial methods for detecting dark matter (DM). Experiments such as XENON1T [578], XENONnT [358], and LUX-ZEPLIN [514] have set an upper limit on the DM-nucleon scattering cross-section, while PandaX-xT [516] and DARWIN/XLZD [517] provides projected limits. In our model, both DMs are weakly coupled with the visible sector and might have a possibility of detection in future direct detection experiments. In Fig . 6.21, we represent the possible Feynman diagram of DM-nucleon scatterings.

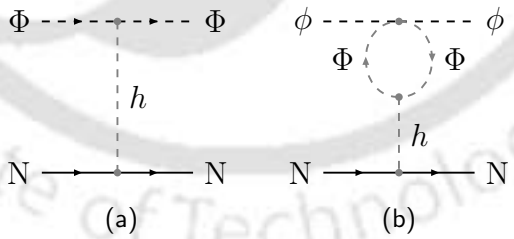

Figure 6.21: The Feynman diagrams are corresponding to the direct detection of WIMP (8.6) and pFIMP (7.2f).

WIMP

The complex scalar WIMP Φ interacts with the target nucleus through a Higgs-mediated process shown in Fig . 8.6, enabled by the Higgs portal interaction. In the WIMP-pFIMP scenario, we use the effective WIMP-nucleon cross-section, which is, $\sigma^{\text{eff}}_{\Phi\text{N}} = (\Omega_{\Phi}\text{h}^2/\Omega_{\text{DM}}\text{h}^2)\sigma^{\text{SI}}_{\Phi\text{N}}$ where $\sigma^{\text{SI}}_{\Phi N}$ is the spin-independent (SI) WIMP-nucleon scattering cross-section. In Fig . 6.22, we illustrate the relic-allowed parameter space in the $m_{\Phi} - \sigma^{\text{eff}}_{\Phi\text{N}}$ plane, with the color bar representing the variation of the parameters as described above the color bar, while the remaining parameters are detailed

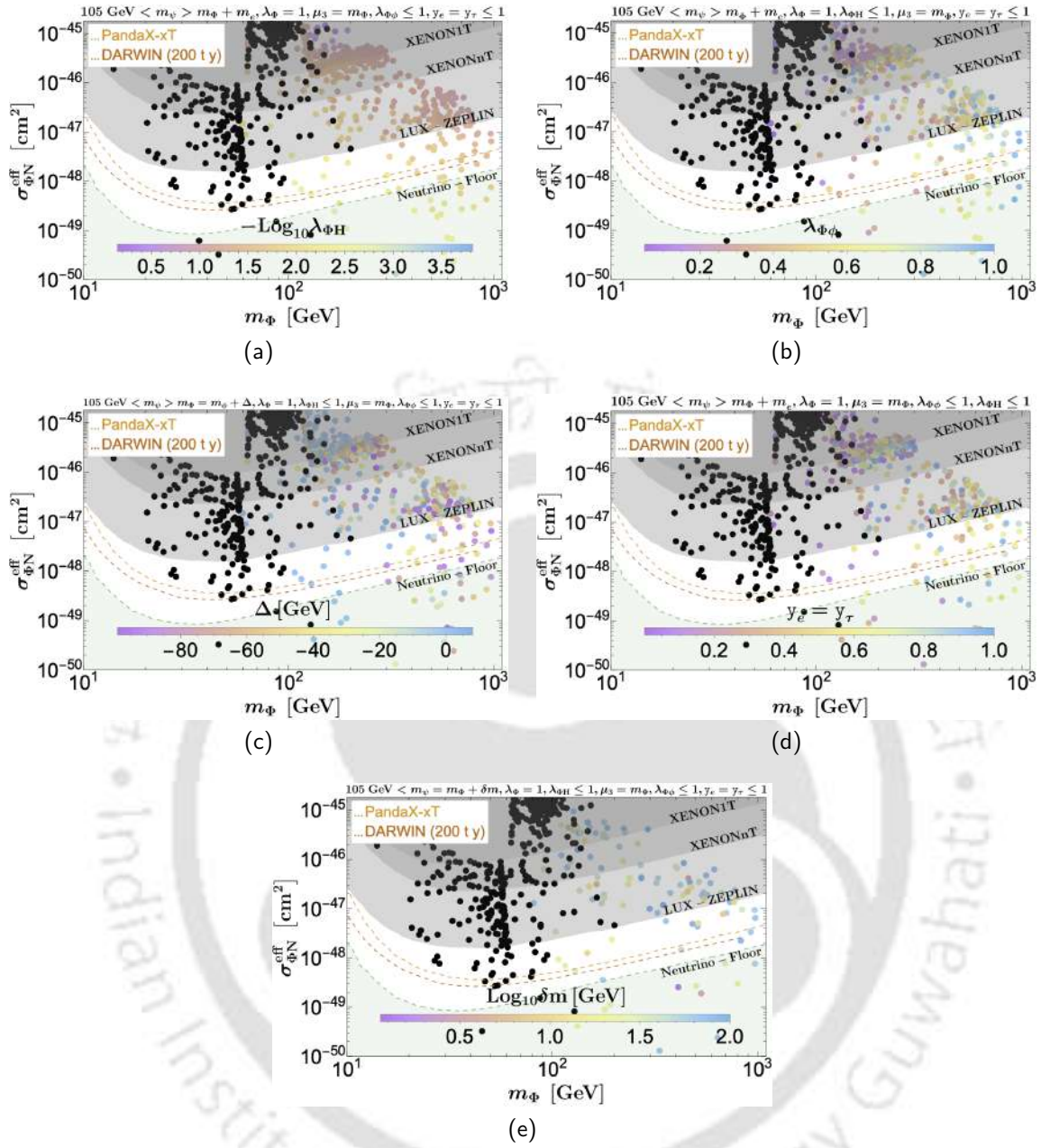

Figure 6.22: In Figs. 6.22a to 6.22e, the relic-allowed parameter space for WIMPs is shown in the $m_\Phi - \sigma^{\rm eff}_{\Phi N}$ plane. The grey-shaded regions are excluded by the observed limits from XENON1T, XENONnT, and LUX-ZEPLIN, while the projected limits from PandaX-xT (orange) and DARWIN/XLZD (brown) are represented by dashed lines. In all plots, we have used $\lambda_{\phi H} = 10^{-12}$, $y_\mu = 10^{-3}$ and the black points are ruled out by the LFV ($\mu^+ \to e^+\gamma$) constraint.

in the figure's inset. In this plane, we also illustrate the LFV constraint, where the process $\mu^+ \to e^+\gamma$ provides the most stringent limit, and the black points violate this limit. Other LFV limits can be ignored as they are less stringent in comparison to this.

In Figs. 6.22a to 6.22e, we show the dependency of $\lambda_{\Phi H}$, $\lambda_{\Phi\phi}$, Δ, $y_e = y_\tau$ and δm, respectively in the relic and DD, through the pastel color-bar. Here, we have defined, $\Delta = m_\Phi - m_\phi$ and $\delta m = m_\psi - m_\Phi$. Below the Higgs resonance, most of the region is excluded by the LFV limit, although it remains viable under the DM relic constraint due to the large lepton portal coupling, and is allowed by the SI DD constraint for small values of $\lambda_{\Phi H}$, regardless of $\lambda_{\Phi\phi}$. In the low mass regime, i.e. below Higgs

mass, the DM relic is adjusted by the other processes that are not involved with $h\Phi\Phi^*$ vertex, which is reflected in Fig . 6.22a. Above the Higgs mass, ψ mass also gradually increases following $m_\psi = m_\Phi + m_e$, hence, the LFV bound is much more relaxed. In this mass regime, $\lambda_{\Phi\phi}$ coupling plays a crucial role in DM relic density, as we see in Fig . 6.22b. However, the DM-DM conversion plays an important role in the DM relic for both DM mass hierarchical scenarios, mostly through the four-point interaction with vertex factor $\lambda_{\Phi\phi}$. In Fig . 6.22c we have shown the effect of DM mass hierarchy through $\Delta = m_\Phi - m_\phi$. If $m_\Phi > m_\phi$, then $\Phi \to \phi$ conversion is more efficient compared to the opposite. For positive Δ, around the Higgs mass, $\Phi \to \phi$ conversion makes the Φ under abundant and ϕ mostly contributes to the total DM relic. This is also true for the higher mass regimes, but all kinds of contributions are feasible. In Fig . 6.22d we have shown the variation of the lepton portal coupling ($\mathrm{y}_e = \mathrm{y}_\tau$) keeping other couplings fixed and $\mathrm{y}_\mu = 10^{-3}$. These couplings are more relevant for a minute Higgs portal coupling to avoid the DD bound. Finally, in Fig . 6.22e, we show the variation of the mass difference between WIMP and charged fermion by δm and represent it through the pastel color bar. This parameter space will be useful for collider analysis.

pFIMP

The real scalar pFIMP (ϕ) interacts with the target nucleus through the WIMP loop and Higgs-mediated process shown in Fig . 7.2f, enabled by the WIMP-Higgs portal and WIMP-pFIMP interactions. Here, we are using the SI effective pFIMP-nucleon cross-section, which is $\sigma^{\rm eff}_{\phi \rm N} = (\Omega_\phi \mathrm{h}^2/\Omega_{\rm DM}\mathrm{h}^2)\sigma^{\rm SI}_{\phi \rm N}$. The pFIMP-nucleon scattering is

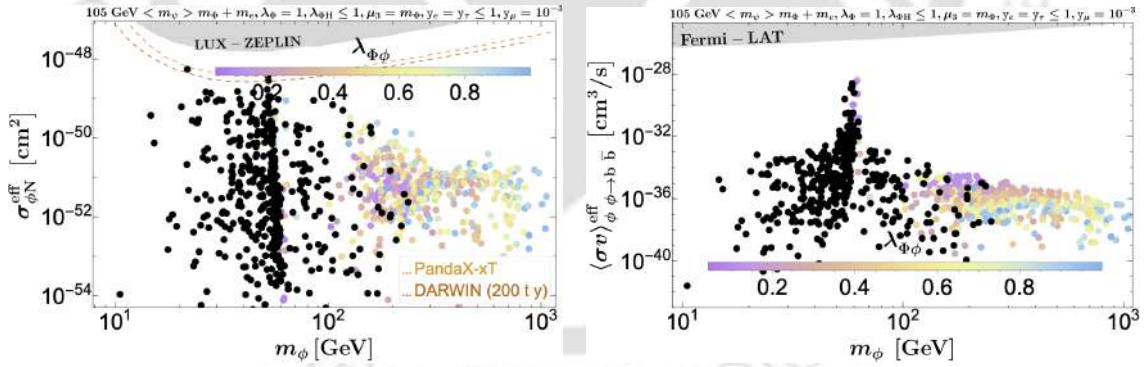

Figure 6.23: pFIMP Relic allowed parameter space in $m_\phi - \sigma^{\rm eff}_{\phi \rm N}$ and $m_\phi - \langle\sigma v\rangle^{\rm eff}_{\phi\phi\to b\bar{b}}$ plane. In all plots, we have used $\lambda_{\phi \rm H} = 10^{-12}$ and the black points are ruled out by the $\mu^+ \to e^+\gamma$ LFV constraint, see Eq . (6.35).

only possible via a 1-loop mediated process, see Fig . 7.2f. This $\sigma^{\rm SI}_{\phi \rm N}$ cross-section predominantly depends on $\lambda_{\Phi \rm H}$ and $\lambda_{\Phi\phi}$, while the effect of the DM mass in the loop is minimal as it only contributes through logarithms. We already have discussed the $\lambda_{\Phi\phi}$ effect in DM relic in Fig . 6.22b, where we have shown the correlation between $\lambda_{\Phi\phi}$ and $\lambda_{\Phi \rm H}$, which is inversely correlated to each other to adjust the DM relic and respect the observed DD limit. The use of a small $\lambda_{\Phi \rm H}$ value allows the WIMP to stay within the current DD limit. However, this also increases the relic of the WIMP, which is then adjusted by the enhancement of $\lambda_{\Phi\phi}$. However, this choice does not impact $\sigma^{\rm SI}_{\phi \rm N}$, and this effect is more noticeable at higher mass ranges. In Figure 6.23a,

the relic-allowed parameter space is depicted in the $m_\phi - \sigma^{\rm eff}_{\phi N}$ plane. As these points depend on the effective relic contribution of pFIMP, the scanning behavior relies on the characteristics of WIMP. However, around the Higgs resonance, some points fall within the direct detection constraint, while above it, the parameter space is mostly open for future detection.

Indirect detection

The AMS-02 experimental data [701, 702] on cosmic ray positrons shows that at high energies, the primary source of positrons is either dark matter annihilation or other astrophysical sources. Therefore, using the AMS-02 data on positron flux sets an upper limit on the rate of dark matter annihilation to electron-positron pairs with a branching ratio of 100%. The gamma-ray observations of Milky Way dSphs from six years of Fermi Large Area Telescope (Fermi-LAT) data [521, 703, 704] reported no significant detections. They presented upper limits on the DM self-annihilation cross-section for 15 dwarf spheroidal satellite galaxies (dSphs) and projected sensitivity for 45 dSphs with 15 years of observation [705]. The DM semi-annihilation cross-section is constrained by gamma-ray observations from Fermi-LAT [519], as well as the projected limits from H.E.S.S [706] and CTA [707].

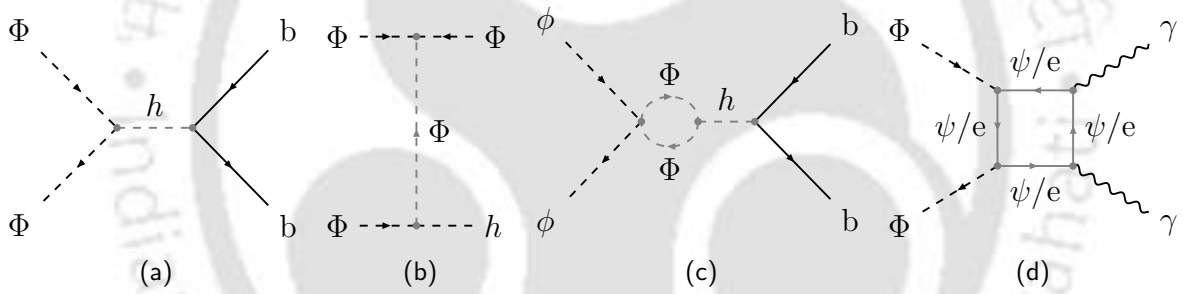

Figure 6.24: The Feynman diagrams are related to the indirect detection of WIMP and pFIMP.

In this work, the key processes depicted in Fig. 6.24 play a crucial role in establishing the limit on the self-annihilation cross-section of WIMPs and pFIMPs, as well as on the semi-annihilation of WIMPs. In Figs. 6.23b and 6.25, we have represented the relic allowed parameter space. Some points are excluded by indirect limits on DM self and semi-annihilation cross-sections from different indirect observations. Here, we use the effective DM annihilation cross-section, which is the DM annihilation cross-section multiplied by the normalized effective DM number density. In Figs. 6.25a to 6.25d, we have represented the relic allowed parameter space in $m_\Phi - \langle\sigma v\rangle^{\rm eff}_{\Phi\Phi^*\to e^-e^+}$, $m_\Phi - \langle\sigma v\rangle^{\rm eff}_{\Phi\Phi^*\to b\bar{b}}$, $m_\Phi - \langle\sigma v\rangle^{\rm eff}_{\Phi\Phi^*\to\gamma\gamma}$, and $m_\Phi - \langle\sigma v\rangle^{\rm eff}_{\Phi\Phi\to\Phi^* h}$ plane, respectively.

WIMP

In Fig. 6.25a, the indirect bound on the DM annihilation to electron-positron pair, using AMS-02 data, excludes some of the relic parameter space in below Higgs mass regime. This is because the larger lepton portal coupling is required to achieve the correct relic. In this regime, the Higgs portal processes are always suppressed. A similar explanation is also applicable to other processes, as shown in Fig. 6.25. In

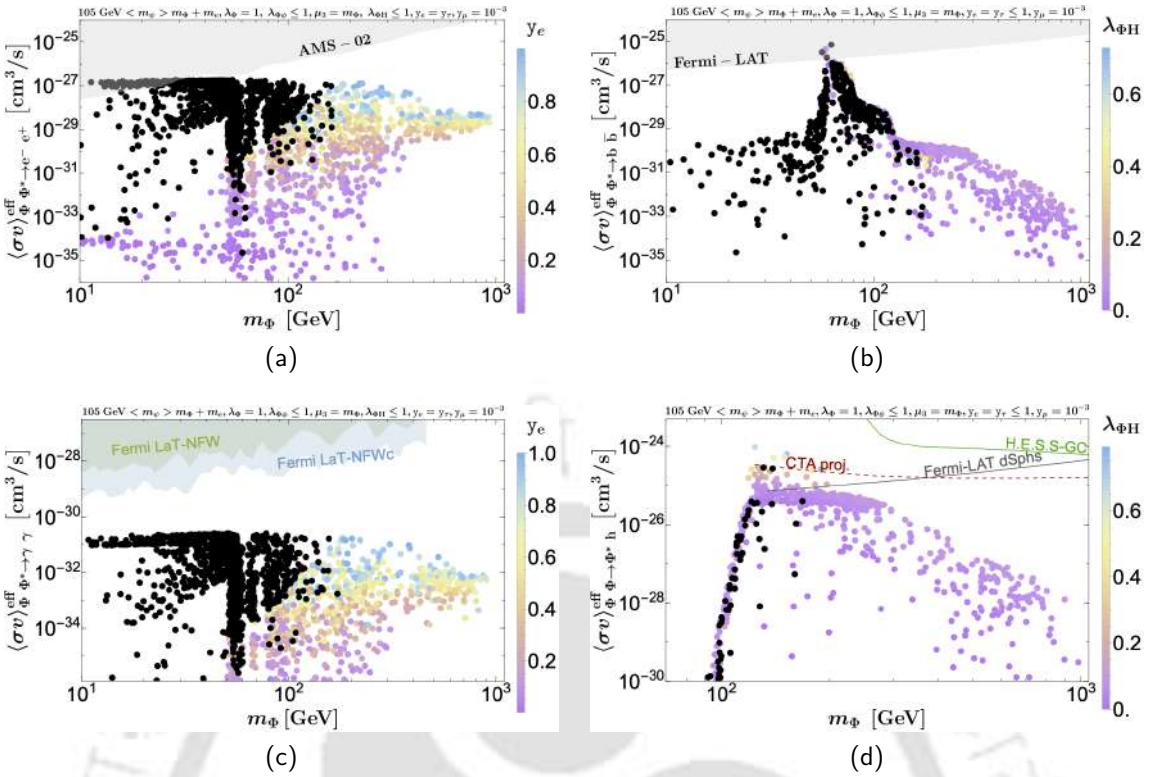

Figure 6.25: In this figure, we represent the relic allowed parameter space. Figs. 6.25a and 6.25b show the exclusion region from AMS-02 and Fermi-LAT limit on WIMP annihilation to electron and bottom pair, respectively. Fig. 6.25c represents the exclusion region using data from Fermi-LAT and Planck, indicated by different color shades. We're narrowing down our parameter space for WIMP semi-annihilation in Fig. 6.25d using H.E.S.S, Fermi-LAT, and CTA data. In all plots, we have used $\lambda_{\phi H} = 10^{-12}$, and the black points are ruled out by the LFV constraint $\mu^+ \to e^+\gamma$, as shown in Eq. (6.35).

Fig. 6.25b, the Higgs resonance regime is excluded by the Fermi-LAT data on DM annihilation to the bottom pair. Additionally, there is a stringent limit from WIMP annihilation into photon pairs based on Fermi-LAT observations. However, this does not constrain the parameter space (Fig. 6.25c), as the process is only possible through 1-loop box diagrams (Fig. 6.24d). Finally, in Fig. 6.25d, some of the WIMP parameter space is also constrained, and near Higgs mass, some points are excluded by the Fermi-LAT, CTA, and H.E.S.S limit on the WIMP semi-annihilation to the Higgs.

pFIMP

The pFIMP annihilation occurs exclusively through a 1-loop mediated process, as shown in Fig. 7.2g. In the case of pFIMPs, most parameter space remains viable, except near the Higgs resonance region. In this area, certain points are excluded due to a significant resonance enhancement of the cross-section, despite the presence of loop suppression, as illustrated in Fig. 6.23b. Alternative indirect detection constraints on pFIMP annihilation and semi-annihilation become ineffective due to the fact that the associated processes are suppressed by loop-level interactions where the 1-loop processes are $\phi\ \phi \to e^-\ e^+$ and $\phi\ \phi \to \phi\ \mathrm{h}$, and the 2-loop process is $\phi\ \phi \to \gamma\ \gamma$.

Sensitivity at collider experiments

In this section, we study the collider sensitivity of the DM candidates. DM searches at colliders are primarily done via missing energy (at Lepton colliders) or missing transverse energy (primarily at Hadron colliders) signals in association with visible particles. Typical DM searches are done concerning mono-X (X = γ, Z, h, j) signal where DM is produced in association with a visible species (X, here). However, such signatures are subjected to huge background contamination, especially at hadron colliders where the hadronic activities are indomitable. Even at lepton colliders, the large SM neutrino background hinders the signal extraction to a great extent. In our model, the possibility of WIMP detection is greatly enhanced by the presence of lepton portal interactions. The lepton portal opens up the di-lepton (also, di-tau) signal possibility, which brings into play a wide range of kinematic observables, aiding in better discrimination of the DM signal from the SM background. Due to the absence of tree-level interaction with the visible sector, pFIMP detection at colliders is possible only through WIMP loop-mediated processes and, hence, always suppressed. In the following sections, we explore the features of di-lepton/di-tau searches at the LHC runs and its possible manifestation at proposed future lepton colliders.

Recasting the LHC limits

Most dark matter searches at the LHC focus on signatures predicted by the Minimal Supersymmetric Standard Model (MSSM), a popular extension of the Standard Model. In the MSSM, supersymmetry (SUSY) introduces new particles, the lightest of which, often a neutralino, serves as a dark matter candidate. These searches primarily look for missing transverse energy (MET) alongside other SUSY particles like squarks, sleptons or gluinos, which could decay into Standard Model particles and dark matter. However, the downside to this strategy is that this renders the analysis to cater only to a specific model. The common practice in such scenarios is to recast the existing LHC analyses in the context of the concerned BSM model. In our case, we recast the LHC di-lepton + MET signal studied at LHC experiments. The process is shown in Fig . 6.27a. Regarding the di-tau signal, τ tagging is usually done concerning the hadronic decay mode of τ lepton (τ decay to pions and neutrino), which emerge as τ jets. The lepton decay mode of τ is disguised as lepton + MET signals and hence is difficult to segregate in processes in which missing particles are already present. However, the hadronic τ tagging turns out to be a strenuous task at the LHC as the light jets (g, u, d, s, c jets), which are omnipotent at the hadron collider, can mimic the τ jets to some extent. This problem is aggravated by the fact that the τ jets emerge from EW processes, whereas the light jets dominantly appear from QCD backgrounds having large cross-sections. Hence, we restrict ourselves to the di-lepton signal only. We recast the ATLAS slepton pair decay to di-lepton and neutralinos (which appear as MET) at 13 TeV LHC at an integrated luminosity of 139 fb^{-1} [708]. The model implementation is done using `FeynRules`. The MC events are generated in `MG5_aMC` [709] and the events are showered using `Pythia8` [710]. The showered events are fed into `CheckMATE2` [711] (build upon `Delphes3` [712] and `Fastjet3` [713–715]). `CheckMATE2` uses CL$_s$ method [716] to determine the 95% C.L. exclusion limits. The events are generated at different (m_ψ, m_Φ) benchmarks. The 95% C.L. exclusion limit is shown in Fig . 6.26. Event selections are made

using the following selection cuts: Opposite sign leptons, $p_T^{\ell\ell} > 25$ GeV, $M_{\ell\ell} > 25$ GeV and $N_b = 0$, where $p_T^{\ell\ell}$ is the vector sum of the p_T of the leptons, $M_{\ell\ell}$ is the invariant mass of the leptons and N_b is the number of b-jets. The signal regions are defined in Table 6.5.

Different flavor leptons, $n_j = 0$	Same flavor leptons, $n_j = 0$
$M_{\ell\ell} > 100$ GeV	$M_{\ell\ell} > 121.2$ GeV
$\not{E}_T > 110$ GeV	$\not{E}_T > 110$ GeV
$\not{E}_T^{sig} > 10\sqrt{\text{GeV}}$	$\not{E}_T^{sig} > 10\sqrt{\text{GeV}}$
$m_{T2} > 100$ GeV	$m_{T2} > 100$ GeV
Different flavor leptons, $n_j = 1$	**Same flavor leptons, $n_j = 1$**
$M_{\ell\ell} > 100$ GeV	$M_{\ell\ell} > 121.2$ GeV
$\not{E}_T > 110$ GeV	$\not{E}_T > 110$ GeV
$\not{E}_T^{sig} > 10\sqrt{\text{GeV}}$	$\not{E}_T^{sig} > 10\sqrt{\text{GeV}}$
$m_{T2} > 100$ GeV	$m_{T2} > 100$ GeV

Table 6.5: Signal regions for ATLAS 13 TeV 139 fb^{-1} recast. Here, n_j is the number of light jets, $\not{E}_T$ is the MET, $\not{E}_T^{sig}$ is the MET significance defined as $\not{E}_T/\sqrt{H_T}$ where H_T is the scalar sum of p_T of visible particles and m_{T2} is the stranverse mass [445–447, 717].

A similar analysis is repeated for HL-LHC 14 TeV 3000 fb^{-1} using `CheckMATE2` projection card `dilepton_HL`. The signal regions are defined to be same as [718]. The 95% C.L. exclusion limit for the HL-LHC projection is shown in Fig. 6.26. We observe that the exclusion limits almost double to that of the LHC 13 TeV case.

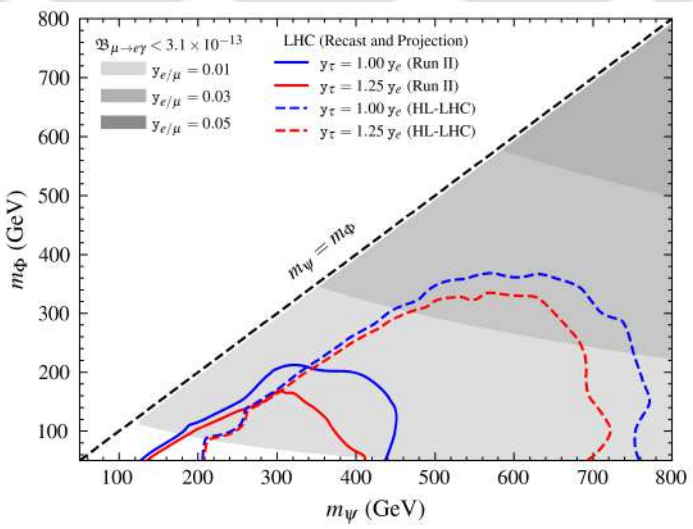

Figure 6.26: Bounds on $m_\psi - m_\Phi$ plane. The colored lines bound the closed region disallowed by *Solid*: Recast of ATLAS dilepton + MET search (13 TeV, 139 fb^{-1}) *Dashed*: Projection of dilepton + MET search at HL-LHC (14 TeV, 3000 fb^{-1}). The grey shaded region corresponds to the parameter space allowed from the LFV μ decay for different $y_{e/\mu}$ (y_τ arbitrary). The region above each shade is allowed indefinitely for that shade. $m_\psi < m_\Phi$ is disallowed from on-shell production of ψ and is separated by the dashed black line.

Search at future lepton colliders

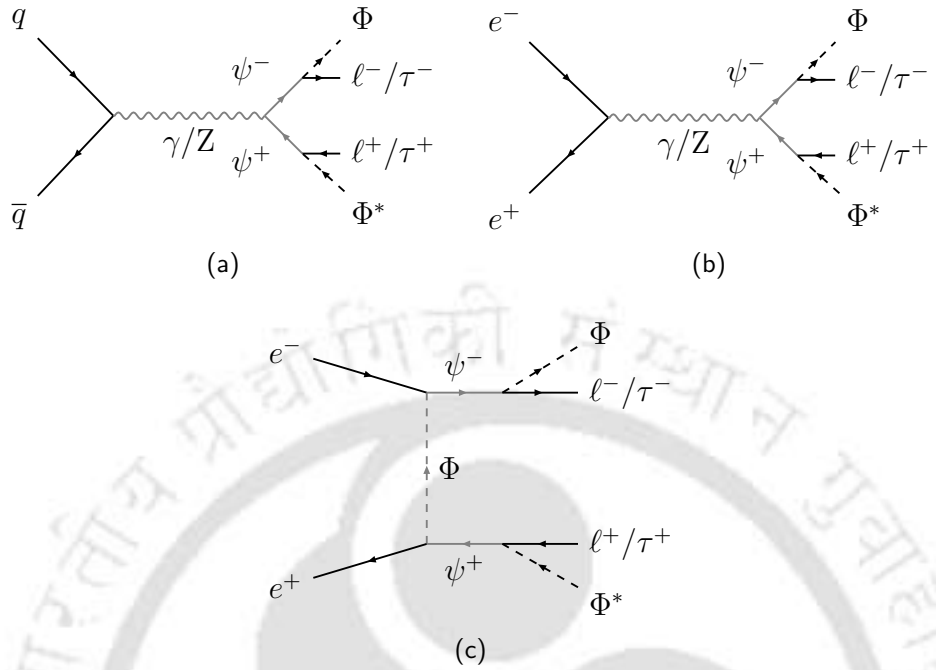

Figure 6.27: Feynman diagrams 6.27a (6.27b, 6.27c) correspond to di-lepton/di-tau + $\not{E}_T(\not{E})$ signal at the LHC (ILC).

The dilepton signal processes corresponding to WIMP production at lepton colliders are shown in Fig. 6.27. The choice of lepton collider has a 3-fold justification. Firstly, the near-absence of hadronic activities at lepton colliders provides a cleaner environment for the study of missing energy signals. The reduced QCD backgrounds ensure lesser contamination of τ jets from light QCD jets. Secondly, the lepton portal connection of the WIMP opens up a t-channel possibility (as shown in Fig. 6.27c), where the lepton portal coupling explicitly enters the production cross-section. However, at low centre-of-mass (CM) energies, the s-channel will dominate, and the effect of the t-channel will be subdued[6]. Thirdly, since lepton colliders have a definite CM energy of the hard processes, this allows us to introduce the variable, missing energy ($\not{E}$), apart from MET. This variable is significant as this encodes information about the mass of the DM and the VLL. This is illustrated for di-lepton/di-tau + $\not{E}$ signal in Fig. 6.28.

We perform the analysis at the ILC ($\sqrt{s} = 1$ TeV). For the di-lepton signal, we choose two opposite sign leptons. We further choose events with no jets. The signal processes are $\ell\ell\Phi\Phi$, $\ell\tau_\ell\Phi\Phi$ and $\tau_\ell\tau_\ell\Phi\Phi$ where, τ_ℓ is the leptonic τ decay products. The relevant SM backgrounds are $\ell\ell\nu\nu$, $\ell\tau_\ell\nu\nu$, $\tau_\ell\tau_\ell\nu\nu$ arising from hard processes like WW, ZZ, $\ell\ell Z$, $\nu\nu Z$, etc. and $\tau_\ell\tau_\ell$ (fully leptonic decay mode of τ pair production). Similarly, for the di-tau signal, we choose two τ jets with no additional leptons or jets in the event. The tagging efficiency of τ jets is 60%, and the efficiency of mistagging a light jet as τ jet is 1%. The signal process is $\tau_h\tau_h\Phi\Phi$, where τ_h is the hadronic tau decay product (τ jet). The relevant SM backgrounds are $\tau_h\tau_h\nu\nu$ arising from hard processes like WW, ZZ, $\tau\tau Z$, $\nu\nu Z$, etc. and $\tau_h\tau_h$ (fully hadronic decay mode

[6]Multi-TeV muon colliders can be better setups to observe significant contributions from the t-channel.

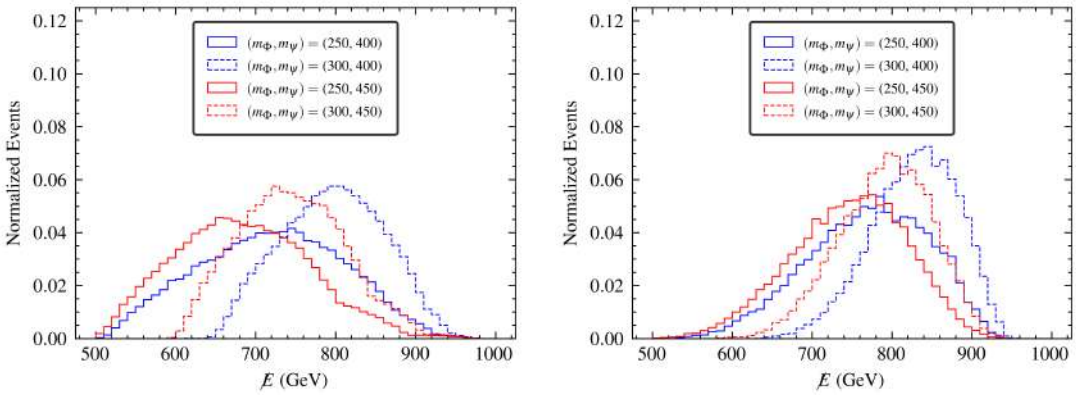

Figure 6.28: Missing energy ($\not{E}$) distributions for di-lepton (left) and di-tau (right) signals for different (m_ψ, m_Φ) benchmarks.

of τ pair production). Contribution to the background from light jet final states is found to be negligible and hence not considered. The relevant kinematic variable distributions for signal and background processes are shown in Fig . 6.29.

The signal and background cross-sections corresponding to the di-lepton and di-tau signal are shown in Table 6.6. For segregation of the signal from the background, we implement the following subsequent cuts, guided by the distributions in Fig . 6.29:

- $\mathcal{C}_1 : M_{\ell\ell}/M_{\tau\tau} > 100$ GeV,
- $\mathcal{C}_2 : \not{E} > 500$ GeV,
- $\mathcal{C}_3 : \Delta R_{\ell\ell}/\Delta R_{\tau\tau} < 3$.

Here, $M_{\ell\ell}$ ($M_{\tau\tau}$) is the invariant mass of the lepton (τ jet) pairs. The variable $\Delta R_{\ell\ell}$ ($\Delta R_{\tau\tau}$) is the distance between the leptons (τ jets) on the detector (η, ϕ) plane. The cuts are chosen identically for both signal processes. The cross-sections prior and posterior to the cuts are tabulated in Table 6.6. Choosing an invariant mass cut,

Signal and Background Processes	σ_0 (in fb)	σ_1 (in fb)	σ_2 (in fb)	σ_3 (in fb)
Signal: $\ell\ell\Phi\Phi$, $\ell\tau_\ell\Phi\Phi$, $\tau_\ell\tau_\ell\Phi\Phi$	33.37	26.68	26.67	19.93
$\tau_\ell\tau_\ell$	8.92	8.22	6.36	0.09
$\tau_\ell\tau_\ell\nu\nu$	2.60	0.88	0.78	0.07
$\ell\tau_\ell\nu\nu$	32.16	26.72	14.04	5.74
$\ell\ell\nu\nu$	249.94	184.49	64.54	43.83
Background (Total)	293.62	220.31	85.72	49.73

Signal and Background Processes	σ_0 (in fb)	σ_1 (in fb)	σ_2 (in fb)	σ_3 (in fb)
Signal: $\tau_h\tau_h\Phi\Phi$	1.14	0.90	0.90	0.66
$\tau_h\tau_h$	16.21	16.07	3.29	0.03
$\tau_h\tau_h\nu\nu$	5.20	2.50	1.75	0.58
Background (Total)	21.41	18.57	5.04	0.61

Table 6.6: Cross sections following subsequent cuts for di-lepton signal, including leptonic τ decays (*top*) and di-tau (hadronic) signal (*bottom*). σ_0, σ_1, σ_2 and σ_3 are the cross section post sequential cuts, $\mathcal{C}_1$, $\mathcal{C}_2$ and $\mathcal{C}_3$ respectively. The signal correspond to the benchmark: $m_\psi = 400$ GeV, $m_\Phi = 250$ GeV, $\mathrm{y}_e = \mathrm{y}_\mu = \mathrm{y}_\tau = 0.01$.

$M_{\ell\ell}/M_{\tau\tau} > 100$ GeV wipes out backgrounds where the leptons/τ jets are products

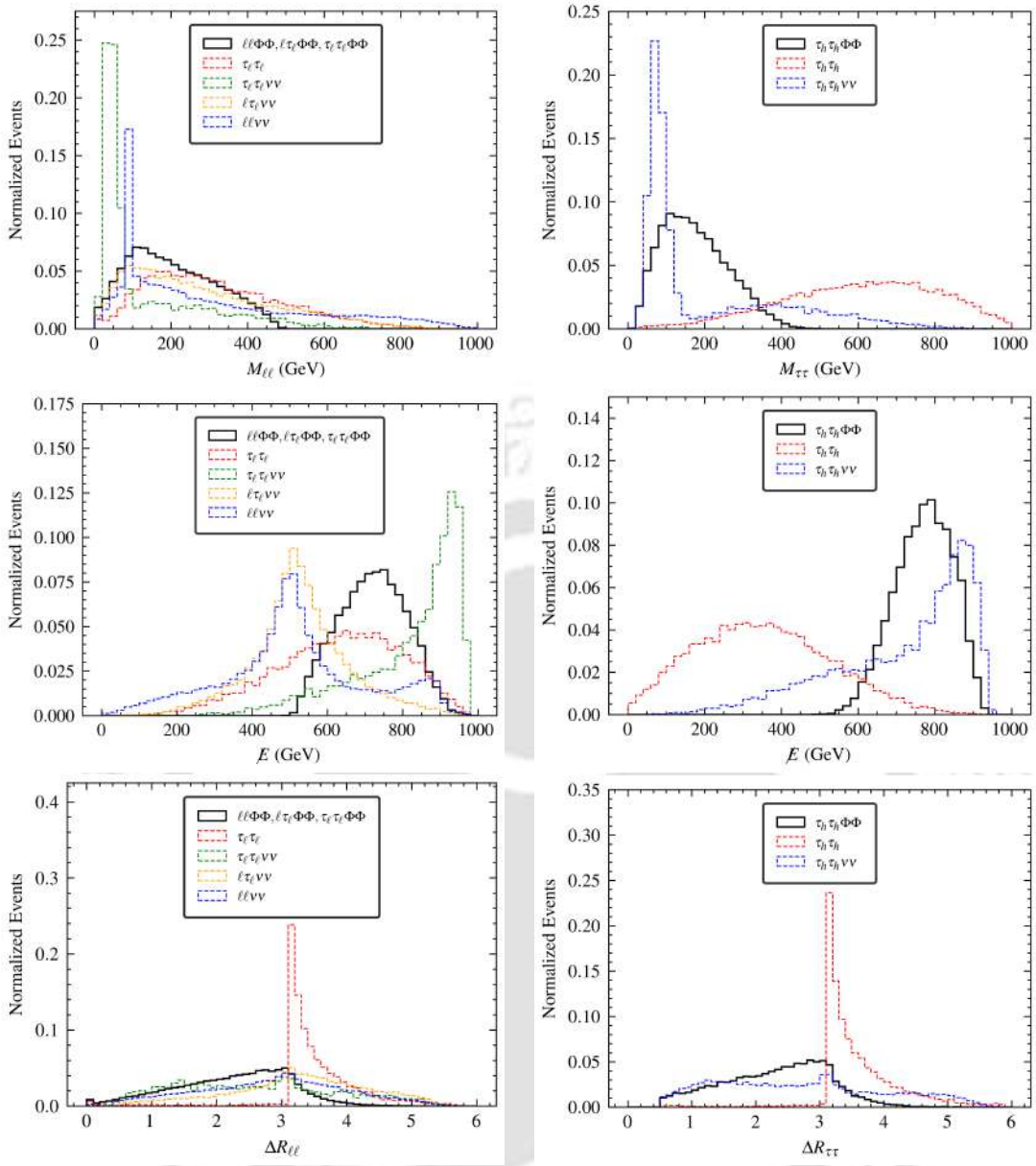

Figure 6.29: Kinematic distributions corresponding to signal and background processes of di-lepton + $\not{E}$ (*left*) and di-tau + $\not{E}$ (*right*) signal at ILC 1 TeV. The signal correspond to the benchmark: $m_\psi = 400$ GeV, $m_\Phi = 250$ GeV, $\mathrm{y}_e = \mathrm{y}_\mu = \mathrm{y}_\tau = 0.01$.

of Z decay. The most important variable is the missing energy of the event. The presence of massive DM results in missing energies to peak at higher values compared to most SM backgrounds. A missing energy cut of $\not{E} > 500$ GeV significantly reduces the major backgrounds in the case of both signals while keeping the signal numbers almost unaltered. Finally, τ pair backgrounds can be significantly reduced by choosing $\Delta R_{\ell\ell}/\Delta R_{\tau\tau}$ to be less than 3. Here, the signal correspond to the benchmark: $m_\psi = 400$ GeV, $m_\Phi = 250$ GeV, $\mathrm{y}_e = \mathrm{y}_\mu = \mathrm{y}_\tau = 0.01$. Tuning these lepton portal couplings alters the branching ratios of ψ decay, which significantly affects the signal cross sections. The signal significance contours plotted on $\mathrm{y}_{e/\mu} - \mathrm{y}_\tau$ plane are shown for both the signal processes in Fig. 6.30. The signal significance is defined as:

$$\text{Significance} = \frac{\sigma_\mathrm{s}}{\sqrt{\sigma_\mathrm{b}}} \times \sqrt{\mathfrak{L}}\,. \tag{6.42}$$

Here, σ_s and σ_b are the signal and background cross sections post cutflow. $\mathfrak{L}$ is the integrated luminosity. The couplings $y_{e/\mu}$ are strongly constrained from $\mu \to e\gamma$ LFV decay, however the same doesn't apply for y_τ. Hence, for certain parameter space regions di-tau may appear to be better choice as signal despite lower cross section. This has been illustrated in the plots. The parameter space is unaffected by future sensitivities of $\mu \to e\gamma$ branching measurements at MEG II.

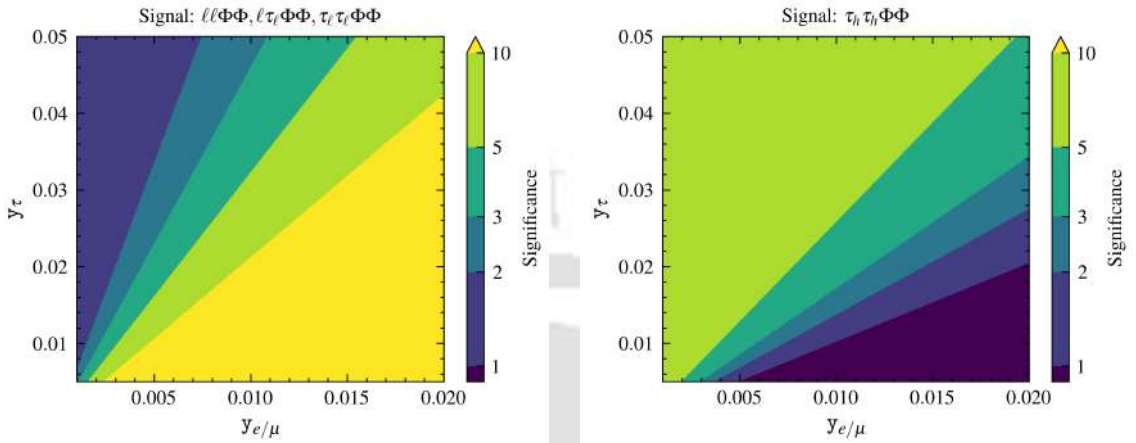

Figure 6.30: Signal significance contours in $y_{e/\mu} - y_\tau$ plane. The integrated luminosity is taken to be $\mathfrak{L} = 100$ fb^{-1}. The signal correspond to the benchmark: $m_\psi = 400$ GeV, $m_\Phi = 250$ GeV.

6.2.5 Summary and Conclusion

In this section, we have studied a minimal extension of the Standard Model (SM) containing a real and a complex scalar DM, stable under $\mathcal{Z}_2 \otimes \mathcal{Z}_3$ symmetry. Additionally, we introduced a Dirac vector-like lepton (VLL) with hypercharge -1, which transforms under $\mathcal{Z}_3$ symmetry in a similar manner to the complex scalar DM. This VLL connects the DM and the lepton sector, hence becoming subjected to constraints from lepton-flavor violation on the DM relic allowed parameter space. In Section 6.2.3, we discussed the constraints from lepton flavor anomalies and lepton flavor violating decays. Although lepton flavor-conserving processes, such as muon $g-2$ and electron $g-2$, are less restrictive in our analysis region ($y_\ell \lesssim 0.1$), the lepton flavor-violating (LFV) decay mode $\mu \to e\gamma$ significantly constrains the parameter space. In our analysis framework, the constraints from Higgs boson decays to di-leptons are less stringent than those from LFV processes and can therefore be disregarded.

In Section 6.2.4, we provide a comprehensive discussion of the DM phenomenology. In the WIMP-pFIMP scenario, the cBEQ has been written in the standard manner, but the only difference arises from the pFIMP interaction terms, most importantly the conversion terms, which is key to thermalization of FIMP, i.e. pFIMP scenario. The total DM relic density, attributed to both WIMPs and pFIMPs, is calculated by solving the cBEQ. This has been discussed in the two subsections that focus on the effective spin-independent WIMP/pFIMP-nucleon scattering cross-section and the production of SM particles through WIMP/pFIMP annihilation. The limits from LFV are also superimposed, resulting in the exclusion of most points below $m_{\rm DM} \sim 100$ GeV. This corresponds to a specific benchmark where $y_\mu = 10^{-3}$, and the limit becomes relaxed for even smaller values of y_μ and stronger for larger

values. In the case of WIMP, some points can still be probed at future DD experiments, PandaX-xT or DARWIN (200 t y), etc. Concurrently, the direct detection of pFIMP is only possible via the WIMP loop and most of the points are consistent with current DD observations, and we look forward to future detection results. The indirect detection limits could also be applicable to the WIMP annihilation to the electron-positron (tree), bottom pair (tree) and photon pair (box-loop), and also semi-annihilation (tree) to the Higgs. So, the observed and projection limits from Fermi-LAT, AMS-02, H.E.S.S, and CTA (projection) also put an exclusion on the relic and DD-allowed parameter space. The WIMP self-annihilation to electron-positron only excludes the low mass regime, while the Higgs resonance regime is excluded by the annihilation to bottom pair. Additionally, around the Higgs mass, certain points are excluded for large Higgs portal coupling ($\lambda_{\Phi H} \gtrsim 0.1$), which is relevant for semi-annihilation of WIMP. However, the annihilation into two photons remains unaffected at current experimental sensitivity. For pFIMPs, annihilation into bottom quark pairs happens only through the WIMP loop process, making them mostly unaffected by Fermi-LAT constraints, except near the Higgs resonance. In Section 6.2.4, we explored how our model could be tested in collider experiments. We recast the results from existing LHC studies on di-lepton + MET events in the context of our model, allowing us to determine the exclusion limits for the masses of the WIMP and VLL. We also estimate how these limits might improve at the HL-LHC run, finding that the exclusion limit roughly doubles. Additionally, we proposed a DM search strategy for future lepton colliders, analyzing di-lepton/di-tau + missing energy events at the 1 TeV run of the ILC. Finally, we compare the two signal processes and highlight the parameter space on the $y_{e/\mu} - y_{\tau}$ plane where each signal is likely to be most significant.

With a minimal extension to the SM that includes a real scalar, a complex scalar, and a VLL, we can successfully explain the DM relic density and LFV constraints. At the same time, this model remains consistent with current limits from direct, indirect, and collider experiments, while allowing for the future detection of WIMPs and pFIMPs in these searches. Not only that, such lepton portal DM models will also leave a signature at LFV decays and can be probed at future low-energy experiments as well. This nice feature occurs due to the presence of the Higgs portal, which is related to direct and indirect searches for DM, as well as lepton portal interactions relevant to LFV decay and collider searches for DM. Through our analysis, we found that both portal interactions significantly contribute to the DM relic density.

To summarise, the detectability of pFIMP at colliders or in direct search depends on the interactions of WIMP partners. We have provided a detailed account on such possibilities for a couple of WIMP-pFIMP models. The segregation of pFIMP signal from the WIMP is, however challenging, as the mass splitting between them is often small, while the pFIMP-SM coupling depends on the WIMP-SM coupling. We plan to work further to see if some exceptions can be thought of.

Chapter 7

Two-component DM and $\mathcal{Z}_N$ symmetry

Contents

More than one dark sector particle transforming under the same symmetry provides one stable dark matter (DM) component which undergoes co-annihilation with the heavier particle(s) decaying to DM. Specific assumptions on the kinematics and on the coupling parameters may render the heavier component(s) stable and contribute as DM. The choices of the charges of the dark sector fields under transformation play a crucial role in the resultant phenomenology. In this chapter, we systematically address the possibility of obtaining two scalar DM components under $\mathcal{Z}_N$ symmetry. We consider both the possibilities of DM being weakly interacting massive particle (WIMP) or pseudofeebly interacting massive particle (pFIMP). We elaborate upon $\mathcal{Z}_3$ symmetric model, confronting the relic density allowed parameter space with recent most direct and indirect search bounds and prospects. We also highlight the possible distinction of the allowed parameter space in single component and two component cases, as well as between WIMP-WIMP and WIMP-pFIMP scenarios. The discussion in this chapter is based on Ref . [307].

7.1 Introduction

In order to satisfy the relic density observed by the anisotropies in CMBR experiments, the DM needs to be stable at the scale of the universe's age. The stability of a fundamental particle is governed by an unbroken symmetry. The lightest dark particle transforming under a symmetry (discrete or continuous) does not possess any tree or loop-level decay terms with the visible sector. Then ideally, two different symmetries are required to have two stable DM particles. However, it is also possible to have one long-lived DM component, where the decay terms are assumed very small and the life time is larger than the age of the universe, which does not necessitate a protection via symmetry. However, the large decay life time requires either a kinematic suppression or the couplings involved in the process to be small or both. We study such possibilities here with a single $\mathcal{Z}_N$ $(N = 2, 3, 4..)$ symmetry, where the heavier dark sector particle is long lived and serves as the second DM component. Our intention is to examine the phenomenology of such cases, especially their implications in direct and indirect search aspects. In this work, how pFIMPs can arise in multicomponent scenarios having single $\mathcal{Z}_N$ symmetry is addressed. We specifically highlight the cases of $\mathcal{Z}_2$ and $\mathcal{Z}_3$ symmetric scenarios and compare it to $\mathcal{Z}_2 \otimes \mathcal{Z}_2'$ and $\mathcal{Z}_3 \otimes \mathcal{Z}_3'$ models. We show the consequent allowed parameter space of the models goes beyond the so-called Higgs resonance region [305].

This chapter is organised as follows: in Section 7.2 we discussed the possibility of getting two stable scalar DM components transforming under a single $\mathcal{Z}_N$ symmetry and in Section 7.3 we discuss briefly the case of $\mathcal{Z}_2$ symmetry. The case pertaining to $\mathcal{Z}_3$ symmetry is elaborated for both WIMP-WIMP and WIMP-pFIMP combinations in Section 7.4. We finally summarise in Section 8.6. Appendices F.1 and F.2 provide some necessary details omitted in the main text.

7.2 Generic discussion on two component DM under $\mathcal{Z}_N$ symmetry

Two stable DM components require two discrete symmetries, as studied in many different contexts [310, 597, 719–723], while some possibilities of having two DMs using a single discrete symmetry [600, 724–726] have also been discussed. However, a systematic study of obtaining all such possibilities under a single symmetry still requires attention. We address it via appropriate assumptions on the coupling parameters of the parent Lagrangian respecting $\mathcal{Z}_N$ symmetry. Our study is limited to scalar DM, while a similar study with vector and/or fermion DM is possible. Similarly, one can also have more than two DM components in a trivial extension of what we present here.

Specifically, we extend the SM with two scalar fields Φ_1 and Φ_2 transforming under a single $\mathcal{Z}_N$ symmetry. The fields Φ_1,Φ_2 might be real or complex, depending on their transformation under the $\mathcal{Z}_N$ symmetry. The lighter component is automatically stable, while the heavier one becomes (kinematically) stable after making some coupling parameters vanishingly small in the non-degenerate case.

In general, the heavier dark sector (DS) particle can have $(n + n')$ body decay as,

$$\text{heavier DS} \to n \text{ lighter DS} + n' \text{ SM}\,, \tag{7.1}$$

with $n,\ n' = 0, 1, 2, 3...,$ and $n + n' \geq 2$; where the exact values of $n(n')$ depend on the model. Now, the tree or loop level decay of this particle can be stopped by appropriate choices of the model parameters:

(a) For $n' = 0$, the heavier DS particle is stable when

$$n\, m_{\rm lighter} > m_{\rm heavier} > m_{\rm lighter}\,. \tag{7.2}$$

(b) When $n' \neq 0$, a kinematic condition $n\, m_{\rm lighter} + n'\, m_{\rm SM} > m_{\rm heavier} > n\, m_{\rm lighter}$ can stop the on-shell decay, but off-shell decays are still possible. The only way to make the heavier DS component stable is to choose appropriate couplings leading to the decay adequately small leading to a long lived particle (LLP) DM.

Further, the DMs can be WIMP, FIMP or SIMP depending on the strength of their couplings to SM. WIMP-WIMP combination is more constrained from direct search than WIMP-FIMP, given that FIMP is mildly constrained from DD/ID experiments (unless the DM-nucleon/electron scattering occurs via a light mediator). On the other hand, pFIMP receives milder constraints than WIMP having feeble DM-SM coupling, but still remains accessible for future sensitivities of DD/ID search via WIMP loop, having sizeable interaction with WIMP. Therefore, we are more interested in obtaining WIMP-pFIMP limit of this model, having either the lighter particle or the heavier one as pFIMP [305, 306]. In order to study two component DM, let us first write the renormalizable scalar potential, $V(\Phi_1, \Phi_2, H)$ (H represents SM Higgs isodoublet), where Φ_1 and Φ_2 are assumed singlets under the SM, but transform non-trivially under $\mathcal{Z}_N$,

$$\mathrm{V}(\Phi_1, \Phi_2, \mathrm{H}) \supset \lambda_1|\Phi_1|^2\mathrm{H}^\dagger\mathrm{H} + \lambda_2|\Phi_2|^2\mathrm{H}^\dagger\mathrm{H} + \lambda_3(\Phi_1\Phi_2 + \Phi_1\Phi_2^* + \mathrm{h.c.})\mathrm{H}^\dagger\mathrm{H} + \mathrm{V}^{\rm int}(\Phi_1, \Phi_2) \tag{7.3}$$

where $\lambda_1,\ \lambda_2,\ \lambda_3$ are dimensionless Higgs portal couplings, and $V^{\rm int}(\Phi_1, \Phi_2)$ contains all possible renormalizable interaction terms (with mass dimension $\mathcal{M}[2]$, $\mathcal{M}[3]$ and $\mathcal{M}[4]$) between Φ_1 and Φ_2 as,

$$\begin{aligned}
&\mathcal{M}[2] : \{\Phi_1\Phi_2,\ \Phi_1\Phi_2^*\} + h.c\,;\\
&\mathcal{M}[3] : \{\Phi_1|\Phi_2|^2,\ \Phi_2|\Phi_1|^2,\ \Phi_1\Phi_2^2,\ \Phi_1\Phi_2^{*2},\ \Phi_1^2\Phi_2\,,\ \Phi_1^2\Phi_2^*\} + h.c\,;\\
&\mathcal{M}[4] : \{\Phi_1^2\Phi_2^2,\ \Phi_1^2\Phi_2^{*2},\ \Phi_1^2|\Phi_2|^2,\ |\Phi_1|^2\Phi_2^2, |\Phi_1|^2|\Phi_2^2,\ \Phi_1\Phi_2^3,\ \Phi_1^*\Phi_2^3,\ \Phi_1^3\Phi_2,\\
&\qquad \Phi_1^3\Phi_2^*,\ \Phi_1\Phi_2|\Phi_1|^2,\ \Phi_1\Phi_2|\Phi_2|^2,\ \Phi_1\Phi_2^*|\Phi_1|^2,\ \Phi_1\Phi_2^*|\Phi_2|^2\} + h.c.
\end{aligned} \tag{7.4}$$

In Eqs. (7.3) and (7.4), we wrote all possible interaction terms, however the choice of the symmetry restricts them. It is obvious that if both Φ_1 and Φ_2 contribute as DM, then to prevent the tree-level decay of the heavier component, λ_3 in Eq. (7.3) needs to be sufficiently small[1], further restrictions arise depending on the possible interaction terms that one can write. If, $\Phi_1 \to \omega_N^{q_1}\Phi_1$ and $\Phi_2 \to \omega_N^{q_2}\Phi_2$ under $\mathcal{Z}_N$ symmetry, where $\omega_N^q = e^{i2\pi(q/N)}$ and $q_{1,2}$ define the charges of the fields, then the choice of $q_{1,2}$ also plays a crucial role in deciding the interaction terms, as shown in Table 7.1. The interaction terms are broadly classified into four cases:

$$\begin{aligned}
&(i) \quad q_1 = q_2, \text{ and } q_1 + q_2 = N\,,\\
&(ii) \quad q_1 = q_2, \text{ but } q_1 + q_2 \neq N\,,\\
&(iii) \quad q_1 \neq q_2, \text{ but } q_1 + q_2 = N\,,\\
&(iv) \quad q_1 \neq q_2, \text{ and } q_1 + q_2 \neq N\,.
\end{aligned} \tag{7.5}$$

[1] Additionally, for WIMP/pFIMP nature, λ_1, λ_2 can be chosen moderate (or small).

For the first three cases in Eq. (7.5), we have to consider both kinematic constraints and choose some couplings vanishingly small for making the heavy DS particle stable. The heavy DS particle in all these cases decay to SM particle plus DM, falling in the case (b) mentioned before. For the fourth condition in Eq. (7.5), i.e. $q_1 \neq q_2$, and $q_1 + q_2 \neq N$, a two-component DM scenario can arise just by imposing kinematic constraints, as here the decay of heavy DS particle occurs within the DS *only*, falling into category (a) discussed above; for some example analysis of such scenarios, see [600, 724–728]. Let us take a closer look into the possible terms that

Two dark sector scalar fields Φ_1 and Φ_2 and interaction terms under $\mathcal{Z}_N$ symmetry		
Symmetry	Transformation	Interaction terms between DS particles
$\mathcal{Z}_N$	$\omega_N^{q_1}, \omega_N^{q_2}$ $(q_1 = q_2)$ and $q_1 + q_2 = N$	$\Phi_1^2,\ \Phi_2^2,\ \Phi_1^4,\ \Phi_2^4,\ \Phi_1\Phi_2,\ \Phi_1^2\Phi_2^2,\ \Phi_1^3\Phi_2,\ \Phi_2^3\Phi_1$
	$\omega_N^{q_1}, \omega_N^{q_2}$ $(q_1 = q_2 = q)$ but $q_1 + q_2 \neq N$	$\lvert\Phi_1\rvert^2,\ \lvert\Phi_2\rvert^2,\ [\Phi_1^3,\ \Phi_2^3]_{\frac{3q}{N}\in\mathbb{N}},\ \lvert\Phi_1\rvert^4,\ \lvert\Phi_2\rvert^4,\ \Phi_1\Phi_2^*,\ \lvert\Phi_1\Phi_2^*\rvert^2,\ (\Phi_1\Phi_2^*)^2,\ \Phi_1\Phi_2^*(\lvert\Phi_1\rvert^2 + \lvert\Phi_2\rvert^2),$ $[\Phi_1^2\Phi_2^2, \Phi_1^3\Phi_2,\ \Phi_2^3\Phi_1,\ \Phi_1^4,\ \Phi_2^4]_{\frac{4q}{N}\in\mathbb{N}},\ [\Phi_1^2\Phi_2,\ \Phi_2^2\Phi_1]_{\frac{3q}{N}\in\mathbb{N}},\ [\Phi_1^3\Phi_2^*,\ \Phi_2^3\Phi_1^*]_{\frac{2q}{N}\in\mathbb{N}},\ [\Phi_1^2\Phi_2^*,\ \Phi_2^2\Phi_1^*]_{\frac{q}{N}\in\mathbb{N}}$
	$\omega_N^{q_1}, \omega_N^{q_2}$ $(q_1 \neq q_2)$ but $q_1 + q_2 = N$	$\lvert\Phi_1\rvert^2,\ \lvert\Phi_2\rvert^2,\ [\Phi_2^3]_{\frac{3q_2}{N}\in\mathbb{N}},\ \lvert\Phi_1\rvert^4,\ \lvert\Phi_2\rvert^4,\ \Phi_1\Phi_2,\ \Phi_1^2\Phi_2^2,\ \lvert\Phi_1\Phi_2\rvert^2,\ \Phi_1\Phi_2(\lvert\Phi_1\rvert^2 + \lvert\Phi_2\rvert^2),$ $[\Phi_1^3,\ \Phi_1^2\Phi_2^*,\ \Phi_2^2\Phi_1^*]_{\frac{3q_1}{N}\in\mathbb{N}},\ [\Phi_1^3\Phi_2^*,\ \Phi_2^3\Phi_1^*,\ \Phi_1^2\Phi_2^{*2},\ \Phi_1^4,\ \Phi_2^4]_{\frac{4q_1}{N}\in\mathbb{N}}$
	$\omega_N^{q_1}, \omega_N^{q_2}$ $(q_1 \neq q_2)$ and $q_1 + q_2 \neq N$	$[\Phi_1^m\Phi_2^n]_{\frac{mq_1+nq_2}{N}\in\mathbb{N}}, [\Phi_1^m\Phi_2^{*n}]_{\frac{mq_1-nq_2}{N}\in\mathbb{N}}$ where $\{m,\ n = 1, 2, 3$ and $q_1^{\max},\ q_2^{\max} = N-1\}$
Examples of some specific symmetries: $\mathcal{Z}_2$, $\mathcal{Z}_3$ and $\mathcal{Z}_4$		
$q_1 = q_2$ and $q_1 + q_2 = N$		
$\mathcal{Z}_2$	$\omega_2,\ \omega_2$	$\Phi_1^2, \Phi_2^2, \Phi_1^4, \Phi_2^4, \Phi_1\Phi_2,\ \Phi_1^2\Phi_2^2,\ \Phi_1^3\Phi_2,\ \Phi_1\Phi_2^3$
$\mathcal{Z}_4$	$\omega_4^2,\ \omega_4^2$	$\Phi_1^2, \Phi_2^2, \Phi_1^4, \Phi_2^4, \Phi_1\Phi_2,\ \Phi_1^2\Phi_2^2,\ \Phi_1^3\Phi_2,\ \Phi_1\Phi_2^3$
$q_1 = q_2$ but $q_1 + q_2 \neq N$		
$\mathcal{Z}_3$	$\omega_3,\ \omega_3$ / $\omega_3^2,\ \omega_3^2$	$\lvert\Phi_1\rvert^2, \lvert\Phi_2\rvert^2, \Phi_1^3, \Phi_2^3, \lvert\Phi_1\rvert^4, \lvert\Phi_2\rvert^4, \Phi_1\Phi_2^*, (\Phi_1\Phi_2^*)^2, \lvert\Phi_1\Phi_2\rvert^2, \Phi_1\Phi_2^2,\ \Phi_1^2\Phi_2,\ \Phi_1\Phi_2^*(\lvert\Phi_1\rvert^2 + \lvert\Phi_2\rvert^2)$
$\mathcal{Z}_4$	$\omega_4,\ \omega_4$ / $\omega_4^3,\ \omega_4^3$	$\lvert\Phi_1\rvert^2, \lvert\Phi_2\rvert^2, \Phi_1^4, \Phi_2^4, \lvert\Phi_1\rvert^4, \lvert\Phi_2\rvert^4, \Phi_1\Phi_2^*, (\Phi_1\Phi_2^*)^2, (\Phi_1\Phi_2)^2, \lvert\Phi_1\Phi_2\rvert^2, \Phi_1^3\Phi_2, \Phi_2^3\Phi_1, \Phi_1\Phi_2^*(\lvert\Phi_1\rvert^2 + \lvert\Phi_2\rvert^2)$
$q_1 \neq q_2$ but $q_1 + q_2 = N$		
$\mathcal{Z}_3$	$\omega_3^2,\ \omega_3$ / $\omega_3,\ \omega_3^2$	$\lvert\Phi_1\rvert^2, \lvert\Phi_2\rvert^2, \Phi_1^3,\ \Phi_2^3,\ \lvert\Phi_1\rvert^4,\ \lvert\Phi_2\rvert^4,\ \Phi_1\Phi_2,\ \Phi_1^2\Phi_2^2,\ \lvert\Phi_1\Phi_2\rvert^2,\ \Phi_2^2\Phi_1^*,\ \Phi_1^2\Phi_2^*,\ \Phi_1\Phi_2(\lvert\Phi_1\rvert^2 + \lvert\Phi_2\rvert^2)$
$\mathcal{Z}_4$	$\omega_4,\ \omega_4^3$ / $\omega_4^3,\ \omega_4$	$\lvert\Phi_1\rvert^2, \lvert\Phi_2\rvert^2,\ \Phi_1^4,\ \Phi_2^4, \lvert\Phi_1\rvert^4,\ \lvert\Phi_2\rvert^4,\ \Phi_1\Phi_2,\ (\Phi_1\Phi_2)^2, (\Phi_1\Phi_2^*)^2,\ \lvert\Phi_1\Phi_2\rvert^2,\ \Phi_1^3\Phi_2^*,\ \Phi_2^3\Phi_1^*,\ \Phi_1\Phi_2(\lvert\Phi_1\rvert^2 + \lvert\Phi_2\rvert^2)$

Table 7.1: Self interaction and interactions between two scalar fields Φ_1 and Φ_2 which transform under a discrete symmetry $\mathcal{Z}_N$ as $\Phi_1 \to \omega_N^{q_1}\Phi_1$ and $\Phi_2 \to \omega_N^{q_2}\Phi_2$ with $\omega_N^{q_i} = e^{i2\pi(q_i/N)}$ and $q_{1,2}$ being the integer charges of $\Phi_{1,2}$ with $q_{1,2} = 1,\ 2,\ 3..,\ N-1$. Depending upon the choice of $q_{1,2}$, the interaction terms are shown. $\mathbb{N}$ denotes set of integer numbers.

one can write involving Φ_1 and Φ_2 depending on their charges under $\mathcal{Z}_N$ transfor-

mation as shown in Table 7.1. The first sub-row of Table 7.1 shows the case when they have same charge: $q_1 = q_2 = q$, with $q = N/2$. As q needs to be an integer, this requires N to be even. In such a situation, Φ_1 and Φ_2 can be two real scalar fields, and only select few terms are allowed amidst all the possibilities listed in Eq . (7.4). The second sub-row in Table 7.1, shows the possible terms when $q_1 = q_2$, but $q_1 + q_2 \neq N$, which restricts us from writing $\Phi_1\Phi_2$ term, but retaining a term like $\Phi_1\Phi_2^*$ is possible, allowing complex scalar fields only. It is obvious but worth reminding that the complex conjugate fields possess $-q_i$ charges as $\Phi_i^* \to \omega_N^{q_i *}\Phi_i^*$ under $\mathcal{Z}_N$. Apart, terms like $\Phi_{1,2}^3$ can only be written if $\dfrac{3q}{N}$ is an integer, i.e., $\dfrac{3q}{N} \in \mathbb{N}$, where $\mathbb{N}$ denotes the set of integer numbers. The third and fourth sub-rows show the interaction terms when $q_1 \neq q_2, q_1 + q_2 = N$, and $q_1 \neq q_2, q_1 + q_2 \neq N$ cases respectively. The restrictions that apply in writing the interaction terms are mentioned in the subscript of the parenthesis. For example, $\Phi_1^m\Phi_2^n$ term can be written for $q_1 \neq q_2, q_1 + q_2 \neq N$ case, only when $\dfrac{mq_1 + nq_2}{N} \in \mathbb{N}$.

In the second part of Table 7.1, we have shown examples of $\mathcal{Z}_2$, $\mathcal{Z}_3$ and $\mathcal{Z}_4$ to write interaction terms between Φ_1, Φ_2 fields. For $\mathcal{Z}_2$, the charges are trivial and only caters to the possibility $q_1 = q_2 = 1, q_1 + q_2 = 2$; but for $\mathcal{Z}_3$ and $\mathcal{Z}_4$, other combination of charges as in Eq . (7.5) are possible. In the table, we have omitted listing $q_1 \neq q_2, q_1 + q_2 \neq N$ case for $\mathcal{Z}_3$ as it doesn't exist, and for $\mathcal{Z}_4$ as it can be stabilised by kinematic constraints without any fine tuning of the couplings. All the possibilities for $\mathcal{Z}_2$ and $\mathcal{Z}_3$ symmetries to contain two DM components will be discussed in this chapter; for $\mathcal{Z}_2$ this turns out to be one combination, while there are six different combinations of choosing vanishingly small parameters for the case of $\mathcal{Z}_3$ to accommodate two DMs. Obviously, the number of possibilities increase with higher N. It is interesting to note that when we choose one or more couplings vanishingly small in the Lagrangian, they may indicate to further restrictions or symmetries imposed to the Lagrangian.

- For example, when $q_1 = q_2$, and $q_1 + q_2 = N$ as in the first case as in Eq . (7.5), imposing the constraints on relevant couplings to have two DM components leads to $\mathcal{Z}_N \otimes \mathcal{Z}'_N$ symmetric Lagrangian. This is *always* the case for $\mathcal{Z}_2$, given the only possible charge combination.

- On the other hand, the second and third possibilities of Eq . (7.5) eventually lead to the fourth scenario $[q_1 \neq q_2, q_1 + q_2 \neq N]$ of a higher symmetry group, after assuming relevant couplings to be vanishingly small to stop heavier DS particle decay. In such circumstances, $\mathcal{Z}_3$ and $\mathcal{Z}_4$ symmetric cases become $\mathcal{Z}_6$ and $\mathcal{Z}_8$ symmetric scenarios respectively. The possible charge combinations of the scalar fields pertaining to $\mathcal{Z}_3$ and $\mathcal{Z}_4$ symmetries for single DM case, and the final charge assignments under $\mathcal{Z}_6$ and $\mathcal{Z}_8$ symmetries having two DMs (after stabilisation of the heavy DS particle) are listed below. We will elaborate on $\mathcal{Z}_3$ later.

$$\mathcal{Z}_3\ [\{q_1, q_2\} :\ (1,1),\ (2,2)] \supset \mathcal{Z}_6\ [\{q_1, q_2\} :\ (2,5),\ (4,1)]\ , \tag{7.6}$$

$$\mathcal{Z}_3\ [\{q_1, q_2\} :\ (1,2),\ (2,1)] \supset \mathcal{Z}_6\ [\{q_1, q_2\} :\ (2,1),\ (4,5)]\ , \tag{7.7}$$

$$\mathcal{Z}_4\ [\{q_1, q_2\} :\ (1,1),\ (3,3)] \supset \mathcal{Z}_8\ [\{q_1, q_2\} :\ (1,5),\ (5,1),\ (3,7),\ (7,3)]\ , \tag{7.8}$$

$$\mathcal{Z}_4\ [\{q_1, q_2\} :\ (1,3),\ (3,1)] \supset \mathcal{Z}_8\ [\{q_1, q_2\} :\ (1,3),\ (3,1),\ (5,7),\ (7,5)]\ . \tag{7.9}$$

7.3 Two scalar DMs under single $\mathcal{Z}_2$ symmetry

$\mathcal{Z}_2$ symmetric model has been studied widely in several contexts with real scalar DM (ϕ_i), odd ($\phi_i \to -\phi_i$) under $\mathcal{Z}_2$ [250–252, 544, 547, 729–733]. We will have a brief discussion here on the possibility of getting two DM components, where two scalar fields ϕ_1 and ϕ_2 are transforming under the same $\mathcal{Z}_2$ symmetry. The corresponding Lagrangian density is,

$$\mathcal{L} = \mathcal{L}_{\rm SM} + \frac{1}{2}\partial_\mu\phi_1\partial^\mu\phi_1 + \frac{1}{2}\partial_\mu\phi_2\partial^\mu\phi_2 - {\rm V}(\phi_1, \phi_2, {\rm H})\,, \tag{7.10}$$

where,

$$\begin{aligned}{\rm V}(\phi_1, \phi_2, {\rm H}) = {}& \frac{1}{2}m_{\phi_1}^2\phi_1^2 + \frac{1}{4!}\lambda_{\phi_1}\phi_1^4 + \frac{1}{2}m_{\phi_2}^2\phi_2^2 + \frac{1}{4!}\lambda_{\phi_2}\phi_2^4 + \frac{1}{2}\lambda_{\phi_1{\rm H}}\phi_1^2({\rm H}^\dagger{\rm H} - \frac{1}{2}v^2) \\ & + \frac{1}{2}\lambda_{\phi_2{\rm H}}\phi_2^2({\rm H}^\dagger{\rm H} - \frac{1}{2}v^2) + \frac{1}{4}\lambda_{\phi_1\phi_2}\phi_1^2\phi_2^2 + \frac{1}{3!}\lambda_{122}\phi_1\phi_2^3 + \frac{1}{3!}\lambda_{112}\phi_1^3\phi_2 \\ & + \mu_{\phi_1\phi_2}^2\phi_1\phi_2 + \lambda_{\phi_1\phi_2{\rm H}}\phi_1\phi_2{\rm H}^\dagger{\rm H}\,. \end{aligned} \tag{7.11}$$

The model parameters obey constraints from unitarity, perturbativity and vacuum stability [251, 300, 734–736]. The presence of $\mu_{\phi_1\phi_2}^2$ term yields a non-diagonal mass term, and upon diagonalization, we get $\mu_{\phi_1\phi_2}^2 = -\frac{1}{2}\lambda_{\phi_1\phi_2 H}v^2$. By default, the model as in Eq . (7.11), represents a single component DM scenario, with lighter of ϕ_1 or ϕ_2 serving as DM; where the heavier DS particle decays to DM and provides co-annihilation channels for the DM to freeze out. In order to make the heavier DS particle stable, we need to analyse the interaction vertices corresponding to the possible decay channels, detailed calculation is furnished in the Appendix F.1. Note for example, the presence of $\phi_1^3\phi_2$ term ($\phi_2^3\phi_1$) can lead $\phi_1(\phi_2)$ to decay into three ϕ_2 (ϕ_1). To stop this decay, one can choose kinematical constraint like $3m_{\rm DM} > m_{\rm DS}$. However, in presence of Higgs portal couplings, two body decay ($\phi_2 \to h\,\phi_1$ or $\phi_1 \to h\,\phi_2$) shown in Fig . F.2 (to on-shell Higgs) and three body decays (via off-shell Higgs) are possible. Notably, the decay of the heavier scalar to di-photon or di-gluon final states via one-loop graph is always possible via off-shell Higgs for non-degenerate m_{ϕ_1,ϕ_2} masses. So, one can choose sufficiently small portal coupling ($\lambda_{\phi_1\phi_2 H}$), so that the decay width of heavy scalar becomes larger than the age of universe. However, one loop decay via $\phi_1^3\phi_2$ and $\phi_2^3\phi_1$ term is still possible, see Fig . F.2. To stop them, λ_{112}, and λ_{122} couplings have to be sufficiently small as well.

Interestingly, when we block these couplings to stabilise the heavier DS particle, we essentially get rid of all terms having combinations of $\phi_1\phi_2$, then the Lagrangian eventually reduces to $\mathcal{Z}_2 \otimes \mathcal{Z}_2'$ symmetric one, well studied in different contexts, like in WIMP-WIMP scenario [300], WIMP-pFIMP scenario [305] etc. The only subtle difference between a pure $\mathcal{Z}_2 \otimes \mathcal{Z}_2'$ symmetric scenario to that of single $\mathcal{Z}_2$ with two DM is that, for the latter, we are getting one stable DM and one LLP, while under two different $\mathcal{Z}_2$ symmetry, we get two stable DMs, although the phenomenology is identical in both the cases.

7.4 Two scalar DMs under single $\mathcal{Z}_3$ symmetry

In this section, we will discuss two complex scalar fields transforming under single $\mathcal{Z}_3$ symmetry and its phenomenology in single and two-component DM scenarios. We will also discuss the comparison with two-component DM scenario in $\mathcal{Z}_3 \otimes \mathcal{Z}_3'$ set up [585].

7.4.1 The model

DS Fields	$\mathcal{Z}_3$
Complex scalar Φ_1	ω/ω^2
Complex scalar Φ_2	ω^2/ω

Table 7.2: Model particle contains and their transformation way, with $\omega = e^{i2\pi/3}$.

The SM extended dark sector Lagrangian containing two complex scalar fields that transform differently under $\mathcal{Z}_3$ symmetry (see Table 7.2) is written as [585, 611, 613, 669, 727, 737–739],

$$\mathcal{L} = \mathcal{L}_{\rm SM} + |\partial_\mu \Phi_1|^2 + |\partial_\mu \Phi_2|^2 - V(\Phi_1, \Phi_2, \mathrm{H}) \,, \tag{7.12}$$

where,

$$\begin{aligned} V(\Phi_1, \Phi_2, \mathrm{H}) \;=\; & -\mu_{\rm H}^2 \mathrm{H}^\dagger \mathrm{H} + \lambda_{\rm H} (\mathrm{H}^\dagger \mathrm{H})^2 + m_{\Phi_1}^2 |\Phi_1|^2 + \lambda_{\Phi_1} |\Phi_1|^4 + m_{\Phi_2}^2 |\Phi_2|^2 + \lambda_{\Phi_2} |\Phi_2|^4 \\ & + \lambda_{1H} |\Phi_1|^2 (\mathrm{H}^\dagger \mathrm{H} - \frac{v^2}{2}) + \lambda_{2H} |\Phi_2|^2 (\mathrm{H}^\dagger \mathrm{H} - \frac{v^2}{2}) + \frac{1}{2} \lambda_{12} (|\Phi_1|^2 |\Phi_2|^2 + |\Phi_1 \Phi_2|^2) \\ & + \frac{1}{2} \lambda_{12H} (\Phi_1 \Phi_2 + h.c.)(\mathrm{H}^\dagger \mathrm{H}) + \frac{1}{2} \lambda'_{12} (\Phi_1^2 \Phi_2^2 + h.c.) + \frac{1}{2} \Big[\mu_1 \Phi_1^* \Phi_2^2 + \mu_2 \Phi_1^2 \Phi_2^* \\ & + \mu_3 \Phi_1^3 + \mu_4 \Phi_2^3 + \mu_{12}^2 \Phi_1 \Phi_2 + h.c. \Big] + \frac{1}{2} \left[\lambda_3 \Phi_1 \Phi_2 |\Phi_1|^2 + \lambda_4 \Phi_1 \Phi_2 |\Phi_2|^2 + h.c. \right] . \end{aligned} \tag{7.13}$$

For $\lambda_H, \lambda_i > 0$ and $\mu_H^2 < 0$, the Higgs field acquires non-zero vev (v), with $\mathrm{H} = \begin{pmatrix} 0 & (h + \mathrm{v})/\sqrt{2} \end{pmatrix}^{\rm T}$, and results in electroweak symmetry breaking (EWSB). The theoretical and experimental constraints on the model parameters are as follows:

• Unitarity
The unitarity bound from infinite scattering limit is given by [740],

$$|\lambda_{iH}| \leq 8\pi, \; |\lambda_i| < 4\pi \,. \tag{7.14}$$

• Perturbativity
To ensure the validity of perturbation theory, loop corrections to the couplings should be smaller than their tree-level values. The perturbative bound for the model is given by [610],

$$|\lambda_{iH}| \leq 4\pi, \; |\lambda_i| < \pi \,. \tag{7.15}$$

• Vacuum stability
The necessary conditions required to stabilise the potential are,

$$\lambda_H > 0,\ \lambda_i > 0,\ \lambda_{iH} + 2\sqrt{\lambda_i \lambda_H} > 0\,. \tag{7.16}$$

The maximal allowed value of the cubic parameters $\mu_{3,4}$ is approximately equal to $\mu_3 = 2\sqrt{\lambda_1} m_{\Phi_1}$, $\mu_4 = 2\sqrt{\lambda_2} m_{\Phi_2}$ [575, 613, 741, 742]. However, we take the cubic coupling up to twice the lightest DM mass for simplicity.

• Higgs invisible decay width
The most sensitive limits on $\mathcal{B}_{h\to\text{inv}}$ are obtained from VBF searches at $\sqrt{s} = 13$ TeV LHC, excluding $\mathcal{B}_{h\to\text{inv}} < 0.18\ (0.10)$ observed (expected) at 95% C.L using 138 fb^{-1} of CMS data [495], and $\mathcal{B}_{h\to\text{inv}} < 0.15\ (0.10)$ using 139 fb^{-1} of ATLAS data [496].

7.4.2 Single component DM

In the potential given by Eq . (7.13), we have written all possible terms are respecting the $\mathcal{Z}_3$ symmetry. Note that the term $\Phi_1\Phi_2$ can be written since both Φ_1 and Φ_2 rotate under the same $\mathcal{Z}_3$, which is not present in $\mathcal{Z}_3 \otimes \mathcal{Z}_3'$ [585]. But, the presence of this term gives us a non-diagonal mass term unless we choose $\mu_{12}^2 = -\lambda_{12H} v^2/2$.

By default, the Lagrangian describes a complex scalar singlet DM, stable under $\mathcal{Z}_3$ symmetry, which has been studied in different contexts [737, 743]. Here we recap this scenario with the trending bounds on DM available from direct and indirect searches. Here, we have taken Φ_1 as our DM, but Φ_2 is equally possible, and DM phenomenology remains unaltered. The relic density of DM is governed by its annihilation channels. Additionally, we can have co-annihilation and semi-annihilation contribution in presence of heavy DS particle. This new degrees of freedom gives more allowed parameter space compared to the only one $\mathcal{Z}_3$ symmetric DM scenario [611, 613]. As we focus on GeV scale DM, $n \to 2$ $(n > 2)$ depletion processes are always subdominant to $2 \to 2$ annihilation process. The heavy DS particle decays to DM via off-shell or on-shell Higgs in tree or loop level, due to sizeable portal couplings: $(\lambda_{12H},\ \lambda_3,\ \mu_2)$. The key free parameters that govern DM analysis are,

$$\{m_{\Phi_i},\ \lambda_j,\ \mu_j,\ \lambda_{iH},\ \lambda_{12H},\ \lambda_{12},\ \lambda_{12}'\}\,. \tag{7.17}$$

where $i = 1, 2$ and $j = 1, ..., 4$ and all of these are taken as real parameters. Mass kinematics and couplings are the key parameters for the heavier DS decay to DM, and to get only one stable DM.

• BEQ and Relic density
The Boltzmann equation (BEQ) in this case is relevant to the total yield, $Y_\Phi = \sum_i Y_i = Y_{\Phi_1} + Y_{\Phi_1^*} + Y_{\Phi_2} + Y_{\Phi_2^*}$ including the complex conjugate fields and heavier dark sector fields as the heavier ones decay to DM, and is given by [306, 585, 724–726, 744],

$$\frac{dY_\Phi}{dx} = -\frac{s}{x\,H(x)}\left[\langle\sigma v\rangle^{\text{eff}}_{\text{SM}}(Y_\Phi^2 - Y_\Phi^{eq^2}) + \frac{1}{2}\langle\sigma v\rangle^{\text{eff}}_{\text{semi}}(Y_\Phi^2 - Y_\Phi Y_\Phi^{eq})\right]\,; \tag{7.18}$$

where,

$$\langle\sigma v\rangle^{\text{eff}}_{\text{SM}} = \sum_{i,j}\langle\sigma v\rangle_{i\ j\to\text{SM SM}}\frac{n_i^{\text{eq}} n_j^{\text{eq}}}{(n_\Phi^{\text{eq}})^2},\quad \langle\sigma v\rangle^{\text{eff}}_{\text{semi}} = \sum_{i,j,k}\langle\sigma v\rangle_{i\ j\to\ k\ \text{SM}}\frac{n_i^{\text{eq}} n_j^{\text{eq}}}{(n_\Phi^{\text{eq}})^2},$$

and

$$n_{\Phi}^{\rm eq} = \sum_i n_i^{\rm eq} = n_{\Phi_1}^{eq} + n_{\Phi_1^*}^{eq} + n_{\Phi_2}^{eq} + n_{\Phi_2^*}^{eq}.$$

We can also express the effective semi-annihilation cross-section as,

$$\langle\sigma v\rangle_{\rm SM}^{\rm eff} = \left[\sum_i g_i m_i^2 K_2\left(\frac{m_i}{T}\right)\right]^{-2} \sum_{i,j}\langle\sigma v\rangle_{ij\to \rm SM\ SM}\, g_i g_j\, m_i^2 m_j^2 K_2\left(\frac{m_i}{T}\right) K_2\left(\frac{m_j}{T}\right) \quad (7.19)$$

where g_i denotes internal degrees of freedom and K_2 denotes Bessel function of second kind. We have numerically solved the BEQ, Eq . (7.18), and verified it using micrOMEGAs [587] after importing the $\mathcal{Z}_3$ symmetric model using FeynRules [699]. The solutions of the BEQ and relic density allowed parameter space in terms of relevant parameters as well as direct and indirect search constraints are shown in Fig . 7.1.

In Fig . 7.1a, we show the relic under abundance in terms of DM mass and Ωh^2. The darkrainbow color bar shows the variation of λ_{1H}. With the presence of Higgs-mediated $s-$channel diagrams, Higgs resonance drop is observed at $m_{\Phi_1} \sim m_h/2$. The presence of a semi-annihilation process, $\Phi_i\Phi_j \to \Phi_k h$ provides another dip near $m_{\Phi_1} \sim m_h$. DM relic density decreases with larger portal and cubic couplings through annihilation, co-annihilation and semi-annihilation. When we move away from Higgs mass regime, the relic density decreases due to less (semi) annihilation contribution and requires larger λ_{1H} coupling. The shape of the parameter space is otherwise very typical to single component scalar DM model connected via Higgs portal. Semi-annihilation and co-annihilation contribution moves the whole spectrum downwards towards smaller relic density and allows smaller values of λ_{1H}.

• Direct detection limit from WIMP-nucleon inelastic scattering

The relic density allowed parameter space is further constrained by non-observation of DM in direct search, resulting in a lower bound on DM nucleon scattering cross section from direct detection experiments like, XENONnT [358] and LUX-ZEPLIN [514] etc,. The self-annihilation and semi-annihilation of this $\mathcal{Z}_3$ WIMP are also constrained by the Fermi-LAT [519], CTA [707], and H.E.S.S. [706] data.

The DM-nuclei scattering is governed mainly by the Higgs portal interaction term $\Phi_1\Phi_1^*(\mathrm{H}^\dagger\mathrm{H})$. For complex scalar DM, the spin-independent DM-nucleon inelastic scattering cross-section is an observed quantity in direct detection experiments,

$$\sigma_{\Phi_1}^{\rm SI} = \frac{\mu_n^2 m_n^2}{4\pi v^2 m_{\Phi_1}^2}\frac{f_n^2}{m_h^4}\lambda_{h\Phi_1\Phi_1^*}^2\,, \quad (7.20)$$

where $\mu_n = \frac{m_n m_{\Phi_1}}{m_n + m_{\Phi_1}}$, $\lambda_{h\Phi_1\Phi_1^*} = \lambda_{1H} v$, and other parameters have usual meaning. Eq . (7.20) show that the spin-independent scattering cross-section depends on the DM mass (m_{Φ_1}) and Higgs portal coupling (λ_{1H}). So, to satisfy direct search bound, we wish to decrease λ_{1H} and adjust other parameters to satisfy relic density, where co-annihilation and semi-annihilation play a major role.

In Fig . 7.1b, we have shown the relic density allowed parameter space in $m_{\Phi_1} - \sigma_{\Phi_1}^{\rm SI}$ plane and color bar represents the mass splitting between Φ_1 and Φ_2, which characterises co-annihilation contribution to relic density. Parameters kept fixed are mentioned in the figure inset.

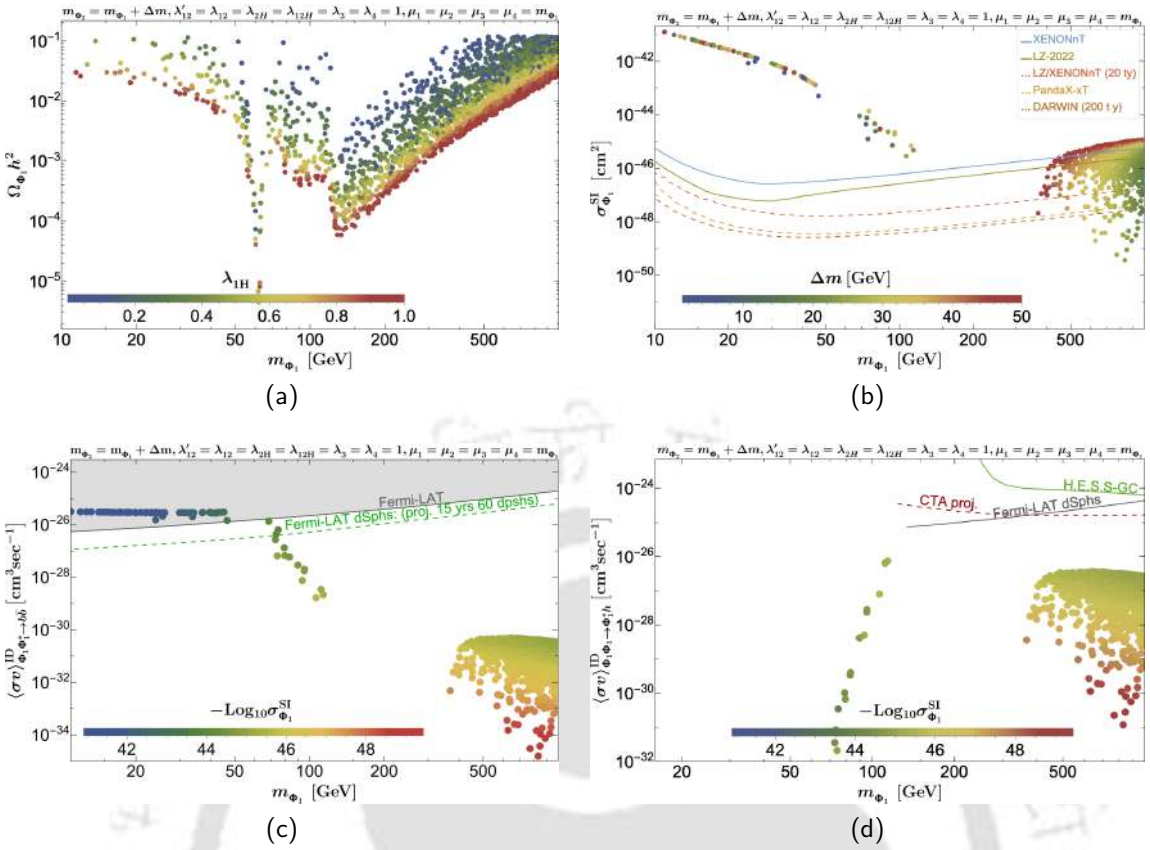

Figure 7.1: Relic density allowed parameter space of the single component DM model with two scalars transforming under the same $\mathcal{Z}_3$ symmetry, confronting direct and indirect search limits. Fig . 7.1a shows relic under abundant ($\Omega_{\Phi_1}h^2 \leq 0.1212$) parameter space in $m_{\Phi_1} - \Omega_{\Phi_1}h^2$ plane where the darkrainbow color bar shows the variation of the Higgs portal coupling (λ_{1H}) with DM (Φ_1) mass. Fig . 7.1b shows relic allowed parameter space in $m_{\Phi_1} - \sigma^{\rm SI}_{\Phi_1}$ plane and the darkrainbow color bar here shows DM mass splitting with the co-annihilating partner Φ_2, i.e, $\Delta m = m_{\Phi_2} - m_{\Phi_1}$. The light blue and olive green colored lines represent the XENONnT and LZ-2022 bound. Fig . 7.1c shows the relic density allowed parameter space in $m_{\Phi_1} - \langle\sigma v\rangle_{\Phi_1\Phi_1^*\to b\bar{b}}$ plane and darkrainbow color bar shows the variation of $\sigma^{\rm SI}_{\Phi_1}$ in unit of $\rm cm^2$. Thick grey and dashed green lines portray Fermi-LAT observation and projected limit, respectively. Fig . 7.1d shows relic density allowed region in $m_{\Phi_1} - \langle\sigma v\rangle_{\Phi_1\Phi_1\to\Phi_1^* h}$ plane and the darkrainbow color bar represents the spin-independent inelastic scattering cross-section ($\sigma^{\rm SI}_{\Phi_1}$) variation. The thick green, thick grey, and dashed blue lines represent the upper bound of the DM semi-annihilation from H.E.S.S, Fermi-LAT and CTA, respectively.

We see that no relic density allowed points are seen at resonance region, or in the semi-annihilation region, they correspond to under abundant region. This is simply due to the range of λ_{1H} chosen for the scan, as it requires much smaller values to satisfy relic, due to enhancement in effective annihilation cross-section in these regions. If the DM mass is adequately large and away from the Higgs mass region, then semi-annihilation is small and we need smaller Δm which enhances co-annihilation. In Fig . 7.1b, some region of the parameter space above the Higgs mass regime is excluded by the recent XENONnT and LZ-2022 bound represented by light blue and olive green lines, respectively. The three dashed lines correspond to the projected limit spin-independent DM direct detection cross-section. The parameter space illustrated here is particular for this benchmark, and one can get more relic density-allowed regions depending on the values of the parameters kept fixed.

• Indirect detection limit on the self-annihilation of WIMP

The limits on DM self-annihilation impose another constraint on the relic and DD-allowed parameter space of the model. Here, we are using the indirect search limit

on DM self-annihilation from Fermi collaboration, six years of observation using 15 dwarf spheroidal galaxies (dSphs) [519] and a projected sensitivity for 45 dSphs and 15 years of observation [520]. The thick grey and dashed green line in Fig . 7.1c represents the observed and projected limit from Fermi-LAT. At the same time, the grey-shaded region is excluded by the observed Fermi-LAT limit on DM self-annihilation into bottom pairs.

The indirect detection limit on the thermal average DM (Φ_1) self-annihilation to the bottom pair is evaluated at the DM freeze-out point, $T^{FO}_{\Phi_1} \sim m_{\Phi_1}/25$, which depends on the DM mass (m_{Φ_1}) and Higgs portal coupling (λ_{1H}). The thermal average cross-section, $\langle\sigma v\rangle_{\Phi_1\Phi_1^*\to b\bar{b}}$, is nearly constant below $m_h/2$ region, but, maximum near Higgs resonance. Near Higgs mass, semi-annihilation helps decrease the λ_{1H} coupling. The DM mass region, near and below the Higgs resonance, is mostly excluded for the specific choice of the benchmark point and allowed above the resonance region. To see the corresponding DD cross section, see the darkrainbow color bar in Fig . 7.1c.

• Indirect detection limit on the semi-annihilation of WIMP
Recently, the gamma-ray observation from Fermi-LAT, H.E.S.S [706] telescope, and also CTA [707] put an upper limit on the DM (Φ_1) semi-annihilation. The presence of cubic interaction in $\mathcal{Z}_3$ symmetric WIMP provides semi-annihilation channel via $\langle\sigma v\rangle_{\Phi_1\Phi_1\to\Phi_1^* h}$ and is evaluated at the freeze-out point of Φ_1. This cross-section depends on m_{Φ_1}, m_{Φ_2}, λ_{1H}, λ_{12H}, μ_2, and μ_3. In Fig . 7.1d, we show the relic density allowed parameter space $m_{\Phi_1} - \langle\sigma v\rangle^{\rm ID}_{\Phi_1\Phi_1\to\Phi_1^* h}$ plane. The color bar shows variation with respect to DD cross-section. We see that for the chosen values of the parameters, relic density allowed points lie below the existing limits. Like other plots, absence of points near Higgs resonance and Higgs mass can be seen, mainly due to the range of parameters chosen for the scan. However, the DM is well allowed up to TeV, due to co-annihilation and self annihilation processes through the presence of additional complex scalar Φ_2, transforming under the same symmetry [611]. .

7.4.3 Two component DM

Eq . (7.12) describes the extension of SM containing two complex scalar fields that transform differently under a single $\mathcal{Z}_3$ symmetry. Interaction terms depend on their transformation charges, see Table 7.3 for details. Such interaction terms in-between Φ_1 and Φ_2, like, $\Phi_1^2\Phi_2^*$ or $\Phi_2^2\Phi_1^*$ etc., open up the decay of the heavier component to the lighter one(s). A suitable choice of mass hierarchy, $2\,m_{\rm lighter} > m_{\rm higher}$ can stop such decay. Further, both fields are connected with the visible sector via Higgs portal interactions. The one connecting both the fields like $\Phi_1\Phi_2|H|^2$ leads to the decay of heavier component to lighter one plus SM at tree level. A mass hierarchy like $m_{\Phi_2} > m_{\Phi_1} + m_h$ can stop such on-shell decay, however, off-shell Higgs decay to di-photon or di-gluon is always permitted for non-degenerate masses of the dark sector particles. Considering sufficiently small portal coupling (λ_{12H}) associated with this term can stop on-shell or off-shell decay of the heavier particle to SM at tree level. However, one loop and two loop decay terms are still possible in the presence of self-interaction terms between Φ_1 and Φ_2. Hence, even after neglecting λ_{12H}, one needs to choose very small λ_3, λ_4, and μ_2 to restrict one-loop decay, although the choice of μ_2 isn't unique. However, after sacrificing all of these parameters, the two-loop

decay (see Fig. F.2) is still possible. To restrict the two-loop decay, different other parameters can be chosen to be small, giving rise to different kinds of scenarios, as shown in Table 7.3. The red colored terms in Table 7.3 can be sacrificed to obtain the second long lived DM component. In the appendix, we have also given an estimate of smallness of these couplings, $\lambda_3,\ \lambda_4,\ \lambda_{12H},\ \mu_2 \lesssim 10^{-15}$, so that the decay lifetime is larger than the age of the universe. Note that for $\mathcal{Z}_3$ model, the possibility of $q_1 \neq q_2, q_1 + q_2 \neq N$ do not arise. Therefore, one has to sacrifice some couplings to make both components stable. Depending on the choice of the couplings required to

Scenarios	Interaction terms of two DMs: Φ_1 and Φ_2 under $\mathcal{Z}_3$ symmetry
$q_1 = 1,\ q_2 = 2$ or $q_1 = 2,\ q_2 = 1$	
A	$\lvert\Phi_1\rvert^2 H^\dagger H,\ \lvert\Phi_2\rvert^2 H^\dagger H,\ \Phi_1^3,\ \Phi_2^3,\ \lvert\Phi_1\rvert^4,\ \lvert\Phi_2\rvert^4,\ \Phi_1\Phi_2 H^\dagger H,\ \Phi_1^2\Phi_2^2,\ \lvert\Phi_1\Phi_2\rvert^2,\ \Phi_2^2\Phi_1^*,\ \Phi_1^2\Phi_2^*,\ \Phi_1\Phi_2(\lvert\Phi_1\rvert^2 + \lvert\Phi_2\rvert^2)$
B	$\lvert\Phi_1\rvert^2 H^\dagger H,\ \lvert\Phi_2\rvert^2 H^\dagger H,\ \Phi_1^3,\ \Phi_2^3,\ \lvert\Phi_1\rvert^4,\ \lvert\Phi_2\rvert^4,\ \Phi_1\Phi_2 H^\dagger H,\ \Phi_1^2\Phi_2^2,\ \lvert\Phi_1\Phi_2\rvert^2,\ \Phi_2^2\Phi_1^*,\ \Phi_1^2\Phi_2^*,\ \Phi_1\Phi_2(\lvert\Phi_1\rvert^2 + \lvert\Phi_2\rvert^2)$
C	$\lvert\Phi_1\rvert^2 H^\dagger H,\ \lvert\Phi_2\rvert^2 H^\dagger H,\ \Phi_1^3,\ \Phi_2^3,\ \lvert\Phi_1\rvert^4,\ \lvert\Phi_2\rvert^4,\ \Phi_1\Phi_2 H^\dagger H,\ \Phi_1^2\Phi_2^2,\ \lvert\Phi_1\Phi_2\rvert^2,\ \Phi_2^2\Phi_1^*,\ \Phi_1^2\Phi_2^*,\ \Phi_1\Phi_2(\lvert\Phi_1\rvert^2 + \lvert\Phi_2\rvert^2)$
$q_1 = q_2 = 1,\ 2$	
D	$\lvert\Phi_1\rvert^2 H^\dagger H,\ \lvert\Phi_2\rvert^2 H^\dagger H,\ \Phi_1^3,\ \Phi_2^3,\ \lvert\Phi_1\rvert^4,\ \lvert\Phi_2\rvert^4,\ \Phi_1\Phi_2^* H^\dagger H,\ (\Phi_1\Phi_2^*)^2,\ \lvert\Phi_1\Phi_2\rvert^2,\ \Phi_2^2\Phi_1,\ \Phi_1^2\Phi_2,\ \Phi_1\Phi_2^*(\lvert\Phi_1\rvert^2 + \lvert\Phi_2\rvert^2)$
E	$\lvert\Phi_1\rvert^2 H^\dagger H,\ \lvert\Phi_2\rvert^2 H^\dagger H,\ \Phi_1^3,\ \Phi_2^3,\ \lvert\Phi_1\rvert^4,\ \lvert\Phi_2\rvert^4,\ \Phi_1\Phi_2^* H^\dagger H,\ (\Phi_1\Phi_2^*)^2,\ \lvert\Phi_1\Phi_2\rvert^2,\ \Phi_2^2\Phi_1,\ \Phi_1^2\Phi_2,\ \Phi_1\Phi_2^*(\lvert\Phi_1\rvert^2 + \lvert\Phi_2\rvert^2)$
F	$\lvert\Phi_1\rvert^2 H^\dagger H,\ \lvert\Phi_2\rvert^2 H^\dagger H,\ \Phi_1^3,\ \Phi_2^3,\ \lvert\Phi_1\rvert^4,\ \lvert\Phi_2\rvert^4,\ \Phi_1\Phi_2^* H^\dagger H,\ (\Phi_1\Phi_2^*)^2,\ \lvert\Phi_1\Phi_2\rvert^2,\ \Phi_2^2\Phi_1,\ \Phi_1^2\Phi_2,\ \Phi_1\Phi_2^*(\lvert\Phi_1\rvert^2 + \lvert\Phi_2\rvert^2)$

Table 7.3: Terms having two dark sector scalar fields transforming under discrete symmetry $\mathcal{Z}_3$. Red color terms are the minimum number of terms to be sacrificed to stop the tree and loop-level decays of the heavier particle.

stabilize the heavier DM component, six possibilities emerge as shown in Table 7.3. The absence of red colored terms indicate the presence of a new discrete symmetry, as mentioned before. For example, scenario A and D correspond to $\mathcal{Z}_3 \otimes \mathcal{Z}_3'$ scenario. Similarly, scenario B and C turns out to be $\mathcal{Z}_6$ symmetry with $q_1 = 4,\ q_2 = 5$ or $q_1 = 2,\ q_2 = 1$ and $q_1 = 5,\ q_2 = 4$ or $q_1 = 1,\ q_2 = 2$, respectively. Scenario E and F falls under $\mathcal{Z}_6$ with $q_1 = 4,\ q_2 = 1$ or $q_1 = 2,\ q_2 = 5$ and $q_1 = 1,\ q_2 = 4$ or $q_1 = 5,\ q_2 = 2$, respectively. Let us recall that when we can have $q_1 \neq q_2, q_1 + q_2 \neq N$, we can stabilise both the components kinematically.

Further, if we want one of the components to be pFIMP, we have to choose the corresponding portal coupling feeble, but DM-DM interaction sizeable. Now the scenarios that arise here, having two DM components, are not all independent. In the following, we elaborate upon scenarios A and B; scenarios C, D, E, and F are somewhat similar to them.

Scenario-A

From Table 7.3, we see that this particular scenario arises via tiny couplings associated with $\Phi_1\Phi_2 H^\dagger H,\ \Phi_1^2\Phi_2^2,\ \Phi_2^2\Phi_1^*,\ \Phi_1^2\Phi_2^*,\ \Phi_1\Phi_2|\Phi_1|^2,\ \Phi_1\Phi_2|\Phi_2|^2$ interaction terms, to

give rise to one LLP and one stable DM. This is then equivalent to $\mathcal{Z}_3 \otimes \mathcal{Z}_3'$ scenario [585]. But, in the two WIMP case, limited parameter space is left for future direct detection. However, WIMP-pFIMP possibility enhances the allowed parameter space, as discussed below.

To make the LLP (Φ_2) pFIMP, we further need λ_{2H} to be very tiny, see Appendix F.1 to know the range of couplings. Then the available parameters, that could be utilised in WIMP-pFIMP phenomenology, are,

$$\{m_{\Phi_1},\ m_{\Phi_2},\ \lambda_1,\ \lambda_2,\ \lambda_{1H},\ \lambda_{12},\ \mu_3,\ \text{and}\ \mu_4\}\,. \tag{7.21}$$

• Relic density

The total relic abundance for this WIMP-pFIMP set-up, comes from Φ_1 as WIMP and Φ_2 as pFIMP, to stipulate to,

$$\Omega_{\rm DM}{\rm h}^2 = 2.744\times 10^8 \sum_{i=1,2} m_{\Phi_i} Y_i[x_\infty]\,, \tag{7.22}$$

where $Y_i = n_i/s$, n_i is number density, and s is the entropy density. The DM yield (Y_i) is calculated by solving coupled BEQ for Φ_1 and Φ_2 numerically using micrOmega. The self-annihilation, semi-annihilation, conversion and semi-conversion are the main number-changing processes that contribute to the DM relic. It is worthy recalling that after stabilisation of the heavy component, there is no co-annihilation contribution.

• Direct detection limits on WIMP and pFIMP

The WIMP is weakly coupled to the visible sector via the Higgs portal interaction and can scatter with the detector nuclei. The effective WIMP-nucleon inelastic scattering cross section at zero transfer momentum limit ($q_h^2 = t \to 0$) turns out to be, see Fig . 7.2a,

$$\sigma^{\rm eff}_{\Phi_1} = \frac{\Omega_{\Phi_1}h^2}{\Omega_{\Phi_1}h^2+\Omega_{\Phi_2}h^2}\frac{\mu_n^2 m_n^2}{4\pi v^2 m_{\Phi_1}^2}\frac{f_n^2}{m_h^4}|\lambda_{h\Phi_1\Phi_1^*}|^2\,. \tag{7.23}$$

In the above, $\mu_n = \frac{m_n m_{\Phi_1}}{m_n+m_{\Phi_1}}$ where m_n is the nucleon mass, $f_n = \frac{2}{9} + \frac{7}{9}\sum_{u,d,s} f^n_{T_q}$ with $f^{p(n)}_{T_u} = 0.018\ (0.013)$, $f^{p(n)}_{T_d} = 0.027\ (0.040)$, and $f^{p(n)}_{T_s} = 0.037\ (0.037)$ [745].

The direct detection of pFIMP is possible only by the WIMP loop-mediated penguin and vertex correction diagrams, see Fig . 7.2f. The effective spin-independent pFIMP-nucleon ($\Phi_2 - N$) inelastic scattering cross-section at zero transfer momentum ($q_h^2 = t \to 0$) limit is given by,

$$\sigma^{\rm eff}_{\Phi_2} = \frac{\Omega_{\Phi_2}h^2}{\Omega_{\Phi_1}h^2+\Omega_{\Phi_2}h^2}\frac{\mu_n^2 m_n^2}{4\pi v^2 m_{\Phi_2}^2}\frac{f_n^2}{m_h^4}|\Gamma^{\rm total}_{h\Phi_2\Phi_2^*}|^2_{t\to 0}\,, \tag{7.24}$$

where, $\mu_n = \frac{m_n m_{\Phi_2}}{m_n+m_{\Phi_2}}$ and $\Gamma^{\rm total}_{h\Phi_2\Phi_2^*} = \Gamma^{7.2f}_{h\Phi_2\Phi_2^*}$. One can easily calculate,

$$\Gamma^{7.2f}_{h\Phi_2\Phi_2^*}\left(q_h^2\right) = -i\lambda^{\rm relic}_{h\Phi_2\Phi_2^*} - i\frac{\lambda_{\Phi_1\Phi_1^*\Phi_2\Phi_2^*}\lambda_{h\Phi_1\Phi_1^*}}{16\pi^2}\int_0^1 dx\,\ln\left[\frac{m_{\Phi_1}^2 - x(1-x)4m_{\Phi_2}^2}{m_{\Phi_1}^2 - x(1-x)q_h^2}\right]\,, \tag{7.25}$$

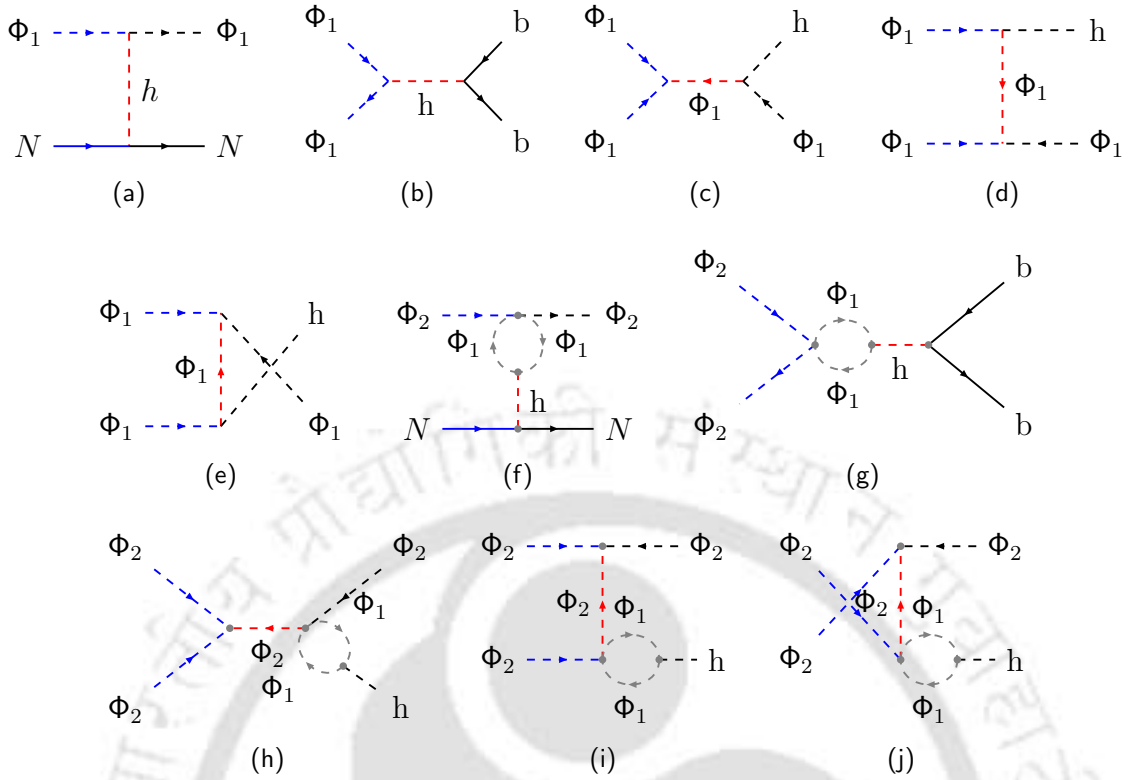

Figure 7.2: Top: Figs . 7.2a and 7.2b represent Feynman diagrams corresponding to the direct and indirect detection of WIMP (Φ_1) respectively. Figs . 7.2c to 7.2e correspond to WIMP semi-annihilation processes contributing to its indirect search. Bottom: Fig . 7.2f shows pFIMP direct search, and Figs . 7.2g to 7.2j represent processes that contribute to indirect detection of pFIMP (Φ_2).

where, q_h is transfer momentum associated with Higgs, $\lambda_{\Phi_1\Phi_1^*\Phi_2\Phi_2^*} = -i\lambda_{12}$, and $\lambda_{h\Phi_1\Phi_1^*} = -i\lambda_{1H}v$. Using Section 7.4.3, we impose the presently available direct detection constraint from LUX-ZEPLIN, XENONnT, and PandaX-xT experiments on the relic density allowed parameter space of the model. Figs . 7.3a and 7.3b, shows the relic density allowed parameter space in $m_{\Phi_1} - \sigma^{\rm eff}_{\Phi_1}$ plane (corresponding to WIMP) while the darkrainbow color bar represents the DM mass difference and λ_{1H} respectively. Here, we have taken $\mu_3 = 2m_{\Phi_1}$ and $\mu_4 = 2m_{\Phi_2}$, which are most useful parameters for DM semi-annihilation. The Higgs resonance ($m_{\Phi_1} \sim m_h/2$) and semi-annihilation ($m_{\Phi_1} \sim m_h$) of WIMP help it to acquire under abundance, while the total relic is adjusted by the pFIMP, and relax the λ_{1H} to come under the present DD bound. Beyond the Higgs resonance or semi-annihilation regime, cross-section decreases and relic density increases, which is adjusted by enhancing the portal coupling λ_{1H}, respecting DD bound.

Figs . 7.3c and 7.3d represent DM relic density allowed parameter space in $m_{\Phi_2} - \sigma^{\rm eff}_{\Phi_2}$ plane corresponding to pFIMP. The spin-independent scattering cross-section, $\sigma^{\rm eff}_{\Phi_2}$ depends on the total loop amplitude ($\Gamma^{\rm total}_{h\Phi_2\Phi_2^*}$), which is function of λ_{12}, λ_{1H}, and μ_1 couplings, and they decide which process in Fig . 7.2f dominantly contribute to pFIMP direct search cross-section. Notably, $\sigma^{\rm eff}_{\Phi_2}$ also depends on the mass splitting Δm and pFIMP relic density $\Omega_{\Phi_2}h^2$, which is small for large conversion rate. The different thick (dashed) colored lines correspond to existing (projected) bounds from the different experiments mentioned in the figure inset. Essentially the part of relic density allowed parameter space with $\lambda_{1H} \gtrsim 0.5$ is under conflict with DD limits.

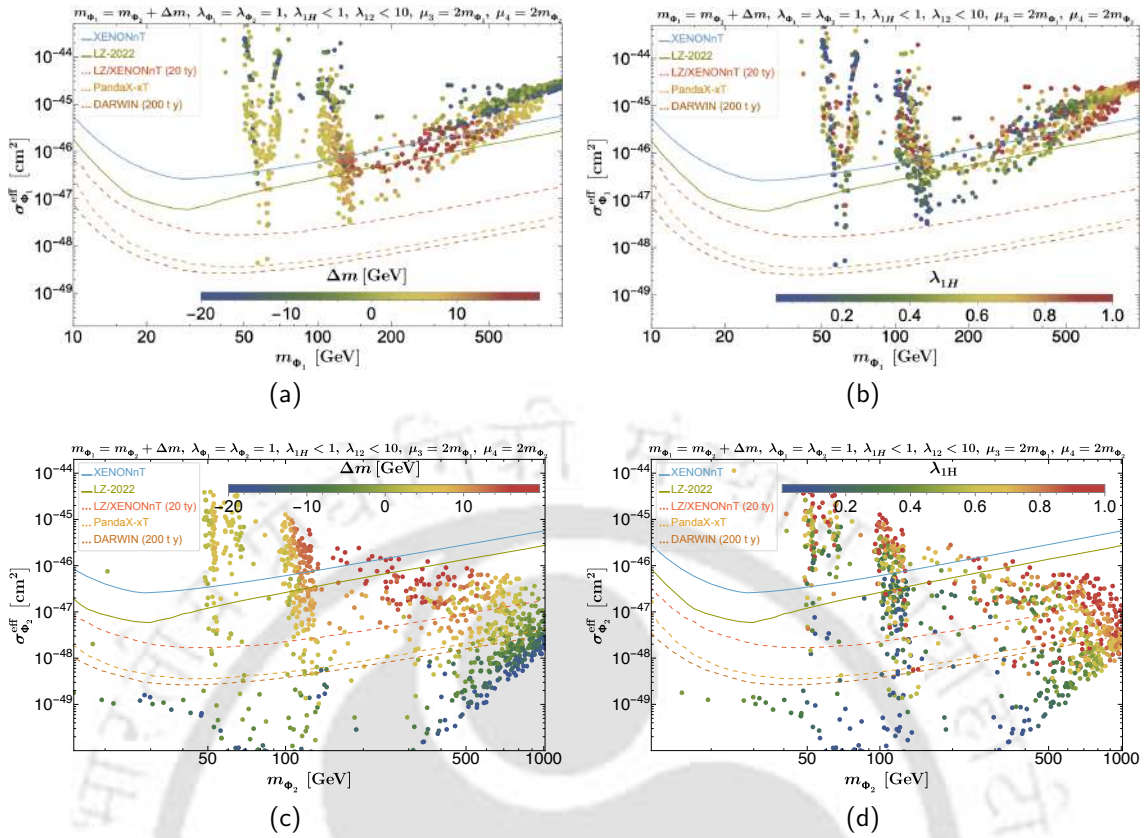

Figure 7.3: In Figs. 7.3a to 7.3d, we have shown the relic density allowed parameter space of the two component WIMP-pFIMP set up, on $m_{\Phi_1} - \sigma^{\rm eff}_{\Phi_1}$ (top panel) and $m_{\Phi_2} - \sigma^{\rm eff}_{\Phi_2}$ planes (bottom panel). We have taken $\lambda'_{12} = \lambda_3 = \lambda_4 = 10^{-20}$ and $\mu_1 = \mu_2 = 10^{-15}$ GeV to stabilise Φ_2, and choose $\lambda_{2H} = 10^{-12}$ to make Φ_2 a pFIMP. Other parameters kept fixed or varied are shown in the figure heading and inset.

• Indirect detection limits on WIMP and pFIMP

The limit on DM self-annihilation into $b\bar{b}$, W^+W^-, ZZ and $t\bar{t}$ is obtained from the data of Fermi collaboration from 6 years of observation of 15 dwarf spheroidal galaxies (dSphs) [519]. They also provide projected sensitivity for 45 dSphs of 16 years of observation [520]. Various gamma-ray observations from Fermi-LAT [519], H.E.S.S. [706] and Cherenkov Telescope Array (CTA) [707] put a bound on DM semi-annihilation $\Phi_i\ \Phi_i \to \Phi_i^*\ h$. We will calculate both the self and semi-annihilation rates in this two component WIMP-pFIMP set up and apply the bounds to find allowed parameter space that can be probed further.

The effective WIMP (Φ_1) self and semi-annihilation cross-section are given by,

$$\langle\sigma v\rangle^{\rm eff}_{\Phi_1\Phi_1^*\to b\bar{b}} = \left(\frac{\Omega_{\Phi_1}h^2}{\Omega_{\Phi_1}h^2+\Omega_{\Phi_2}h^2}\right)^2 \langle\sigma v\rangle_{\Phi_1\Phi_1^*\to b\bar{b}}\,. \tag{7.26}$$

and

$$\langle\sigma v\rangle^{\rm eff}_{\Phi_1\Phi_1\to\Phi_1^*h} = \left(\frac{\Omega_{\Phi_1}h^2}{\Omega_{\Phi_1}h^2+\Omega_{\Phi_2}h^2}\right) \langle\sigma v\rangle_{\Phi_1\Phi_1\to\Phi_1^*h}\,. \tag{7.27}$$

In Eqs. (7.26) and (7.27), the thermal average of self and semi-annihilation cross-sections are evaluated at the WIMP freeze-out point, $T^{\rm FO}_{\Phi_1} \sim m_{\Phi_1}/25$ and plotted in $m_{\Phi_1} - \langle\sigma v\rangle^{\rm eff}_{\Phi_1\Phi_1^*\to b\bar{b}}$ plane in Figs. 7.4a and 7.4b, respectively. The darkrainbow

color bar shows the spin-independent direct detection cross-section of pFIMP in cm^2 unit. The effective self and semi-annihilation cross-section of WIMP depend on λ_{1H}, WIMP mass and also on the effective WIMP contribution to the total DM relic. Fermi-LAT observation and projection data are shown by thick grey and dashed green lines, respectively. We see that most of the parameter space probed here obey the limit.

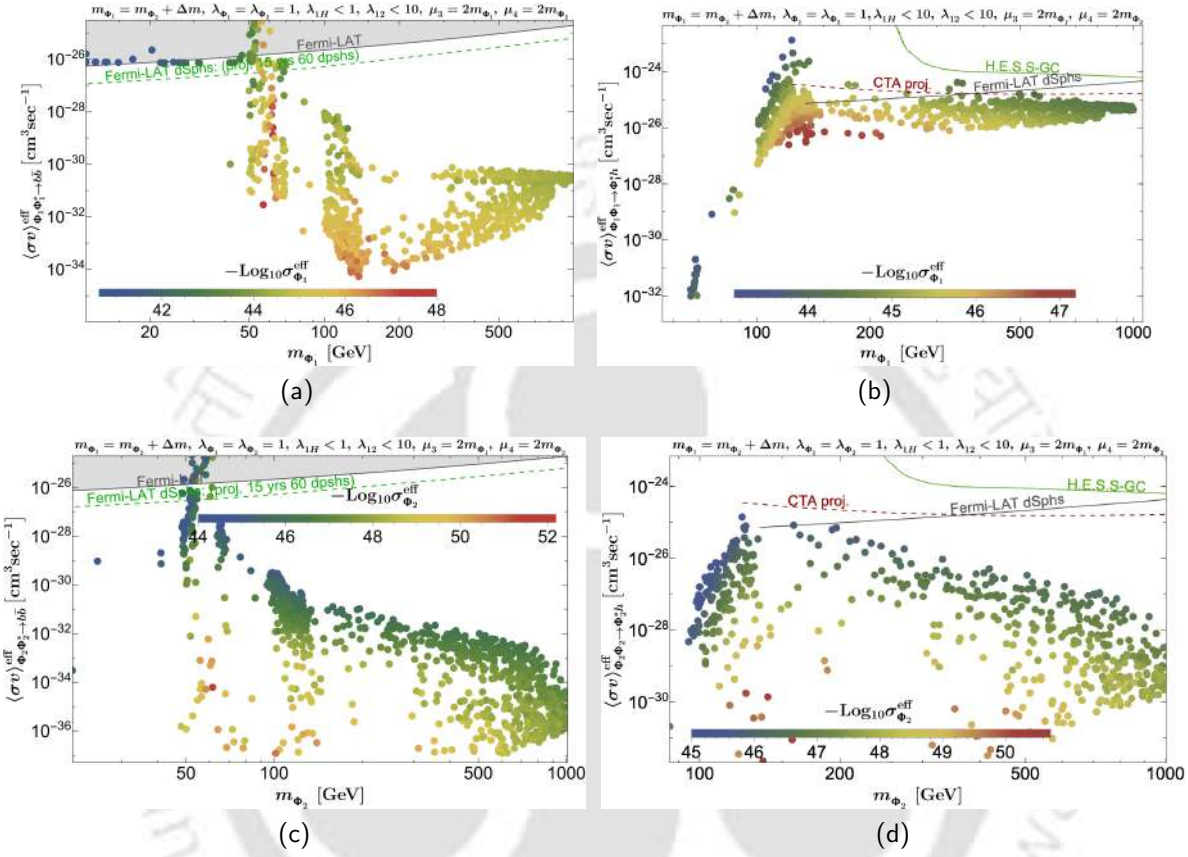

Figure 7.4: Figs. 7.4a and 7.4c show the relic allowed parameter space $m_{\Phi_1} - \langle\sigma v\rangle^{\rm eff}_{\Phi_1\Phi_1^*\to b\bar{b}}$ and $m_{\Phi_2} - \langle\sigma v\rangle^{\rm eff}_{\Phi_2\Phi_2^*\to b\bar{b}}$ plane, respectively for WIMP and pFIMP while Figs. 7.4b and 7.4d corresponds to WIMP and pFIMP semi-annihilation. We have taken $\lambda'_{12} = \lambda_3 = \lambda_4 = 10^{-20}$ and $\mu_1 = \mu_2 = 10^{-15}$GeV to stabilise the heavier DM and $\lambda_{2H} = 10^{-12}$ to become Φ_2 as pFIMP.

pFIMP Φ_2 connects with the visible sector via WIMP loop-mediated interaction, as shown in Figs. 7.2g to 7.2j. These diagrams are subdominant to the tree-level processes. The effective self-annihilation cross-section of pFIMP (Φ_2) is given by,

$$\langle\sigma v\rangle^{\rm eff}_{\Phi_2\Phi_2^*\to b\bar{b}} = \left(\frac{\Omega_{\Phi_2}h^2}{\Omega_{\Phi_1}h^2+\Omega_{\Phi_2}h^2}\right)^2 \langle\sigma v\rangle_{\Phi_2\Phi_2^*\to b\bar{b}}\,, \tag{7.28}$$

and the pFIMP semi-annihilation cross-section is given by,

$$\langle\sigma v\rangle^{\rm eff}_{\Phi_2\Phi_2\to\Phi_2^* h} = \left(\frac{\Omega_{\Phi_2}h^2}{\Omega_{\Phi_1}h^2+\Omega_{\Phi_2}h^2}\right) \langle\sigma v\rangle_{\Phi_2\Phi_2\to\Phi_2^* h}\,. \tag{7.29}$$

The dominant self-annihilation of Φ_2 to SM pair comes from diagram Fig. 7.2g, while others are suppressed due to tiny couplings assumed for the stability of Φ_2. We also need to remove the divergence contribution from the vertex correction diagram

Fig . 7.2g. We take $q_h^2 = 4m_{\Phi_2}^2$ as our renormalisation scale [305]. Then, we have calculated the thermal average annihilation cross-section at the pFIMP freeze-out point $\mathrm{T}_{\Phi_2}^{\mathrm{FO}} \sim \mathrm{m}_{\Phi_2}/25$.

Figs . 7.4c and 7.4d show the relic density allowed parameter space in $m_{\Phi_2} - \langle\sigma v\rangle^{\rm eff}_{\Phi_2\Phi_2^*\to b\bar{b}}$ and $m_{\Phi_2} - \langle\sigma v\rangle^{\rm eff}_{\Phi_2\Phi_2\to\Phi_2^* h}$ planes, respectively. The pFIMP effective semi-annihilation cross-section is written in Eq . (7.29) and is proportional to the λ_{1H}, λ_{12}, and μ_4 couplings. Among these three, λ_{1H} and λ_{12} contribute to the pFIMP DD cross-section. With larger λ_{1H}, both the self-annihilation and direct detection cross-section of pFIMP increases, which is also reflected in Fig . 7.4c. Finally, we constrain the parameter space by imposing the Fermi-LAT observation and projection bound in $m_{\Phi_2} - \langle\sigma v\rangle^{\rm eff}_{\Phi_2\Phi_2^*\to b\bar{b}}$ plane and the color bar represents the variation of effective pFIMP direct detection cross-section. The pFIMP semi-annihilation is also mediated via WIMP loop, see Figs . 7.2h to 7.2j. We have used the bound on DM semi-annihilation from H.E.S.S (green), Fermi-LAT (grey), and CTA (dashed red) in Fig . 7.4d. These constraints exclude some regions, which are also excluded by the presently available DD bounds.

In summary, the two component DM scenario of type A after stabilising the heavier component by adjusting coupling parameters behaves like $\mathcal{Z}_3 \otimes \mathcal{Z}_3'$ scenario. Additionally, when the heavier DM component behaves like pFIMP having tiny portal interaction, the under abundant parameter space of WIMP is adequately utilised by the second component and enhance the allowed parameter space. Having the second component as pFIMP reduces the DD and ID bounds as they are primarily governed by loop mediated interactions and allows one to exploit larger parameter space compared to the WIMP-WIMP case [585]. Both DMs are allowed within $\mathrm{GeV\ to\ TeV}$ range, where semi-annihilation and conversion play crucial roles for yielding correct DM relic density.

Scenario-B

In scenario B (Table 7.3), the absence of Φ_2^3 helps in the stabilisation of the heavier particle. This parameter doesn't have any significance in WIMP-pFIMP set up. But the presence of $\Phi_1^2\Phi_2^2$ and $\Phi_2^2\Phi_1^*$ terms has an important role in the semi-annihilation of Φ_2 for the WIMP-WIMP scenario. They open up many conversion and semi-conversion channels, shown in Fig . F.4, which are absent in scenario A or WIMP-WIMP set up under $\mathcal{Z}_3 \otimes \mathcal{Z}_3'$ model. We will do a similar kind of analysis to understand the benefits, such as the scenario A. We study both (I) WIMP$-$WIMP ($\lambda_{2H} \neq 0$), and (II) WIMP-pFIMP ($\lambda_{2H} \to 0$) cases below.

• WIMP-WIMP

In case of a real scalar singlet WIMP as a single component DM, some breathing space is left near the Higgs resonance region, or in the high mass regime, $\gtrsim 1$ TeV, but the direct detection sensitivity is less for the latter. In the two-component real scalar singlet WIMP scenario, the choices could be: (I) one is near Higgs resonance, and another in the higher mass regime, $m_{\rm DM} \gtrsim 1$ TeV, or (II) both DM masses are far above the Higgs resonance. In scenario B, the presence Φ_1^3 term opens up semi-annihilation channels, which brings more relic and DD-allowed parameter space.

However, in two-component complex scalar WIMP scenario as in here, Φ_2 semi-annihilation is inefficient due to the feeble Φ_2^3, but opens the door for conversion,

semi-conversion channels via $\Phi_1^2\Phi_2^2$ and $\Phi_2^2\Phi_1^*$ terms. Along with the standard DM-DM conversion via $|\Phi_1|^2|\Phi_2|^2$ term, we then have Φ_1 semi-annihilation ($\Phi_1\Phi_1 \to \Phi_1^* h$) due to Φ_1^3 and Φ_2 mediated DM-DM conversion Figs. F.4h and F.4k, and semi-conversion ($\Phi_2\Phi_2 \to \Phi_1^* h$) Figs. F.4m and F.4n in due to the presence of $\Phi^2\Phi_1^*$ term, all of which help in acquiring correct relic, without perturbing DD or ID searches. The $\Phi_1 - \Phi_2$ conversion can also be possible via Higgs mediation and Φ_2 mediation along with the four-point scattering. So, the Higgs resonance effect is not only limited to DM annihilation to SM particles but also to DM-DM conversion. The s-channel semi-conversion of $\Phi_2\Phi_2 \to \Phi_1^* h$ is more effective near the Higgs mass regime. These processes help to relax the Higgs portal coupling, but keep adequate depletion via conversion processes and save the DM components from DD constraints. In Fig. 7.5, we have shown the relic density allowed parameter space

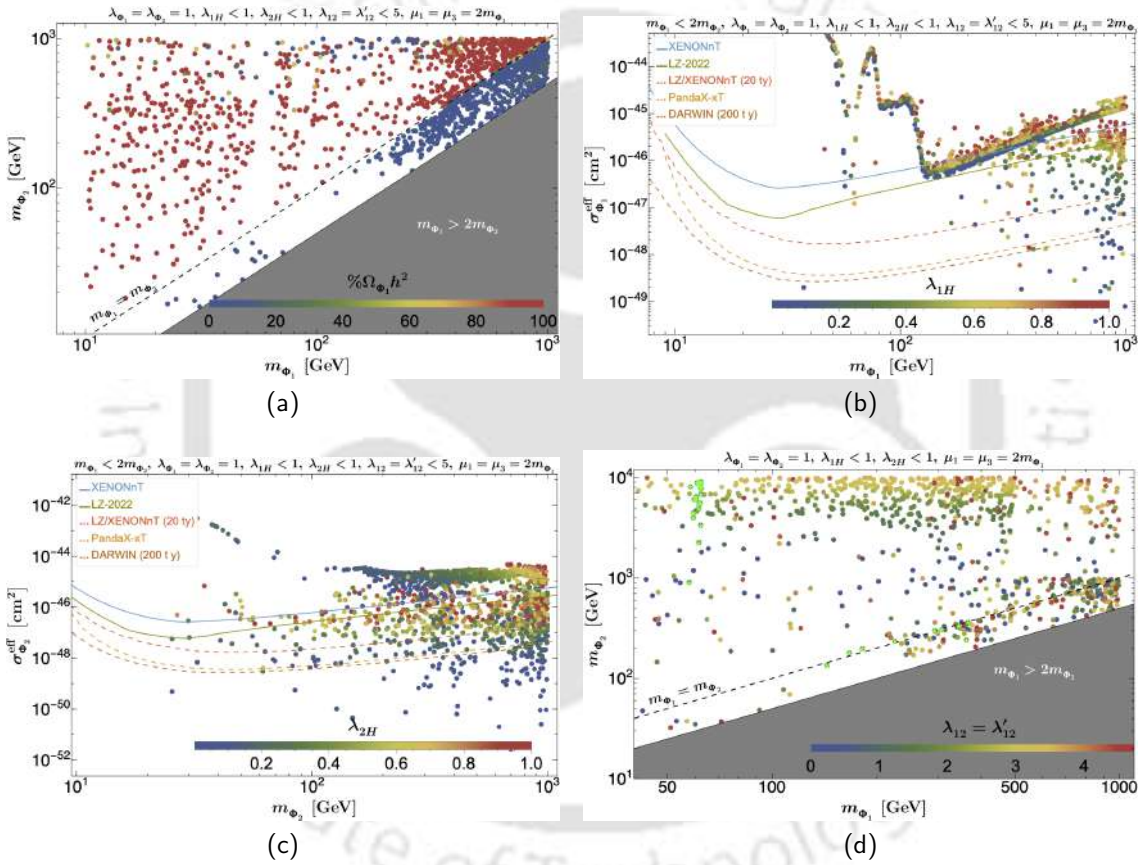

Figure 7.5: Figs. 7.5b and 7.5c shows the relic density allowed parameter space for two-component WIMP in category B (Table 7.3) in $m_{\Phi_1} - \sigma^{\rm eff}_{\Phi_1}$, and $m_{\Phi_2} - \sigma^{\rm eff}_{\Phi_2}$ planes respectively. Figs. 7.5a and 7.5d show the relic allowed parameter space in $m_{\Phi_1} - m_{\Phi_2}$ plane, where darkrainbow color depicts variation in $\Omega_{\Phi_1}h^2$ and λ_{12} respectively. The couplings $(\mu_2, \mu_4, \lambda_3, \lambda_4)$ are taken adequately small ($\sim 10^{-20}$) to stabilise the heavier DM component. The grey-shaded region is excluded from the heavier particle stability. In Fig. 7.5d green star points depict the case where both DM components obey the stringent limit on spin-independent DM-nucleon scattering cross section from LZ-2022.

and incorporated possible direct detection bounds. Fig. 7.5a represents the relic allowed parameter space in $m_{\Phi_1} - m_{\Phi_2}$ plane, while the darkrainbow color bar shows the variation of percentage contribution of Φ_1 in the total relic. If $m_{\Phi_1} > m_{\Phi_2}$, then Φ_1 relic is subdominant due to conversion of Φ_1 to Φ_2 decrease the Φ_1 number density but Φ_2 number density is enhanced simultaneously. Around the Higgs resonance and semi-annihilation region, the conversion effect could be ignored, and equal contribution arises; see green color points in Fig. 7.5a. Figs. 7.5b and 7.5c represents the

relic allowed point in $m_{\Phi_1} - \sigma^{\rm eff}_{\Phi_1}$ and $m_{\Phi_2} - \sigma^{\rm eff}_{\Phi_2}$ plane, respectively. In Fig . 7.5b, we see two kinks, m_{Φ_1} around the Higgs resonance and Higgs-mass region, where semi-annihilation process is more effective because of the presence of Φ_1^3 term. Beyond the Higgs mass, semi-annihilation and also self-annihilation cross-section decreases, which can be adjusted by λ_{1H}, and λ_{12}, but λ_{1H} is strongly restricted by DD. On the contrary, as the trilinear coupling of Φ_2 is very tiny to keep it stable, there is no kink due to semi-annihilation near Higgs mass in Fig . 7.5c. So, with larger mass, the decrease in cross-section is adjusted by the enhancement of λ_{2H}. Although semi-annihilation of Φ_2 is not active in absence of Φ_2^3 term, but semi-conversion channels are there due to $\Phi_2^2\Phi_1^*$ terms, which help to relax the λ_{2H} coupling. In Fig . 7.5d, we show the effect of conversion in $m_{\Phi_1} - m_{\Phi_2}$ plane.

The main outcome of this scenario is that we are getting relic and DD-allowed points near the Higgs resonance, Higgs mass, and also some above the Higgs mass, represented by the green stars in Fig . 7.5. Indirect search limits are less stringent than DD and do not alter the allowed parameter space.

• **WIMP-pFIMP**

In scenario-B (Table 7.3), we have identified Φ_2 as pFIMP by choosing $\lambda_{2H} \sim 10^{-12}$, so that it doesn't have a direct SM connection, however sizeable λ_{12} keeps it in thermal bath via interaction with Φ_1.

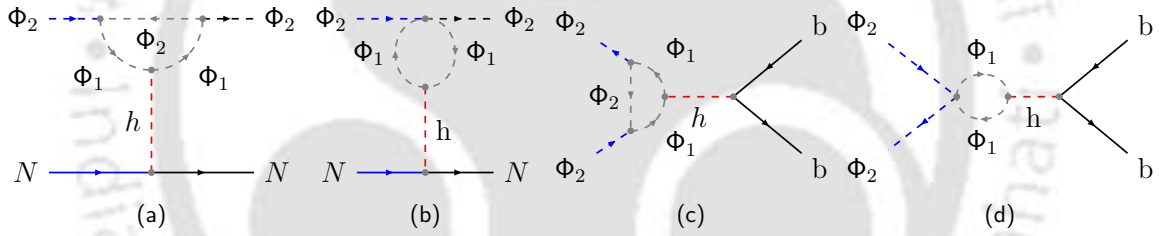

Figure 7.6: Figs . 7.6a and 7.6b, Figs . 7.6c and 7.6d represent the Feynman diagrams related to the direct and indirect detection of pFIMP (Φ_2), respectively.

The relic density in WIMP-pFIMP limit is calculated by solving cBEQ, using micrOMEGAs [587]; for relevant Feynman diagrams related to annihilation, semi-annihilation and conversion channels, see Fig . F.4. The WIMP and pFIMP relic density allowed parameter spaces are shown in Figs . 7.7 and 7.8. As before, the direct and indirect detection of WIMP is possible through the Higgs portal λ_{1H}, but the pFIMP detection is only possible via the WIMP loop-mediated diagrams, see Fig . 7.6. The loop divergences have been taken care of using the on-shell renormalisation scheme, while the renormalization scale is chosen at $\sim 4m^2_{\Phi_2}$.

Fig . 7.7 show the WIMP and pFIMP relic density allowed parameter space in $m_{\Phi_1} - \sigma^{\rm eff}_{\Phi_1}$, $m_{\Phi_2} - \sigma^{\rm eff}_{\Phi_2}$ planes, and the color bar shows the variation of different relevant parameters as mentioned in figure insets. The different colored lines correspond to the lower bounds from different direct detection experiments, while thick and dashed lines represent the observed and projected limits on the spin-independent DM-nucleon scattering cross-section. We see that along with the Higgs resonance, the semi-annihilation region is also available. One important point to note that we can also have $\sim$ 500 GeV WIMP mass, where the mass splitting $|\Delta m|$ can go up to 100 GeV, see Fig . 7.7c. This is unlike 5 GeV mass splitting for two real scalar WIMP-pFIMP DM scenario [305]. The reason for this is the presence of additional

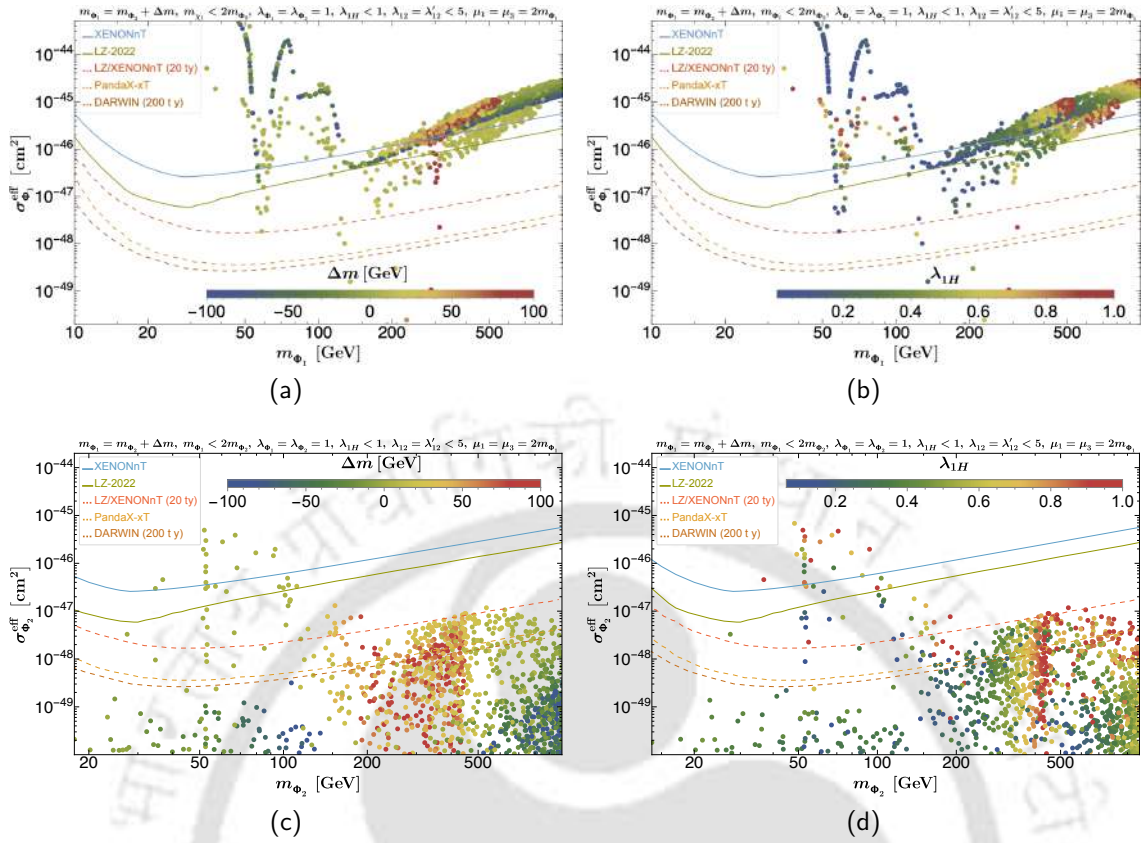

Figure 7.7: Figs. 7.7a to 7.7d show the relic density allowed parameter space in $m_{\Phi_1} - \sigma^{\rm eff}_{\Phi_1}$ and $m_{\Phi_2} - \sigma^{\rm eff}_{\Phi_2}$ plane, respectively. The couplings $(\mu_2, \mu_4, \lambda_3, \lambda_4)$ are taken adequately small to stabilise the heavier DM Φ_2 so that it falls in category B of two component DM (Table 7.3). The darkrainbow color bar show the variation of Δm (left) and λ_{1H} (right). The thick and dashed lines correspond to the lower limits on the observed and projected DM-nucleon spin-independent DD cross-section respectively, while different colors refer to the experiments as mentioned in the figure inset.

semi-conversion channel $\Phi_2\Phi_2 \to \Phi_1^* h$ (Fig. F.4m) here, which is strongly active when $m_{\Phi_1} \sim m_h$. Fig. 7.7d show the relic density allowed parameter space in $m_{\Phi_2} - \sigma^{\rm eff}_{\Phi_2}$, and the color bar show the variation of WIMP-Higgs portal coupling (λ_{1H}). The pFIMP-nucleon cross-section is directly proportional to $(\mu_1, \lambda_{12}, \lambda_{1H})$, depends on the WIMP and pFIMP masses via loop factor, and on the effective relic density contribution. Due to this reason, around the Higgs-resonance regime, the WIMP relic is very small compared to pFIMP, and the effective relic contribution decreases with larger pFIMP mass, as visible in Fig. 7.7c.

Fig. 7.8 shows indirect detection limit on the DM self-annihilation and semi-annihilation in the relic-allowed parameter space of the WIMP-pFIMP set up. The Fermi-LAT, H.E.S.S and CTA put limits on the annihilation of WIMP and pFIMP into $b\bar{b}$. Figs. 7.8a and 7.8c show the relic allowed parameter space in $m_{\Phi_1} - \langle\sigma v\rangle^{\rm eff}_{\Phi_1\Phi_1^* \to b\bar{b}}$ and $m_{\Phi_2} - \langle\sigma v\rangle^{\rm eff}_{\Phi_2\Phi_2^* \to b\bar{b}}$ plane, while the color bar show the variation of $-{\rm Log}_{10}\sigma^{\rm eff}_{\Phi_1}$ and $-{\rm Log}_{10}\sigma^{\rm eff}_{\Phi_2}$ respectively. For both the plots, near Higgs resonance, some points are disallowed by the Fermi-LAT data. Semi-annihilation bounds from indirect searches are not applicable to pFIMP due to the absence of the Φ_2^3 term. Fig. 7.8d show relic density allowed points $m_{\Phi_1} - m_{\Phi_2}$ plane where the grey shaded region is excluded by the DM decay kinematics. The relic and DD allowed points, denoted by green stars lie in the vicinity of mass degenerate line. This is in contrast to the WIMP-WIMP situation described before (see Fig. 7.5d).

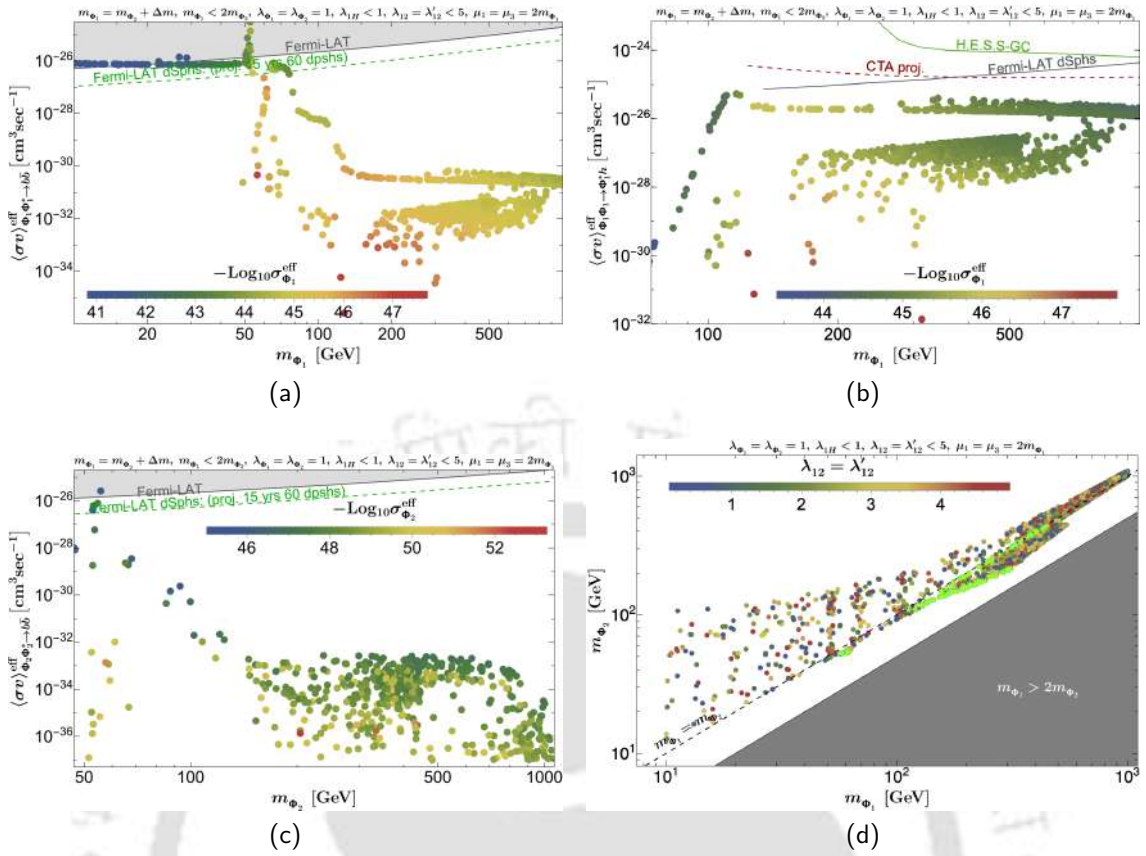

Figure 7.8: Figs. 7.8a and 7.8c represent indirect detection limit on the self-annihilation of WIMP and pFIMP into $\to b\bar{b}$ channel in the relic density allowed parameter space. Fig. 7.8b shows the indirect observational constraints on the WIMP semi-annihilation. In Fig. 7.8d, we show the relic density allowed parameter space in $m_{\Phi_1} - m_{\Phi_2}$ plane where WIMP and pFIMP DD allowed points are indicated by green star. The thick and dashed lines correspond to the observed and projected limits of the experiments as mentioned in the figure(s).

7.5 Summary

The motivation of our study is to find the possible multicomponent DM frameworks when SM is extended with more than one scalar fields, but transforming under a single symmetry. Such efforts have already been done in many papers, however under what circumstances such scenarios evolve has not been elaborated systematically. The heavier component usually have decay terms to DM and to SM. In our paper, we show that the stabilisation of the heavier component depend strictly on the charges of the dark fields under symmetry transformation. For example, whenever, under $\mathcal{Z}_N$ symmetry, $q_1 \neq q_2, q_1 + q_2 \neq N$, the heavier component decays only to dark sector particle, thus allowing it to be stabilized by imposing simple kinematical constraint. However, if the above condition on dark sector particle charges is not obeyed, then heavier component can decay to DM and SM both. Such decays at tree level, one loop and two loop level can only be stopped when we make some couplings vanishingly small. After that the scenario either resembles to $\mathcal{Z}_N \otimes \mathcal{Z}'_N$ case, or $q_1 \neq q_2, q_1 + q_2 \neq N'$ case of a $\mathcal{Z}_{N'}$ group, where $N' > N$. We have explicitly demonstrated all the possibilities for having two DM components in $\mathcal{Z}_2$, $\mathcal{Z}_3$ and $\mathcal{Z}_4$ symmetric cases. We should note here that as there is no choice pertaining to $q_1 \neq q_2, q_1 + q_2 \neq N$ for $\mathcal{Z}_2$ and $\mathcal{Z}_3$ symmetric cases; forcing to compromise some of the couplings of these models to make the heavier DM component stable.

We specifically elaborate the phenomenology associated to $\mathcal{Z}_3$. Interestingly, the choices of terms that should be neglected (or assumed small) are not unique. This gives rise to different possible scenarios in $\mathcal{Z}_3$ symmetry after stabilising the heavier component. Like one can have $\mathcal{Z}_3 \otimes \mathcal{Z}_3'$ or $\mathcal{Z}_6$ with $\{q_1, q_2\} = \{2, 5\}, \{4, 1\}$ etc. They also provide different phenomenological implications. In this chapter, we have discussed two such examples. Conversion, semi conversion and semi-annihilations are some of the key processes that dictate the allowed parameter space of the two component DM model and their compatibility with DD/ID searches. Note that after the heavy particle becomes a stable DM candidate, co-annihilation process stops contributing. This reduces allowed parameter space of the model, particularly to comply with non-observation of DM in DD/ID experiments.

Further, the two DM components can be WIMP or pFIMP depending on the strength of the corresponding Higgs portal couplings. Both WIMP-WIMP case, and WIMP-pFIMP cases are illustrated here and we show that WIMP-pFIMP case enjoys a larger parameter space as the pFIMP detection relies on loop level WIMP mediated interactions. There is another interesting feature that comes out of the specific WIMP-pFIMP analysis in $\mathcal{Z}_3$ symmetry that here pFIMP not only relies on conversion with WIMP to thermalise, but also semi-conversion plays a crucial role for the same, which makes a crucial distinction that one can choose a large mass splitting between WIMP and pFIMP unlike the $\mathcal{Z}_2$ case with two real scalars [305]. This in turn can help distinguishing WIMP and pFIMP in direct search and collider search experiments via a kink or a double hump missing energy distribution, which is otherwise difficult with smaller mass splitting.

Chapter 8

Two-component Dark Matter and particle-antiparticle asymmetry

Contents

The observable cosmos exhibits sizable baryon asymmetry, small active neutrino masses, and the presence of dark matter (DM). To address these phenomena together, we propose a two component DM scenario in an extension of Scotogenic model, imposing $\mathcal{Z}_2 \otimes \mathcal{Z}_2'$ symmetry. The electroweak sphaleron process converts the Y_{B-L} yield, generated through the Leptogenesis mechanism, into the baryon asymmetry ($Y_{\Delta B}$) at $T_{sph} \sim 131.7$ GeV, the sphalerons decoupling temperature. In this framework, the CP asymmetry as well as the radiative neutrino mass generation explicitly involve the two DM particles, thus establishing a correlation between the baryon asymmetry, DM and observed active neutrino masses. We study in details the allowed parameter space available after considering all the constraints from the three phenomena as well as from the collider search limits, and outline the region which could potentially be tested in future DM detection experiments through direct or indirect detection searches, lepton flavor-violating decays, etc. The discussion in this chapter is based on Ref . [746].

8.1 Introduction

In this work, we propose a two-component DM model where both DMs are directly responsible for the baryon asymmetry production in the universe while being consistent with the neutrino oscillation data. To the best of our knowledge, this is attempted for the first time. Although there are efforts where DM particle generates the CP asymmetry by entering into the one-loop diagrams [180, 747], or co-genesis with two component DM [748], but the DM parameter space mostly remains independent of the leptogenesis. In the proposed model, the same DM coupling that generates diagrams for the CP asymmetry also determines the DM relic density and thus are correlated. The particle content of our model is an extension of the minimal scotogenic model that includes two inert doublets, two right-handed neutrinos (RHNs), and a real scalar. The low-scale leptogenesis requires the introduction of two new interaction vertices, along with the minimal scotogenic vertex, which doesn't affect neutrino mass generation, giving rise to RHN mass relaxation. These new vertices can contain DMs after ensuring the particles' stability by appropriate $\mathcal{Z}_2 \otimes \mathcal{Z}_2'$ symmetry assignments. A similar scenario was studied in [749, 750], where the CP asymmetry is generated by introducing a real scalar particle (not a DM) in type-I seesaw model. Additionally, few more studies [751–753] known as N_2 leptogenesis, assumes the decay of heavy RHN ($m_{N_2} > m_{N_1}$) relevant for asymmetry generation, but without direct involvement of DM. However, in our framework, the asymmetry generated by the tree and 1-loop decays of the lightest RHN, contain two DMs, which are the lightest stable particles under each discrete symmetries $\mathcal{Z}_2 \otimes \mathcal{Z}_2'$. By this choice, we were also able to prohibit the lepton number violating (LNV) decays involving the SM Higgs and only allow the symmetry singlet terms. For simplicity, we assume that all the model parameters are real, except for the Yukawa couplings related to the tree-level LNV decay to explain the observed BAU. In this way, the asymmetry generation directly involves the masses of two DMs and the couplings associated with interaction with DMs, which are also responsible for the DM analysis. Therefore, the BAU satisfied points are constrained by the DM bounds. Apart, the radiative diagrams for neutrino mass generation also have a strong connection with the DM, thus connecting all the three phenomena together.

There is also a phenomenological advantage for the presence of two DMs in this model. In an inert doublet model, the DM is tightly constrained and can't produce the correct relic density unless the DM mass is around the Higgs mass or approximately 600 GeV. Introducing an additional DM component shares the remaining relic density and enhances the allowed parameter space via DM-DM conversion.

The chapter is organized as follows. In Section 8.2, we provide a general discussion of the model and its motivations. In Section 8.3, we explore the collider and lepton flavor constraints on the model parameters. The thermal leptogenesis and dark matter phenomenology, including DM relic density and direct (indirect) detection prospects, are discussed in detail in Sections 8.4 and 8.5, respectively. Finally, we summarize and conclude in Section 8.6. Several appendices provide the details of the relevant calculations.

8.2 The Model and motivations

The minimal scotogenic model [134], proposed to generate neutrino mass at one loop level, successfully addresses the BAU and DM in the universe. The one-loop neutrino mass generation relaxes the constraints coming from the neutrino masses to Leptogenesis. The well-known Davidson Ibarra (DI) bound lowers down to around $m_{N_1} \sim 10\mathrm{T}eV$ [180, 753, 754] from $m_{N_1} \sim 10^{10}\ GeV$ in the type-I seesaw model [755]. However, with two right-handed neutrinos, the scale of Leptogenesis again pushes to $m_{N_2} \gtrsim 10^{10}\ GeV$ [180, 751]. Depending on the lightest $\mathcal{Z}_2$ odd state, the lightest neutral component of the inert doublet or the lightest right-handed neutrino can be a DM candidate in the scotogenic model. In the case of the scalar DM scenario, three RHNs participate in Leptogenesis. In such a case leptogenesis is possible at the TeV scale independent of DM parameters. In the case of the fermionic DM scenario, two RHNs participate in leptogenesis and the observed asymmetry can be generated around $m_{N_2} \sim 10^{10}\ GeV$. With two RHNs responsible for CP asymmetry generation, the lightest RHN N_1, being DM only enters the leptogenesis scenario by scattering washouts [751]. The scattering washouts are insignificant compared to the huge washout from the inverse decay of N_2. Therefore the leptogenesis parameter space remains independent of DM parameter space. In this work, we propose an extension of the scotogenic model where a DM particle directly generates the CP asymmetry in LNV decays. A two-component DM scenario naturally emerges in the model.

We extend the SM with two copies of RHNs ($N_{1,2}$), two scalar inert doublets ($\eta_{1,2}$), and a real singlet scalar (ϕ). All the SM fields are even under an imposed $\mathcal{Z}_2 \otimes \mathcal{Z}_2'$ symmetry while the new fields transform non-trivially as shown in Table 8.1. The neutrinos get mass by the scotogenic mechanism [134] as shown in Fig. G.2 of Appendix G.2. We keep the right-handed neutrinos N_i to be heavier than the doublet scalars η_i and the singlet scalar ϕ. A net lepton asymmetry can be generated from the out-of-equilibrium decay of the lightest RHN ($N_1 \longrightarrow l_\alpha \eta_1$). Due to the imposed $\mathcal{Z}_2 \otimes \mathcal{Z}_2'$ symmetry the singlet scalar enters the vertex correction diagram generating the required CP asymmetry. The additional $\mathcal{Z}_2$ symmetry naturally leads to a two-component DM scenario. Under these circumstances, the lightest of the inert doublets could be a viable WIMP due to its gauge portal interaction. At the same time, the singlet scalar ϕ can be any DM, depending on the strength of its Higgs portal interaction and its interaction rate with the WIMP. Finally, we could get a WIMP-WIMP [300], WIMP-FIMP [301], WIMP-pFIMP [305–307], etc. However, this chapter focuses solely on the WIMP-WIMP scenario.

Fields	$SU(3)_c \otimes \mathrm{SU(2)_L} \otimes \mathrm{U(1)_Y}$	$\mathcal{Z}_2$	$\mathcal{Z}_2'$
N_1	(1,1,0)	-1	1
N_2	(1,1,0)	1	-1
η_1	(1,2,1/2)	-1	1
η_2	(1,2,1/2)	1	-1
ϕ	(1,1,0)	-1	-1

Table 8.1: Particle content of the extended model and their corresponding charges.

$$\mathcal{L} = \mathcal{L}_{\rm SM} + \frac{1}{2}|\partial_\mu \phi|^2 + \sum_{k=1,2}\left(i\overline{N}_k \partial\!\!\!/ N_k + |\mathcal{D}_\mu \eta_k|^2\right) + \mathcal{L}_{Yuk} - \mathcal{V}\,. \tag{8.1}$$

Here the Lagrangian $\mathcal{L}_{Yuk}$ contain the Yukawa couplings as well as the Majorana mass term for the RHNs and is given by,

$$\mathcal{L}_{Yuk} \;=\; -\sum_{i=1,2}\left(h_{ii\alpha}\overline{L}_\alpha \tilde{\eta}_i N_i + h.c\right) - \frac{1}{2}\sum_{i=1,2} m_{N_i}\overline{N_i^c}N_i. \tag{8.2}$$

The scalar potential $\mathcal{V}$ is given by

$$\begin{aligned}\mathcal{V} =& \mu_{\eta_i}^2\left(\eta_i^\dagger\eta_i\right) + \frac{1}{4}\lambda_{ij}\left|\eta_i^\dagger\eta_j + \eta_j^\dagger\eta_i\right|^2 + \frac{1}{2}\mu_\phi^2\phi^2 + \frac{1}{4!}\lambda_\phi\phi^4 + \lambda_{iiH}\left(H^\dagger\eta_i\right)\left(\eta_i^\dagger H\right)\\ &+\lambda'_{iiH}\left(\eta_i^\dagger\eta_i\right)\left(H^\dagger H\right) + \frac{1}{2}\left[\lambda''_{iiH}\left(\eta_i^\dagger H\right)\left(\eta_i^\dagger H\right) + h.c.\right] + \frac{1}{2}\lambda_{\phi H}\phi^2\left(H^\dagger H\right)\\ &+\frac{1}{2}\lambda_{ii\phi}\left(\eta_i^\dagger\eta_i\right)\phi^2 + \frac{1}{2}\sum_{i\neq j}\left(y_{ij\phi}\overline{N_i^c}N_j\phi + \mu_{ij\phi}\eta_i^\dagger\eta_j\phi + h.c.\right)\,.\end{aligned} \tag{8.3}$$

where, we assumed real $y_{ij\phi}$ and inert doublets ($\eta_j s$) has the following forms,

$$\eta_j = \frac{1}{\sqrt{2}}\begin{pmatrix}\sqrt{2}\eta_j^+\\ \eta_{R_j}^0 + i\eta_{I_j}^0\end{pmatrix}\,. \tag{8.4}$$

After the electroweak symmetry breaking, the masses of the physical scalars would be,

$$m_\phi^2 = \mu_\phi^2 + \frac{1}{2}\lambda_{\phi H}v^2\,, \tag{8.5}$$

$$m_{\eta_i^+}^2 \text{[1]} = \mu_{\eta_i}^2 + \lambda'_{iiH}v^2\,, \tag{8.6}$$

$$m_{\eta_{R_i}^0}^2 = m_{\eta_i^+}^2 + \frac{1}{2}\left(\lambda_{iiH} + \lambda''_{iiH}\right)v^2\,, \tag{8.7}$$

$$m_{\eta_{I_i}^0}^2 = m_{\eta_i^+}^2 + \frac{1}{2}\left(\lambda_{iiH} - \lambda''_{iiH}\right)v^2\,. \tag{8.8}$$

8.3 Constraints on model parameters

8.3.1 Collider constraints

LHC and LEP experiments put constraints on the decay of SM gauge bosons [462, 463, 756]. One such constraint on the model appears from $Z \longrightarrow \eta_R\eta_I$ requiring $m_Z < m_{\eta_R} + m_{\eta_I}$.

$$\Gamma_{\rm Z\to invisible} < \begin{cases}506 \pm 13\ {\rm MeV} \quad ({\rm ATLAS})\,,\\ 523 \pm 16\ {\rm MeV} \quad ({\rm CMS})\,,\\ 498 \pm 17{\rm MeV} \quad ({\rm L3})\,.\end{cases} \tag{8.9}$$

[1] $\mu_{\eta_i}^2 > 0 \implies m_{\eta_i^+}^2 > \lambda'_{iiH}v^2$ required for the stability of inert doublets.

In the parameter space $m_h/2 > m_{\eta_R}, m_{\eta_I}$ the constraints from the Higgs invisible decay is applied. The observed (expected) upper limit on the invisible branching fraction of the Higgs boson corresponds to an integrated luminosity of 138 fb^{-1}, at 95% confidence level [460, 461] with total decay width of 125.1 GeV Higgs is $3.2^{+2.8}_{-2.2}$ MeV [757],

$$\mathcal{B}_{\mathrm{h}\to\mathrm{invisible}} < \begin{cases} 0.107\ (0.077) \quad (\mathrm{ATLAS})\,, \\ 0.15\ (0.08) \quad (\mathrm{CMS})\,. \end{cases} \tag{8.10}$$

This constrain our model parameters $(\lambda_{iiH} + \lambda'_{iiH} \pm \lambda''_{iiH})$, $\lambda_{\phi H}$ to be less than around 10^{-3} in the regime $m_{\eta_R}, m_{\eta_I}, m_\phi < m_h/2$. Additionally LEP precision data rule a parameter space $m_{\eta_R} < 80\ GeV$, $m_{\eta_I} < 100\ GeV$ and $m_{\eta_I} - m_{\eta_R} > 8\ GeV$ [758]. From LHC and LEP, [759–761], the charge scalar mass is constrained and $m_{\eta_j^\pm} > 90\ GeV$.

8.3.2 Lepton Flavor constraints

The MEG II experiment, which searches for the decay $\mu^+ \to e^+\gamma$, reports that no excess of events over the expected background has been observed, yielding an upper limit on the branching ratio [225, 762],

$$\mathcal{B}(\mu^+ \to \mathrm{e}^+\gamma) < 3.1 \times 10^{-13}\ (90\%\ \mathrm{C.L.})\,, \tag{8.11}$$

The branching fraction corresponds to $\ell_\alpha \to \ell_\beta\gamma$ is given by [763–766],

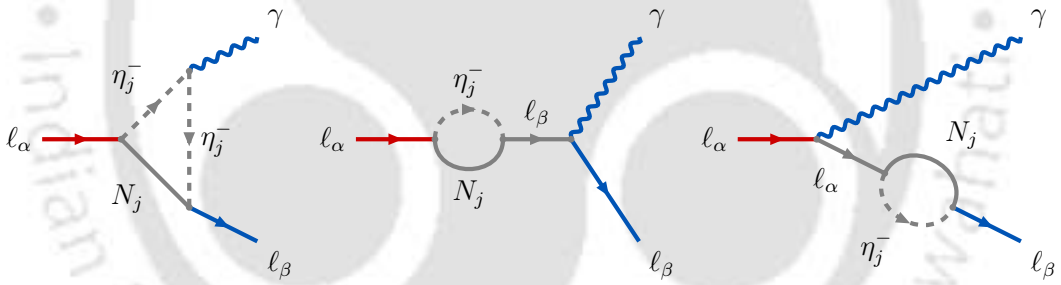

Figure 8.1: 1-loop Feynman diagrams related to $\ell_\alpha \to \ell_\beta\gamma$.

$$\mathcal{B}(\ell_\alpha \to \ell_\beta\gamma) = \frac{3(4\pi)^3\alpha_{\mathrm{em}}}{4G_F^2}|F_D|^2\ \mathrm{BR}(\ell_\alpha \to \ell_\beta\nu_\alpha\overline{\nu_\beta})\,, \tag{8.12}$$

where α_{em} and G_F are the electromagnetic fine structure and Fermi constant, respectively. For SM leptonic decay branching, $\ell_\alpha \to \ell_\beta\nu_\alpha\overline{\nu_\beta}$, see [18]. F_D is the dipole form factor, given by,

$$F_D = \sum_{i=1}^{2} \frac{h^*_{ii\beta}h_{ii\alpha}}{2(4\pi)^2}\frac{1}{m^2_{\eta_i^+}}G(x_i)\,, \tag{8.13}$$

where, $x_i = \dfrac{m^2_{N_i}}{m^2_{\eta_i^+}}$ and $G(x) = \dfrac{1 - 6x + 3x^2 + 2x^3 - 6x^2\ \log\ x}{6(1-x)^4}$.

During our analysis, we consistently account for this limit. Since the required Yukawa couplings are very small ($|h_{ii\alpha}| \sim 10^{-5}$), we don't need to be concerned about this limit. However, other limits, such as $\mu \to eee$, would be more suppressed, as the same couplings contribute to these processes.

8.4 Thermal Leptogensis analysis

In the minimal scotogenic model, a net lepton asymmetry can be generated from the decay of the lightest right-handed neutrino. The Yukawa coupling involved in Leptogenesis is subjected to satisfy the light neutrino data through the Casas-Ibarra (CI) parametrization [767, 768]. The Yukawa couplings are determined by the scalar quartic coupling λ''_{iiH} and the active and right-handed neutrino masses [180]. While for three right-handed neutrinos, the Yukawa couplings of the lightest right-handed neutrino can be made small by fixing the lightest active neutrino mass, we don't have such a choice with two right-handed neutrinos [751]. With two right-handed neutrinos, the Yukawa couplings of the lightest right-handed neutrino are always large, resulting in strong washouts of the lepton asymmetry. In Fig. 8.2 we show the decay parameter $K_{N_1} = \Gamma_{N_1}/H(z=1)$ with mass of the lightest right handed neutrino (m_{N_1}). The left panel plot of Fig. 8.2 show the decay parameter with two RHNs in the minimal scotogenic model is always greater than one, while the right panel corresponds to our model. This suggests that we are always in a strong washout region. Due to the strong washouts, the scale of Leptogenesis is pushed beyond $m_{N_1} \sim 10^9$ GeV. This lower bound for a vanilla leptogenesis mechanism is known as the Davidson Ibarra (DI) bound [755]. In the case of the minimal scotogenic model, the DI bound can be found in [180]. The singlet DM enters the one loop vertex correction diagram of $N_1 \longrightarrow l_\alpha \eta_1$ in this model. Although we still are in a strong washout region with only two RHNs (see right panel of Fig. 8.2), we now have a coupling in the leptogenesis loop free from the neutrino mass generation. One can sufficiently enhance the asymmetry parameter ε_{N_1} by fixing the $y_{ij\phi}$. The DI bound for the minimal scotogenic model is no longer applicable in this case.

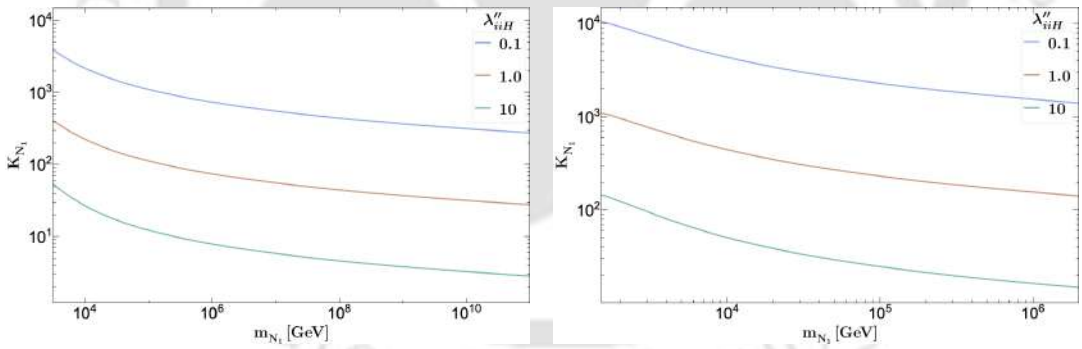

Figure 8.2: We have used $\{m_{N_1} > \mu_{\eta_2} + m_\phi,\ \lambda'_{iiH} = 0.01,\ m_{\eta^0_{I_1}} = 0.5\ TeV,\ m_\phi = 0.4\ TeV,\ m_{\eta^0_{I_2}} = m_{\eta^0_{I_1}} + m_\phi + 1\ GeV,\ \mu_{12\phi} = m_\phi,\ y_{12\phi} = 1,\ m_{N_2} = 3m_{N_1},\ m_{\eta^+_i} = m_{\eta^0_{I_i}} + 3\ \text{GeV},\ m_{\eta^0_{R_i}} = (m^2_{\eta^0_{I_i}} + \lambda''_{iiH} v^2)^{1/2},\ a = 0.1,\ b = 0.3\}$ to calculate the decay parameter, K_{N_1}.

We calculate the CP asymmetry (ε_{N_1}) parameter arising from the decay $N_1 \longrightarrow l_\alpha \eta_1$ in Appendix G.3. In Fig. 8.3, we show the variation of the asymmetry parameter through the dark rainbow color bar ε_{N_1} in $m_{N_1} - \lambda''_{ii\mathrm{H}}$ plane. On the left panel plot of the Fig. 8.3, asymmetry parameter ε_{N_1} is plotted for the minimal scotogenic model while, on the right panel plot, it is shown for the extended model. In the left panel plot, it can be seen that there exists a correlation of the asymmetry parameter with the quartic coupling $\lambda''_{ii\mathrm{H}}$ as well as m_{N_1}. With the decrease in $\lambda_{ii\mathrm{H}}$ the Yukawa couplings $h_{11\alpha}$ increases increasing asymmetry parameter ε_{N_1}. However, one can not decrease the $\lambda''_{ii\mathrm{H}}$ to arbitrarily small values, as it would increase

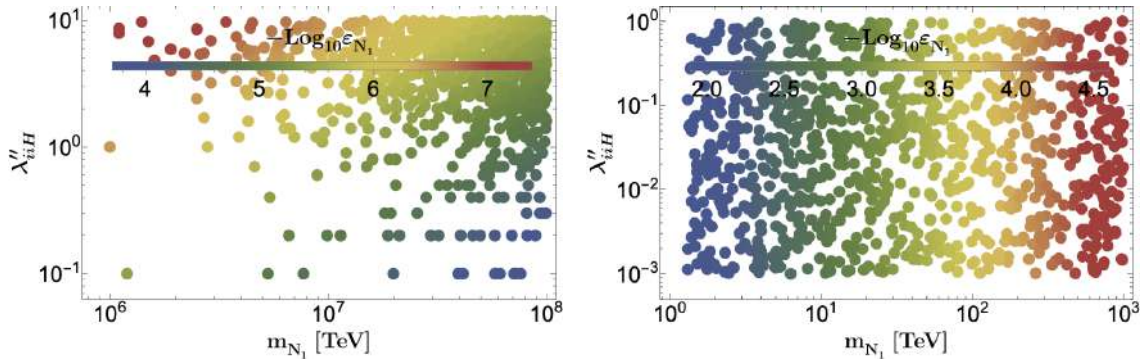

Figure 8.3: Scan plot for the asymmetry parameter in $m_{N_1} - \lambda''_{iiH}$ plane. For the left panel plot, the other important parameters are mentioned in the figure inset (for 2 RHN and one inert). The figure on the right corresponds to our model and uses the same parameters as those in Fig . 8.2.

the washouts leading to a strong washout of the generated asymmetry. With the increase in the masses of the RHNs, the corresponding Yukawa couplings increase, increasing the asymmetry parameter. On the right panel plot, it is seen that the correlation of the asymmetry parameter ε_{N_1} with λ''_{iiH} vanishes. The dependence of ε_{N_1} on λ''_{iiH} is through the Yukawa coupling $h_{ii\alpha}$, by the Casas Ibarra parameterization given in Eq . (G.18). Due to the presence of the Yukawa coupling $y_{12\phi}$ and $\mu_{12\phi}$ in the vertex correction diagram, the dependence of the asymmetry parameter on the Yukawa couplings $h_{11\alpha}$ vanishes.

In this model, we found that the asymmetry parameter ε_{N_1} is independent of the scalar couplings λ_{11H}, unlike the minimal scotogenic model. Required kinematics for Leptogenesis:

$$m_{N_1} > \mu_{\eta_2} + m_\phi\,,\ \mu_{\eta_2} > \mu_{\eta_1} + m_\phi\,,\ m_{N_2} > m_{N_1} + m_\phi\,. \tag{8.14}$$

The relevant coupled Boltzmann Equations for Leptogenesis is written as,

$$\begin{aligned}
\frac{dY_{N_1}}{dz} =& -D_{N_1}\left(Y_{N_1} - Y_{N_1,0}\right) - \frac{s}{H(z)z}\left(Y^2_{N_1} - Y^2_{N_1,0}\right)\left[\langle\sigma v\rangle_{N_1N_1\longrightarrow\phi\phi} + \langle\sigma v\rangle_{N_1N_1\longrightarrow\eta_1\eta_1^\dagger} + \langle\sigma v\rangle_{N_1N_1\longrightarrow\ell_\alpha\bar{\ell}_\beta}\right]\,,\\
& - \frac{s}{H(z)z}\left(Y_{N_1} - Y_{N_1,0}\right)\left[Y_{\phi,0}\langle\sigma v\rangle_{N_1\phi\longrightarrow l_\alpha\eta_2^\dagger} + Y_{\eta_1,0}\langle\sigma v\rangle_{N_1\eta_1\longrightarrow l_\alpha V_\mu} + Y_{N_2,0}\langle\sigma v\rangle_{N_1N_2\longrightarrow\eta_1\eta_2^\dagger}\right]\,,\\
\frac{dY_{B-L}}{dz} =& -\varepsilon_{N_1}D_{N_1}\left(Y_{N_1} - Y_{N_1,0}\right) - W_{\rm ID}Y_{B-L} - \frac{s}{H(z)z}Y_{B-L}\left[2\sum_{i=1,2}Y_{\eta_i,0}\langle\sigma v\rangle_{l_\alpha\eta_i^\dagger\longrightarrow\bar{l}_\beta\eta_i}\right.\\
& \left. + 2Y_{l,0}\sum_{i=1,2}r^2_{\eta_i}\langle\sigma v\rangle_{\eta_i^\dagger\eta_i^\dagger\longrightarrow l_\alpha l_\beta} + Y_{l,0}\sum_{i\neq j}r_{N_i}r_\phi\langle\sigma v\rangle_{N_i\phi\longrightarrow l_\alpha\eta_j^\dagger} + Y_{l,0}\sum_{i=1,2}r_{N_i}r_{\eta_i}\langle\sigma v\rangle_{\eta_iN_i\longrightarrow l_\alpha V_\mu}\right]\,.
\end{aligned} \tag{8.15}$$

The Boltzmann equations are written in terms of the dimensionless variable $z = \mathrm{m}_{\mathrm{N}_1}/\mathrm{T}$, i^{th} particle co-moving number density Y_i and equilibrium number density $Y_{i,0} = Y_i^{\rm eq}$. Here D_{N_1} and $W_{\rm ID}$ are the decay and inverse decay terms for N_1 defined as

$$D_{N_1} = K_{N_1}z\frac{\kappa_1(z)}{\kappa_2(z)}, \tag{8.16}$$

$$W_{\rm ID} = \frac{1}{4}K_{N_1}z^3\kappa_1(z)\,, \tag{8.17}$$

where $K_{N_1} = \Gamma_{N_1}/H(z=1)$ is known as the decay parameter and κ_i's are the modified Bessel functions of second kind. $\langle\sigma v\rangle_{\rm AB\longrightarrow CD}$ represents the thermal averaged

cross-section for a given process $A + B \longrightarrow C + D$. Here $r_j = Y_{j,0}/Y_{l,0}$. The detailed derivation of neutrino mass and asymmetry parameters (ε_{N_1}) is available in the Appendix G.2 and G.3, respectively. The relevant Feynman diagrams corresponding to the leptogenesis scenarios are shown in Fig . G.1.

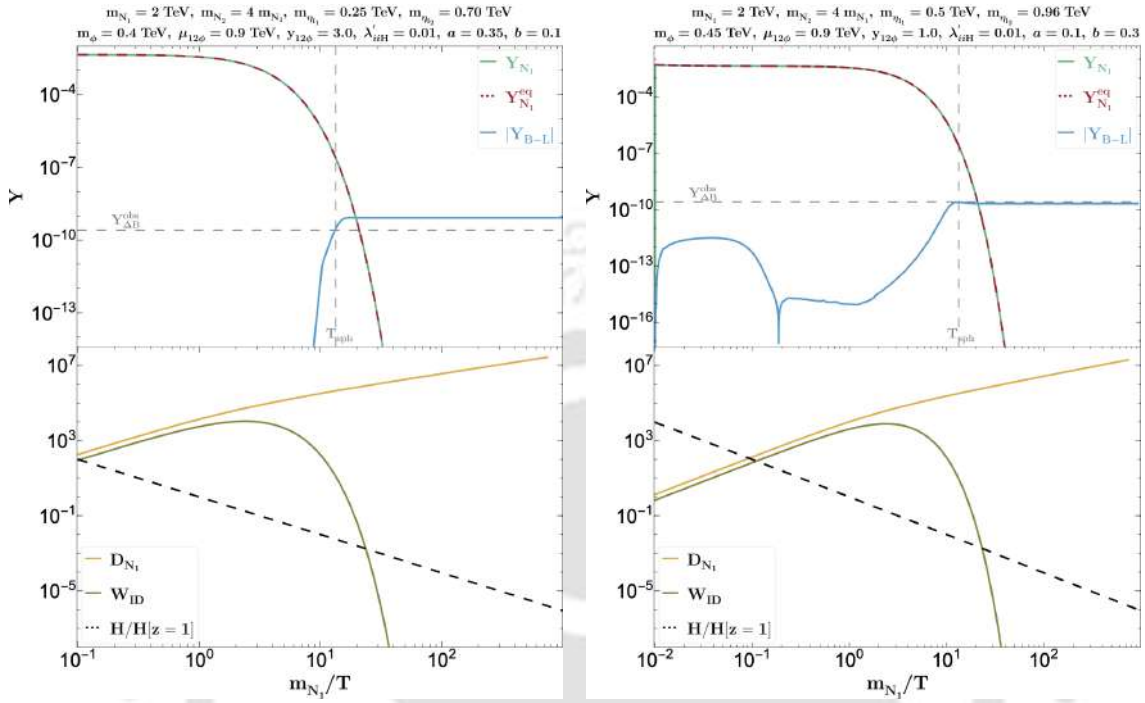

Figure 8.4: The left figure corresponds to the initial condition $Y_{N_1} = Y^{eq}_{N_1}$, while for the right figure $Y_{N_1} \sim 10^{-20}$. The horizontal and vertical gray dashed lines indicate $Y^{obs}_{\Delta B}$ and T_{sph}, respectively. The other solid and dashed lines represent the variation of parameters with $z = m_{N_1}/T$, as indicated in the figure's inset. The masses of the real and charged components of the inert doublet are defined as $m_{\eta^0_{R_i}} = m_{\eta^0_{I_i}} + 2$ and $m_{\eta^+_i} = m_{\eta^0_{I_i}} + 3$, respectively.

In Fig . 8.4, we have represented the solution of cBEQ (Eq . (8.15)), yielding the Y_{B-L} and Y_{N_1} evaluation with z. In Leptogenesis, the observed baryon asymmetry is generated by the sphaleron process, where the sphaleron freeze-out occurs at T_{sph}, transform Y_{B-L} asymmetry to the $Y_{\Delta B}$ asymmetry. We solve it for two benchmark points in the left and right panel of Fig . 8.4. The blue and green solid lines depict the evolution of $|Y_{B-L}|$ and Y_{N_1}, respectively, while the dark red and black dashed lines represent $Y^{eq}_{N_1}$ and $H/H(z = 1)$, respectively. The figures in the bottom panel illustrate how the decay and inverse decay rates vary with z. The intersection of D_{N_1} and W_{ID} with $H/H(z = 1)$, decide the asymmetry production and washout. At the first and second intersections, both are becoming in and out-equilibrium processes. Although the rates are equal at equilibrium, the production and washout are also influenced by Y_{N_1} and Y_{B-L}, leading to fascinating dynamics. In the bottom panel of Fig . 8.4, we have not shown the scattering rate relevant for asymmetry evaluation, as they are less significant compared to the decay (D_{N_1}) and inverse decay (W_{ID}). However, some scattering processes significantly impact the number density of N_1 keeping it near its equilibrium abundance, reducing the asymmetry.

In Fig . 8.4, we show two plots representing two different scenarios: the left plot assumes that N_1 is initially in equilibrium, while the right plot considers a case where N_1 is not in equilibrium and starts from a very small initial abundance. In the left panel of Fig . 8.4, N_1 is initially in equilibrium so the decay $(N_1 \to l\eta_1)$ and the inverse

decay ($l\eta_1 \to N_1$) rates are almost close to each other at high temperature, $z \lesssim 9$. Because of this, at high temperatures, the produced asymmetry is washed out and the remaining asymmetry is negligible, $|\mathrm{Y_{B-L}}| \lesssim 10^{-14}$. But, when the temperature falls below m_{N_1}, the inverse decay rate would start to fall and finally go below the Hubble rate. During this time ($9 < z < 20$), the decay will become dominant and the produced asymmetry will survive due to the gradual decrease in strength of the inverse decay washout. The gradual increase in asymmetry will not continue indefinitely. It will stop when $\mathrm{Y}^{\mathrm{eq}}_{\mathrm{N}_1}$ falls to a very small value due to the decays and can no longer produce asymmetry at low temperatures ($z \gtrsim 20$) and it freezes in. A similar explanation applies to the right panel plots in Fig. 8.4 when $z \gtrsim 2$. However, below it *i.e.* $z \lesssim 2$ the asymmetry is generated through the out-of-equilibrium decay of N_1 and strongly washed out when it comes into thermal equilibrium. Once it does, it mimics the behavior seen in the left panel plot.

Since numerous parameters play a significant role in Leptogenesis, we are fixing some at specific values and expressing others in terms of $\{m_{\eta^0_{I_1}},\, m_\phi,\, m_{N_1},\, y_{12\phi},\, \mu_{12\phi}\}$:

$$\begin{aligned} &m_{N_2} = 3m_{N_1},\; m_{\eta^0_{R_i}} = m_{\eta^0_{I_i}} + 2\ \mathrm{GeV},\; m_{\eta^+_i} = m_{\eta^0_{I_i}} + 3\ \mathrm{GeV},\; a = 1,\; b = 0.4\,, \\ &m_\phi < \mu_{12\phi} < 2m_\phi,\; \lambda'_{11H} = \lambda'_{22H} = 0.1,\; m_{\eta^0_{I_2}} = m_{\eta^0_{I_1}} + m_\phi + 1\ \mathrm{GeV},\; m_{N_1} > m_{\eta^0_{I_2}} + m_\phi\,. \end{aligned} \tag{8.18}$$

The choice of $a,\ b$ is not unique, and the dependency is shown in Fig. G.4 for a sample benchmark.

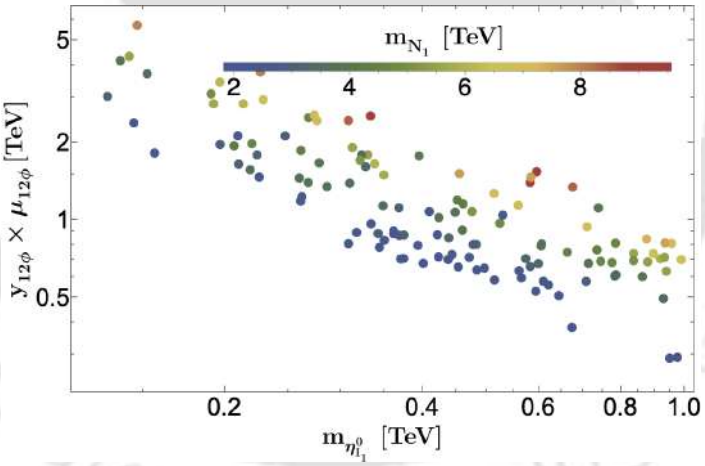

Figure 8.5: In this figure, the dark rainbow-colored points represent the RHN mass m_{N_1}. All of these points respect the observed baryon asymmetry ($Y^{\mathrm{obs}}_{\Delta B} \simeq 8.75^{+0.23}_{-0.23} \times 10^{-11}$) and account for the correct active neutrino masses.

In Fig. 8.5 we show the points in $m_{\eta^0_{I_1}} - y_{12\phi}\mu_{12\phi}$ plane that satisfies the neutrino mass and baryon asymmetry while respecting the current LEP constraints on the charged scalar. Since the free couplings $y_{12\phi}$ and $\mu_{12\phi}$ both positively contribute to the asymmetry parameter ε_{N_1} we keep $y_{12\phi}\mu_{12\phi}$ in the y-axis. The dimension-full coupling $\mu_{12\phi}$ is defined as a function of m_ϕ and is varied within the range, $1 < \mu_{12\phi}/m_\phi < 2$. The different values of m_{N_1} are shown as a rainbow color bar. From Fig. 8.5 it is seen that there exist a positive correlation between m_{N_1} and $y_{12\phi}\mu_{12\phi}$. In Eq. (G.36), it is clear that, the asymmetry parameter ε_{N_1} decreases with the increase in m_{N_1} and increases with the enhancement of η_1 ($\equiv m^2_{\eta^0_{I_1}}/m^2_{N_1}$). Therefore it is required to increase the free couplings $y_{12\phi}\mu_{12\phi}$ to generate sufficient asymmetry.

Hence a larger value of m_{N_1} require larger $y_{12\phi}\mu_{12\phi}$ to satisfy the observed baryon asymmetry. Similarly, in Fig. 8.5 it is seen that the points satisfying the observed asymmetry have a negative gradient with $m_{\eta^0_{I_1}}$. It is also due to the dependency of ε_{N_1} on η_1. For a fixed m_{N_1}, with the increase in $m_{\eta^0_{I_1}}$ the asymmetry parameter ε_{N_1} increases. To compensate for this, we need smaller values of $y_{12\phi}\mu_{12\phi}$. Before concluding this section, we have illustrated several points, in Table 8.2, that meet the constraints on active neutrino masses and the observed baryon asymmetry. However, the LFV constraints are not applicable in this context, as the asymmetry-respecting parameter $|h_{ii\alpha}|$ is effectively negligible.

BM	$m_{\eta^0_{I_1}}$ [GeV]	m_ϕ [GeV]	m_{N_1} [TeV]	$\mu_{12\phi}$ [GeV]	$y_{12\phi}$
I	232.37	656.80	6.388	1037.20	2.555
II	786.91	124.31	3.670	222.43	2.603
III	355.11	365.58	2.205	384.67	2.608
IV	340.88	467.62	5.932	598.88	2.688
V	130.78	618.41	3.661	1220.52	3.001

Table 8.2: The sample benchmark (BM) points are giving the observed baryon asymmetry after addressing the active neutrino masses, while other parameters are considered following the Eq. (8.18).

8.5 Dark Matter analysis

The lightest particle under a discrete symmetry is stable and becomes a DM. In Table 8.1, we have define the particles charges under $\mathcal{Z}_2 \otimes \mathcal{Z}_2'$ symmetry. We have chosen the $\eta^0_{I_1}$ (CP-odd part of inert doublet η_1) and ϕ (real scalar singlet) as our DMs by considering other parameter masses larger than these two. The required kinematics for the stabilisation of DMs ($\eta^0_{I_1}$, ϕ):

$$m_{\eta^0_{I_2}} > m_{\eta^0_{I_1}} + m_\phi\,,\; m_{N_2} > m_{\eta^0_{I_2}}\,, m_{\eta^0_{R_i}} > m_{\eta^0_{I_i}}\,,\; m_{\eta_i^+} > m_{\eta^0_{I_i}}\,,\; m_{N_1} > m_{\eta^0_{I_1}}\,. \quad (8.19)$$

The heavier dark sector particles contribute to relics through co-annihilation channels. In this two-component real scalar DM scenario, both DMs interact with the visible sector via gauge and Higgs portal interactions. In Eq. (8.3), we see that two inert doublets have gauge portal interactions, by which $\eta^0_{I_1}$ is in thermal equilibrium, and the lightest one acts as a viable thermal dark matter candidate. In contrast, ϕ interacts with the visible sector only via the Higgs portal interactions. It's also coupled to the inert doublets through $\eta_1^\dagger\eta_2\phi$ and $\eta_i^\dagger\eta_i\phi^2$ terms. Interestingly, the mass coupling associated with $\eta_1^\dagger\eta_2\phi$ is also contributed in baryon asymmetry along with DM masses $m_{\eta^0_{I_1}}$ and m_ϕ. However, Depending on the value of $\lambda_{\phi H}$, two scenarios

arise: (i) WIMP-WIMP, for $\lambda_{\phi H} \sim 0.1$, and (ii) WIMP-pFIMP, for $\lambda_{\phi H} \sim 10^{-12}$, with dark matter masses in the $GeV - TeV$ range. In this chapter, we exclusively focus on the WIMP-WIMP scenario; and we leave the alternate possibilities for future works.

In a two-component DM scenario, the relic density of DM is calculated by solving the coupled Boltzmann Equation (cBEQ). For simplicity, we can neglect some of the processes that are ineffective in DM freezeout. RHNs (N_i) masses $(\sim TeV)$ are quite larger than DMs masses, necessary to account for both the correct baryon asymmetry and neutrino masses. So, (N_i)s remained out of thermal equilibrium and couldn't participate in DM freezeout, which occurs at $\mathrm{T_{FO}}$ is smaller than the sphaleron decoupling temperature, $T_{\rm sph}$ where the $\mathrm{Y_{B-L}}$ is transferred into $\mathrm{Y_{\Delta B}}$. Finally, the coupled Boltzmann equations are written as,

$$\begin{aligned}
\frac{dY_{\eta_1}}{dz} &= -\frac{s}{H\left(\frac{m_{\eta_1}}{m_{N_1}}z\right)\left(\frac{m_{\eta_1}}{m_{N_1}}\right)z}\left[(Y^2_{\eta_1}-Y^2_{\eta_1,0})\langle\sigma v\rangle^{\rm eff}_{\eta_1\eta_1\longrightarrow \rm SM\ SM}+\left(Y^2_{\eta_1}-Y^2_{\phi}\frac{Y^2_{\eta_1,0}}{Y^2_{\phi,0}}\right)\langle\sigma v\rangle^{\rm eff}_{\eta_1\eta_1\longrightarrow\phi\phi}\right], \\
\frac{dY_{\phi}}{dz} &= -\frac{s}{H\left(\frac{m_{\phi}}{m_{N_1}}z\right)\left(\frac{m_{\phi}}{m_{N_1}}\right)z}\left[(Y^2_{\phi}-Y^2_{\phi,0})\,\langle\sigma v\rangle_{\phi\phi\longrightarrow \rm SM\ SM}+\left(Y^2_{\phi}-Y^2_{\eta_1}\frac{Y^2_{\phi,0}}{Y^2_{\eta_1,0}}\right)\langle\sigma v\rangle^{\rm eff}_{\phi\phi\longrightarrow\eta_1\eta_1}\right].
\end{aligned} \tag{8.20}$$

where $Y_{i,0} = Y_i^{\rm eq}$, $z = \mathrm{m_{N_1}/T}$, $\langle\sigma v\rangle^{\rm eff}$ denoted the effective annihilation cross section because of the co-annihilating particles, which eventually decay into the DM [647, 769] and other parameters carried their usual meaning. We have solved the cBEQ using MicrOMEGAs-6.0 [513], and the results are presented in the subsequent sections. Although different cosmological and astrophysical observations confirm the existence of DM, its detection still has not been confirmed. We will also discuss its possible detection prospects via direct and indirect searches in the below sections.

Before delving into the discussion on DM detection, let us simplify the model by reducing the number of free parameters. To reduce the model parameters we fix the parameters $\{m_{\eta^0_{I_1}},\ m_\phi,\ \mu_{12\phi}, \lambda_{11\phi},\ \lambda'_{11\rm H}\}$ at specific values and express others in terms them:

$$\begin{aligned}
|h_{ii\ell}| = 7.2\times10^{-6}\ (a=0,\ b=0.175),\ \lambda_{ij}=1,\ \lambda_{22\phi}=\lambda_{11\phi}\,, \\
y_{12\phi}=1,\ 0<\mu_{12\phi}<2m_\phi,\ \lambda'_{22H}=1,\ m_{\eta^0_{I_2}}=m_{\eta^0_{I_1}}+m_\phi+1\ \mathrm{GeV}, \\
m_{N_1}=2m_{\eta^0_{I_2}}, m_{N_2}=3m_{N_1},\ m_{\eta^0_{R_i}}=m_{\eta^0_{I_i}}+5\ \mathrm{GeV},\ m_{\eta^+_i}=m_{\eta^0_{I_i}}+5\ \mathrm{GeV}\,.
\end{aligned} \tag{8.21}$$

8.5.1 Direct detection limits

The most sensible method to detect a thermal DM is by observing the DM-nuclear/electron scattering rate through inelastic scattering with SM particles in direct detection experiments. The unobserved DM direct detection signal, from different underground experiments like XENON1T [578], XENONnT [358], LUX-ZEPLIN [514], DARWIN/XLZD (projected) [518], PandaX-xT (projected) [516], puts an upper limit on the DM-nucleon scattering cross-section. There is a lower limit obtained from the coherent elastic neutrino-nucleus scatterings, known as neutrino-fog, where the discrimination of DM signal from neutrino background is challenging [770].

Here, the direct detection of $\eta^0_{I_1}$ and ϕ is possible via the Higgs mediated diagrams shown in Fig. 8.6. In a two-component scalar DM setup, the effective spin-

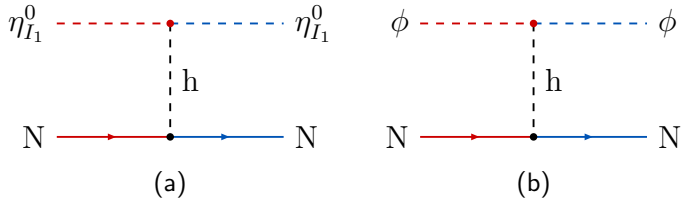

Figure 8.6: Feynman diagrams correspond to the direct detection of $\eta^0_{I_1}$ (left) and ϕ (right).

independent DM-nucleon scattering cross section is written as [300],

$$\sigma^{\rm eff}_{{\rm N}\eta^0_{I_1}} = \frac{\Omega_{\eta^0_{I_1}}}{\Omega_{\eta^0_{I_1}} + \Omega_\phi}\sigma^{\rm SI}_{{\rm N}\eta^0_{I_1}}\,, \quad \text{and} \quad \sigma^{\rm eff}_{{\rm N}\phi} = \frac{\Omega_\phi}{\Omega_{\eta^0_{I_1}} + \Omega_\phi}\sigma^{\rm SI}_{{\rm N}\phi}\,. \tag{8.22}$$

In Fig . 8.7, we have represented the relic allowed parameter space in $m_{\eta^0_{I_1}} - \sigma^{\rm eff}_{{\rm N}\eta^0_{I_1}}$ (left panel) and $m_\phi - \sigma^{\rm eff}_{{\rm N}\phi}$ plane (right panel). In one inert doublet scenario [771–773], the CP-odd scalar DM also acts as DM, the relic parameter space between $\sim m_h$ and $600\,GeV$, is purely under abundant. However, this range would be changed depending on the mass difference between the charged and neutral CP-even scalar. Here, in the presence of a second inert doublet, more co-annihilation will add up and become more underabundant. It's possible to evolve to the correct relic in the presence of another DM (ϕ) that has shared the remaining relic. Because of these, all plots in Fig . 8.7 are filled with color points in between 25 GeV to 700 GeV. Following the Eq . (8.21), we have shown the variation of relic and DD with Δm, $\lambda_{\phi {\rm H}}$, $\lambda'_{11{\rm H}}$, $\mu_{12\phi}$. The coupling associated with $h\phi\phi$ and $h\eta^0_{I_1}\eta^0_{I_1}$ is strongly constrained by the present observed SI DD constraint. So, It would be better to keep off the process containing these vertices in DM freeze-out by choosing sufficient small coupling so that DMs remain in DD allowed. In this scenario, the DM-DM conversion plays a crucial role in relic, especially in an underabundant regime of $\eta^0_{I_1}$. The gray-shaded regions in Fig . 8.7 are excluded by the present SI direct detection experiments, while the stringent set by LUX-ZEPLIN experiments. The dashed lines correspond to the future projection limits set by PandaX-xT and XLZD experiments. As we said, in the middle region is the total relic allowed shared by two DMs, and extreme regions are overabundant regimes. However, the lower and upper mass of $\eta^0_{I_1}$ depends on the mass difference between the charged and neutral scalar of η_1.The rainbow color bar represents the variation of Δm (top), $\mu_{12\phi}$ (middle), and $\%\Omega_i h^2$ (bottom).

In Figs . 8.7a and 8.7b, we have shown the role of Δm coupling in the relic-allowed parameter space. The (effective) conversion processes, $\eta_i^\dagger \eta_i \to \phi\phi$, helps to ϕ come under relic as $\lambda_{\phi H}$ is small constrained by DD. For this, $m_\phi > m_{\eta^0_{I_1}}$ regime is fitted with relic otherwise in the opposite hierarchy ϕ becomes overabundant. The conversion rate depends on the ratio of the equilibrium number density of both DMs, which causes the small mass hierarchy $(\Delta m \lesssim 10)$ to be needed for more conversion of ϕ to $\eta^0_{I_1}$. This has been clearly visible in the top panel figures. Another factor in conversion is the coupling $\mu_{12\phi}$. Although it has a proportional dependency on the conversion rate, simultaneously, it enhanced the effective annihilation cross-section and became more underabundant. For this reason, the parameter space in Figs . 8.7c and 8.7d show mixed color points, which mostly depend on Δm. Finally, in Figs . 8.7e and 8.7f, we show the effective contribution of DMs in total relic, de-

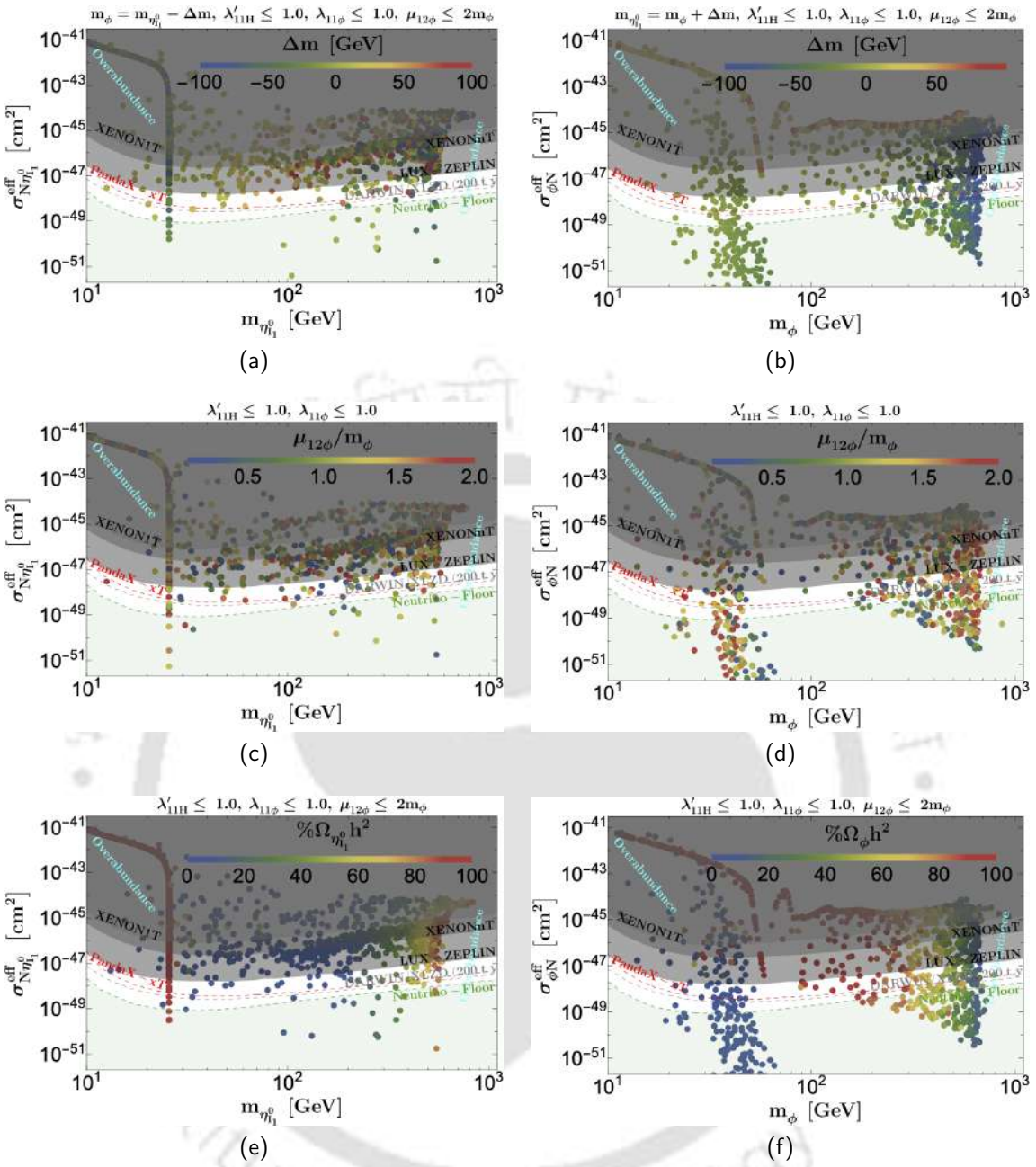

Figure 8.7: Figs. 8.7a, 8.7c, 8.7e and 8.7b, 8.7d, 8.7f, represents the relic allowed parameter space in $m_{\eta^0_{I_1}} - \sigma^{\rm eff}_{N\eta^0_{I_1}}$ and $m_\phi - \sigma^{\rm eff}_{N\phi}$ plane, respectively. The rainbow colorbar represents the variation of $\mu_{12\phi}$, $\Delta m = m_{\eta^0_{I_1}} - m_\phi$, and $\%\Omega_i h^2 = \Omega_i h^2 \left(\sum_i \Omega_i h^2\right)^{-1} 100$, where $i = \eta^0_{I_1}$ and ϕ, has mentioned above the colorbar. The observed SI DD limit excludes the grey-shaded regions from XENON1T, XENONnT, and LUX-ZEPLIN, while the dashed lines correspond to projected limits from PandaX-xT and DARWIN/XLZD (200 t y). Light green represents the neutrino floor.

picted by the rainbow color bar. These two figures complement each other while the extreme regions are $\eta^0_{I_1}$ dominant, and the middle region is dominated by ϕ where $\eta^0_{I_1}$ is badly underabundant.

8.5.2 Indirect detection limits

The self-annihilation of DM particles at the galactic core can produce SM particles, like gamma rays, neutrinos, positrons, etc., which could be possible to detect by various telescopes and detectors. However, the non-observation of the excess in these signals, gamma rays (Fermi-LAT), cosmic rays (AMS-02), and neutrinos (IceCube), etc., allows us to set an upper limit on the DM self-annihilation cross section guided us for the theoretical models and future searching for DM. In this framework,

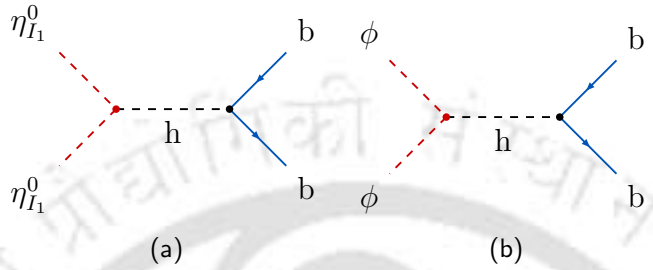

Figure 8.8: The Feynman diagrams represents the self annihilation of $\eta^0_{I_1}$ and ϕ into $b\,\bar{b}$ shown in Figs. 8.8a and 8.8b, respectively.

we have estimated the self-annihilation of $\eta^0_{I_1}$ and ϕ, is possible via the Higgs mediated diagrams shown in Fig. 8.8, into the bottom pair as it gives the most stringent constraint for DM annihilation set by Fermi-LAT observation. More interestingly, In a two-component scalar DM setup, the effective DM self-annihilation cross-sections are written as [300],

$$\langle\sigma v\rangle^{\rm eff}_{\phi\ \phi\to \rm b\ \bar{b}} = \frac{\Omega^2_{\phi}}{(\Omega_{\eta^0_{I_1}}+\Omega_{\phi})^2}\langle\sigma v\rangle_{\phi\ \phi\to \rm b\ \bar{b}}\,, \tag{8.23}$$

$$\langle\sigma v\rangle^{\rm eff}_{\eta^0_{I_1}\eta^0_{I_1}\to \rm b\ \bar{b}} = \frac{\Omega^2_{\eta^0_{I_1}}}{(\Omega_{\eta^0_{I_1}}+\Omega_{\phi})^2}\langle\sigma v\rangle_{\eta^0_{I_1}\eta^0_{I_1}\to \rm b\ \bar{b}}\,, \tag{8.24}$$

where the cross-section is calculated at the WIMP freeze-out temperature, $T_{\rm FO} \sim m_{\rm DM}/25$. The annihilation cross-section, $\langle\sigma v\rangle_{\eta^0_{I_1}\eta^0_{I_1}\to \rm b\ \bar{b}}$, proportionally depends on the parameters $m_{\eta^0_{I_1}}$ and $\lambda_{h\eta^0_{I_1}\eta^0_{I_1}} = (\lambda_{11H}+\lambda'_{11H}-\lambda''_{11H})v = (2m^2_{\eta^0_{I_1}}-2m^2_{\eta^+_1})/v+\lambda'_{11H}v$, on the contrary $\langle\sigma v\rangle_{\phi\phi\to \rm b\ \bar{b}}$ depends on the m_ϕ and $\lambda_{h\phi\phi} = \lambda_{\phi H}v$. In Fig. 8.9, we have shown the variation of these parameters through the rainbow colorbar. In all plots, the gray regions are excluded by the upper limit on the DM annihilation to the bottom pair from Fermi-LAT, and this is stringent compared to other indirect observations. In case of $\eta^0_{I_1}$, with the enhancement of λ'_{1H} the $\langle\sigma v\rangle_{\eta^0_{I_1}\eta^0_{I_1}\to \rm b\ \bar{b}}$ is increased which depicted in Fig. 8.9a. If the DM mass $m_{\eta^0_{I_1}} \sim m_h/2$, some points are excluded by Fermi-LAT due to the Higgs resonance enhancement in the cross-section, and the same explanation is also valid for the second DM ϕ which has been illustrated in Fig. 8.9b. Below $m_h/2$, the cross-section gradually decreases, and some points go inside the Fermi-LAT exclusion regime. As these couplings are also involved in SI direct detection of $\eta^0_{I_1}$ and ϕ, so its decrement also decreases the DD cross-sections, as we see in Figs. 8.9c and 8.9d. Here, the gradual decrement of both DD and ID cross-section with the vertex factor $\lambda_{h\eta^0_{I_1}\eta^0_{I_1}}$ and $\lambda_{h\phi\phi}$, is portrayed by the transition of color gradient from blue to red.

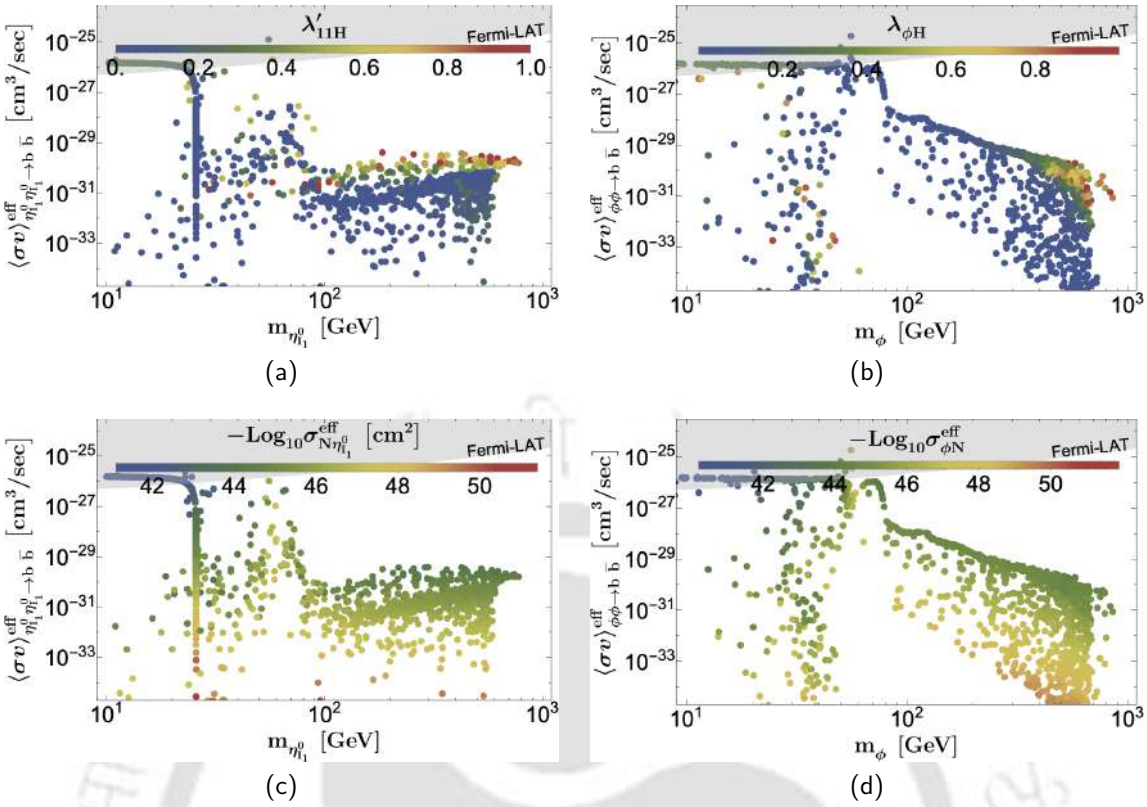

Figure 8.9: Figures are shown the Indirect detection limit on relic allowed parameter space in $m_i - \langle\sigma v\rangle^{\mathrm{eff}}_{i\,i\to b\,\bar{b}}$ plane, where $i = \eta^0_{I_1}$, and ϕ. The grey-shaded regions are excluded from the recent Fermi-LAT limit on the DM annihilation bottom pair. In this scan, we have taken: $\mu_{12\phi} \leq 2m_\phi$ and $\lambda_{11\phi} \leq 1.0$. The rainbow color shows the variation of the respective parameters mentioned above in the color bar.

Here, we connect three frameworks, (i) Neutrino mass: $\{m_{\eta^0_{R_k}}, m_{\eta^0_{I_k}}, m_{N_k}, h_{kk\alpha}\}$, (ii) Baryon asymmetry: $\{m_{\eta^0_{R_k}}, m_{\eta^0_{I_k}}, m_{\eta^+_k}, m_{N_k}, m_\phi, y_{12\phi}, \mu_{12\phi}, h_{kk\alpha}\}$, and (iii) DM relic density and its detection possibilities: $\{m_{\eta^0_{R_k}}, m_{\eta^0_{I_k}}, m_{\eta^+_k}, m_\phi, \lambda_{\phi H}, \lambda'_{kkH}, \mu_{12\phi}, \lambda_{mn}, \lambda_{kk\phi}\}$ in a one plane, where, $\{k, m, n = 1, 2\}$. RHNs are much heavier than DMs, and it doesn't play any role in the DM relic. All of these are directly connected by common parameters $\{m_{\eta^0_{R_k}}, m_{\eta^0_{I_k}}\}$. So, by fine-tuning other parameters, we can adjust the corresponding observed observables. If we start from neutrino mass is adjusted by $\{m_{\eta^0_{R_k}}, m_{\eta^0_{I_k}}, m_{N_k}, h_{kk\alpha}\}$ while along with these values fine-tuning the remaining terms, $\{m_{\eta^+_k}, m_{N_k}, m_\phi, y_{12\phi}, \mu_{12\phi}\}$, get observed BAU. Lastly, the DM relic is adjusted by $\{\lambda_{\phi H}, \lambda'_{kkH}, \lambda_{mn}, \lambda_{kk\phi}\}$ while $\lambda_{\phi H}$ is directly connected with DD and ID of DM. After all of these three constraints, the unobserved Lepton flavor-violating decays $(\ell_\alpha \to \ell_\beta\gamma)$ put an upper limit on $h_{kk\alpha}$, it isn't applicable in our scenario. Only strong limits on charged scalar mass from LEP observation put a lower limit $\sim 90\ GeV$.

In Fig. 8.10, we have shown the relic density of DM, neutrino mass, baryon asymmetry satisfied, and DD, ID, and flavor violating decays allowed parameter space in $m_{\eta^0_{I_1}} - m_\phi$ plane. However, the analysis followed the methodology outlined in Eq. (8.21). The red points in the left panel represent the parameter space allowed by the DM relic density, while the blue points correspond to regions consistent with both the relic density and DD constraints. Here, we have used the stringent exclusion limit from recently observed SI DM-nucleon scattering cross-sections

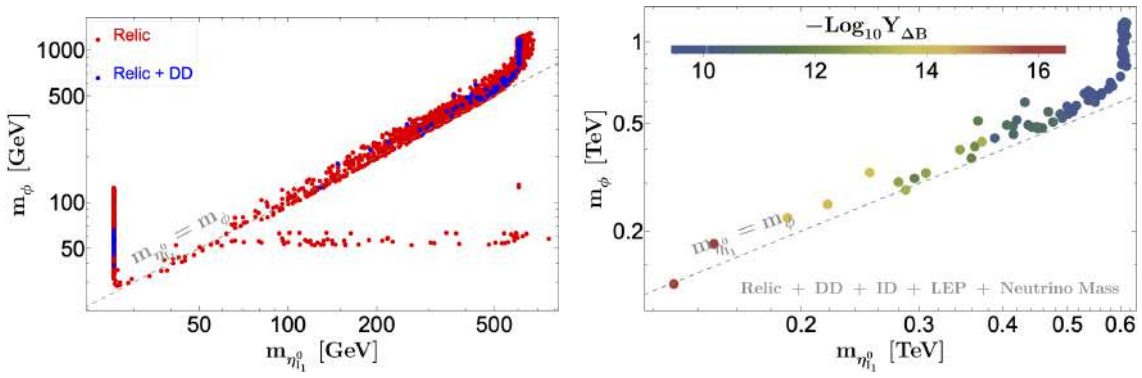

Figure 8.10: The red points represent the total relic density satisfied by both DM candidates. The blue points correspond to the total relic density satisfied and allowed by the DD constraint from the LZ-2022 experiment for both DMs. Lastly, the rainbow color points indicate the regions where the relic density, DD, ID provided by Fermi-LAT, and LEP limits on charged scalars mass are satisfied by both DM candidates. The color bar shows the baryon asymmetry, $Y_{\Delta B}(z_{\rm sph})$, corresponding to each point, while $Y^{\rm obs}_{\Delta B}$ indicated by cyan line on the legendbar.

provided by the LUX-ZEPLIN experiment. A real scalar singlet DM (under only one inert doublet model) results in an underabundant relic density in the range $\mathrm{m_h}/2 < \mathrm{m_{DM}} < 500$ GeV, which is here compensated by partner DM ϕ. Here, we restrict the DM mass ratio up to three for simplicity, but it could be relaxable, which has already been discussed in the above sections. The self-annihilation of ϕ into SM particles is possible only via the Higgs portal interactions, and its freeze-out point depends on the $\lambda_{\phi \mathrm{H}}$, which DD also constrains. However, it could be relaxed in the presence of the DM-DM conversion processes, which help to become underabundant and left for future detection, as we see in the left figure.

The right figure in Fig. 8.10, we show the variation of the baryon asymmetry in $m_{\eta^0_{I_1}} - m_\phi$ plane, while all points respect the DM relic density and neutrino mass, and DD, ID and LEP constraint on charged scalar mass. The Fermi-LAT recent observation puts an upper limit on the DM annihilation to bottom pairs, which are less effective compared to DD constrained. Due to this, the allowed parameter space remains unaltered after imposing ID constraints. However, the parameters $h_{kk\alpha}$, $y_{12\phi}$, m_{N_1}, m_{N_2} is responsible for Leptogenesis and related to active neutrino mass generation, but does not have any role in DM relic or its detections due to its heaviness. Using this freedom, we calculated the yield of baryon asymmetry $(\mathrm{Y_{\Delta B}})$. The rainbow color bar shows the variation of $\mathrm{Y_{\Delta B}}$ while the green line on the color bar represents the observed baryon asymmetry $(\mathrm{Y^{obs}_{\Delta B}})$. But, still, the mass dependency of DMs is present via the decay of N_1 $(\to \ell_\alpha\, \eta_1)$ in the asymmetry parameter, which is reflected in the plot. With the increase in the mass of $\eta^0_{I_1}$, the m_{N_1} (as described by Eq. (8.21)) also increases, leading to an increase in Γ_{N_1}, which in turn increases the asymmetry. Finally, we have implemented the LEP constrained on the charged scalar mass $(m_{\eta^+_1})$, which is $\sim 90\ GeV$.

8.6 Summary

The simplest scenario that addresses neutrino mass generation and BAU is type-I seesaw model, where the right-handed neutrinos (RHNs) need to be heavy, $\sim 10^{10}\ TeV$ to satisfy the active neutrino masses and baryon asymmetry within the observed limit. On the contrary, the WIMP (mass $\sim GeV$) freeze out occurs much

later. So, having a separate DM candidate added to such a framework won't correlate all the phenomena together. The simplest way to connect them is to consider the scotogenic model, where DM freeze-out and leptogenesis could happen nearly at the same scale, and the masses of RHNs get down to $\sim TeV$ scale. However, the BAU and DM phenomena are not directly coupled in such a framework. Our primary focus was to find out a model setup with minimal particle content that not only addresses all of them together, but also provides an inter dependence, so that the prediction in one sector affects the other.

We find out that an extension of scotogenic model that includes two RHNs, two inert doublets, and one real scalar, stabilised appropriately under $\mathcal{Z}_2 \otimes \mathcal{Z}_2'$ symmetry with two real scalar DM components, does the job, establishing a novel connection between the DM phenomenology and the matter-antimatter asymmetry. The asymmetry generation in leptogenesis strongly depends on the DM masses and coupling with the RHNs through the vertex correction of N_1 decays into $\ell\eta_1$. On the other hand, neutrino mass generation strongly depends on the inert doublet masses and $h_{kk\alpha}$ couplings, which also play a significant role in leptogenesis. Due to the presence of $N\ell\eta$ vertex, the radiative lepton flavor violating decay becomes possible, but the limit from MEG-II is less sensitive for the parameter space relevant for us. As the LEP experiments already put a stringent lower limit on the singly charged scalar $\sim 90\ GeV$, excludes some of our parameter space.

Operationally, we perform all the detailed calculations to arrive at our final results. We have solved the cBEQ of $\mathrm{Y_{N_1}}$ and $\mathrm{Y_{B-L}}$ numerically for some chosen benchmark points that address the correct active neutrino mass limits. We also provide a scan plot in $m_{\eta^0_{I_1}} - (y_{12\phi} \times \mu_{12\phi})$ plane, where the points are explaining the observed baryon asymmetry and neutrino masses simultaneously. We do the DM calculation via solving coupled BEQs as well as scanning it via micrOmegas. The mass hierarchy between DM components plays a crucial role in leptogenesis, as both the DMs are considered as on-shell particles in the 1-loop vertex correction calculation. The parameters $\{m_{\eta^0_{I_1}},\ m_\phi,\ \mu_{12\phi}\}$ relevant for Leptogenesis, also turns crucial for DM phenomenology. In the minimal scotogenic model, with one inert doublet, the relic density allowed parameter space is very restrictive, depends on the mass splitting between the charged and neutral components of the inert doublet, and most of the parameter space accessible to collider observation is under-abundant due to the presence of gauge portal interactions. Here, on the contrary, in the presence of two DM components, the parameter space available for both leptogenesis and DM constraints, is enhanced, allowing a future detection of the charged component of the inert doublet in the collider, indicating to a specific parameter space relevant for DM, leptogenesis and neutrino mass generation. A summary plot also indicates the future detectability of DM in the Direct and Indirect searches after addressing the relevant constraints.

Chapter 9

Summary and Future prospects

The thesis studies DM sector of the universe, which is motivated from several astrophysical and cosmological experiments, but still awaiting a discovery signal. We consider particles having different spins, masses and genesis (like WIMP, FIMP or SIMP) to co-exist and consist the dark sector. The thesis mainly aims to elaborate upon the cosmological and phenomenological consequences of such scenarios, which mainly stems from the interaction between the DM components. We show that DM detectability is also crucially governed by such cases, which may show up in upcoming sensitivities of direct, indirect or collider search experiments. We also try to connect to other motivations of physics beyond the SM, like neutrino masses, matter-anti matter asymmetry of the universe etc.

The thesis begins with an introduction to SM of particle physics, and some of the compelling issues which makes us believe that there exists physics beyond the SM. We then study in details DM phenomenology. We particularly highlight different manifestations like WIMP, SIMP and FIMP type DM, from the perspective of a simple model extensions via scalar singlet, but choosing the couplings in a judicious way to render different limits of the same DM. We elaborate thereafter DM detection prospects in direct, indirect and collider searches.

The main projects that consists the thesis starts from Chapter 3. Here we propose a two-component vector-scalar (WIMP-WIMP) model to show that the combined event rate differs from that of a single-component DM and exhibits a distinct kink, when one of the DM is light and the other is heavy. The challenge was to find a parameter space where such curvature is seen after satisfying the cosmological, theoretical and phenomenological constraints. To the best of our knowledge, this was done for the first time in literature. Excepting DM mass, other model parameters related to DM number densities and DM-nucleus scattering cross-sections, also play a significant role in the visibility of the curvature. The analysis also shows that distinguishability of such two component framework from a single component one is restricted to a particular region of the parameter space and limited to a class of models.

In Chapter 4, we go beyond WIMP-WIMP to WIMP-FIMP combination. We study the same scalar vector model as studied in the previous chapter, but the vector boson DM becomes FIMP here. We highlight the distinction in the available parameter space of the model for DM freeze-in or freeze-out before and after Electroweak

Symmetry Breaking (EWSB). If the relic density saturates before EWSB, we find that DM masses should be heavy $\gtrsim 4\ TeV$. However, this constraint gets relaxed for DM freeze in or freeze out after EWSB. The detection of FIMP is usually challenging, but we show that its presence can be inferred indirectly through direct and indirect searches of thermal DM partner in both pre- and post- EWSB epochs.

In Chapter 5, we study the case when the interaction between WIMP and FIMP is not feeble; so that the FIMP reaches thermal equilibrium and freezes out. We study the dynamics of such particles in model independent way and see that there are some generic features that can be attributed. We therefore classify such particles as a new kind of DM called pseudo-FIMP (pFIMP). pFIMPs don't have a direct SM connection, therefore its detection could be possible via the thermal DM loop. The fate of pFIMP heavily depends on the partner DM and the interaction between them. We study the simplest WIMP-pFIMP model with two real scalar DMs stabilised under $\mathcal{Z}_2 \otimes \mathcal{Z}_2'$ symmetry. pFIMPs can also arise in presence of a SIMP type DM. We have also demonstrated it by replacing a real scalar with a complex scalar DM (stable under $\mathcal{Z}_3$), which resembles a SIMP DM.

The detection prospect of pFIMP is illustrated next in Chapter 6, where we draw all possible WIMP loops for scalar, fermion and vector boson. We then study a vector-like fermionic WIMP and a real scalar pFIMP setup, assuming the Higgs portal coupling to be very feeble. The key finding of this model is that above the LEP exclusion limit ($103\ GeV$), both WIMP and pFIMP are accessible for direct and indirect searches, while obeying the existing limits. Here, pFIMP detection is dominantly governed by the penguin loop of fermionic DM, and UV divergence is handled using on-shell renormalization scheme. In the subsequent section of this chapter, we illustrate another example of WIMP-pFIMP setup consisting of real and complex scalar DM. Additionally, we introduce a vector-like charged lepton, which couples only to right-handed charged leptons, so that WIMP can participate in both lepton-flavor-violating and lepton-flavor-conserving processes, so that some of the parameter space is excluded by LFV ($\mu \to e\gamma$) decay constraints. We further analyze missing energy plus opposite-sign lepton (electron and muon) and di-tau signals at an e^+e^- collider (ILC) for points allowed by cosmological, theoretical and collider limits. We demonstrate a 5σ discovery potential in di-lepton and di-tau searches.

In Chapter 7, we study how one can achieve two stable DM components with a single discrete symmetry $\mathcal{Z}_N$, with two complex scalar fields. We study the different kinematic conditions so that the heavier component becomes long lived. This gives rise to several possibilities. For $\mathcal{Z}_2$ symmetry, preventing the decay of heavier particle to the lighter one (or lighter particles plus SMs) leads to $\mathcal{Z}_2 \otimes \mathcal{Z}_2'$ model. However, for $\mathcal{Z}_3$ symmetry, it can yield $\mathcal{Z}_3 \otimes \mathcal{Z}_3'$ scenario, as well as situations like $q_1 \neq q_2$, with $q_1 + q_2 \neq N$ when $q_{1,2}$ are the charges for DM and both are stable, and phenomenologically distinguishable from the $\mathcal{Z}_3 \otimes \mathcal{Z}_3'$ scenario.

In Chapter 8, we have shown a connection between neutrino mass, matter-antimatter asymmetry, and dark matter (DM). This connection has been established in a scotogenic model consisting of two inert doublets, two right-handed neutrinos, and a real scalar field, having two DM components. For an appropriate choice of the dark sector particle charges under the $\mathcal{Z}_2 \otimes \mathcal{Z}_2'$ symmetry, the lepton number-violating one-loop decays involve both DMs and the couplings that generate lepton asymmetry, are also relevant for DM relic density. In this way, the three phenomena are correlated to each other and provides a larger accessible parameter space than the

minimal scotogenic scenario.

In summary, the thesis explores several interesting cosmological and phenomenological features that multicomponent DM frameworks can provide. In particular, we highlight the detectability of such models. However, we see that the distinction of two component set ups from one component case is often limited. The issues that the thesis couldn't touch upon are the possibilities of first-order phase transition and resulting gravitational wave signal, and its potential to distinguish single and multipartite dark sector. Apart we also wish to study DM production using non-standard cosmology, and its potential distinguishability from the standard case, the possibility of multicomponent DMs having different temperatures, the possibility of axion DM coexisting with others etc. The question of DM discovery is making the particle physicists anxious and the author hopes that it will soon be achieved, so that new era opens up in exploring early universe cosmology and physics beyond the SM.

Appendix A

Boltzmann Equation for Dark Matter

For a significant portion of its early history, the universe's constituents existed in thermal equilibrium, making an equilibrium-based description a robust approximation. However, several critical phenomena mark significant departures from this equilibrium, including neutrino decoupling, the decoupling of the CMBR, primordial nucleosynthesis, and, within more speculative frameworks, inflation, baryogenesis, and the decoupling of relic WIMPs, among others. As previously emphasized, in the absence of such departures from thermal equilibrium, the current state of the universe would be entirely determined by its present temperature. These deviations from equilibrium have given rise to several significant relics, such as the light elements, the neutrino background, the net baryon asymmetry, relic WIMPs, and other cosmologically relevant features.

A fundamental criterion to determine whether a particle species remains coupled or becomes decoupled is the comparison between its interaction rate, Γ, and the expansion rate of the universe, $\mathcal{H}$:

$$\begin{aligned} \Gamma &\gtrsim \mathcal{H} \quad (\text{Coupled}) \,, \\ \Gamma &\lesssim \mathcal{H} \quad (\text{Decoupled}) \,, \end{aligned} \tag{A.1}$$

where Γ represents the interaction rate per particle for the reaction(s) responsible for maintaining the species in thermal equilibrium, while the units of Γ are expressed as time^{-1}. To accurately address the phenomenon of decoupling, one must analyze the microscopic evolution of the particle's phase-space distribution function, denoted $f(p^\mu, x^\mu)$. This evolution is governed by the Boltzmann equation, expressed as:

$$\hat{\mathbf{L}}[f] = \mathbf{C}[f], \tag{A.2}$$

where $f = f(\vec{p}, \vec{x}, t)$ represents the phase-space density to be determined, $\hat{\mathbf{L}}$ is the **Liouville operator**, describing the temporal evolution of the phase-space density, and $\mathbf{C}$ is the **collision operator**, which accounts for the net gain or loss of particles within a phase-space volume per unit time.

In the non-relativistic regime, the Liouville operator can be interpreted as a total time derivative, expressed as:

$$\hat{\mathbf{L}}_{\text{NR}} = \frac{d}{dt} + \frac{d\vec{x}}{dt} \cdot \vec{\nabla}_x + \frac{d\vec{v}}{dt} \cdot \vec{\nabla}_v = \frac{d}{dt} + \vec{v} \cdot \vec{\nabla}_x + \frac{\vec{\mathbf{F}}}{m} \cdot \vec{\nabla}_v \,, \tag{A.3}$$

where $\vec{v}$ is the velocity, $\vec{\mathbf{F}}$ represents the force, and m is the particle's mass.

In the relativistic framework, the covariant form of the Liouville operator is given by:

$$\hat{\mathbf{L}}_{\text{cov}} = p^{\alpha}\frac{\partial}{\partial x^{\alpha}} - \Gamma^{\alpha}_{\beta\gamma}p^{\beta}p^{\gamma}\frac{\partial}{\partial p^{\alpha}}, \tag{A.4}$$

where gravitational effects are encapsulated by the affine connection $\Gamma^{\alpha}_{\beta\gamma}$. In the context of the Friedmann Robertson Walker (FRW) cosmological model, the phase-space density is assumed to be spatially homogeneous and isotropic. Consequently, $f(\vec{x},\vec{p},t)$ simplifies to $f(|\vec{p}|,t)$ or, equivalently, $f(E,t)$, where E denotes the particle energy. The FRW metric possesses the following non-zero Christoffel symbols:

$$\boxed{\Gamma^{0}_{ij} = \delta_{ij}\dot{a}a}, \quad \boxed{\Gamma^{i}_{0j} = \Gamma^{i}_{j0} = \delta_{ij}\frac{\dot{a}}{a}},$$

where δ_{ij} is the Kronecker delta with $i,\ j = \{1,2,3\}$, $a(t)$ is the scale factor, and $\dot{a}$ represents its time derivative. Employing these coefficients, the Liouville operator simplifies as follows:

$$\begin{aligned}\hat{\mathbf{L}}[f] &= E\frac{\partial f}{\partial t} - \Gamma^{i}_{0j}p^{0}p^{j}\frac{\partial f}{\partial p^{i}} - \Gamma^{i}_{j0}p^{j}p^{0}\frac{\partial f}{\partial p^{i}} - \Gamma^{0}_{ij}p^{i}p^{j}\frac{\partial f}{\partial p^{0}} \\ &= E\frac{\partial f}{\partial t} - \delta_{ij}a\ \dot{a}p^{i}p^{j}\frac{\partial f}{\partial E} \\ &= E\frac{\partial f}{\partial t} - \frac{\dot{a}}{a}|\vec{p}|^{2}\frac{\partial f}{\partial E}\,.\end{aligned} \tag{A.5}$$

Here, E denotes the energy of the particle, $\vec{p}$ is the spatial momentum,$|\mathbf{p}|^2 = p^i p_i g^{ii}$ encapsulates the squared magnitude of the spatial momentum and g^{ii} represents the components of the inverse metric.

Here, we focus on particle number densities, specifically by integrating over momenta in the phase-space distribution, along with the energy and pressure densities. The equilibrium number, energy, and pressure density are defined as follows:

$$n_i(t) = \frac{1}{(2\pi)^3}\int d^3p_i\ f_i(E_i,t)\,, \tag{A.6}$$

$$\rho_i(t) = \frac{1}{(2\pi)^3}\int d^3p_i\ E_i\ f_i(E_i,t)\,, \tag{A.7}$$

$$\mathcal{P}_i(t) = \frac{1}{(2\pi)^3}\int d^3p_i\ \frac{|\mathbf{p}_i|^2}{3E_i}\ f_i(E_i,t)\,, \tag{A.8}$$

where $n_i,\ \rho_i,\ \mathcal{P}_i$ are the number density, energy density, and pressure of a dilute weakly interacting gas of particles with internal degrees of freedom g_i written in terms of its phase space distribution function $f(|\mathbf{p}|)$.

The Fermi-Dirac (FD), Bose-Einstein (BE), and Maxwell Boltzmann (MB) distributions are given by,

$$\begin{aligned} f(\mathbf{p}) &\sim \quad g e^{-(E-\mu)/T} && [\text{MB}]\,, \\ f(\mathbf{p}) &\sim \ g\left(e^{(E-\mu)/T}+1\right)^{-1} && [\text{FD}]\,, \\ f(\mathbf{p}) &\sim \ g\left(e^{(E-\mu)/T}-1\right)^{-1} && [\text{BE}]\,. \end{aligned} \tag{A.9}$$

As at the equilibrium, particle numbers are conserved, so the chemical potential (μ) must be vanishes. We can redefine our phase space density is likely: $f = ge^{-\mu/T} f^{\rm eq} \equiv \frac{n}{n^{\rm eq}} f^{\rm eq}$ [MB] (see A.6), where

$$\begin{aligned} f^{\rm eq} &= ge^{-E/T} && [\text{MB}]\,, \\ f^{\rm eq} &= g\left(e^{E/T}-1\right)^{-1} && [\text{BE}]\,, \\ f^{\rm eq} &= g\left(e^{E/T}+1\right)^{-1} && [\text{FD}]\,. \end{aligned} \tag{A.10}$$

Now, the energy density is defined as,

$$\rho_i = g_i \int \frac{d^3p_i}{(2\pi)^3} E_i e^{-(E_i-\mu_i)/T} = \frac{n_i}{n_{i,0}(T)} \rho_{i,0}(T)\,. \tag{A.11}$$

where,

$$n_{i,0}(T) = \frac{T}{2\pi^2} g_i m_i^2 K_2\left(m_i/T\right)\,, \tag{A.12}$$

$$\rho_{i,0}(T) = \int \frac{d^3p_i}{(2\pi)^3} E_i f_i^{eq} = \frac{g_i m_i^3}{2\pi^2/T}\left[K_3\left(m_i/T\right) - \frac{T}{m_i} K_2\left(m_i/T\right)\right]\,. \tag{A.13}$$

Using the recursion relation of modified Bessel function of second kind order n:

$$K_{n-1}(x) - K_{n+1}(x) = -2\frac{n}{x} K_n(x)\,, \tag{A.14}$$

and Eq . (A.13) becomes,

$$\rho_{i,0}(T) = \frac{g_i m_i^3}{2\pi^2 \beta'}\left[K_1\left(m_i/T\right) + \frac{3}{(m_i/T)} K_2\left(m_i/T\right)\right]\,, \tag{A.15}$$

and similarly,

$$\mathcal{P}_i = \frac{n_1}{n_{i,0}(T)} \mathcal{P}_{i,0}(T)\,, \tag{A.16}$$

$$\mathcal{P}_{i,0}(T) = \int \frac{d^3p_i}{(2\pi)^3} \frac{|\mathbf{p}_i|^2}{3E_i} f_i^{eq} = \frac{1}{3}\rho_{i,0}(T) - \frac{g_i m_i^3}{6\pi^2/T} K_1\left(m_i/T\right) \equiv T n_{i,0}(T)\,. \tag{A.17}$$

Species Type	Number Density (Equilibrium)	Energy Density (Equilibrium)
Non-relativistic($T \ll m_i$)	$n_{i,0} = g_i \left(\frac{m_i T}{2\pi}\right)^{3/2} e^{-(m_i-\mu_i)/T}$	$\rho_{i,0} = n_{i,0} m_i$
Ultra-relativistic($T \gg m_i, \mu_i$)	$n_{i,0} = \frac{\zeta(3)}{\pi^2} g_i T^3 \begin{cases} 1 & \text{(bosons)} \\ \frac{3}{4} & \text{(fermions)} \end{cases}$	$\rho_{i,0} = \frac{\pi^2}{30} g_i T^4 \begin{cases} 1 & \text{(bosons)} \\ \frac{7}{8} & \text{(fermions)} \end{cases}$

where $\zeta(3) = \sum_{n=1}^{\infty} n^{-3} \simeq 1.2026$ is the Riemann zeta function of order 3, $n_{i,0}$ is the equilibrium number density, $\rho_{i,0}$ is the equilibrium energy density, g_i represents the degeneracy factor, m_i is the particle mass, and T is the bath temperature. For a system comprising multiple particle species in thermal equilibrium, where the species i exhibit a thermal distribution characterized by temperature T_i, the total energy density can be expressed to a high degree of precision as:

$$\rho_{\rm tot} = \frac{\pi^2}{30} g_*(T) T^4\,. \tag{A.18}$$

Here, $g_*(T)$ represents the effective number of relativistic (effectively massless) degrees of freedom at temperature T. It is given by:

$$g_*(T) = \sum_{b\in\text{bosons}} g_b \left(\frac{T_b}{T}\right)^4 + \frac{7}{8}\sum_{f\in\text{fermions}} g_f \left(\frac{T_f}{T}\right)^4 , \tag{A.19}$$

where g_b and g_f denote the intrinsic degrees of freedom for bosons and fermions, respectively, while T_b and T_f are their associated temperatures relative to the reference temperature T. During the radiation-dominated (RD) era, where the scale factor evolves as $a(t) \propto \sqrt{t}$, the Hubble parameter can be expressed as:

$$\mathcal{H}^2 = \frac{8\pi G_N}{3}\rho_{\text{tot}} = \frac{8\pi G_N}{3}\frac{\pi^2}{30}g_*(T)T^4 \simeq \left(1.66\sqrt{g_*(T)}\frac{T^2}{m_{\text{Pl}}}\right)^2 . \tag{A.20}$$

Here, $G_N = 6.6743\times10^{-11}m^3kg^{-3}s^{-2}$ is the Newtonian constant of gravitation, and $m_{\text{Pl}} \simeq 1.221\times10^{19}$ denotes the Planck mass ($\equiv 1/\sqrt{G_N}$).

Let us rewrite the Eq. (A.2) in accordance with the preceding expressions:

$$\begin{aligned}
&\int \hat{\mathbf{L}}[f]g\frac{d^3p}{(2\pi)^3} = \int \hat{\mathbf{C}}[f]g\frac{d^3p}{(2\pi)^3}\\
\implies &\frac{g}{(2\pi)^3}\int\left[\frac{\partial f}{\partial t} - \frac{\dot a}{a}\frac{|\vec p|^2}{E}\frac{\partial f}{\partial E}\right]d^3p = \frac{g}{(2\pi)^3}\int\hat{\mathbf{C}}[f]\frac{d^3p}{E}\\
\implies &\frac{\partial}{\partial t}\left[g\int\frac{d^3p}{(2\pi)^3}f\right] - \frac{g}{(2\pi)^3}\frac{\dot a}{a}\left[4\pi\int p^3df\right] = \frac{g}{(2\pi)^3}\int\hat{\mathbf{C}}[f]\frac{d^3p}{E}\\
\implies &\frac{dn}{dt} + \frac{g}{(2\pi)^3}\frac{\dot a}{a}\left[4\pi\int 3p^2dp\, f\right] = \frac{g}{(2\pi)^3}\int\hat{\mathbf{C}}[f]\frac{d^3p}{E}\\
\implies &\frac{dn}{dt} + 3\mathcal{H}n = \frac{g}{(2\pi)^3}\int\hat{\mathbf{C}}[f]\frac{d^3p}{E} ,
\end{aligned} \tag{A.21}$$

where $\mathcal{H} = \dot a/a$ denotes the Hubble rate.

In general collision term for the process $\psi + a + b + ... \leftrightarrow i + j + ...$, where we are focussing on the evaluation of ψ, on is given by [62, 774],

$$\begin{aligned}
&\frac{g_\psi}{(2\pi)^3}\int\hat{\mathbf{C}}[f_\psi]\frac{d^3p_\psi}{E_\psi}\\
&= -\int d\Pi_\psi d\Pi_a d\Pi_b ... d\Pi_i d\Pi_j ... (2\pi)^4\delta^4(p_\psi + p_a + p_b ... - p_i - p_j ...)\left[|\mathcal{M}|^2_{\psi+a+b+...\to i+j+...}\right.\\
&\left. f_\psi f_a f_b ...(1\pm f_i)(1\pm f_j)... - |\mathcal{M}|^2_{i+j+...\leftarrow\psi+a+b+...} f_i f_j ...(1\pm f_\psi)(1\pm f_a)(1\pm f_b)...\right] ,
\end{aligned} \tag{A.22}$$

where $f_i, f_j, ..., f_a, f_b, ...$ are the phase space densities of species $i, j, ..., a, b, ...$; f_ψ is the phase space density of ψ; $(+)$ applies to bosons; $(-)$ applies to fermions; and

$$d\Pi_i \equiv \frac{1}{(2\pi)^3}\frac{d^3p_i}{2E_i} . \tag{A.23}$$

In Eq. (A.22), the four-dimensional Dirac delta function ensures the conservation of energy and three-momentum. The squared matrix element, $|\mathcal{M}|^2_{i+j+\cdots\to\psi+a+b+\cdots}$, corresponding to the process $i+j+\cdots\to\psi+a+b+\cdots$, is averaged over the spins of the initial and final states. Additionally, it incorporates the appropriate symmetry factors to account for indistinguishable particles in either the initial or final states. To simplify Eq. (A.22), we employ two well-justified approximations:

- **T (or CP) Invariance:** We assume time-reversal (or charge-parity) invariance, which implies the equality of matrix elements for forward and reverse processes, $|\mathcal{M}|^2_{i+j+\cdots\to\psi+a+b+\ldots} = |\mathcal{M}|^2_{\psi+a+b+\cdots\to i+j+\ldots} \equiv |\mathcal{M}|^2$.
- **Maxwell-Boltzmann Statistics:** We approximate the distribution functions of all species using MB statistics instead of FD for fermions and BE for bosons. In the absence of Bose-Einstein condensation or Fermi degeneracy, the factors associated with quantum effects, $1 \pm f$, can be approximated as 1, and the distribution functions take the form $f_i(E_i) = \exp[-(E_i - \mu_i)/T]$ for all species in kinetic equilibrium.

Under these two assumptions, the BEQ can be expressed in the familiar form using Eq . (A.21) and Eq . (A.22):

$$\dot{n}_\psi + 3\mathcal{H}n_\psi = -\int d\Pi_\psi d\Pi_a \ldots d\Pi_i d\Pi_j \ldots (2\pi)^4 |\mathcal{M}|^2 \delta^4\left(p_\psi + p_a \ldots - p_i - p_j \ldots\right)\left[f_\psi f_a \ldots - f_i f_j \ldots\right] . \tag{A.24}$$

The significance of the individual terms is evident: the term $3\mathcal{H}n_\psi$ represents the dilution effect resulting from the expansion of the universe, while the right-hand side of Eq . (A.24) captures the contributions of interactions that modify the number density of ψ-particles. In the absence of such interactions, the solution to Eq . (A.24) is $n_\psi \propto a^{-3}$. It is usually useful to scale out the effect of the expansion of the universe; it is often advantageous to evaluate the evolution of the particle number within a moving volume. This approach involves utilizing the entropy density (s) with $\dot{s} = -3\mathcal{H}s$, and defining the dimensionless variable called as yield $Y_\psi \equiv \dfrac{n_\psi}{s}$. Now, the BEQ is written in terms of yield:

$$\frac{dn_\psi}{dt} + 3\mathcal{H}n_\psi = s\frac{dY_\psi}{dt} . \tag{A.25}$$

Moreover, because the interaction term typically exhibits an explicit dependence on temperature rather than time, it is advantageous to define an alternative independent variable $x = \dfrac{m}{T}$, where m represents a convenient mass scale, commonly chosen as the mass of the particle under consideration, here is m_ψ. During the *radiation-dominated epoch*, x and t are related by $t = 1/(2\mathcal{H})$ and $dt = dx/x$. Incorporating all these ingredients, Eq . (A.22) simplifies to describe the $\psi\, a \to i\, j$ process as follows:

$$\frac{dY_\psi}{dx} = -\frac{1}{s\mathcal{H}x}\int d\Pi_\psi d\Pi_a d\Pi_i d\Pi_j (2\pi)^4 |\mathcal{M}|^2 \delta^4(p_\psi + p_a - p_i - p_j)\left[f_\psi f_a - f_i f_j\right] . \tag{A.26}$$

If we assume $i,\ j$ particles are in equilibrium, just for simplicity, then $f_i f_j = f_i^{\rm eq} f_j^{\rm eq} = f_\psi^{\rm eq} f_a^{\rm eq}$ using energy conservation, $E_\psi + E_a = E_i + E_j$. Furthermore, for non-equilibrium particle $f_{\psi,a} = f^{\rm eq}_{\psi,a} e^{-\mu_{\psi,a}/T}$ which can easily be simplified to $n_{\psi,a} = n^{\rm eq}_{\psi,a} e^{-\mu_{\psi,a}/T}$. Therefore, the last distribution factor in Eq . (A.26) will be,

$$\left[f_\psi f_a - f_i f_j\right] = \frac{f_\psi^{\rm eq} f_a^{\rm eq}}{n_{i,0} n_{j,0}}\left[n_\psi n_a - n_{\psi,0} n_{a,0}\right] , \tag{A.27}$$

Finally, the BEQ is written as,

$$\frac{dY_\psi}{dx} = -\frac{s}{\mathcal{H}x}\langle\sigma_{\psi\ a\to i\ j} v_{\rm rel}\rangle\left[Y_\psi Y_a - Y_{\psi,0} Y_{a,0}\right] . \tag{A.28}$$

In the above equation, the thermal averaged annihilation cross-section times velocity is given by,

$$\langle \sigma v \rangle_{\psi\ a\to i\ j} = \frac{\int (\sigma v_{\rm rel}) e^{-E_\psi/T} e^{-E_a/T} d^3p_\psi d^3p_a}{\int e^{-E_\psi/T} e^{-E_a/T} d^3p_\psi d^3p_a} \,. \tag{A.29}$$

After doing a few mathematical steps, we get the relative velocity, (v) between ψ and a, in terms of Mandelstam variable s as, $v_{\rm rel}^2 = s^2 \frac{\left[s-(m_\psi+m_a)^2\right]\left[s-(m_\psi-m_a)^2\right]}{(s+m_\psi^2-m_a^2)^2(s-m_\psi^2+m_a^2)^2}$. However, the denominator and numerator part of Eq . (A.29) are given by,

$$\int\int e^{-E_\psi/T} e^{-E_a/T} d^3p_\psi d^3p_a = \left(4\pi m_\psi^2 T K_2\left(\frac{m_\psi}{T}\right)\right)\left(4\pi m_a^2 T K_2\left(\frac{m_a}{T}\right)\right) \,, \tag{A.30}$$

and

$$\begin{aligned}\int\int (\sigma v_{\rm rel}) e^{-E_\psi/T} e^{-E_a/T} d^3p_\psi d^3p_a \\ = 2\pi^2 T \int_{s_{\rm min}}^{\infty} \sigma(s) \left(s-(m_\psi+m_a)^2\right)\left(s-(m_\psi-m_a)^2\right)^{1/2} K_1\left(\frac{\sqrt{s}}{T}\right) ds \,,\end{aligned} \tag{A.31}$$

where the lower limit of the integration over s is $s_{\rm min} = \max\left[(m_\psi+m_a)^2, (m_i+m_j)^2\right]$. In the above equations, we have used K_n is the modified Bessel function of the second kind n^{th} order, has the following form:

$$\mathbf{K}_n(t) = \frac{\sqrt{\pi}}{\Gamma\left(n+\frac{1}{2}\right)}\left(\frac{t}{2}\right)^n \int_1^\infty e^{-tx}\left(x^2-1\right)^{n-\frac{1}{2}} dx; \;\; Re(n) > -\frac{1}{2}, \; Re(t) > 0 \,. \tag{A.32}$$

Finally, solving the Eq . (A.28), we can find out the present time abundance of the ψ species using the the relic density formula, $\Omega_\psi = \frac{\rho_\psi}{\rho_c}$. The present entropy density is $2893/\mathrm{cm}^3$ and $\rho_c \sim 1.054\times10^{-5}h^2\ GeV/\mathrm{cm}^3$ [7]. Therefore, the present ψ abundance is given by,

$$\Omega_\psi h^2 \simeq 2.744\times10^8 m_\psi Y_\psi|_{x\to\infty} \,. \tag{A.33}$$

In this context, we have presented the single-particle BEQ in Eq . (A.28). However, it is straightforward to derive the BEQs for the evaluation of the two-particle number density following this approach. In equilibrium, using the detailed balanced condition, we can write:

$$\langle \sigma v \rangle_{\psi\ a\to i\ j} n_{\psi,0} n_{a,0} = \langle \sigma v \rangle_{\psi\ a\to i\ j} n_{i,0} n_{j,0} \,. \tag{A.34}$$

This expression is usually very useful when writing the n-component coupled BEQ, although, in this thesis, we have only focused on the 2-component coupled BEQ.

Appendix B

Direct Search for WIMP-WIMP model

B.1 Feynman diagrams for DM relic density

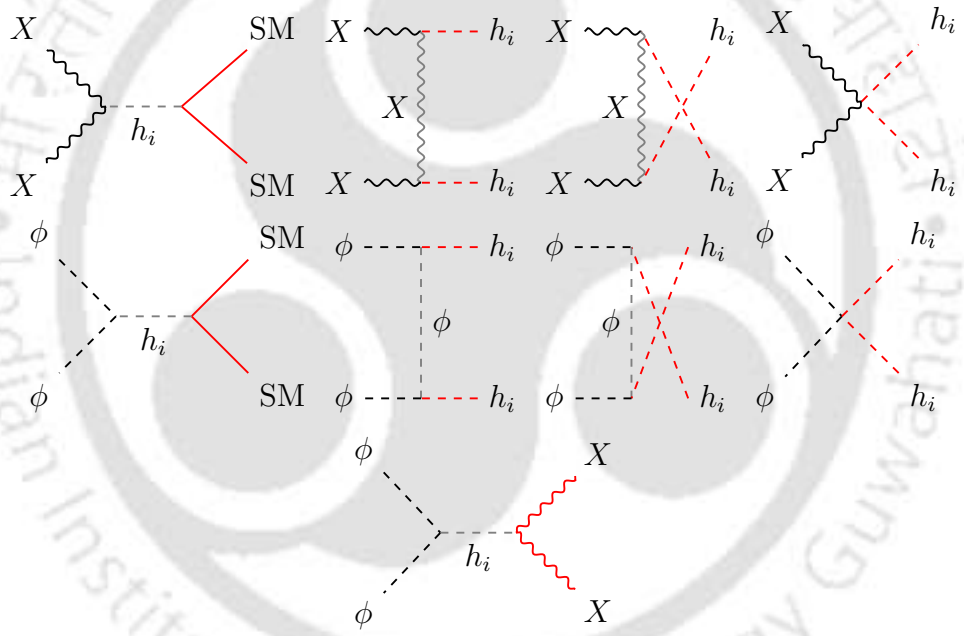

Figure B.1: Feynman diagrams relevant for DM annihilation: $\phi\,\phi \to$ SM SM and X X $\to$ SM SM, where SM $\in \{h_i,$ quarks, leptons, $W^{\pm}$, Z$\}$, and $i = 1, 2$. The bottom panel Feynman diagram shows the DM-DM conversion: $\phi\,\phi \to$ X X.

In the two component DM model, constructed of a VBDM (X) and a scalar singlet (ϕ) in thermal bath as described in Section 3.2, their annihilation cross-sections to the SM particles and conversion amongst themselves crucially decide the relic densities of the individual components. The Feynman graphs are shown in Fig . B.1. The individual relic densities also dictate the effective direct and indirect search cross-sections.

B.2 Thermal equilibrium for h_2

The key assumption in solving the cBEQ for obtaining ϕ and X relic densities, is that during DM freeze-out, h_2 remains in chemical and kinetic equilibrium, i.e.,

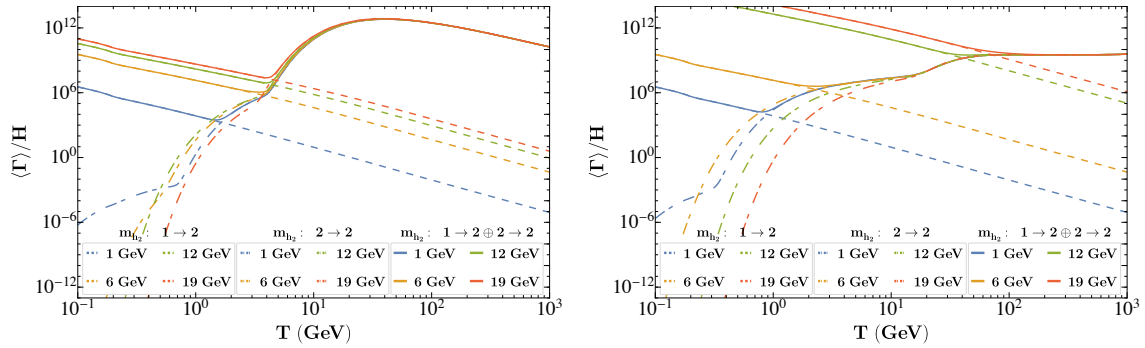

Figure B.2: $\langle\Gamma\rangle/H$ versus bath temperature T plotted for h_2. The dashed, dot-dashed, and thick color lines show the interaction rate of h_2 for decay, scattering, and the combined decay plus scattering processes, respectively. The parameters kept constant are: $g_X = 10^{-2}$, $\sin\vartheta = 10^{-3}$, $\lambda_{\phi S} = 10^{-1}$, $\lambda_{\phi H} = 10^{-2}$, while for left : $\{\mathrm{m}_\phi = 50\ \mathrm{GeV},\ \text{and}\ \mathrm{m_X} = 10\ \mathrm{GeV}\}$, and for right : $\{\mathrm{m}_\phi = 100\ \mathrm{GeV},\ \text{and},\ \mathrm{m_X} = 5\ \mathrm{GeV}\}$, with four distinct colors representing different values of m_{h_2}.

$n_{h_2}(T) = n_{h_2,0}(T)$, and shares the same thermal bath temperature. The kinetic and chemical equilibria are maintained via scattering with relativistic SM fermions and annihilation and decay to the light SM fermions, respectively. The results are shown in Fig . B.2, where $\langle\Gamma\rangle/H$ is plotted against bath temperature (T) for some allowed parameters of the model to show that in all cases including decay and scattering, h_2 remains in thermal bath.

Appendix C

Freeze-In/Out before and after EWSB

C.1 Decoupling of the bath particle decaying to FIMP

In our analysis, we have seen that $s \to XX$ (bEWSB) and $h_2 \to XX$ (aEWSB) plays a major role for X yield (Ω_X) when kinematically accessible with $m_s \gtrsim 2m_X$ or $m_{h_2} \gtrsim 2m_X$. However, it is important to note that the decay can occur when $s(h_2)$ is in thermal bath and also after it decouples from the bath. The contribution to X yield after the decoupling is referred to as 'late decay'. The late decay is taken care of in the FIMP BEQ via an additional interaction as shown in Eq. (4.35). The same is shown for freeze-in production of X aEWSB in Eq. (4.42). This additional term stems from a cBEQ involving s and X, where s freezes-out and X freezes-in. The relevant cBEQs are given by:

$$\begin{aligned}
\frac{dY_s}{dx} =& -\frac{0.264\,\mathrm{M_{Pl}}\,m_s}{x^2}\frac{g_*^s}{\sqrt{g_*^\rho}}\left[Y_s^2-(Y_s^{eq})^2\right]\left[\sum_{i=H,\phi,X}\langle\sigma_{ss\to ii}\,v\rangle+\frac{\langle\Gamma_{s\to XX}\rangle}{Y_s^{eq}\frac{2\pi^2}{45}g_*^s\left(\frac{m_s}{x}\right)^3}\right];\\
\frac{dY_X}{dx} =& \frac{45\,\mathrm{M_{Pl}}\,\Gamma_{s\to XX}}{1.67\times 2\pi^4\,m_s^2}\frac{K_1[x]\,x^3}{g_*^s\sqrt{g_*^\rho}}+\frac{0.264\,\mathrm{M_{Pl}}\,m_s}{x^2}\frac{g_*^s}{\sqrt{g_*^\rho}}\left[Y_s^2-(Y_s^{eq})^2\right]\frac{\langle\Gamma_{s\to XX}\rangle}{Y_s^{eq}\frac{2\pi^2}{45}g_*^s\left(\frac{m_s}{x}\right)^3};
\end{aligned} \tag{C.1}$$

where $x = m_s/T$. As shown in Fig. 4.7e, the late decay contribution essentially comes from the freeze-out yield of $s(h_2)$. The freeze-out yield of s, in turn depends on the annihilation cross-sections of s via the channels as shown in Feynman graphs in Fig. 4.6. The cross-sections at the threshold (denoted by σ^0) where center of mass energy ($\mathtt{s}$) is just enough for the production process to occur are given below :

$$\begin{aligned}
\sigma^0_{ss\to HH^\dagger}|_{\mathtt{s}=4m_s^2} =& \frac{\lambda_{HS}^2}{8\pi g_X^4 m_s^7}\sqrt{m_s^2-m_H^2}\left(g_X^4m_s^4-2g_X^2m_s^2m_X^2\lambda_{HS}+m_X^4\lambda_{HS}^2\right),\\
\sigma^0_{ss\to\phi\phi}|_{\mathtt{s}=4m_s^2} =& \frac{\lambda_{\phi S}^2}{16\pi g_X^4 m_s^7}\sqrt{m_s^2-m_\phi^2}\left(-2g_X^2m_s^2m_X^2\lambda_{\phi S}+g_X^4m_s^4+m_X^4\lambda_{\phi S}^2\right),\\
\sigma^0_{ss\to XX}|_{\mathtt{s}=4m_s^2} =& \frac{g_X^4}{4\pi m_s^7}\sqrt{m_s^2-m_X^2}\left(-20m_s^2m_X^2+11m_s^4+12m_X^4\right).
\end{aligned} \tag{C.2}$$

Note that the annihilation cross-section at threshold has the most dominant contribution for freeze out. The expressions for cross-sections of h_2 decoupling is pretty

similar, involves additionally the mixing angle $(\sin\theta)$ between the SM isodoublet and singlet.

C.2 Higgs mass and constraints

The scalar potential bEWSB (in terms of m_H, m_s, m_ϕ) is given by,

$$\begin{aligned} V(H,s,\phi)\Big|_{\rm bEWSB} &= \underbrace{(\mu_H^2+\frac{1}{2}\lambda_{HS}v_s^2)}_{m_H^2}(H^\dagger H)+\lambda_H(H^\dagger H)^2+\frac{1}{2}\underbrace{(\mu_\phi^2+\frac{1}{2}\lambda_{\phi S}v_s^2)}_{m_\phi^2}\phi^2+\frac{1}{4!}\lambda_\phi\phi^4 \\ &+\frac{1}{2}\underbrace{(\mu_S^2+3\lambda_S v_s^2)}_{m_s^2}s^2+\frac{1}{4}\lambda_S s^4+\lambda_S v_s s^3+\frac{1}{2}\lambda_{\phi H}(\phi^2 H^\dagger H)+\lambda_{HS}v_s(sH^\dagger H) \\ &+\frac{1}{2}\lambda_{\phi S}v_s(s\phi^2)+\frac{1}{2}\lambda_{HS}(s^2H^\dagger H)+\frac{1}{4}\lambda_{\phi S}(s^2\phi^2)+(\lambda_S v_s^3-\mu_S^2 v_s)s \\ &+(\frac{1}{4}\lambda_S v_s^4-\frac{1}{2}\mu_S^2 v_s^2). \end{aligned} \tag{C.3}$$

The potential aEWSB can be written (in terms of m_H, m_s, m_ϕ) as:

$$\begin{aligned} V(h,s,\phi)\Big|_{\rm aEWSB} &= \frac{1}{2}m_H^2(\mathtt{v}+h)^2+\frac{1}{4}\lambda_H(\mathtt{v}+h)^4+\frac{1}{2}m_\phi^2\phi^2+\frac{1}{4!}\lambda_\phi\phi^4 \\ &+\frac{1}{2}m_s^2s^2+\frac{1}{4}\lambda_S s^4+\lambda_S v_s s^3+\frac{1}{4}\lambda_{\phi H}\phi^2(\mathtt{v}+h)^2+\frac{1}{2}\lambda_{HS}v_s(v+h)^2s \\ &+\frac{1}{2}\lambda_{\phi S}v_s\phi^2 s+\frac{1}{4}\lambda_{HS}(\mathtt{v}+h)^2s^2+\frac{1}{4}\lambda_{\phi S}\phi^2s^2+(\lambda_S v_s^3-\mu_S^2 v_s)s \\ &+(\frac{1}{4}\lambda_S v_s^4-\frac{1}{2}\mu_S^2 v_s^2). \end{aligned} \tag{C.4}$$

Following above, there is a mixing between h, s fields aEWSB. The mass matrix $\mathcal{M}$ in the basis $\{h, s, \phi\}$ can be written as,

$$\mathcal{M}^2=\begin{pmatrix} m_H^2+3\lambda_H\mathtt{v}^2 & \lambda_{HS}\mathtt{v}v_s & 0 \\ \lambda_{HS}\mathtt{v}v_s & m_s^2+\frac{1}{2}\lambda_{HS}\mathtt{v}^2 & 0 \\ 0 & 0 & m_\phi^2+\frac{1}{2}\lambda_{\phi H}v^2 \end{pmatrix}. \tag{C.5}$$

Upon diagonalisation, the mass eigenvalues of the matrix are given by,

$$\begin{aligned} 2m_{h_{1,2}}^2 &= m_H^2+m_s^2+3\lambda_H\mathtt{v}^2+\frac{1}{2}\lambda_{HS}v^2\mp\sqrt{(m_s^2+\frac{1}{2}\lambda_{HS}\mathtt{v}^2-m_H^2-3\lambda_H\mathtt{v}^2)^2+4\lambda_{HS}^2\mathtt{v}^2v_s^2}; \\ \mathfrak{m}_\phi^2 &= m_\phi^2+\frac{1}{2}\lambda_{\phi H}\mathtt{v}^2. \end{aligned} \tag{C.6}$$

The physical eigenstates are given by

$$\begin{aligned} h_1 &= \cos\theta\, h-\sin\theta\, s\,, \\ h_2 &= \sin\theta\, h+\cos\theta\, s\,; \end{aligned} \tag{C.7}$$

where the mixing angle can be written as,

$$\tan 2\theta = \frac{2\lambda_{HS}\mathrm{v}v_s}{m_s^2 + \frac{1}{2}\lambda_{HS}\mathrm{v}^2 - m_H^2 - 3\lambda_H\mathrm{v}^2}\,. \tag{C.8}$$

The mixing is restricted by LHC data as $|\sin[\theta]| \lesssim 0.3$ (see text). Now, h_1 is identified with SM Higgs so that $m_{h_1} = 125.1$ GeV and h_2 is assumed to be another neutral scalar, which is dominantly a singlet and can be heavy or light. When $m_s < 2m_X$, immaterial to whether the freeze-in or freeze-out occurs bEWSB, h, s mixing as stated above occurs and results in a SM Higgs as observed currently. So, even in bEWSB epoch, m_H, m_s needs to be chosen in such a way that we obtain correct Higgs mass and respect the mixing angle limit. This is what we have done for the scans done in the DM analysis. The correct choices of parameters $\{m_H, m_s, \lambda_{HS}, v_s\}$ is indicated in Fig . C.1, which shows the correlation between $m_H - m_s$ bEWSB allowed by these mass constraints for fixed values of other couplings.

Here, we would also like to point out to a caveat that when $m_s \gtrsim 2m_X$ and FIMP freezes-in before EWSB by in-equilibrium decay and late decay of s, due to complete depletion of s before EWSB, mixing does not arise after EWSB $(\sin\theta \sim 0)$ and therefore we only obtain one physical scalar h_1 with mass $m_{h_1} = 125.1$ GeV. Then the relation between m_H bEWSB and m_{h_1} aEWSB is simply given by

$$m_{h_1}^2 = m_H^2 + 3\lambda_H\mathrm{v}^2, \;\; m_H^2 = \frac{1}{2}m_{h_1}^2. \tag{C.9}$$

The scalar potential can be written only in terms of h_1, h_2, θ is given by

$$\begin{aligned} V(h_1,h_2,\phi)\Big|_{\text{aEWSB}} =& \frac{\mu_H^2}{2}(\mathrm{v} + h_1\cos\theta + h_2\sin\theta)^2 + \frac{\lambda_H}{4}(\mathrm{v} + h_1\cos\theta + h_2\sin\theta)^4 + \frac{\mu_\phi^2}{2}\phi^2 \\ &+ \frac{\lambda_\phi}{4!}\phi^4 + \frac{\mu_S^2}{2}(v_s - h_1\sin\theta + h_2\cos\theta)^2 + \frac{\lambda_S}{4}(v_s - h_1\sin\theta + h_2\cos\theta)^4 \\ &+ \frac{\lambda_{\phi H}}{4}\phi^2(\mathrm{v} + h_1\cos\theta + h_2\sin\theta)^2 + \frac{\lambda_{\phi S}}{4}\phi^2(v_s - h_1\sin\theta + h_2\cos\theta)^2 \\ &+ \frac{\lambda_{HS}}{4}(\mathrm{v} + h_1\cos\theta + h_2\sin\theta)^2(v_s - h_1\sin\theta + h_2\cos\theta)^2\,. \end{aligned} \tag{C.10}$$

Using the extremisation condition of the potential

$$\left(\frac{\partial V(h_1,h_2,\phi)}{\partial h_1}\right), \left(\frac{\partial V(h_1,h_2,\phi)}{\partial h_2}\right)\Bigg|_{h_{1,2},\phi=0} = 0 \tag{C.11}$$

we obtain the following conditions,

$$\begin{aligned} \mathrm{v}\cos\theta\left(\lambda_{HS}v_s^2 + 2\mu_H^2 + 2\lambda_H\mathrm{v}^2\right) - v_s\sin\theta\left(\mathrm{v}^2\lambda_{HS} + 2\lambda_S v_s^2 + 2\mu_S^2\right) = 0\,, \\ \mathrm{v}\sin\theta\left(\lambda_{HS}v_s^2 + 2\mu_H^2 + 2\lambda_H\mathrm{v}^2\right) + v_s\cos\theta(\mathrm{v}^2\lambda_{HS} + 2\lambda_S v_s^2 + 2\mu_S^2) = 0\,. \end{aligned} \tag{C.12}$$

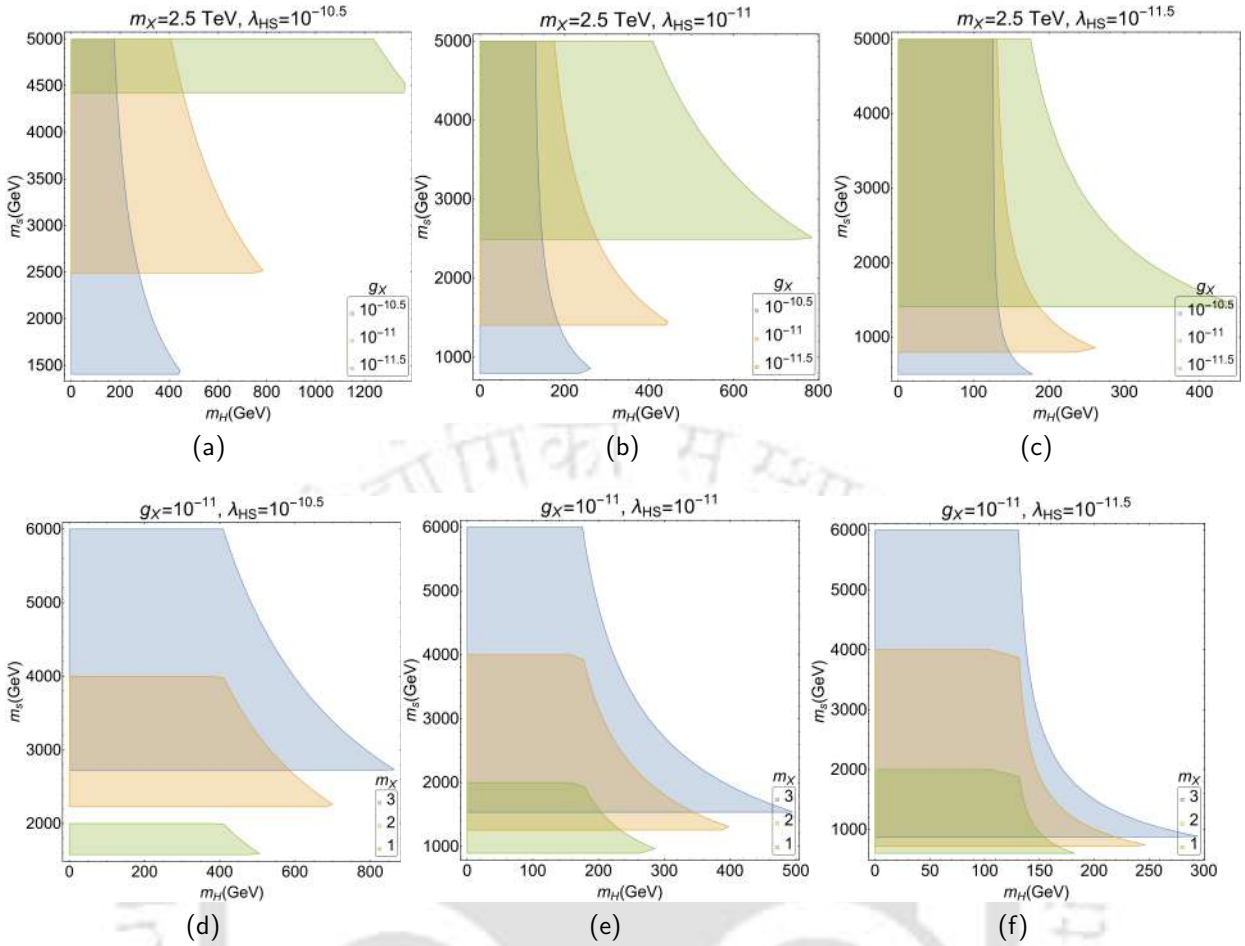

Figure C.1: Allowed parameter space in $m_H - m_s$ plane constrained by the requirement of obtaining 125.1 GeV SM Higgs after EWSB. $|\sin[\theta]| \lesssim 0.3$ and $0 < \lambda_H \leq 4\pi$. FIMP mass (m_X) is varied in TeV scale in Figs . C.1d to C.1f.

$$
\begin{aligned}
\left.\frac{\partial^2 V_{\text{scalar}}}{\partial h_1^2}\right|_{h_{1,2}=\phi=0} &= m_{h_1}^2 = (3v^2\lambda_H + \frac{1}{2}v_s^2\lambda_{HS} + \mu_H^2)\cos^2\theta - \mathrm{v}v_s\lambda_{HS}\sin 2\theta \\
&\quad + (3v_s^2\lambda_S + \frac{1}{2}v^2\lambda_{HS} + \mu_S^2)\sin^2\theta\,, \\
\left.\frac{\partial^2 V_{\text{scalar}}}{\partial \phi^2}\right|_{h_{1,2}=\phi=0} &= \mathfrak{m}_\phi^2 = \frac{1}{2}\left(2\mu_\phi^2 + \lambda_{\phi S}v_s^2 + \mathrm{v}^2\lambda_{\phi H}\right)\,, \\
\left.\frac{\partial^2 V_{\text{scalar}}}{\partial h_2^2}\right|_{h_{1,2}=\phi=0} &= m_{h_2}^2 = (3\mathrm{v}^2\lambda_H + \frac{1}{2}v_s^2\lambda_{HS} + \mu_H^2)\sin^2\theta + \mathrm{v}v_s\lambda_{HS}\sin 2\theta \\
&\quad + (3v_s^2\lambda_S + \frac{1}{2}\mathrm{v}^2\lambda_{HS} + \mu_S^2)\cos^2\theta\,.
\end{aligned}
\tag{C.13}
$$

After mixing, off-diagonal mass terms of physical fields h_1 and h_2 are absent; then $\partial^2 V_{\text{scalar}}/\partial h_1 \partial h_2 = 0$ gives us,

$$
\cos 2\theta\ \mathrm{v}v_s\lambda_{HS} + \frac{1}{2}\sin 2\theta\left[3(\mathrm{v}^2\lambda_H - v_s^2\lambda_S) + \frac{1}{2}\lambda_{HS}(v_s^2 - \mathrm{v}^2) - (\mu_S^2 - \mu_H^2)\right] = 0\,. \tag{C.14}
$$

Finally, the expressions of mixing angle (θ) and internal parameters $(\mu_H, \mu_\phi, \mu_S, \lambda_H, \lambda_S, \lambda_{HS})$ in terms of the external parameters are given by:

$$\begin{aligned}
\mu_H^2 &= -(\lambda_H \mathrm{v}^2 + \frac{1}{2}\lambda_{HS} v_s^2), \\
\mu_\phi^2 &= \mathfrak{m}_\phi^2 - \frac{1}{2}\lambda_{\phi S} v_s^2 - \frac{1}{2}\lambda_{\phi H}\mathrm{v}^2, \\
\mu_S^2 &= -(\lambda_S v_s^2 + \frac{1}{2}\lambda_{HS}\mathrm{v}^2), \\
v_s &= \frac{m_X}{g_X}, \\
\lambda_H &= \frac{1}{2\mathrm{v}^2}\left(m_{h_1}^2 \cos^2\theta + m_{h_2}^2 \sin^2\theta\right), \\
\lambda_S &= \frac{1}{2v_s^2}\left(m_{h_2}^2 \cos^2\theta + m_{h_1}^2 \sin^2\theta\right), \\
\lambda_{HS} &= \frac{\sin 2\theta}{2v_s\mathrm{v}}\left(m_{h_2}^2 - m_{h_1}^2\right).
\end{aligned} \tag{C.15}$$

C.3 Invisible decay width of Higgs

In Higgs portal scenarios, where DM couples to SM Higgs, Higgs boson can always decay to a pair of DM particles when kinematically accessible, contributing to invisible Higgs decay width. In our model, the possible invisible decay channels of Higgs include $h_1 \to \phi\phi, h_1 \to XX, h_1 \to h_2 h_2$ with decay widths are given by:

$$\begin{aligned}
\Gamma_{h_1\to\phi\phi} &= \frac{(\lambda_{\phi S} m_X \sin\theta - \lambda_{\phi H} g_X \mathrm{v}\cos\theta)^2}{32\pi g_X^2 m_{h_1}^2}(m_{h_1}^2 - 4\mathfrak{m}_\phi^2)^{1/2}\Theta(m_{h_1} - 2\mathfrak{m}_\phi) \\
\Gamma_{h_1\to XX} &= \frac{g_X^2 \sin^2\theta}{32\pi m_{h_1}^2 m_X^2}(m_{h_1}^2 - 4m_X^2)^{1/2}(m_{h_1}^4 - 4m_{h_1}^2 m_X^2 + 12 m_X^4)\Theta(m_{h_1} - 2m_X) \\
\Gamma_{h_1\to h_2 h_2} &= \frac{(m_X \sin\theta - v g_X \cos\theta)^2}{32\pi \mathrm{v}^2 m_{h_1}^2 m_X^2}\sin^2\theta\cos^2\theta(m_{h_1}^2 + 2m_{h_2}^2)^2(m_{h_1}^2 - 4m_{h_2}^2)^{1/2}\Theta(m_{h_1} - 2m_{h_2})
\end{aligned} \tag{C.16}$$

The expression for the Higgs invisible decay branching ratio is,

$$\Gamma_{h_1\to\text{inv}} = \frac{\Gamma_{h_1\to\phi\phi} + \Gamma_{h_1\to XX} + \Gamma_{h_1\to h_2 h_2}}{\Gamma_{h_1}^{\text{SM}} + \Gamma_{h_1\to\phi\phi} + \Gamma_{h_1\to XX} + \Gamma_{h_1\to h_2 h_2}}. \tag{C.17}$$

Invisible Higgs decay widths and branching ratio is heavily restricted by the observed Higgs data at LHC as mentioned in Eq . (E.1) and therefore, we do not scan the parameter space that comes within.

C.4 Direct Search possibilities

In this two component WIMP-FIMP DM model, FIMP X coupling to SM Higgs (H) (via s) λ_{HS} is very small in order to facilitate non-thermal production. Therefore, FIMP-nucleon cross-section is negligible. In case of WIMP ϕ, it can talk to SM through the portals $\lambda_{\phi H}$ and $\lambda_{\phi S}$, given the mixing between $s-h$ present after EWSB, where the physical states become h_1 and h_2, out of which h_1 is assumed as SM Higgs,

and h_2 is dominantly a singlet as explained in Appendix C.2. The Feynman graph for direct search cross-section is shown in Fig. C.2. The relative dominance of the mediators h_1, h_2 in the DM-nucleon scattering cross-section depends on the mass of new scalar h_2, which can be either heavy or light.

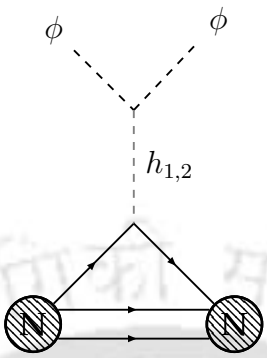

Figure C.2: Feynman diagrams for the direct detection of WIMP DM ϕ.

The spin-independent scattering cross section of ϕ-Nucleon, mediated by both the physical scalars after mixing, is given by,

$$\sigma^{\rm SI}_{n_\phi} = \frac{\Omega_\phi}{\Omega_\phi+\Omega_X}\frac{f_N^2\mu_n^2 m_n^2}{4\pi v^2 \mathfrak{m}_\phi^2}\left(\cos\theta\frac{\lambda_{h_1\phi\phi}}{m_{h_1}^2}+\sin\theta\frac{\lambda_{h_2\phi\phi}}{m_{h_2}^2}\right)^2, \tag{C.18}$$

where $f_N = 0.308\pm0.018$ [775] represents the form factor of nucleon and $\mu_n = \frac{m_n\mathfrak{m}_\phi}{m_n+\mathfrak{m}_\phi}$ stands for the reduced mass and n stands for nucleon. Also note that the maximum direct search cross-section for ϕ is folded by the fraction of relic density that ϕ possess in the total DM relic density in a two component framework given by $\frac{\Omega_\phi}{\Omega_\phi+\Omega_X}$. The expressions of $\lambda_{h_1\phi\phi}$ and $\lambda_{h_2\phi\phi}$ in terms of our model parameters are given by

$$\begin{aligned}\lambda_{h_1\phi\phi} &= -\mathrm{v}\cos\theta\lambda_{\phi H}+\frac{m_X}{g_X}\sin\theta\lambda_{\phi S}\,,\\ \lambda_{h_2\phi\phi} &= -\mathrm{v}\sin\theta\lambda_{\phi H}-\frac{m_X}{g_X}\cos\theta\lambda_{\phi S}.\end{aligned} \tag{C.19}$$

In our analysis, the h_2 mediation in the direct detection cross-section is suppressed by small mixing angle. Also, there will be some propagator suppression due to h_2 which is assumed heavier than the SM Higgs. It is to be noted that if $\sin\theta \sim 0$, ie, mixing is absent, Eq. (C.18) boils down to the typical scalar singlet direct detection cross-section, mediated by SM Higgs. The constraint on the mixing is propagated to constraining λ_{HS}, as per Eq. (C.15), and importantly affects both WIMP and FIMP under abundance. The SI direct search limit from XENON1T is mentioned in Section 4.4.2.

We further note that even if freeze-out occurs before EWSB, one can have direct search possibility as described above. Even the FIMP under abundant region gets constrained by direct search bound due to the presence of $\lambda_{\phi S}$ in both the cases. Only when s decay completes before EWSB, it does not mix with h aEWSB and then FIMP has absolutely no connection to SM and no constraints from direct search.

Appendix D

Pseudo-FIMP: construction and solution of coupled BEQ

D.1 Semi-analytic solution of the cBEQ for WIMP-pFIMP scenario

A two-component WIMP-pFIMP framework is governed by a coupled Boltzmann equations (cBEQ),

$$\begin{aligned}
\frac{dY_1}{dx} =& -\frac{2\pi^2 \mathrm{M_{pl}}}{45\times 1.67}\frac{g^s_\star}{\sqrt{g^\rho_\star}}\frac{\mu_{12}}{x^2}\left[\langle\sigma v\rangle_{11\to \mathrm{SM}}\left(Y_1^2 - Y_1^{\mathrm{eq}^2}\right) + \langle\sigma v\rangle_{11\to 22}\left(Y_1^2 - \frac{Y_1^{\mathrm{eq}^2}}{Y_2^{\mathrm{eq}^2}}Y_2^2\right)\right], \\
\frac{dY_2}{dx} =& \frac{2\mathrm{M_{pl}}}{1.67\times\sqrt{g^\rho_\star}}\frac{x}{\mu_{12}^2}\langle\Gamma_{\mathrm{SM}\to 22}\rangle(Y^{\mathrm{eq}}_{\mathrm{SM}} - \frac{Y_2^2}{Y_2^{\mathrm{eq}^2}}Y^{\mathrm{eq}}_{\mathrm{SM}}) + \frac{4\pi^2\mathrm{M_{pl}}}{45\times 1.67}\frac{g^s_\star}{\sqrt{g^\rho_\star}}\frac{\mu_{12}}{x^2} \\
& \left[\langle\sigma v\rangle_{\mathrm{SM}\to 22}\left(Y^{\mathrm{eq}^2}_{\mathrm{SM}} - \frac{Y_2^2}{Y_2^{\mathrm{eq}^2}}Y^{\mathrm{eq}^2}_{\mathrm{SM}}\right) + \langle\sigma v\rangle_{11\to 22}\left(Y_1^2 - \frac{Y_1^{\mathrm{eq}^2}}{Y_2^{\mathrm{eq}^2}}Y_2^2\right)\right].
\end{aligned} \tag{D.1}$$

We elaborate upon the semi analytical solution of the cBEQ as in Eq. (D.1) in WIMP-pFIMP limit, for both the hierarchies:

- Case-I: WIMP mass > pFIMP mass (i.e. $m_1 > m_2$).
- Case-II: WIMP mass < pFIMP mass (i.e. $m_1 < m_2$).

The methodology follows the procedure in [597].

Case-I ($m_1 > m_2$)

In WIMP-pFIMP limit, we neglect the pFIMP production from the visible sector as the pFIMP coupling with SM is very small, compared to the conversion cross-section. So, in the following we consider, $\Gamma_{\mathrm{SM}\to 22} = \langle\sigma v\rangle_{\mathrm{SM}\to 22} = 0$. For notational ease, let us also use, $\langle\sigma v\rangle_{11\to\mathrm{SM}} = \sigma_1$, $\langle\sigma v\rangle_{11\to 22} = \sigma_{12}$, $\langle\sigma v\rangle_{22\to 11} = \sigma_{21}$, $[(2\pi^2\sqrt{\mathrm{g}^\rho_\star})/(45\times 1.66)]\mathrm{M_{pl}} = \mathrm{n_f}$ with Planck mass $\mathrm{M_{pl}} = 1.22\times 10^{19}$ GeV. Recall that $\sigma_{12} = \sigma_{21}\,(n_2^{eq}/n_1^{eq})^2$.

With above, the cBEQ in terms of bath temperature (T) becomes,

$$\begin{aligned}\frac{dY_1}{dT} &= n_f\left[\sigma_1\left(Y_1^2 - Y_1^{\mathrm{eq}^2}\right) + \sigma_{12}\left(Y_1^2 - \frac{Y_1^{\mathrm{eq}^2}}{Y_2^{\mathrm{eq}^2}}Y_2^2\right)\right], \\ \frac{dY_2}{dT} &= -2n_f\left[\sigma_{12}\left(Y_1^2 - \frac{Y_1^{\mathrm{eq}^2}}{Y_2^{\mathrm{eq}^2}}Y_2^2\right)\right].\end{aligned} \tag{D.2}$$

The equilibrium yield is given by Maxwell-Boltzmann distribution,

$$Y_i^{\mathrm{eq}}(T) = 0.145\frac{g}{g_\star^s}\left(\frac{m_i}{T}\right)^{3/2}\exp\left(-\frac{m_i}{T}\right) = A_i T^{-3/2}e^{-m_i/T} \text{ with } A_i = 0.145\frac{g}{g_\star^s}m_i^{3/2}.$$

Defining $Y_1^{eq^2}\left(\frac{\sigma_1}{\sigma_1+\sigma_{12}} + \frac{\sigma_{12}}{\sigma_1+\sigma_{12}}\frac{Y_2^2}{Y_2^{eq^2}}\right) = y_1^{eq^2}$, Eq. (D.2) becomes,

$$\begin{aligned}\frac{dY_1}{dT} &= n_f(\sigma_1+\sigma_{12})\left(Y_1^2 - y_1^{\mathrm{eq}^2}\right), \\ \frac{dY_2}{dT} &= -2n_f\left[\sigma_{12}\left(Y_1^2 - \frac{Y_1^{\mathrm{eq}^2}}{Y_2^{\mathrm{eq}^2}}Y_2^2\right)\right].\end{aligned} \tag{D.3}$$

In order to solve the cBEQ analytically, it would be convenient to divide this whole scenario in three regions on the bath temperature: **Region A**: $T \gg T_{f_i}$, **Region B**: $T \simeq T_{f_i}$ and **Region C**: $T \ll T_{f_i}$ where T_{f_i} denotes the freeze-out temperature of both species $i = 1, 2$. Let use consider the difference of DM yield from equilibrium yield as $\Delta_1 = Y_1 - y_1^{\mathrm{eq}}$ and $\Delta_2 = Y_2 - Y_2^{\mathrm{eq}}$. Using these relations, Eq. (D.3) becomes,

$$\begin{aligned}\frac{d\Delta_1}{dT} + \frac{dy_1^{eq}}{dT} &= n_f(\sigma_1+\sigma_{12})\left(\Delta_1^2 + 2\Delta_1 y_1^{\mathrm{eq}}\right), \\ \frac{d\Delta_2}{dT} + \frac{dY_2^{eq}}{dT} &= -2n_f\sigma_{12}\left[\left(\Delta_1 + y_1^{\mathrm{eq}}\right)^2 - \frac{Y_1^{\mathrm{eq}^2}}{Y_2^{\mathrm{eq}^2}}\left(\Delta_2 + Y_2^{\mathrm{eq}}\right)^2\right].\end{aligned} \tag{D.4}$$

- **Region A:**

For $T \gg T_{f_i}$, $\frac{d\Delta_i}{dT}$ is negligible and Eq. (D.4) becomes,

$$\frac{dy_1^{eq}}{dT} = n_f(\sigma_1+\sigma_{12})\left(\Delta_1^2 + 2\Delta_1 y_1^{\mathrm{eq}}\right), \tag{D.5}$$

$$\frac{dY_2^{eq}}{dT} = -2n_f\sigma_{12}\left[\left(\Delta_1 + y_1^{\mathrm{eq}}\right)^2 - \frac{Y_1^{\mathrm{eq}^2}}{Y_2^{\mathrm{eq}^2}}\left(\Delta_2 + Y_2^{\mathrm{eq}}\right)^2\right]. \tag{D.6}$$

- **Region B:**

Let us suppose $T_{f_2} > T_{f_1}$, then both Eq. (D.5) and Eq. (D.6) hold at T_{f_2}, but only Eq. (D.5) holds at T_{f_1} as pFIMP already freezes out at T_{f_1}. In the vicinity of $T \simeq T_f$, we may further assume $\Delta_1(T_{f_1}) = c_1 y_1^{eq}(T_{f_1})$ and $\Delta_2(T_{f_2}) = c_2 Y_2^{eq}(T_{f_2})$ [62], where c_i's are unknown constants whose values are determined by matching the analytical result with the numerical one. Substituting in Eq. (D.5) and Eq. (D.6), we get,

$$y_1^{eq'}(T_{f_1}) \approx n_f(\sigma_1+\sigma_{12})\,c_1(c_1+2)y_1^{eq^2}(T_{f_1}), \tag{D.7}$$

$$2n_f(\sigma_1+\sigma_{12})\sigma_{12}\left[(c_2+1)^2 Y_1^{eq^2}(T_{f_2}) - y_1^{eq^2}(T_{f_2})\right] \approx (\sigma_1+\sigma_{12})Y_2^{eq'}(T_{f_2}) + 2\sigma_{12}y_1^{eq'}(T_{f_2}) \tag{D.8}$$

In the above,

$$Y_i^{\mathrm{eq}'}(T) = \left(-\frac{3}{2T} + \frac{m_i}{T^2}\right) Y_i^{\mathrm{eq}}(T)\,, \tag{D.9}$$

$$y_1^{eq^2}(T_{f_2}) = Y_1^{eq^2}(T_{f_2}) \left(\frac{\sigma_1}{\sigma_1+\sigma_{12}} + \frac{\sigma_{12}}{\sigma_1+\sigma_{12}}\,(c_2+1)^2\right)\,, \tag{D.10}$$

$$y_1^{eq^2}(T_{f_1}) = Y_1^{eq^2}(T_{f_1}) \left(\frac{\sigma_1}{\sigma_1+\sigma_{12}} + (c_2+1)^2\frac{\sigma_{12}}{\sigma_1+\sigma_{12}}\frac{Y_2^{eq^2}(T_{f_2})}{Y_2^{eq^2}(T_{f_1})}\right)\,, \tag{D.11}$$

$$\begin{aligned} y_1^{eq'}(T_{f_2}) = \frac{Y_1^{eq^2}(T_{f_2})}{y_1^{eq}(T_{f_2})} \Bigg[&\left(-\frac{3}{2T_{f_2}} + \frac{m_1}{T_{f_2}^2}\right)\left(\frac{\sigma_1}{\sigma_1+\sigma_{12}} + \frac{\sigma_{12}}{\sigma_1+\sigma_{12}}\,(c_2+1)^2\right) \\ &- \left(-\frac{3}{2T_{f_2}} + \frac{m_2}{T_{f_2}^2}\right)\frac{\sigma_{12}}{\sigma_1+\sigma_{12}} c_2\,(c_2+1)\Bigg]\,, \end{aligned} \tag{D.12}$$

$$y_1^{eq'}(T_{f_1}) = \frac{Y_1^{eq^2}(T_{f_1})}{y_1^{eq}(T_{f_1})} \left[\left(-\frac{3}{2T_{f_1}} + \frac{m_1}{T_{f_1}^2}\right)\frac{\sigma_1}{\sigma_1+\sigma_{12}} + \frac{\sigma_{12}}{\sigma_1+\sigma_{12}}\,(c_2+1)^2\,\frac{m_1-m_2}{T_{f_1}^2}\left(\frac{T_{f_1}}{T_{f_2}}\right)^3 e^{-2\frac{m_2}{T_{f_2}}} e^{2\frac{m_2}{T_{f_1}}}\right]\,. \tag{D.13}$$

Eq. (D.7) and Eq. (D.8) can be written further as,

$$y_1^{eq'}(T_{f_1}) = n_f\,(\sigma_1+\sigma_{12})\,c_1(c_1+2)y_1^{eq^2}(T_{f_1})\,, \tag{D.14}$$

$$P\,T_{f_2}^{-1/2} = 2\sigma_{12}QT_{f_2}e^{\frac{m_1}{T_{f_2}}} + (\sigma_1+\sigma_{12})\left(-\tfrac{3}{2}+\tfrac{m_2}{T_{f_2}}\right)\left(\tfrac{m_2}{m_1}\right)^{3/2} e^{2\frac{m_1}{T_{f_2}}} e^{-\frac{m_2}{T_{f_2}}}\,; \tag{D.15}$$

where,

$$P = 2A_1 n_f \sigma_1\sigma_{12}c_2\,(c_2+2)\,, \tag{D.16}$$

$$\begin{aligned} Q = \left[\left(-\frac{3}{2T_{f_2}} + \frac{m_1}{T_{f_2}^2}\right)\left(\frac{\sigma_1}{\sigma_1+\sigma_{12}} + \frac{\sigma_{12}}{\sigma_1+\sigma_{12}}\,(c_2+1)^2\right) - \left(-\frac{3}{2T_{f_2}} + \frac{m_2}{T_{f_2}^2}\right)\frac{\sigma_{12}}{\sigma_1+\sigma_{12}} c_2\,(c_2+1)\right] \\ \times\left[\frac{\sigma_1}{\sigma_1+\sigma_{12}} + \frac{\sigma_{12}}{\sigma_1+\sigma_{12}}\,(c_2+1)^2\right]^{-1/2}\,. \end{aligned} \tag{D.17}$$

Eq. (D.14) and Eq. (D.15) are transcendental equations, analytical solutions are difficult to obtain, but using numerical method it is possible to extract the values of freeze-out temperature T_{f_1} and T_{f_2}, which we did.

- **Region C:**

When $T \ll T_{f_i}$, then, Y_i^{eq}, $Y_i^{\mathrm{eq}'}$ and $\frac{Y_1^{eq^2}}{Y_2^{eq^2}}$ are exponentially suppressed, so, $\Delta_i \gg Y_i^{\mathrm{eq}}$ and Eq. (D.4) becomes,

$$\frac{d\Delta_1}{dT} \approx n_f(\sigma_1+\sigma_{12})\Delta_1^2\,, \tag{D.18}$$

$$\frac{d\Delta_2}{dT} \approx -2n_f\sigma_{12}\Delta_1^2\,. \tag{D.19}$$

After solving the differential equations between T_{f_i} to T with $\Delta_i(T) \gg \Delta_i(T_{f_i})$, we get,

$$\Delta_1(T) \approx \left[\frac{1}{\Delta_1(T_{f_1})} + n_f(\sigma_1+\sigma_{12})\,(T_{f_1}-T)\right]^{-1}, \tag{D.20}$$

$$\Delta_2(T) \approx \Delta_2(T_{f_2}) - 2n_f\sigma_{12}(T-T_{f_2})\Big[\left(\frac{1}{\Delta_1(T_{f_1})} + n_f(\sigma_1+\sigma_{12})(T_{f_1}-T)\right)\left(\frac{1}{\Delta_1(T_{f_1})} + n_f(\sigma_1+\sigma_{12})(T_{f_1}-T_{f_2})\right)\Big]^{-1}. \tag{D.21}$$

Following, $\Delta_1(T_{f_1}) \approx c_1 y_1^{\rm eq}(T_{f_1})$, $\Delta_2(T_{f_2}) \approx c_2 Y_2^{\rm eq}(T_{f_2})$, at $T = T_{\rm CMB} = 2.35 \times 10^{-13}$GeV, the DM yields are,

$$\Delta_1(T_{\rm CMB}) \approx Y_1(T_{\rm CMB}) \approx \left(\frac{1}{\Delta_1(T_{f_1})} + n_f(T_{f_1}-T_{\rm CMB})(\sigma_1+\sigma_{12})\right)^{-1}, \tag{D.22}$$

$$\Delta_2(T_{\rm CMB}) \approx Y_2(T_{\rm CMB}) \approx \Delta_2(T_{f_2}) + 2n_f\sigma_{12}\int_{T_{\rm CMB}}^{T_{f_2}} \Delta_1^2(T)\,dT\,. \tag{D.23}$$

Using the analytical approximate solutions, relic density as a function of conversion cross-section for both WIMP and pFIMP have been shown in Fig . D.1. They show reasonably good agreement, the tiny mismatch with numeric result at low and high conversion region is only due to the entropy d.o.f (g_*^s) and matter d.o.f (g_*^ρ) which depends on temperature (specifically $T \lesssim 5$ GeV) but for simplicity we have neglected this temperature dependence and chosen a fixed value of $g_*^\rho = g_*^s \simeq 75$ for the semi analytical solution.

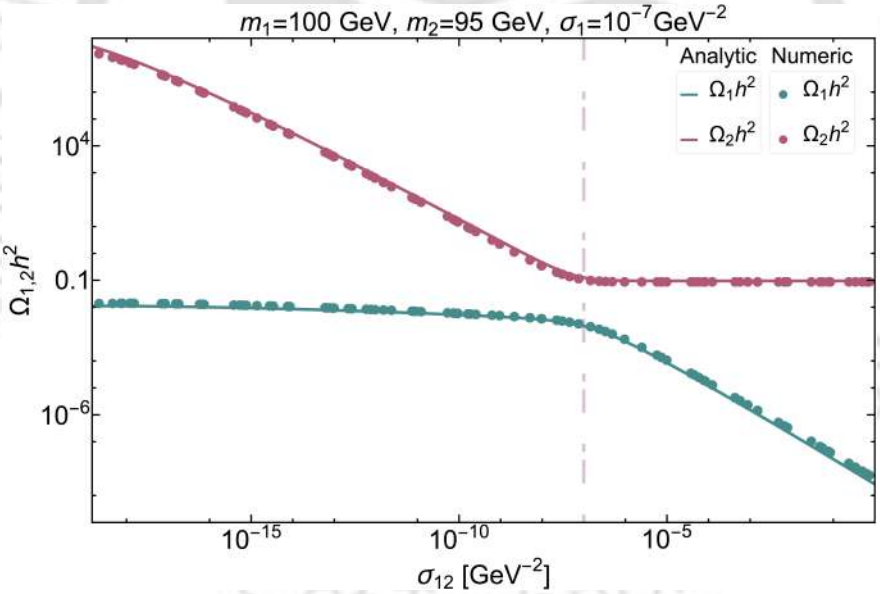

Figure D.1: Analytic solution of the cBEQ (represented by thick line) and numerical solution (represented by points) of Eq. (D.1) for pFIMP-WIMP case is shown as a function of conversion cross-section. The unknown constants are chosen as $c_1 = 2$ and $c_2 = 7$. The vertical dot-dashed line is corresponding to $\sigma_{12} = \sigma_1$.

In the similar way it is easy to evaluate the present DM relic for the inverse mass hierarchy ($m_1 < m_2$) where one necessary input is $T_{f_1} > T_{f_2}$ and $\Delta_2(T_{f_2}) = c_2 y_2^{eq}(T_{f_2})$ with $y_2^{eq} = Y_1 \frac{Y_2^{eq}}{Y_1^{eq}}$. The transition of FIMP into a pFIMP depends not only

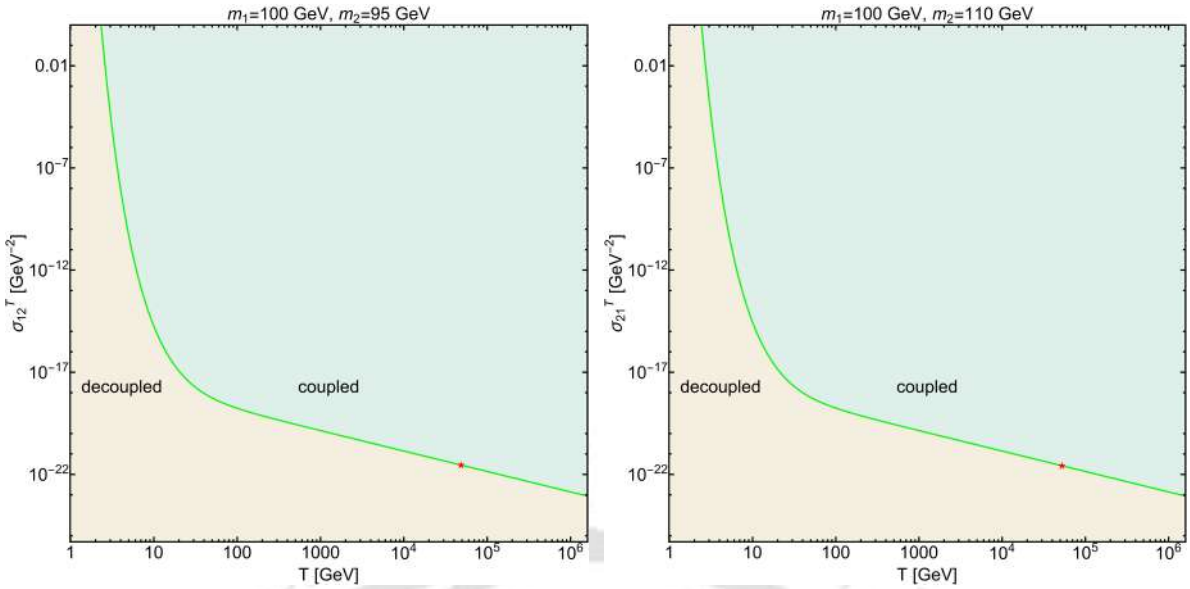

Figure D.2: In-equilibrium ($\Gamma > \mathrm{H}$) (green shade) and out-of-equilibrium ($\Gamma < \mathrm{H}$) (yellow shade) possibilities for pFIMP. Green line corresponds to $\Gamma(\mathrm{T}) = \mathrm{H}(\mathrm{T})$ and red star corresponds to $\mathrm{T} = \mathrm{T_{RH}}$. Both mass hierarchies $m_1 > m_2$ (left), $m_2 > m_1$ (right) are plotted.

on the temperature but also on the interaction rate. This can be understood, just by analysing the relation between interaction rate (Γ) and Hubble expansion rate (H). Fig . D.2 depicts it for both mass hierarchies: $m_1 > m_2$ (left), $m_2 > m_1$ (right). $\Gamma \simeq \mathrm{H}$ has been represented by the green curve. The red star points correspond to $\Gamma(\mathrm{T} \sim \mathrm{T_{RH}}) = \mathrm{H}(\mathrm{T} \sim \mathrm{T_{RH}})$ in both the figures. In our model-independent analysis, we have neglected the temperature dependence of the conversion cross-section, which may alter the high temperature behaviour of the plot.

D.2 Dynamics of the pFIMP in presence of a SIMP

The pFIMP behaviour could also be achieved in presence of SIMP [254] when DM-DM conversion is sufficiently large ($\sim$ weak scale). The cBEQ for pFIMP-SIMP scenario can be written as:

$$\frac{dY_{\mathrm{w}}}{dx} = \frac{2\,\mathbf{s}}{x\,H(x)}\Bigg[\frac{1}{\mathbf{s}}\left(Y_{\mathrm{SM}}^{\mathrm{eq}} - Y_{\mathrm{SM}}^{\mathrm{eq}}\frac{Y_{\mathrm{w}}^2}{Y_{\mathrm{w}}^{\mathrm{eq}^2}}\right)\langle\Gamma\rangle_{\mathrm{SM}\to \mathrm{w\ w}} + \left(Y_{\mathrm{SM}}^{\mathrm{eq}^2} - Y_{\mathrm{SM}}^{\mathrm{eq}^2}\frac{Y_{\mathrm{w}}^2}{Y_{\mathrm{w}}^{\mathrm{eq}^2}}\right)\langle\sigma v\rangle_{\mathrm{SM\ SM}\to \mathrm{w\ w}} + \left(Y_{\mathrm{s}}^2 - Y_{\mathrm{s}}^{\mathrm{eq}^2}\frac{Y_{\mathrm{w}}^2}{Y_{\mathrm{w}}^{\mathrm{eq}^2}}\right)\langle\sigma v\rangle_{\mathrm{s\ s}\to \mathrm{w\ w}}\Bigg], \tag{D.24}$$

$$\frac{dY_{\mathrm{s}}}{dx} = -\frac{\mathbf{s}}{x\,H(x)}\Bigg[\left(Y_{\mathrm{s}}^2 - Y_{\mathrm{s}}^{\mathrm{eq}^2}\right)\langle\sigma v\rangle_{\mathrm{s\ s}\to \mathrm{SM\ SM}} + \mathbf{s}\left(Y_{\mathrm{s}}^3 - Y_{\mathrm{s}}^2 Y_{\mathrm{s}}^{\mathrm{eq}}\right)\langle\sigma v^2\rangle_{3s\to 2s} + \left(Y_{\mathrm{s}}^2 - Y_{\mathrm{s}}^{\mathrm{eq}^2}\frac{Y_{\mathrm{w}}^2}{Y_{\mathrm{w}}^{\mathrm{eq}^2}}\right)\langle\sigma v\rangle_{\mathrm{s\ s}\to \mathrm{w\ w}}\Bigg]. \tag{D.25}$$

In the above subscripts s denote SIMP and w denote pFIMP, $\mu = 1/\left(\frac{1}{m_{\mathrm{w}}} + \frac{1}{m_{\mathrm{s}}}\right)^{-1}$, $x = \mu/T$, $H(x) = 1.67\sqrt{g_*^{\rho}}\mu^2 x^{-2}\mathrm{M_{pl}^{-1}}$, $\mathbf{s} = \frac{2\pi^2}{45}g_*^{\mathbf{s}}\left(\frac{\mu}{x}\right)^3$, $\langle\sigma v\rangle_{\mathrm{w\ w}\to \mathrm{s\ s}} = \langle\sigma v\rangle_{\mathrm{s\ s}\to \mathrm{w\ w}}\left(Y_{\mathrm{s}}^{\mathrm{eq}}/Y_{\mathrm{w}}^{\mathrm{eq}}\right)^2$, $Y_i^{\mathrm{eq}} = \frac{45}{4\pi^4}\frac{g_i}{g_*^{\mathbf{s}}}\left(\frac{m_i}{\mu}x\right)^2 K_2\left(\frac{m_i}{\mu}x\right)$. For simplicity we only have taken $3\mathrm{DM} \to 2\mathrm{DM}$ depletion process for SIMP, but ($n\mathrm{DM} \to 2\mathrm{DM}$ with $n > 3$) can also be taken to show

the same effect. We solve the cBEQ with increasing order of conversion cross-section to show the change from FIMP to pFIMP case in Fig . D.3 for both mass hierarchies $m_{\rm w} > m_{\rm s}$ (left panel) and $m_{\rm w} < m_{\rm s}$ (right panel). The features remain very similar to pFIMP-WIMP scenario.

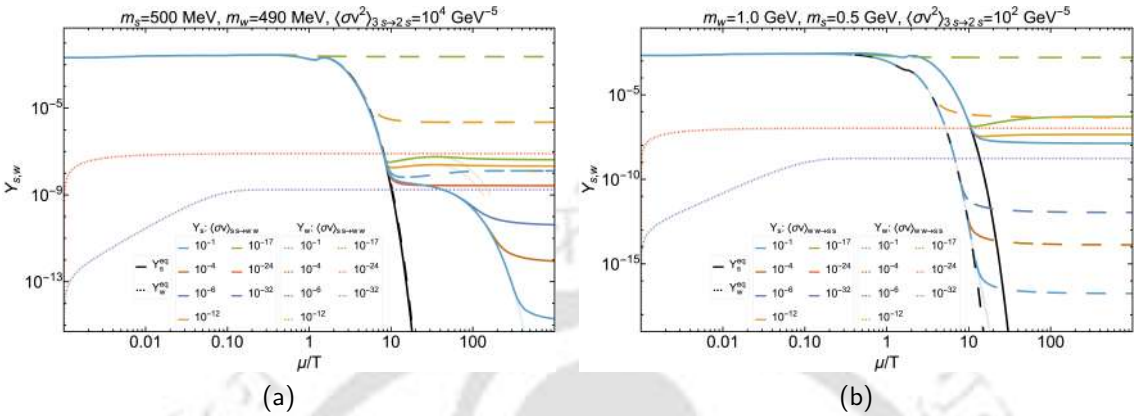

Figure D.3: DM yield with $x = \mu/T$ in pFIMP-SIMP case for fixed DM masses and conversion cross-sections, where the black solid (dashed) curves denote equilibrium distribution for SIMP (pFIMP) corresponding to (a) $m_{\rm s} > m_{\rm w}$ and (b) $m_{\rm s} < m_{\rm w}$. For all the plots $\langle\sigma v\rangle_{\rm s\,s\to SM\,SM} = 10^{-10}{\rm GeV}^{-2}$, $\langle\Gamma\rangle_{\rm SM\to w\,w} = 10^{-23}{\rm GeV}^{-1}$, $\langle\sigma v\rangle_{\rm SM\,SM\to w\,w} = 10^{-32}{\rm GeV}^{-2}$ and $m_{\rm SM} = 10$ GeV have been assumed.

D.3 Solution to cBEQ for two component scalar DM model

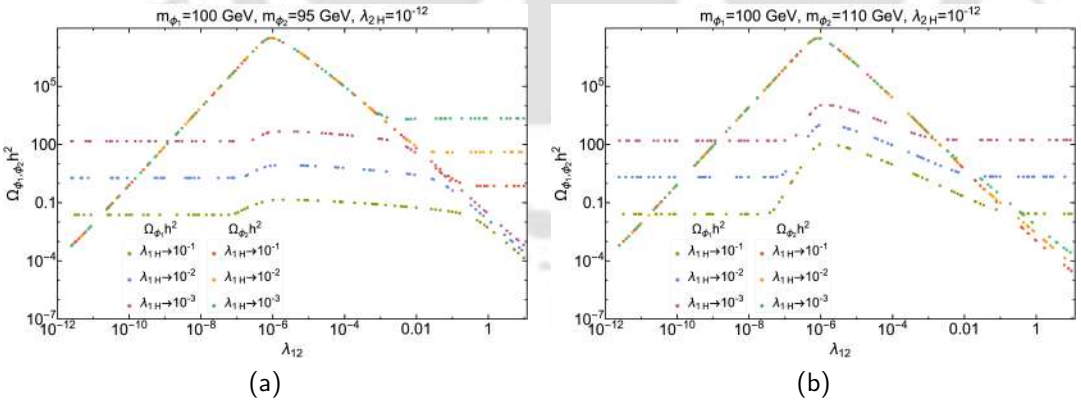

Figure D.4: Variation of relic density with λ_{12} for the the two component scalar DM model, where ϕ_1 is WIMP and ϕ_2 is pFIMP for $m_{\phi_1} > m_{\phi_2}$ (a) and $m_{\phi_1} < m_{\phi_2}$ (b). See figure insets and headings for other parameters kept fixed for the plot.

In Fig . D.4, we show the relic density of the DM components ϕ_1, ϕ_2 for a two component scalar DM scenario, as a function of the DM-DM interaction coupling λ_{12}. Both the hierarchies $m_{\phi_1} > m_{\phi_2}$ (a) and $m_{\phi_1} < m_{\phi_2}$ (b) are shown. We see a spectacularly similar feature to that of model independent analysis presented in fig. 1 of the main text, showing that the generic properties assigned to pFIMP are generically valid.

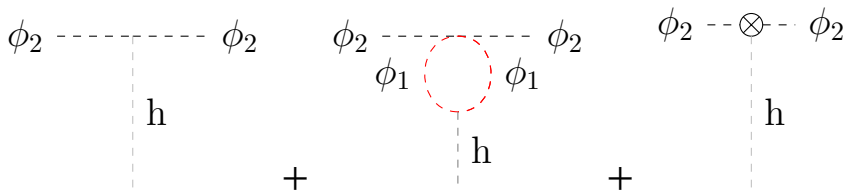

Figure D.5: The Feynman diagrams for pFIMP (ϕ_2) to interact with SM via Higgs. Sum of these tree (left), 1-loop (middle) and counter (right) diagram gives the total renormalized $\lambda_{h\phi_2\phi_2}$ coupling at 1-loop level.

D.4 Direct search prospect of pFIMP via WIMP loop

We will now provide the details of direct search prospect of the pFIMP (ϕ_2) in the two component scalar singlet model. The renormalized amplitude is given by (see Fig . D.5),

$$\begin{aligned}\Gamma_{h\phi_2\phi_2} &= \Gamma^{\text{tree}}_{h\phi_2\phi_2} + \Gamma^{1-\text{loop}}_{h\phi_2\phi_2} + \Gamma^{\text{counter}}_{h\phi_2\phi_2}\,, \\ &= -i\lambda_{h\phi_2\phi_2} + \Gamma^{1-\text{loop}}_{h\phi_2\phi_2} - i\delta_{\lambda_{h\phi_2\phi_2}}\,. \end{aligned} \tag{D.26}$$

Here,

$$\Gamma^{1-\text{loop}}_{h\phi_2\phi_2}(q_h) = \frac{1}{2}\mu^{4-d}\left(-i\lambda_{\phi_1\phi_1\phi_2\phi_2}\right)\left(-i\lambda_{h\phi_1\phi_1}\right)\int \frac{d^dk}{(2\pi)^d}\frac{i}{k^2-m^2_{\phi_1}}\frac{i}{(k-q_h)^2-m^2_{\phi_1}}\,. \tag{D.27}$$

The transfer momentum q_h is momentum transfer from initial to final state particles and $1/2$ is the symmetry factor due to the scalar loop. The dimension regularization parameter μ (mass scale) is introduced to keep couplings dimensionless in $d = 4-2\epsilon$ dimension when $\epsilon \to 0_+$. Now the 1-loop amplitude in Eq . (D.27) becomes,

$$\begin{aligned}\Gamma^{1-\text{loop}}_{h\phi_2\phi_2}(q_h^2) &= \frac{1}{2}\left(-i\lambda_{\phi_1\phi_1\phi_2\phi_2}\right)\left(-i\lambda_{h\phi_1\phi_1}\right)\frac{-i}{16\pi^2}\int_0^1 dx\left(\frac{4\pi\mu^2}{\Delta}\right)^{\epsilon}\Gamma(\epsilon) \qquad \text{where, } \Delta = m^2_{\phi_1} - x(1-x)q_h^2\,, \\ &= \frac{1}{2}\left(-i\lambda_{\phi_1\phi_1\phi_2\phi_2}\right)\left(-i\lambda_{h\phi_1\phi_1}\right)\frac{-i}{16\pi^2}\int_0^1 dx\left(\frac{1}{\epsilon}-\gamma_E+\ln\left[4\pi\mu^2\right]-\ln\left[\Delta\right]\right)\,, \\ &= \frac{1}{2}\left(-i\lambda_{\phi_1\phi_1\phi_2\phi_2}\right)\left(-i\lambda_{h\phi_1\phi_1}\right)\frac{-i}{16\pi^2}\int_0^1 dx\left(\frac{1}{\epsilon}-\gamma_E+\ln\left[4\pi\mu^2\right]-\ln\left[m^2_{\phi_1}-x(1-x)q_h^2\right]\right)\,. \end{aligned} \tag{D.28}$$

There is an ambiguity of choosing the renormalisation scale, its unknown essentially. The direct search cross-section depends on the choice. For, $q_h^2 \to 0$, the cross-section is vanishingly small [308], however if we choose $q_h^2 = 4m^2_{\phi_2}$, a scale relevant for the pFIMP production, the contribution is substantial [745]. So we choose $q_h^2 = 4m^2_{\phi_2}$ as the renormalization condition setting point and calculate the counter term which removes the divergence from 1-loop amplitude $\Gamma^{1-\text{loop}}_{h\phi_2\phi_2}$ to yield,

$$\Gamma^{\text{total}}_{h\phi_2\phi_2}(q_h^2) = -i\lambda^{\text{relic}}_{h\phi_2\phi_2} - \frac{i}{32\pi^2}\left(\lambda_{\phi_1\phi_1\phi_2\phi_2}\lambda_{h\phi_1\phi_1}\right)\int_0^1 dx\ln\left[\frac{m^2_{\phi_1}-x(1-x)4m^2_{\phi_2}}{m^2_{\phi_1}-x(1-x)q_h^2}\right]\,. \tag{D.29}$$

Therefore, using Eq . (D.29) the effective spin-independent DM-nucleon direct-detection cross-section in zero transfer momentum ($q_h^2 = t \to 0$) limit turns out to be,

$$\sigma^{\text{SI}}_{\phi_{2\text{eff}}} = \frac{\Omega_{\phi_2}h^2}{\Omega_{\phi_1}h^2+\Omega_{\phi_2}h^2}\frac{\mu_n^2 m_n^2}{4\pi v^2 m^2_{\phi_2}}\frac{f_n^2}{m_h^4}|\Gamma^{\text{total}}_{h\phi_2\phi_2}|^2_{t\to 0}\,. \tag{D.30}$$

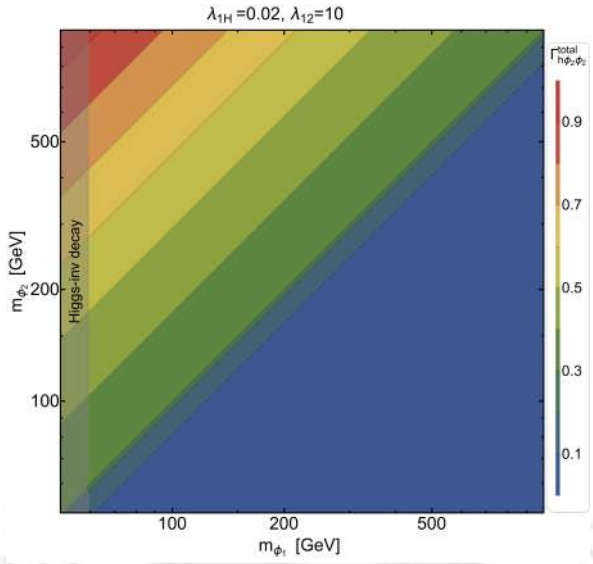

Figure D.6: Contour plot in $m_{\phi_1} - m_{\phi_2}$ plane to represent the absolute 1-loop amplitude $|\Gamma^{\rm total}_{h\phi_2\phi_2}|_{t\to 0}$ for some chosen values of λ_{1H} and λ_{12} as mentioned in the figure heading.

In the above, $\mu_n = \frac{m_n m_{\phi_2}}{m_n + m_{\phi_2}}$ where m_n is the nucleon mass, $f_n = \frac{2}{9} + \frac{7}{9}\sum_{u,d,s} f^n_{T_q}$ with $f^{p(n)}_{T_u} = 0.018(0.013)$, $f^{p(n)}_{T_d} = 0.027(0.040)$, and $f^{p(n)}_{T_s} = 0.037(0.037)$ [745]. We use Eq . (D.30) for pFIMP direct search cross-section while scanning the parameter space as shown in the main text.

D.5 The semi-analytical solution of a SIMP

The Boltzmann equation for the number density n_s of the SIMP type DM (s),

$$\dot{n_s} + 3Hn_s = -\left(n_s^3 - n_s^2 n_s^{\rm eq}\right)\langle\sigma v^2\rangle_{3\to 2} - \left(n_s^2 - n_s^{\rm eq^2}\right)\langle\sigma v\rangle_{\rm ann}\,. \tag{D.31}$$

As the necessity condition for SIMP is $\Gamma_{3\to 2} \gtrsim \Gamma_{\rm ann}$ so we can safely neglect the $\langle\sigma v\rangle_{\rm ann}$ term, and the BEQ becomes.

$$\frac{dY_s}{dx} = -\frac{n_f}{x^5}\left(Y_s^3 - Y_s^2 Y_s^{\rm eq}\right)\,, \tag{D.32}$$

where $x = m_s/T$, $n_f = \dfrac{\mathrm{s}^2 x^4}{\mathcal{H}(x)}\langle\sigma v^2\rangle_{3\to 2}$ with s and $\mathcal{H}(x)$ are entropy density and Hubble parameter, respectively. The equilibrium yield of SIMP is given by Maxwell-Boltzmann distribution, as during freeze out SIMP is in the non-relativistic regime, $Y_s^{\rm eq} = 0.145(g_s/g_\star^{\rm s})x^{3/2}e^{-x} = A\,x^{3/2}e^{-x}$ where $A = 0.145(g_s/g_\star^s)$. Another important assumption is that the entropy and matter degrees of freedom are nearly equal during SIMP freezes out ($x_{\rm FO} \sim 25$) and constant $g_\star^{\rm s} \simeq g_\star^\rho \sim 10$.

To solve the BEQ analytically, it would be convenient to divide the whole scenario into three different regions on value of x: **Region I:** $x \ll x_{\rm FO}$, **Region II:** $x \simeq x_{\rm FO}$ and **Region III:** $x \gg x_{\rm FO}$. Let us define the difference of SIMP yield from its equilibrium yield as $\Delta = Y_s - Y_s^{\rm eq}$ and Eq . (D.32) becomes,

$$\frac{dY_s^{\rm eq}}{dx} + \frac{d\Delta}{dx} = -\frac{n_f}{x^5}\Delta\left(\Delta + Y_s^{\rm eq}\right)^2\,. \tag{D.33}$$

- **Region I**
  For $x \ll x_{\rm FO}$, $\dfrac{d\Delta}{dx}$ is negligible and Eq . (D.33) becomes,

$$\frac{dY_s^{\rm eq}}{dx} = -\frac{n_f}{x^5}\Delta\left(\Delta + Y_s^{\rm eq}\right)^2 . \tag{D.34}$$

- **Region II**
  In the vicinity of $x \simeq x_{\rm FO}$, we may further assume $\Delta = c\, Y_s^{\rm eq}(x_{\rm FO})$ where c is unknown constants whose values are determined by matching the analytical result with the numerical one. Substituting in Eq . (D.34), we get

$$\left.\frac{dY_s^{\rm eq}}{dx}\right|_{x=x_{\rm FO}} = -\frac{n_f}{x_{\rm FO}^5} c\,(c+1)^2\, Y_s^{\rm eq^3}(x_{\rm FO}) . \tag{D.35}$$

  After simplification, we get,

$$x_{\rm FO}^2 e^{2x_{\rm FO}} - \frac{3}{2} x_{\rm FO} e^{2x_{\rm FO}} = \underbrace{n_f\, A^2\, c\,(c+1)^2}_{P} . \tag{D.36}$$

  The solution of Eq . (D.36) gives us the freeze out point of SIMP is,

$$x_{\rm FO} \approx \ln\sqrt{P} - \ln\ln\sqrt{P} . \tag{D.37}$$

- **Region III**
  When $x \gg x_{\rm FO}$, then, $Y_s^{\rm eq}$ and $\dfrac{dY_s^{\rm eq}}{dx}$ are exponentially suppressed, so, $\Delta \gg Y_s^{\rm eq}$ and Eq . (D.33) becomes,

$$\frac{d\Delta}{dx} = -\frac{n_f}{x^5}\Delta^3 . \tag{D.38}$$

  After solving the differential equation between $x_{\rm FO}$ to x with $\Delta(x) \gg \Delta(x_{\rm FO})$, we get,

$$\Delta(x) = \left[\frac{1}{\Delta(x_{\rm FO})^2} - \frac{n_f}{2}\left(\frac{1}{x^4} - \frac{1}{x_{\rm FO}^4}\right)\right]^{-\frac{1}{2}} . \tag{D.39}$$

  Following $\Delta(x_{\rm FO}) \approx cY_s^{\rm eq}(x_{\rm FO})$ at $x = x_{\rm CMB} = m_s/T_{\rm CMB}$, the SIMP yields is

$$Y_s(x_{\rm CMB}) \approx \Delta(x_{\rm CMB}) \approx \left[\frac{1}{\Delta(x_{\rm FO})^2} - \frac{n_f}{2}\left(\frac{1}{x_{\rm CMB}^4} - \frac{1}{x_{\rm FO}^4}\right)\right]^{-\frac{1}{2}} . \tag{D.40}$$

D.6 Possible Feynman diagrams related to DM phenomenology

We have calculated the squared matrix amplitude for non-relativistic DMs using FeynCalc [776] and CalcHEP [777].

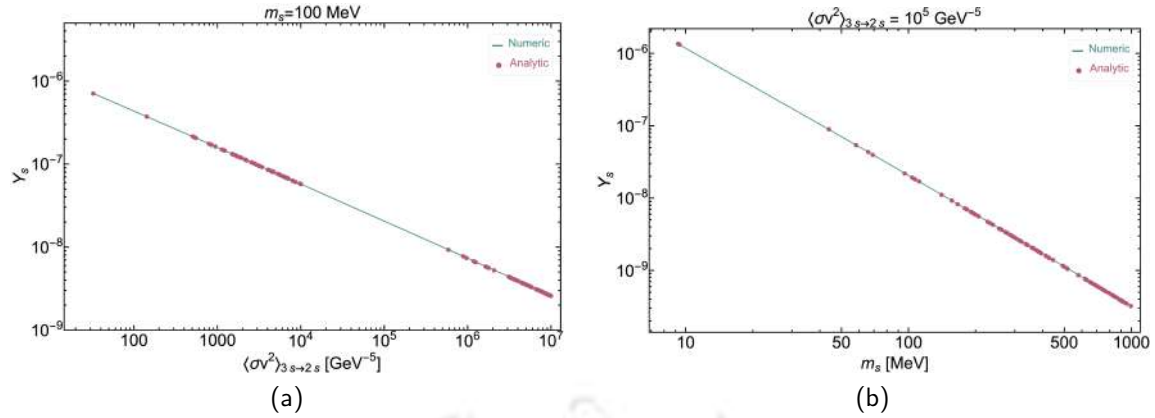

Figure D.7: A comparison plot analytic vs numeric solution of BEQ where we have considered $g_\star^s = g_\star^\rho = 10.75$, $g_s = 2$ (for complex scalar) and have chosen $c(c+1)^2 = 4.5$.

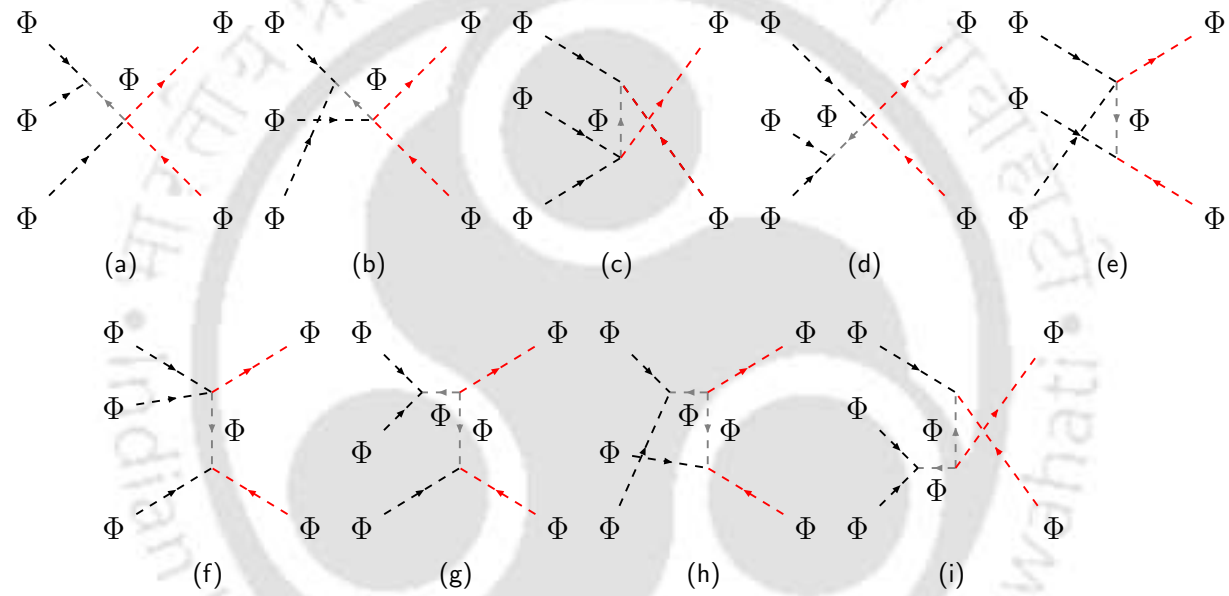

Figure D.8: Self annihilation via $\Phi(p_1)\Phi(p_2)\Phi(p_3) \to \Phi(p_4)\Phi^*(p_5)$ process.

$$\overline{|\mathcal{M}_{D.8}|^2} = \frac{9\mu_3^2}{4m_\Phi^8}\left(4\lambda_\Phi m_\Phi^2 + 9\mu_3^2\right)^2 . \tag{D.41}$$

and

$$\langle\sigma v^2\rangle_{\Phi\Phi\Phi\to\Phi\Phi^*} = \frac{1}{64\pi m_\Phi^3}\left(\frac{K_1(m_\Phi/T)}{K_2(m_\Phi/T)}\right)^3 \frac{\sqrt{5}}{6}\overline{|\mathcal{M}_{\Phi\Phi\Phi\to\Phi\Phi^*}|^2} . \tag{D.42}$$

$$\overline{|\mathcal{M}_{D.9}|^2} = \frac{\mu_3^2}{64m_\Phi^8}\left(117\mu_3^2 - 148\lambda_\Phi m_\Phi^2\right)^2 . \tag{D.43}$$

and

$$\langle\sigma v^2\rangle_{\Phi\Phi^*\Phi^*\to\Phi\Phi} = \frac{1}{64\pi m_\Phi^3}\left(\frac{K_1(m_\Phi/T)}{K_2(m_\Phi/T)}\right)^3 \frac{\sqrt{5}}{6}\overline{|\mathcal{M}_{\Phi\Phi^*\Phi^*\to\Phi\Phi}|^2} . \tag{D.44}$$

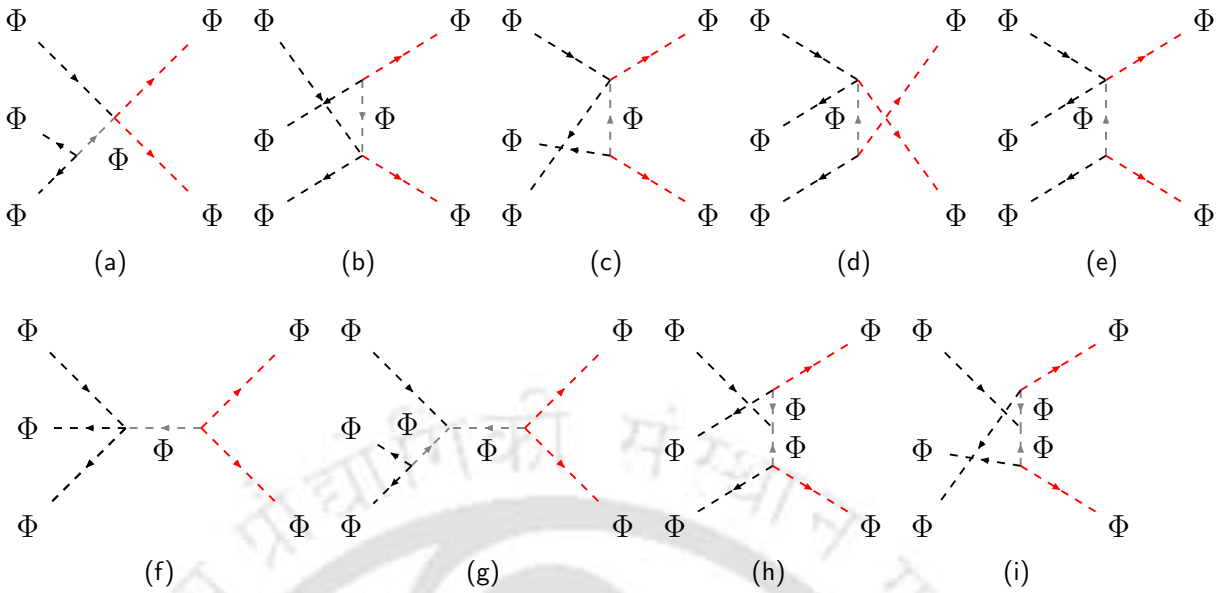

Figure D.9: Self-annihilation of SIMP via $\Phi\Phi^*\Phi^* \to \Phi\Phi$ process.

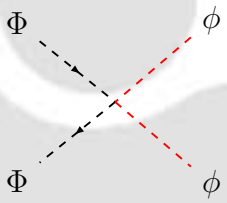

Figure D.10: Conversion of SIMP to pFIMP via $\Phi\Phi^* \to \phi\phi$ process.

D.7 Dark Matter self-interaction

In single component complex scalar SIMP scenario, The effective DM self-scattering cross-section over mass is written as [262],

$$\frac{\sigma_{\rm self}}{m_{\rm DM}} = \frac{1}{m_\Phi}\left(\frac{\Omega_\Phi^2}{\Omega_{\rm DM}^2}\sigma_{\Phi\Phi\to\Phi\Phi} + \frac{\Omega_{\Phi^*}^2}{\Omega_{\rm DM}^2}\sigma_{\Phi^*\Phi^*\to\Phi^*\Phi^*} + \frac{\Omega_\Phi}{\Omega_{\rm DM}}\frac{\Omega_{\Phi^*}}{\Omega_{\rm DM}}\sigma_{\Phi\Phi^*\to\Phi\Phi^*}\right). \tag{D.45}$$

In the multicomponent scenario, we take DM mass as effective $\rm m_{DM}$ weighted by effective relic contribution for a particular DM and the analytic expression could be written as [302],

$$\begin{aligned}\frac{\sigma_{\rm self}}{m_{\rm DM}} = &\left(\frac{\Omega_\Phi}{\Omega_{\rm DM}}\right)^2\frac{1}{m_\Phi}\left(\sigma_{\Phi\Phi\to\Phi\Phi} + \sigma_{\Phi^*\Phi^*\to\Phi^*\Phi^*} + \sigma_{\Phi\Phi^*\to\Phi\Phi^*} + \sigma_{\Phi\Phi^*\to\phi\phi}\right)\\ &+\left(\frac{\Omega_\phi}{\Omega_{\rm DM}}\right)^2\frac{1}{m_\phi}\sigma_{\phi\phi\to\phi\phi} + \frac{\Omega_\Phi}{\Omega_{\rm DM}}\frac{\Omega_\phi}{\Omega_{\rm DM}}\frac{2}{m_\Phi+m_\phi}\left(\sigma_{\phi\Phi\to\phi\Phi} + \sigma_{\phi\Phi^*\to\phi\Phi^*}\right).\end{aligned} \tag{D.46}$$

where,

$$\sigma_{\Phi\Phi\to\Phi\Phi} = \frac{1}{16\pi(m_\Phi+m_\Phi)^2}\left(|\mathcal{M}_{\Phi\Phi\to\Phi\Phi}|^2 + |\mathcal{M}_{\Phi^*\Phi^*\to\Phi^*\Phi^*}|^2\right), \tag{D.47}$$

$$\sigma_{\Phi\Phi^*\to\Phi\Phi^*} = \frac{1}{16\pi(m_\Phi+m_{\Phi^*})^2}|\mathcal{M}_{\Phi\Phi^*\to\Phi\Phi^*}|^2, \tag{D.48}$$

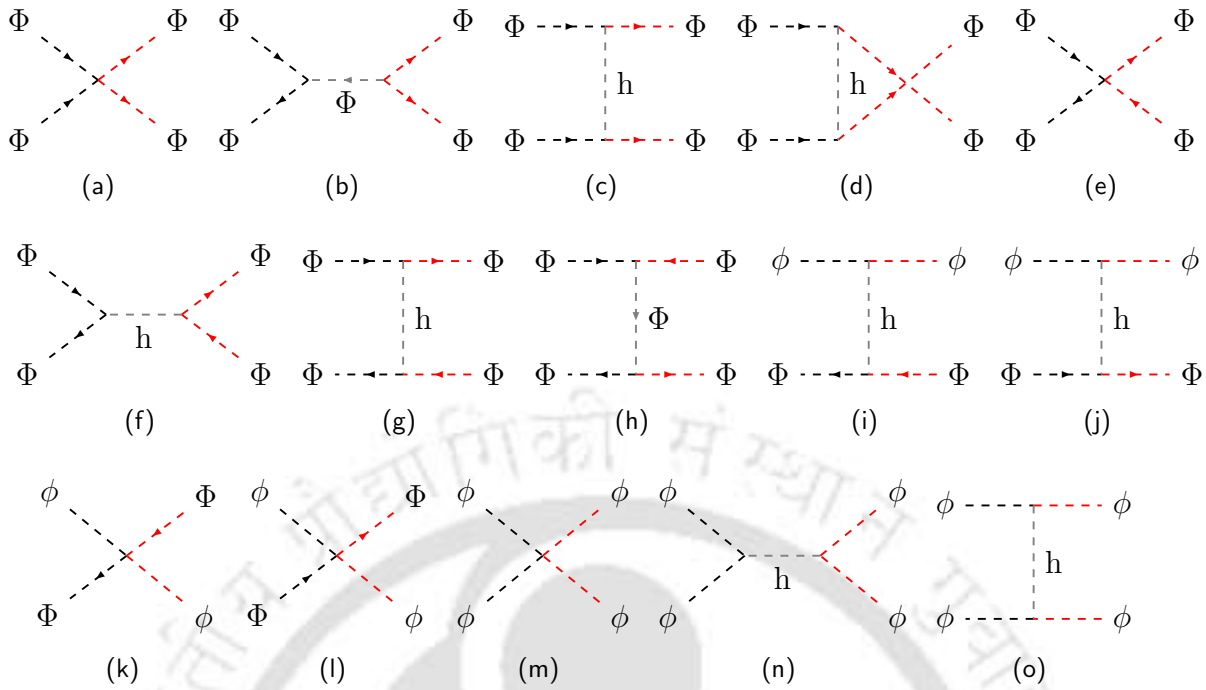

Figure D.11: Dark matter self scattering

$$\sigma_{\Phi\Phi^*\to\phi\phi} = \frac{1}{16\pi(m_\Phi + m_{\Phi^*})^2}|\mathcal{M}_{\Phi\Phi^*\to\phi\phi}|^2\,, \tag{D.49}$$

$$\sigma_{\phi\phi\to\phi\phi} = \frac{1}{16\pi(m_\phi + m_\phi)^2}|\mathcal{M}_{\phi\phi\to\phi\phi}|^2\,, \tag{D.50}$$

$$\sigma_{\phi\Phi\to\phi\Phi} = \frac{1}{16\pi(m_\phi + m_\Phi)^2}\left(|\mathcal{M}_{\phi\Phi\to\phi\Phi}|^2 + |\mathcal{M}_{\phi\Phi^*\to\phi\Phi^*}|^2\right)\,, \tag{D.51}$$

with,

$$|\mathcal{M}_{\Phi\Phi\to\Phi\Phi}|^2 = \frac{\left(m_h^2(3\mu_3^2 + 4\lambda_\Phi m_\Phi^2) - 2\lambda_{\Phi H}^2 v^2 m_\Phi^2\right)^2}{2m_\Phi^4 m_h^4}\,, \tag{D.52}$$

$$|\mathcal{M}_{\Phi\Phi^*\to\Phi\Phi^*}|^2 = \frac{\left(m_h^2(4m_\Phi^2 - m_h^2)(9\mu_3^2 - 4\lambda_\Phi m_\Phi^2) - 2\lambda_{\Phi H}^2 v^2 m_\Phi^2(m_h^2 - 2m_\Phi^2)\right)^2}{m_\Phi^4 m_h^4 (m_h^2 - 4m_\Phi^2)^2}\,, \tag{D.53}$$

$$|\mathcal{M}_{\Phi\Phi^*\to\phi\phi}|^2 = \frac{\left(4\lambda_{\Phi\phi}m_\Phi^2 - \lambda_{\Phi\phi}m_h^2 + \lambda_{\Phi H}\lambda_{\phi H}v^2\right)^2}{2(m_h^2 - 4m_\Phi^2)^2}\,, \tag{D.54}$$

$$|\mathcal{M}_{\Phi\phi\to\Phi\phi}|^2 = \frac{\left(\lambda_{\Phi\phi}\left((m_\Phi - m_\phi)^2 - m_h^2\right) - \lambda_{\Phi H}\lambda_{\phi H}v^2\right)^2}{\left((m_\Phi - m_\phi)^2 - m_h^2\right)^2}\,, \tag{D.55}$$

$$|\mathcal{M}_{\phi\phi\to\phi\phi}|^2 = \frac{\left(\lambda_\phi(m_h^4 - 4m_h^2 m_\phi^2) + \lambda_{\phi H}^2(8m_\phi^2 - 3m_h^2)v^2\right)^2}{2m_h^4(m_h^2 - 4m_\phi^2)^2}\,. \tag{D.56}$$

and $\Omega_\Phi = \Omega_s/2$, $\Omega_{\rm DM} = \Omega_s + \Omega_\phi$.

D.8 DM Kinetic equilibriation

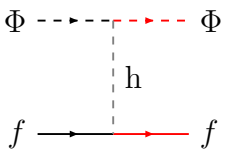

Figure D.12: The Feynman diagram represent the DM (Φ) and SM fermions (f) scattering.

We already discussed that the kinetic equilibrium of SIMP with SM is achieved after considering an appropriate choice of portal coupling. Only relativistic fermions are available during SIMP freezes-out, and contributing to kinetic decoupling condition is written regarding DM-SM scattering, Fig . D.12, rate as,

$$2\sum_{f}\Gamma_{\Phi f\to\Phi\to f} = 2\sum_{f}\langle\sigma v\rangle_{\Phi f\to\Phi f} n_f^{\rm eq}(T) \gtrsim \mathcal{H}(T)\,. \tag{D.57}$$

where,

$$\langle\sigma v\rangle_{\Phi f\to\Phi f} = \frac{\int_{(m_\Phi+m_f)^2}^{\infty}\sigma_{\Phi f\to\Phi f}K_1\left(\frac{\sqrt{s}}{T}\right)\sqrt{s-(m_\Phi-m_f)^2}\,(s-(m_\Phi+m_f)^2)\,ds}{8Tm_\Phi^2 m_f^2 K_2\left(\frac{m_\Phi}{T}\right)K_2\left(\frac{m_f}{T}\right)}\,. \tag{D.58}$$

and two factors come from SM fermion and anti-fermion contribution. Fig . D.13 rep-

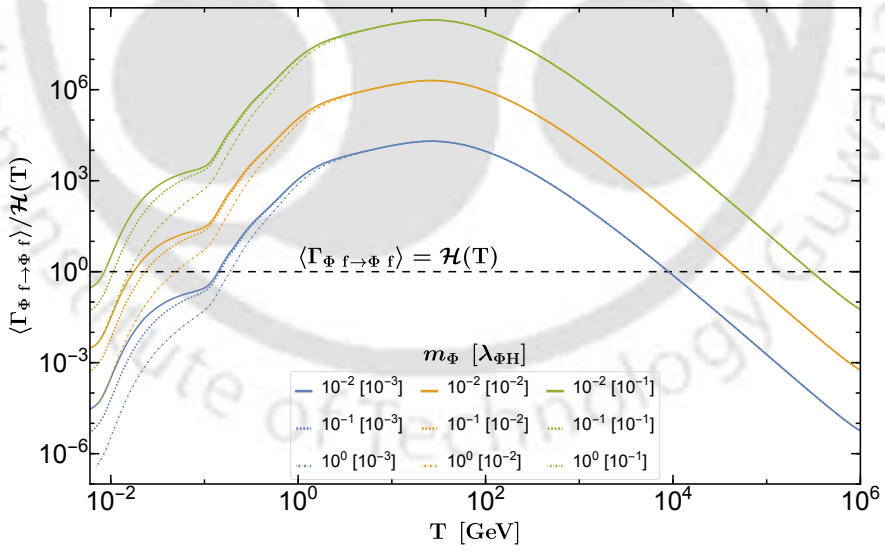

Figure D.13: The evaluation of DM (Φ)-fermion elastic scattering rate with temperature. The different color lines represent the different m_Φ masses in the GeV unit, and coupling is mentioned in the figure inset.

resents the evolution of DM-SM elastic scattering rate with the SM bath temperature (T). Our work focuses on sub-MeV DMs and suitable choice of $\lambda_{\Phi H} \sim 0.1$, without affecting DM relic, to achieve kinetic equilibrium between DM and SM bath.

The kinetic equilibriation, with thermal bath, of Φ ensures the pFIMP (ϕ) kinetic equilibriation also because of the presence of strong self-interaction among themselves. For this reason, there is no necessity to do similar kinds of analysis for ϕ.

Appendix E

Pseudo-FIMP detection via WIMP loop

E.1 Higgs and Z Invisible decay widths

The observed (expected) upper limit on the invisible branching fraction of the Higgs boson at 95% confidence level [495, 496] having the total decay width of 125.1 GeV Higgs given by $3.2^{+2.8}_{-2.2}$ MeV [757] is,

$$\mathcal{B}_{\rm h\to invisible} < \begin{cases} 0.145(0.103) \quad (\text{ATLAS})\,. \\ 0.18(0.10) \quad (\text{CMS})\,. \end{cases} \tag{E.1}$$

In this model, the invisible branching ratio comes from Higgs decay to both WIMP and pFIMP given by,

$$\Gamma_{h\to\phi\phi} = \frac{\mathbb{L}_h^2}{32\pi m_h}\left(1-4\frac{m_\phi^2}{m_h^2}\right)^{1/2}\Theta[m_h-2m_\phi]\,, \tag{E.2}$$

$$\Gamma_{h\to\chi_1\bar{\chi}_1} = \frac{\sin^4 2\theta}{32\pi v^2} m_h (m_{\chi_1}-m_{\chi_2})^2\left(1-4\frac{m_{\chi_1}^2}{m_h^2}\right)^{3/2}\Theta[m_h-2m_{\chi_1}]\,. \tag{E.3}$$

In the above, $\mathbb{L}_h$ is 1-loop corrected $h\to\phi\phi$ vertex as elaborated later. The recent Invisible decay width bound on the Z-boson comes from various experiments like [463, 671],

$$\Gamma_{\rm Z\to invisible} < \begin{cases} 523\pm 16\ \text{MeV} \quad (\text{CMS})\,. \\ 503\pm 16\ \text{MeV} \quad (\text{LEPComb.})\,. \\ 498\pm 17\text{MeV} \quad (\text{L3})\,. \end{cases} \tag{E.4}$$

Invisible Z boson decay can have contributions from both WIMP and pFIMP, given by,

$$\Gamma_{Z\to\phi\phi} = \frac{\mathbb{L}_Z^2 m_Z}{16\pi}\left(1-4\frac{m_\phi^2}{m_Z^2}\right)^{3/2}\Theta[m_Z-2m_\phi]\,, \tag{E.5}$$

$$\Gamma_{Z\to\chi_1\bar{\chi}_1} = \frac{m_Z^3\sin^4\theta\sin^4\theta_w}{12\pi v^2}\left(1+2\frac{m_{\chi_1}^2}{m_Z^2}\right)\left(1-4\frac{m_{\chi_1}^2}{m_Z^2}\right)^{1/2}\Theta[m_Z-2m_{\chi_1}]\,. \tag{E.6}$$

Here $\mathbb{L}_Z$ is 1-loop corrected $Z\to\phi\phi$ vertex. The explicit expressions for $\mathbb{L}_h$ and $\mathbb{L}_Z$ will be given in Appendix E.3. If DM masses are below $m_h/2(m_Z/2)$, it is severely constrained by the invisible Higgs and Z decay constraints.

E.2 BEQ with coannihilation in WIMP-pFIMP framework

Let us consider, n_i dark sector particles have the same Z_2 symmetry, masses m_i (m_1 being the mass of DM), and internal d.o.f g_i. The evolution of the number density n_i of particle i can be written as,

$$\dot{n}_i + 3Hn_i = -\sum_j \langle\sigma v\rangle_{ij\to \text{SM}} \left(n_i n_j - n_i^{\text{eq}} n_j^{\text{eq}}\right) . \tag{E.7}$$

Since all the dark sector particles with $i > 1$, will eventually decay to the stable DM candidate after their respective freeze-outs, the total DM density will be result of the combined yield of all the dark sector particles. Therefore, its final abundance (n) can be described by the sum of the density of all the dark sector particles that transform under the same Z_2 symmetry,

$$n = \sum_i n_i \, . \tag{E.8}$$

Corresponding evolution equation for n can be written as follows [643, 647],

$$\dot{n} = -3Hn - \sum_{i,j} \langle\sigma v\rangle_{ij\to \text{SM}} \left(n_i n_j - n_i^{\text{eq}} n_j^{\text{eq}}\right) . \tag{E.9}$$

In the above, we have assumed that n_i dark sector particles are initially in thermal bath with SM and n_i^{eq} denotes the equilibrium number density. Using $\frac{n_i}{n} = \frac{n_i^{\text{eq}}}{n^{\text{eq}}}$, Eq . (E.9) becomes,

$$\begin{aligned} \dot{n} + 3Hn &= -\sum_{ij} \langle\sigma v\rangle_{ij\to \text{SM}} \left(n_i^{\text{eq}} \frac{n}{n^{\text{eq}}} n_j^{\text{eq}} \frac{n}{n^{\text{eq}}} - n_i^{\text{eq}} n_j^{\text{eq}}\right) \\ &= -\langle\sigma v\rangle^{\text{eff}}_{\text{SM}} \left(n^2 - n^{\text{eq}^2}\right) , \end{aligned} \tag{E.10}$$

where,

$$\langle\sigma v\rangle^{\text{eff}} = \sum_{i,j} \langle\sigma v\rangle_{ij} \frac{n_i^{\text{eq}} n_j^{\text{eq}}}{n_{\text{eq}}^2} \quad \text{and} \quad n^{\text{eq}} = \sum_i n_i^{\text{eq}} . \tag{E.11}$$

Following Eq . (E.11), it is straightforward to calculate the $\langle\sigma v\rangle^{\text{eff}}$ for all possible channels relevant for our case as in Eqs . (6.20) and (6.21),

$$\langle\Gamma\rangle^{\text{eff}}_{\psi_2\to\chi_1\phi} = \sum_i \langle\Gamma\rangle_{\psi_2\to i\phi} \, . \tag{E.12}$$

$$\langle\sigma v\rangle^{\text{eff}}_{\chi_1\bar{\psi}_2\to h\phi} = \left[\sum_i g_i m_i^2 K_2\left(\frac{m_i}{T}\right)\right]^{-1} \sum_i \langle\sigma v\rangle_{i\bar{\psi}_2\to h\phi} g_i m_i^2 K_2\left(\frac{m_i}{T}\right) . \tag{E.13}$$

$$\langle\sigma v\rangle^{\text{eff}}_{\phi} = \left[\sum_i g_i m_i^2 K_2\left(\frac{m_i}{T}\right)\right]^{-2} \sum_{i,j} 2\langle\sigma v\rangle_{ij\to\phi\phi} g_i g_j m_i^2 m_j^2 K_2\left(\frac{m_i}{T}\right) K_2\left(\frac{m_j}{T}\right) . \tag{E.14}$$

$$\langle\sigma v\rangle^{\text{eff}}_{\psi_2} = \left[\sum_i g_i m_i^2 K_2\left(\frac{m_i}{T}\right)\right]^{-2} \sum_{i,j} 2\langle\sigma v\rangle_{ij\to\psi_2\bar{\psi}_2} g_i g_j m_i^2 m_j^2 K_2\left(\frac{m_i}{T}\right) K_2\left(\frac{m_j}{T}\right) . \tag{E.15}$$

$$\langle\sigma v\rangle^{\text{eff}}_{\text{SM}} = \left[\sum_i g_i m_i^2 K_2\left(\frac{m_i}{T}\right)\right]^{-2} \sum_{i,j} 2\langle\sigma v\rangle_{ij\to \text{SM SM}} g_i g_j m_i^2 m_j^2 K_2\left(\frac{m_i}{T}\right) K_2\left(\frac{m_j}{T}\right) . \tag{E.16}$$

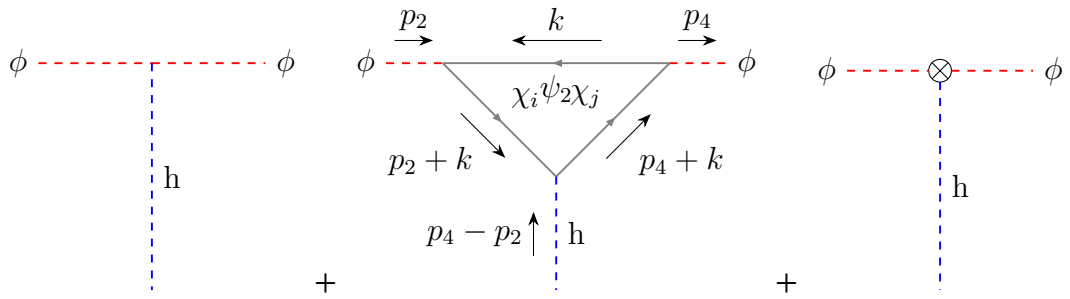

Figure E.1: Tree-level, one-loop and counter-term interaction vertex for the $h\phi\phi$ interaction vertex where $\{i,j=1,2\}$[27, 29].

E.3 Relevant fermion loop calculations for direct search

We consider first the three-point vertex and its one-loop contribution for the $\phi\phi h$ interaction, which plays crucial role in the direct detection of the pFIMP. The one-loop amplitude can be written as a sum of three contributions, the tree level amplitude, one loop and counterterm,

$$\mathbb{L}_h = -i\lambda_{h\phi\phi} + \sum_{i,j=1,2} \Gamma_{ij}^{1-\text{loop}} + \delta_{ij}^{\lambda}\,. \tag{E.17}$$

Here we have assumed that at tree level $\lambda_{\phi H}$ is very small. The one-loop diagram contributing to $h\phi\phi$ vertex is shown in the middle of Fig. E.1, and the amplitude is given by,

$$\begin{aligned}\Gamma_{ij}^{1-\text{loop}} &= \int \frac{d^4k}{(2\pi)^4}(-1)\text{Tr}\left[\frac{(-\text{i}\lambda_{\phi\psi_2\chi_\text{j}})\text{i}(\not{k}+\text{m}_{\psi_2})}{\left[\text{k}^2-\text{m}_{\psi_2}^2+\text{i}\epsilon\right]}\frac{(-\text{i}\lambda_{\phi\psi_2\chi_\text{i}})\text{i}(\not{p}_2+\not{k}+\text{m}_{\chi_\text{i}})}{\left[(\text{p}_2+\text{k})^2-\text{m}_{\chi_\text{i}}^2+\text{i}\epsilon\right]}\frac{(-\text{i}\lambda_{\text{h}\chi_\text{i}\chi_\text{j}})\text{i}(\not{p}_4+\not{k}+\text{m}_{\chi_\text{j}})}{\left[(\text{p}_4+\text{k})^2-\text{m}_{\chi_\text{j}}^2+\text{i}\epsilon\right]}\right],\\ &= -4\int \frac{d^4k}{(2\pi)^4}\frac{m_{\chi_i}m_{\chi_j}m_{\psi_2}+m_{\psi_2}(m_\phi^2-\frac{t}{2})+(m_{\chi_i}+m_{\chi_j}+m_{\psi_2})k^2+(m_{\psi_2}+m_{\chi_j})k.p_2+(m_{\psi_2}+m_{\chi_i})k.p_4}{\left[k^2-m_{\psi_2}^2+i\epsilon\right]\left[(k+p_2)^2-m_{\chi_i}^2+i\epsilon\right]\left[(k+p_4)^2-m_{\chi_j}^2+i\epsilon\right]}\\ &\qquad\times\lambda_{h\chi_i\chi_j}\lambda_{\phi\psi_2\chi_j}\lambda_{\phi\psi_2\chi_i}\,.\end{aligned} \tag{E.18}$$

Using, $l = k + yp_2 + zp_4$,

$$\Delta_{ij} = (y+z)(y+z-1)m_\phi^2 - tyz + xm_{\psi_2}^2 + ym_{\chi_i}^2 + zm_{\chi_j}^2,$$

$$\delta m_{ij} = m_{\psi_2}\left(m_{\chi_i}m_{\chi_j} + m_\phi^2(1-y-z)^2 - \frac{t}{2}(1-y-z+2yz)\right) + m_\phi^2(m_{\chi_i}+m_{\chi_j})(y+z)(y+z-1) +$$

$$\frac{t}{2}m_{\chi_i}y(1-2z) + \frac{t}{2}m_{\chi_j}z(1-2y)\,,\ \text{and}\ c_{ij} = m_{\psi_2}+m_{\chi_i}+m_{\chi_j}\,.$$

Therefore,

$$\begin{aligned}\Gamma_{ij}^{1-\text{loop}} &= -8\lambda_{h\chi_i\chi_j}\lambda_{\phi\psi_2\chi_j}\lambda_{\phi\psi_2\chi_i}\int\frac{d^4l}{(2\pi)^4}\int_0^1 dx\,dy\,dz\frac{\delta m_{ij}+c_{ij}\,l^2}{(l^2-\Delta_{ij}+i\epsilon)^3}\delta(x+y+z-1)\\ &= 8i\lambda_{h\chi_i\chi_j}\lambda_{\phi\psi_2\chi_j}\lambda_{\phi\psi_2\chi_i}\int_0^1 dx\,dy\,dz\left[\frac{\delta m_{ij}}{32\pi^2}\frac{\Gamma(1+\epsilon)}{\Delta_{ij}^{1+\epsilon}}\left(4\pi\mu^2\right)^\epsilon - \frac{c_{ij}}{32\pi^2}(2-\epsilon)\frac{\Gamma(\epsilon)}{\Delta_{ij}^{\epsilon}}\left(4\pi\mu^2\right)^\epsilon\right]\delta(x+y+z-1)\,,\end{aligned} \tag{E.19}$$

In the above, μ is the dimension regularization parameter (basically a mass scale) introduced to keep λ dimensionless and $d = 4-2\epsilon$, in the limit $\epsilon \to 0_+$. At $\epsilon \to 0_+$

limit we have the following expansions,

$$\begin{aligned}\Gamma(\epsilon) &\simeq \frac{1}{\epsilon} - \gamma_E + \mathcal{O}(\epsilon),\\ \frac{1}{\Delta^\epsilon} &\simeq 1 - \frac{\epsilon}{2}\ln\Delta^2 + \mathcal{O}(\epsilon),\\ \mu^\epsilon &\simeq 1 + \frac{\epsilon}{2}\ln\mu^2 + \mathcal{O}(\epsilon)\,.\end{aligned} \tag{E.20}$$

Where $\gamma_E \approx 0.5772156649$ is the Euler-Mascheroni constant. Note that, we have multiplied Eq . (E.19) by a factor of 2, because of the antiparticles in the loop, which also contributes equally. Then,

$$\Gamma_{ij}^{1-\text{loop}} = \frac{i}{2\pi^2}\lambda_{h\chi_i\chi_j}\lambda_{\phi\psi_2\chi_j}\lambda_{\phi\psi_2\chi_i}\int_0^1 dx\,dy\,dz\left[\frac{\delta m_{ij}}{\Delta_{ij}} - 2c_{ij}\left(\frac{1}{\epsilon} - \gamma_E + \ln[4\pi] - \frac{1}{2} + \ln\frac{\mu^2}{\Delta_{ij}}\right) + \mathcal{O}(\epsilon)\right] \delta(x+y+z-1)\,. \tag{E.21}$$

Here, we are using the on-shell renormalization scheme to remove the divergence from $\sum_{i,j}\Gamma_{ij}^{1-\text{loop}}$ by calculating the total counter term $\sum_{i,j}\delta_{ij}^{\lambda}$ from Higgs mediated annihilation amplitude $\sum_{i,j}\Gamma_{ij}^{\prime 1-\text{loop}} \equiv \sum_{i,j}\Gamma_{ij}^{1-\text{loop}}\,(p_4 \to -p_4)$, and we are choosing DM relic density observation scale as the physical renormalization scale, i.e. $q_h^2 = (p_2+p_4)^2 = 4m_\phi^2$ [305] to cancel the pole in the Eq . (E.21),

$$\sum_{i,j}\delta_{ij}^{\lambda} = -\sum_{i,j}\Gamma_{ij}^{\prime 1-\text{loop}}\Big|_{q_h^2\to 4m_\phi^2}\,. \tag{E.22}$$

The total amplitude at $\epsilon \to 0$ and $t \to 0$ then becomes,

$$\mathbb{L}_h = -i\lambda_{h\phi\phi} + \sum_{i,j}\Gamma_{ij}^{1-\text{loop}}\Big|_{t\to 0} - \sum_{i,j}\Gamma_{ij}^{\prime 1-\text{loop}}\Big|_{q_h^2\to 4m_\phi^2}\,. \tag{E.23}$$

with,

$$\lambda_{h\overline{\chi}_2\chi_2} = \frac{Y_1}{\sqrt{2}}\sin 2\theta\,,$$

$$\lambda_{h\overline{\chi}_1\chi_1} = -\frac{Y_1}{\sqrt{2}}\sin 2\theta\,,$$

$$\lambda_{\phi\psi_2\overline{\chi}_2} = \lambda_{\phi\overline{\psi}_2\chi_2} = Y_2\sin\theta\,,$$

$$\lambda_{\phi\psi_2\overline{\chi}_1} = \lambda_{\phi\overline{\psi}_2\chi_1} = -Y_2\cos\theta\,,$$

$$\lambda_{h\overline{\chi}_1\chi_2} = \lambda_{h\overline{\chi}_2\chi_1} = -\frac{Y_1}{\sqrt{2}}\cos 2\theta\,.$$

In Fig . E.2, we show the variation of Higgs-mediated loop amplitude $\mathbb{L}_h$ in color bar in the $\Delta m - Y_2$ plane.

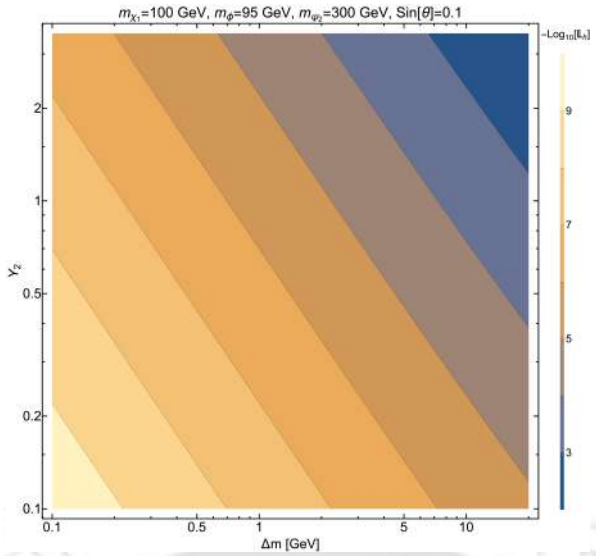

Figure E.2: One-loop amplitude for the Higgs-mediated process.

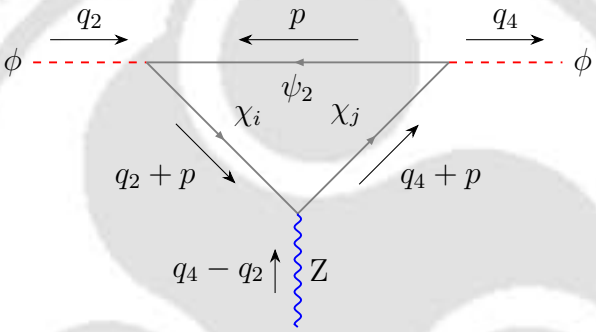

Figure E.3: One-loop Feynman diagrams contributing to the $Z\phi\phi$ interaction term, where $\{i,j=1,2\}$.

Next we calculate the one-loop contribution of the Z-mediated diagram, see Fig . E.3, for the pFIMP-nucleon direct search cross-section.

$$\mathbb{L}_\mu^{ij} = (-1)\int \frac{d^4p}{(2\pi)^4}\mathrm{Tr}\left[\frac{(-\mathrm{i}\lambda_{\phi\psi_2\chi_\mathrm{j}})\mathrm{i}(\not{p}+\mathrm{m}_{\psi_2})}{\left[\mathrm{p}^2-\mathrm{m}^2_{\psi_2}+\mathrm{i}\epsilon\right]}\frac{(-\mathrm{i}\lambda_{\phi\psi_2\chi_\mathrm{i}})\mathrm{i}(\not{q}_2+\not{p}+\mathrm{m}_{\chi_\mathrm{i}})}{\left[(\mathrm{q}_2+\mathrm{p})^2-\mathrm{m}^2_{\chi_\mathrm{i}}+\mathrm{i}\epsilon\right]}\frac{(-\mathrm{i}\gamma_\mu\lambda_{\mathrm{Z}\chi_\mathrm{i}\chi_\mathrm{j}})\mathrm{i}(\not{q}_4+\not{p}+\mathrm{m}_{\chi_\mathrm{j}})}{\left[(\mathrm{q}_4+\mathrm{p})^2-\mathrm{m}^2_{\chi_\mathrm{j}}+\mathrm{i}\epsilon\right]}\right],$$

$$= -4\lambda_{\phi\psi_2\chi_j}\lambda_{\phi\psi_2\chi_i}\lambda_{Z\chi_i\chi_j}\int\frac{d^4p}{(2\pi)^4}\left[\frac{(m_{\psi_2}m_{\chi_j}+p.p+p.q_4)q_{2_\mu}+(m_{\psi_2}m_{\chi_i}+p.p+p.q_2)q_{4_\mu}}{\left[p^2-m^2_{\psi_2}+i\epsilon\right]\left[(q_2+p)^2-m^2_{\chi_i}+i\epsilon\right]\left[(q_4+p)^2-m^2_{\chi_j}+i\epsilon\right]}\right.$$
$$\left.+\frac{(m_{\chi_i}m_{\chi_j}+m_{\psi_2}m_{\chi_i}+m_{\psi_2}m_{\chi_j}+p.p-q_2.q_4)p_\mu}{\left[p^2-m^2_{\psi_2}+i\epsilon\right]\left[(q_2+p)^2-m^2_{\chi_i}+i\epsilon\right]\left[(q_4+p)^2-m^2_{\chi_j}+i\epsilon\right]}\right]. \tag{E.24}$$

Using Feynman parametrization $l=p+yq_2+zq_4$, we define,

$$\Delta^{ij} = (y+z)(y+z-1)m_\phi^2 - tyz + xm^2_{\psi_2} + ym^2_{\chi_i} + zm^2_{\chi_j}\,, \tag{E.25}$$

$$\delta m_\mu^{ij} = \left[m_{\psi_2}m_{\chi_j} - (m_{\psi_2}m_{\chi_j}+m_{\psi_2}m_{\chi_i}+m_{\chi_i}m_{\chi_j})y + tyz(y-1) - m_\phi^2(z+(y-1)(y+z)^2)\right]q_{2_\mu} +$$
$$\left[m_{\psi_2}m_{\chi_i} - (m_{\psi_2}m_{\chi_i}+m_{\psi_2}m_{\chi_j}+m_{\chi_i}m_{\chi_j})z + tyz(z-1) - m_\phi^2(y+(z-1)(y+z)^2)\right]q_{4_\mu}\,, \tag{E.26}$$

$$c_\mu = (1-y)q_{2_\mu} + (1-z)q_{4_\mu}\,, \tag{E.27}$$

and using the dimensional regularisation method, we can write,

$$\mathbb{L}_{\mu}^{ij} = -8\lambda_{\phi\psi_2\chi_j}\lambda_{\phi\psi_2\chi_i}\lambda_{Z\chi_i\chi_j}\int_0^1 dx\,dy\,dz\int\frac{d^4l}{(2\pi)^4}\frac{\delta m_{\mu}^{ij}+c_{\mu}l^2-2yq_2^{\alpha}l_{\alpha}l_{\mu}-2zq_4^{\beta}l_{\beta}l_{\mu}}{[l^2-\Delta^{ij}+i\epsilon]^3}\delta(x+y+z-1)$$
$$= \frac{i}{4\pi^2}\lambda_{\phi\psi_2\chi_j}\lambda_{\phi\psi_2\chi_i}\lambda_{Z\chi_i\chi_j}\int_0^1 dx\,dy\,dz\left[\frac{\delta m_{\mu}^{ij}}{\Delta^{ij}}-(2c_{\mu}-yq_{2_{\mu}}-zq_{4_{\mu}})\left(\frac{1}{\epsilon}-\gamma_E+\ln[4\pi\mu^2]-\ln\Delta^{ij}\right)\right.$$
$$\left.+c_{\mu}+\mathcal{O}(\epsilon)\right]\delta(x+y+z-1)\,, \quad \text{(E.28)}$$

where,

$$\lambda_{\phi\psi_2\overline{\chi}_1} = \lambda_{\phi\overline{\psi}_2\chi_1} = -Y_2\cos\theta,$$
$$\lambda_{\phi\psi_2\overline{\chi}_2} = \lambda_{\phi\overline{\psi}_2\chi_2} = Y_2\sin\theta,$$
$$\lambda_{Z\overline{\chi}_1\chi_1} = \frac{g}{2\cos\theta_w}\sin^2\theta = \frac{m_Z}{v}\sin^2\theta,$$
$$\lambda_{Z\overline{\chi}_2\chi_2} = \frac{g}{2\cos\theta_w}\cos^2\theta = \frac{m_Z}{v}\cos^2\theta,$$
$$\lambda_{Z\overline{\chi}_1\chi_2} = \lambda_{Z\overline{\chi}_2\chi_1} = \frac{g}{2\cos\theta_w}\sin\theta\cos\theta = \frac{m_Z}{v}\sin\theta\cos\theta\,.$$

In a similar way to the Higgs mediated diagram, here also a factor 2 is multiplied in Eq . (E.28) for the anti-particles in the loop and the total amplitude becomes,

$$\mathbb{L}_{\mu}^{Z} = 2\sum_{i,j=1,2}\mathbb{L}_{\mu}^{ij}\,,$$
$$= \frac{i}{2\pi^2}\sum_{i,j=1,2}\lambda_{\phi\psi_2\chi_j}\lambda_{\phi\psi_2\chi_i}\lambda_{Z\chi_i\chi_j}\int_0^1 dx\,dy\,dz\left[\frac{\delta m_{\mu}^{ij}}{\Delta^{ij}}\right.$$
$$\left.-(2c_{\mu}-yq_{2_{\mu}}-zq_{4_{\mu}})\left(\frac{1}{\epsilon}-\gamma_E+\ln[4\pi\mu^2]-\ln\Delta^{ij}\right)+c_{\mu}+\mathcal{O}(\epsilon)\right]\delta(x+y+z-1)\,,$$
$$\underset{\epsilon\to 0}{=}\frac{i}{2\pi^2}\sum_{i,j=1,2}\lambda_{\phi\psi_2\chi_j}\lambda_{\phi\psi_2\chi_i}\lambda_{Z\chi_i\chi_j}\int_0^1 dx\,dy\,dz\left[\frac{\delta m_{\mu}^{ij}}{\Delta^{ij}}+(2c_{\mu}-yq_{2_{\mu}}-zq_{4_{\mu}})\ln\Delta^{ij}\right]\delta(x+y+z-1)\,,$$
$$\xrightarrow[m_{\chi_1}=m_{\chi_2}]{} 0\,.$$
$$\xrightarrow[m_{\chi_1}\neq m_{\chi_2}]{} \mathbb{L}_Z(q_{2_{\mu}}+q_{4_{\mu}})\,.$$

We have cross-checked our analytical solution with Package-X [778] and FeynCalc [779]. In Fig . E.4, the color bar represents the variation of Z-mediated loop amplitude $\mathbb{L}_Z$ in $\Delta m - Y_2$ plane.

E.4 Direct detection cross-section of pFIMP and WIMP

After the amplitude, we calculate the cross-section here. The Feynman diagrams for DM ϕ scattering off a nucleon at tree-level and one-loop level are shown in Fig . 6.10. For the Higgs mediator, the tree-level contribution is negligible because of tiny $h\phi\phi$ coupling that we have assumed, justifiably, in the pFIMP scenario. The dominant

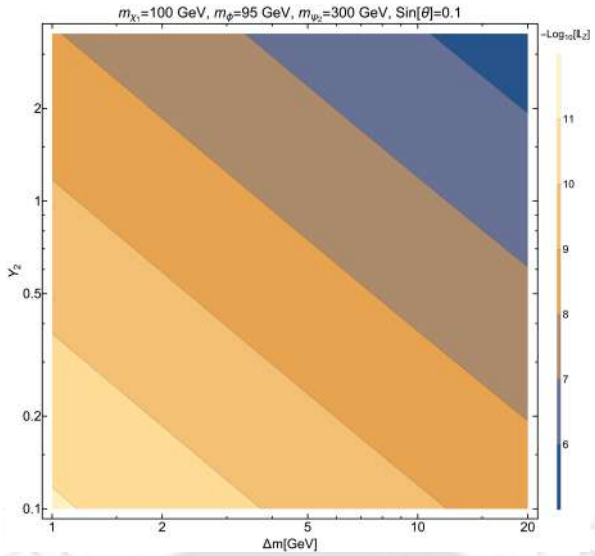

Figure E.4: One-loop amplitude for the Z-mediated process.

Higgs-mediated contribution therefore comes from one-loop diagram. The two interaction vertices involved in the loop-induced Higgs-mediated process are $\mathbb{L}_h h\phi\phi$ and $\frac{m_q}{v} hq\bar{q}$, the effective Lagrangian at the parton level can be written as,

$$\mathcal{L}^h_{eff} = \mathbb{L}_h \frac{m_q}{v}\frac{1}{m_h^2} q\bar{q}\phi\phi = f^h_q q\bar{q}\phi\phi. \tag{E.29}$$

The matrix element for a scattering $N\phi \to N\phi$ via Higgs-mediation, where N stands for nucleon, is the following:

$$i\mathcal{M}^h_{N\phi} = \alpha^h_N \left[\overline{u}_N(q_3)u_N(q_1)\right], \tag{E.30}$$

where α^h_N is the effective DM-nucleon coupling and the relation with quark level coupling is,

$$\frac{\alpha^h_N}{m_N} = \sum_{q=u,d,s} f^N_{T_q}\frac{f^{\rm h}_q}{m_q} + \frac{2}{27}(1 - \sum_{q=u,d,s} f^N_{T_q}) \sum_{q=c,b,t}\frac{f^{\rm h}_q}{m_q}. \tag{E.31}$$

The nuclear form-factors are defined by [1, 780] ,

$$\langle N|m_q\bar{q}q|N\rangle \equiv m_N f^N_{T_q}\langle N|N\rangle (q = u, d, s)\,. \tag{E.32}$$

The matrix element squared for the Higgs mediated process then turns out to be,

Nucleon	$f^N_{T_u}$	$f^N_{T_d}$	$f^N_{T_s}$	$f^N_{T_G}$	$f^N_{T_c}$	$f^N_{T_b}$	$f^N_{T_t}$
Proton	0.018(5)	0.027(7)	0.037(17)	0.917(19)	0.078(2)	0.072(2)	0.069(1)
Neutron	0.013(3)	0.040(10)	0.037(17)	0.910(20)	0.078(2)	0.071(2)	0.068(2)

Table E.1: Values of the Nuclear form factors $f^N_{T_{q,G}}$.

$$\overline{|\mathcal{M}^h_{N\phi}|^2} = \frac{1}{2}\sum_{\text{all spin}} |\mathcal{M}^h_{N\phi}|^2 = 4m_N^2|\alpha^h_N|^2\,. \tag{E.33}$$

The effective Lagrangian for Z mediator direct search process can be written as,

$$\begin{aligned}
\mathcal{L}^{Z}_{eff} &= \bar{q}\left[\frac{g}{\cos\theta_W}\gamma^{\mu}\frac{1}{2}\left(c^{q}_{V}-c^{q}_{A}\gamma^{5}\right)\right]q\frac{\mathbb{L}_Z}{m^2_Z}\phi(q_{2_\mu}+q_{4_\nu})\phi\,, && \text{(SI + SD)}\\
&\to \frac{m_Z}{v}c^{q}_{V}\frac{\mathbb{L}_Z}{m^2_Z}\bar{q}\gamma^{\mu}q\phi(q_{2_\mu}+q_{4_\mu})\phi\,, && \text{(SI)}\\
&= \frac{c^{q}_{V}}{v}\frac{\mathbb{L}_Z}{m_Z}\bar{q}\gamma^{\mu}q\phi(q_{2_\mu}+q_{4_\mu})\phi\,,\\
&= b^{Z}_{q}\bar{q}\gamma^{\mu}q\phi(q_{2_\mu}+q_{4_\mu})\phi\,. && \text{(E.34)}
\end{aligned}$$

The matrix element for Z-mediated pFIMP-nucleon scattering $N\phi \to N\phi$ is as follows assuming Let, $\mathbb{L}^{Z}_{\mu} = \mathbb{L}_{Z}(q_{2_\mu}+q_{4_\mu})$,

$$i\mathcal{M}^{Z}_{N\phi} = b^{Z}_{N}\left[\overline{u}_N(q_3)\gamma^{\mu}u_N(q_1)\right](q_{2_\mu}+q_{4_\mu})\,. \tag{E.35}$$

Here b^{Z}_{N} is the $\mathrm{DM}-\mathrm{nucleon}$ effective coupling. As the sea-quarks and the gluons do not contribute to the vector current, only valence quark contributions add up due to the conservation of the vector current, which gives us $b_p = 2b_u + b_d$ and $b_n = b_u + 2b_d$. So the effective DM-nucleon couplings can be recast in terms of quark level couplings as [781],

$$\begin{aligned}
b^{Z}_{p} &= 2b^{Z}_{u} + b^{Z}_{d}\,,\\
b^{Z}_{n} &= b^{Z}_{u} + 2b^{Z}_{d}\,;\ \text{where}\ b^{Z}_{q} = \frac{c^{q}_{V}}{v}\frac{\mathbb{L}_Z}{m_Z}.
\end{aligned} \tag{E.36}$$

The matrix element squared turns out to be,

$$\begin{aligned}
\overline{|\mathcal{M}^{Z}_{N\phi}|^2} &= \frac{|b^{Z}_{N}|^2}{2}\mathrm{Tr}\left[(\not{q}_3+\mathrm{m_N})\gamma^{\mu}(\not{q}_1+\mathrm{m_N})\gamma^{\nu}\right](\mathrm{q}_{2_\mu}+\mathrm{q}_{4_\mu})(\mathrm{q}_{2_\nu}+\mathrm{q}_{4_\nu})\,, && \text{(E.37)}\\
&= 4|b^{Z}_{N}|^2 4m^2_{\phi}m^2_{N} \qquad \text{as initially the nucleus is in rest, } q_1 \sim \{m_N, \vec{0}\}\,.
\end{aligned}$$

The Z and Higgs mediated cross-term is,

$$\begin{aligned}
\overline{|\mathcal{M}^{Z}_{N\phi}|^{\dagger}|\mathcal{M}^{h}_{N\phi}|} &= \frac{1}{2}\sum_{\text{all spin}}\left[b^{Z}_{N}\left(\overline{u}_N(q_3)\gamma^{\mu}u_N(q_1)\right)(q_{2_\mu}+q_{4_\mu})\right]^{\dagger}\left[\alpha^{h}_{N}\left(\overline{u}_N(q_3)u_N(q_1)\right)\right]\,,\\
&= 2m_N b^{Z^{\dagger}}_{N}\alpha^{h}_{N}4m_{\phi}m_N\,, \qquad \text{as initially the nucleus is in rest, } q_1 \sim \{m_N, \vec{0}\}\\
&= 8m^2_N m_{\phi} b^{Z^{\dagger}}_{N}\alpha^{h}_{N}\,. && \text{(E.38)}
\end{aligned}$$

In a similar way,

$$\begin{aligned}
\overline{|\mathcal{M}^{Z}_{N\phi}||\mathcal{M}^{h}_{N\phi}|^{\dagger}} &= \frac{1}{2}\sum_{\text{all spin}}\left[b^{Z}_{N}\left(\overline{u}_N(q_3)\gamma^{\mu}u_N(q_1)\right)(q_{2_\mu}+q_{4_\mu})\right]\left[\alpha^{h}_{N}\left(\overline{u}_N(q_3)u_N(q_1)\right)\right]^{\dagger}\,,\\
&= 8m^2_N m_{\phi} b^{Z}_{N}\alpha^{h^{\dagger}}_{N}\,. && \text{(E.39)}
\end{aligned}$$

The spin-independent $\mathrm{pFIMP}-\mathrm{nucleon}$ scattering cross-section in the non-relativistic limit, assuming the initial nucleon is at rest, is given by [782],

$$\begin{aligned}\sigma_{\phi\mathrm{N}} &= \frac{1}{4m_\phi m_N|w-v_N|}\int \frac{d^3q_3}{(2\pi)^3 2m_N}\frac{d^3q_4}{(2\pi)^3 2m_\phi}\overline{|\mathcal{M}^Z_{N\phi}+\mathcal{M}^h_{N\phi}|^2}(2\pi)^4\delta^4(q_1+q_2-q_3-q_4)\\ &= \int \frac{\overline{|\mathcal{M}^Z_{N\phi}+\mathcal{M}^h_{N\phi}|^2}}{4\pi^2(4m_\phi m_N)^2|w-v_N|}d^3q_3\, d^3q_4\delta(E_1+E_2-E_3-E_4)\delta^3(\vec{q}_1+\vec{q}_2-\vec{q}_3-\vec{q}_4)\,.\end{aligned} \tag{E.40}$$

From energy conservation,

$$\begin{aligned}2\mu_{\phi N}\vec{q}_2.\vec{q}_3 &= m_\phi|\vec{q}_3|^2\,,\\ |\vec{q}_3| &= 2\mu_{\phi N}w\cos\theta\,,\end{aligned} \tag{E.41}$$

where w, v_N are the initial velocities of DM and nucleus. We have assumed that in Lab-frame, the nucleus initially is at rest, $|\vec{v}_N|=0$, so the relative velocity between DM and nucleus becomes w. The angle between $\vec{q}_2$ and $\vec{q}_3$ is θ. Then Eq. (E.40) becomes,

$$\begin{aligned}\sigma_{\phi\mathrm{N}} &= \int \frac{\overline{|\mathcal{M}^Z_{N\phi}+\mathcal{M}^h_{N\phi}|^2}}{4\pi^2(4m_\phi m_N)^2 w}(\pi|\vec{q}_3|d\cos\theta\, d|\vec{q}_3|^2)\, d^3q_4\delta(E_1+E_2-E_3-E_4)\delta^3(\vec{q}_2-\vec{q}_3-\vec{q}_4)\,,\\ &= \frac{\mu^2_{\phi N}}{4\pi m^2_\phi}\left|\alpha^h_N+2m_\phi b^{Z^\dagger}_N\right|^2\,.\end{aligned} \tag{E.42}$$

Let us now turn to WIMP direct search cross-section. The Feynman diagrams corresponding to WIMP DM χ_1 scattering off a nucleon at tree level are shown in Fig. 6.22. The two relevant interaction vertices for Higgs mediated interaction are $\lambda_{h\chi_1\overline{\chi}_1}h\chi_1\overline{\chi}_1$ and $\frac{m_q}{v}hq\bar{q}$. Effective Lagrangian for spin-independent direct search process can be written as,

$$\mathcal{L}^h_{eff} = \frac{m_q}{v}\frac{1}{m^2_h}\lambda_{h\chi_1\overline{\chi}_1}q\bar{q}\chi_1\overline{\chi}_1 = F^h_q q\bar{q}\chi_1\overline{\chi}_1\,, \tag{E.43}$$

where $\lambda_{h\chi_1\overline{\chi}_1}=-\frac{Y_1}{\sqrt{2}}\sin 2\theta$ in our model. The matrix element for a scattering $N\chi_1\to N\chi_1$ via Higgs mediation (N stands for nucleon) is the following:

$$i\mathcal{M}^h_{N\chi_1} = \beta^h_N\Big[\overline{u}_N(q_3)u_N(q_1)\Big]\Big[\overline{u}_{\chi_1}(q_4)u_{\chi_1}(q_2)\Big]\,, \tag{E.44}$$

where β^h_N is the DM-nucleon coupling, related to the quark level coupling F^h_q following Eq. (E.31). The amplitude squared is,

$$\overline{|\mathcal{M}^h_{N\chi_1}|^2} = \frac{1}{4}\sum_{\text{spin}}|\mathcal{M}^h_{N\chi_1}|^2 = 16m^2_{\chi_1}m^2_N|\beta^h_N|^2\,. \tag{E.45}$$

For Z mediator, only the vector term contributes to SI cross-section and the effective Lagrangian is,

$$\begin{aligned}\mathcal{L}^Z_{eff} &= \frac{m_Z}{v}\frac{1}{m^2_Z}\lambda_{Z\chi_1\overline{\chi}_1}\overline{q}\gamma^\mu\left(c^q_V-c^q_A\gamma^5\right)q\overline{\chi}_1\gamma_\mu\chi_1 && (\mathrm{SI}+\mathrm{SD})\\ &\to \frac{m_Z}{v}\frac{c^q_V}{m^2_Z}\lambda_{Z\chi_1\overline{\chi}_1}\overline{q}\gamma^\mu q\overline{\chi}_1\gamma_\mu\chi_1 && (\mathrm{SI})\\ &= B_q\overline{\chi}_1\gamma^\mu\chi_1\bar{q}\gamma_\mu q\,, &&\end{aligned} \tag{E.46}$$

where, $\lambda_{Z\chi_1\bar{\chi}_1} = \frac{m_Z}{v}\sin^2\theta$.

The matrix element for $N\chi_1 \to N\chi_1$ scattering via Z mediation is,

$$i\mathcal{M}^Z_{N\chi_1} = B^Z_N\left[\overline{u}_N(q_3)\gamma^\mu u_N(q_1)\right]\left[\overline{u}_{\chi_1}(q_4)\gamma_\mu u_{\chi_1}(q_2)\right], \tag{E.47}$$

where B^Z_N is the DM-nucleon coupling is related to the quark level coupling B_q ollowed by the Eq. (E.36). Finally the amplitude squared for Z-mediation is,

$$\overline{|\mathcal{M}^Z_{N\chi_1}|^2} = \frac{1}{4}\sum_{\text{spin}}|\mathcal{M}^Z_{N\chi_1}|^2 = 16m^2_{\chi_1}m^2_N|B^Z_N|^2\,. \tag{E.48}$$

In a two-component framework, the effective spin-independent $\chi_1 N$ scattering cross section becomes, [324, 783],

$$\sigma^{\text{SI}}_{\chi_1 N_{\text{eff}}} = \frac{\Omega_{\chi_1}}{\Omega_{\chi_1}+\Omega_\phi}\frac{\mu^2_{\chi_1 N}}{\pi}\left|\beta^h_N + B^Z_N\right|^2, \tag{E.49}$$

where $\mu_{\chi_1 N} = m_{\chi_1}m_N/(m_{\chi_1}+m_N)$ is the WIMP-nucleon reduced mass, with $m_N \sim 0.939$ GeV. The Z mediated direct search for the WIMP provides a stringent constraint on the WIMP parameter space reducing the singlet-doublet mixing angle significantly.

Appendix F

Stability of two DM components in $\mathcal{Z}_N$ symmetry

F.1 Heavy DM stability criteria from two and three body decays

The two-body decay width in the rest frame of the decaying particle (A_0), $A_0(m_0) \to A_1(m_1)\ A_2(m_2)$ (Fig . F.1a), is given by [679],

$$\Gamma_{A_0 \to A_1\ A_2} = \frac{1}{64\pi^2 m_0}\sqrt{\left[1-\left(\frac{m_1+m_2}{m_0}\right)^2\right]\left[1-\left(\frac{m_1-m_2}{m_0}\right)^2\right]}\int \overline{|\mathcal{M}|^2} d\Omega\,. \quad \text{(F.1)}$$

Let us consider a process like $\mathrm{A_0(m_0) \to A_1(m_1)\ A_2(m_2)\ A_3(m_3)}$ where three particles can be produced by three different kinds of processes as shown in fig. F.1. The

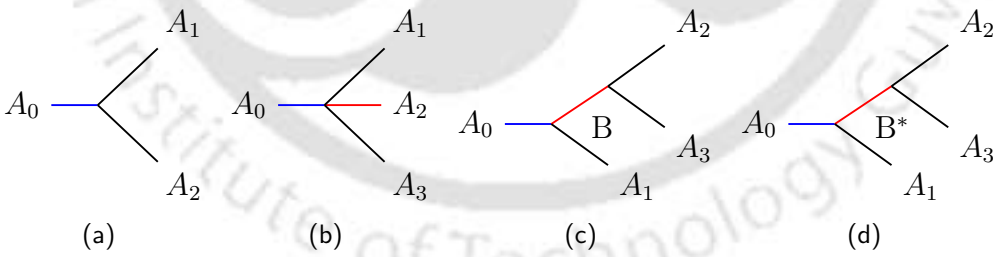

Figure F.1: Fig. F.1a show the two-body decay when $m_0 > \sum_{i=1}^{2} m_i$. The rest of the figures show the possible three-body decay: four-point (F.1b), off-shell B (F.1c), on-shell B (F.1d).

three-body decay width in the rest frame of the decaying particle (A_0) is given by [757],

$$\Gamma_{A_0 \to A_1 A_2 .. A_n} = S_k \frac{1}{2m_0}\left(\prod_{i=1}^{n}\int \frac{d^3 p_i'}{(2\pi)^3 2E_i'}\right)(2\pi)^4\delta^4(p-\sum_{i=1}^{n} p_i')\overline{|\mathcal{M}|^2}_{A_0 \to A_1 A_2 .. A_n}\,, \quad \text{(F.2)}$$

$S_k = 1/k!$ is the corresponding symmetry factor, with k the number of identical final state particles. In the CM reference frame, the expression for the three body decay width [784],

$$\Gamma_{A_0\to A_1\ A_2\ A_3} = S_k \frac{1}{(2\pi)^3}\frac{1}{32m_0^3}\int dm_{12}^2 \int dm_{23}^2\ \overline{|\mathcal{M}|^2}_{A_0\to A_1\ A_2\ A_3}\,, \tag{F.3}$$

where,

$$m_{23}^2|_{\max} = (E_2^* + E_3^*)^2 - \left(\sqrt{E_2^{*2} - m_2^2} - \sqrt{E_3^{*2} - m_3^2}\right)^2\,, \tag{F.4}$$

$$m_{23}^2|_{\min} = (E_2^* + E_3^*)^2 - \left(\sqrt{E_2^{*2} - m_2^2} + \sqrt{E_3^{*2} - m_3^2}\right)^2\,, \tag{F.5}$$

$$m_{12}^2|_{\max} = (m_0 - m_3)^2 \text{ and } m_{12}^2|_{\min} = (m_1 + m_2)^2\,, \tag{F.6}$$

$$E_2^* = (m_{12}^2 - m_1^2 + m_2^2)/2m_{12} \text{ and } E_3^* = (m_0^2 - m_{12}^2 - m_3^2)/2m_{12}\,. \tag{F.7}$$

First alternative way

$$\Gamma_{A_0\to A_1\ A_2\ A_3} = \frac{1}{(2\pi)^3}\frac{1}{8m_0}\int_{E_1^{\min}}^{E_1^{\max}} dE_1 \int_{E_2^{\min}}^{E_2^{\max}} dE_2 \overline{|\mathcal{M}|^2}_{A_0\to A_1\ A_2\ A_3}\,, \tag{F.8}$$

where the minimum and maximum energy of the particles in the CM frame are [302, 784],

$$E_2^{\min} = \frac{1}{2m_{23}^2}\left[(m_0 - E_1)\, m_{23}^2 - \sqrt{(E_1^2 - m_1^2)\,\lambda(m_{23}^2, m_2^2, m_3^2)}\right]\,, \tag{F.9}$$

$$E_2^{\max} = \frac{1}{2m_{23}^2}\left[(m_0 - E_1)\, m_{23}^2 + \sqrt{(E_1^2 - m_1^2)\,\lambda(m_{23}^2, m_2^2, m_3^2)}\right]\,; \tag{F.10}$$

with

$$m_{23}^2 = m_0^2 + m_1^2 - 2m_0E_1\,, \tag{F.11}$$

$$\lambda(a,b,c) \equiv a^2 + b^2 + c^2 - 2ab - 2bc - 2ca\,, \tag{F.12}$$

$$E_1^{\min} = m_1\,, \qquad E_1^{\max} = \frac{1}{2m_0}\left(m_0^2 + m_1^2 - 4m_2^2\right)\,. \tag{F.13}$$

and λ is the Källén function.

Second alternative way [784, 785]

$$d\Gamma_{A_0\to A_1\ A_2\ A_3} = \frac{1}{64m_0^3}\frac{1}{(2\pi)^3}\frac{\sqrt{\lambda(m_0^2, m_1^2, q^2)\lambda(q^2, m_2^2, m_3^2)}}{q^2} dq^2 d\cos\theta^* |\mathcal{M}|^2_{A_0\to A_1\ A_2\ A_3}\,. \tag{F.14}$$

where, $q = p_0 - p_1$, $q^2_{\min} = (m_2 + m_3)^2$, $q^2_{\max} = (m_0 - m_1)^2$.

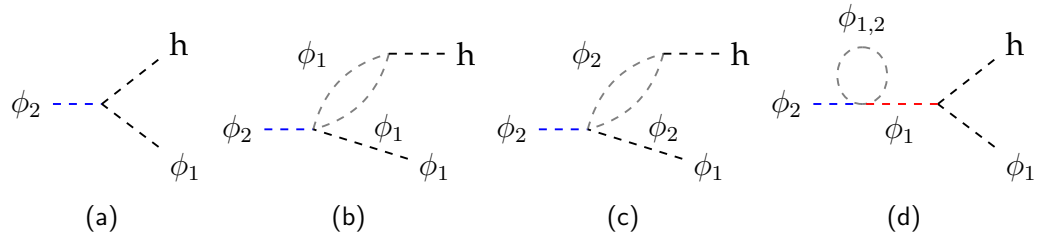

Figure F.2: Figs. F.2a to F.2c and Fig. F.2d are corresponding to the tree and 1-loop level decays of ϕ_2 to ϕ_1 plus on-shell Higgs, under the assumption $m_{\phi_2} > m_{\phi_1}$, respectively. However, the Higgs off-shell decay to di-photon or di-gluon would always be there for two non-degenerate DMs.

Tree and loop level decay of the heavy DM with $\mathcal{Z}_2$ symmetry

The presence of the Higgs portal interaction for ϕ_1 and ϕ_2, as described in Eq. (7.11), allows the heavier particle decay to the lighter particle along with a Higgs boson. The Higgs, whether on-shell or off-shell, can substantially decay into a pair of photons or gluons. The decay of the heavier particle in a non-degenerate scenario imposes stringent constraints on the associated couplings, implying that the mass hierarchy is not limited to just the Higgs mass. Fig. F.2 illustrates the decay of the heavier particle into the lighter one plus an on-shell Higgs. The decay width involving an off-shell Higgs, which decays into light fermions or massless bosons, is significantly suppressed, so we consider only the on-shell Higgs in the total decay width calculation (tree-level + loop correction) to derive stringent limits on the couplings associated with the $\phi_2 \to \phi_1 h$ decay. We don't delve into the details of the complicated loop calculation; instead, we provide an approximate estimate of the coupling required to stabilise the heavier DM particle. The vertex factor corresponding to the tree-level decay process, shown in Fig. F.2a, is $\lambda_{\phi_1\phi_2 H} v$. We aim to determine the stringent limit on this coupling such that the decay time of the heavier particle, τ_{ϕ_2}, exceeds the age of the universe: $\tau_{\rm univ} = 6.4 \times 10^{41} {\rm GeV}^{-1}$. the decay time for the tree-level $\phi_2 \to \phi_1 {\rm h}$ process is

$$\tau_{\phi_2}^{-1} = \frac{\lambda_{\phi_1\phi_2 H}^2 v^2}{16\pi m_{\phi_2}} \sqrt{\left[1 - \left(\frac{m_{\phi_1} + m_h}{m_{\phi_2}}\right)^2\right]\left[1 - \left(\frac{m_{\phi_1} - m_h}{m_{\phi_2}}\right)^2\right]}. \tag{F.15}$$

The tree-level decay shown in Fig. F.2a indicates that a coupling of $\lambda_{\phi_1\phi_2 H} \lesssim 10^{-22}$ is sufficient to ensure that τ_{ϕ_2} exceeds the age of the universe, $\tau_{\rm univ}$. At the next order, a 1-loop decay is also possible. However, we disregard diagrams involving the $h\phi_1\phi_2$ vertex in 1-loop decay, as these would be suppressed compared to the tree-level decay. The relevant decay diagrams are shown in Figs. F.2b to F.2d. Stringent limits on the λ_{112} and λ_{122} couplings are necessary to stabilize the heavier particle. These couplings are expected to be $\gtrsim \lambda_{\phi_1\phi_2 H}$ due to the loop suppression factor of $1/(16\pi^2)$. However, a proper loop calculation is required to determine the upper limit accurately. Ideally, the total decay width of ϕ_2 should include contributions from both the tree-level and all relevant 1-loop decays. However, the presence of UV divergences in the loop diagrams adds complexity to this process, which we have not explored in detail here. Instead, we focus on finding the appropriate combination of m_{ϕ_1}, m_{ϕ_2}, $\lambda_{\phi_1\phi_2 H}$, λ_{112}, and λ_{122} that stabilises ϕ_2, ensuring that $\tau_{\phi_2} > \tau_{\rm univ}$, while keeping the other parameters within a weak ordering regime.

Tree and loop level decay of the heavy DM with $\mathcal{Z}_3$ symmetry

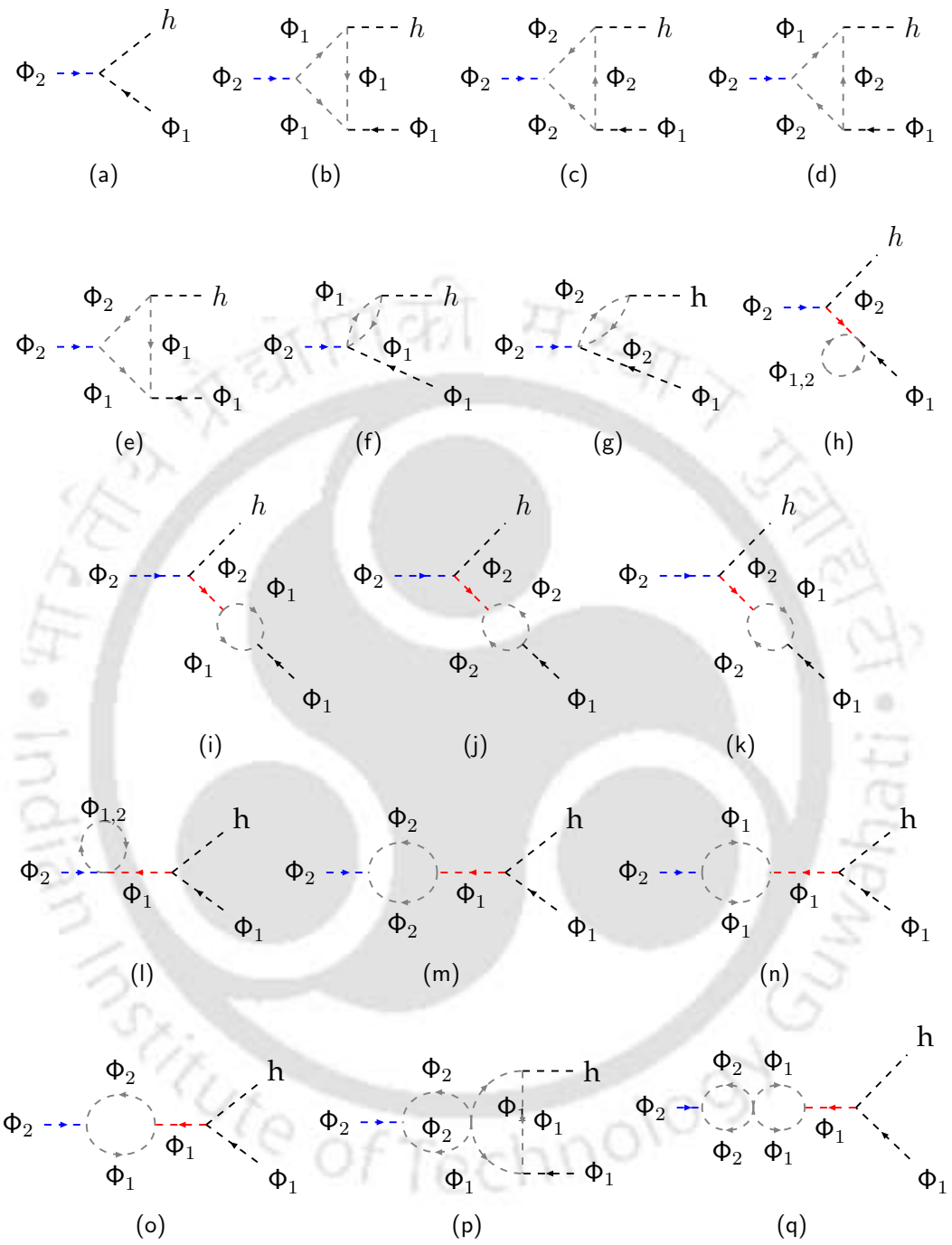

Figure F.3: Fig . F.3a, is the Feynman diagram corresponding to the tree level decay: $\Phi_2 \to \Phi_1\, h$. After ignoring the diagrams involves $h\Phi_1\Phi_2$ vertex, the remaining Feynman diagrams: Figs . F.3b to F.3o represented the 1-loop mediated decay. After the appropriate choice, see Table 7.3, of sacrificing coupling associated with the 1-loop decay, and there are still possible 2-loop decay processes, see Figs . F.3p and F.3q.

Similar to the case with $\mathcal{Z}_2$ symmetry, there are decay channels for the heavier DM particle under $\mathcal{Z}_3$ symmetry as well. The interactions between the DM particles and visible sectors, as shown in Eq . (7.13), give rise to tree-level, 1-loop, and 2-loop decay processes. Let's analyse these decay processes step by step, assuming $m_{\Phi_2} > m_{\Phi_1}$. However, the decay constraints are equally applicable to the opposite mass hierarchy.

- The tree-level decay process $\Phi_2 \to \Phi_1^* + h$ (see Fig . F.3a) is mediated by the coupling λ_{12H}. According to Appendix F.1, to ensure $\tau_{\Phi_2} > \tau_{\text{univ}}$ in the presence of this tree-level decay, we require $\lambda_{12H} \lesssim 4 \times 10^{-22}$.
- If we ignore the diagrams involving the λ_{12H} coupling, we obtain 1-loop decay diagrams, as shown in Figs . F.3b to F.3o. The associated interaction terms and their corresponding couplings, whose small values contribute to the stability of Φ_2, present various scenarios, as summarised in Table 7.3.
- In specific cases, there may also be 2-loop decay processes, such as those depicted in Figs . F.3p and F.3q. To stabilise Φ_2, the couplings associated with these decays must be minimised, although the constraints will be less stringent than the 1-loop limits due to the suppression factor $(16\pi^2)^{-2}$.

Although we have imposed constraints on the couplings associated with each decay process, the total decay width is the sum of contributions from tree-level, 1-loop, and 2-loop processes. Calculating the total decay width is a highly complicated task, and while the precise limits on the couplings may shift slightly with a more accurate computation, the overall phenomenology remains unchanged.

F.2 Relevant Feynmann diagrams for two-component DM in $\mathcal{Z}_3$ scenario

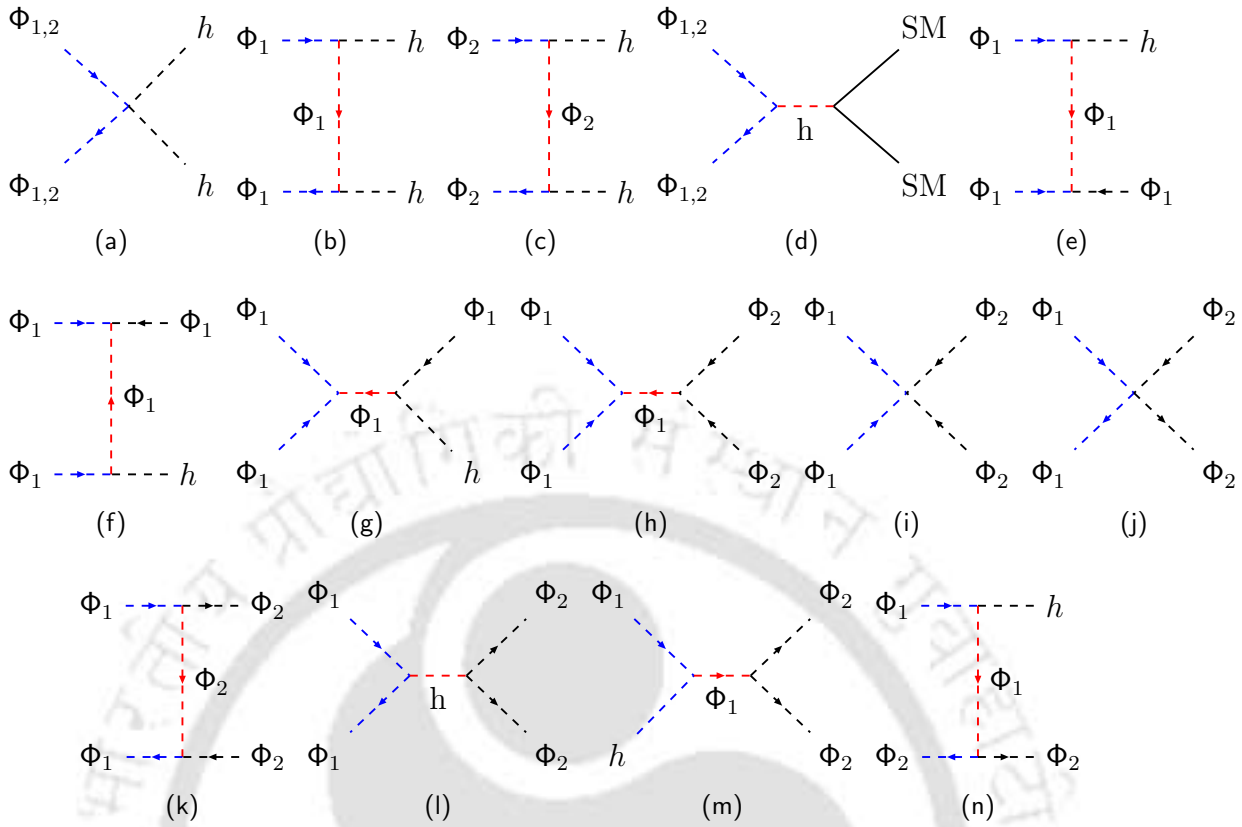

Figure F.4: The Feynman diagrams, Figs. F.4a to F.4d, represents the self-annihilation of Φ_1 and Φ_2 DM where SM = {Higgs, quark, lepton, $W^{\pm}$ and Z boson}. The Feynman diagrams, Figs. F.4e to F.4g, Figs. F.4h to F.4l, and Figs. F.4m and F.4n represent the semi-annihilation, conversion and semi-conversion channels of Φ_1 relevant for Scenario-A and B.

Appendix G

Neutrino mass and CP asymmetry

G.1 Parameters before EWSB

$$\eta_i = \begin{pmatrix} \eta_i^+ \\ \eta_i^0 \end{pmatrix} \; ; \quad H = \begin{pmatrix} H^+ \\ H^0 \end{pmatrix} \; ; \quad \mathbb{L} = \begin{pmatrix} \nu_\ell \\ \ell \end{pmatrix} . \tag{G.1}$$

$$\mathcal{D}_\mu = \partial_\mu + ig\frac{\tau^a}{2}W_\mu^a + ig'YB_\mu = \partial_\mu + \frac{i}{2}\begin{pmatrix} gW_\mu^3 + g'B_\mu & \sqrt{2}gW_\mu^+ \\ \sqrt{2}gW_\mu^- & -gW_\mu^3 + g'B_\mu \end{pmatrix} . \tag{G.2}$$

$$\begin{aligned}
(\mathcal{D}^\mu\eta_i)^\dagger(\mathcal{D}_\mu\eta_i) =& \partial^\mu\eta_i^\dagger\partial_\mu\eta_i + \frac{1}{4}\begin{pmatrix} \eta_i^- & \eta_i^{0^*} \end{pmatrix}\begin{pmatrix} gW_\mu^3 + g'B_\mu & \sqrt{2}gW_\mu^+ \\ \sqrt{2}gW_\mu^- & -gW_\mu^3 + g'B_\mu \end{pmatrix}\begin{pmatrix} gW_\mu^3 + g'B_\mu & \sqrt{2}gW_\mu^+ \\ \sqrt{2}gW_\mu^- & -gW_\mu^3 + g'B_\mu \end{pmatrix} \\
& \begin{pmatrix} \eta_i^+ \\ \eta_i^0 \end{pmatrix} - \frac{i}{2}\left[\begin{pmatrix} \eta_i^- & \eta_i^{0^*} \end{pmatrix}\begin{pmatrix} gW_\mu^3 + g'B_\mu & \sqrt{2}gW_\mu^+ \\ \sqrt{2}gW_\mu^- & -gW_\mu^3 + g'B_\mu \end{pmatrix}\begin{pmatrix} \partial^\mu\eta_i^+ \\ \partial^\mu\eta_i^0 \end{pmatrix} - h.c.\right] \\
=& \partial^\mu\eta_i^\dagger\partial_\mu\eta_i + \frac{1}{4}\left[2g^2W_\mu^+W^{\mu^-}(\eta_i^+\eta_i^- + \eta_i^0\eta_i^{0^*}) + 2\sqrt{2}gg'(B_\mu W^{\mu^-}\eta_i^+\eta_i^{0^*} + h.c.)\right] \\
& - \frac{i}{2}\left[\left(gW_\mu^3 + g'B_\mu\right)\left(\partial^\mu\eta_i^+\right)\eta_i^- + \sqrt{2}gW_\mu^+\left(\partial^\mu\eta_i^0\right)\eta_i^- + \sqrt{2}gW_\mu^-\left(\partial^\mu\eta_i^+\right)\eta_i^{0^*}\right. \\
& \left. + \left(g'B_\mu - gW_\mu^3\right)\left(\partial^\mu\eta_i^0\right)\eta_i^{0^*} - h.c.\right] + \frac{1}{4}\left[|g'B_\mu + gW_\mu^3|^2\eta_i^+\eta_i^- + |g'B_\mu - gW_\mu^3|^2\eta_i^0\eta_i^{0^*}\right] .
\end{aligned} \tag{G.3}$$

$$\begin{aligned}
& \overline{\mathbb{L}}_L i\gamma^\mu\mathcal{D}_\mu\mathbb{L}_L + \overline{\ell}_R i\gamma^\mu\mathcal{D}_\mu\ell_R \\
=& \overline{\mathbb{L}}_L i\gamma^\mu\left(\partial_\mu + ig\frac{\tau^a}{2}W_\mu^a - i\frac{g'}{2}B_\mu\right)\mathbb{L}_L + \overline{\ell}_R i\gamma^\mu\left(\partial_\mu - ig'B_\mu\right)\ell_R \\
=& \begin{pmatrix} \overline{\nu}_{\ell_L} & \overline{\ell}_L \end{pmatrix}\left(i\partial\!\!\!/ - \frac{1}{2}\gamma^\mu\begin{pmatrix} gW_\mu^3 - g'B_\mu & \sqrt{2}gW_\mu^+ \\ \sqrt{2}gW_\mu^- & -gW_\mu^3 - g'B_\mu \end{pmatrix}\right)\begin{pmatrix} \nu_{\ell_L} \\ \ell_L \end{pmatrix} + \overline{\ell}_R\left(i\partial\!\!\!/ + \gamma^\mu g'B_\mu\right)\ell_R \\
=& \overline{\ell}i\partial\!\!\!/\ell - (gW_\mu^3 - g'B_\mu)\overline{\nu_\ell}\frac{1}{2}\gamma^\mu\mathbb{P}_L\nu_\ell + \overline{\ell}\gamma^\mu\left[\frac{1}{2}(gW_\mu^3 + g'B_\mu)\mathbb{P}_L + g'B_\mu\mathbb{P}_R\right]\ell - \frac{g}{\sqrt{2}}\left(W_\mu^+\overline{\nu}_\ell\gamma^\mu\mathbb{P}_L\ell + h.c.\right) .
\end{aligned} \tag{G.4}$$

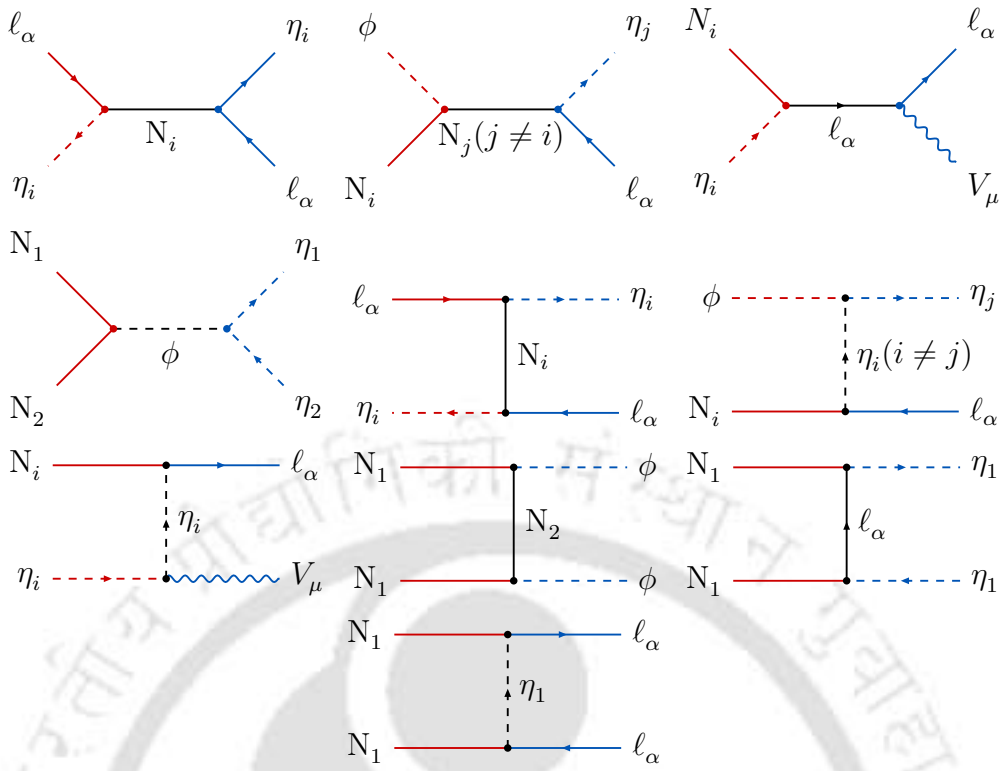

Figure G.1: The relevant Feynman diagrams for Leptogenesis where $i = 1, 2$; $V_\mu = B_\mu$, W^3_μ, $W^\pm_\mu$ [158, 786] and α define the lepton generation.

G.2 Neutrino mass generation

In this scenario, neutrino mass is generated via a one-loop radiative diagram, as shown in Fig . G.2. and the 1-loop correction due to this self-energy graph is written

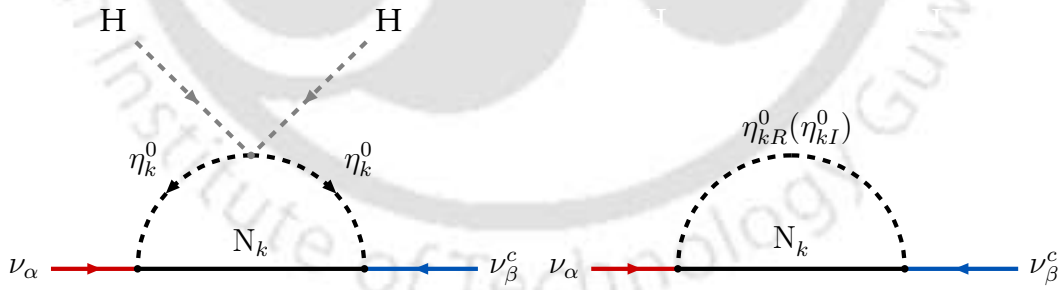

Figure G.2: Radiative neutrino majorana mass generation where i, j are generation indices and $k = 1, 2$. The left and right figures correspond to before and after EWSB, respectively.

as,

$$\overline{u}_{L_{\nu_\alpha}}(p)\Sigma_{\alpha\beta}(p)u^c_{L_{\nu_\beta}}(p) = \overline{u}_{L_{\nu_\alpha}}(p)\sum_{k=1,2}\left(\Sigma_{\alpha\beta}(p,\eta^0_{kR}) + \Sigma_{\alpha\beta}(p,\eta^0_{kI})\right)u^c_{L_{\nu_\beta}}(p)\,. \tag{G.5}$$

$$-i\Sigma_{\alpha\beta}\left(p,\eta^0_{kR(I)}\right) = -C^{\alpha k}_{R(I)}\int\frac{d^4l}{(2\pi)^4}\frac{i}{(p-l)^2 - m^2_{\eta^0_{kR(I)}}}\frac{i(\not{l}+M_k)}{l^2-M^2_k}C^{\beta k}_{R(I)}\,. \tag{G.6}$$

Here $C^{\alpha k}_{R(I)}$ and $C^{\beta k}_{R(I)}$ are the couplings, given by

$$C^{\alpha k}_{R(I)} = \frac{f_{R(I)}}{\sqrt{2}} h^*_{kk\alpha} \quad \text{and} \quad C^{\beta k}_{R(I)} = \frac{f_{R(I)}}{\sqrt{2}} h^*_{kk\beta}\,, \tag{G.7}$$

with $f_R = 1$ and $f_I = i$.

$$\mathbb{M}^k_{\alpha\beta} = \Sigma_{\alpha\beta}(0, \eta^0_{kR}) + \Sigma_{\alpha\beta}(0, \eta^0_{kI})\,. \tag{G.8}$$

Eq . G.6 is also valid for $p = 0$, so we set this limit during mass matrix calculation. The odd power of l should vanish after integration.

$$\begin{aligned}\Sigma_{\alpha\beta}(0, \eta^0_{kR(I)}) &= iC^{\alpha k}_{R(I)} \int \frac{d^4l}{(2\pi)^4} \frac{1}{l^2 - m^2_{\eta^0_{kR(I)}}} \frac{(\not{l} + M_k)}{l^2 - M^2_k} C^{\beta k}_{R(I)} \\ &\equiv iC^{\alpha k}_{R(I)} C^{\beta k}_{R(I)} \int \frac{d^4l}{(2\pi)^4} \frac{1}{l^2 - m^2_{\eta^0_{kR(I)}}} \frac{M_k}{l^2 - M^2_k}\,;\end{aligned} \tag{G.9}$$

$$\mathbb{M}_{\alpha\beta} = \sum_{k=1,2} \mathbb{M}^k_{\alpha\beta} = \sum_{k=1,2} \Sigma_{\alpha\beta}(0, \eta^0_{kR}) + \Sigma_{\alpha\beta}(0, \eta^0_{kI})\,; \tag{G.10}$$

$$\begin{aligned}\mathbb{M}^k_{\alpha\beta} &= i\frac{h^*_{kk\alpha} h^*_{kk\beta} M_k}{2} \int \frac{d^4l}{(2\pi)^4} \left(\frac{1}{(l^2 - m^2_{\eta^0_{kR}})(l^2 - M^2_k)} - \frac{1}{(l^2 - m^2_{\eta^0_{kI}})(l^2 - M^2_k)} \right) \\ &= h^*_{kk\alpha} \left[\frac{M_k}{32\pi^2} \left(\frac{m^2_{\eta^0_{kR}}}{m^2_{\eta^0_{kR}} - M^2_k} \ln \frac{m^2_{\eta^0_{kR}}}{M^2_k} - \frac{m^2_{\eta^0_{kI}}}{m^2_{\eta^0_{kI}} - M^2_k} \ln \frac{m^2_{\eta^0_{kI}}}{M^2_k} \right) \right] h^*_{kk\beta}\,.\end{aligned}$$

The neutrino mass generated from the diagrams shown in Fig . G.2 is given by

$$(\mathcal{M})_{\alpha\beta} = \sum_{i=1}^{2} \frac{h^*_{ii\alpha} h^*_{ii\beta} M_i}{32\pi^2} \left[L(m^2_{\eta_{iR}}) - L(m^2_{\eta_{iI}}) \right], \tag{G.11}$$

where the function L has the following form

$$L(m^2) = \frac{m^2}{m^2 - M^2_i} ln \left(\frac{m^2}{M^2_i} \right). \tag{G.12}$$

$$\begin{aligned}\mathbb{M}_{\alpha\beta} &= \sum_k h^*_{kk\alpha} (\Lambda_{kk})^{-1} h^*_{kk\beta} \\ &= h^*_{11\alpha} (\Lambda_{11})^{-1} h^*_{11\beta} + h^*_{22\alpha} (\Lambda_{22})^{-1} h^*_{22\beta} \\ &= \begin{pmatrix} h^*_{11\alpha} & h^*_{22\alpha} \end{pmatrix} \begin{pmatrix} \frac{1}{\Lambda_{11}} & 0 \\ 0 & \frac{1}{\Lambda_{22}} \end{pmatrix} \begin{pmatrix} h^*_{11\beta} \\ h^*_{22\beta} \end{pmatrix}\,;\end{aligned} \tag{G.13}$$

$$\mathbb{M} = \begin{pmatrix} h^*_{111} & h^*_{221} \\ h^*_{112} & h^*_{222} \\ h^*_{113} & h^*_{223} \end{pmatrix} \begin{pmatrix} \frac{1}{\Lambda_{11}} & 0 \\ 0 & \frac{1}{\Lambda_{22}} \end{pmatrix} \begin{pmatrix} h^*_{111} & h^*_{112} & h^*_{113} \\ h^*_{221} & h^*_{222} & h^*_{223} \end{pmatrix} \equiv h^* \Lambda^{-1} (h^*)^T = h^* \Lambda^{-1} h^\dagger\,, \tag{G.14}$$

where

$$h = \begin{pmatrix} h_{111} & h_{221} \\ h_{112} & h_{222} \\ h_{113} & h_{223} \end{pmatrix} \text{ and } \Lambda^{-1} = \begin{pmatrix} \dfrac{1}{\Lambda_{11}} & 0 \\ 0 & \dfrac{1}{\Lambda_{22}} \end{pmatrix}, \tag{G.15}$$

and

$$\Lambda_{ii} = \frac{4\pi^2}{m^2_{\eta_{Ri}} - m^2_{\eta_{Ii}}} \xi_i M_i = \frac{4\pi^2}{\lambda''_{iiH}} \xi_i \frac{M_i}{v^2}. \tag{G.16}$$

The loop functions ξ_i are given by

$$\xi_i = \left(\frac{1}{8} \frac{M_i^2}{m^2_{\eta_{Ri}} - m^2_{\eta_{Ii}}} \left[L(m^2_{\eta_{Ri}}) - L(m^2_{\eta_{Ii}}) \right] \right)^{-1}. \tag{G.17}$$

Now, the light neutrino mass is diagonalized using the usual PMNS matrix U, with Majorana and Dirac phases, which is determined from neutrino oscillation data and

$$\mathbb{M}_\nu = \mathrm{diag}(\mathrm{m_1}, \mathrm{m_2}, \mathrm{m_3}) = \mathrm{U}^\dagger \mathbb{M} \mathrm{U}^* = \mathrm{U}^\dagger \mathrm{h}^* \sqrt{\Lambda^{-1}} \sqrt{\Lambda^{-1}} \mathrm{h}^\dagger \mathrm{U}^* ,$$

$$\mathbb{M}_{\sqrt{\nu}} \mathbb{M}_{\sqrt{\nu}} = \mathrm{U}^\dagger \mathrm{h}^* \sqrt{\Lambda^{-1}} \sqrt{\Lambda^{-1}} \mathrm{h}^\dagger \mathrm{U}^* ,$$

$$\mathbb{I} = \mathbb{M}_{\sqrt{\nu^{-1}}} \mathrm{U}^\dagger \mathrm{h}^* \sqrt{\Lambda^{-1}} \sqrt{\Lambda^{-1}} \mathrm{h}^\dagger \mathrm{U}^* \mathbb{M}_{\sqrt{\nu^{-1}}} = \left[\sqrt{\Lambda^{-1}} \mathrm{h}^\dagger \mathrm{U}^* \mathbb{M}_{\sqrt{\nu^{-1}}} \right]^{\mathrm{T}} \left[\sqrt{\Lambda^{-1}} \mathrm{h}^\dagger \mathrm{U}^* \mathbb{M}_{\sqrt{\nu^{-1}}} \right] \equiv \mathbb{R}^{\mathrm{T}} \mathbb{R} .$$

where $\mathbb{R}$ is any 2×3 orthogonal matrix. Then, the Yuakawa coupling matrix satisfying the neutrino data can be written as,

$$h = U^* \mathbb{M}_{\sqrt{\nu}} \mathbb{R}^\dagger \sqrt{\Lambda} \tag{G.18}$$

where [787],

$$\mathbb{M}_{\sqrt{\nu}} = \begin{pmatrix} \sqrt{m_1} & 0 & 0 \\ 0 & \sqrt{m_2} & 0 \\ 0 & 0 & \sqrt{m_3} \end{pmatrix} \text{ and } \sqrt{\Lambda} = \begin{pmatrix} \sqrt{\Lambda_{11}} & 0 \\ 0 & \sqrt{\Lambda_{22}} \end{pmatrix} \tag{G.19}$$

$$U = \begin{pmatrix} c_{12}c_{13} & s_{12}c_{13} & s_{13}e^{-i\delta} \\ -s_{12}c_{23} - c_{12}s_{23}s_{13}e^{i\delta} & c_{12}c_{23} - s_{12}s_{23}s_{13}e^{i\delta} & s_{23}c_{13} \\ s_{12}s_{23} - c_{12}c_{23}s_{13}e^{i\delta} & -c_{12}s_{23} - s_{12}c_{23}s_{13}e^{i\delta} & c_{23}c_{13} \end{pmatrix} \tag{G.20}$$

Neutrino oscillation experiments only measure two neutrino mass squared differences [788, 789].

$$\left.\begin{aligned} m_1 &= 0 \\ m_2 &= \sqrt{\Delta m^2_{21}} \\ m_3 &= \sqrt{\Delta m^2_{31}} \end{aligned}\right\} \quad \text{NO} \quad \left\{\begin{aligned} &\theta_{12}/^\circ = 33.44,\ \theta_{23}/^\circ = 49.2,\ \theta_{13}/^\circ = 8.57,\ \delta_{CP} = 197 \\ &\Delta m^2_{21} = 7.42 \times 10^{-5}\ \mathrm{eV}^2 \\ &\Delta m^2_{31} = 2.517 \times 10^{-5}\ \mathrm{eV}^2 \end{aligned}\right.$$

$$\left.\begin{aligned} m_1 &= \sqrt{-\Delta m^2_{32} - \Delta m^2_{21}} \\ m_2 &= \sqrt{-\Delta m^2_{32}} \\ m_3 &= 0 \end{aligned}\right\} \quad \text{IO} \quad \left\{\begin{aligned} &\theta_{12}/^\circ = 33.45,\ \theta_{23}/^\circ = 49.3,\ \theta_{13}/^\circ = 8.60,\ \delta_{CP} = 282 \\ &\Delta m^2_{21} = 7.42 \times 10^{-5}\ \text{eV}^2 \\ &\Delta m^2_{32} = -2.498 \times 10^{-5}\ \text{eV}^2 \end{aligned}\right.$$

$$\mathbb{R}^{\text{NO}} = \begin{pmatrix} 0 & \cos z & \sin z \\ 0 & -\sin z & \cos z \end{pmatrix} \text{ and } \mathbb{R}^{\text{IO}} = \begin{pmatrix} \cos z & \sin z & 0 \\ -\sin z & \cos z & 0 \end{pmatrix}$$

where $z = a + i\,b$ and $\{a,\ b\}$ are our free parameters. Also, one can find the relations

$$\sum_{\alpha=1}^{3} h_{11\alpha} h^*_{11\alpha} = Tr(h^{'} h^{\dagger}) \quad \text{and} \quad \sum_{\alpha=1}^{3} h_{22\alpha} h^*_{11\alpha} = Tr(h^{''} h^{\dagger}), \tag{G.21}$$

where

$$h^{'} = \begin{pmatrix} h_{111} & h_{221} \\ h_{112} & h_{222} \\ h_{113} & h_{223} \end{pmatrix} \begin{pmatrix} 1 & 0 \\ 0 & 0 \end{pmatrix} = \begin{pmatrix} h_{111} & 0 \\ h_{112} & 0 \\ h_{113} & 0 \end{pmatrix}, \tag{G.22}$$

and

$$h^{''} = \begin{pmatrix} h_{111} & h_{221} \\ h_{112} & h_{222} \\ h_{113} & h_{223} \end{pmatrix} \begin{pmatrix} 0 & 0 \\ 1 & 0 \end{pmatrix} = \begin{pmatrix} h_{221} & 0 \\ h_{222} & 0 \\ h_{223} & 0 \end{pmatrix}. \tag{G.23}$$

G.3 CP-asymmetry calculation

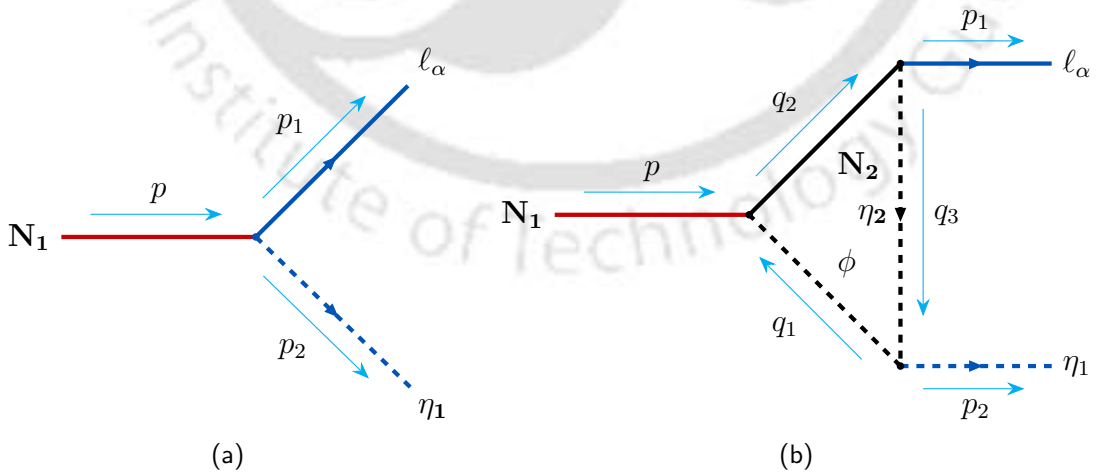

Figure G.3: Feynman diagrams corresponds to $N_1 \to \ell_\alpha \eta_1$ is relevant for Leptogenesis.

The vertex factors for the processes in Fig . G.3 is,

$$N_j \to \ell_\alpha \eta_j : \ -ih_{jj\alpha} P_R; \tag{G.24}$$

$$N_2 \to N_1 \phi : \ iy_{12\phi} C^{\dagger}; \quad \eta_2 \to \eta_1 \phi : \ -i\mu_{12\phi}\,. \tag{G.25}$$

$$\Gamma_{N_1\to\ell_\alpha\bar{\eta}_1}=\Gamma_{N_1\to\bar{\ell}_\alpha\eta_1}=2\frac{h_{11\alpha}h^*_{11\alpha}}{32\pi m^3_{N_1}}(m^2_{N_1}+m^2_\alpha-m^2_{\eta_1})\sqrt{(m^2_{N_1}-m^2_\alpha+m^2_{\eta_1})^2-4m^2_{\eta_1}m^2_{N_1}}\,. \tag{G.26}$$

In the above equation, the factor 2 arises due to the presence of two potential decay channels, $N_1\to\nu\eta^0_1$ and $N_1\to l^-\eta^+_1$.

The cross term which related to CP asymmetry parameter $\varepsilon=\dfrac{2\int_{\text{phase space}} Im[\mathcal{M}_{tree}\mathcal{M}^\dagger_{loop}]}{\Gamma_{N_1}}$

$$\begin{aligned}\mathcal{I}_{\text{vertex}}&=\int\frac{d^4q_2}{(2\pi)^4}\overline{u}_\alpha(-ih_{22\alpha}P_R)\frac{-i(\not{q}_2+m_{N_2})C}{q^2_2-m^2_{N_2}+i\epsilon}(iy_{12\phi}C^\dagger)\frac{u^c_{N_1}(-i\mu_{12\phi})}{q^2_3-m^2_{\eta_2}+i\epsilon}\frac{1}{q^2_1-m^2_\phi+i\epsilon}\underbrace{\left[\overline{u}_\alpha(-ih_{11\alpha}P_R)u^c_{N_1}\right]^\dagger}_{\mathcal{M}^\dagger_{tree}}\\&=(-ih_{22\alpha}y_{12\phi}\mu_{12\phi}h^*_{11\alpha})\int\frac{d^4q_2}{(2\pi)^4}\frac{\overline{u}_\alpha P_R(\not{q}_2+m_{N_2})}{q^2_2-m^2_{N_2}+i\epsilon}\frac{u^c_{N_1}}{q^2_3-m^2_{\eta_2}+i\epsilon}\frac{(u^T_{N_1}C^\dagger P_L u_\alpha)}{q^2_1-m^2_\phi+i\epsilon}\,.\end{aligned} \tag{G.27}$$

After summing over final spins and averaging over initial spins, we get,

$$\begin{aligned}\mathcal{I}_{\text{vertex}}&=(-ih_{22\alpha}y_{12\phi}\mu_{12\phi}h^*_{11\alpha})\frac{1}{2}\int\frac{d^4q_2}{(2\pi)^4}\frac{Tr\left[P_R(\not{q}_2+m_{N_2})(-\not{p}+m_{N_1})P_L(\not{p}_1+m_\alpha)\right]}{(q^2_2-m^2_{N_2}+i\epsilon)(q^2_3-m^2_{\eta_2}+i\epsilon)(q^2_1-m^2_\phi+i\epsilon)}\\&=(ih_{22\alpha}y_{12\phi}\mu_{12\phi}h^*_{11\alpha})\int\frac{d^4q_2}{(2\pi)^4}\frac{m_{N_2}p.p_1-m_{N_1}p_1.q_2}{(q^2_2-m^2_{N_2}+i\epsilon)(q^2_3-m^2_{\eta_2}+i\epsilon)(q^2_1-m^2_\phi+i\epsilon)}\,.\end{aligned} \tag{G.28}$$

To calculate the imaginary part of the amplitude, which is related to the discontinuity of the amplitude, we use the cutting rule to calculate this. The proper cutting through the propagators associated with momenta q_1 and q_3. Thus, we make the replacement,

$$\frac{1}{q^2_1-m^2_\phi+i\epsilon}\to-2\pi i\delta(q^2_1-m^2_\phi)\Theta(E_\phi)=-2\pi i\delta((p-q_2)^2-m^2_\phi)\Theta(m_{N_1}-E_{N_2})\,,$$

$$\frac{1}{q^2_3-m^2_{\eta_2}+i\epsilon}\to-2\pi i\delta((p_1-q_2)^2-m^2_{\eta_2})\Theta(E_{\eta_2})\,,$$

where,

$$2p.p_1=m^2_{N_1}+m^2_\alpha-m^2_{\eta_1}\,.$$

$$p_1.q_2=E_\alpha E_{N_2}-|\mathbf{p}_1||\mathbf{q}_2|\cos\theta\ \text{ and }\ |\mathbf{p}_1|=|\mathbf{p}_2|=\frac{1}{2m_{N_1}}\sqrt{(m^2_{N_1}+m^2_{\eta_1}-m^2_\alpha)^2-4m^2_{N_1}m^2_{\eta_1}}\,.$$

and θ is the angle between $\mathbf{p}_1$ and $\mathbf{q}_2$. Putting all of these together we obtain ($\epsilon\to0$),

$$\begin{aligned}\text{Disc}(\mathcal{I}'_{\text{vertex}})&=\frac{-i}{4\pi^2}\int dE_{N_2}d^3q_2\frac{m_{N_2}p.p_1-m_{N_1}(E_\alpha E_{N_2}-|\mathbf{p}_1||\mathbf{q}_2|\cos\theta))}{q^2_2-m^2_{N_2}}\\&\times\delta[(p-q_2)^2-m^2_\phi]\delta[(p_1-q_2)^2-m^2_{\eta_2}]\Theta(m_{N_1}-E_{N_2})\Theta(E_\alpha-E_{N_2})\end{aligned} \tag{G.29}$$

$$\delta[(p-q_2)^2-m^2_\phi]=\delta[E^2_{N_2}-2m_{N_1}E_{N_2}+m^2_{N_1}-|\mathbf{q}_2|^2-m^2_\phi]=-\frac{\delta[E_{N_2}-(m_{N_1}-\sqrt{|\mathbf{q}_2|^2+m^2_\phi})]}{2\sqrt{|\mathbf{q}_2|^2+m^2_\phi}}$$

$$\text{Disc}(\mathcal{I}^{'}_{\text{vertex}}) = \frac{i}{4\pi^2}\int \frac{|\mathbf{q_2}|^2}{2\sqrt{|\mathbf{q_2}|^2+m_\phi^2}} d|\mathbf{q_2}| d\Omega \frac{m_{N_2} p.p_1 - m_{N_1}\left[E_\alpha(m_{N_1}-\sqrt{|\mathbf{q_2}|^2+m_\phi^2}) - |\mathbf{p_1}||\mathbf{q_2}|\cos\theta\right]}{m_{N_1}^2 - m_{N_2}^2 + m_\phi^2 - 2m_{N_1}\sqrt{|\mathbf{q_2}|^2+m_\phi^2}}$$
$$\times\delta[m_\alpha^2 + m_{N_1}^2 + m_\phi^2 - m_{\eta_2}^2 - 2E_\alpha(m_{N_1}-\sqrt{|\mathbf{q_2}|^2+m_\phi^2}) - 2m_{N_1}\sqrt{|\mathbf{q_2}|^2+m_\phi^2} + 2|\mathbf{p_1}||\mathbf{q_2}|\cos\theta]$$
$$\times\Theta[(m_{N_1}-\sqrt{|\mathbf{q_2}|^2+m_\phi^2}) - E_\alpha]$$

$$\delta\left[\cos\theta - \frac{1}{2|\mathbf{p_1}||\mathbf{q_2}|}(-m_{N_1}^2 + m_{\eta_2}^2 - m_\phi^2 - m_\alpha^2 + \sqrt{|\mathbf{p_1}|^2+m_\alpha^2}(m_{N_1}-\sqrt{|\mathbf{q_2}|^2+m_\phi^2}) + 2m_{N_1}\sqrt{|\mathbf{q_2}|^2+m_\phi^2})\right]\frac{1}{2|\mathbf{p_1}||\mathbf{q_2}|}, \tag{G.30}$$

$$\text{Disc}(\mathcal{I}^{'}_{\text{vertex}}) = \frac{i}{8\pi}\int \frac{|\mathbf{q_2}|^2}{\sqrt{|\mathbf{q_2}|^2+m_\phi^2}} d|\mathbf{q_2}| \frac{m_{N_2}m_{N_1}E_\alpha - E_\alpha m_{N_1}^2 + E_\alpha m_{N_1}\sqrt{|\mathbf{q_2}|^2+m_\phi^2} + m_{N_1}|\mathbf{p_1}||\mathbf{q_2}|\cos\theta}{m_{N_1}^2 - m_{N_2}^2 + m_\phi^2 - 2m_{N_1}\sqrt{|\mathbf{q_2}|^2+m_\phi^2}}$$
$$\times \frac{\delta\left[\cos\theta - \frac{(-m_{N_1}^2+m_{\eta_2}^2-m_\phi^2-m_\alpha^2+\sqrt{|\mathbf{p_1}|^2+m_\alpha^2}(m_{N_1}-\sqrt{|\mathbf{q_2}|^2+m_\phi^2})+2m_{N_1}\sqrt{|\mathbf{q_2}|^2+m_\phi^2})}{2|\mathbf{p_1}||\mathbf{q_2}|}\right] d\cos\theta}{|\mathbf{p_1}||\mathbf{q_2}|}$$
$$\times\Theta[(m_{N_1}-\sqrt{|\mathbf{q_2}|^2+m_\phi^2}) - E_\alpha]$$

$$\text{Disc}(\mathcal{I}^{'}_{\text{vertex}}) = \frac{-i}{8\pi}\int_0^A \frac{m_{N_1}^2|\mathbf{q_0}|\, d|\mathbf{q_0}|}{\sqrt{|\mathbf{q_0}|^2+m_\phi^2}\times\sqrt{(m_{N_1}^2-m_\alpha^2+m_{\eta_1}^2)^2 - 4m_{\eta_1}^2 m_{N_1}^2}}$$
$$\times\frac{\left(m_{N_1} - m_{\eta_1} + m_\alpha - \frac{m_{N_1}}{m_{N_2}}(m_{N_1}^2 + m_\alpha^2 - m_{\eta_1}^2) + m_\phi^2 - 2m_{N_1}\sqrt{|\mathbf{q_0}|^2+m_\phi^2}\right)}{m_{N_1}^2 - m_{N_2}^2 + m_\phi^2 - 2m_{N_1}\sqrt{|\mathbf{q_0}|^2+m_\phi^2}}, \tag{G.31}$$

where the upper limit of the integration

$$A = \sqrt{\left(m_{N_1} - \frac{(m_{N_1}^2 + m_\alpha^2 - m_{\eta_1}^2)}{2m_{N_1}}\right)^2 - m_\phi^2}$$

comes from the theta function $\Theta(m_{N_1}-\sqrt{|\mathbf{q_2}|^2+m_\phi^2}) - E_\alpha)$.

$$\text{Disc}(\mathcal{I}^{'}_{\text{vertex}}) = -\frac{m_{N_1}\left((\sqrt{5-2C+C^2-4G}-2\sqrt{\sigma}) + (D-r+\sqrt{r}\,G)\ln\left[\frac{1-r+\sigma-(2-G)}{1-r+\sigma-2\sqrt{\sigma}}\right]\right)}{2\sqrt{(2-G)^2-4\eta_1}}, \tag{G.32}$$

where

$$C = (\eta_1 - l'),\ D = (\eta_2 - l'),\ G = (1-\eta_1+l'),$$
$$\eta_1 = \frac{m_{\eta_1}^2}{m_{N_1}^2},\ \eta_2 = \frac{m_{\eta_2}^2}{m_{N_1}^2},\ \sigma = \frac{m_\phi^2}{m_{N_1}^2},\ r = \frac{m_{N_2}^2}{m_{N_1}^2},\ l' = \frac{m_\alpha^2}{m_{N_1}^2}$$

Now the imaginary part of $\mathrm{Im}(\mathcal{I}'_{\mathrm{vertex}}) = \dfrac{1}{2i}\mathrm{Disc}(\mathcal{I}'_{\mathrm{vertex}})$

$$\Gamma_{\mathrm{total}} = \Gamma + \overline{\Gamma} = 2\Gamma_{N_1\to\ell_\alpha\eta_1}$$

2-body phase space factor $V_{N_1\longrightarrow\eta_1 l} = 2\dfrac{|\mathbf{p_1}|}{8\pi E_{cm}^2} = 2\dfrac{|\mathbf{p_1}|}{8\pi m_{N_1}^2}$

$$\varepsilon_{N_1\to\ell_\alpha\eta_1} = -\frac{4}{\Gamma_{\mathrm{tot}}}\mathrm{Im}(\mathcal{F}_{\mathrm{vertex}})\mathrm{Im}(\mathcal{I}'_{\mathrm{vertex}})V_{N_1\to\ell\eta_1}, \tag{G.33}$$

where $\mathrm{Im}(\mathcal{F}_{\mathrm{vertex}})$ is the vertex factor of the loop integration written as

$$\mathrm{Im}(\mathcal{F}_{\mathrm{vertex}}) = \mathrm{Im}(h_{22\alpha}y_{12\phi}\mu_{12\phi}h^*_{11\alpha}). \tag{G.34}$$

Finally the CP asymmetry from N_1 decay can be written as $\varepsilon_{N_1} = \sum_{\alpha=1}^{3}\varepsilon_{N_1\to\ell_\alpha\eta_1}$

$$\varepsilon_{N_1} = \sum_{\alpha=1}^{3}\frac{\mathrm{Im}(\mathcal{F}_{\mathrm{vertex}})}{8\pi M_{N_1}}\frac{\left((\sqrt{(1-C)^2+4(1-G)}-2\sqrt{\sigma})+(D-r+\sqrt{r}G)\ln\left[\dfrac{1-r+\sigma-(2-G)}{1-r+\sigma-2\sqrt{\sigma}}\right]\right)}{(h_{11\alpha}h^*_{11\alpha})\,G\,\sqrt{(2-G)^2-4\eta_1}}. \tag{G.35}$$

With the approximation $l' \to 0$ this expression will look like

$$\varepsilon_{N_1} = \sum_{\alpha=1}^{3}\frac{\mathrm{Im}(\mathcal{F}_{\mathrm{vertex}})}{8\pi M_1}\frac{\left[(1+\eta_1)-2\sqrt{\sigma}+\left(\eta_2-r+(1-\eta_1)\sqrt{r}\right)\left(\ln\left[\sigma-r-\eta_1\right]-\ln\left[1-r+\sigma-2\sqrt{\sigma}\right]\right)\right]}{(h_{11\alpha}h^*_{11\alpha})(1-\eta_1)^2}. \tag{G.36}$$

Further with additional approximations $\eta_1 \to 0,\ \eta_2 \to 0$ and $\sigma \to 0$, this expression will transform to

$$\varepsilon_{N_1} = \sum_{\alpha=1}^{3}\frac{\mathrm{Im}(\mathcal{F}_{\mathrm{vertex}})}{8\pi(h_{11\alpha}h^*_{11\alpha})M_1}\left(1+r\ln\left[1-\frac{1}{r}\right]-\sqrt{r}\ln\left[1-\frac{1}{r}\right]\right). \tag{G.37}$$

We have verified our asymmetry parameter in the limit $m_{\eta_{1,2}} \to 0$ and $m_\phi \to 0$, comparing it with the results from [749], except for a negative sign. In Fig . G.4, we illustrate the role of the rotation angle $\mathrm{z} = a + i\,b$ in the asymmetry parameter ε_{N_1}, taking into account the active neutrino masses. While a and b are unconstrained by theoretical or experimental limits, their influence on ε_{N_1} remains largely constant, with typical values around $\varepsilon_{N_1} \sim 10^{-2.5}$. However, a notable decrease in ε_{N_1} is observed within the yellow-shaded region, where it drops to $\lesssim 10^{-4}$. The maximum value of ε_{N_1} ($\sim 10^{-1}$) occurs for $\{a = 1,\ b = 0.4\}$. Beyond this point, increasing a results in periodic variations in ε_{N_1}.

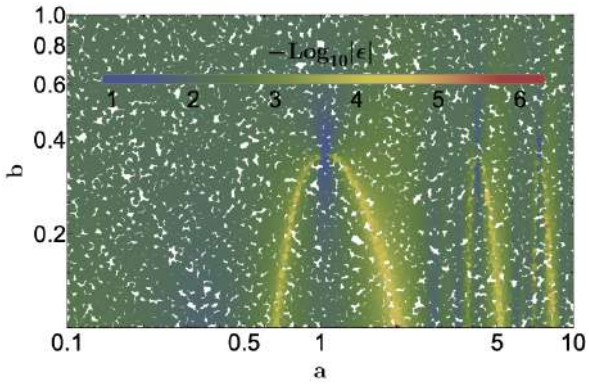

Figure G.4: This figure illustrates the dependency of the parameters a and b on the asymmetry (ε_{N_1}) after accounting for the constraints imposed by neutrino masses. We are fixing other parameters as: $\mathrm{m}_{\mathrm{N}_1} = 2\ \mathrm{TeV}$, $\mathrm{m}_{\mathrm{N}_2} = 6\ \mathrm{TeV}$, $\mathrm{m}_{\phi} = 0.5\ \mathrm{TeV}$, $\mathrm{m}_{\eta^0_{\mathrm{I}_1}} = 0.4\ \mathrm{TeV}$, $\mathrm{m}_{\eta^0_{\mathrm{I}_2}} = \mathrm{m}_{\eta^0_{\mathrm{I}_1}} + \mathrm{m}_{\phi} + 1\ \mathrm{GeV}$, $\mathrm{m}_{\eta^0_{\mathrm{R}_k}} = \mathrm{m}_{\eta^0_{\mathrm{I}_k}} + 2\ \mathrm{GeV}$, $\mathrm{m}_{\eta^+_{\mathrm{k}}} = \mathrm{m}_{\eta^0_{\mathrm{I}_k}} + 3\ \mathrm{GeV}$, $\mu_{12\phi} = \mathrm{m}_{\phi}$, $\mathrm{y}_{12\phi} = 1$, $\lambda_{kkH} = 0.01$, with $k = 1,\ 2$.

Bibliography

[1] G. Bertone, D. Hooper and J. Silk, *Particle dark matter: Evidence, candidates and constraints*, *Phys. Rept.* **405** (2005) 279 [hep-ph/0404175].

[2] G. Bertone and D. Hooper, *History of dark matter*, *Rev. Mod. Phys.* **90** (2018) 045002 [1605.04909].

[3] F. Zwicky, *On the Masses of Nebulae and of Clusters of Nebulae*, *Astrophys. J.* **86** (1937) 217.

[4] F. Zwicky, *Die Rotverschiebung von extragalaktischen Nebeln*, *Helv. Phys. Acta* **6** (1933) 110.

[5] Y. Sofue and V. Rubin, *Rotation curves of spiral galaxies*, *Ann. Rev. Astron. Astrophys.* **39** (2001) 137 [astro-ph/0010594].

[6] E. Hayashi and S. D. M. White, *How Rare is the Bullet Cluster?*, *Mon. Not. Roy. Astron. Soc.* **370** (2006) L38 [astro-ph/0604443].

[7] Planck collaboration, *Planck 2018 results. VI. Cosmological parameters*, *Astron. Astrophys.* **641** (2020) A6 [1807.06209].

[8] A. Friedmann, *Über die Krümmung des Raumes*, *Zeitschrift fur Physik* **10** (1922) 377.

[9] G. Lemaître, *Un Univers homogène de masse constante et de rayon croissant rendant compte de la vitesse radiale des nébuleuses extra-galactiques*, *Annales de la Société Scientifique de Bruxelles* **47** (1927) 49.

[10] A. Salam and J. C. Ward, *Electromagnetic and weak interactions*, *Phys. Lett.* **13** (1964) 168.

[11] S. Weinberg, *A Model of Leptons*, *Phys. Rev. Lett.* **19** (1967) 1264.

[12] Y. Nambu, *String-Like Configurations in the Weinberg-Salam Theory*, *Nucl. Phys. B* **130** (1977) 505.

[13] J. J. Thomson, *Xl. cathode rays*, *The London, Edinburgh, and Dublin Philosophical Magazine and Journal of Science* **44** (1897) 293 [https://doi.org/10.1080/14786449708621070].

[14] J. J. Thomson, *Lviii. on the masses of the ions in gases at low pressures*, *The London, Edinburgh, and Dublin Philosophical Magazine and Journal of Science* **48** (1899) 547 [https://doi.org/10.1080/14786449908621447].

[15] P. W. Higgs, *Broken Symmetries and the Masses of Gauge Bosons*, *Phys. Rev. Lett.* **13** (1964) 508.

[16] ATLAS collaboration, *Observation of a new particle in the search for the Standard Model Higgs boson with the ATLAS detector at the LHC*, *Phys. Lett. B* **716** (2012) 1 [1207.7214].

[17] CMS collaboration, *Observation of a New Boson at a Mass of 125 GeV with the CMS Experiment at the LHC*, *Phys. Lett. B* **716** (2012) 30 [1207.7235].

[18] Particle Data Group collaboration, *Review of particle physics*, *Phys. Rev. D* **110** (2024) 030001.

[19] B. Altschul, *Bound on the Photon Charge from the Phase Coherence of Extragalactic Radiation*, *Phys. Rev. Lett.* **98** (2007) 261801 [hep-ph/0703126].

[20] C. Caprini, S. Biller and P. G. Ferreira, *Constraints on the electrical charge asymmetry of the universe*, *JCAP* **02** (2005) 006 [hep-ph/0310066].

[21] D. D. Ryutov, *Using Plasma Physics to Weigh the Photon*, *Plasma Phys. Control. Fusion* **49** (2007) B429.

[22] C.-M. Chang, J.-J. Wei, K.-L. Meng, S.-B. Zhang, H.-X. Gao, J.-J. Geng et al., *Bounding the photon mass with gravitationally lensed fast radio bursts*, 2412.09806.

[23] D. D. Ryutov, *Relating the Proca Photon Mass and Cosmic Vector Potential via Solar Wind*, *Phys. Rev. Lett.* **103** (2009) 201803.

[24] A. S. Goldhaber and M. M. Nieto, *Photon and Graviton Mass Limits*, *Rev. Mod. Phys.* **82** (2010) 939 [0809.1003].

[25] L. Bonetti, J. Ellis, N. E. Mavromatos, A. S. Sakharov, E. K. Sarkisyan-Grinbaum and A. D. A. M. Spallicci, *FRB 121102 Casts New Light on the Photon Mass*, *Phys. Lett. B* **768** (2017) 326 [1701.03097].

[26] F. Halzen and A. D. Martin, *QUARKS AND LEPTONS: AN INTRODUCTORY COURSE IN MODERN PARTICLE PHYSICS*. 1984.

[27] M. D. Schwartz, *Quantum Field Theory and the Standard Model*. Cambridge University Press, 3, 2014.

[28] P. B. Pal, *An Introductory Course of Particle Physics*. CRC Press, 7, 2014, 10.1201/b17199.

[29] M. E. Peskin and D. V. Schroeder, *An Introduction to quantum field theory*. Addison-Wesley, Reading, USA, 1995, 10.1201/9780429503559.

[30] T.-P. .-.-.-. Cheng and L.-F. .-.-.-. Li, *Gauge Theory of Elementary Particle Physics*. Oxford University Press, Oxford, UK, 1984.

[31] J. Goldstone, *Field Theories with Superconductor Solutions*, *Nuovo Cim.* **19** (1961) 154.

[32] J. Goldstone, A. Salam and S. Weinberg, *Broken Symmetries*, *Phys. Rev.* **127** (1962) 965.

[33] C. S. Wu, E. Ambler, R. W. Hayward, D. D. Hoppes and R. P. Hudson, *Experimental Test of Parity Conservation in β Decay*, *Phys. Rev.* **105** (1957) 1413.

[34] M. Goldhaber, L. Grodzins and A. W. Sunyar, *Helicity of Neutrinos*, *Phys. Rev.* **109** (1958) 1015.

[35] Gargamelle Neutrino collaboration, *Observation of Neutrino Like Interactions Without Muon Or Electron in the Gargamelle Neutrino Experiment*, *Phys. Lett. B* **46** (1973) 138.

[36] ALEPH, DELPHI, L3, OPAL, SLD, LEP Electroweak Working Group, SLD Electroweak Group, SLD Heavy Flavour Group collaboration, *Precision electroweak measurements on the Z resonance*, *Phys. Rept.* **427** (2006) 257 [hep-ex/0509008].

[37] F. Jegerlehner, *The hierarchy problem of the electroweak Standard Model revisited*, 1305.6652.

[38] G. Burdman, *New solutions to the hierarchy problem*, *Braz. J. Phys.* **37** (2007) 506 [hep-ph/0703194].

[39] N. Arkani-Hamed, S. Dimopoulos and G. R. Dvali, *The Hierarchy problem and new dimensions at a millimeter*, *Phys. Lett. B* **429** (1998) 263 [hep-ph/9803315].

[40] H. Georgi, H. R. Quinn and S. Weinberg, *Hierarchy of Interactions in Unified Gauge Theories*, *Phys. Rev. Lett.* **33** (1974) 451.

[41] J. Schwichtenberg, *Gauge Coupling Unification without Supersymmetry*, *Eur. Phys. J. C* **79** (2019) 351 [1808.10329].

[42] J. R. Ellis, K. Enqvist, D. V. Nanopoulos and F. Zwirner, *Aspects of the Superunification of Strong, Electroweak and Gravitational Interactions*, *Nucl. Phys. B* **276** (1986) 14.

[43] H. Georgi and S. L. Glashow, *Unity of All Elementary Particle Forces*, *Phys. Rev. Lett.* **32** (1974) 438.

[44] M. Sher, *Electroweak Higgs Potentials and Vacuum Stability*, *Phys. Rept.* **179** (1989) 273.

[45] G. Isidori, G. Ridolfi and A. Strumia, *On the metastability of the standard model vacuum*, *Nucl. Phys. B* **609** (2001) 387 [hep-ph/0104016].

[46] J. Elias-Miro, J. R. Espinosa, G. F. Giudice, G. Isidori, A. Riotto and A. Strumia, *Higgs mass implications on the stability of the electroweak vacuum*, *Phys. Lett. B* **709** (2012) 222 [1112.3022].

[47] G. Hiller, T. Höhne, D. F. Litim and T. Steudtner, *Vacuum stability in the Standard Model and beyond*, *Phys. Rev. D* **110** (2024) 115017 [2401.08811].

[48] S. M. Barr, *Solving the Strong CP Problem Without the Peccei-Quinn Symmetry*, *Phys. Rev. Lett.* **53** (1984) 329.

[49] S. M. Barr, *The Strong CP Problem in Unified Models*, *Phys. Rev. D* **23** (1981) 2434.

[50] J. E. Kim, *Weak Interaction Singlet and Strong CP Invariance*, *Phys. Rev. Lett.* **43** (1979) 103.

[51] R. D. Peccei and H. R. Quinn, *CP Conservation in the Presence of Instantons*, *Phys. Rev. Lett.* **38** (1977) 1440.

[52] E. Corbelli and P. Salucci, *The Extended Rotation Curve and the Dark Matter Halo of M33*, *Mon. Not. Roy. Astron. Soc.* **311** (2000) 441 [astro-ph/9909252].

[53] E. Corbelli, *Dark matter and visible baryons in M33*, *Mon. Not. Roy. Astron. Soc.* **342** (2003) 199 [astro-ph/0302318].

[54] WMAP Science Team collaboration, *Results from the Wilkinson Microwave Anisotropy Probe*, *PTEP* **2014** (2014) 06B102 [1404.5415].

[55] K. G. Begeman, A. H. Broeils and R. H. Sanders, *Extended rotation curves of spiral galaxies: Dark haloes and modified dynamics*, *Mon. Not. Roy. Astron. Soc.* **249** (1991) 523.

[56] WMAP collaboration, *Three-year Wilkinson Microwave Anisotropy Probe (WMAP) observations: temperature analysis*, *Astrophys. J. Suppl.* **170** (2007) 288 [astro-ph/0603451].

[57] D. Clowe, M. Bradac, A. H. Gonzalez, M. Markevitch, S. W. Randall, C. Jones et al., *A direct empirical proof of the existence of dark matter*, *Astrophys. J. Lett.* **648** (2006) L109 [astro-ph/0608407].

[58] A. G. Riess et al., *A Comprehensive Measurement of the Local Value of the Hubble Constant with 1 km s^{-1} Mpc^{-1} Uncertainty from the Hubble Space Telescope and the SH0ES Team*, *Astrophys. J. Lett.* **934** (2022) L7 [2112.04510].

[59] T. D. Brandt, *Constraints on MACHO Dark Matter from Compact Stellar Systems in Ultra-Faint Dwarf Galaxies*, *Astrophys. J. Lett.* **824** (2016) L31 [1605.03665].

[60] S. Profumo, L. Giani and O. F. Piattella, *An Introduction to Particle Dark Matter*, *Universe* **5** (2019) 213 [1910.05610].

[61] A. Del Popolo, *Nonbaryonic Dark Matter in Cosmology*, *Int. J. Mod. Phys. D* **23** (2014) 1430005 [1305.0456].

[62] E. W. Kolb and M. S. Turner, *The Early Universe*, vol. 69. 1990, 10.1201/9780429492860.

[63] D. Feldman, Z. Liu and P. Nath, *The Stueckelberg Z-prime Extension with Kinetic Mixing and Milli-Charged Dark Matter From the Hidden Sector*, *Phys. Rev. D* **75** (2007) 115001 [hep-ph/0702123].

[64] Z. Bogorad and N. Toro, *Ultralight millicharged dark matter via misalignment*, *JHEP* **07** (2022) 035 [2112.11476].

[65] S. Davidson, S. Hannestad and G. Raffelt, *Updated bounds on millicharged particles*, *JHEP* **05** (2000) 003 [hep-ph/0001179].

[66] K. Griest, A. M. Cieplak and M. J. Lehner, *Experimental Limits on Primordial Black Hole Dark Matter from the First 2 yr of Kepler Data*, *Astrophys. J.* **786** (2014) 158 [1307.5798].

[67] R. Murgia, G. Scelfo, M. Viel and A. Raccanelli, *Lyman-α Forest Constraints on Primordial Black Holes as Dark Matter*, *Phys. Rev. Lett.* **123** (2019) 071102 [1903.10509].

[68] K. K. Rogers and H. V. Peiris, *Strong Bound on Canonical Ultralight Axion Dark Matter from the Lyman-Alpha Forest*, *Phys. Rev. Lett.* **126** (2021) 071302 [2007.12705].

[69] V. Iršič, M. Viel, M. G. Haehnelt, J. S. Bolton and G. D. Becker, *First constraints on fuzzy dark matter from Lyman-α forest data and hydrodynamical simulations*, *Phys. Rev. Lett.* **119** (2017) 031302 [1703.04683].

[70] W. Hu, R. Barkana and A. Gruzinov, *Cold and fuzzy dark matter*, *Phys. Rev. Lett.* **85** (2000) 1158 [astro-ph/0003365].

[71] M. A. Amin and M. Mirbabayi, *A Lower Bound on Dark Matter Mass*, *Phys. Rev. Lett.* **132** (2024) 221004 [2211.09775].

[72] M. Cirelli, A. Strumia and J. Zupan, *Dark Matter*, 2406.01705.

[73] PLANET, MICROFUN, OGLE collaboration, *Limb-darkening measurements for a cool red giant in microlensing event OGLE 2004-BLG-482*, *Astron. Astrophys.* **525** (2011) A15 [0912.2312].

[74] C. Boehm, M. J. Dolan and C. McCabe, *A Lower Bound on the Mass of Cold Thermal Dark Matter from Planck*, *JCAP* **08** (2013) 041 [1303.6270].

[75] K. Griest and M. Kamionkowski, *Unitarity Limits on the Mass and Radius of Dark Matter Particles*, *Phys. Rev. Lett.* **64** (1990) 615.

[76] H. Kim and E. Kuflik, *Superheavy Thermal Dark Matter*, *Phys. Rev. Lett.* **123** (2019) 191801 [1906.00981].

[77] A. Berlin and N. Blinov, *Thermal Dark Matter Below an MeV*, *Phys. Rev. Lett.* **120** (2018) 021801 [1706.07046].

[78] D. V. Nguyen, D. Sarnaaik, K. K. Boddy, E. O. Nadler and V. Gluscevic, *Observational constraints on dark matter scattering with electrons*, *Phys. Rev. D* **104** (2021) 103521 [2107.12380].

[79] Q. Decant, J. Heisig, D. C. Hooper and L. Lopez-Honorez, *Lyman-α constraints on freeze-in and superWIMPs*, *JCAP* **03** (2022) 041 [2111.09321].

[80] B. Dasgupta and J. Kopp, *Sterile Neutrinos*, *Phys. Rept.* **928** (2021) 1 [2106.05913].

[81] D. Naredo-Tuero, M. Escudero, E. Fernández-Martínez, X. Marcano and V. Poulin, *Critical look at the cosmological neutrino mass bound*, *Phys. Rev. D* **110** (2024) 123537 [2407.13831].

[82] C. Di Paolo, F. Nesti and F. L. Villante, *Phase space mass bound for fermionic dark matter from dwarf spheroidal galaxies*, *Mon. Not. Roy. Astron. Soc.* **475** (2018) 5385 [1704.06644].

[83] W. Pauli, *Dear radioactive ladies and gentlemen*, *Phys. Today* **31N9** (1978) 27.

[84] F. Reines and C. L. Cowan, *Detection of the free neutrino*, *Phys. Rev.* **92** (1953) 830.

[85] C. L. Cowan, F. Reines, F. B. Harrison, H. W. Kruse and A. D. McGuire, *Detection of the free neutrino: A Confirmation*, *Science* **124** (1956) 103.

[86] R. Davis, Jr., D. S. Harmer and K. C. Hoffman, *Search for neutrinos from the sun*, *Phys. Rev. Lett.* **20** (1968) 1205.

[87] V. N. Gribov and B. Pontecorvo, *Neutrino astronomy and lepton charge*, *Phys. Lett. B* **28** (1969) 493.

[88] Super-Kamiokande collaboration, *Study of the atmospheric neutrino flux in the multi-GeV energy range*, *Phys. Lett. B* **436** (1998) 33 [hep-ex/9805006].

[89] Super-Kamiokande collaboration, *Evidence for oscillation of atmospheric neutrinos*, *Phys. Rev. Lett.* **81** (1998) 1562 [hep-ex/9807003].

[90] SNO collaboration, *Direct evidence for neutrino flavor transformation from neutral current interactions in the Sudbury Neutrino Observatory*, *Phys. Rev. Lett.* **89** (2002) 011301 [nucl-ex/0204008].

[91] KamLAND collaboration, *First results from KamLAND: Evidence for reactor anti-neutrino disappearance*, *Phys. Rev. Lett.* **90** (2003) 021802 [hep-ex/0212021].

[92] B. Pontecorvo, *Mesonium and anti-mesonium*, *Sov. Phys. JETP* **6** (1957) 429.

[93] B. Pontecorvo, *Inverse beta processes and nonconservation of lepton charge*, *Zh. Eksp. Teor. Fiz.* **34** (1957) 247.

[94] Z. Maki, M. Nakagawa and S. Sakata, *Remarks on the unified model of elementary particles*, *Prog. Theor. Phys.* **28** (1962) 870.

[95] B. Pontecorvo, *Neutrino Experiments and the Problem of Conservation of Leptonic Charge*, *Zh. Eksp. Teor. Fiz.* **53** (1967) 1717.

[96] E. Majorana, *Teoria simmetrica dell'elettrone e del positrone*, *Nuovo Cim.* **14** (1937) 171.

[97] S. M. Bilenky and B. Pontecorvo, *Lepton Mixing and Neutrino Oscillations*, *Phys. Rept.* **41** (1978) 225.

[98] S. M. Bilenky, J. Hosek and S. T. Petcov, *On Oscillations of Neutrinos with Dirac and Majorana Masses*, *Phys. Lett. B* **94** (1980) 495.

[99] M. Gell-Mann, P. Ramond and R. Slansky, *Complex Spinors and Unified Theories*, *Conf. Proc. C* **790927** (1979) 315 [1306.4669].

[100] Z.-z. Xing and S. Zhou, *Neutrinos in particle physics, astronomy and cosmology*. 2011.

[101] P. F. de Salas, D. V. Forero, S. Gariazzo, P. Martínez-Miravé, O. Mena, C. A. Ternes et al., *2020 global reassessment of the neutrino oscillation picture*, *JHEP* **02** (2021) 071 [2006.11237].

[102] KATRIN collaboration, *Direct neutrino-mass measurement based on 259 days of KATRIN data*, 2406.13516.

[103] KamLAND-Zen collaboration, *Search for Majorana Neutrinos with the Complete KamLAND-Zen Dataset*, 2406.11438.

[104] S. Weinberg, *Baryon and Lepton Nonconserving Processes*, *Phys. Rev. Lett.* **43** (1979) 1566.

[105] R. N. Mohapatra and G. Senjanovic, *Neutrino Mass and Spontaneous Parity Nonconservation*, *Phys. Rev. Lett.* **44** (1980) 912.

[106] G. Anamiati, O. Castillo-Felisola, R. M. Fonseca, J. C. Helo and M. Hirsch, *High-dimensional neutrino masses*, *JHEP* **12** (2018) 066 [1806.07264].

[107] X. Marcano Imaz, *Lepton flavor violation from low scale seesaw neutrinos with masses reachable at the LHC*, Ph.D. thesis, U. Autonoma, Madrid (main), 6, 2017. 1710.08032. 10.1007/978-3-319-94604-7.

[108] K. Hamaguchi, *Cosmological baryon asymmetry and neutrinos: Baryogenesis via leptogenesis in supersymmetric theories*, Ph.D. thesis, Tokyo U., 1, 2002. hep-ph/0212305.

[109] I. Masina, *The Problem of neutrino masses in extensions of the standard model*, *Int. J. Mod. Phys. A* **16** (2001) 5101 [hep-ph/0107220].

[110] S. S. C. Law, *Neutrino Models and Leptogenesis*, Ph.D. thesis, Melbourne U., 2008. 0901.1232.

[111] R. Cepedello Pérez, *Radiative neutrino masses: A window to new physics*, Ph.D. thesis, Valencia U., IFIC, 2021. 2105.01896.

[112] Y. F. P. Gonzalez, *Massive Neutrinos: Phenomenological and Cosmological Consequences*, Ph.D. thesis, Universidade de São Paulo, Brasil, Sao Paulo U., 2017. 1712.06675. 10.11606/T.43.2017.tde-14122017-162727.

[113] F.-X. Josse-Michaux, *Recent developments in thermal leptogenesis: the role of flavours in various seesaw realisations*, Ph.D. thesis, Orsay, LPT, 2008. 0809.4960.

[114] T. Yanagida, *Horizontal gauge symmetry and masses of neutrinos*, *Conf. Proc. C* **7902131** (1979) 95.

[115] P. Minkowski, $\mu \to e\gamma$ *at a Rate of One Out of* 10^9 *Muon Decays?*, *Phys. Lett. B* **67** (1977) 421.

[116] H. Fritzsch, M. Gell-Mann and P. Minkowski, *Vector - Like Weak Currents and New Elementary Fermions*, *Phys. Lett. B* **59** (1975) 256.

[117] R. N. Mohapatra and G. Senjanovic, *Neutrino Masses and Mixings in Gauge Models with Spontaneous Parity Violation*, *Phys. Rev. D* **23** (1981) 165.

[118] W. Konetschny and W. Kummer, *Nonconservation of Total Lepton Number with Scalar Bosons*, *Phys. Lett. B* **70** (1977) 433.

[119] T. P. Cheng and L.-F. Li, *Neutrino Masses, Mixings and Oscillations in* $SU(2)$ *x* $U(1)$ *Models of Electroweak Interactions*, *Phys. Rev. D* **22** (1980) 2860.

[120] Y. Cheng, X.-G. He, Z.-L. Huang and M.-W. Li, *Type-II seesaw triplet scalar effects on neutrino trident scattering*, *Phys. Lett. B* **831** (2022) 137218 [2204.05031].

[121] S. Mandal, O. G. Miranda, G. Sanchez Garcia, J. W. F. Valle and X.-J. Xu, *Toward deconstructing the simplest seesaw mechanism*, *Phys. Rev. D* **105** (2022) 095020 [2203.06362].

[122] P. S. B. Dev, B. Dutta, T. Ghosh, T. Han, H. Qin and Y. Zhang, *Leptonic scalars and collider signatures in a UV-complete model*, *JHEP* **03** (2022) 068 [2109.04490].

[123] R. Foot, H. Lew, X. G. He and G. C. Joshi, *Seesaw Neutrino Masses Induced by a Triplet of Leptons*, *Z. Phys. C* **44** (1989) 441.

[124] E. Ma, *Pathways to naturally small neutrino masses*, *Phys. Rev. Lett.* **81** (1998) 1171 [hep-ph/9805219].

[125] I. Dorsner and P. Fileviez Perez, *Upper Bound on the Mass of the Type III Seesaw Triplet in an* $SU(5)$ *Model*, *JHEP* **06** (2007) 029 [hep-ph/0612216].

[126] A. Batra, P. Bharadwaj, S. Mandal, R. Srivastava and J. W. F. Valle, *Phenomenology of the simplest linear seesaw mechanism*, *JHEP* **07** (2023) 221 [2305.00994].

[127] S. M. Boucenna, S. Morisi and J. W. F. Valle, *The low-scale approach to neutrino masses*, *Adv. High Energy Phys.* **2014** (2014) 831598 [1404.3751].

[128] A. Das, S. Goswami, K. N. Vishnudath and T. Nomura, *Constraining a general* $U(1)'$ *inverse seesaw model from vacuum stability, dark matter and collider*, *Phys. Rev. D* **101** (2020) 055026 [1905.00201].

[129] E. Fernandez-Martinez, M. Pierre, E. Pinsard and S. Rosauro-Alcaraz, *Inverse Seesaw, dark matter and the Hubble tension*, *Eur. Phys. J. C* **81** (2021) 954 [2106.05298].

[130] A. Zee, *A Theory of Lepton Number Violation, Neutrino Majorana Mass, and Oscillation*, *Phys. Lett. B* **93** (1980) 389.

[131] K. S. Babu and J. Julio, *Two-Loop Neutrino Mass Generation through Leptoquarks*, *Nucl. Phys. B* **841** (2010) 130 [1006.1092].

[132] L. M. Krauss, S. Nasri and M. Trodden, *A Model for neutrino masses and dark matter*, *Phys. Rev. D* **67** (2003) 085002 [hep-ph/0210389].

[133] M. Gustafsson, J. M. No and M. A. Rivera, *Predictive Model for Radiatively Induced Neutrino Masses and Mixings with Dark Matter*, *Phys. Rev. Lett.* **110** (2013) 211802 [1212.4806].

[134] E. Ma, *Verifiable radiative seesaw mechanism of neutrino mass and dark matter*, *Phys. Rev. D* **73** (2006) 077301 [hep-ph/0601225].

[135] S. Saad, *Simplest Radiative Dirac Neutrino Mass Models*, *Nucl. Phys. B* **943** (2019) 114636 [1902.07259].

[136] M. Reig, D. Restrepo, J. W. F. Valle and O. Zapata, *Bound-state dark matter and Dirac neutrino masses*, *Phys. Rev. D* **97** (2018) 115032 [1803.08528].

[137] C. Bonilla, E. Ma, E. Peinado and J. W. F. Valle, *Two-loop Dirac neutrino mass and WIMP dark matter*, *Phys. Lett. B* **762** (2016) 214 [1607.03931].

[138] J. W. F. Valle and C. A. Vaquera-Araujo, *Dynamical seesaw mechanism for Dirac neutrinos*, *Phys. Lett. B* **755** (2016) 363 [1601.05237].

[139] E. Ma and R. Srivastava, *Dirac or inverse seesaw neutrino masses with $B - L$ gauge symmetry and S_3 flavor symmetry*, *Phys. Lett. B* **741** (2015) 217 [1411.5042].

[140] Y. Farzan and E. Ma, *Dirac neutrino mass generation from dark matter*, *Phys. Rev. D* **86** (2012) 033007 [1204.4890].

[141] M. Kawasaki and K. Murai, *Lepton asymmetric universe*, *JCAP* **08** (2022) 041 [2203.09713].

[142] I. M. Oldengott and D. J. Schwarz, *Improved constraints on lepton asymmetry from the cosmic microwave background*, *EPL* **119** (2017) 29001 [1706.01705].

[143] E. Aver, D. A. Berg, K. A. Olive, R. W. Pogge, J. J. Salzer and E. D. Skillman, *Improving helium abundance determinations with Leo P as a case study*, *JCAP* **03** (2021) 027 [2010.04180].

[144] A. Matsumoto et al., *EMPRESS. VIII. A New Determination of Primordial He Abundance with Extremely Metal-poor Galaxies: A Suggestion of the Lepton Asymmetry and Implications for the Hubble Tension*, *Astrophys. J.* **941** (2022) 167 [2203.09617].

[145] R. J. Cooke, M. Pettini and C. C. Steidel, *One Percent Determination of the Primordial Deuterium Abundance*, *Astrophys. J.* **855** (2018) 102 [1710.11129].

[146] B. Fields and S. Sarkar, *Big-Bang nucleosynthesis (2006 Particle Data Group mini-review)*, astro-ph/0601514.

[147] A. Strumia, *Baryogenesis via leptogenesis*, in *Les Houches Summer School on Theoretical Physics: Session 84: Particle Physics Beyond the Standard Model*, pp. 655–680, 8, 2006, hep-ph/0608347.

[148] A. D. Sakharov, *Violation of CP Invariance, C asymmetry, and baryon asymmetry of the universe*, *Pisma Zh. Eksp. Teor. Fiz.* **5** (1967) 32.

[149] M. B. Gavela, P. Hernandez, J. Orloff and O. Pene, *Standard model CP violation and baryon asymmetry*, *Mod. Phys. Lett. A* **9** (1994) 795 [hep-ph/9312215].

[150] M. Yoshimura, *Unified Gauge Theories and the Baryon Number of the Universe*, *Phys. Rev. Lett.* **41** (1978) 281.

[151] S. Weinberg, *Cosmological Production of Baryons*, *Phys. Rev. Lett.* **42** (1979) 850.

[152] D. V. Nanopoulos and S. Weinberg, *Mechanisms for Cosmological Baryon Production*, *Phys. Rev. D* **20** (1979) 2484.

[153] A. G. Cohen, D. B. Kaplan and A. E. Nelson, *Progress in electroweak baryogenesis*, *Ann. Rev. Nucl. Part. Sci.* **43** (1993) 27 [hep-ph/9302210].

[154] P. Huet and E. Sather, *Electroweak baryogenesis and standard model CP violation*, *Phys. Rev. D* **51** (1995) 379 [hep-ph/9404302].

[155] I. Affleck and M. Dine, *A New Mechanism for Baryogenesis*, *Nucl. Phys. B* **249** (1985) 361.

[156] M. Dine, L. Randall and S. D. Thomas, *Baryogenesis from flat directions of the supersymmetric standard model*, *Nucl. Phys. B* **458** (1996) 291 [hep-ph/9507453].

[157] W. Buchmuller, P. Di Bari and M. Plumacher, *The Neutrino mass window for baryogenesis*, *Nucl. Phys. B* **665** (2003) 445 [hep-ph/0302092].

[158] A. Pilaftsis and T. E. J. Underwood, *Resonant leptogenesis*, *Nucl. Phys. B* **692** (2004) 303 [hep-ph/0309342].

[159] M. A. Luty, *Baryogenesis via leptogenesis*, *Phys. Rev. D* **45** (1992) 455.

[160] M. Plumacher, *Baryogenesis and lepton number violation*, *Z. Phys. C* **74** (1997) 549 [hep-ph/9604229].

[161] R. Barbieri, P. Creminelli, A. Strumia and N. Tetradis, *Baryogenesis through leptogenesis*, *Nucl. Phys. B* **575** (2000) 61 [hep-ph/9911315].

[162] M. Fukugita and T. Yanagida, *Baryogenesis Without Grand Unification*, *Phys. Lett. B* **174** (1986) 45.

[163] A. D. Dolgov, *NonGUT baryogenesis*, *Phys. Rept.* **222** (1992) 309.

[164] S. Skadhauge, *Sphalerons and electroweak baryogenesis*, Ph.D. thesis, Copenhagen U., 1996.

[165] M. D'Onofrio, K. Rummukainen and A. Tranberg, *The Sphaleron Rate through the Electroweak Cross-over*, *JHEP* **08** (2012) 123 [1207.0685].

[166] J. A. Harvey and M. S. Turner, *Cosmological baryon and lepton number in the presence of electroweak fermion number violation*, *Phys. Rev. D* **42** (1990) 3344.

[167] S. Y. Khlebnikov and M. E. Shaposhnikov, *The Statistical Theory of Anomalous Fermion Number Nonconservation*, *Nucl. Phys. B* **308** (1988) 885.

[168] T. Inui, T. Ichihara, Y. Mimura and N. Sakai, *Cosmological baryon asymmetry in supersymmetric Standard Models and heavy particle effects*, *Phys. Lett. B* **325** (1994) 392 [hep-ph/9310268].

[169] M. Bolz, W. Buchmuller and M. Plumacher, *Baryon asymmetry and dark matter*, *Phys. Lett. B* **443** (1998) 209 [hep-ph/9809381].

[170] S. F. King, S. K. Manna, R. Roshan and A. Sil, *Leptogenesis with Majoron Dark Matter*, 2412.14121.

[171] A. Liu, Z.-L. Han, Y. Jin and F.-X. Yang, *Leptogenesis and dark matter from a low scale seesaw mechanism*, *Phys. Rev. D* **101** (2020) 095005 [2001.04085].

[172] F.-X. Josse-Michaux and E. Molinaro, *A Common Framework for Dark Matter, Leptogenesis and Neutrino Masses*, *Phys. Rev. D* **84** (2011) 125021 [1108.0482].

[173] Y. Cui and M. Shamma, *WIMP Cogenesis for Asymmetric Dark Matter and the Baryon Asymmetry*, *JHEP* **12** (2020) 046 [2002.05170].

[174] A. Falkowski, E. Kuflik, N. Levi and T. Volansky, *Light Dark Matter from Leptogenesis*, *Phys. Rev. D* **99** (2019) 015022 [1712.07652].

[175] A. Falkowski, J. T. Ruderman and T. Volansky, *Asymmetric Dark Matter from Leptogenesis*, *JHEP* **05** (2011) 106 [1101.4936].

[176] P. Di Bari, P. O. Ludl and S. Palomares-Ruiz, *Unifying leptogenesis, dark matter and high-energy neutrinos with right-handed neutrino mixing via Higgs portal*, *JCAP* **11** (2016) 044 [1606.06238].

[177] P.-H. Gu and U. Sarkar, *Radiative Neutrino Mass, Dark Matter and Leptogenesis*, *Phys. Rev. D* **77** (2008) 105031 [0712.2933].

[178] R. Kitano, H. Murayama and M. Ratz, *Unified origin of baryons and dark matter*, *Phys. Lett. B* **669** (2008) 145 [0807.4313].

[179] W. Buchmuller, L. Covi, K. Hamaguchi, A. Ibarra and T. Yanagida, *Gravitino Dark Matter in R-Parity Breaking Vacua*, *JHEP* **03** (2007) 037 [hep-ph/0702184].

[180] T. Hugle, M. Platscher and K. Schmitz, *Low-Scale Leptogenesis in the Scotogenic Neutrino Mass Model*, *Phys. Rev. D* **98** (2018) 023020 [1804.09660].

[181] X. Qi and H. Sun, *Interplay between dark matter and leptogenesis in a common framework*, *JHEP* **09** (2023) 118 [2208.13345].

[182] A. Ahriche, A. Arhrib, A. Jueid, S. Nasri and A. de La Puente, *Mono-Higgs Signature in the Scotogenic Model with Majorana Dark Matter*, *Phys. Rev. D* **101** (2020) 035038 [1811.00490].

[183] D. Borah, P. S. B. Dev and A. Kumar, *TeV scale leptogenesis, inflaton dark matter and neutrino mass in a scotogenic model*, *Phys. Rev. D* **99** (2019) 055012 [1810.03645].

[184] A. Beniwal, J. Herrero-García, N. Leerdam, M. White and A. G. Williams, *The ScotoSinglet Model: a scalar singlet extension of the Scotogenic Model*, *JHEP* **21** (2020) 136 [2010.05937].

[185] I. M. Ávila, V. De Romeri, L. Duarte and J. W. F. Valle, *Phenomenology of scotogenic scalar dark matter*, *Eur. Phys. J. C* **80** (2020) 908 [1910.08422].

[186] V. De Romeri, M. Puerta and A. Vicente, *Dark matter in a charged variant of the Scotogenic model*, *Eur. Phys. J. C* **82** (2022) 623 [2106.00481].

[187] L. Sarma, P. Das and M. K. Das, *Scalar dark matter and leptogenesis in the minimal scotogenic model*, *Nucl. Phys. B* **963** (2021) 115300 [2004.13762].

[188] P. A. M. Dirac, *The Quantum theory of electron. 2.*, *Proc. Roy. Soc. Lond. A* **118** (1928) 351.

[189] T. Aoyama, M. Hayakawa, T. Kinoshita and M. Nio, *Complete Tenth-Order QED Contribution to the Muon g-2*, *Phys. Rev. Lett.* **109** (2012) 111808 [1205.5370].

[190] S. Laporta, *High-precision calculation of the 4-loop contribution to the electron g-2 in QED*, *Phys. Lett. B* **772** (2017) 232 [1704.06996].

[191] T. Aoyama, M. Hayakawa, T. Kinoshita and M. Nio, *Quantum electrodynamics calculation of lepton anomalous magnetic moments: Numerical approach to the perturbation theory of QED*, *PTEP* **2012** (2012) 01A107.

[192] S. J. Brodsky and J. D. Sullivan, *W BOSON CONTRIBUTION TO THE ANOMALOUS MAGNETIC MOMENT OF THE MUON*, *Phys. Rev.* **156** (1967) 1644.

[193] T. Burnett and M. J. Levine, *Intermediate vector boson contribution to the muon's anomalous magnetic moment*, *Phys. Lett. B* **24** (1967) 467.

[194] R. Jackiw and S. Weinberg, *Weak interaction corrections to the muon magnetic moment and to muonic atom energy levels*, *Phys. Rev. D* **5** (1972) 2396.

[195] I. Bars and M. Yoshimura, *Muon magnetic moment in a finite theory of weak and electromagnetic interactions*, *Phys. Rev. D* **6** (1972) 374.

[196] K. Fujikawa, B. W. Lee and A. I. Sanda, *Generalized Renormalizable Gauge Formulation of Spontaneously Broken Gauge Theories*, *Phys. Rev. D* **6** (1972) 2923.

[197] T. V. Kukhto, E. A. Kuraev, Z. K. Silagadze and A. Schiller, *The Dominant two loop electroweak contributions to the anomalous magnetic moment of the muon*, *Nucl. Phys. B* **371** (1992) 567.

[198] S. Peris, M. Perrottet and E. de Rafael, *Two loop electroweak corrections to the muon g-2: A New class of hadronic contributions*, *Phys. Lett. B* **355** (1995) 523 [hep-ph/9505405].

[199] A. Czarnecki, B. Krause and W. J. Marciano, *Electroweak corrections to the muon anomalous magnetic moment*, *Phys. Rev. Lett.* **76** (1996) 3267 [hep-ph/9512369].

[200] A. Czarnecki, W. J. Marciano and A. Vainshtein, *Refinements in electroweak contributions to the muon anomalous magnetic moment*, *Phys. Rev. D* **67** (2003) 073006 [hep-ph/0212229].

[201] C. Gnendiger, D. Stöckinger and H. Stöckinger-Kim, *The electroweak contributions to $(g-2)_\mu$ after the Higgs boson mass measurement*, *Phys. Rev. D* **88** (2013) 053005 [1306.5546].

[202] M. Hoferichter, B.-L. Hoid, B. Kubis, S. Leupold and S. P. Schneider, *Pion-pole contribution to hadronic light-by-light scattering in the anomalous magnetic moment of the muon*, *Phys. Rev. Lett.* **121** (2018) 112002 [1805.01471].

[203] G. Colangelo, M. Hoferichter, M. Procura and P. Stoffer, *Rescattering effects in the hadronic-light-by-light contribution to the anomalous magnetic moment of the muon*, *Phys. Rev. Lett.* **118** (2017) 232001 [1701.06554].

[204] T. Blum, N. Christ, M. Hayakawa, T. Izubuchi, L. Jin, C. Jung et al., *Connected and Leading Disconnected Hadronic Light-by-Light Contribution to the Muon Anomalous Magnetic Moment with a Physical Pion Mass*, *Phys. Rev. Lett.* **118** (2017) 022005 [1610.04603].

[205] A. Gérardin, H. B. Meyer and A. Nyffeler, *Lattice calculation of the pion transition form factor $\pi^0 \to \gamma^*\gamma^*$*, *Phys. Rev. D* **94** (2016) 074507 [1607.08174].

[206] J. Green, O. Gryniuk, G. von Hippel, H. B. Meyer and V. Pascalutsa, *Lattice QCD calculation of hadronic light-by-light scattering*, *Phys. Rev. Lett.* **115** (2015) 222003 [1507.01577].

[207] M. Davier, A. Hoecker, B. Malaescu and Z. Zhang, *A new evaluation of the hadronic vacuum polarisation contributions to the muon anomalous magnetic moment and to $\alpha(m_Z^2)$*, *Eur. Phys. J. C* **80** (2020) 241 [1908.00921].

[208] G. Colangelo, M. Hoferichter and P. Stoffer, *Two-pion contribution to hadronic vacuum polarization*, *JHEP* **02** (2019) 006 [1810.00007].

[209] RBC, UKQCD collaboration, *Calculation of the hadronic vacuum polarization contribution to the muon anomalous magnetic moment*, *Phys. Rev. Lett.* **121** (2018) 022003 [1801.07224].

[210] Budapest-Marseille-Wuppertal collaboration, *Hadronic vacuum polarization contribution to the anomalous magnetic moments of leptons from first principles*, *Phys. Rev. Lett.* **121** (2018) 022002 [1711.04980].

[211] M. Della Morte, A. Francis, V. Gülpers, G. Herdoíza, G. von Hippel, H. Horch et al., *The hadronic vacuum polarization contribution to the muon $g-2$ from lattice QCD*, *JHEP* **10** (2017) 020 [1705.01775].

[212] F. Jegerlehner, *Muon g – 2 theory: The hadronic part*, *EPJ Web Conf.* **166** (2018) 00022 [1705.00263].

[213] B. Chakraborty, C. T. H. Davies, P. G. de Oliviera, J. Koponen, G. P. Lepage and R. S. Van de Water, *The hadronic vacuum polarization contribution to a_μ from full lattice QCD*, *Phys. Rev. D* **96** (2017) 034516 [1601.03071].

[214] RBC, UKQCD collaboration, *The long-distance window of the hadronic vacuum polarization for the muon g-2*, 2410.20590.

[215] A. Kurz, T. Liu, P. Marquard and M. Steinhauser, *Hadronic contribution to the muon anomalous magnetic moment to next-to-next-to-leading order*, *Phys. Lett. B* **734** (2014) 144 [1403.6400].

[216] G. Colangelo, M. Hoferichter, A. Nyffeler, M. Passera and P. Stoffer, *Remarks on higher-order hadronic corrections to the muon $g-2$*, *Phys. Lett. B* **735** (2014) 90 [1403.7512].

[217] Muon g-2 collaboration, *Measurement of the Positive Muon Anomalous Magnetic Moment to 0.20 ppm*, *Phys. Rev. Lett.* **131** (2023) 161802 [2308.06230].

[218] Muon g-2 collaboration, *Measurement of the negative muon anomalous magnetic moment to 0.7 ppm*, *Phys. Rev. Lett.* **92** (2004) 161802 [hep-ex/0401008].

[219] L. Morel, Z. Yao, P. Cladé and S. Guellati-Khélifa, *Determination of the fine-structure constant with an accuracy of 81 parts per trillion*, *Nature* **588** (2020) 61.

[220] R. H. Parker, C. Yu, W. Zhong, B. Estey and H. Müller, *Measurement of the fine-structure constant as a test of the Standard Model*, *Science* **360** (2018) 191 [1812.04130].

[221] X. Fan, T. G. Myers, B. A. D. Sukra and G. Gabrielse, *Measurement of the Electron Magnetic Moment*, *Phys. Rev. Lett.* **130** (2023) 071801 [2209.13084].

[222] T. Aoyama, T. Kinoshita and M. Nio, *Theory of the Anomalous Magnetic Moment of the Electron*, *Atoms* **7** (2019) 28.

[223] ATLAS collaboration, *Tau anomalous magnetic moment measurements at ATLAS and CMS*, .

[224] M. Verducci, C. Roda, V. Cavasinni and N. Vignaroli, *Study of the measurement of the τ lepton anomalous magnetic moment in high energy lead-lead collisions at the LHC*, *Phys. Rev. D* **110** (2024) 052001 [2307.15160].

[225] MEG II collaboration, *A search for $\mu^+ \to e^+\gamma$ with the first dataset of the MEG II experiment*, *Eur. Phys. J. C* **84** (2024) 216 [2310.12614].

[226] MEG II collaboration, *The design of the MEG II experiment*, *Eur. Phys. J. C* **78** (2018) 380 [1801.04688].

[227] SINDRUM collaboration, *Search for the Decay $\mu^+ \to e^+e^+e^-$*, *Nucl. Phys. B* **299** (1988) 1.

[228] A. Blondel et al., *Research Proposal for an Experiment to Search for the Decay $\mu \to eee$*, 1301.6113.

[229] S. M. Barr, R. S. Chivukula and E. Farhi, *Electroweak Fermion Number Violation and the Production of Stable Particles in the Early Universe*, *Phys. Lett. B* **241** (1990) 387.

[230] D. B. Kaplan, *A Single explanation for both the baryon and dark matter densities*, *Phys. Rev. Lett.* **68** (1992) 741.

[231] S. Nussinov, *TECHNOCOSMOLOGY: COULD A TECHNIBARYON EXCESS PROVIDE A 'NATURAL' MISSING MASS CANDIDATE?*, *Phys. Lett. B* **165** (1985) 55.

[232] D. E. Kaplan, M. A. Luty and K. M. Zurek, *Asymmetric Dark Matter*, *Phys. Rev. D* **79** (2009) 115016 [0901.4117].

[233] M. L. Graesser, I. M. Shoemaker and L. Vecchi, *Asymmetric WIMP dark matter*, *JHEP* **10** (2011) 110 [1103.2771].

[234] M. J. Baker, J. Kopp and A. J. Long, *Filtered Dark Matter at a First Order Phase Transition*, *Phys. Rev. Lett.* **125** (2020) 151102 [1912.02830].

[235] D. Chway, T. H. Jung and C. S. Shin, *Dark matter filtering-out effect during a first-order phase transition*, *Phys. Rev. D* **101** (2020) 095019 [1912.04238].

[236] A. Azatov, M. Vanvlasselaer and W. Yin, *Dark Matter production from relativistic bubble walls*, *JHEP* **03** (2021) 288 [2101.05721].

[237] A. M. Green and B. J. Kavanagh, *Primordial Black Holes as a dark matter candidate*, *J. Phys. G* **48** (2021) 043001 [2007.10722].

[238] B. Carr and F. Kuhnel, *Primordial Black Holes as Dark Matter: Recent Developments*, *Ann. Rev. Nucl. Part. Sci.* **70** (2020) 355 [2006.02838].

[239] B. Carr, F. Kuhnel and M. Sandstad, *Primordial Black Holes as Dark Matter*, *Phys. Rev. D* **94** (2016) 083504 [1607.06077].

[240] S. Clesse and J. García-Bellido, *Seven Hints for Primordial Black Hole Dark Matter*, *Phys. Dark Univ.* **22** (2018) 137 [1711.10458].

[241] F. Capela, M. Pshirkov and P. Tinyakov, *Constraints on Primordial Black Holes as Dark Matter Candidates from Star Formation*, *Phys. Rev. D* **87** (2013) 023507 [1209.6021].

[242] M. Garny, M. Sandora and M. S. Sloth, *Planckian Interacting Massive Particles as Dark Matter*, *Phys. Rev. Lett.* **116** (2016) 101302 [1511.03278].

[243] J. Ren and H.-J. He, *Probing Gravitational Dark Matter*, *JCAP* **03** (2015) 052 [1410.6436].

[244] M. Garny, A. Palessandro, M. Sandora and M. S. Sloth, *Theory and Phenomenology of Planckian Interacting Massive Particles as Dark Matter*, *JCAP* **02** (2018) 027 [1709.09688].

[245] Y. Ema, K. Nakayama and Y. Tang, *Production of Purely Gravitational Dark Matter*, *JHEP* **09** (2018) 135 [1804.07471].

[246] C. Gross, S. Karamitsos, G. Landini and A. Strumia, *Gravitational Vector Dark Matter*, *JHEP* **03** (2021) 174 [2012.12087].

[247] M. A. G. Garcia, M. Pierre and S. Verner, *New window into gravitationally produced scalar dark matter*, *Phys. Rev. D* **108** (2023) 115024 [2305.14446].

[248] L. Husdal, *On Effective Degrees of Freedom in the Early Universe*, *Galaxies* **4** (2016) 78 [1609.04979].

[249] D. J. Fixsen, *The Temperature of the Cosmic Microwave Background*, *Astrophys. J.* **707** (2009) 916 [0911.1955].

[250] J. M. Cline, K. Kainulainen, P. Scott and C. Weniger, *Update on scalar singlet dark matter*, *Phys. Rev. D* **88** (2013) 055025 [1306.4710].

[251] W.-L. Guo and Y.-L. Wu, *The Real singlet scalar dark matter model*, *JHEP* **10** (2010) 083 [1006.2518].

[252] GAMBIT collaboration, *Status of the scalar singlet dark matter model*, *Eur. Phys. J. C* **77** (2017) 568 [1705.07931].

[253] S. Bhattacharya, P. Ghosh and S. Verma, *SIMPler realisation of Scalar Dark Matter*, *JCAP* **01** (2020) 040 [1904.07562].

[254] Y. Hochberg, E. Kuflik, T. Volansky and J. G. Wacker, *Mechanism for Thermal Relic Dark Matter of Strongly Interacting Massive Particles*, *Phys. Rev. Lett.* **113** (2014) 171301 [1402.5143].

[255] N. Bernal and X. Chu, $\mathbb{Z}_2$ *SIMP Dark Matter*, *JCAP* **01** (2016) 006 [1510.08527].

[256] S.-Y. Ho, *An asymmetric SIMP dark matter model*, *JHEP* **10** (2022) 182 [2207.13373].

[257] Y. Hochberg, E. Kuflik and H. Murayama, *SIMP Spectroscopy*, *JHEP* **05** (2016) 090 [1512.07917].

[258] D. Chowdhury and and S. Show, *SIMP dark matter during reheating*, 2410.02871.

[259] S.-Y. Ho, T. Toma and K. Tsumura, *A Radiative Neutrino Mass Model with SIMP Dark Matter*, *JHEP* **07** (2017) 101 [1705.00592].

[260] S.-M. Choi and H. M. Lee, *Resonant SIMP dark matter*, *Phys. Lett. B* **758** (2016) 47 [1601.03566].

[261] S.-M. Choi, H. M. Lee and M.-S. Seo, *Cosmic abundances of SIMP dark matter*, *JHEP* **04** (2017) 154 [1702.07860].

[262] S.-M. Choi and H. M. Lee, *SIMP dark matter with gauged Z_3 symmetry*, *JHEP* **09** (2015) 063 [1505.00960].

[263] S.-M. Choi, Y. Hochberg, E. Kuflik, H. M. Lee, Y. Mambrini, H. Murayama et al., *Vector SIMP dark matter*, *JHEP* **10** (2017) 162 [1707.01434].

[264] Y. Hochberg, *SIMP Dark Matter*, *SciPost Phys. Lect. Notes* **59** (2022) 1.

[265] L. J. Hall, K. Jedamzik, J. March-Russell and S. M. West, *Freeze-In Production of FIMP Dark Matter*, *JHEP* **03** (2010) 080 [0911.1120].

[266] F. Elahi, C. Kolda and J. Unwin, *UltraViolet Freeze-in*, *JHEP* **03** (2015) 048 [1410.6157].

[267] B. Barman, S. Bhattacharya and B. Grzadkowski, *Feebly coupled vector boson dark matter in effective theory*, *JHEP* **12** (2020) 162 [2009.07438].

[268] B. Barman, S. Bhattacharya and M. Zakeri, *Non-Abelian Vector Boson as FIMP Dark Matter*, *JCAP* **02** (2020) 029 [1905.07236].

[269] N. Bernal, F. Elahi, C. Maldonado and J. Unwin, *Ultraviolet Freeze-in and Non-Standard Cosmologies*, *JCAP* **11** (2019) 026 [1909.07992].

[270] A. Biswas, S. Ganguly and S. Roy, *Fermionic dark matter via UV and IR freeze-in and its possible X-ray signature*, *JCAP* **03** (2020) 043 [1907.07973].

[271] S.-L. Chen and Z. Kang, *On UltraViolet Freeze-in Dark Matter during Reheating*, *JCAP* **05** (2018) 036 [1711.02556].

[272] J. McDonald, *Warm Dark Matter via Ultra-Violet Freeze-In: Reheating Temperature and Non-Thermal Distribution for Fermionic Higgs Portal Dark Matter*, *JCAP* **08** (2016) 035 [1512.06422].

[273] R. Frumkin, Y. Hochberg, E. Kuflik and H. Murayama, *Thermal Dark Matter from Freeze-Out of Inverse Decays*, *Phys. Rev. Lett.* **130** (2023) 121001 [2111.14857].

[274] N. Bernal, M. Heikinheimo, T. Tenkanen, K. Tuominen and V. Vaskonen, *The Dawn of FIMP Dark Matter: A Review of Models and Constraints*, *Int. J. Mod. Phys. A* **32** (2017) 1730023 [1706.07442].

[275] C. E. Yaguna, *The Singlet Scalar as FIMP Dark Matter*, *JHEP* **08** (2011) 060 [1105.1654].

[276] F. D'Eramo and A. Lenoci, *Lower mass bounds on FIMP dark matter produced via freeze-in*, *JCAP* **10** (2021) 045 [2012.01446].

[277] A. Del Popolo and M. Le Delliou, *Small scale problems of the ΛCDM model: a short review*, *Galaxies* **5** (2017) 17 [1606.07790].

[278] S. Tulin and H.-B. Yu, *Dark Matter Self-interactions and Small Scale Structure*, *Phys. Rept.* **730** (2018) 1 [1705.02358].

[279] F. Governato, A. Zolotov, A. Pontzen, C. Christensen, S. H. Oh, A. M. Brooks et al., *Cuspy No More: How Outflows Affect the Central Dark Matter and Baryon Distribution in Lambda CDM Galaxies*, *Mon. Not. Roy. Astron. Soc.* **422** (2012) 1231 [1202.0554].

[280] W. J. G. de Blok, *The Core-Cusp Problem*, *Adv. Astron.* **2010** (2010) 789293 [0910.3538].

[281] M. Boylan-Kolchin and C.-P. Ma, *Major mergers of galaxy haloes: Cuspy or cored inner density profile?*, *Mon. Not. Roy. Astron. Soc.* **349** (2004) 1117 [astro-ph/0309243].

[282] J. S. Bullock, *Notes on the Missing Satellites Problem*, 1009.4505.

[283] M. S. Bovill and M. Ricotti, *Pre-reionization Fossils, Ultra-faint Dwarfs and the Missing Galactic Satellite Problem*, *Astrophys. J.* **693** (2009) 1859 [0806.2340].

[284] S. Kazantzidis, L. Mayer, C. Mastropietro, J. Diemand, J. Stadel and B. Moore, *Density profiles of cold dark matter substructure: Implications for the missing satellites problem*, *Astrophys. J.* **608** (2004) 663 [astro-ph/0312194].

[285] A. A. Klypin, A. V. Kravtsov, O. Valenzuela and F. Prada, *Where are the missing Galactic satellites?*, *Astrophys. J.* **522** (1999) 82 [astro-ph/9901240].

[286] M. Tomozeiu, L. Mayer and T. Quinn, *Tidal stirring of satellites with shallow density profiles prevents them from being too big to fail*, *The Astrophysical Journal Letters* **827** (2016) L15.

[287] M. Boylan-Kolchin, J. S. Bullock and M. Kaplinghat, *Too big to fail? The puzzling darkness of massive Milky Way subhaloes*, *Mon. Not. Roy. Astron. Soc.* **415** (2011) L40 [1103.0007].

[288] M. Boylan-Kolchin, J. S. Bullock and M. Kaplinghat, *Too big to fail? the puzzling darkness of massive milky way subhaloes*, *Monthly Notices of the Royal Astronomical Society: Letters* **415** (2011) L40.

[289] R. Kuzio de Naray, G. D. Martinez, J. S. Bullock and M. Kaplinghat, *The Case Against Warm or Self-Interacting Dark Matter as Explanations for Cores in Low Surface Brightness Galaxies*, *Astrophys. J. Lett.* **710** (2010) L161 [0912.3518].

[290] K. A. Oman et al., *The unexpected diversity of dwarf galaxy rotation curves*, *Mon. Not. Roy. Astron. Soc.* **452** (2015) 3650 [1504.01437].

[291] E. Romano-Diaz, I. Shlosman, Y. Hoffman and C. Heller, *Erasing Dark Matter Cusps in Cosmological Galactic Halos with Baryons*, *Astrophys. J. Lett.* **685** (2008) L105 [0808.0195].

[292] D. Cole, W. Dehnen and M. Wilkinson, *Weakening dark-matter cusps by clumpy baryonic infall*, *Mon. Not. Roy. Astron. Soc.* **416** (2011) 1118 [1105.4050].

[293] O. D. Elbert, J. S. Bullock, M. Kaplinghat, S. Garrison-Kimmel, A. S. Graus and M. Rocha, *A Testable Conspiracy: Simulating Baryonic Effects on Self-Interacting Dark Matter Halos*, *Astrophys. J.* **853** (2018) 109 [1609.08626].

[294] A. Del Popolo, *The Cusp/Core problem and the Secondary Infall Model*, *Astrophys. J.* **698** (2009) 2093 [0906.4447].

[295] A. M. Brooks, M. Kuhlen, A. Zolotov and D. Hooper, *A Baryonic Solution to the Missing Satellites Problem*, *Astrophys. J.* **765** (2013) 22 [1209.5394].

[296] M. H. Eriksen, M. T. Frandsen and M. H. From, *A cusp-core-like challenge for modified Newtonian dynamics*, *Astron. Astrophys.* **656** (2021) A123 [1906.07823].

[297] D. C. Rodrigues, P. L. de Oliveira, J. C. Fabris and G. Gentile, *Modified gravity models and the central cusp of dark matter haloes in galaxies*, *Mon. Not. Roy. Astron. Soc.* **445** (2014) 3823 [1409.7524].

[298] F. Lelli, S. S. McGaugh, J. M. Schombert and M. S. Pawlowski, *One law to rule them all: the radial acceleration relation of galaxies*, *The Astrophysical Journal* **836** (2017) 152.

[299] M. Milgrom, *A Modification of the Newtonian dynamics as a possible alternative to the hidden mass hypothesis*, *Astrophys. J.* **270** (1983) 365.

[300] S. Bhattacharya, P. Poulose and P. Ghosh, *Multipartite Interacting Scalar Dark Matter in the light of updated LUX data*, *JCAP* **04** (2017) 043 [1607.08461].

[301] S. Bhattacharya, S. Chakraborti and D. Pradhan, *Electroweak symmetry breaking and WIMP-FIMP dark matter*, *JHEP* **07** (2022) 091 [2110.06985].

[302] S.-M. Choi, J. Kim, P. Ko and J. Li, *A multi-component SIMP model with* $U(1)_X \to Z_2 \times Z_3$, *JHEP* **09** (2021) 028 [2103.05956].

[303] S.-Y. Ho, P. Ko and C.-T. Lu, *Scalar and fermion two-component SIMP dark matter with an accidental* $\mathbb{Z}_4$ *symmetry*, *JHEP* **03** (2022) 005 [2201.06856].

[304] M. Pandey, D. Majumdar and K. P. Modak, *Two Component Feebly Interacting Massive Particle (FIMP) Dark Matter*, *JCAP* **06** (2018) 023 [1709.05955].

[305] S. Bhattacharya, D. Pradhan and J. Lahiri, *Dynamics of pseudofeebly interacting massive particles in presence of thermal dark matter*, *Phys. Rev. D* **108** (2023) L111702 [2212.07622].

[306] S. Bhattacharya, J. Lahiri and D. Pradhan, *Detection possibility of a pseudo-FIMP in the presence of a thermal WIMP*, *Phys. Rev. D* **109** (2024) 095031 [2212.14846].

[307] S. Bhattacharya, L. Kolay and D. Pradhan, *Multiparticle scalar dark matter with $\mathbb{Z}_N$ symmetry*, 2410.16275.

[308] B. Díaz Sáez, K. Möhling and D. Stöckinger, *Two real scalar WIMP model in the assisted freeze-out scenario*, *JCAP* **10** (2021) 027 [2103.17064].

[309] A. Abada, D. Ghaffor and S. Nasri, *A Two-Singlet Model for Light Cold Dark Matter*, *Phys. Rev. D* **83** (2011) 095021 [1101.0365].

[310] L. Bian, R. Ding and B. Zhu, *Two Component Higgs-Portal Dark Matter*, *Phys. Lett. B* **728** (2014) 105 [1308.3851].

[311] A. Ahriche, A. Arhrib and S. Nasri, *Higgs Phenomenology in the Two-Singlet Model*, *JHEP* **02** (2014) 042 [1309.5615].

[312] A. Arhrib and M. Maniatis, *The two-real-singlet Dark Matter model*, *Phys. Lett. B* **796** (2019) 15 [1807.03554].

[313] A. Dutta Banik, M. Pandey, D. Majumdar and A. Biswas, *Two component WIMP–FImP dark matter model with singlet fermion, scalar and pseudo scalar*, *Eur. Phys. J. C* **77** (2017) 657 [1612.08621].

[314] S. Peyman Zakeri, S. Mohammad Moosavi Nejad, M. Zakeri and S. Yaser Ayazi, *A Minimal Model For Two-Component FIMP Dark Matter: A Basic Search*, *Chin. Phys. C* **42** (2018) 073101 [1801.09115].

[315] F. Costa, S. Khan and J. Kim, *A two-component vector WIMP — fermion FIMP dark matter model with an extended seesaw mechanism*, *JHEP* **12** (2022) 165 [2209.13653].

[316] M. W. Goodman and E. Witten, *Detectability of Certain Dark Matter Candidates*, *Phys. Rev. D* **31** (1985) 3059.

[317] D. N. Spergel and W. H. Press, *Effect of hypothetical, weakly interacting, massive particles on energy transport in the solar interior*, *Astrophys. J.* **294** (1985) 663.

[318] W. H. Press and D. N. Spergel, *Capture by the sun of a galactic population of weakly interacting massive particles*, *Astrophys. J.* **296** (1985) 679.

[319] I. Goldman and S. Nussinov, *Weakly Interacting Massive Particles and Neutron Stars*, *Phys. Rev. D* **40** (1989) 3221.

[320] A. K. Drukier, K. Freese and D. N. Spergel, *Detecting Cold Dark Matter Candidates*, *Phys. Rev. D* **33** (1986) 3495.

[321] J. Rich, D. Lloyd Owen and M. Spiro, *EXPERIMENTAL PARTICLE PHYSICS WITHOUT ACCELERATORS*, *Phys. Rept.* **151** (1987) 239.

[322] K. Griest, *Cross-Sections, Relic Abundance and Detection Rates for Neutralino Dark Matter*, *Phys. Rev. D* **38** (1988) 2357.

[323] K. Griest, *Calculations of Rates for Direct Detection of Neutralino Dark Matter*, *Phys. Rev. Lett.* **61** (1988) 666.

[324] G. Jungman, M. Kamionkowski and K. Griest, *Supersymmetric dark matter*, *Phys. Rept.* **267** (1996) 195 [hep-ph/9506380].

[325] R. J. Gaitskell, *Direct detection of dark matter*, *Ann. Rev. Nucl. Part. Sci.* **54** (2004) 315.

[326] I. M. Bloch, R. Essig, K. Tobioka, T. Volansky and T.-T. Yu, *Searching for Dark Absorption with Direct Detection Experiments*, *JHEP* **06** (2017) 087 [1608.02123].

[327] J. A. Dror, G. Elor and R. Mcgehee, *Directly Detecting Signals from Absorption of Fermionic Dark Matter*, *Phys. Rev. Lett.* **124** (2020) 18 [1905.12635].

[328] J. A. Dror, G. Elor and R. Mcgehee, *Absorption of Fermionic Dark Matter by Nuclear Targets*, *JHEP* **02** (2020) 134 [1908.10861].

[329] J. A. Dror, G. Elor, R. McGehee and T.-T. Yu, *Absorption of sub-MeV fermionic dark matter by electron targets*, *Phys. Rev. D* **103** (2021) 035001 [2011.01940].

[330] G. Afek, D. Carney and D. C. Moore, *Coherent Scattering of Low Mass Dark Matter from Optically Trapped Sensors*, *Phys. Rev. Lett.* **128** (2022) 101301 [2111.03597].

[331] F. Monteiro, G. Afek, D. Carney, G. Krnjaic, J. Wang and D. C. Moore, *Search for composite dark matter with optically levitated sensors*, *Phys. Rev. Lett.* **125** (2020) 181102 [2007.12067].

[332] M. Geller and O. Telem, *Self-destructing atomic dark matter*, *Phys. Rev. D* **104** (2021) 035010 [2001.11514].

[333] Y. Grossman, R. Harnik, O. Telem and Y. Zhang, *Self-Destructing Dark Matter*, *JHEP* **07** (2019) 017 [1712.00455].

[334] J. Bramante, J. Kumar and N. Raj, *Dark matter astrometry at underground detectors with multiscatter events*, *Phys. Rev. D* **100** (2019) 123016 [1910.05380].

[335] J. Bramante, B. Broerman, R. F. Lang and N. Raj, *Saturated Overburden Scattering and the Multiscatter Frontier: Discovering Dark Matter at the Planck Mass and Beyond*, *Phys. Rev. D* **98** (2018) 083516 [1803.08044].

[336] W. Yin, *Highly-boosted dark matter and cutoff for cosmic-ray neutrinos through neutrino portal*, *EPJ Web Conf.* **208** (2019) 04003 [1809.08610].

[337] T. Bringmann and M. Pospelov, *Novel direct detection constraints on light dark matter*, *Phys. Rev. Lett.* **122** (2019) 171801 [1810.10543].

[338] N. F. Bell, J. B. Dent, B. Dutta, S. Ghosh, J. Kumar, J. L. Newstead et al., *Cosmic-ray upscattered inelastic dark matter*, *Phys. Rev. D* **104** (2021) 076020 [2108.00583].

[339] J. Alvey, T. Bringmann and H. Kolesova, *No room to hide: implications of cosmic-ray upscattering for GeV-scale dark matter*, *JHEP* **01** (2023) 123 [2209.03360].

[340] S. Bhowmick, D. Ghosh and D. Sachdeva, *Blazar boosted dark matter — direct detection constraints on $\sigma e\chi$: role of energy dependent cross sections*, *JCAP* **07** (2023) 039 [2301.00209].

[341] M. Pospelov, *Secluded $U(1)$ below the weak scale*, *Phys. Rev. D* **80** (2009) 095002 [0811.1030].

[342] A. Berlin, D. Hooper and G. Krnjaic, *Thermal Dark Matter From A Highly Decoupled Sector*, *Phys. Rev. D* **94** (2016) 095019 [1609.02555].

[343] M. Pospelov, A. Ritz and M. B. Voloshin, *Secluded WIMP Dark Matter*, *Phys. Lett. B* **662** (2008) 53 [0711.4866].

[344] P. W. Graham, R. Harnik, S. Rajendran and P. Saraswat, *Exothermic Dark Matter*, *Phys. Rev. D* **82** (2010) 063512 [1004.0937].

[345] D. Tucker-Smith and N. Weiner, *Inelastic dark matter*, *Phys. Rev. D* **64** (2001) 043502 [hep-ph/0101138].

[346] D. Tucker-Smith and N. Weiner, *The Status of inelastic dark matter*, *Phys. Rev. D* **72** (2005) 063509 [hep-ph/0402065].

[347] C. A. J. O'Hare, A. M. Green, J. Billard, E. Figueroa-Feliciano and L. E. Strigari, *Readout strategies for directional dark matter detection beyond the neutrino background*, *Phys. Rev. D* **92** (2015) 063518 [1505.08061].

[348] P. Grothaus, M. Fairbairn and J. Monroe, *Directional Dark Matter Detection Beyond the Neutrino Bound*, *Phys. Rev. D* **90** (2014) 055018 [1406.5047].

[349] J. Kopp, T. Schwetz and J. Zupan, *Global interpretation of direct Dark Matter searches after CDMS-II results*, *JCAP* **02** (2010) 014 [0912.4264].

[350] G. Belanger, F. Boudjema, A. Pukhov and A. Semenov, *Dark matter direct detection rate in a generic model with micrOMEGAs 2.2*, *Comput. Phys. Commun.* **180** (2009) 747 [0803.2360].

[351] P. Ullio, M. Kamionkowski and P. Vogel, *Spin dependent WIMPs in DAMA?*, *JHEP* **07** (2001) 044 [hep-ph/0010036].

[352] A. L. Fitzpatrick, W. Haxton, E. Katz, N. Lubbers and Y. Xu, *The Effective Field Theory of Dark Matter Direct Detection*, *JCAP* **02** (2013) 004 [1203.3542].

[353] N. Anand, A. L. Fitzpatrick and W. C. Haxton, *Weakly interacting massive particle-nucleus elastic scattering response*, *Phys. Rev. C* **89** (2014) 065501.

[354] J. Herrero-Garcia, A. Scaffidi, M. White and A. G. Williams, *On the direct detection of multi-component dark matter: implications of the relic abundance*, *JCAP* **01** (2019) 008 [1809.06881].

[355] J. Herrero-Garcia, A. Scaffidi, M. White and A. G. Williams, *On the direct detection of multi-component dark matter: sensitivity studies and parameter estimation*, *JCAP* **11** (2017) 021 [1709.01945].

[356] LZ collaboration, *Dark Matter Search Results from 4.2 Tonne-Years of Exposure of the LUX-ZEPLIN (LZ) Experiment*, 2410.17036.

[357] PandaX-4T collaboration, *Dark Matter Search Results from the PandaX-4T Commissioning Run*, *Phys. Rev. Lett.* **127** (2021) 261802 [2107.13438].

[358] XENON collaboration, *First Dark Matter Search with Nuclear Recoils from the XENONnT Experiment*, *Phys. Rev. Lett.* **131** (2023) 041003 [2303.14729].

[359] SuperCDMS collaboration, *Results from the Super Cryogenic Dark Matter Search Experiment at Soudan*, *Phys. Rev. Lett.* **120** (2018) 061802 [1708.08869].

[360] DarkSide-50 collaboration, *Search for low-mass dark matter WIMPs with 12 ton-day exposure of DarkSide-50*, *Phys. Rev. D* **107** (2023) 063001 [2207.11966].

[361] DEAP collaboration, *Search for dark matter with a 231-day exposure of liquid argon using DEAP-3600 at SNOLAB*, *Phys. Rev. D* **100** (2019) 022004 [1902.04048].

[362] LUX collaboration, *Results of a Search for Sub-GeV Dark Matter Using 2013 LUX Data*, *Phys. Rev. Lett.* **122** (2019) 131301 [1811.11241].

[363] XENON collaboration, *Search for Light Dark Matter Interactions Enhanced by the Migdal Effect or Bremsstrahlung in XENON1T*, *Phys. Rev. Lett.* **123** (2019) 241803 [1907.12771].

[364] XENON collaboration, *Light Dark Matter Search with Ionization Signals in XENON1T*, *Phys. Rev. Lett.* **123** (2019) 251801 [1907.11485].

[365] SuperCDMS collaboration, *Search for Low-Mass Dark Matter with CDMSlite Using a Profile Likelihood Fit*, *Phys. Rev. D* **99** (2019) 062001 [1808.09098].

[366] SuperCDMS collaboration, *Search for low-mass dark matter via bremsstrahlung radiation and the Migdal effect in SuperCDMS*, *Phys. Rev. D* **107** (2023) 112013 [2302.09115].

[367] CRESST collaboration, *First results from the CRESST-III low-mass dark matter program*, *Phys. Rev. D* **100** (2019) 102002 [1904.00498].

[368] CRESST collaboration, *Results on sub-GeV dark matter from a 10 eV threshold CRESST-III silicon detector*, *Phys. Rev. D* **107** (2023) 122003 [2212.12513].

[369] DAMIC collaboration, *Results on low-mass weakly interacting massive particles from a 11 kg-day target exposure of DAMIC at SNOLAB*, *Phys. Rev. Lett.* **125** (2020) 241803 [2007.15622].

[370] NEWS-G collaboration, *First results from the NEWS-G direct dark matter search experiment at the LSM*, *Astropart. Phys.* **97** (2018) 54 [1706.04934].

[371] Y. Kahn and T. Lin, *Searches for light dark matter using condensed matter systems*, *Rept. Prog. Phys.* **85** (2022) 066901 [2108.03239].

[372] R. Essig, J. Mardon and T. Volansky, *Direct Detection of Sub-GeV Dark Matter*, *Phys. Rev. D* **85** (2012) 076007 [1108.5383].

[373] R. Catena, T. Emken, M. Matas, N. A. Spaldin and E. Urdshals, *Crystal responses to general dark matter-electron interactions*, *Phys. Rev. Res.* **3** (2021) 033149 [2105.02233].

[374] M. J. Dolan, F. Kahlhoefer and C. McCabe, *Directly detecting sub-GeV dark matter with electrons from nuclear scattering*, *Phys. Rev. Lett.* **121** (2018) 101801 [1711.09906].

[375] D. Baxter, Y. Kahn and G. Krnjaic, *Electron Ionization via Dark Matter-Electron Scattering and the Migdal Effect*, *Phys. Rev. D* **101** (2020) 076014 [1908.00012].

[376] M. Ibe, W. Nakano, Y. Shoji and K. Suzuki, *Migdal Effect in Dark Matter Direct Detection Experiments*, *JHEP* **03** (2018) 194 [1707.07258].

[377] J. D. Vergados and H. Ejiri, *The role of ionization electrons in direct neutralino detection*, *Phys. Lett. B* **606** (2005) 313 [hep-ph/0401151].

[378] N. F. Bell, J. B. Dent, B. Dutta, S. Ghosh, J. Kumar and J. L. Newstead, *Low-mass inelastic dark matter direct detection via the Migdal effect*, *Phys. Rev. D* **104** (2021) 076013 [2103.05890].

[379] J. E. Gunn, B. W. Lee, I. Lerche, D. N. Schramm and G. Steigman, *Some Astrophysical Consequences of the Existence of a Heavy Stable Neutral Lepton*, *Astrophys. J.* **223** (1978) 1015.

[380] L. Baldini, *Space-Based Cosmic-Ray and Gamma-Ray Detectors: a Review*, 1407.7631.

[381] F. W. Stecker, *The Cosmic Gamma-Ray Background from the Annihilation of Primordial Stable Neutral Heavy Leptons*, *Astrophys. J.* **223** (1978) 1032.

[382] M. Cirelli, P. D. Serpico and G. Zaharijas, *Bremsstrahlung gamma rays from light Dark Matter*, *JCAP* **11** (2013) 035 [1307.7152].

[383] J. R. Ellis, R. A. Flores, K. Freese, S. Ritz, D. Seckel and J. Silk, *Cosmic Ray Constraints on the Annihilations of Relic Particles in the Galactic Halo*, *Phys. Lett. B* **214** (1988) 403.

[384] ANTARES collaboration, *Search of Dark Matter Annihilation in the Galactic Centre using the ANTARES Neutrino Telescope*, *JCAP* **10** (2015) 068 [1505.04866].

[385] IceCube collaboration, *Search for neutrinos from decaying dark matter with IceCube*, *Eur. Phys. J. C* **78** (2018) 831 [1804.03848].

[386] C. A. Argüelles, A. Diaz, A. Kheirandish, A. Olivares-Del-Campo, I. Safa and A. C. Vincent, *Dark matter annihilation to neutrinos*, *Rev. Mod. Phys.* **93** (2021) 035007 [1912.09486].

[387] M. S. Turner and F. Wilczek, *Positron Line Radiation from Halo WIMP Annihilations as a Dark Matter Signature*, *Phys. Rev. D* **42** (1990) 1001.

[388] I. Cholis, L. Goodenough, D. Hooper, M. Simet and N. Weiner, *High Energy Positrons From Annihilating Dark Matter*, *Phys. Rev. D* **80** (2009) 123511 [0809.1683].

[389] AMS 02 collaboration, *The antimatter spectrometer (AMS-02): A particle physics detector in space*, *Nucl. Instrum. Meth. A* **588** (2008) 227.

[390] M. Cirelli, N. Fornengo, M. Taoso and A. Vittino, *Anti-helium from Dark Matter annihilations*, *JHEP* **08** (2014) 009 [1401.4017].

[391] E. Carlson, A. Coogan, T. Linden, S. Profumo, A. Ibarra and S. Wild, *Antihelium from Dark Matter*, *Phys. Rev. D* **89** (2014) 076005 [1401.2461].

[392] A. Shukla, A. Datta, P. von Doetinchem, D.-M. Gomez-Coral and C. Kanitz, *Large-scale Simulations of Antihelium Production in Cosmic-ray Interactions*, *Phys. Rev. D* **102** (2020) 063004 [2006.12707].

[393] J. Silk and M. Srednicki, *Cosmic Ray anti-Protons as a Probe of a Photino Dominated Universe*, *Phys. Rev. Lett.* **53** (1984) 624.

[394] F. W. Stecker, S. Rudaz and T. F. Walsh, *Galactic antiprotons from photinos*, *Phys. Rev. Lett.* **55** (1985) 2622.

[395] R. J. Protheroe, *Cosmic Ray Anti-protons in the Closed Galaxy Model*, *Astrophys. J.* **251** (1981) 387.

[396] F. Donato, N. Fornengo and P. Salati, *Anti-deuterons as a signature of supersymmetric dark matter*, *Phys. Rev. D* **62** (2000) 043003 [hep-ph/9904481].

[397] H. Baer and S. Profumo, *Low energy antideuterons: shedding light on dark matter*, *JCAP* **12** (2005) 008 [astro-ph/0510722].

[398] C. B. Brauninger and M. Cirelli, *Anti-deuterons from heavy Dark Matter*, *Phys. Lett. B* **678** (2009) 20 [0904.1165].

[399] Fermi-LAT collaboration, *Fermi-LAT Observations of High-Energy γ-Ray Emission Toward the Galactic Center*, *Astrophys. J.* **819** (2016) 44 [1511.02938].

[400] M. Ackermann, M. Ajello, W. Atwood, L. Baldini, G. Barbiellini, D. Bastieri et al., *Constraints on the galactic halo dark matter from fermi-lat diffuse measurements*, *The Astrophysical Journal* **761** (2012) 91.

[401] MAGIC, Fermi-LAT collaboration, *Limits to Dark Matter Annihilation Cross-Section from a Combined Analysis of MAGIC and Fermi-LAT Observations of Dwarf Satellite Galaxies*, *JCAP* **02** (2016) 039 [1601.06590].

[402] C. Thorpe-Morgan, D. Malyshev, C.-A. Stegen, A. Santangelo and J. Jochum, *Annihilating dark matter search with 12 yr of Fermi LAT data in nearby galaxy clusters*, *Mon. Not. Roy. Astron. Soc.* **502** (2021) 4039 [2010.11006].

[403] Fermi-LAT collaboration, *Search for extended gamma-ray emission from the Virgo galaxy cluster with Fermi-LAT*, *Astrophys. J.* **812** (2015) 159 [1510.00004].

[404] Fermi-LAT collaboration, *Search for Dark Matter Satellites using the FERMI-LAT*, *Astrophys. J.* **747** (2012) 121 [1201.2691].

[405] Fermi-LAT collaboration, *Limits on Dark Matter Annihilation Signals from the Fermi LAT 4-year Measurement of the Isotropic Gamma-Ray Background*, *JCAP* **09** (2015) 008 [1501.05464].

[406] VERITAS collaboration, *Dark Matter Constraints from a Joint Analysis of Dwarf Spheroidal Galaxy Observations with VERITAS*, *Phys. Rev. D* **95** (2017) 082001 [1703.04937].

[407] VERITAS collaboration, *Hunting for dark matter subhalos among the Fermi-LAT sources with VERITAS*, *PoS* **ICRC2015** (2016) 1216 [1509.00085].

[408] J. Aleksić et al., *Optimized dark matter searches in deep observations of Segue 1 with MAGIC*, *JCAP* **02** (2014) 008 [1312.1535].

[409] MAGIC collaboration, *Indirect dark matter searches in the dwarf satellite galaxy Ursa Major II with the MAGIC Telescopes*, *JCAP* **03** (2018) 009 [1712.03095].

[410] MAGIC collaboration, *A search for dark matter in Triangulum II with the MAGIC telescopes*, *Phys. Dark Univ.* **28** (2020) 100529 [2003.05260].

[411] H.E.S.S. collaboration, *Search for dark matter annihilation signatures in H.E.S.S. observations of Dwarf Spheroidal Galaxies*, *Phys. Rev. D* **90** (2014) 112012 [1410.2589].

[412] H.E.S.S. collaboration, *Search for dark matter signals towards a selection of recently detected DES dwarf galaxy satellites of the Milky Way with H.E.S.S.*, *Phys. Rev. D* **102** (2020) 062001 [2008.00688].

[413] H.E.S.S. collaboration, *H.E.S.S. Limits on Linelike Dark Matter Signatures in the 100 GeV to 2 TeV Energy Range Close to the Galactic Center*, *Phys. Rev. Lett.* **117** (2016) 151302 [1609.08091].

[414] A. Albert et al., *Results from the search for dark matter in the Milky Way with 9 years of data of the ANTARES neutrino telescope*, *Phys. Lett. B* **769** (2017) 249 [1612.04595].

[415] ANTARES collaboration, *Search for dark matter towards the Galactic Centre with 11 years of ANTARES data*, *Phys. Lett. B* **805** (2020) 135439 [1912.05296].

[416] IceCube collaboration, *Search for Dark Matter Annihilation in the Galactic Center with IceCube-79*, *Eur. Phys. J. C* **75** (2015) 492 [1505.07259].

[417] IceCube collaboration, *The IceCube Neutrino Observatory - Contributions to ICRC 2015 Part IV: Searches for Dark Matter and Exotic Particles*, 1510.05226.

[418] IceCube collaboration, *Search for neutrino lines from dark matter annihilation and decay with IceCube*, *Phys. Rev. D* **108** (2023) 102004 [2303.13663].

[419] A. D. Avrorin et al., *Dark matter constraints from an observation of dSphs and the LMC with the Baikal NT200*, *J. Exp. Theor. Phys.* **125** (2017) 80 [1612.03836].

[420] BAIKAL collaboration, *A search for neutrino signal from dark matter annihilation in the center of the Milky Way with Baikal NT200*, *Astropart. Phys.* **81** (2016) 12 [1512.01198].

[421] D. Maurin, H. Dembinski, J. Gonzalez, I. C. Maris and F. Melot, *Cosmic-Ray Database Update: Ultra-High Energy, Ultra-Heavy, and Antinuclei Cosmic-Ray Data (CRDB v4.0)*, *Universe* **6** (2020) 102 [2005.14663].

[422] HAWC collaboration, *Search for decaying dark matter in the Virgo cluster of galaxies with HAWC*, *Phys. Rev. D* **109** (2024) 043034 [2309.03973].

[423] MAGIC collaboration, *Constraining Dark Matter lifetime with a deep gamma-ray survey of the Perseus Galaxy Cluster with MAGIC*, *Phys. Dark Univ.* **22** (2018) 38 [1806.11063].

[424] LHAASO collaboration, *Constraints on Ultraheavy Dark Matter Properties from Dwarf Spheroidal Galaxies with LHAASO Observations*, *Phys. Rev. Lett.* **133** (2024) 061001 [2406.08698].

[425] A. Acharyya et al., *Search for Ultraheavy Dark Matter from Observations of Dwarf Spheroidal Galaxies with VERITAS*, *Astrophys. J.* **945** (2023) 101 [2302.08784].

[426] V. D. Shiltsev, *High energy particle colliders: past 20 years, next 20 years and beyond*, *Phys. Usp.* **55** (2012) 965 [1205.3087].

[427] S. Holmes, R. S. Moore and V. Shiltsev, *Overview of the Tevatron Collider Complex: Goals, Operations and Performance*, *JINST* **6** (2011) T08001 [1106.0909].

[428] *LHC Design Report Vol.1: The LHC Main Ring*, .

[429] *LHC Design Report. 3. The LHC injector chain*, .

[430] *LHC Design Report. 2. The LHC infrastructure and general services*, .

[431] *Site Specific Conceptual Design of the Superconducting Supercollider*, .

[432] FCC collaboration, *FCC-ee: The Lepton Collider: Future Circular Collider Conceptual Design Report Volume 2*, *Eur. Phys. J. ST* **228** (2019) 261.

[433] FCC collaboration, *FCC Physics Opportunities: Future Circular Collider Conceptual Design Report Volume 1*, *Eur. Phys. J. C* **79** (2019) 474.

[434] FCC collaboration, *FCC-hh: The Hadron Collider: Future Circular Collider Conceptual Design Report Volume 3*, *Eur. Phys. J. ST* **228** (2019) 755.

[435] J. Tang et al., *Concept for a Future Super Proton-Proton Collider*, 1507.03224.

[436] R. Assmann, M. Lamont and S. Myers, *A brief history of the LEP collider*, *Nucl. Phys. B Proc. Suppl.* **109** (2002) 17.

[437] ILC collaboration, *The International Linear Collider Technical Design Report - Volume 2: Physics*, 1306.6352.

[438] *The International Linear Collider Technical Design Report - Volume 1: Executive Summary*, 1306.6327.

[439] M. Ruan et al., *Reconstruction of physics objects at the Circular Electron Positron Collider with Arbor*, *Eur. Phys. J. C* **78** (2018) 426 [1806.04879].

[440] CLIC ACCELERATOR collaboration, *The Compact Linear Collider (CLIC) - Project Implementation Plan*, 1903.08655.

[441] M. Gyulassy, *The QGP discovered at RHIC*, in *NATO Advanced Study Institute: Structure and Dynamics of Elementary Matter*, pp. 159–182, 3, 2004, nucl-th/0403032.

[442] NICA/MPD collaboration, *The Nuclotron-based Ion Collider Facility Project. The Physics Programme for the Multi-Purpose Detector*, *J. Phys. Conf. Ser.* **1390** (2019) 012121.

[443] G. A. Voss and B. H. Wiik, *The Electron proton collider HERA*, *Ann. Rev. Nucl. Part. Sci.* **44** (1994) 413.

[444] S. Zhou, J. Hua, W. Lu, W. An, W. B. Mori and C. Joshi, *High efficiency uniform wakefield acceleration of a positron beam using stable asymmetric mode in a hollow channel plasma*, 2012.06095.

[445] C. G. Lester and D. J. Summers, *Measuring masses of semiinvisibly decaying particles pair produced at hadron colliders*, *Phys. Lett. B* **463** (1999) 99 [hep-ph/9906349].

[446] H.-C. Cheng and Z. Han, *Minimal Kinematic Constraints and $m(T2)$*, *JHEP* **12** (2008) 063 [0810.5178].

[447] A. Barr, C. Lester and P. Stephens, *$m(T2)$: The Truth behind the glamour*, *J. Phys. G* **29** (2003) 2343 [hep-ph/0304226].

[448] A. A. Petrov and W. Shepherd, *Searching for dark matter at LHC with Mono-Higgs production*, *Phys. Lett. B* **730** (2014) 178 [1311.1511].

[449] N. F. Bell, J. B. Dent, A. J. Galea, T. D. Jacques, L. M. Krauss and T. J. Weiler, *Searching for Dark Matter at the LHC with a Mono-Z*, *Phys. Rev. D* **86** (2012) 096011 [1209.0231].

[450] Y. Bai, P. J. Fox and R. Harnik, *The Tevatron at the Frontier of Dark Matter Direct Detection*, *JHEP* **12** (2010) 048 [1005.3797].

[451] J. L. Feng, S. Su and F. Takayama, *Lower limit on dark matter production at the large hadron collider*, *Phys. Rev. Lett.* **96** (2006) 151802 [hep-ph/0503117].

[452] T. Alanne, G. Arcadi, F. Goertz, V. Tenorth and S. Vogl, *Model-independent constraints with extended dark matter EFT*, *JHEP* **10** (2020) 172 [2006.07174].

[453] T. Alanne and F. Goertz, *Extended Dark Matter EFT*, *Eur. Phys. J. C* **80** (2020) 446 [1712.07626].

[454] A. Berlin, S. Gori, T. Lin and L.-T. Wang, *Pseudoscalar Portal Dark Matter*, *Phys. Rev. D* **92** (2015) 015005 [1502.06000].

[455] M. R. Buckley, D. Feld and D. Goncalves, *Scalar Simplified Models for Dark Matter*, *Phys. Rev. D* **91** (2015) 015017 [1410.6497].

[456] E. Bernreuther, F. Kahlhoefer, M. Krämer and P. Tunney, *Strongly interacting dark sectors in the early Universe and at the LHC through a simplified portal*, *JHEP* **01** (2020) 162 [1907.04346].

[457] S. Baek, P. Ko and J. Li, *Minimal renormalizable simplified dark matter model with a pseudoscalar mediator*, *Phys. Rev. D* **95** (2017) 075011 [1701.04131].

[458] N. F. Bell, G. Busoni and I. W. Sanderson, *Self-consistent Dark Matter Simplified Models with an s-channel scalar mediator*, *JCAP* **03** (2017) 015 [1612.03475].

[459] S. P. Liew, M. Papucci, A. Vichi and K. M. Zurek, *Mono-X Versus Direct Searches: Simplified Models for Dark Matter at the LHC*, *JHEP* **06** (2017) 082 [1612.00219].

[460] ATLAS collaboration, *Combination of searches for invisible decays of the Higgs boson using 139 fb−1 of proton-proton collision data at s=13 TeV collected with the ATLAS experiment*, *Phys. Lett. B* **842** (2023) 137963 [2301.10731].

[461] CMS collaboration, *A search for decays of the Higgs boson to invisible particles in events with a top-antitop quark pair or a vector boson in proton-proton collisions at* $\sqrt{s} = 13$ *TeV*, *Eur. Phys. J. C* **83** (2023) 933 [2303.01214].

[462] ATLAS collaboration, *Measurement of the Z boson invisible width at s=13 TeV with the ATLAS detector*, *Phys. Lett. B* **854** (2024) 138705 [2312.02789].

[463] CMS collaboration, *Precision measurement of the Z boson invisible width in pp collisions at s=13 TeV*, *Phys. Lett. B* **842** (2023) 137563 [2206.07110].

[464] S. Bhattacharya and D. Pradhan, *Direct Search signal of two-component Dark Matter*, 2501.17862.

[465] S. Bhattacharya, P. Ghosh, J. Lahiri and B. Mukhopadhyaya, *Mono-X signal and two component dark matter: New distinction criteria*, *Phys. Rev. D* **108** (2023) L111703 [2211.10749].

[466] S. Bhattacharya, P. Ghosh, J. Lahiri and B. Mukhopadhyaya, *Distinguishing two dark matter component particles at* e^+e^- *colliders*, *JHEP* **12** (2022) 049 [2202.12097].

[467] Q.-H. Cao, E. Ma, J. Wudka and C. P. Yuan, *Multipartite dark matter*, 0711.3881.

[468] ATLAS collaboration, *Combined Measurement of the Higgs Boson Mass from the* $H\to\gamma\gamma$ *and* $H\to ZZ^*\to 4\ell$ *Decay Channels with the ATLAS Detector Using s=7, 8, and 13 TeV pp Collision Data*, *Phys. Rev. Lett.* **131** (2023) 251802 [2308.04775].

[469] T. Biekötter, S. Heinemeyer and G. Weiglein, *The CMS di-photon excess at 95 GeV in view of the LHC Run 2 results*, *Phys. Lett. B* **846** (2023) 138217 [2303.12018].

[470] H. B. Nielsen and S. Chadha, *On How to Count Goldstone Bosons*, *Nucl. Phys. B* **105** (1976) 445.

[471] S. R. Coleman, *There are no Goldstone bosons in two-dimensions*, *Commun. Math. Phys.* **31** (1973) 259.

[472] C. P. Burgess, *Goldstone and pseudoGoldstone bosons in nuclear, particle and condensed matter physics*, *Phys. Rept.* **330** (2000) 193 [hep-th/9808176].

[473] G. Bhattacharyya and D. Das, *Scalar sector of two-Higgs-doublet models: A minireview*, *Pramana* **87** (2016) 40 [1507.06424].

[474] J. Horejsi and M. Kladiva, *Tree-unitarity bounds for THDM Higgs masses revisited*, *Eur. Phys. J. C* **46** (2006) 81 [hep-ph/0510154].

[475] S. Bhattacharya, P. Ghosh, A. K. Saha and A. Sil, *Two component dark matter with inert Higgs doublet: neutrino mass, high scale validity and collider searches*, *JHEP* **03** (2020) 090 [1905.12583].

[476] I. Baldes and K. Petraki, *Asymmetric thermal-relic dark matter: Sommerfeld-enhanced freeze-out, annihilation signals and unitarity bounds*, *JCAP* **09** (2017) 028 [1703.00478].

[477] J. Smirnov and J. F. Beacom, *TeV-Scale Thermal WIMPs: Unitarity and its Consequences*, *Phys. Rev. D* **100** (2019) 043029 [1904.11503].

[478] D. Bhatia and S. Mukhopadhyay, *Unitarity limits on thermal dark matter in (non-)standard cosmologies*, *JHEP* **03** (2021) 133 [2010.09762].

[479] Z. Zhou, G. Liu, Y. Mu and L. Xu, *Limit on the dark matter mass from its interaction with photons*, *Phys. Rev. D* **105** (2022) 103509 [2205.08070].

[480] G. Krnjaic and S. D. McDermott, *Implications of BBN Bounds for Cosmic Ray Upscattered Dark Matter*, *Phys. Rev. D* **101** (2020) 123022 [1908.00007].

[481] K. M. Nollett and G. Steigman, *BBN And The CMB Constrain Light, Electromagnetically Coupled WIMPs*, *Phys. Rev. D* **89** (2014) 083508 [1312.5725].

[482] P. F. Depta, M. Hufnagel, K. Schmidt-Hoberg and S. Wild, *BBN constraints on the annihilation of MeV-scale dark matter*, *JCAP* **04** (2019) 029 [1901.06944].

[483] P. D. Serpico and G. G. Raffelt, *MeV-mass dark matter and primordial nucleosynthesis*, *Phys. Rev. D* **70** (2004) 043526 [astro-ph/0403417].

[484] C. M. Ho and R. J. Scherrer, *Limits on MeV Dark Matter from the Effective Number of Neutrinos*, *Phys. Rev. D* **87** (2013) 023505 [1208.4347].

[485] K. M. Nollett and G. Steigman, *BBN And The CMB Constrain Neutrino Coupled Light WIMPs*, *Phys. Rev. D* **91** (2015) 083505 [1411.6005].

[486] N. Sabti, J. Alvey, M. Escudero, M. Fairbairn and D. Blas, *Refined Bounds on MeV-scale Thermal Dark Sectors from BBN and the CMB*, *JCAP* **01** (2020) 004 [1910.01649].

[487] ATLAS collaboration, *Constraints on new phenomena via Higgs boson couplings and invisible decays with the ATLAS detector*, *JHEP* **11** (2015) 206 [1509.00672].

[488] K. Tuominen, *Cold Particle Dark Matter*, *Symmetry* **13** (2021) 1945.

[489] G. Chalons, D. Lopez-Val, T. Robens and T. Stefaniak, *The Higgs singlet extension at LHC Run 2*, *PoS* **DIS2016** (2016) 113 [1606.07793].

[490] T. Robens and T. Stefaniak, *Status of the Higgs Singlet Extension of the Standard Model after LHC Run 1*, *Eur. Phys. J. C* **75** (2015) 104 [1501.02234].

[491] G. Chalons, D. Lopez-Val, T. Robens and T. Stefaniak, *The Higgs singlet extension at LHC Run 2*, *PoS* **ICHEP2016** (2016) 1180 [1611.03007].

[492] T. N. Robens, *Constraining extended scalar sectors at current and future colliders*, *PoS* **CORFU2021** (2022) 031 [2203.17016].

[493] T. Robens, *A short overview on low mass scalars at future lepton colliders – LCWS23 proceedings*, in *International Workshop on Future Linear Colliders*, 7, 2023, 2307.15962.

[494] S. D. Lane, I. M. Lewis and M. Sullivan, *Resonant multiscalar production in the generic complex singlet model in the multi-TeV region*, *Phys. Rev. D* **110** (2024) 055017 [2403.18003].

[495] CMS collaboration, *Search for invisible decays of the Higgs boson produced via vector boson fusion in proton-proton collisions at s=13 TeV*, *Phys. Rev. D* **105** (2022) 092007 [2201.11585].

[496] ATLAS collaboration, *Search for invisible Higgs-boson decays in events with vector-boson fusion signatures using 139 fb^{-1} of proton-proton data recorded by the ATLAS experiment*, *JHEP* **08** (2022) 104 [2202.07953].

[497] LHC Higgs Cross Section Working Group collaboration, *Handbook of LHC Higgs Cross Sections: 4. Deciphering the Nature of the Higgs Sector*, 1610.07922.

[498] CMS collaboration, *Search for a standard model-like Higgs boson in the mass range between 70 and 110 GeV in the diphoton final state in proton-proton collisions at $\sqrt{s} = 13$ TeV*, 2405.18149.

[499] ATLAS collaboration, *Search for diphoton resonances in the 66 to 110 GeV mass range using 140 fb^{-1} of 13 TeV pp collisions collected with the ATLAS detector*, .

[500] ATLAS collaboration, *Search for diphoton resonances in the 66 to 110 GeV mass range using pp collisions at $\sqrt{s} = 13$ TeV with the ATLAS detector*, 2407.07546.

[501] T. Biekötter, S. Heinemeyer and G. Weiglein, *95.4 GeV diphoton excess at ATLAS and CMS*, *Phys. Rev. D* **109** (2024) 035005 [2306.03889].

[502] S. Yaser Ayazi, M. Hosseini, S. Paktinat Mehdiabadi and R. Rouzbehi, *Vector dark matter and LHC constraints, including a 95 GeV light Higgs boson*, *Phys. Rev. D* **110** (2024) 055004 [2405.01132].

[503] S. Gao, S.-M. Zhao, L. Ruan, X.-X. Dong and T.-F. Feng, *A 95 GeV Higgs Boson in the $U(1)_X$ model*, 2411.13261.

[504] P. Janot, *The infamous 95 GeV $b\bar{b}$ excess at LEP: two b or not two b?*, *JHEP* **10** (2024) 223 [2407.10948].

[505] G. Steigman, *Neutrinos And Big Bang Nucleosynthesis*, *Adv. High Energy Phys.* **2012** (2012) 268321 [1208.0032].

[506] M. Kaplinghat, S. Tulin and H.-B. Yu, *Direct Detection Portals for Self-interacting Dark Matter*, *Phys. Rev. D* **89** (2014) 035009 [1310.7945].

[507] G. Belanger, A. Mjallal and A. Pukhov, *WIMP and FIMP dark matter in the inert doublet plus singlet model*, *Phys. Rev. D* **106** (2022) 095019 [2205.04101].

[508] A. Fradette and M. Pospelov, *BBN for the LHC: constraints on lifetimes of the Higgs portal scalars*, *Phys. Rev. D* **96** (2017) 075033 [1706.01920].

[509] M. Pospelov and J. Pradler, *Big Bang Nucleosynthesis as a Probe of New Physics*, *Ann. Rev. Nucl. Part. Sci.* **60** (2010) 539 [1011.1054].

[510] M. Duch, B. Grzadkowski and D. Huang, *Strongly self-interacting vector dark matter via freeze-in*, *JHEP* **01** (2018) 020 [1710.00320].

[511] J. D. Clarke, R. Foot and R. R. Volkas, *Phenomenology of a very light scalar (100 MeV $< m_h <$ 10 GeV) mixing with the SM Higgs*, *JHEP* **02** (2014) 123 [1310.8042].

[512] K. Schmidt-Hoberg, F. Staub and M. W. Winkler, *Constraints on light mediators: confronting dark matter searches with B physics*, *Phys. Lett. B* **727** (2013) 506 [1310.6752].

[513] G. Alguero, G. Belanger, F. Boudjema, S. Chakraborti, A. Goudelis, S. Kraml et al., *micrOMEGAs 6.0: N-component dark matter*, *Comput. Phys. Commun.* **299** (2024) 109133 [2312.14894].

[514] LZ collaboration, *First Dark Matter Search Results from the LUX-ZEPLIN (LZ) Experiment*, *Phys. Rev. Lett.* **131** (2023) 041002 [2207.03764].

[515] XENON collaboration, *First Search for Light Dark Matter in the Neutrino Fog with XENONnT*, 2409.17868.

[516] PandaX collaboration, *PandaX-xT: a Multi-ten-tonne Liquid Xenon Observatory at the China Jinping Underground Laboratory*, 2402.03596.

[517] L. Baudis, *Dual-phase xenon time projection chambers for rare-event searches*, *Phil. Trans. Roy. Soc. Lond. A* **382** (2023) 20230083 [2311.05320].

[518] L. Baudis, *DARWIN/XLZD: A future xenon observatory for dark matter and other rare interactions*, *Nucl. Phys. B* **1003** (2024) 116473 [2404.19524].

[519] Fermi-LAT collaboration, *Searching for Dark Matter Annihilation from Milky Way Dwarf Spheroidal Galaxies with Six Years of Fermi Large Area Telescope Data*, *Phys. Rev. Lett.* **115** (2015) 231301 [1503.02641].

[520] Fermi-LAT collaboration, *Sensitivity Projections for Dark Matter Searches with the Fermi Large Area Telescope*, *Phys. Rept.* **636** (2016) 1 [1605.02016].

[521] Fermi-LAT collaboration, *Updated search for spectral lines from Galactic dark matter interactions with pass 8 data from the Fermi Large Area Telescope*, *Phys. Rev. D* **91** (2015) 122002 [1506.00013].

[522] EDELWEISS collaboration, *First germanium-based constraints on sub-MeV Dark Matter with the EDELWEISS experiment*, *Phys. Rev. Lett.* **125** (2020) 141301 [2003.01046].

[523] COSINE-100 collaboration, *Lowering threshold of NaI(Tl) scintillator to 0.7 keV in the COSINE-100 experiment*, *JINST* **19** (2024) P12013 [2408.14688].

[524] PICO collaboration, *Dark Matter Search Results from the Complete Exposure of the PICO-60 C_3F_8 Bubble Chamber*, *Phys. Rev. D* **100** (2019) 022001 [1902.04031].

[525] J. D. Lewin and P. F. Smith, *Review of mathematics, numerical factors, and corrections for dark matter experiments based on elastic nuclear recoil*, *Astropart. Phys.* **6** (1996) 87.

[526] R. H. Helm, *Inelastic and Elastic Scattering of 187-Mev Electrons from Selected Even-Even Nuclei*, *Phys. Rev.* **104** (1956) 1466.

[527] B. J. Kavanagh, T. Emken and R. Catena, *Measuring the local dark matter density in the laboratory*, *Phys. Rev. D* **104** (2021) 083023 [2004.01621].

[528] P. F. de Salas and A. Widmark, *Dark matter local density determination: recent observations and future prospects*, *Rept. Prog. Phys.* **84** (2021) 104901 [2012.11477].

[529] Y. Sofue, *Rotation Curve of the Milky Way and the Dark Matter Density*, *Galaxies* **8** (2020) 37 [2004.11688].

[530] M. C. Smith et al., *The RAVE Survey: Constraining the Local Galactic Escape Speed*, *Mon. Not. Roy. Astron. Soc.* **379** (2007) 755 [astro-ph/0611671].

[531] P. R. Kafle, S. Sharma, G. F. Lewis and J. Bland-Hawthorn, *On the Shoulders of Giants: Properties of the Stellar Halo and the Milky Way Mass Distribution*, *Astrophys. J.* **794** (2014) 59 [1408.1787].

[532] R. Foot, *Hidden sector dark matter explains the DAMA, CoGeNT, CRESST-II and CDMS/Si experiments*, *Phys. Rev. D* **88** (2013) 025032 [1209.5602].

[533] P. G. Staudt, J. S. Bullock, M. Boylan-Kolchin, D. Kirkby, A. Wetzel and X. Ou, *Sliding into DM: determining the local dark matter density and speed distribution using only the local circular speed of the galaxy*, *JCAP* **08** (2024) 022 [2403.04122].

[534] T. Markkanen, A. Rajantie and S. Stopyra, *Cosmological Aspects of Higgs Vacuum Metastability*, *Front. Astron. Space Sci.* **5** (2018) 40 [1809.06923].

[535] J. Khoury and T. Steingasser, *Gauge hierarchy from electroweak vacuum metastability*, 2108.09315.

[536] S. M. Bilenky and S. T. Petcov, *Massive neutrinos and neutrino oscillations*, *Rev. Mod. Phys.* **59** (1987) 671.

[537] J. Schechter and J. W. F. Valle, *Neutrino Masses in $SU(2)$ x $U(1)$ Theories*, *Phys. Rev. D* **22** (1980) 2227.

[538] M. E. Shaposhnikov, *Baryon Asymmetry of the Universe in Standard Electroweak Theory*, *Nucl. Phys. B* **287** (1987) 757.

[539] D. E. Morrissey and M. J. Ramsey-Musolf, *Electroweak baryogenesis*, *New J. Phys.* **14** (2012) 125003 [1206.2942].

[540] S. Heeba, F. Kahlhoefer and P. Stöcker, *Freeze-in production of decaying dark matter in five steps*, *JCAP* **11** (2018) 048 [1809.04849].

[541] C. Delaunay, T. Ma and Y. Soreq, *Stealth decaying spin-1 dark matter*, *JHEP* **02** (2021) 010 [2009.03060].

[542] G. Choi, T. T. Yanagida and N. Yokozaki, *Feebly interacting $U(1)_{B-L}$ gauge boson warm dark matter and XENON1T anomaly*, *Phys. Lett. B* **810** (2020) 135836 [2007.04278].

[543] B. Barman and A. Ghoshal, *Scale Invariant FIMP Miracle*, 2109.03259.

[544] J. McDonald, *Gauge singlet scalars as cold dark matter*, *Phys. Rev. D* **50** (1994) 3637 [hep-ph/0702143].

[545] T. G. Steele, Z.-W. Wang, D. Contreras and R. B. Mann, *Viable dark matter via radiative symmetry breaking in a scalar singlet Higgs portal extension of the standard model*, *Phys. Rev. Lett.* **112** (2014) 171602 [1310.1960].

[546] V. Silveira and A. Zee, *SCALAR PHANTOMS*, *Phys. Lett.* **161B** (1985) 136.

[547] C. P. Burgess, M. Pospelov and T. ter Veldhuis, *The Minimal model of nonbaryonic dark matter: A Singlet scalar*, *Nucl. Phys.* **B619** (2001) 709 [hep-ph/0011335].

[548] T. Hambye, *Hidden vector dark matter*, *JHEP* **01** (2009) 028 [0811.0172].

[549] T. Hambye and M. H. G. Tytgat, *Confined hidden vector dark matter*, *Phys. Lett. B* **683** (2010) 39 [0907.1007].

[550] S. Bhattacharya, J. L. Diaz-Cruz, E. Ma and D. Wegman, *Dark Vector-Gauge-Boson Model*, *Phys. Rev. D* **85** (2012) 055008 [1107.2093].

[551] Y. Farzan and A. R. Akbarieh, *VDM: A model for Vector Dark Matter*, *JCAP* **10** (2012) 026 [1207.4272].

[552] Z. Hu, C. Cai, Y.-L. Tang, Z.-H. Yu and H.-H. Zhang, *Vector dark matter from split $SU(2)$ gauge bosons*, *JHEP* **07** (2021) 089 [2103.00220].

[553] S. Baek, P. Ko, W.-I. Park and E. Senaha, *Higgs Portal Vector Dark Matter : Revisited*, *JHEP* **05** (2013) 036 [1212.2131].

[554] P. Ko, W.-I. Park and Y. Tang, *Higgs portal vector dark matter for* GeV *scale γ-ray excess from galactic center*, *JCAP* **09** (2014) 013 [1404.5257].

[555] M. Duch, B. Grzadkowski and M. McGarrie, *A stable Higgs portal with vector dark matter*, *JHEP* **09** (2015) 162 [1506.08805].

[556] M. Duch and B. Grzadkowski, *Resonance enhancement of dark matter interactions: the case for early kinetic decoupling and velocity dependent resonance width*, *JHEP* **09** (2017) 159 [1705.10777].

[557] S. Yaser Ayazi and A. Mohamadnejad, *Conformal vector dark matter and strongly first-order electroweak phase transition*, *JHEP* **03** (2019) 181 [1901.04168].

[558] G. Choi, T. T. Yanagida and N. Yokozaki, *Dark photon dark matter in the minimal $B - L$ model*, *JHEP* **01** (2021) 057 [2008.12180].

[559] O. Lebedev, H. M. Lee and Y. Mambrini, *Vector Higgs-portal dark matter and the invisible Higgs*, *Phys. Lett. B* **707** (2012) 570 [1111.4482].

[560] H. Davoudiasl and I. M. Lewis, *Dark Matter from Hidden Forces*, *Phys. Rev. D* **89** (2014) 055026 [1309.6640].

[561] S. Bhattacharya and J. Wudka, *Effective Theories with Dark Matter Applications*, 2104.01788.

[562] F. Fortuna, P. Roig and J. Wudka, *Effective field theory analysis of dark matter-standard model interactions with spin one mediators*, *JHEP* **02** (2021) 223 [2008.10609].

[563] S. Matsumoto, S. Mukhopadhyay and Y.-L. S. Tsai, *Singlet Majorana fermion dark matter: a comprehensive analysis in effective field theory*, *JHEP* **10** (2014) 155 [1407.1859].

[564] N. F. Bell, Y. Cai, J. B. Dent, R. K. Leane and T. J. Weiler, *Dark matter at the LHC: Effective field theories and gauge invariance*, *Phys. Rev. D* **92** (2015) 053008 [1503.07874].

[565] A. De Simone and T. Jacques, *Simplified models vs. effective field theory approaches in dark matter searches*, *Eur. Phys. J. C* **76** (2016) 367 [1603.08002].

[566] Q.-H. Cao, C.-R. Chen, C. S. Li and H. Zhang, *Effective Dark Matter Model: Relic density, CDMS II, Fermi LAT and LHC*, *JHEP* **08** (2011) 018 [0912.4511].

[567] K. Cheung, P.-Y. Tseng, Y.-L. S. Tsai and T.-C. Yuan, *Global Constraints on Effective Dark Matter Interactions: Relic Density, Direct Detection, Indirect Detection, and Collider*, *JCAP* **05** (2012) 001 [1201.3402].

[568] G. Busoni, A. De Simone, E. Morgante and A. Riotto, *On the Validity of the Effective Field Theory for Dark Matter Searches at the LHC*, *Phys. Lett. B* **728** (2014) 412 [1307.2253].

[569] M. Duch, B. Grzadkowski and J. Wudka, *Classification of effective operators for interactions between the Standard Model and dark matter*, *JHEP* **05** (2015) 116 [1412.0520].

[570] M. Carena, A. Megevand, M. Quiros and C. E. M. Wagner, *Electroweak baryogenesis and new TeV fermions*, *Nucl. Phys. B* **716** (2005) 319 [hep-ph/0410352].

[571] M. J. Baker and L. Mittnacht, *Variations on the Vev Flip-Flop: Instantaneous Freeze-out and Decaying Dark Matter*, *JHEP* **05** (2019) 070 [1811.03101].

[572] V. De Romeri, D. Karamitros, O. Lebedev and T. Toma, *Neutrino dark matter and the Higgs portal: improved freeze-in analysis*, *JHEP* **10** (2020) 137 [2003.12606].

[573] M. Chianese and S. F. King, *The Dark Side of the Littlest Seesaw: freeze-in, the two right-handed neutrino portal and leptogenesis-friendly fimpzillas*, *JCAP* **09** (2018) 027 [1806.10606].

[574] J. Elias-Miro, J. R. Espinosa, G. F. Giudice, H. M. Lee and A. Strumia, *Stabilization of the Electroweak Vacuum by a Scalar Threshold Effect*, *JHEP* **06** (2012) 031 [1203.0237].

[575] K. Kannike, *Vacuum Stability of a General Scalar Potential of a Few Fields*, *Eur. Phys. J. C* **76** (2016) 324 [1603.02680].

[576] J. Chakrabortty, P. Konar and T. Mondal, *Copositive Criteria and Boundedness of the Scalar Potential*, *Phys. Rev. D* **89** (2014) 095008 [1311.5666].

[577] WMAP collaboration, *Nine-Year Wilkinson Microwave Anisotropy Probe (WMAP) Observations: Cosmological Parameter Results*, *Astrophys. J. Suppl.* **208** (2013) 19 [1212.5226].

[578] XENON collaboration, *Dark Matter Search Results from a One Ton-Year Exposure of XENON1T*, *Phys. Rev. Lett.* **121** (2018) 111302 [1805.12562].

[579] XENON collaboration, *Projected WIMP sensitivity of the XENONnT dark matter experiment*, *JCAP* **11** (2020) 031 [2007.08796].

[580] V. Barger, P. Langacker, M. McCaskey, M. J. Ramsey-Musolf and G. Shaughnessy, *LHC Phenomenology of an Extended Standard Model with a Real Scalar Singlet*, *Phys. Rev. D* **77** (2008) 035005 [0706.4311].

[581] E. Fuchs, O. Matsedonskyi, I. Savoray and M. Schlaffer, *Collider searches for scalar singlets across lifetimes*, *JHEP* **04** (2021) 019 [2008.12773].

[582] CMS collaboration, *Searches for Higgs boson rare and invisible decays at CMS*, *PoS* **ICHEP2020** (2021) 070.

[583] ATLAS collaboration, *Combination of searches for invisible Higgs boson decays with the ATLAS experiment*, .

[584] S. Okawa and Y. Omura, *Light mass window of lepton portal dark matter*, *JHEP* **02** (2021) 231 [2011.04788].

[585] S. Bhattacharya, P. Ghosh, T. N. Maity and T. S. Ray, *Mitigating Direct Detection Bounds in Non-minimal Higgs Portal Scalar Dark Matter Models*, *JHEP* **10** (2017) 088 [1706.04699].

[586] J. Buch, P. Ralegankar and V. Rentala, *Late decaying 2-component dark matter scenario as an explanation of the AMS-02 positron excess*, *JCAP* **10** (2017) 028 [1609.04821].

[587] G. Bélanger, F. Boudjema, A. Goudelis, A. Pukhov and B. Zaldivar, *micrOMEGAs5.0 : Freeze-in*, *Comput. Phys. Commun.* **231** (2018) 173 [1801.03509].

[588] J. C. Criado, A. Djouadi, M. Perez-Victoria and J. Santiago, *A complete effective field theory for dark matter*, *JHEP* **07** (2021) 081 [2104.14443].

[589] A. Falkowski, G. Isabella and C. S. Machado, *On-shell effective theory for higher-spin dark matter*, *SciPost Phys.* **10** (2021) 101 [2011.05339].

[590] W. R. Inc., "Mathematica, Version 12.3.1.0."

[591] J. Redondo and M. Postma, *Massive hidden photons as lukewarm dark matter*, *JCAP* **02** (2009) 005 [0811.0326].

[592] M. J. Baker, M. Breitbach, J. Kopp and L. Mittnacht, *Dynamic Freeze-In: Impact of Thermal Masses and Cosmological Phase Transitions on Dark Matter Production*, *JHEP* **03** (2018) 114 [1712.03962].

[593] S. Bhattacharya, D. Pradhan and J. Thakkar., *Pseudo-FIMP dark matter in presence of a SIMP*, 2411.15108.

[594] G. Belanger, A. Mjallal and A. Pukhov, *Two dark matter candidates: the case of inert doublet and singlet scalars*, 2108.08061.

[595] F. Costa, S. Khan and J. Kim, *A two-component dark matter model and its associated gravitational waves*, *JHEP* **06** (2022) 026 [2202.13126].

[596] G. Belanger and J.-C. Park, *Assisted freeze-out*, *JCAP* **03** (2012) 038 [1112.4491].

[597] S. Bhattacharya, A. Drozd, B. Grzadkowski and J. Wudka, *Two-Component Dark Matter*, *JHEP* **10** (2013) 158 [1309.2986].

[598] T. N. Maity and T. S. Ray, *Exchange driven freeze out of dark matter*, *Phys. Rev. D* **101** (2020) 103013 [1908.10343].

[599] S. Bhattacharya, P. Ghosh and N. Sahu, *Multipartite Dark Matter with Scalars, Fermions and signatures at LHC*, *JHEP* **02** (2019) 059 [1809.07474].

[600] C. E. Yaguna and O. Zapata, *Fermion and scalar two-component dark matter from a Z4 symmetry*, *Phys. Rev. D* **105** (2022) 095026 [2112.07020].

[601] W. Abdallah, S. Choubey and S. Khan, *Two Component FIMP DM in a $U(1)_{B-L}$ Extension of the SM*, in *International Conference on Neutrinos and Dark Matter*, 4, 2020, DOI [2004.13211].

[602] P. Ghosh, P. Konar, A. K. Saha and S. Show, *Self-interacting freeze-in dark matter in a singlet doublet scenario*, *JCAP* **10** (2022) 017 [2112.09057].

[603] G. Bélanger, F. Boudjema, A. Pukhov and A. Semenov, *micrOMEGAs4.1: two dark matter candidates*, *Comput. Phys. Commun.* **192** (2015) 322 [1407.6129].

[604] T. Binder, T. Bringmann, M. Gustafsson and A. Hryczuk, *Early kinetic decoupling of dark matter: when the standard way of calculating the thermal relic density fails*, *Phys. Rev. D* **96** (2017) 115010 [1706.07433].

[605] K. Ala-Mattinen and K. Kainulainen, *Precision calculations of dark matter relic abundance*, *JCAP* **09** (2020) 040 [1912.02870].

[606] H. M. Lee and M.-S. Seo, *Communication with SIMP dark mesons via Z' -portal*, *Phys. Lett. B* **748** (2015) 316 [1504.00745].

[607] L. Hui, *Unitarity bounds and the cuspy halo problem*, *Phys. Rev. Lett.* **86** (2001) 3467 [astro-ph/0102349].

[608] A. Kamada, S. Kobayashi and T. Kuwahara, *Perturbative unitarity of strongly interacting massive particle models*, *JHEP* **02** (2023) 217 [2210.01393].

[609] M. H. Namjoo, T. R. Slatyer and C.-L. Wu, *Enhanced n-body annihilation of dark matter and its indirect signatures*, *JHEP* **03** (2019) 077 [1810.09455].

[610] R. N. Lerner and J. McDonald, *Gauge singlet scalar as inflaton and thermal relic dark matter*, *Phys. Rev. D* **80** (2009) 123507 [0909.0520].

[611] G. Belanger, K. Kannike, A. Pukhov and M. Raidal, *Z_3 Scalar Singlet Dark Matter*, *JCAP* **01** (2013) 022 [1211.1014].

[612] B. W. Lee, C. Quigg and H. B. Thacker, *Weak Interactions at Very High-Energies: The Role of the Higgs Boson Mass*, *Phys. Rev. D* **16** (1977) 1519.

[613] A. Hektor, A. Hryczuk and K. Kannike, *Improved bounds on $\mathbb{Z}_3$ singlet dark matter*, *JHEP* **03** (2019) 204 [1901.08074].

[614] F. C. Adams, *General solutions for tunneling of scalar fields with quartic potentials*, *Phys. Rev. D* **48** (1993) 2800 [hep-ph/9302321].

[615] E. D. Carlson, M. E. Machacek and L. J. Hall, *Self-interacting dark matter*, *Astrophys. J.* **398** (1992) 43.

[616] N. Bernal, C. Garcia-Cely and R. Rosenfeld, *WIMP and SIMP Dark Matter from the Spontaneous Breaking of a Global Group*, *JCAP* **04** (2015) 012 [1501.01973].

[617] N. Bernal, X. Chu, C. Garcia-Cely, T. Hambye and B. Zaldivar, *Production Regimes for Self-Interacting Dark Matter*, *JCAP* **03** (2016) 018 [1510.08063].

[618] D. N. Spergel and P. J. Steinhardt, *Observational evidence for selfinteracting cold dark matter*, *Phys. Rev. Lett.* **84** (2000) 3760 [astro-ph/9909386].

[619] D. Clowe, A. Gonzalez and M. Markevitch, *Weak lensing mass reconstruction of the interacting cluster 1E0657-558: Direct evidence for the existence of dark matter*, *Astrophys. J.* **604** (2004) 596 [astro-ph/0312273].

[620] M. Markevitch, A. H. Gonzalez, D. Clowe, A. Vikhlinin, L. David, W. Forman et al., *Direct constraints on the dark matter self-interaction cross-section from the merging galaxy cluster 1E0657-56*, *Astrophys. J.* **606** (2004) 819 [astro-ph/0309303].

[621] S. W. Randall, M. Markevitch, D. Clowe, A. H. Gonzalez and M. Bradac, *Constraints on the Self-Interaction Cross-Section of Dark Matter from Numerical Simulations of the Merging Galaxy Cluster 1E 0657-56*, *Astrophys. J.* **679** (2008) 1173 [0704.0261].

[622] F. Kahlhoefer, K. Schmidt-Hoberg, J. Kummer and S. Sarkar, *On the interpretation of dark matter self-interactions in Abell 3827*, *Mon. Not. Roy. Astron. Soc.* **452** (2015) L54 [1504.06576].

[623] A. H. G. Peter, M. Rocha, J. S. Bullock and M. Kaplinghat, *Cosmological Simulations with Self-Interacting Dark Matter II: Halo Shapes vs. Observations*, *Mon. Not. Roy. Astron. Soc.* **430** (2013) 105 [1208.3026].

[624] M. Rocha, A. H. G. Peter, J. S. Bullock, M. Kaplinghat, S. Garrison-Kimmel, J. Onorbe et al., *Cosmological Simulations with Self-Interacting Dark Matter I: Constant Density Cores and Substructure*, *Mon. Not. Roy. Astron. Soc.* **430** (2013) 81 [1208.3025].

[625] M. Battaglieri et al., *US Cosmic Visions: New Ideas in Dark Matter 2017: Community Report*, in *U.S. Cosmic Visions: New Ideas in Dark Matter*, 7, 2017, 1707.04591.

[626] C. Giovanetti, M. Lisanti, H. Liu and J. T. Ruderman, *Joint Cosmic Microwave Background and Big Bang Nucleosynthesis Constraints on Light Dark Sectors with Dark Radiation*, *Phys. Rev. Lett.* **129** (2022) 021302 [2109.03246].

[627] DAMIC-M collaboration, *First Constraints from DAMIC-M on Sub-GeV Dark-Matter Particles Interacting with Electrons*, 2302.02372.

[628] DarkSide collaboration, *Low-Mass Dark Matter Search with the DarkSide-50 Experiment*, *Phys. Rev. Lett.* **121** (2018) 081307 [1802.06994].

[629] J. Liao, Y. Gao, Z. Liang, Z. Ouyang, Z. Peng, L. Zhang et al., *Introduction to a low-mass dark matter project, ALETHEIA: A Liquid hElium Time projection cHambEr In dArk matter*, 2203.07901.

[630] DarkSide-20k collaboration, *DarkSide-20k: A 20 tonne two-phase LAr TPC for direct dark matter detection at LNGS*, *Eur. Phys. J. Plus* **133** (2018) 131 [1707.08145].

[631] LDMX collaboration, *Light Dark Matter eXperiment (LDMX)*, 1808.05219.

[632] P. Athron, C. Balázs, D. H. J. Jacob, W. Kotlarski, D. Stöckinger and H. Stöckinger-Kim, *New physics explanations of a_μ in light of the FNAL muon $g-2$ measurement*, *JHEP* **09** (2021) 080 [2104.03691].

[633] J. Kawamura, S. Okawa and Y. Omura, *Current status and muon $g-2$ explanation of lepton portal dark matter*, *JHEP* **08** (2020) 042 [2002.12534].

[634] L3 collaboration, *Search for heavy neutral and charged leptons in e^+e^- annihilation at LEP*, *Phys. Lett. B* **517** (2001) 75 [hep-ex/0107015].

[635] ALEPH collaboration, *Absolute lower limits on the masses of selectrons and sneutrinos in the MSSM*, *Phys. Lett. B* **544** (2002) 73 [hep-ex/0207056].

[636] OPAL collaboration, *Search for anomalous production of dilepton events with missing transverse momentum in e+ e- collisions at s**(1/2) = 183-Gev to 209-GeV*, *Eur. Phys. J. C* **32** (2004) 453 [hep-ex/0309014].

[637] DELPHI collaboration, *Searches for supersymmetric particles in e+ e- collisions up to 208-GeV and interpretation of the results within the MSSM*, *Eur. Phys. J. C* **31** (2003) 421 [hep-ex/0311019].

[638] L3 collaboration, *Search for scalar leptons and scalar quarks at LEP*, *Phys. Lett. B* **580** (2004) 37 [hep-ex/0310007].

[639] J. Lahiri, D. Pradhan and A. Sarkar, *The Influence of Lepton Portal on the WIMP-pFIMP framework*, 2410.19734.

[640] P. Gondolo and G. Gelmini, *Cosmic abundances of stable particles: Improved analysis*, *Nucl. Phys. B* **360** (1991) 145.

[641] F. del Aguila, L. Ametller, G. L. Kane and J. Vidal, *Vector Like Fermion and Standard Higgs Production at Hadron Colliders*, *Nucl. Phys. B* **334** (1990) 1.

[642] CMS collaboration, *Search for invisible decays of a Higgs boson produced through vector boson fusion in proton-proton collisions at $\sqrt{s} = 13$ TeV*, *Phys. Lett. B* **793** (2019) 520 [1809.05937].

[643] K. Griest and D. Seckel, *Three exceptions in the calculation of relic abundances*, *Phys. Rev. D* **43** (1991) 3191.

[644] R. T. D'Agnolo, D. Pappadopulo and J. T. Ruderman, *Fourth Exception in the Calculation of Relic Abundances*, *Phys. Rev. Lett.* **119** (2017) 061102 [1705.08450].

[645] R. T. D'Agnolo, C. Mondino, J. T. Ruderman and P.-J. Wang, *Exponentially Light Dark Matter from Coannihilation*, *JHEP* **08** (2018) 079 [1803.02901].

[646] C.-K. Chua and R.-C. Hsieh, *Study of Dirac fermionic dark matter*, *Phys. Rev. D* **88** (2013) 036011 [1305.7008].

[647] J. Edsjo and P. Gondolo, *Neutralino relic density including coannihilations*, *Phys. Rev. D* **56** (1997) 1879 [hep-ph/9704361].

[648] M. Dutta, S. Bhattacharya, P. Ghosh and N. Sahu, *Singlet-Doublet Majorana Dark Matter and Neutrino Mass in a minimal Type-I Seesaw Scenario*, *JCAP* **03** (2021) 008 [2009.00885].

[649] G. Duda, G. Gelmini, P. Gondolo, J. Edsjo and J. Silk, *Indirect detection of a subdominant density component of cold dark matter*, *Phys. Rev. D* **67** (2003) 023505 [hep-ph/0209266].

[650] P. Ullio, L. Bergstrom, J. Edsjo and C. G. Lacey, *Cosmological dark matter annihilations into gamma-rays - a closer look*, *Phys. Rev. D* **66** (2002) 123502 [astro-ph/0207125].

[651] Fermi-LAT collaboration, *Dark Matter search in dwarf irregular galaxies with the Fermi Large Area Telescope*, *PoS* **ICRC2021** (2021) 509 [2109.11291].

[652] Super-Kamiokande collaboration, *Indirect search for dark matter from the Galactic Center and halo with the Super-Kamiokande detector*, *Phys. Rev. D* **102** (2020) 072002 [2005.05109].

[653] H.E.S.S. collaboration, *Search for Dark Matter Annihilation Signals in the H.E.S.S. Inner Galaxy Survey*, *Phys. Rev. Lett.* **129** (2022) 111101 [2207.10471].

[654] IceCube collaboration, *Observation and Characterization of a Cosmic Muon Neutrino Flux from the Northern Hemisphere using six years of IceCube data*, *Astrophys. J.* **833** (2016) 3 [1607.08006].

[655] IceCube collaboration, *Searches for connections between dark matter and high-energy neutrinos with IceCube*, *JCAP* **10** (2023) 003 [2205.12950].

[656] IceCube collaboration, *Search for GeV-scale dark matter annihilation in the Sun with IceCube DeepCore*, *Phys. Rev. D* **105** (2022) 062004 [2111.09970].

[657] B. Díaz Sáez, P. Escalona, S. Norero and A. R. Zerwekh, *Fermion singlet dark matter in a pseudoscalar dark matter portal*, *JHEP* **10** (2021) 233 [2105.04255].

[658] A. Reinert and M. W. Winkler, *A Precision Search for WIMPs with Charged Cosmic Rays*, *JCAP* **01** (2018) 055 [1712.00002].

[659] G. Guedes and J. Santiago, *New leptons with exotic decays: collider limits and dark matter complementarity*, *JHEP* **01** (2022) 111 [2107.03429].

[660] S. Bhattacharya, S. Jahedi and J. Wudka, *Probing heavy charged fermions at e^+e^- collider using the Optimal Observable Technique*, 2106.02846.

[661] ATLAS collaboration, *Statistical Combination of ATLAS Run 2 Searches for Charginos and Neutralinos at the LHC*, *Phys. Rev. Lett.* **133** (2024) 031802 [2402.08347].

[662] ATLAS collaboration, *The quest to discover supersymmetry at the ATLAS experiment*, 2403.02455.

[663] CMS collaboration, *Combined search for electroweak production of winos, binos, higgsinos, and sleptons in proton-proton collisions at s=13 TeV*, *Phys. Rev. D* **109** (2024) 112001 [2402.01888].

[664] Y. Bai and J. Berger, *Lepton Portal Dark Matter*, *JHEP* **08** (2014) 153 [1402.6696].

[665] PandaX collaboration, *Search for lepton portal dark matter in the PandaX-4T experiment*, 2408.14730.

[666] B. Díaz Sáez and K. Ghorbani, *Z_3 scalar dark matter with strong positron fluxes*, *JCAP* **02** (2023) 002 [2203.09282].

[667] P. Asadi, A. Radick and T.-T. Yu, *Interplay of freeze-in and freeze-out: Lepton-flavored dark matter and muon colliders*, *Phys. Rev. D* **110** (2024) 035022 [2312.03826].

[668] R. Mandal, *Fermionic dark matter in leptoquark portal*, *Eur. Phys. J. C* **78** (2018) 726 [1808.07844].

[669] P. Athron, J. M. Cornell, F. Kahlhoefer, J. Mckay, P. Scott and S. Wild, *Impact of vacuum stability, perturbativity and XENON1T on global fits of $\mathbb{Z}_2$ and $\mathbb{Z}_3$ scalar singlet dark matter*, *Eur. Phys. J. C* **78** (2018) 830 [1806.11281].

[670] CMS collaboration, *Measurement of the Higgs boson width and evidence of its off-shell contributions to ZZ production*, *Nature Phys.* **18** (2022) 1329 [2202.06923].

[671] CMS collaboration, *Precision measurement of the Z invisible width with the CMS experiment in pp collisions at $\sqrt{s} = 13$ TeV* , .

[672] Z. Chacko and G. D. Kribs, *Constraints on lepton flavor violation in the MSSM from the muon anomalous magnetic moment measurement*, *Phys. Rev. D* **64** (2001) 075015 [hep-ph/0104317].

[673] M. Lindner, M. Platscher and F. S. Queiroz, *A Call for New Physics : The Muon Anomalous Magnetic Moment and Lepton Flavor Violation*, *Phys. Rept.* **731** (2018) 1 [1610.06587].

[674] D. Barducci, A. Deandrea, S. Moretti, L. Panizzi and H. Prager, *Characterizing dark matter interacting with extra charged leptons*, *Phys. Rev. D* **97** (2018) 075006 [1801.02707].

[675] H. Acaroğlu, P. Agrawal and M. Blanke, *Lepton-flavoured scalar dark matter in Dark Minimal Flavour Violation*, *JHEP* **05** (2023) 106 [2211.03809].

[676] J. P. Leveille, *The Second Order Weak Correction to (G-2) of the Muon in Arbitrary Gauge Models*, *Nucl. Phys. B* **137** (1978) 63.

[677] H. Acaroğlu, M. Blanke and M. Tabet, *Opening the Higgs portal to lepton-flavoured dark matter*, *JHEP* **11** (2023) 079 [2309.10700].

[678] A. D'Alise et al., *Standard model anomalies: lepton flavour non-universality, $g-2$ and W-mass*, *JHEP* **08** (2022) 125 [2204.03686].

[679] P. Pal, *An Introductory Course of Particle Physics*. Taylor & Francis, 2014.

[680] Muon g-2 collaboration, *Measurement of the Positive Muon Anomalous Magnetic Moment to 0.46 ppm*, *Phys. Rev. Lett.* **126** (2021) 141801 [2104.03281].

[681] A. Datta, D. Marfatia and L. Mukherjee, *$B \to K \nu \nu^-$, MiniBooNE and muon g-2 anomalies from a dark sector*, *Phys. Rev. D* **109** (2024) L031701 [2310.15136].

[682] BaBar collaboration, *Searches for Lepton Flavor Violation in the Decays tau+- —> e+- gamma and tau+- —> mu+- gamma*, *Phys. Rev. Lett.* **104** (2010) 021802 [0908.2381].

[683] Belle collaboration, *Search for lepton-flavor-violating tau-lepton decays to $\ell\gamma$ at Belle*, *JHEP* **10** (2021) 19 [2103.12994].

[684] CMS collaboration, *Search for the Higgs boson decay to a pair of electrons in proton-proton collisions at s=13TeV*, *Phys. Lett. B* **846** (2023) 137783 [2208.00265].

[685] ATLAS collaboration, *A detailed map of Higgs boson interactions by the ATLAS experiment ten years after the discovery*, *Nature* **607** (2022) 52 [2207.00092].

[686] CMS collaboration, *Search for the lepton-flavor violating decay of the Higgs boson and additional Higgs bosons in the $e\mu$ final state in proton-proton collisions at $\sqrt{s} =$ 13 TeV*, *Phys. Rev. D* **108** (2023) 072004 [2305.18106].

[687] CMS collaboration, *Search for lepton-flavor violating decays of the Higgs boson in the $\mu\tau$ and $e\tau$ final states in proton-proton collisions at $\sqrt{s} = 13$ TeV*, *Phys. Rev. D* **104** (2021) 032013 [2105.03007].

[688] ATLAS collaboration, *Searches for lepton-flavour-violating decays of the Higgs boson into $e\tau$ and $\mu\tau$ in $\sqrt{s} = 13$ TeV pp collisions with the ATLAS detector*, *JHEP* **07** (2023) 166 [2302.05225].

[689] T. T. Hong, H. T. Hung, H. H. Phuong, L. T. T. Phuong and L. T. Hue, *Lepton-flavor-violating decays of the SM-like Higgs boson $h \to e_i e_j$, and $e_i \to e_j \gamma$ in a flipped 3-3-1 model*, *PTEP* **2020** (2020) 043B03 [2002.06826].

[690] S. Fajfer, J. F. Kamenik and M. Tammaro, *Interplay of New Physics effects in $(g-2)_\ell$ and $h \to \ell^+\ell^-$ — lessons from SMEFT*, *JHEP* **06** (2021) 099 [2103.10859].

[691] A. Stebbins and G. Krnjaic, *New Limits on Charged Dark Matter from Large-Scale Coherent Magnetic Fields*, *JCAP* **12** (2019) 003 [1908.05275].

[692] J. B. Muñoz and A. Loeb, *A small amount of mini-charged dark matter could cool the baryons in the early Universe*, *Nature* **557** (2018) 684 [1802.10094].

[693] A. De Rujula, S. L. Glashow and U. Sarid, *CHARGED DARK MATTER*, *Nucl. Phys. B* **333** (1990) 173.

[694] P. Agrawal, F.-Y. Cyr-Racine, L. Randall and J. Scholtz, *Make Dark Matter Charged Again*, *JCAP* **05** (2017) 022 [1610.04611].

[695] K. Kadota, T. Sekiguchi and H. Tashiro, *A new constraint on millicharged dark matter from galaxy clusters*, 1602.04009.

[696] E. Iles, S. Heeba and K. Schutz, *Direct Detection of the Millicharged Background*, 2407.21096.

[697] A. Berlin and D. Hooper, *High-energy neutrinos from millicharged dark matter annihilation in the Sun*, *Phys. Rev. D* **110** (2024) 075018 [2407.04768].

[698] D. F. G. Fiorillo and E. Vitagliano, *Self-Interacting Dark Sectors in Supernovae Can Behave as a Relativistic Fluid*, *Phys. Rev. Lett.* **133** (2024) 251004 [2404.07714].

[699] N. D. Christensen and C. Duhr, *FeynRules - Feynman rules made easy*, *Comput. Phys. Commun.* **180** (2009) 1614 [0806.4194].

[700] A. Alloul, N. D. Christensen, C. Degrande, C. Duhr and B. Fuks, *FeynRules 2.0 - A complete toolbox for tree-level phenomenology*, *Comput. Phys. Commun.* **185** (2014) 2250 [1310.1921].

[701] A. Ibarra, A. S. Lamperstorfer and J. Silk, *Dark matter annihilations and decays after the AMS-02 positron measurements*, *Phys. Rev. D* **89** (2014) 063539 [1309.2570].

[702] AMS collaboration, *Towards Understanding the Origin of Cosmic-Ray Positrons*, *PoS* **ICRC2019** (2020) 091.

[703] R. Essig, E. Kuflik, S. D. McDermott, T. Volansky and K. M. Zurek, *Constraining Light Dark Matter with Diffuse X-Ray and Gamma-Ray Observations*, *JHEP* **11** (2013) 193 [1309.4091].

[704] Fermi-LAT, DES collaboration, *Searching for Dark Matter Annihilation in Recently Discovered Milky Way Satellites with Fermi-LAT*, *Astrophys. J.* **834** (2017) 110 [1611.03184].

[705] Fermi-LAT collaboration, *Dark Matter Searches with the Fermi Large Area Telescope*, *AIP Conf. Proc.* **719** (2009) 1085 [0904.2348].

[706] H.E.S.S. collaboration, *Search for dark matter annihilations towards the inner Galactic halo from 10 years of observations with H.E.S.S*, *Phys. Rev. Lett.* **117** (2016) 111301 [1607.08142].

[707] H. Silverwood, C. Weniger, P. Scott and G. Bertone, *A realistic assessment of the CTA sensitivity to dark matter annihilation*, *JCAP* **03** (2015) 055 [1408.4131].

[708] ATLAS collaboration, *Search for electroweak production of charginos and sleptons decaying into final states with two leptons and missing transverse momentum in $\sqrt{s} = 13$ TeV pp collisions using the ATLAS detector*, *Eur. Phys. J. C* **80** (2020) 123 [1908.08215].

[709] J. Alwall, M. Herquet, F. Maltoni, O. Mattelaer and T. Stelzer, *MadGraph 5 : Going Beyond*, *JHEP* **06** (2011) 128 [1106.0522].

[710] T. Sjostrand, S. Mrenna and P. Z. Skands, *A Brief Introduction to PYTHIA 8.1*, *Comput. Phys. Commun.* **178** (2008) 852 [0710.3820].

[711] D. Dercks, N. Desai, J. S. Kim, K. Rolbiecki, J. Tattersall and T. Weber, *CheckMATE 2: From the model to the limit*, *Comput. Phys. Commun.* **221** (2017) 383 [1611.09856].

[712] DELPHES 3 collaboration, *DELPHES 3, A modular framework for fast simulation of a generic collider experiment*, *JHEP* **02** (2014) 057 [1307.6346].

[713] M. Cacciari and G. P. Salam, *Dispelling the N^3 myth for the k_t jet-finder*, *Phys. Lett. B* **641** (2006) 57 [hep-ph/0512210].

[714] M. Cacciari, G. P. Salam and G. Soyez, *The anti-k_t jet clustering algorithm*, *JHEP* **04** (2008) 063 [0802.1189].

[715] M. Cacciari, G. P. Salam and G. Soyez, *FastJet User Manual*, *Eur. Phys. J. C* **72** (2012) 1896 [1111.6097].

[716] A. L. Read, *Presentation of search results: The CL_s technique*, *J. Phys. G* **28** (2002) 2693.

[717] Y. Bai, H.-C. Cheng, J. Gallicchio and J. Gu, *Stop the Top Background of the Stop Search*, *JHEP* **07** (2012) 110 [1203.4813].

[718] ATLAS collaboration, *Search for direct production of charginos, neutralinos and sleptons in final states with two leptons and missing transverse momentum in pp collisions at $\sqrt{s} = 8$ TeV with the ATLAS detector*, *JHEP* **05** (2014) 071 [1403.5294].

[719] K. M. Zurek, *Multi-Component Dark Matter*, *Phys. Rev. D* **79** (2009) 115002 [0811.4429].

[720] S. Profumo, K. Sigurdson and L. Ubaldi, *Can we discover multi-component WIMP dark matter?*, *JCAP* **12** (2009) 016 [0907.4374].

[721] M. V. Medvedev, *Cosmological Simulations of Multicomponent Cold Dark Matter*, *Phys. Rev. Lett.* **113** (2014) 071303 [1305.1307].

[722] S. Esch, M. Klasen and C. E. Yaguna, *A minimal model for two-component dark matter*, *JHEP* **09** (2014) 108 [1406.0617].

[723] M. Aoki and T. Toma, *Implications of Two-component Dark Matter Induced by Forbidden Channels and Thermal Freeze-out*, *JCAP* **01** (2017) 042 [1611.06746].

[724] C. E. Yaguna and O. Zapata, *Multi-component scalar dark matter from a Z_N symmetry: a systematic analysis*, *JHEP* **03** (2020) 109 [1911.05515].

[725] C. E. Yaguna and O. Zapata, *Two-component scalar dark matter in Z_{2n} scenarios*, *JHEP* **10** (2021) 185 [2106.11889].

[726] G. Bélanger, A. Pukhov, C. E. Yaguna and O. Zapata, *The Z_5 model of two-component dark matter*, *JHEP* **09** (2020) 030 [2006.14922].

[727] G. Bélanger, K. Kannike, A. Pukhov and M. Raidal, *Minimal semi-annihilating $\mathbb{Z}_N$ scalar dark matter*, *JCAP* **06** (2014) 021 [1403.4960].

[728] X. Qi and H. Sun, *Inflation and dark matter in the Z $_5$ model*, *JCAP* **05** (2023) 051 [2303.15169].

[729] S. Profumo, L. Ubaldi and C. Wainwright, *Singlet Scalar Dark Matter: monochromatic gamma rays and metastable vacua*, *Phys. Rev. D* **82** (2010) 123514 [1009.5377].

[730] A. Djouadi, A. Falkowski, Y. Mambrini and J. Quevillon, *Direct Detection of Higgs-Portal Dark Matter at the LHC*, *Eur. Phys. J. C* **73** (2013) 2455 [1205.3169].

[731] L. Feng, S. Profumo and L. Ubaldi, *Closing in on singlet scalar dark matter: LUX, invisible Higgs decays and gamma-ray lines*, *JHEP* **03** (2015) 045 [1412.1105].

[732] M. Duerr, P. Fileviez Perez and J. Smirnov, *Scalar Singlet Dark Matter and Gamma Lines*, *Phys. Lett. B* **751** (2015) 119 [1508.04418].

[733] H. Han and S. Zheng, *New Constraints on Higgs-portal Scalar Dark Matter*, *JHEP* **12** (2015) 044 [1509.01765].

[734] C. E. Yaguna, *Gamma rays from the annihilation of singlet scalar dark matter*, *JCAP* **03** (2009) 003 [0810.4267].

[735] A. Goudelis, Y. Mambrini and C. Yaguna, *Antimatter signals of singlet scalar dark matter*, *JCAP* **12** (2009) 008 [0909.2799].

[736] M. Gonderinger, Y. Li, H. Patel and M. J. Ramsey-Musolf, *Vacuum Stability, Perturbativity, and Scalar Singlet Dark Matter*, *JHEP* **01** (2010) 053 [0910.3167].

[737] K. Kannike, K. Loos and M. Raidal, *Gravitational wave signals of pseudo-Goldstone dark matter in the $\mathbb{Z}_3$ complex singlet model*, *Phys. Rev. D* **101** (2020) 035001 [1907.13136].

[738] P. Ko and Y. Tang, *Semi-annihilating Z_3 dark matter for XENON1T excess*, *Phys. Lett. B* **815** (2021) 136181 [2006.15822].

[739] A. Liu, Z.-L. Han, Y. Jin and H. Li, *Sterile neutrino portal dark matter with Z3 symmetry*, *Phys. Rev. D* **108** (2023) 075021 [2306.14091].

[740] F. Kahlhoefer, K. Schmidt-Hoberg, T. Schwetz and S. Vogl, *Implications of unitarity and gauge invariance for simplified dark matter models*, *JHEP* **02** (2016) 016 [1510.02110].

[741] K. Kannike, *Vacuum Stability Conditions From Copositivity Criteria*, *Eur. Phys. J. C* **72** (2012) 2093 [1205.3781].

[742] Y. Cai and A. P. Spray, *The galactic center excess from $\mathbb{Z}_3$ scalar semi-annihilations*, *JHEP* **06** (2016) 156 [1511.09247].

[743] Z. Kang, P. Ko and T. Matsui, *Strong first order EWPT & strong gravitational waves in Z_3-symmetric singlet scalar extension*, *JHEP* **02** (2018) 115 [1706.09721].

[744] G. Bélanger, A. Pukhov, C. E. Yaguna and O. Zapata, *The Z_7 model of three-component scalar dark matter*, *JHEP* **03** (2023) 100 [2212.07488].

[745] T. Abe and R. Sato, *Quantum corrections to the spin-independent cross section of the inert doublet dark matter*, *JHEP* **03** (2015) 109 [1501.04161].

[746] S. Bhattacharya, D. Mahanta, N. Mondal and D. Pradhan, *Two-component Dark Matter and low scale Thermal Leptogenesis*, 2412.21202.

[747] D. Croon, H. Davoudiasl and R. Houtz, *Leptogenesis enabled by dark matter*, *Phys. Rev. D* **106** (2022) 035006 [2204.07584].

[748] D. Borah, A. Dasgupta and S. K. Kang, *Two-component dark matter with cogenesis of the baryon asymmetry of the Universe*, *Phys. Rev. D* **100** (2019) 103502 [1903.10516].

[749] M. Le Dall and A. Ritz, *Leptogenesis and the Higgs Portal*, *Phys. Rev. D* **90** (2014) 096002 [1408.2498].

[750] T. Alanne, T. Hugle, M. Platscher and K. Schmitz, *Low-scale leptogenesis assisted by a real scalar singlet*, *JCAP* **03** (2019) 037 [1812.04421].

[751] D. Mahanta and D. Borah, *Fermion dark matter with N_2 leptogenesis in minimal scotogenic model*, *JCAP* **11** (2019) 021 [1906.03577].

[752] Y. Abe, T. Ito and K. Yoshioka, *Leptonic CP asymmetry and Light flavored scalar*, *JHEP* **01** (2023) 019 [2110.11096].

[753] D. K. Ghosh, P. Ghosh, K. Mukherjee and N. Narendra, *A singlet scalar assisted N_2 Leptogenesis and Pseudo-Scalar Dark Matter*, 2409.17067.

[754] S. Bhattacharya, N. Mondal, R. Roshan and D. Vatsyayan, *Leptogenesis, dark matter and gravitational waves from discrete symmetry breaking*, *JCAP* **06** (2024) 029 [2312.15053].

[755] S. Davidson and A. Ibarra, *A Lower bound on the right-handed neutrino mass from leptogenesis*, *Phys. Lett. B* **535** (2002) 25 [hep-ph/0202239].

[756] L3 collaboration, *Results from the L3 experiment at LEP*, *Phys. Rept.* **236** (1993) 1.

[757] Particle Data Group collaboration, *Review of Particle Physics*, *PTEP* **2022** (2022) 083C01.

[758] E. Lundstrom, M. Gustafsson and J. Edsjo, *The Inert Doublet Model and LEP II Limits*, *Phys. Rev. D* **79** (2009) 035013 [0810.3924].

[759] A. Pierce and J. Thaler, *Natural Dark Matter from an Unnatural Higgs Boson and New Colored Particles at the TeV Scale*, *JHEP* **08** (2007) 026 [hep-ph/0703056].

[760] M. Hashemi, M. Krawczyk, S. Najjari and A. F. Żarnecki, *Production of Inert Scalars at the high energy e^+e^- colliders*, *JHEP* **02** (2016) 187 [1512.01175].

[761] J. Kalinowski, W. Kotlarski, T. Robens, D. Sokolowska and A. F. Zarnecki, *Benchmarking the Inert Doublet Model for e^+e^- colliders*, *JHEP* **12** (2018) 081 [1809.07712].

[762] MEG collaboration, *Search for the lepton flavour violating decay $\mu^+ \to e^+\gamma$ with the full dataset of the MEG experiment*, *Eur. Phys. J. C* **76** (2016) 434 [1605.05081].

[763] T. Toma and A. Vicente, *Lepton Flavor Violation in the Scotogenic Model*, *JHEP* **01** (2014) 160 [1312.2840].

[764] A. Vicente and C. E. Yaguna, *Probing the scotogenic model with lepton flavor violating processes*, *JHEP* **02** (2015) 144 [1412.2545].

[765] P. E. Valiente, *Neutrino Masses and Lepton Flavor Physics Beyond the Standard Model*, Ph.D. thesis, U. Valencia (main), 2023.

[766] R. S. Hundi, *Lepton flavor violating Z and Higgs decays in the scotogenic model*, *Eur. Phys. J. C* **82** (2022) 505 [2201.03779].

[767] J. A. Casas and A. Ibarra, *Oscillating neutrinos and $\mu \to e, \gamma$*, *Nucl. Phys. B* **618** (2001) 171 [hep-ph/0103065].

[768] W. M. Alberico and S. M. Bilenky, *Neutrino oscillations, masses and mixing*, *Phys. Part. Nucl.* **35** (2004) 297 [hep-ph/0306239].

[769] K. Griest and D. Seckel, *Three exceptions in the calculation of relic abundances*, *Phys. Rev. D* **43** (1991) 3191.

[770] J. Tang and B.-L. Zhang, *Asymptotic analysis of binned likelihoods and the neutrino floor*, *Phys. Rev. D* **108** (2023) 062004 [2304.13665].

[771] L. Lopez Honorez, E. Nezri, J. F. Oliver and M. H. G. Tytgat, *The Inert Doublet Model: An Archetype for Dark Matter*, *JCAP* **02** (2007) 028 [hep-ph/0612275].

[772] R. Barbieri, L. J. Hall and V. S. Rychkov, *Improved naturalness with a heavy Higgs: An Alternative road to LHC physics*, *Phys. Rev. D* **74** (2006) 015007 [hep-ph/0603188].

[773] L. Lopez Honorez and C. E. Yaguna, *The inert doublet model of dark matter revisited*, *JHEP* **09** (2010) 046 [1003.3125].

[774] P. Gondolo and J. Edsjo, *Neutralino relic density including coannihilations*, *Phys. Atom. Nucl.* **61** (1998) 1081.

[775] M. Hoferichter, P. Klos, J. Menéndez and A. Schwenk, *Improved limits for Higgs-portal dark matter from LHC searches*, *Phys. Rev. Lett.* **119** (2017) 181803 [1708.02245].

[776] V. Shtabovenko, R. Mertig and F. Orellana, *FeynCalc 10: Do multiloop integrals dream of computer codes?*, *Comput. Phys. Commun.* **306** (2025) 109357 [2312.14089].

[777] A. Belyaev, N. D. Christensen and A. Pukhov, *CalcHEP 3.4 for collider physics within and beyond the Standard Model*, *Comput. Phys. Commun.* **184** (2013) 1729 [1207.6082].

[778] H. H. Patel, *Package-X 2.0: A Mathematica package for the analytic calculation of one-loop integrals*, *Comput. Phys. Commun.* **218** (2017) 66 [1612.00009].

[779] V. Shtabovenko, R. Mertig and F. Orellana, *FeynCalc 9.3: New features and improvements*, *Comput. Phys. Commun.* **256** (2020) 107478 [2001.04407].

[780] J. Ellis, N. Nagata and K. A. Olive, *Uncertainties in WIMP Dark Matter Scattering Revisited*, *Eur. Phys. J. C* **78** (2018) 569 [1805.09795].

[781] P. Agrawal, Z. Chacko, C. Kilic and R. K. Mishra, *A Classification of Dark Matter Candidates with Primarily Spin-Dependent Interactions with Matter*, 1003.1912.

[782] T. Lin, *Dark matter models and direct detection*, *PoS* **333** (2019) 009 [1904.07915].

[783] J. Hisano, R. Nagai and N. Nagata, *Effective Theories for Dark Matter Nucleon Scattering*, *JHEP* **05** (2015) 037 [1502.02244].

[784] V. Ilisie, *Concepts in Quantum Field Theory*, UNITEXT for Physics. Springer, 2016, 10.1007/978-3-319-22966-9.

[785] T. Han, *Collider phenomenology: Basic knowledge and techniques*, in *Theoretical Advanced Study Institute in Elementary Particle Physics: Physics in D ≧ 4*, pp. 407–454, 8, 2005, DOI [hep-ph/0508097].

[786] G. F. Giudice, A. Notari, M. Raidal, A. Riotto and A. Strumia, *Towards a complete theory of thermal leptogenesis in the SM and MSSM*, *Nucl. Phys. B* **685** (2004) 89 [hep-ph/0310123].

[787] S. Antusch, P. Di Bari, D. A. Jones and S. F. King, *Leptogenesis in the Two Right-Handed Neutrino Model Revisited*, *Phys. Rev. D* **86** (2012) 023516 [1107.6002].

[788] I. Esteban, M. C. Gonzalez-Garcia, A. Hernandez-Cabezudo, M. Maltoni and T. Schwetz, *Global analysis of three-flavour neutrino oscillations: synergies and tensions in the determination of θ_{23}, δ_{CP}, and the mass ordering*, *JHEP* **01** (2019) 106 [1811.05487].

[789] I. Esteban, M. C. Gonzalez-Garcia, M. Maltoni, T. Schwetz and A. Zhou, *The fate of hints: updated global analysis of three-flavor neutrino oscillations*, *JHEP* **09** (2020) 178 [2007.14792].